

## Abram Isaakovich Alikhanov—Scientist, Director, Personality

Yu. G. Abov

*Institute of Theoretical and Experimental Physics,  
Bol'shaya Cheremushkinskaya ul. 25, Moscow, 117259 Russia*

Received April 14, 2003; in final form, September 8, 2003

Abram Isaakovich Alikhanov was born on March 4, 1904, in the town of Elizavetpol' in the Tiflis province [later on, the town of Kirovabad (presently, Ganja), Azerbaijan].

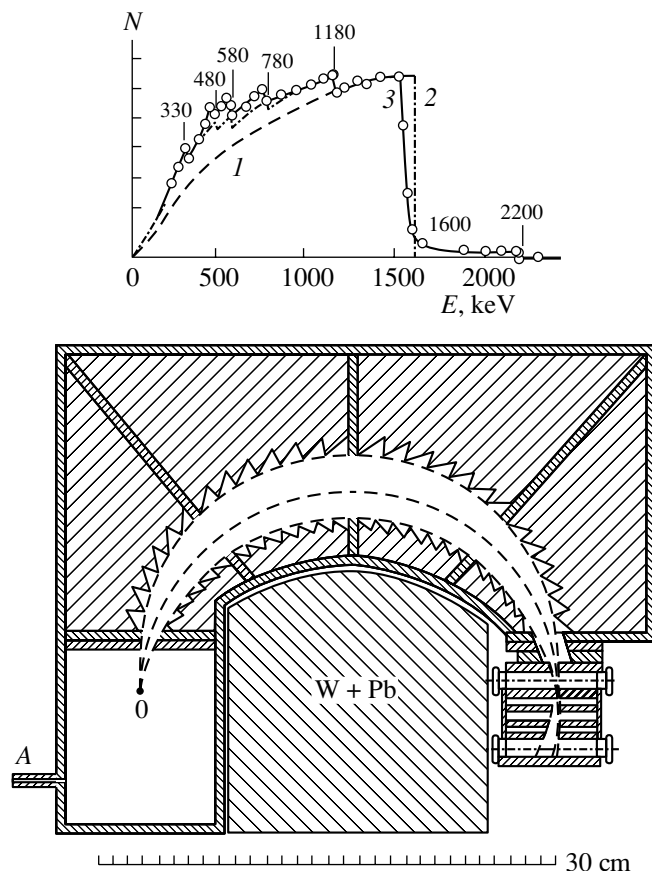
Abram Alikhanov attended a secondary school in Tiflis and, upon graduating from it in 1921, joined the Tiflis Polytechnic Institute, but, for want of means of subsistence, Alikhanov had to interrupt his studies. In 1923, Abram Isaakovich became a first-year student of the Second Petersburg Polytechnic Institute. (The First and the Second Petersburg Polytechnic Institute merged in 1924.) In 1927, when he was still a student, Abram Isaakovich was invited to work at the Leningrad Institute for Physics and Technology, where he immediately began his investigations into solid-state physics, the main subject of research there. His first studies were devoted to exploring the propagation of x rays in metals and alloys in connection with the problem of age hardening of metals. Before long, however, he proceeded to study the properties of x rays themselves. Together with L.A. Artsimovich, Alikhanov performed a series of studies in x ray optics. Among these, the investigation of the total internal reflection of x rays from thin layers of transparent and nontransparent (absorbing) substances is worthy of special note. This involved measuring the radiation-penetration depth in the course of total reflection. Very complicated and subtle measurements were performed, and the results of those measurements were in agreement with the results of the calculations performed by these two authors themselves. It was shown that the processes of refraction and total absorption of hard x rays are in accord with laws of classical optics (Maxwell, Fresnel) [1–3]. The results of his studies, Alikhanov summarized in the monograph *X-Ray Optics* [2].

In 1933, the subject of Alikhanov's studies changed again, this time drastically. He and his disciples and colleagues addressed nuclear-physics problems. It was to his great credit that Academician A.F. Ioffe, director of the Leningrad Institute for Physics and Technology, perceived the need for rapidly deploying investigations in these realms. For this, the Nuclear

Physics Department, headed by I.V. Kurchatov, was organized in that institution. In his department (Department of Solid-State Physics), Ioffe created the Positron Laboratory (1934), headed by Alikhanov. Thus, there appeared, at the Leningrad Institute for Physics and Technology, the first nuclear-physics school in the Soviet Union, which, later on, played a key role in developing and creating nuclear weapons in the country. Switching to nuclear-physics realms was not accidental in those years. At the end of 1932 (December), C. Anderson reported on the discovery of positive electrons (that is, positrons) in cosmic rays. The discovery was made with the aid of a Wilson chamber placed in a magnetic field. This was a rather bold claim. In fact, other researchers had also seen tracks of “incorrect” (inverse) curvature. D.V. Skobeltsyn found such tracks in 1931, but he did not interpret them as positron traces, assuming that these were electrons going in the opposite direction. Even when, in Wilson chambers, researchers saw vees—that is, an electron and a positron track originating from one point (Skobeltsyn, I. Curie and F. Joliot)—they did not find sufficient grounds to reject the possibility that these vees resulted from a random superposition of tracks due to two electrons traveling in opposite directions. Nevertheless, the discovery of Anderson was confirmed by other experimentalists very soon after the publication of his results. Any doubt was dispelled, and Anderson was awarded a Nobel prize in 1936.

Immediately after the discovery of positrons in cosmic rays, attempts were made to reveal “terrestrial” sources of positrons. In the course of such investigations, I. Curie and Joliot showed that positron radiation emerges upon the irradiation of some nuclei with alpha rays. Specifically, they were dealing with  $(\alpha, n)$  and  $(\alpha, p)$  nuclear reactions that led to the formation of radioactive products. In this way, induced radioactivity was discovered in January 1934, and I. Curie and Joliot were awarded a Nobel prize for this [4].

In dealing with a Wilson chamber, the curvature of a track must be measured in order to determine the



Spectrum of RaC positrons (top). Numbers stand for gamma-line energies. The notation for the curves is given in the main body of the text. Layout of the spectrometer (bottom). A uniform magnetic field is orthogonal to the figure plane.

momentum of an electron or a positron (method of a trochoid). Since intense radiation sources cannot be used in doing this, it is rather difficult to measure the energy spectrum of electrons (positrons). Nonetheless, all research groups employed Wilson chambers in this region at that time.

Alikhanov decided to apply a magnetic spectrometer of the Danysz type to this problem. The spectrometer was upgraded both in order to improve its resolution and in order to reduce the background of scattered photons and electrons, the latter being necessary for rendering the use of intense radiation sources possible. A telescope consisting of two Geiger–Müller counters operating in the coincidence mode was employed to record particles. For the first time, the Rossi coincidence scheme was implemented in nuclear physics with electronic lamps of high amplification. This marked the beginning of nuclear electronics in the Soviet Union [5]. It was M.S. Kozodaev who was in charge of electronics in Alikhanov's group. This instrument was used to perform systematic investigations of the energy spectra of electrons and positrons emitted by natural and man-made sources. The latter were obtained in  $(\alpha, n)$  and

$(\alpha, p)$  nuclear reactions (at that time, it was already clear that alpha-ray-induced nuclear transformations occur there). Man-made radioactive nuclides were obtained independently of the studies performed by I. Curie and Joliot, but the publications that reported on obtaining such sources appeared in the literature a few months later [6].<sup>1)</sup> The most important articles that were written by Alikhanov and his colleagues within that period were collected in [3].

At the end of 1933 to the beginning of 1934, the phenomenon of external pair conversion of gamma rays had already been firmly established in experiments and considered theoretically. However, Alikhanov and his colleagues were the first to study in detail the spectrum of positrons from external pair conversion over the entire energy range. Among other things, they showed that, in accord with relevant theoretical results, the maximum of the spectrum occurs in the vicinity of the positron energy equal to half the endpoint energy.

<sup>1)</sup>It should be noted that, in those years, induced radioactivity, immediately after its discovery, was referred to as a new form of radioactivity.

As to the process of internal pair conversion, this phenomenon had not been reliably discovered in experiments and had not been described theoretically at the time when the studies of Alikhanov's group began. It should be recalled that the phenomenon of external pair conversion consists in that hard gamma rays incident on a target that contains heavy nuclei produce electron–positron pairs in the Coulomb field of these nuclei. Usually, lead foils are taken for a target—that is, for a converter of gamma rays. As to the phenomenon of internal pair conversion, it consists in that the excitation energy of a nucleus is removed via the emission of a virtual photon that converts into an electron–positron pair escaping from the nucleus rather than via the emission of a real photon. Alikhanov observed, in his spectrometer, the production of such pairs without converters. The shape of the energy spectrum of positrons from internal pair conversion differs from the shape of the spectra of positrons from external pair conversion. The endpoint energy of internal-conversion positrons is obviously equal to  $E_{\max} = E - 1.02 \text{ MeV}$ . At the end of the spectrum, there arises a sharp downfall, which differs from the gamma-line energy  $E$  by 1.02 MeV. An example of the spectrum of internal-pair-conversion positrons that was obtained by Alikhanov and Kozodaev is displayed in the figure.

In the figure, curve 1 was calculated with allowance for only one previously known gamma line of energy about 1600 keV. Curve 2 was calculated with allowance for all discovered gamma lines, while curve 3 represents experimental data. It can be seen that curves 2 and 3 are nearly coincident. It should be noted that (see [3]) the authors did not immediately understand that they had obtained a new powerful tool for nuclear spectroscopy at their disposal. Only upon improving the resolution of the spectrometer were they able to discover that the excess of positrons was due to the presence of previously unknown gamma transitions.

Thus, those investigations made it possible to reveal gamma lines that had previously been unknown, whereby it was possible to reconstruct the diagrams of decays of excited nuclei. This initiated the development of modern nuclear spectroscopy, a science to which B.S. Dzheleпов, one of Alikhanov's disciples, who later became a corresponding member of the Russian Academy of Sciences, devoted all his activities to the end of his life and in which he was a commonly recognized leader.

In the course of studying internal pair conversion, Alikhanov and his colleagues measured for the first time ever the internal-conversion coefficient  $\alpha_{\text{pair}} = N_{\text{pair}}/N_{\gamma}$ , which is the ratio of the number of electron–positron pairs to the number of photons in a given transition. Since  $\alpha_{\text{pair}} \sim 10^{-4}$  and since

it is necessary to isolate a given transition against the background of all other transitions, one can easily perceive the complexity of such measurements. The results proved to be in agreement with the theory. In the period between the years 1934 and 1940, the group headed by Alikhanov became a leader in these realms worldwide. In addition to the aforesaid, it should be mentioned that Alikhanov and his colleagues also investigated the distribution of the angles of divergence of electrons and positrons. In a dedicated experiment, they measured thoroughly the angular distribution of photons from the annihilation of an electron–positron pair and, for soft positrons, showed that two photons fly apart at an angle of  $180^\circ$ . This proved that the law of energy–momentum conservation holds in the microcosm as well and put an end to long-term discussions on the subject that were initiated long ago by N. Bohr. Alikhanov and his colleagues were the first to discover and investigate the effect of the Coulomb field of a nucleus on the shape of the beta spectrum (both of positrons and of electrons) in its soft part; moreover, they made an attempt at studying the beta spectrum in the vicinity of its endpoint, where the intensity of the spectrum is close to zero. Those investigations were aimed at measuring the neutrino mass, but, at that time (in the 1930s), such attempts were premature; moreover, the choice of object of the investigation, RaE, was extremely unfavorable, since this substance is characterized by an anomalous shape of the spectrum (see below). However, honors should be given to the bravest!

Completing this brief description of Alikhanov's studies at the Leningrad Institute for Physics and Technology, I would also like to mention his investigations of the propagation and scattering of relativistic electrons, since those investigations proved the validity of the predictions of relativistic quantum mechanics. From the aforesaid, it is clearly seen that Alikhanov's studies within the period between the years 1933 and 1940 were at the highest scientific level worthy of a Nobel prize. No wonder that, in 1935, Alikhanov was immediately awarded a PhD degree in physics and mathematics and that he was elected to corresponding membership in USSR Academy of Sciences in 1939 and to full membership in 1943. More details on Alikhanov's scientific activities within that period can be found in the article of Gasparyan *et al.* [7].

In 1942 and 1943, Alikhanov became interested in cosmic-ray physics. Having analyzed data available worldwide on the composition of cosmic rays, he arrived at the conclusion that, in addition to two known components, a soft (electrons and photons) and a hard (muons—“mesons” at that time) one, cosmic rays feature a third component, a proton one.

This prediction was confirmed by two independent research groups that worked in the Pamir mountains (a group from the Institute of Physics, Moscow) and in the mountains of Armenia (Alikhanov and Alikhanyan) [3]. Alikhanov did not terminate investigations in these realms despite the hard times of World War II and despite the fact that he took on new responsibilities (see below). Here, one comment of paramount importance is in order. A scientist should have the right of committing an error; otherwise, he is deprived of freedom, in which case no creative activity is possible. It would suffice to recall that Einstein made errors, but he remained Einstein; Reines was awarded a Nobel prize in 1995 despite the fact that, in 1980, he made a grave error, stating that he had discovered neutrino oscillations. Errors must not outweigh obvious achievements. However, the methodological error that Alikhanov and Alikhanyan made in “discovering” so-called varitrons has not been forgiven thus far.

In 1943, work on creating nuclear weapons was deployed in the Soviet Union. Alikhanov was involved in this project from the very beginning. The project was headed by Academician Kurchatov, a friend of Alikhanov. Kurchatov organized a research center called Laboratory no. 2 (USSR Academy of Sciences) at that time (presently, Russian Research Centre Kurchatov Institute). The main effort there was aimed at creating nuclear reactors where graphite was used for a moderator of neutrons. Alikhanov organized a research center that was then called Laboratory no. 3 (USSR Academy of Sciences) and which is presently known as the Institute of Theoretical and Experimental Physics (ITEP, Moscow). There, attention was given predominantly to heavy-water reactors. To the end of his days, Alikhanov remained a renowned head and a strong advocate of this line in reactor engineering. However, preference was given to graphite reactors, which are cheaper.

Naturally, there arises the question of whether the disaster at Chernobyl could have been avoided if the choice had been in favor of heavy-water reactors. It should be emphasized from the outset that a violation of the conditions of proper operation can provoke an accident at any reactor. Heavy-water reactors possess a number of advantages, which will not be described here. It should only be noted that they can operate with natural uranium; that is, heavy-water reactors do not require enriching a fuel. But at the present time, a different feature of such reactors is of greater value: heavy-water reactors have a high negative temperature coefficient of power; therefore, an uncontrolled reactor runaway that ends up in an explosion is hardly possible. In a report that

Alikhanov and his colleagues presented at the International Conference on Peaceful Uses of Atomic Energy in 1955 (see [8]), it is emphasized that the following conclusions can be drawn from the experience of running the ITEP heavy-water reactor: A significant negative temperature coefficient renders the control of the reactor quite stable. After heating and equilibration of the concentration of poisoning xenon-135, the reactor can operate in a steady-state mode for an indefinitely long time with regulators switched off or completely removed from the apparatus. The self-control of power owing to a negative temperature coefficient rules out the possibility of accidents in case of regulator damage. If all of the regulators are removed from the shutdown apparatus, the power increases fast . . . , whereupon it decreases and gradually approaches a fixed value that is determined by heat removal [8]. This property was obviously missing in the Chernobyl apparatus! Of course, one can imagine a situation where a heavy-water reactor also acquires a positive temperature coefficient. This danger arises if the water system for cooling the fuel is out of order. Under such conditions, the heating of the fuel (so-called void effect) can lead to a positive temperature coefficient; in the case of the failure of the control system and emergency protection, an increase in the power will then be indefinite.

At ITEP, a method was proposed and implemented that removes this void effect almost completely. A heavy-water reactor was created where gas cooling was used for heat-releasing elements [8]. Since a gas (for example, CO<sub>2</sub>) does not absorb neutrons, the interruption of the gas supply to the reactor core has virtually no effect on the reactor reactivity. Of course, heavy-water reactors are expensive since the production of heavy water requires great expenditures. Moreover, beta-active tritium is accumulated in the reactor core; therefore, it is desirable to purify water from tritium sometimes, this entailing additional expenses. However, it has long since been known that the cheapest solutions are not always the best ones.

In accordance with the decree of the Council of Ministers, Laboratory no. 3 was organized on December 25, 1945. At the Institute of Theoretical and Experimental Physics, this day is presently commemorated as ITEP day. The staff of Laboratory no. 3 was rather small, but Alikhanov was able to gather a group of highly talented physicists around him. As a result, the design of the reactor was ready in 1947; the reactor was built in 1948 and was put into operation in April 1949. It should be emphasized that no information came from abroad at that time. Alikhanov and his colleagues made everything themselves: they developed the theory of reactors and conducted the necessary experiments. The first start-up of the reactor (critical zero-power experiment) was

performed secretly at night, in the absence of officials. When top-ranking officials of the respective ministry came to the laboratory in the morning, they were told that the start-up had already been accomplished. Although victors are rarely condemned, the officials were dissatisfied.

The fate of Alikhanov was such that he stirred up an ever growing discontent. A non-Party director was especially odious to functionaries in the Defense Department of the Central Committee of the Soviet Communist Party. The main reason for this was that Alikhanov could not conceal his attitude to people. He hated functionaries who wanted to exercise control over things with which they were not conversant. This did not concern officials of the ministry exclusively. By way of example, I would like to recall the following funny incident. The chief of the fire brigade of the laboratory entered Alikhanov's study and, pointing to the parquet floor, said that it should be replaced with a fireproof one. The response of the director was curt, "It is easier for me to replace you," and this was indeed done.

In the Ministry for Medium Machine Building (the Ministry for Atomic Industry at the present time), Alikhanov was on very good terms with Minister E.P. Slavsky and Deputy Minister V.S. Emel'yanov. He addressed the minister directly, avoiding any contact with the head of the respective department. Naturally, this irritated the functionaries.

Upon the start-up of a heavy-water reactor, a series of experiments were performed on it under the supervision of Alikhanov with the aim of measuring parameters that are necessary for a precise calculation of a commercial apparatus. In particular, various configurations ("lattice") of the reactor core were tested and contrasted against the results of relevant calculations, the reactor reactivity under various conditions was explored with the aid of a "boiler oscillator," and the cross sections for the production of various fissile nuclides were measured. A commercial version of a heavy-water reactor was implemented before long (see [9]). After that, research reactors were constructed in China and Yugoslavia. Also, a power nuclear reactor employing a gas heat carrier was created under the supervision of Alikhanov.

The commissioning of a commercial heavy-water reactor completed fulfillment of the government task. In 1954, Alikhanov became a recipient of the title of a Hero of Socialist Labour. Since heavy-water reactors were not to become pivotal in nuclear power engineering in the Soviet Union, the focus of investigations at ITEP switched to the realms of nuclear physics. It should be noted that, soon after the commissioning of the reactor, a cyclotron was put into operation at ITEP and was used to measure, by the time-of-flight technique, effective neutron cross

sections not only for fissile but also for some other elements, the precision of those measurements being high for that time. As far back as the early 1950s, Alikhanov and Deputy Director V.V. Vladimirovsky planned the construction of a hard-focusing proton accelerator, which was to become the first one in the Soviet Union. A hard-focusing proton accelerator rated to a proton energy of 7 GeV began operating at ITEP in 1961. It was an operating model of the 70-GeV proton accelerator that was simultaneously under construction in the neighborhood of Serpukhov (Protvino) and which was then the largest proton accelerator in the world.

Let us, however, return somewhat to the past, to the times when investigations at the ITEP proton accelerator were launched. In the period between 1957 and 1960, Alikhanov headed a number of studies devoted to parity violation in beta decay. Those studies were initiated by the experiment of Wu and her colleagues [10], who, in 1957, discovered parity violation in beta decay, an effect that was predicted theoretically by Lee and Yang in 1956. The investigations at ITEP were aimed not only at confirming the very phenomenon in other experiments but also, which was the most important, at exploring the structure of weak interaction—that is, at revealing the type of interactions involved in beta decay.

The entire history of this discovery and the work performed at ITEP in this connection are described in detail by Alikhanov in his monograph [11]. Alikhanov himself participated in a series of measurements of the longitudinal polarization of beta-decay electrons. Those investigations revealed that, both for allowed and for forbidden unique and Coulomb transitions, the longitudinal polarization of electrons is equal, in accord with theoretical predictions, to  $v/c$  (that is, to the ratio of the speed of the electrons to the speed of light—see [12–16]), irrespective of the transition energy. It was known that the energy spectrum of the  $1^+ \rightarrow 0^-$  Coulomb beta transition in RaE has an anomalous shape. It was mentioned above that, in the early 1930s, Alikhanov explored the energy spectrum of electrons originating from this transition. The anomalous character of the shape of this spectrum attracted the attention of researchers long before the discovery of parity violation in beta decay. The shape of the spectrum of electrons from RaE could be understood under the assumption that leading contributions are canceled in the probability of RaE beta decay. In fact, these energy-independent terms are compensated to 1% of their magnitude. In view of this, the shape of the spectrum is sizably affected by other terms, which are usually suppressed. They depend on the energy of the electrons and distort the "standard" shape of the beta spectrum. A fit to respective experimental data was constructed by

introducing a correction factor that depends on the ratio of matrix elements. Alikhanov assumed that the longitudinal polarization of electrons originating from the beta decay of RaE differs from  $v/c$ . An experiment confirmed this assumption [12]. In the case of time-inversion-invariance violation, the weak-interaction coupling constants become complex-valued, with the result that the compensating factor changes. Moreover, it was shown theoretically at ITEP [17] that, in the case of time-inversion-invariance violation, the longitudinal polarization of electrons from the beta decay of RaE must appear to be energy-dependent. For the VA and ST versions of weak-interaction theory, the longitudinal polarization of the electrons was calculated and was predicted to be energy-dependent. The results of the measurements were in agreement with the (V - A) version of weak-interaction theory, and no energy dependence of the polarization was observed. The degree of polarization proved to be  $-(0.73 \pm 0.04)v/c$  [15], where the coefficient 0.73 is independent of energy. It was shown that the phase shift of the matrix elements of V and A interactions can differ from  $180^\circ$  by no more than  $\Delta\theta \sim 4^\circ$  [that is, this is indeed the (V - A) version!].

A higher accuracy was achieved only many years later in experiments devoted to measuring a triple correlation in free-neutron decay:  $\sigma_n \cdot [\mathbf{p}_e \times \mathbf{p}_\gamma]$ , where  $\sigma_n$  is the neutron spin and  $[\mathbf{p}_e \times \mathbf{p}_\gamma]$  is the vector product of the electron and neutrino momenta. Thus, Alikhanov's group was able to demonstrate, to a high degree of precision, that invariance under time inversion holds in weak interaction.

Since 1961—that is, after the commissioning of the proton synchrotron—elementary-particle physics has been the main subject of investigations at ITEP. The program of investigations at the accelerator was composed under the supervision of Alikhanov. He took part himself in a number of studies there [18]. However, destiny was extremely malevolent to him. He had to suffer a number of heavy blows. In 1956, after the XX Congress of the Soviet Communist Party, young communists ventured remarks at a party meeting of the institute that were rather audacious at that time. The essence of those speeches amounted to the question of whether there are guarantees that such violations will not be repeated. Obviously, similar speeches were delivered at other institutions. The Communist leaders of the Soviet Union decided to restore order and chose to make ITEP a scapegoat. The Communist organization of the institute was disbanded. There appeared rumors of forthcoming persecutions. Under these circumstances, the non-Party director had to take extraordinary measures, since the whole institute was in a precarious situation. A difficult conversation between Alikhanov and Khrushchev took place. As a matter of fact, this

conversation saved the institute. It was necessary to dismiss four members of the staff; they were expelled from the Communist Party and deprived of access to secret materials (at that time, one was not allowed to work at ITEP without this access). Among the dismissed persons, special mention should be made of Yu.F. Orlov, who became very famous later on and who was immediately invited to work at the Yerevan Physics Institute, headed, at that time, by A.I. Alikhanian, Alikhanov's brother. A few more researchers were expelled from the Communist Party, but they remained at ITEP, successfully continued their studies, and received doctorate degrees. Somewhat earlier, when there arose the so-called case of the physicians in the early 1950s, Alikhanov also had to defend his colleagues. Of course, there were victims, but he was able to minimize them. The decision of the ministry to take the unfinished Serpukhov accelerator away from ITEP was the next irreparable blow for Alikhanov. Since elementary-particle physics became the main subject of studies at ITEP, this decision deprived the institute of any prospects for further development. Abram Isaakovich could not withstand this blow—he suffered a severe stroke. It is not true that this decision was a consequence of the fact that the construction of the accelerator was not as fast as was desired. This could be used as a pretext. In fact, the decision in question was taken at the very beginning of the work on constructing the accelerator, as the present author knew at the Defense Department in the Central Committee of the Soviet Communist Party.

The rebellion of A.S. Kronrod, head of the Mathematical Laboratory at ITEP, was a next heavy blow for Alikhanov. Kronrod declared that he wanted to put his laboratory on a self-supporting basis; as a matter of fact, this meant the separation of the Mathematical Laboratory from ITEP. There had long since been a conflict between the ITEP physicists and mathematicians—the mathematicians refused to participate in data processing, while the physicists were unable at that time to write computer programs. The director was seriously ill and could not “strike his fist on the table,” as he sometimes used to do in the past. The fact that the ITEP mathematicians signed a letter in defense of the dissenter A. Esenin-Vol'pin was a coup de grace for Abram Isaakovich. The ministry lost all patience and insisted on the dismissal of Kronrod. However, almost all of the mathematicians left ITEP in his wake in protest against this.

Alikhanov resigned from the post of director. Two years later, in December 1970, Abram Isaakovich passed away.

Not only was Alikhanov an outstanding physicist endowed with excellent organizing abilities, but he

was also a strong personality of rigorous moral principles. Life is difficult for such people, but the memory of them is cherished forever by all of those who had a privilege to know them. Not one monument was erected for Alikhanov, but he created his monument himself—it is the Institute of Theoretical and Experimental Physics, which was organized owing to his efforts and which was recently named after him.

The ITEP organizing committee of the Conference of the Department of Physical Sciences (Russian Academy of Science) on Fundamental Problems in Elementary Particle Physics decided to dedicate to the memory of Alikhanov the proceedings of this conference, which are published in the present issue of the journal *Physics of Atomic Nuclei*.

#### REFERENCES

1. A. I. Alichanov and L. A. Artsimovich, *Z. Phys.* **69**, 853 (1931); **82**, 489 (1933); *Zh. Éksp. Teor. Fiz.* **3**, 115 (1933).
2. A. I. Alikhanov, *X-ray Optics* (Gostekhizdat, Leningrad; Moscow, 1933) [in Russian].
3. A. I. Alikhanov, *Selected Papers* (Nauka, Moscow, 1975) [in Russian].
4. I. Curie and F. Joliot, *J. Phys.* **198**, 502 (1934).
5. A. I. Alichanov and M. S. Kozodaev, *Zh. Éksp. Teor. Fiz.* **4**, 531 (1934); A. I. Alikhanov, *Selected Papers* (Nauka, Moscow, 1975) [in Russian], p. 39.
6. A. I. Alichanov, A. I. Alichanian, and B. S. Dzelepov, *Nature* **133**, 871 (1934); A. I. Alikhanov, *Selected Papers* (Nauka, Moscow, 1975) [in Russian], p. 120.
7. B. G. Gasparyan, A. P. Grindberg, and V. Ya. Frenkel', in *A. I. Alikhanov. Memorials, Letters, Documents* (Nauka, Leningrad; Moscow, 1989) [in Russian], p. 5.
8. A. I. Alikhanov, *Selected Papers* (Nauka, Moscow, 1975) [in Russian], p. 269.
9. N. N. Nikolaev, in *A. I. Alikhanov. Memorials, Letters, Documents* (Nauka, Leningrad; Moscow, 1989) [in Russian], p. 98.
10. C. S. Wu *et al.*, *Phys. Rev.* **105**, 1413 (1957).
11. A. I. Alikhanov, *Weak Interactions: Up-to-Date Researches in  $\beta$ -Decay* (Fizmatgiz, Moscow, 1960) [in Russian].
12. A. I. Alikhanov, G. P. Eliseev, V. A. Lyubimov, and B. V. Érshler, *Zh. Éksp. Teor. Fiz.* **32**, 1344 (1957) [*Sov. Phys. JETP* **5**, 1097 (1957)]; *Selected Papers* (Nauka, Moscow, 1975) [in Russian], p. 165.
13. A. I. Alikhanov, G. P. Eliseev, V. A. Lyubimov, and B. V. Éshler, *Zh. Éksp. Teor. Fiz.* **39**, 785 (1960); *Selected Papers* (Nauka, Moscow, 1975) [in Russian], p. 171.
14. A. I. Alikhanov, G. P. Eliseev, and V. A. Lyubimov, *Zh. Éksp. Teor. Fiz.* **39**, 1046 (1960) [*Sov. Phys. JETP* **12**, 728 (1960)]; *Selected Papers* (Nauka, Moscow, 1975) [in Russian], p. 186.
15. A. I. Alikhanov, G. P. Eliseev, and V. A. Lyubimov, *Zh. Éksp. Teor. Fiz.* **35**, 1061 (1959) [*Sov. Phys. JETP* **8**, 740 (1959)]; A. I. Alichanov *et al.*, *Nucl. Phys.* **13**, 541 (1959); *Selected Papers* (Nauka, Moscow, 1975) [in Russian], p. 203.
16. A. I. Alikhanov, G. P. Eliseev, and V. A. Lyubimov, *Zh. Éksp. Teor. Fiz.* **39**, 587 (1960) [*Sov. Phys. JETP* **12**, 414 (1960)]; *Selected Papers* (Nauka, Moscow, 1975) [in Russian], p. 212.
17. V. V. Geshkenbeĭn, S. A. Nemirovskaya, and A. P. Rudik, *Zh. Éksp. Teor. Fiz.* **36**, 526 (1959) [*Sov. Phys. JETP* **39**, 366 (1959)].
18. A. I. Alikhanov, *Selected Papers* (Nauka, Moscow, 1975) [in Russian], p. 269.

*Translated by A. Isaakyan*

---

---

NUCLEI  
Experiment

---

---

## Double-Beta-Decay Experiments: Present Status and Prospects for the Future

A. S. Barabash

*Institute of Theoretical and Experimental Physics,  
Bol'shaya Cheremushkinskaya ul. 25, Moscow, 117259 Russia*

Received March 31, 2003

**Abstract**—The present status of experiments seeking double-beta decay is surveyed. The results of the most sensitive experiments are discussed. Particular attention is given to describing the NEMO-3 detector, which is intended for seeking the neutrinoless double-beta decay of various isotopes ( $^{100}\text{Mo}$ ,  $^{82}\text{Se}$ , etc.) with a sensitivity as high as  $T_{1/2} \sim 10^{25}$  yr, which corresponds to a sensitivity to the Majorana neutrino mass at a level of 0.1 to 0.3 eV. The first results obtained with the NEMO-3 detector are presented. A review of the existing projects of double-beta-decay experiments where it is planned to reach a sensitivity to the Majorana neutrino mass at a level of 0.01 to 0.1 eV is given. © 2004 MAIK “Nauka/Interperiodica”.

### 1. INTRODUCTION

The main reason behind current interest in neutrinoless double-beta [ $2\beta(0\nu)$ ] decay is that the very fact of the existence of this process is closely related to the following fundamental aspects of elementary-particle physics [1–3]: (i) lepton-number nonconservation, (ii) the presence of a neutrino mass and its origin, (iii) the existence of right-handed currents in electroweak interaction, (iv) the existence of the Majoron, (v) the structure of the Higgs sector, (vi) supersymmetry, (vii) the existence of leptoquarks, (viii) the existence of a heavy sterile neutrino, and (ix) the existence of a composite neutrino.

All of these issues are beyond the standard model of electroweak interaction; therefore, the detection of  $2\beta(0\nu)$  decay would imply the discovery of new physics. Of course, interest in this process is caused primarily by the problem of a neutrino mass: if  $2\beta(0\nu)$  decay is discovered, then, according to currently prevalent concepts, this will automatically mean that the rest mass of at least one neutrino flavor is nonzero and is of Majorana origin.

Interest in  $2\beta(0\nu)$  decay has been quickened significantly in recent years by the fact that, from an analysis of the results obtained for atmospheric [4] and solar [5–9] neutrinos, it was deduced that there exist neutrino oscillations (see, for example, the relevant discussion in [10–12]). This conclusion was recently confirmed in the KamLAND experiment with reactor antineutrinos [13]. However, experiments studying neutrino oscillations are not sensitive to the origin of the neutrino mass (a Dirac versus a Majorana mass) and furnish no information about the absolute scale of the neutrino masses, since

such experiments measure the quantity  $\Delta m^2$ . The detection and investigation of  $2\beta(0\nu)$  decay may clarify the following problems of neutrino physics (see the relevant discussions in [14–16]): (i) the origin of the neutrino mass (a Dirac versus a Majorana mass), (ii) absolute scale of the neutrino mass (measurement of  $m_1$  or derivation of a limit on it), (iii) the type of hierarchy (normal, inverse, or quasidegenerate one), and (iv)  $CP$  violation in the lepton sector (measurement of the Majorana  $CP$ -odd phase).

Let us consider three main modes of  $2\beta$  decay:<sup>1)</sup>

$$(A, Z) \rightarrow (A, Z + 2) + 2e^- + 2\bar{\nu}, \quad (1)$$

$$(A, Z) \rightarrow (A, Z + 2) + 2e^-, \quad (2)$$

$$(A, Z) \rightarrow (A, Z + 2) + 2e^- + \chi^0. \quad (3)$$

The spectra of the total electron energy for all of these processes are shown in Fig. 1.

**$2\beta(2\nu)$  decay** [process (1)] is a second-order process, which is not forbidden by any conservation law. The detection of this process furnishes information about nuclear matrix elements for  $2\nu$  transitions, and this makes it possible to test the existing models for calculating these nuclear matrix elements

---

<sup>1)</sup>The decay modes also include  $(A, Z) \rightarrow (A, Z - 2)$  processes proceeding via (i) the emission of two positrons ( $2\beta^+$  processes), (ii) the emission of one positron accompanied by  $K$  capture ( $K\beta^+$  processes), and (iii) the capture of two orbital electrons ( $2K$  capture). For the sake of simplicity, we will consider  $2\beta^-$  decay. In each case where it will be desirable to invoke  $2\beta^+$ ,  $K\beta^+$ , or  $2K$  processes, this will be indicated specifically.

and contributes to obtaining deeper insight into the nuclear-physics aspect of the problem of double-beta decay. It is expected that the accumulation of experimental information about  $2\beta(2\nu)$  processes will permit improving the quality of the calculation of the relevant nuclear matrix elements both for  $2\nu$  and for  $0\nu$  decay. Moreover, a precision investigation of the process in question is of interest from the point of view of seeking the time dependence of the coupling constant for weak interaction [17, 18].

**$2\beta(0\nu)$  decay** [process (2)] violates the law of lepton-number conservation ( $\Delta L = 2$ ) and requires that the Majorana neutrino have a nonzero rest mass or that an admixture of right-handed currents be present in weak interaction. Also, this process is possible in some supersymmetric models, where  $2\beta(0\nu)$  decay is initiated by the exchange of supersymmetric particles. Moreover, this decay arises in models featuring an extended Higgs sector within electroweak-interaction theory and in some other cases [1].

**$2\beta(0\nu\chi^0)$  decay** [process (3)] requires the existence of a Majoron—it is a massless Goldstone boson that arises upon a global breakdown of  $(B - L)$  symmetry, where  $B$  and  $L$  are, respectively, the baryon and the lepton number. The Majoron, if any, could play a significant role in the history of the early Universe and in the evolution of stars; it could also have a direct bearing on the solar-neutrino problem. The model of a triplet Majoron [19] was disproved in 1989 by the data on the decay width of the  $Z^0$  boson that were obtained at the LEP accelerator (CERN, Switzerland). Despite this, some new models were proposed [20, 21], where  $2\beta(0\nu\chi^0)$  decay is possible and where there are no contradictions with the LEP data. Also, a  $2\beta$ -decay model that involves the emission of two Majorons was proposed within supersymmetric theories [22]. A few new models of the Majoron were proposed in the 1990s. By the term “Majoron,” one means here massless or light bosons that are associated with neutrinos. In these models, the Majoron can carry a lepton charge and is not bound to be a Goldstone boson [23]. A decay process that involves the emission of two “Majorons” is also possible [24]. In models featuring a vector Majoron, the Majoron is the longitudinal component of a massive gauge boson emitted in  $2\beta$  decay [25]. For the sake of simplicity, each such object is referred to as a Majoron.

In [26], the model of a “bulk” Majoron was proposed within models featuring extra dimensionalities (“brane-bulk” scenario for elementary-particle physics).

In view of all of the aforesaid, searches for  $2\beta$  decay involving Majoron emission is a problem of importance and interest.

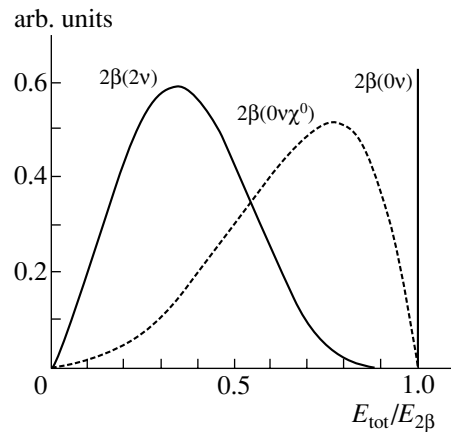


Fig. 1. Spectra of the total electron energy for  $2\beta(0\nu)$ ,  $2\beta(0\nu\chi^0)$ , and  $2\beta(2\nu)$  decays.

Neutrinoless double-beta decay has not yet been recorded, but the existing experimental data make it possible to set constraints on the mass of the Majorana neutrino ( $\langle m_\nu \rangle$ ), on the parameters characterizing the admixture of right-handed currents in electroweak interaction ( $\langle \eta \rangle$  and  $\langle \lambda \rangle$ ), on the Majoron-neutrino coupling constant ( $\langle g_{ee} \rangle$ ), and on some other relevant quantities. The reliability and the accuracy of these constraints greatly depend on the quality of the calculation of  $0\nu$  matrix elements. At the present time, the accuracy of these calculations is insufficiently high, their values in the calculations of different authors varying within a factor of 1.5 to 2. Nonetheless, the use of the most conservative values of the  $0\nu$  nuclear matrix elements permits obtaining quite reliable constraints on all of the aforementioned parameters.

## 2. RESULTS OF EXPERIMENTAL INVESTIGATIONS

The number of possible candidates for objects undergoing double-beta decay is quite great—there are approximately 30 nuclei.<sup>2)</sup> However, nuclei for which the double-beta-transition energy  $E_{2\beta}$  is in excess of 2 MeV are of greatest interest, since the double-beta-decay probability strongly depends on the transition energy. In transitions to excited states of the daughter nucleus, the excitation energy is removed via the emission of one or two photons, which can be detected, and this can therefore serve as an additional source of information about double-beta decay. By way of example, Fig. 2 shows the diagram of energy levels in the  $^{100}\text{Mo}$ – $^{100}\text{Tc}$ – $^{100}\text{Ru}$  nuclear triplet.

<sup>2)</sup> Approximately the same number of nuclei can undergo  $2K$  capture, while twenty nuclei and six nuclei can undergo, respectively,  $K\beta^+$  and  $2\beta^+$  capture (see the tables in [27]).

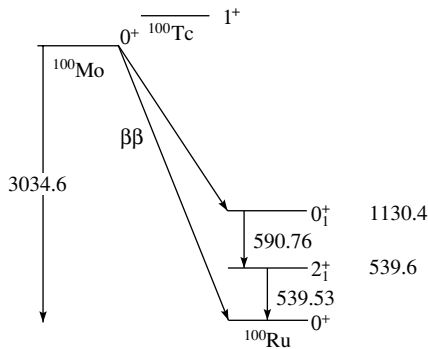


**Fig. 2.** Diagram of energy levels in the  $^{100}\text{Mo}$ – $^{100}\text{Tc}$ – $^{100}\text{Ru}$  nuclear triplet. The displayed energies are given in keV.

The first experiment aimed at searches for double-beta decay was performed in 1948 with the aid of Geiger counters [28]. This experiment resulted in setting a limit on the  $^{124}\text{Sn}$  half-life:  $T_{1/2}^{0\nu} > 3 \times 10^{15}$  yr. In the next few years, the “discovery” of double-beta decay was reported several times, but, each time, these discoveries were then disproved by new, more sensitive experiments. This was not so only for geochemical experiments, where the double-beta decay of  $^{130}\text{Te}$  was indeed discovered (see below).

Up to the mid-1960s, the sensitivity of direct experiments employing counters was not higher than that of about  $10^{17}$  to  $10^{18}$  yr. A first qualitative jump in the sensitivity of experiments seeking double-beta decay occurred in the late 1960s and early 1970s: for a few nuclei ( $^{48}\text{Ca}$ ,  $^{82}\text{Se}$ ,  $^{76}\text{Ge}$ ), it was increased up

**Table 1.** Averaged and recommended values of  $T_{1/2}(2\nu)$  [36]

Isotope	$T_{1/2}(2\nu)$ , yr
$^{48}\text{Ca}$	$4.3_{-1.0}^{+2.1} \times 10^{19}$
$^{76}\text{Ge}$	$1.42_{-0.07}^{+0.09} \times 10^{21}$
$^{82}\text{Se}$	$(0.9 \pm 0.1) \times 10^{20}$
$^{96}\text{Zr}$	$2.1_{-0.4}^{+0.8} \times 10^{19}$
$^{100}\text{Mo}$	$(8.0 \pm 0.7) \times 10^{18}$
$^{100}\text{Mo}$ – $^{100}\text{Ru}(0_1^+)$	$(6.8 \pm 1.2) \times 10^{20}$
$^{116}\text{Cd}$	$3.3_{-0.3}^{+0.4} \times 10^{19}$
$^{128}\text{Te}$	$(2.5 \pm 0.4) \times 10^{24}$
$^{130}\text{Te}$	$(0.9 \pm 0.15) \times 10^{21}$
$^{150}\text{Nd}$	$(7.0 \pm 1.7) \times 10^{18}$
$^{238}\text{U}$	$(2.0 \pm 0.6) \times 10^{21}$

to about  $10^{21}$  yr for  $0\nu$  decay and up to about  $10^{19}$  for  $2\nu$  decay.

In the early 1980s, the growth of interest in double-beta decay resulted in a new improvement of the level and quality of relevant experiments. At the present time, the sensitivity of such experiments is about  $10^{23}$  to  $10^{25}$  yr for  $0\nu$  decay and about  $10^{19}$  to  $10^{21}$  yr for  $2\nu$  decay.

### 2.1. Two-Neutrino Double-Beta Decay

This decay was first recorded in 1949 in a geochemical experiment with  $^{130}\text{Te}$  [29]; in 1967, it was also found for  $^{82}\text{Se}$  [30]. Attempts at revealing this decay in a direct experiment employing counters had been futile for a long time. Only in 1987 could M. Moe, who used a time-projection chamber (TPC), observe  $2\beta(2\nu)$  decay in  $^{82}\text{Se}$  for the first time [31]. Within the next few years, experiments employing counters were able to detect  $2\beta(2\nu)$  decay in  $^{76}\text{Ge}$ ,  $^{100}\text{Mo}$ ,  $^{150}\text{Nd}$ ,  $^{116}\text{Cd}$ ,  $^{48}\text{Ca}$ , and  $^{96}\text{Zr}$ . In  $^{100}\text{Mo}$ ,  $2\beta(2\nu)$  decay to the  $0^+$  excited state of the daughter nucleus at an excitation energy of 1130.29 keV was recorded for the first time in [32]. Also, the  $2\beta(2\nu)$  decay of  $^{238}\text{U}$  was detected in a radiochemical experiment [33]; positive results for  $^{96}\text{Zr}$  were obtained in geochemical experiments [34, 35]. Table 1 displays the present-day averaged and recommended values of  $T_{1/2}(2\nu)$  from [36]. The results of individual experiments can be found in the tables given in [27].

At the present-time, experiments devoted to detecting  $2\beta(2\nu)$  decay are approaching a qualitatively new level at which it is already insufficient to restrict oneself to recording the decay process, but it is necessary to measure all parameters of this process to a high precision. Tracking detectors that are able to record both the energy of each electron and the angle of their divergence are the most appropriate instruments for solving this problem.

### 2.2. Neutrinoless Double-Beta Decay

In contrast to two-neutrino decay, neutrinoless double-beta decay has not yet been observed, although, from the experimental point of view, it is easier to detect it, since, in that case, one seeks, in the experimental spectrum, a peak of energy equal to the double-beta-transition energy and of width determined by detector resolution. Various methods and facilities were applied in searches for  $0\nu$  decay. The most significant advances have been made with germanium semiconductor detectors, which are characterized by a high energy resolution ( $\Delta E = 2$ – $4$  keV) and by comparatively small dimensions. Owing to the last circumstance, it was possible to create

**Table 2.** Compendium of the best results on searches for  $2\beta(0\nu)$  decay (all constraints were obtained at a 90% C.L.; in calculating constraints on the effective value of the Majorana neutrino mass  $\langle m_\nu \rangle$ , use was made of the nuclear matrix elements computed in [48–53] and of the phase-space volumes from [54])

Isotope	$T_{1/2}$ , yr	$\langle m_\nu \rangle$ , eV
$^{48}\text{Ca}$	$>6.8 \times 10^{21}$ [55]	$<36$
$^{76}\text{Ge}$	$>1.9 \times 10^{25}$ [38]	$<0.33\text{--}1$
$^{82}\text{Se}$	$>1.4 \times 10^{22}$ [56]	$<4.7\text{--}13.1$
$^{96}\text{Zr}$	$>1 \times 10^{21}$ [57]	$<16.3\text{--}40$
$^{100}\text{Mo}$	$>1 \times 10^{23}$ [47]	$<0.9\text{--}2$
$^{116}\text{Cd}$	$>7 \times 10^{22}$ [46]	$<2.2\text{--}4.6$
$^{128}\text{Te}$	$>2 \times 10^{24}$ (geochemistry) [58]	$<1.8\text{--}4.9$
$^{130}\text{Te}$	$>2.1 \times 10^{23}$ [45]	$<1.2\text{--}5.2$
$^{136}\text{Xe}$	$>4.4 \times 10^{23}$ [44]	$<2.2\text{--}5.2$
$^{150}\text{Nd}$	$>1.2 \times 10^{21}$ [59]	$<8.5\text{--}29.6$

detectors manufactured from ultrapure materials and surrounded by a passive shield of low radioactivity, this making it possible to reach an extremely low level of background.

Advances that have been made over the last 15 years are especially impressive: in the region of  $2\beta(0\nu)$  decay, the background index was reduced by a factor greater than 100. The use of germanium detectors manufactured from germanium enriched in  $^{76}\text{Ge}$  to about 86%, which is approximately ten times as great as the content of  $^{76}\text{Ge}$  in natural germanium, was a second important advancement. This immediately increased the sensitivity of the experiment by a factor of about 10, all other conditions being the same. For the first time ever, a detector from enriched germanium was used in an experiment performed by a joint group from the Institute of Theoretical and Experimental Physics (ITEP, Moscow) and Yerevan Physics Institute (YerPhI, Yerevan) between 1987 and 1990 (ITEP–YerPhI experiment) [37]. In 1990, the Heidelberg–Moscow Collaboration [Max Planck Institute from Heidelberg and Kurchatov Institute of Atomic Energy (IAE) from Moscow, simply Kurchatov Institute at present] launched a new experiment that is based on the use of detectors from enriched germanium and which has been continued to the present. The experiment is being performed at the Gran Sasso underground laboratory (Italy) at a depth of 3500 mwe. Five HPGe detectors manufactured from enriched germanium (the degree of enrichment is 86%) are surrounded by a passive shield. The total weight of the detectors is 11 kg. For the  $2\beta(0\nu)$  decay of  $^{76}\text{Ge}$ , the authors present the constraint  $T_{1/2} > 1.9 \times 10^{25}$  yr [38], which corresponds to the

following constraint on the mass of the Majorana neutrino:  $\langle m_\nu \rangle < 0.33\text{--}1$  eV.<sup>3)</sup>

The constraint  $T_{1/2} > 1.57 \times 10^{25}$  yr was obtained in the IGEX experiment involving three detectors from enriched germanium (their total weight is 6 kg) [43].

Constraints at a level of  $10^{23}$  yr were obtained for  $^{136}\text{Xe}$  [44],  $^{130}\text{Te}$  [45],  $^{116}\text{Cd}$  [46], and  $^{100}\text{Mo}$  [47] in direct experiments employing counters.

The present-day constraints associated with the existence of  $2\beta(0\nu)$  decay are quoted in Table 2 for nuclei that are the most promising in this respect. All of these results, with the exception of those for  $^{128}\text{Te}$ , were obtained in experiments employing counters. In the case of  $^{128}\text{Te}$ , a “positive” result for  $2\beta(2\nu)$  decay simultaneously serves as a constraint for  $2\beta(0\nu)$  decay. In calculating constraints on  $\langle m_\nu \rangle$ , use was made of the results obtained for nuclear matrix elements in [48–53]. It is advisable to employ the calculations from precisely those studies, because these calculations are the most thorough and take into account the most recent theoretical achievements. The respective phase-space volumes were borrowed from [54].

### 2.3. Double-Beta Decay Involving Majoron Emission

Table 3 displays the best present-day constraints for a “standard” (triplet) Majoron.

<sup>3)</sup>Here, we do not consider the report on the “observation” of the neutrinoless double-beta decay of  $^{76}\text{Ge}$  [39], since the respective conclusion does not seem justified—this result received a great deal of criticism in [40–42].

**Table 3.** Compendium of the best results on searches for  $2\beta(0\nu\chi^0)$  decay involving a standard Majoron (all constraints were obtained at a 90% C.L.; in calculating constraints on the Majoron–neutrino coupling constant  $\langle g_{ee} \rangle$ , use was made of the nuclear matrix elements computed in [48–53] and of the phase-space volumes from [54])

Isotope	$T_{1/2}, \text{yr}$	$\langle g_{ee} \rangle$
$^{48}\text{Ca}$	$> 7.2 \times 10^{20}$ [60]	$< 1.2 \times 10^{-3}$
$^{76}\text{Ge}$	$> 6.4 \times 10^{22}$ [38]	$< (1.2\text{--}3.5) \times 10^{-4}$
$^{82}\text{Se}$	$> 2.4 \times 10^{21}$ [61]	$< (1.7\text{--}4.7) \times 10^{-4}$
$^{96}\text{Zr}$	$> 3.9 \times 10^{20}$ [57]	$< (3.5\text{--}8.5) \times 10^{-4}$
$^{100}\text{Mo}$	$> 5.8 \times 10^{21}$ [104]	$< (0.4\text{--}0.9) \times 10^{-4}$
$^{116}\text{Cd}$	$> 3.7 \times 10^{21}$ [46]	$< (1.3\text{--}2.8) \times 10^{-4}$
$^{128}\text{Te}$	$> 2 \times 10^{24}$ (geochemistry) [58]	$< (0.6\text{--}1.6) \times 10^{-4}$
$^{130}\text{Te}$	$> 3.1 \times 10^{21}$ [45]	$< (1.6\text{--}7) \times 10^{-4}$
$^{136}\text{Xe}$	$> 7.2 \times 10^{21}$ [44]	$< (2.8\text{--}6.5) \times 10^{-4}$
$^{150}\text{Nd}$	$> 2.8 \times 10^{20}$ [59]	$< (2.2\text{--}5.5) \times 10^{-4}$

**Table 4.** Nine possible models of the Majoron (according to [22, 25, 62])

Model	Decay mode	Goldstone boson	$L$	$n$	Matrix element
IB	$2\beta\chi^0$	No	0	1	$M_F - M_{GT}$
IC	$2\beta\chi^0$	Yes	0	1	$M_F - M_{GT}$
ID	$2\beta\chi^0\chi^0$	No	0	3	$M_{F\omega 2} - M_{GT\omega 2}$
IE	$2\beta\chi^0\chi^0$	Yes	0	3	$M_{F\omega 2} - M_{GT\omega 2}$
IIB	$2\beta\chi^0$	No	-2	1	$M_F - M_{GT}$
IIC	$2\beta\chi^0$	Yes	-2	3	$M_{CR}$
IID	$2\beta\chi^0\chi^0$	No	-1	3	$M_{F\omega 2} - M_{GT\omega 2}$
IIE	$2\beta\chi^0\chi^0$	Yes	-1	7	$M_{F\omega 2} - M_{GT\omega 2}$
IIF	$2\beta\chi^0$	Gauge boson	-2	3	$M_{CR}$

A few new models of the Majoron were proposed in the 1990s. Nine possible models of the Majoron are quoted in Table 4 (according to [22, 25, 62]). The table is broken down into two parts comprising models that respect (I) and violate (II) the law of lepton-number conservation. The second column of the table gives the number of emitted Majorons—one or two. The third column indicates whether the Majoron is or is not a Goldstone boson (or is a gauge boson in the case of a vector Majoron—the IIF model). The fourth column presents lepton-charge values, while the fifth column displays a “special index”  $n$  that determines the form of the energy spectrum of emitted electrons:  $G \sim (Q_{\beta\beta} - T)^n$  (here,  $G$  is the phase space,  $Q_{\beta\beta}$  is the double-beta-transition energy, and  $T$  is the total kinetic energy of two electrons). The

respective matrix elements are given in the last column of Table 4. By way of example, the spectra of various modes of double-beta decay accompanied by the emission of one or two Majorons are shown in Fig. 3 for  $^{100}\text{Mo}$ . Only the spectrum for the “bulk” Majorons with the spectral index of  $n = 2$  is not shown. The “nonstandard” models of the Majoron were experimentally tested in [63] for  $^{76}\text{Ge}$  and in [64] for  $^{100}\text{Mo}$ ,  $^{116}\text{Cd}$ ,  $^{82}\text{Se}$ , and  $^{96}\text{Zr}$ . Constraints on the decay modes involving the emission of two Majorons were also obtained for  $^{100}\text{Mo}$  [65],  $^{116}\text{Cd}$  [46], and  $^{130}\text{Te}$  [66]. For  $n = 2, 3$ , and 7, Table 5 gives the best experimental constraints on decays accompanied by the emission of one or two Majorons.

Thus, only limits for double-beta decay accompanied by Majoron emission have been obtained to

**Table 5.** Best experimental constraints (at a 90% C.L.) for the decays accompanied by the emission of one or two Majorons for the  $n = 2, n = 3,$  and  $n = 7$  modes

Isotope	$T_{1/2}, \text{yr}$		
	$n = 2$	$n = 3$	$n = 7$
$^{76}\text{Ge}$	$>7 \times 10^{21*}$	$>5.8 \times 10^{21}$ [63]	$>6.6 \times 10^{21}$ [63]
$^{82}\text{Se}$	$>1 \times 10^{21**}$	$>6.3 \times 10^{20}$ [64]	$>1.1 \times 10^{20}$ [64]
$^{96}\text{Zr}$	$>1 \times 10^{20**}$	$>6.3 \times 10^{19}$ [64]	$>2.4 \times 10^{19}$ [64]
$^{100}\text{Mo}$	$>3 \times 10^{20**}$	$>1.6 \times 10^{20}$ [64]	$>4.1 \times 10^{19}$ [64]
$^{116}\text{Cd}$	$>5 \times 10^{20**}$	$>5.9 \times 10^{20}$ [46]	$>3.1 \times 10^{19}$ [64]
$^{130}\text{Te}$	$>2 \times 10^{21***}$	$>1.1 \times 10^{21}$ [45]	–

The conservative estimates according to [63], [64], and [45] are labeled with \*, \*\*, and \*\*\*, respectively.

date (see Tables 3, 5). The most stringent constraints come from a geochemical experiment for  $^{128}\text{Te}$  and from experiments for  $^{100}\text{Mo}, ^{116}\text{Cd}, ^{76}\text{Ge},$  and  $^{82}\text{Se}$  with counters.

*2.4. Double-Beta Transitions to Excited States of Daughter Nuclei*

Considerable advances in studying such transitions have been made over the past decade. The level of sensitivity of present-day experiments is usually  $T_{1/2} \sim 10^{21} - 10^{22}$  yr, reaching a value of about  $8 \times 10^{23}$  yr for the  $0\nu(0^+ - 2^+)$  transition to  $^{76}\text{Ge}$  [67]. The improvement of the experimental sensitivity resulted in that the transition to the  $0_1^+$  excited state of  $^{100}\text{Ru}$  was recorded for the first time for  $^{100}\text{Mo}$  [32]; in all probability, transitions of this type will be recorded for some other nuclei ( $^{150}\text{Nd}, ^{96}\text{Zr}, ^{82}\text{Se}$ ) in the near future. Previously, it was believed that  $2\beta(2\nu)$  decay to the  $2^+$  excited state of the daughter nucleus is strongly suppressed and is almost inaccessible to detection. However, it was recently shown that the suppression factor is not very large, and the half-lives of some nuclei ( $^{136}\text{Xe}, ^{116}\text{Cd}, ^{82}\text{Se}, ^{100}\text{Mo}$ ) may range between about  $10^{21}$  and  $10^{23}$  yr [68–70], in which case there arises the possibility of recording such transitions. In this respect, it is important to note that, within the quasiparticle random-phase approximation (QRPA), the dependence of nuclear matrix elements on the parameter  $g_{pp}$  for  $2\nu$  transitions to the ground state ( $0_{\text{g.s.}}^+$ ) differs drastically from that for respective transitions to an excited state ( $0_1^+$ ). Thus, the detection of  $2\beta(2\nu)$  decay to the  $0_1^+$  excited state furnishes additional information about nuclear matrix elements, and this makes it possible to test various schemes for calculating nuclear matrix elements (see [54]).

As to  $2\beta(0\nu)$  transitions to excited states of daughter nuclei, a clear-cut signature of such decays is worthy of special note here: in addition to two electrons of fixed total energy, there appears one ( $0^+ - 2_1^+$  transition) or two ( $0^+ - 0_1^+$  transition) photons, their energies being strictly fixed as well. In a would-be experiment detecting all decay products with a high efficiency and a high energy resolution, the background could be reduced nearly to zero. Possibly, this circumstance will be used in future experiments featuring a large mass of the substance under study (in facilities like MAJORANA [71], CUORE [72], GENIUS [1, 73], KamLAND [74], or BOREXINO [75, 76]). Table 6 gives a compendium of the best

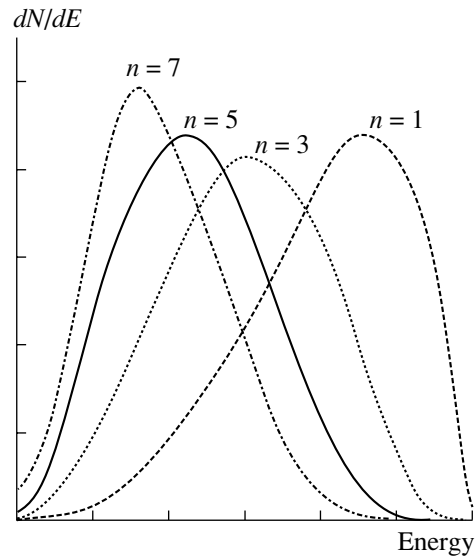


**Fig. 3.** Spectra of various modes of double-beta decay accompanied by the emission of one or two Majorons ( $n = 1, 3, 7$ ) and of two-neutrino double-beta decay ( $n = 5$ ) for  $^{100}\text{Mo}$ .

**Table 6.** Compendium of the best results on searches for double-beta decay to excited state of daughter nuclei (all of the constraints were obtained at a 90% C.L.;  $J_f^\pi$  are quantum numbers of the respective excited state;  $Q_{\beta\beta}$  is the double-beta-transition energy)

Isotope	$J_f^\pi$ (energy, keV)	$Q_{\beta\beta}$ , keV	Decay type	$T_{1/2}$ , yr	References	
$^{48}\text{Ca}$	$2_1^+$ (983.5)	3288.5	$0\nu$	$>1 \times 10^{21}$	[60]	
			$0\nu + 2\nu$	$>1.8 \times 10^{20}$	[77]	
	$2_2^+$ (2421.0)	1851	$0\nu + 2\nu$	$>1.5 \times 10^{20}$	[77]	
$^{76}\text{Ge}$	$0_1^+$ (2997.2)	1274.8	$0\nu + 2\nu$	$>1.5 \times 10^{20}$	[77]	
	$2_1^+$ (559.1)	1480	$0\nu$	$>8.2 \times 10^{23}$	[67]	
			$0\nu + 2\nu$	$>1.1 \times 10^{21}$	[78]	
	$0_1^+$ (1122.3)	916.7	$0\nu + 2\nu$	$>6.2 \times 10^{21}$	[79]	
$^{82}\text{Se}$			$0\nu$	$>1.3 \times 10^{22}$	[80]	
	$2_2^+$ (1216.1)	823	$0\nu + 2\nu$	$>1.4 \times 10^{21}$	[78]	
	$2_1^+$ (776.49)	2218.5	$0\nu$	$>2.8 \times 10^{21}$	[61]	
			$0\nu + 2\nu$	$>1.4 \times 10^{21}$	[81]	
$^{96}\text{Zr}$	$2_2^+$ (1474.84)	1520.2	$0\nu + 2\nu$	$>1.6 \times 10^{21}$	[81]	
	$0_1^+$ (1487.5)	1507.5	$0\nu + 2\nu$	$>3.0 \times 10^{21}$	[81]	
	$2_1^+$ (778.22)	2572.2	$0\nu$	$>3.9 \times 10^{20}$	[57]	
			$0\nu + 2\nu$	$>7.9 \times 10^{19}$	[82]	
$^{100}\text{Mo}$	$0_1^+$ (1147.9)	2202.5	$0\nu + 2\nu$	$>6.8 \times 10^{19}$	[82]	
	$2_2^+$ (1497.8)	1852.6	$0\nu + 2\nu$	$>6.1 \times 10^{19}$	[82]	
	$2_3^+$ (1625.9)	1724.5	$0\nu + 2\nu$	$>5.4 \times 10^{19}$	[82]	
	$2_1^+$ (539.53)	2494.5	$0\nu$	$>7 \times 10^{21}$	[83]	
			$0\nu + 2\nu$	$>1.6 \times 10^{21}$	[32]	
$^{116}\text{Cd}$	$0_1^+$ (1130.29)	1903.7	$0\nu + 2\nu$	$= (6.8 \pm 1.2) \times 10^{20}$	[32]	
	$2_2^+$ (1362.06)	1671.9	$0\nu + 2\nu$	$>1.3 \times 10^{21}$	[32]	
	$0_2^+$ (1740.7)	1293.3	$0\nu + 2\nu$	$>1.3 \times 10^{21}$	[32]	
	$2_1^+$ (1293.54)	1511.5	$0\nu + 2\nu$	$>2.3 \times 10^{21}$	[84]	
			$0\nu$	$>1.3 \times 10^{22}$	[46]	
	$0_1^+$ (1756.8)	1048.2	$0\nu + 2\nu$	$>2.0 \times 10^{21}$	[84]	
			$0\nu$	$>7 \times 10^{21}$	[46]	
$^{128}\text{Te}$	$0_2^+$ (2027.3)	777.7	$0\nu + 2\nu$	$>2.0 \times 10^{21}$	[84]	
	$2_2^+$ (2112.2)	692.8	$0\nu + 2\nu$	$>1.1 \times 10^{20}$	[85]	
	$2_3^+$ (2225.3)	579.7	$0\nu + 2\nu$	$>0.6 \times 10^{20}$	[85]	
	$2_1^+$ (442.88)	424.3	$0\nu + 2\nu$	$>2.9 \times 10^{21}$	[86]	
$^{130}\text{Te}$	$2_1^+$ (536.09)	1992.7	$0\nu + 2\nu$	$>2.8 \times 10^{21}$	[86]	
			$0\nu$	$>1.4 \times 10^{23}$	[45]	
	$2_2^+$ (1122.15)	1406.7	$0\nu + 2\nu$	$>2.7 \times 10^{21}$	[87]	
$^{136}\text{Xe}$	$0_1^+$ (1793.5)	735.3	$0\nu$	$>3.1 \times 10^{22}$	[45]	
			$0\nu + 2\nu$	$>2.3 \times 10^{21}$	[87]	
	$2_1^+$ (818.6)	1649.4	$0\nu$	$>6.5 \times 10^{21}$	[88]	
	$^{150}\text{Nd}$	$2_1^+$ (333.94)	3033.6	$0\nu + 2\nu$	$>9.1 \times 10^{19}$	[89]
		$0_1^+$ (740.4)	2627.1	$0\nu + 2\nu$	$>1.0 \times 10^{20}$	[89]
			$>1.5 \times 10^{20}$	[79]		
	$2_2^+$ (1046.3)	2321.2	$0\nu + 2\nu$	$>1.4 \times 10^{20}$	[90]	
	$2_3^+$ (1193.8)	2173.7	$0\nu + 2\nu$	$>2.7 \times 10^{18}$	[91]	
	$0_2^+$ (1256.6)	2110.9	$0\nu + 2\nu$	$>2.0 \times 10^{20}$	[89]	

results on searches for double-beta decay to excited states of daughter nuclei.

### 2.5. $2\beta^+$ , $K\beta^+$ , and $2K$ Processes

Much less attention has been given to  $(A, Z) \rightarrow (A, Z - 2)$  processes, since there was no hope for detecting them at currently available low-background facilities. Processes of the  $2\beta^+(2\nu)$  and  $K\beta^+(2\nu)$  types are strongly suppressed in relation to  $2\beta^-$  decay because of the Coulomb barrier for positrons and a substantially lower kinetic energy realized in such transitions. However, these processes are appealing from the experimental point of view owing to the possibility of recording them in the mode of coincidence of four (two) annihilation photons and two (one) positrons. Moreover, these processes can be studied by recording only annihilation photons—for example, with the aid of germanium semiconductor detectors. For  $2K(2\nu)$  processes, the kinetic energy of the transition can be quite high (up to about 2.8 MeV), positrons being absent from the final state. However, it is difficult to record this process because only characteristic radiation is accessible to detection in it.

Nonetheless, both theorists and experimentalists have recently shown greater interest in such processes. Theorists performed precise calculations of the phase space by using relativistic wave functions [92] and computed nuclear matrix elements for the most promising nuclei [54, 93, 94]. On their side, experimentalists improved substantially the sensitivity of experiments and indicated that searches for such transitions to  $0_1^+$  excited states of daughter nuclei are quite promising [95]. As a result, it became clear that, by using currently available low-background facilities, one can record  $K\beta^+(2\nu)$ ,  $2K(2\nu)$ , and  $2K(2\nu; 0^+ - 0_1^+)$  processes in some nuclei ( $^{78}\text{Kr}$ ,  $^{124}\text{Xe}$ ,  $^{106}\text{Cd}$ ,  $^{130}\text{Ba}$ ,  $^{136}\text{Ce}$ ).

In [94], it was also emphasized that searches for  $2\beta^+(0\nu)$  and  $K\beta^+(0\nu)$  processes are of importance since this information (even only respective limits!) may prove to be useful if the  $2\beta^-$  decay of some nucleus is detected. In this case, information about  $2\beta^+(0\nu)$  and especially about  $K\beta^+(0\nu)$  transitions may contribute to clarifying the mechanism (neutrino mass versus right-handed currents) responsible for  $2\beta^-(0\nu)$  decay.

Table 7 gives a compendium of the best present-day constraints for  $2\beta^+$ ,  $K\beta^+$ , and  $2K$  processes and the result of the geochemical experiment that employed  $^{130}\text{Ba}$  and which yielded the first indication of the observation of  $2K(2\nu)$  capture.

## 3. FURTHER PROSPECTS

Tables 1–3 and 5–7 illustrate the experimental situation at the end of 2002. The majority of the most sensitive experiments either had been completed by that time (for example, IGEX [43], ELEGANT-5 [103, 104], the experiment for Xe with a TPC [44], NEMO-2 [57, 61], MIBETA [45]) or are hardly able to improve substantially their sensitivity (for example, the Heidelberg–Moscow experiment and the scintillation experiment with  $^{116}\text{Cd}$  in Solotvino). Therefore, a further improvement of sensitivity can be expected only in new experiments of larger scale.

### 3.1. *New Experiments Occurring at the Stage of Implementation*

In this subsection, we will discuss experiments that are being performed at the present time and experiments that will begin to yield results in the near future. Among new experiments, that with the NEMO-3 detector, which was commissioned in June 2002 (the first results from this experiment will be given below), is worthy of note above all. In all probability, the first physics results for  $^{130}\text{Te}$  in the CUORICINO experiment [66, 105] and for  $^{136}\text{Xe}$  from the TPC at ITEP [106] will be obtained in 2003.

**3.1.1. NEMO-3 Experiment** [107, 108]. This is a tracking experiment that, in contrast to experiments with  $^{76}\text{Ge}$ , detects not only the total energy deposition but also the remaining parameters of the process, including the energy of individual electrons, their divergence angle, and the coordinate of an event in the source plane. The main properties of the detector were studied by using the NEMO-2 prototype [57, 61, 109]. Since June 2002, the NEMO-3 detector has operated at the Frejus underground laboratory (France) located at a depth of 4800 mwe. The detector has a cylindrical structure and consists of 20 identical sectors (see Fig. 4). A thin (about 30–60 mg/cm<sup>2</sup>) source containing beta-decaying nuclei and having a total area of 20 m<sup>2</sup> and a weight of up to 10 kg is placed at the detector center. The basic principles of detection are identical to those used in the NEMO-2 detector: the energy of the electrons is measured by plastic scintillators (1940 individual counters), while the tracks are reconstructed on the basis of information obtained in the planes of Geiger cells (6180 cells) surrounding the source on both sides. The tracking volume of the detector is filled with a mixture consisting of 96% He and 4% spirit at normal pressure. In addition, a magnetic field of strength about 30 G parallel to the detector axis is created by a solenoid surrounding the detector. The magnetic field is used to identify electron–positron pairs and, hence, to suppress this source of background.

**Table 7.** Experimental constraints for  $2\beta^+$ ,  $K\beta^+$ , and  $KK$  processes (all constraints were obtained at a 90% C.L.)

Decay type	Nucleus	$T_{1/2}$ , yr	References
$2K(0\nu)$	$^{130}\text{Ba}$	$>4 \times 10^{21}$	[96]
	$^{132}\text{Ba}$	$>3 \times 10^{20}$	[96]
	$^{58}\text{Ni}$	$>1.3 \times 10^{19}$	[97]
$= 2K(2\nu)$	$^{130}\text{Ba}$	$>4 \times 10^{21}$	[96]
		$= (2.2 \pm 0.5) \times 10^{21}$	[98]
$K\beta^+(0\nu)$	$^{132}\text{Ba}$	$>3 \times 10^{20}$	[96]
	$^{130}\text{Ba}$	$>4 \times 10^{21}$	[96]
$K\beta^+(2\nu)$	$^{78}\text{Kr}$	$>2.5 \times 10^{21}$	[99]
	$^{58}\text{Ni}$	$>4.4 \times 10^{20}$	[100]
	$^{106}\text{Cd}$	$>3.7 \times 10^{20}$	[101]
	$^{92}\text{Mo}$	$>1.9 \times 10^{20}$	[102]
	$^{130}\text{Ba}$	$>4 \times 10^{21}$	[96]
$2\beta^+(0\nu)$	$^{58}\text{Ni}$	$>4.4 \times 10^{20}$	[100]
	$^{106}\text{Cd}$	$>4.1 \times 10^{20}$	[101]
	$^{92}\text{Mo}$	$>1.9 \times 10^{20}$	[102]
	$^{78}\text{Kr}$	$>7 \times 10^{19}$	[99]
	$^{130}\text{Ba}$	$>4 \times 10^{21}$	[96]
$2\beta^+(2\nu)$	$^{78}\text{Kr}$	$>1 \times 10^{21}$	[99]
	$^{106}\text{Cd}$	$>2.4 \times 10^{20}$	[102]
	$^{130}\text{Ba}$	$>4 \times 10^{21}$	[96]
$2\beta^+(2\nu)$	$^{130}\text{Ba}$	$>4 \times 10^{21}$	[96]
	$^{78}\text{Kr}$	$>1 \times 10^{21}$	[99]
	$^{106}\text{Cd}$	$>2.4 \times 10^{20}$	[101]

**Table 8.** Isotopes studied with the NEMO-3 detector

Isotope	$^{100}\text{Mo}$	$^{82}\text{Se}$	$^{130}\text{Te}$	$^{116}\text{Cd}$	$^{150}\text{Nd}$	$^{96}\text{Zr}$	$^{48}\text{Ca}$
Enrichment, %	97	97	89	93	91	57	73
Isotope mass, g	6914	932	454	405	36.6	9.4	7.0

The main parameters of the detector are the following: the energy resolution of the scintillation counters lies in the interval 14–17% of FWHM for electrons of energy 1 MeV; the time resolution is 250 ps for an electron energy of 1 MeV; and the accuracy in reconstructing the vertex of  $2e^-$  events is about 1 cm.

The detector is surrounded by a passive shield consisting of 20 cm of steel and 30 cm of water. The level of radioactive admixtures in structural materials of the detector and of the passive shield was tested

in measurements with low-background HPGe detectors.

Measurements with the NEMO-3 detector revealed that tracking information, combined with time and energy measurements, makes it possible to suppress the background efficiently. By using data from these measurements and the results of the calculations, it was shown that, within five years of measurements, the sensitivity of the NEMO experiment in determining the respective half-lives can become as high as about  $10^{25}$  yr for the  $0\nu$  decay ( $\langle m_\nu \rangle \approx 0.1$ –

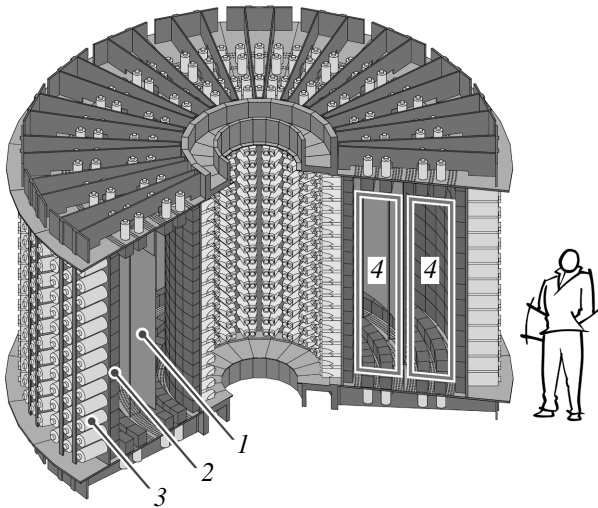


**Fig. 4.** Layout of the NEMO-3 detector: (1) source, (2) plastic scintillators, (3) multiplier phototubes of low radioactivity; and (4) tracking volume.

0.3 eV), about  $10^{23}$  yr for the  $0\nu\chi^0$  decay ( $\langle g_{ee} \rangle \approx 10^{-5}$ ), and  $10^{22}$  yr for the  $2\nu$  decay of  $^{100}\text{Mo}$ . That NEMO-3 can be used to investigate almost all isotopes of interest is a distinctive feature of this facility. At the present time, such investigations are being performed there for seven isotopes; these are  $^{100}\text{Mo}$ ,  $^{82}\text{Se}$ ,  $^{116}\text{Cd}$ ,  $^{150}\text{Nd}$ ,  $^{96}\text{Zr}$ ,  $^{130}\text{Te}$ , and  $^{48}\text{Ca}$  (see Table 8). In addition, foils from copper and natural (not enriched) tellurium are placed in the detector for performing background measurements.

Figure 5 displays the spectrum of  $2\beta(2\nu)$  events in  $^{100}\text{Mo}$  that were collected over 690 hours, while Fig. 6 shows the angular distribution in these events. The total number of useful events is about 12 000, which is much greater than the total statistics of all of the preceding experiments with  $^{100}\text{Mo}$ . It should also be noted that the background is as low as about 2% of the total number of useful events. By employing the calculated values of the detection efficiencies for  $2\beta(2\nu)$ ,  $2\beta(0\nu)$ , and  $2\beta(0\nu\chi^0)$  events, the following preliminary results were obtained for  $^{100}\text{Mo}$ :

$$T_{1/2}(2\nu) = [8 \pm 0.08(\text{stat.}) \pm 1.5(\text{syst.})] \times 10^{18} \text{ yr}, \quad (4)$$

$$T_{1/2}(0\nu) > 1 \times 10^{23} \text{ yr}, \quad (5)$$

$$T_{1/2}(0\nu\chi^0) > 3 \times 10^{21} \text{ yr}. \quad (6)$$

It should be emphasized that the value of  $T_{1/2}(2\nu)$  complies well with the results of preceding experiments (see Table 1). The systematic error will be reduced substantially upon performing dedicated calibration measurements and can be made as low as

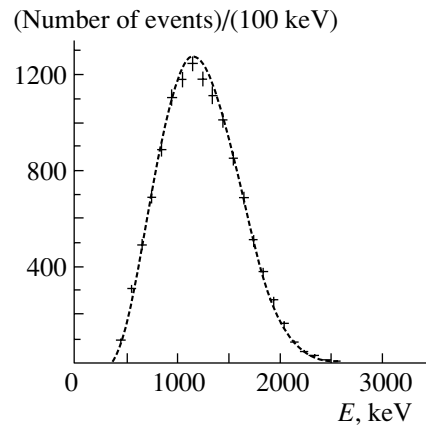


**Fig. 5.** Spectrum of  $2\beta(2\nu)$  events in  $^{100}\text{Mo}$  that were accumulated over 690 hours of measurements.

some 5 to 7%. The constraint for  $2\beta(0\nu)$  decay is more stringent than the best of the previous results from [103].

By using the constraints obtained for the  $2\beta(0\nu)$  and  $2\beta(0\nu\chi^0)$  decays of  $^{100}\text{Mo}$ , one can derive constraints on the effective value of the Majorana neutrino mass,  $\langle m_\nu \rangle$ , and on the Majoron–neutrino coupling constant,  $\langle g_{ee} \rangle$ :  $\langle m_\nu \rangle < 0.9\text{--}2$  eV and  $\langle g_{ee} \rangle < (0.5\text{--}1.2) \times 10^{-4}$ , respectively. It should be noted that this constraint on  $\langle g_{ee} \rangle$  is one of the most stringent among present-day constraints on this quantity and that the constraint on  $\langle m_\nu \rangle$  already goes beyond the interval bounded in experiments with  $^{76}\text{Ge}$  (see Tables 2, 3).

The NEMO-3 experiment is being continued, and new interesting results are expected from it in the near future.

**3.1.2. CUORICINO** [66, 105]. This project is the first stage of the larger scale CUORE experiment

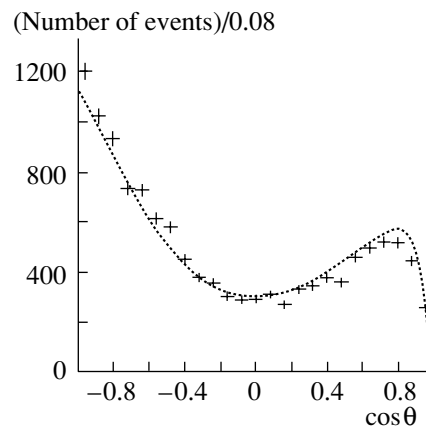


**Fig. 6.** Angular distribution of  $2\beta(2\nu)$  events in  $^{100}\text{Mo}$  that were accumulated over 690 hours of measurements ( $\theta$  is the angle between the electron momenta).

(see Subsection 3.2.2 below). The experiment will be performed at the Gran Sasso underground laboratory. The main idea consists in employing low-temperature detectors based on  $^{\text{nat}}\text{TeO}_2$  crystals. The use of natural tellurium is quite justified in this case, because the content of  $^{130}\text{Te}$  in it is rather high, 33.8%. The detector will consist of 56 individual crystals, their total weight being 42 kg. It is assumed that the energy resolution will be about 5 keV at an energy of 2.6 MeV. One of the main methodological tasks of the CUORICINO experiment is to demonstrate the possibility of substantially reducing the background level in relation to the background in the previous experiment with  $\text{TeO}_2$  detectors that was reported in [45].

The sensitivity of the experiment to the  $0\nu$  mode will be  $T_{1/2} \sim 10^{25}$  yr over five years of measurements, the corresponding sensitivity to the effective mass of the Majorana neutrino being about 0.2 to 0.7 eV. It is planned to begin measurements in 2003.

**3.1.3. TPC-ITEP** [106]. The experimental facility is deployed at ITEP (Moscow). It includes a TPC of volume  $13 \text{ m}^3$  placed in a large magnet. Electrons from the double-beta decay of  $^{136}\text{Xe}$  located in the central part of the TPC are detected in two adjacent volumes separated by a thin Mylar film. With the aim of suppressing multiple rescattering of low-energy electrons (0.3–2 MeV), these volumes are filled with methane. In order to improve the efficiency of detection of useful events and to measure electron energies, the TPC is placed in a magnetic field of strength 1 kG. The event coordinates are measured by multiwire proportional chambers arranged in the central part of the detector. The dimensions of the TPC are  $3 \times 3 \times 1.5 \text{ m}^3$ . The chamber operates at atmospheric pressure and may house up to 10 kg of Xe (its optimum weight is 6 kg). The expected sensitivity of the experiment over one year of measurements is  $T_{1/2} \sim (2\text{--}4) \times 10^{24}$  yr for the  $0\nu$  mode and  $T_{1/2} \sim 3 \times 10^{21}$  yr for the  $2\nu$  mode.

At present, the chamber is operating, and measurements with  $^{\text{nat}}\text{Xe}$  have begun. In all probability, measurements with 6 kg of  $^{136}\text{Xe}$  (enrichment to 95%) will begin in 2003.

### 3.2. Planned Experiments

In this section, mention is made of experimental projects that can be implemented within the next five to ten years.

**3.2.1. SUPERNEMO** [110]. The NEMO Collaboration considers the possibility of performing an experiment that would employ 100 kg of  $^{82}\text{Se}$  with the aim of reaching the sensitivity to the  $0\nu$  decay

of this isotope at a level of  $T_{1/2} \sim (1\text{--}2) \times 10^{26}$  yr (the corresponding sensitivity to the neutrino mass is about 0.04 to 0.15 eV). In order to accomplish this goal, it is proposed to use the experimental procedure identical to that in the NEMO-3 experiment (see Subsection 3.1.1). However, the new detector will have planar geometry and will consist of four identical sections, each having dimensions of about  $2 \times 3 \times 20 \text{ m}^3$ . A  $^{82}\text{Se}$  source having a thickness of about  $60 \text{ mg/cm}^2$  and a very low content of radioactive admixtures is placed at the center of the sections. The detector will record all features of double-beta decay: the electron energy will be recorded by counters based on plastic scintillators ( $\Delta E/E \approx 10\text{--}12\%$  at  $E = 1 \text{ MeV}$ ), while tracks will be reconstructed with the aid of Geiger counters.

The same facility can be used to investigate  $^{100}\text{Mo}$ ,  $^{116}\text{Cd}$ , and  $^{130}\text{Te}$  with a sensitivity to  $2\beta(0\nu)$  decay at a level of about  $(0.5\text{--}1) \times 10^{26}$  yr.

The use of an already tested experimental technique is an appealing feature of this experiment. It is planned to arrange the equipment at the Frejus underground laboratory (the respective depth being 4800 mwe).

**3.2.2. CUORE** [72]. The experiment is to be performed at the Gran Sasso underground laboratory. It is planned to investigate 760 kg of  $^{\text{nat}}\text{TeO}_2$ —that is, 206 kg of  $^{130}\text{Te}$ . One thousand low-temperature ( $T \approx 10 \text{ mK}$ ) detectors, each having a weight of 760 g, will be manufactured and arranged in 25 towers (one tower is approximately equivalent to the CUORICINO detector—see Subsection 3.1.2). One of the main problems here is to reduce the background level by a factor of about 100 to 1000 in relation to the background level achieved in the 20-crystal  $\text{TeO}_2$  detector [45]. Upon reaching a background level of 0.001  $(\text{keV kg yr})^{-1}$ , the sensitivity of the experiment to the  $0\nu$  decay of  $^{130}\text{Te}$  will become approximately  $3.5 \times 10^{26}$  yr ( $\langle m_\nu \rangle \sim 0.03\text{--}0.13 \text{ eV}$ ).

**3.2.3. GENIUS** [1, 73]. In this experiment, it is planned to use 1 t of germanium enriched in  $^{76}\text{Ge}$  to about 85% (approximately 300 HPGe detectors). In order to suppress an external background, the detector will be placed in a tank filled with liquid nitrogen ( $\varnothing 12 \times 12 \text{ m}^3$ ). Referring to the success achieved by the BOREXINO Collaboration in purifying water and a liquid scintillator, the authors of this project hope to purify liquid nitrogen to a level of  $10^{-16} \text{ g/g}$  for  $^{238}\text{U}$  and  $^{232}\text{Th}$  and to a level of  $0.5 \text{ mBq/m}^3$  for  $^{222}\text{Rn}$ . In the opinion of those authors, the background can then be reduced by a factor of  $10^3$  to  $10^4$  in relation to the background in the Heidelberg–Moscow experiment [38]. As a result, the background over

one year of measurements in the region of the  $0\nu$  decay of  $^{76}\text{Ge}$  will be 0.8 of an event. At this background level, the sensitivity of the experiment will be about  $2 \times 10^{27}$  yr (at a 90% C.L.), the corresponding sensitivity to the neutrino mass being  $\langle m_\nu \rangle \sim 0.03\text{--}0.1$  eV. Over 10 years of measurements under such background conditions, the respective sensitivities will become about  $6 \times 10^{27}$  yr (at a 90% C.L.) and 0.017–0.058 eV.

By and large, the project seems quite promising, but it would be difficult to reach the declared background reduction. Moreover, a verification of a long-term operation of unshielded HPGe detectors in liquid nitrogen seems crucial for it.

**3.2.4. MAJORANA** [71]. The MAJORANA facility will consist of 210 sectioned HPGe detectors manufactured from enriched germanium (the degree of enrichment is about 86%). The total mass of enriched germanium will be 500 kg. The facility is designed in such a way that it will consist of ten individual supercryostats manufactured from radioactive copper, each containing 21 HPGe detectors. The entire facility will be surrounded by a passive shield and will be arranged at an underground laboratory in the United States.

Only the total energy deposition will be employed in measuring the  $2\beta(0\nu)$  decay of  $^{76}\text{Ge}$  to the ground state ( $0^+$ ) of the daughter nucleus. The use of sectioned HPGe detectors, an analysis of signals in shape, anticoincidences, and the application of structural materials characterized by low radioactivity will make it possible to reduce the background level to a value below  $3 \times 10^{-4}$  (keV kg yr) $^{-1}$  and to reach a sensitivity of about  $4 \times 10^{27}$  yr within ten years of measurements. The corresponding sensitivity to the effective mass of the Majorana neutrino is about 0.02 to 0.07 eV.

The measurement of the  $2\beta(0\nu)$  decay of  $^{76}\text{Ge}$  to the  $0^+$  excited state of the daughter nucleus will be performed by recording two cascade photons and two beta electrons. The planned sensitivity is about  $10^{27}$  yr.

**3.2.5. EXO** [111]. In this project, it is planned to implement Moe's proposal of 1991 [112] to record both ionization electrons and the  $\text{Ba}^+$  ion originating from the double-beta-decay process  $^{136}\text{Xe} \rightarrow ^{136}\text{Ba}^{++} + 2e^-$ . In [111], it is proposed to explore 1 t of  $^{136}\text{Xe}$ . An actual project of the experiment has not yet been developed. One of the possible schemes for its implementation is as follows. There is a gas TPC of volume  $40 \text{ m}^3$  filled with enriched xenon to a pressure of 5 to 10 atm. For the background from the  $2\nu$  decay of  $^{136}\text{Xe}$  to be avoided, the energy resolution

of the detector must not be poorer than 2.5% ( $\sigma$ ) at an energy of 1.6 MeV.

In the  $0\nu$  decay of  $^{136}\text{Xe}$ , the TPC will measure the energy of two electrons and the coordinates of a useful event to within a few millimeters. After that, a laser beam will be directed to the region of a useful event, and a  $\text{Ba}^+$  ion will be recorded by resonance excitation (a system of photodetectors is intended for this). For  $\text{Ba}^{++}$  to undergo a transition to a state of  $\text{Ba}^+$ , a special gas is added to xenon. The authors of the project assume that the background will be reduced to zero within five years of measurements; at a 70% efficiency of detection of useful events, this will make it possible to reach a sensitivity of about  $8 \times 10^{26}$  yr for the  $^{136}\text{Xe}$  half-life and a sensitivity of about 0.05 to 0.12 eV for the neutrino mass.

Those authors also considered a detector version in which the mass of  $^{136}\text{Xe}$  is 10 t, but this is probably beyond present-day capabilities. It should be recalled that about 120 t of usual xenon are required for obtaining 10 t of  $^{136}\text{Xe}$ , but this is in excess of the xenon amount produced worldwide over a few years.

To conclude this section, we note that the main difficulty in this experiment is associated with detecting a  $\text{Ba}^+$  ion with a reasonably high efficiency and under conditions of a relatively low optical background. This issue calls for thorough experimental tests, and positive results along these lines have yet to be obtained.

**3.2.6. MOON** [113]. The project is aimed at implementing an experiment that would simultaneously study the double-beta decay of  $^{100}\text{Mo}$  and record solar neutrinos by the reaction  $\nu + ^{100}\text{Mo} \rightarrow ^{100}\text{Tc} + e^-$  (its threshold being 168 keV). It is planned to employ 3.3 t of  $^{100}\text{Mo}$  (or 34 t of natural molybdenum) purified to a level below  $10^{-3}$  Bq/t in  $^{238}\text{U}$  and  $^{232}\text{Th}$ .

Methodologically, the project is still underdeveloped—even the general scheme of an experiment is not quite clear. One of the possible versions of project implementation is to use the procedure developed for the MINOS detector. The dimensions of the MOON detector are  $6 \times 6 \times 5 \text{ m}^3$ ; it consists of 1950 modules ( $6 \text{ m} \times 6 \text{ m} \times 0.25 \text{ cm}$ ). Each module contains 30 plates of a plastic scintillator with dimensions  $600 \times 20 \times 0.25 \text{ cm}^3$ . A Mo foil of thickness 0.05 g/cm $^2$  is placed between the modules. Light from each of the scintillating modules is collected with the aid of 222 WLS fibers located at intervals of 2.7 cm along the  $x$  axis (on one side of the module) and along the  $y$  axis (on the other side of the module). The authors of the project hope to obtain reasonably high energy [7% (FWHM) at  $E = 3 \text{ MeV}$ ], spatial ( $\Delta x \approx \Delta y = 0.5 \text{ cm}$ ), and time (about one nanosecond) resolutions. As a result, the expected sensitivity over one

year of measurements will be about  $(2-3) \times 10^{26}$  yr, which corresponds to a sensitivity to the neutrino mass at a level of 0.02 to 0.05 eV.

### 3.2.7. Use of the BOREXINO Detector in Double-Beta-Decay Searches.

(i) In 1994, Raghavan proposed employing detectors of the BOREXINO type in searches for the double-beta decay of  $^{136}\text{Xe}$  [75]. The idea consisted in dissolving 2% of Xe in a liquid scintillator. Since it is planned to reach a very low background level in the BOREXINO experiment, there arises the possibility of attaining a high sensitivity to the neutrinoless double-beta decay of  $^{136}\text{Xe}$ .

In 2000, this idea was revisited by Caccianiga and Giammarchi [76] in connection with the actual features of the Counting Test Facility (CTF) and the expected features of BOREXINO. It was shown that, for the half-life, the sensitivity achieved within one year of measurements will be about  $2 \times 10^{24}$  yr for CTF and about  $2 \times 10^{26}$  yr for BOREXINO. In the last case, it is planned to use 1500 kg of enriched xenon. It is assumed that, upon the completion of the program of measurement of the solar-neutrino flux, the BOREXINO facility could be used in double-beta-decay searches.

(ii) In [114], it was proposed to use the CTF and BOREXINO in searches for the double-beta decay of  $^{116}\text{Cd}$  (CAMEO project). In this case, it is planned to place  $^{116}\text{CdWO}_4$  crystals at the center of a vessel containing a liquid scintillator. In employing the CTF, there will be 24 crystals of total weight 64 kg (the weight of  $^{116}\text{Cd}$  is 19.3 kg). In this case, the sensitivity will reach a value of about  $10^{26}$  yr within five to eight years of measurements. In employing the BOREXINO detector, it is planned to manufacture 370 crystals of total weight 1000 kg (the weight of  $^{116}\text{Cd}$  is 290 kg). In this case, the expected sensitivity over five to eight years of measurements will be  $T_{1/2} \sim 10^{27}$  yr, the corresponding sensitivity to the neutrino mass being  $\langle m_\nu \rangle \sim 0.02-0.04$  eV.

It should be emphasized that the proposals outlined in Subsection 3.2.7 can be implemented with the aid of the KamLAND detector as well [74].

## 4. CONCLUSION

Thus, two-neutrino double-beta decay has so far been recorded for ten nuclei ( $^{48}\text{Ca}$ ,  $^{76}\text{Ge}$ ,  $^{82}\text{Se}$ ,  $^{96}\text{Zr}$ ,  $^{100}\text{Mo}$ ,  $^{116}\text{Cd}$ ,  $^{128}\text{Te}$ ,  $^{130}\text{Te}$ ,  $^{150}\text{Nd}$ ,  $^{238}\text{U}$ ). In addition, the  $2\beta(2\nu)$  decay of  $^{100}\text{Mo}$  to an excited state of the daughter nucleus and the  $2K(2\nu)$  process in  $^{130}\text{Ba}$  were recorded. Experiments studying two-neutrino

double-beta decay are presently approaching a qualitatively new level, where high-precision measurements are performed not only for half-lives but also for all other parameters of the process. At the same time, the sensitivity of experiments aimed at searches for double-beta decay to excited states of daughter nuclei and for  $2\beta^+$ ,  $K\beta^+$ , and  $2K$  processes is being continuously improved. As a result, a trend is emerging toward thoroughly investigating all aspects of two-neutrino double-beta decay, and this will furnish very important information about the values of nuclear matrix elements, the parameters of various theoretical models, and so on. In this connection, one may expect advances in the calculation of nuclear matrix elements and in the understanding of the nuclear-physics facets of double-beta decay.

Neutrinoless double-beta decay has not yet been recorded, the most stringent limit on the effective value of the Majorana neutrino mass being obtained in experiments with  $^{76}\text{Ge}$  (0.33–1 eV). Within the next few years, the sensitivity to the neutrino mass in the NEMO and CUORICINO experiments will be improved to become about 0.1 to 0.3 eV in measurements with  $^{100}\text{Mo}$  and  $^{130}\text{Te}$ . With the NEMO-3 detector, a similar level of sensitivity can be reached for some other nuclei as well ( $^{82}\text{Se}$ , for example). It is precisely these two experiments (NEMO and CUORICINO) that will establish, within the nearest five to seven years, the level of investigations in the realm of double-beta decay. Next-generation experiments, where the mass of the isotopes being studied will be as great as about 100 to 1000 kg, will have started within five to ten years. In all probability, they will make it possible to reach the sensitivity to the neutrino mass at a level of 0.1 to 0.01 eV.

## REFERENCES

1. H. V. Klapdor-Kleingrothaus, J. Hellmig, and M. Hirsch, *J. Phys. G* **24**, 483 (1998).
2. A. Faessler and F. Simkovic, *Prog. Part. Nucl. Phys.* **46**, 233 (2001).
3. J. D. Vergados, *Phys. Rep.* **361**, 1 (2002).
4. H. Sobel *et al.*, *Nucl. Phys. B (Proc. Suppl.)* **91**, 127 (2001).
5. B. T. Cleveland *et al.*, *Astrophys. J.* **496**, 505 (1998).
6. S. Fukuda *et al.*, *Phys. Rev. Lett.* **86**, 5651 (2001); **86**, 5656 (2001).
7. V. N. Gavrin *et al.*, *Nucl. Phys. B (Proc. Suppl.)* **91**, 36 (2001).
8. M. Altman *et al.*, *Phys. Lett. B* **490**, 16 (2000).
9. Q. R. Ahmad *et al.*, *Phys. Rev. Lett.* **89**, 011301 (2002); **89**, 011302 (2002).
10. P. C. de Holanda and A. Yu. Smirnov, *Phys. Rev. D* **66**, 113005 (2002).
11. J. N. Bahcall *et al.*, hep-ph/0204314.
12. M. Maltoni *et al.*, hep-ph/0207227.

13. K. Eguchi *et al.*, hep-ex/0212021.
14. A. Yu. Smirnov, Czech. J. Phys. **52**, 439 (2002).
15. S. Pascoli, S. T. Petcov, and W. Rodejohann, hep-ph/0209059.
16. B. Kayser, hep-ph/0211134.
17. A. S. Barabash, Pis'ma Zh. Éksp. Teor. Fiz. **68**, 3 (1998)[JETP Lett. **68**, 1 (1998)].
18. A. S. Barabash, Eur. Phys. J. A **8**, 137 (2000).
19. G. Gelmini and M. Roncadelli, Phys. Lett. B **99B**, 1411 (1981).
20. R. N. Mohapatra and P. B. Pal, *Massive Neutrinos in Physics and Astrophysics* (World Sci., Singapore, 1991).
21. Z. G. Berezhiani, A. Yu. Smirnov, and J. W. F. Valle, Phys. Lett. B **291**, 99 (1992).
22. R. N. Mohapatra and E. Takasugi, Phys. Lett. B **211**, 192 (1988).
23. C. P. Burgess and J. M. Cline, Phys. Lett. B **298**, 141 (1993); Phys. Rev. D **49**, 5925 (1994).
24. P. Bamert, C. P. Burgess, and R. N. Mohapatra, Nucl. Phys. B **449**, 25 (1995).
25. C. D. Carone, Phys. Lett. B **308**, 85 (1993).
26. R. N. Mohapatra, A. Perez-Lorenzana, and C. A. S. Pires, Phys. Lett. B **491**, 143 (2000).
27. V. I. Tretyak and Yu. G. Zdesenko, At. Data Nucl. Data Tables **80**, 83 (2002).
28. E. L. Fireman, Phys. Rev. **74**, 1238 (1948).
29. M. G. Inghram and J. H. Reynolds, Phys. Rev. **76**, 1265 (1949); **78**, 822 (1950).
30. T. Kirsten, W. Gentner, and O. A. Schaeffer, Z. Phys. **202**, 273 (1967).
31. S. R. Elliott, A. A. Hahn, and M. K. Moe, Phys. Rev. Lett. **59**, 2020 (1987).
32. A. S. Barabash *et al.*, Phys. Lett. B **345**, 408 (1995).
33. A. L. Turkevich, T. E. Economou, and G. A. Cowan, Phys. Rev. Lett. **67**, 3211 (1991).
34. A. Kawashima, K. Takahashi, and A. Masuda, Phys. Rev. C **47**, 2452 (1993).
35. M. E. Wieser and J. R. De Laeter, Phys. Rev. C **64**, 024308 (2001).
36. A. S. Barabash, Czech. J. Phys. **52**, 567 (2002).
37. A. A. Vasenko *et al.*, Mod. Phys. Lett. A **5**, 1299 (1990).
38. H. V. Klapdor-Kleingrothaus *et al.*, Eur. Phys. J. A **12**, 147 (2001).
39. H. V. Klapdor-Kleingrothaus *et al.*, Mod. Phys. Lett. A **16**, 2409 (2001).
40. C. E. Aalseth *et al.*, Mod. Phys. Lett. A **17**, 1475 (2002).
41. F. Feruglio, A. Strumia, and F. Vissani, Nucl. Phys. B **637**, 345 (2002).
42. Yu. G. Zdesenko, F. A. Danevich, and V. I. Tretyak, Phys. Lett. B **546**, 206 (2002).
43. C. E. Aalseth *et al.*, Phys. Rev. C **65**, 092007 (2002).
44. R. Luescher *et al.*, Phys. Lett. B **434**, 407 (1998).
45. C. Arnaboldi *et al.*, hep-ex/0211071.
46. F. A. Danevich *et al.*, Phys. Rev. C **62**, 045501 (2000).
47. NEMO Collab.
48. F. Simkovic *et al.*, Phys. Rev. C **60**, 055502 (1999).
49. J. Suhonen, Phys. Lett. B **477**, 99 (2000).
50. J. Suhonen, Phys. Rev. C **62**, 042501 (2000).
51. S. Stoica and H. V. Klapdor-Kleingrothaus, Nucl. Phys. A **694**, 269 (2001).
52. E. Caurier *et al.*, Nucl. Phys. A **654**, 973c (1999).
53. J. H. Hirsch, O. Castanos, and P. O. Hess, Nucl. Phys. A **582**, 124 (1995).
54. J. Suhonen and O. Sivitarese, Phys. Rep. **300**, 123 (1998).
55. K. You *et al.*, Phys. Lett. B **265**, 53 (1991).
56. S. R. Elliot *et al.*, Phys. Rev. C **46**, 1535 (1992).
57. R. Arnold *et al.*, Nucl. Phys. A **658**, 299 (1999).
58. O. K. Manuel, J. Phys. G **17**, 221 (1991).
59. A. De Silva, M. K. Moe, M. A. Nelson, and M. A. Vient, Phys. Rev. C **56**, 2451 (1997).
60. A. S. Barabash, Phys. Lett. B **216**, 257 (1989).
61. R. Arnold *et al.*, Nucl. Phys. A **636**, 209 (1998).
62. M. Hirsch *et al.*, Phys. Lett. B **372**, 8 (1996).
63. M. Gunther *et al.*, Phys. Rev. D **55**, 54 (1997).
64. R. Arnold *et al.*, Nucl. Phys. A **678**, 341 (2000).
65. J. Tanaka and H. Ejiri, Phys. Rev. D **48**, 5412 (1993).
66. O. Cremonesi, hep-ex/0210007.
67. B. Maier, Nucl. Phys. B (Proc. Suppl.) **35**, 358 (1994).
68. S. K. Dhiman and P. K. Raina, Phys. Rev. C **50**, R2660 (1994).
69. O. Civitarese and J. Suhonen, Nucl. Phys. A **575**, 251 (1994).
70. J. Toivanen and J. Suhonen, Phys. Rev. C **55**, 2314 (1997).
71. C. E. Aalseth *et al.*, hep-ex/0201021.
72. C. Arnaboldi *et al.*, hep-ex/0212053.
73. H. V. Klapdor-Kleingrothaus *et al.*, hep-ph/0103074.
74. A. Piepke, Nucl. Phys. B (Proc. Suppl.) **91**, 99 (2001).
75. R. S. Raghavan, Phys. Rev. Lett. **72**, 1411 (1994).
76. B. Caccianiga and M. G. Giammarchi, Astropart. Phys. **14**, 15 (2000).
77. A. Bakalyarov *et al.*, Pis'ma Zh. Éksp. Teor. Fiz. **76**, 643 (2002)[JETP Lett. **76**, 545 (2002)].
78. A. S. Barabash *et al.*, Z. Phys. A **352**, 231 (1995).
79. A. A. Klimenko *et al.*, Czech. J. Phys. **52**, 589 (2002).
80. A. Morales *et al.*, Nuovo Cimento A **100**, 525 (1988).
81. J. Suhonen *et al.*, Z. Phys. A **358**, 297 (1997).
82. A. S. Barabash *et al.*, J. Phys. G **22**, 487 (1996).
83. H. Ejiri *et al.*, Nucl. Phys. A **611**, 85 (1996).
84. A. Piepke *et al.*, Nucl. Phys. A **577**, 121 (1994).
85. A. S. Barabash, A. V. Kopylov, and V. I. Cherehovskiy, Phys. Lett. B **249**, 186 (1990).
86. E. Bellotti *et al.*, Europhys. Lett. **3**, 889 (1987).
87. A. S. Barabash *et al.*, Eur. Phys. J. A **11**, 143 (2001).
88. E. Bellotti *et al.*, J. Phys. G **17**, S231 (1991).
89. C. Arpesella *et al.*, Nucl. Phys. B (Proc. Suppl.) **70**, 249 (1999).
90. C. Arpesella *et al.*, Nucl. Phys. B (Proc. Suppl.) **48**, 247 (1996).

91. E. Bellotti *et al.*, Lett. Nuovo Cimento **33**, 273 (1982).
92. M. Doi and T. Kotani, Prog. Theor. Phys. **87**, 1207 (1992).
93. J. Suhonen, Phys. Rev. C **48**, 574 (1993).
94. M. Hirsch *et al.*, Z. Phys. A **347**, 151 (1994).
95. A. S. Barabash, Pis'ma Zh. Éksp. Teor. Fiz. **59**, 644 (1994)[JETP Lett. **59**, 677 (1994)].
96. A. S. Barabash and R. R. Saakyan, Yad. Fiz. **59**, 197 (1996)[Phys. At. Nucl. **59**, 179 (1996)].
97. E. B. Norman and M. A. De Faccio, Phys. Lett. B **148B**, 31 (1984).
98. A. P. Meshik *et al.*, Phys. Rev. C **64**, 035205 (2001).
99. C. Saenz *et al.*, Phys. Rev. C **50**, 1170 (1994).
100. S. I. Vasil'ev *et al.*, Pis'ma Zh. Éksp. Teor. Fiz. **57**, 614 (1993)[JETP Lett. **57**, 320 (1993)].
101. P. Belli *et al.*, Astropart. Phys. **10**, 115 (1999).
102. A. S. Barabash *et al.*, Z. Phys. A **357**, 351 (1997).
103. H. Ejiri *et al.*, Phys. Rev. C **63**, 065501 (2001).
104. H. Ejiri *et al.*, Phys. Lett. B **531**, 190 (2002).
105. C. Brofferio *et al.*, Czech. J. Phys. **52**, 531 (2002).
106. V. A. Artemiev *et al.*, Yad. Fiz. **63**, 1312 (2000) [Phys. At. Nucl. **63**, 1238 (2000)].
107. NEMO-3 Proposal, Preprint No. 94-29, LAL (Orsay, 1994).
108. NEMO Collab., Preprint No. 02-30, LAL (Orsay, 2002).
109. R. Arnold *et al.*, Nucl. Instrum. Methods Phys. Res. A **354**, 338 (1995).
110. A. S. Barabash, Czech. J. Phys. **52**, 575 (2002).
111. M. Danilov *et al.*, Phys. Lett. B **480**, 12 (2000).
112. M. Moe, Phys. Rev. C **44**, R931 (1991).
113. H. Ejiri, Phys. Rev. Lett. **85**, 2917 (2000).
114. G. Bellini *et al.*, Phys. Lett. B **493**, 216 (2000).

*Translated by A. Isaakyan*

---

---

NUCLEI  
Experiment

---

---

## Double-Beta Decay of $^{150}\text{Nd}$ to the First $0^+$ Excited State of $^{150}\text{Sm}$ : Current State\*

A. S. Barabash<sup>1)\*\*</sup>, F. Hubert<sup>2)</sup>, Ph. Hubert<sup>2)</sup>, and V. I. Umatov<sup>1)</sup>

Received March 31, 2003

**Abstract**—Two-neutrino double-beta decay of  $^{150}\text{Nd}$  to the first  $0^+$  excited state in  $^{150}\text{Sm}$  is investigated with the 400-cm<sup>3</sup> low-background HPGe detector. Preliminary data analysis for 6843 h shows an excess of events at 333.9 and 406.5 keV. If this excess is assigned to the investigated transition, then its half-life can be estimated at  $[1.2_{-0.3}^{+0.5} \pm 0.4(\text{syst.})] \times 10^{20}$  yr. © 2004 MAIK “Nauka/Interperiodica”.

### 1. INTRODUCTION

The main interest in double-beta decay is connected with the neutrinoless mode ( $0\nu\beta\beta$ ) as a probe for physics beyond the Standard Model of electroweak interactions. Its existence is connected with fundamental aspects of particle physics, i.e., the lepton number nonconservation, the existence and nature of neutrino mass, the existence of right-handed currents in the electroweak interaction, the existence of a massless Goldstone boson, the Majoron, supersymmetry, etc. (see, for instance, [1–4]).

In connection with  $0\nu\beta\beta$  decay, the detection of double-beta decay with the emission of two neutrinos ( $2\nu\beta\beta$ ), which is an allowed process of second order in the Standard Model, enables the experimental determination of nuclear matrix elements involved in the double-beta-decay processes. This, in turn, leads to the development of theoretical schemes for nuclear-matrix-element calculations in connection both with  $2\nu\beta\beta$  decays and with  $0\nu\beta\beta$  decays.

The  $\beta\beta$  decay can proceed through transitions to the ground state as well as to various excited states of the daughter nuclide. Studies of the latter transitions allow one to obtain supplementary information about  $\beta\beta$  decay. Because of smaller transition energies, the probabilities for  $\beta\beta$ -decay transitions to excited states are substantially suppressed in comparison with transitions to the ground state. But as was shown [5], by using low-background HPGe detectors, the  $2\nu\beta\beta$  decay to the  $0_1^+$  level in the daughter nucleus may be detected for such nuclei as  $^{100}\text{Mo}$ ,

$^{96}\text{Zr}$ , and  $^{150}\text{Nd}$ . In this case, the energies involved in the  $\beta\beta$  transitions are large enough (1903, 2202, and 2627 keV, respectively), and the expected half-lives are of the order of  $10^{20}$ – $10^{21}$  yr. The required sensitivity was reached only for  $^{100}\text{Mo}$  and the transition was detected in three experiments [6–8] with the half-life lying within  $(6$ – $9) \times 10^{20}$  yr. Recently, additional isotopes,  $^{82}\text{Se}$ ,  $^{130}\text{Te}$ ,  $^{116}\text{Cd}$ , and  $^{76}\text{Ge}$ , have become of interest to studies of  $2\nu\beta\beta$  decay to the  $0_1^+$  level too (see review [9]).

Theoretical estimates of  $2\nu\beta\beta$  decay to a  $2^+$  excited state have shown that, for a few nuclei ( $^{82}\text{Se}$ ,  $^{96}\text{Zr}$ ,  $^{100}\text{Mo}$ , and  $^{130}\text{Te}$ ), the half-lives can be  $\sim 10^{22}$ – $10^{23}$  yr [4]. This would mean that the detection of such decays becomes possible using the present and new installations in the near future.

It is very important to note that, in the framework of QRPA models, the behavior of nuclear matrix elements with  $g_{pp}$  parameter is completely different for transitions to the ground and excited ( $2^+$  and  $0^+$ ) states [4, 10]. This is why the decay to excited states may probe different aspects of the calculational method than the decay to the ground states. Thus, the search for  $\beta\beta$  transitions to the excited states has its own special interest.

In this article, the first preliminary results of an experimental investigation of the  $\beta\beta$  decay of  $^{150}\text{Nd}$  to the first  $0^+$  excited state in  $^{150}\text{Sm}$  are presented. The decay scheme is shown in Fig. 1. A search for  $\beta\beta$  transitions of  $^{150}\text{Nd}$  to the first  $0^+$  excited state in  $^{150}\text{Sm}$  has been carried out using a germanium detector to look for  $\gamma$ -ray lines corresponding to the decay scheme.

### 2. EXPERIMENTAL

The experimental work is being performed in the Modane Underground Laboratory (depth of

---

\*This article was submitted by the authors in English.

<sup>1)</sup>Institute of Theoretical and Experimental Physics, Bol'shaya Cheremushkinskaya ul. 25, Moscow, 117259 Russia.

<sup>2)</sup>Centre d'Etudes Nucléaires, IN2P3-CNRS et Université de Bordeaux, France.

\*\* e-mail: Alexander.Barabash@itep.ru

Analysis of events in the range of peaks under study

Peak, keV	333.9 ± 1.12			406.5 ± 1.12	
Number of events	416			394	
Continuous background	342			319	
Isotopes	<sup>214</sup> Bi	<sup>227</sup> Th	<sup>228</sup> Ac	<sup>214</sup> Bi	<sup>211</sup> Pb
$E_\gamma$ , keV	333.31; 334.78	334.37	332.37	405.74	404.853
Contributions from isotopes	5.7	3.4	2.0	9.1	2.0
Excess of events	63 ± 27			64 ± 27	

4800 mwe). A 400-cm<sup>3</sup> low-background HPGe detector is being used for investigation of 3046 g of Nd<sub>2</sub>O<sub>3</sub> powder placed into a special Marinelli delrin box which has been put on the detector endcap. Taking into account the natural abundance (5.64%), 153 g of <sup>150</sup>Nd is exposed. Data collected for 6843 h have been used for analysis.

The HPGe detector is surrounded by a passive shield consisting of 2 cm of archaeological lead, 10 cm of OFHC copper, and 15 cm of ordinary lead. To reduce the <sup>222</sup>Rn gas, which is one of the main sources of the background, special efforts were made to minimize the free space near the detector. In addition, the passive shield was enclosed in an aluminum box flushed with high-purity nitrogen. The cryostat, the endcap, and the critical mechanical components of the HPGe detector are made of very pure Al–Si alloy. Finally, the cryostat has a J-type geometry to shield the crystal from possible radioactive impurities in the dewar.

The electronics consist of currently available spectrometric amplifiers and an 8192 channel ADC. The energy calibration was adjusted to cover the energy range from 50 keV to 3.5 MeV. The energy resolution was 1.9 keV for the 1332-keV line of <sup>60</sup>Co. The electronics were stable during the experiment due to the constant conditions in the laboratory (temperature of

23°C, relative humidity of 50%). A daily check on the apparatus functioning is made.

The detection photopeak efficiencies are equal to 2.38% at 333.9 keV and 2.35% at 406.5 keV. The efficiencies have been computed with the CERN Monte Carlo code GEANT3.21. Special calibration measurements with radioactive sources and powders containing well-known <sup>226</sup>Ra activities confirmed that the accuracy of these efficiencies is about 10%.

The dominant detector backgrounds come from natural <sup>40</sup>K, radioactive chains of <sup>232</sup>Th and <sup>235,238</sup>U, and man-made and/or cosmogenic activities of <sup>137</sup>Cs and <sup>60</sup>Co. The sample was found to have considerable activity of <sup>40</sup>K (48 mBq/kg). Additionally, long-lived radioactive impurities were observed in the sample, but with much weaker activities. In our case, the most important isotopes contributing to energy ranges of the investigated transition are <sup>214</sup>Bi (1.1 mBq/kg), <sup>228</sup>Ac (1.1 mBq/kg), <sup>227</sup>Ac (0.17 mBq/kg), and their daughters.

### 3. ANALYSIS AND RESULTS

Figures 2 and 3 show the energy spectrum in the ranges under interest. As one can see, there is an excess of events above the continuous background at the investigated energies. <sup>214</sup>Bi contributes to both investigated ranges through  $\gamma$  rays with energies of 333.9-keV peak and 405.74 keV (0.17%) for the 406.5-keV peak. <sup>228</sup>Ac touches the 333.9-keV-peak range with its  $\gamma$  (332.37 keV, 0.40%). <sup>227</sup>Ac exhibits, through its daughters, <sup>227</sup>Th (334.37 keV, 1.14%) and <sup>211</sup>Pb (404.853 keV, 3.78%).

The table presents the results of the analysis for the two peak energy ranges under study. A peak shape is described as a Gaussian with a standard deviation of ~0.56 keV at the energies investigated. For the analysis, a peak range is taken within four standard deviations ( $E \pm 2\sigma$ ), i.e., 0.9545 of a peak area. As

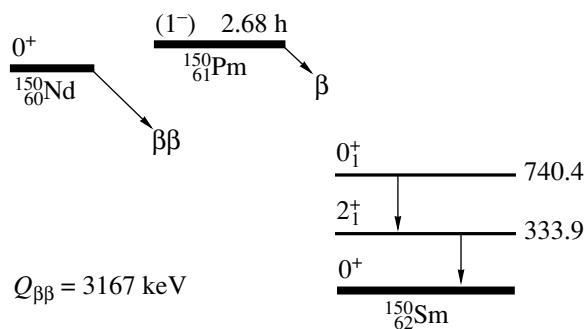


Fig. 1. Decay scheme of <sup>150</sup>Nd. Energies of levels are in keV.

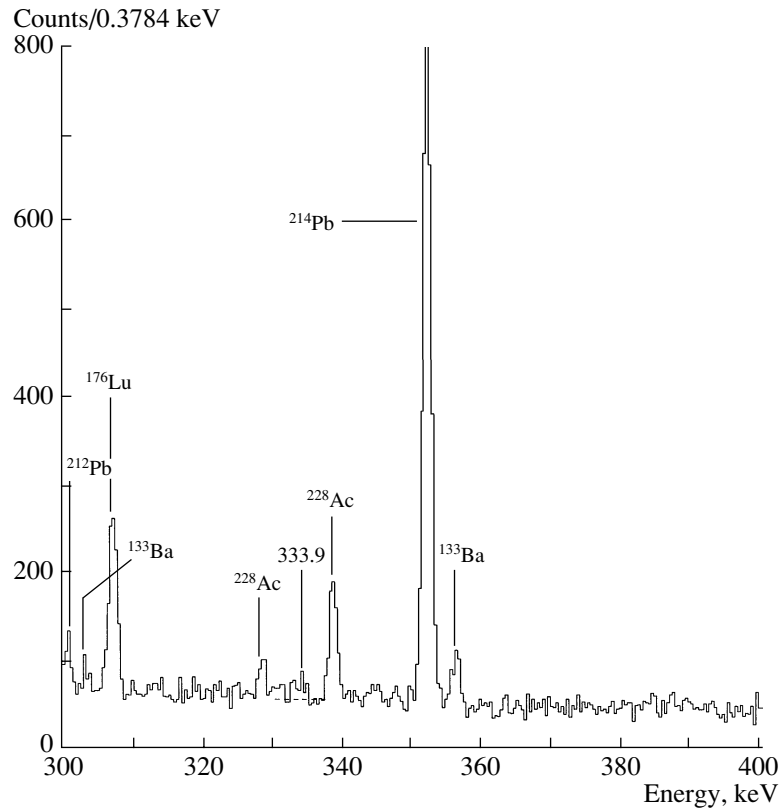


Fig. 2. Energy spectrum in the range of 333.9 keV. Dashed line is continuous background used in the analysis.

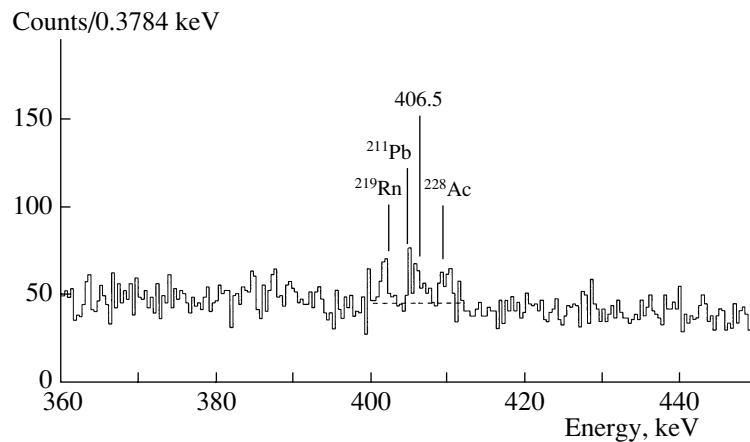


Fig. 3. Energy spectrum in the range of 406.5 keV. Dashed line is continuous background used in the analysis.

one can see, there is an excess of events for each peak under study. If these event excesses are connected with the  $2\nu\beta\beta$  decay of  $^{150}\text{Nd}$  to the first  $0^+$  excited state of  $^{150}\text{Sm}$ , then by summing the two peaks we obtain an effect of  $133 \pm 40$  events, corresponding to a half-life  $T_{1/2} = [1.2^{+0.5}_{-0.3} \pm 0.4(\text{syst.})] \times 10^{20}$  yr.

Previous experiments gave only limits on this transition,  $>1 \times 10^{20}$  yr [11] and  $>1.5 \times 10^{20}$  yr [12]. Taking into account all errors, our result is not in con-

tradiction with the previous limits. Our measurement is still going on, and we hope to obtain a more reliable and clearer effect.

#### ACKNOWLEDGMENTS

We would like to thank the Modane Underground Laboratory staff for their technical assistance in running the experiment.

Portions of this work were supported by INTAS, grant no. 00-00362.

## REFERENCES

1. H. V. Klapdor-Kleingrothaus, Nucl. Phys. B (Proc. Suppl.) **77**, 357 (1999).
2. A. Faessler and F. Šimcovic, J. Phys. G **24**, 2139 (1998).
3. P. Vogel, nucl-th/0005020.
4. J. Suhonen and O. Civitarese, Phys. Rep. **300**, 123 (1998).
5. A. S. Barabash, Pis'ma Zh. Éksp. Teor. Fiz. **51**, 180 (1990)[JETP Lett. **51**, 207 (1990)].
6. A. S. Barabash *et al.*, Phys. Lett. B **345**, 408 (1995).
7. A. S. Barabash *et al.*, Yad. Fiz. **62**, 2211 (1999)[Phys. At. Nucl. **62**, 2039 (1999)].
8. L. De Braekeleer *et al.*, Phys. At. Nucl. **63**, 1214 (2000).
9. A. S. Barabash, Czech. J. Phys. **50**, 447 (2000).
10. M. Aunola and J. Suhonen, Nucl. Phys. A **602**, 133 (1996).
11. C. Arpesella *et al.*, Nucl. Phys. B (Proc. Suppl.) **70**, 249 (1999).
12. A. A. Klimenko *et al.*, Czech. J. Phys. **52**, 589 (2002).

## Nuclear-Structure Corrections to the Energy Spectra of Ordinary and Muonic Deuterium

A. P. Martynenko\* and R. N. Faustov<sup>1)</sup>\*\*

Samara State University, ul. Akademika Pavlova 1, Samara, 443011 Russia

Received March 20, 2003; in final form, June 27, 2003

**Abstract**—One-loop nuclear-structure-induced corrections of order  $(Z\alpha)^5$  to the Lamb shift and to the hyperfine structure of deuterium are calculated. The contribution of deuteron-structure effects to the  $(ep)$ – $(ed)$  and  $(\mu p)$ – $(\mu d)$  isotopic shifts for the  $1S$ – $2S$  splitting is obtained with the aid of modern experimental data on the electromagnetic form factors for the deuteron. A comparison with the analogous contributions to the Lamb shift for ordinary and muonic hydrogen shows that the relative contribution of corrections associated with the nuclear structure increases as we go over from the hydrogen to the deuterium atom owing to the growth of the nuclear size. © 2004 MAIK “Nauka/Interperiodica”.

### 1. INTRODUCTION

Experimental and theoretical investigation of the Lamb shift and of the hyperfine structure of muonic hydrogen and muonic deuterium can lead to considerable advances in determining some fundamental properties of the proton and the deuteron and to a better understanding of effects associated with the structure and polarizability of the nuclei of these hydrogen-like atoms [1–5]. It is the nuclear-structure corrections and the corrections due to the nuclear polarizabilities that introduce the main theoretical uncertainty both in the Lamb shift for the hydrogen atom and in its hyperfine structure. One of the latest investigations of these effects in the hyperfine structure of ordinary and muonic hydrogen revealed [6] that, in the case of ordinary hydrogen, nearly 70% of the quantity  $(\Delta E_{\text{QED}}^{\text{HFS}} - \Delta E_{\text{expt}}^{\text{HFS}}) = 0.046$  MHz (the QED contribution  $\Delta E_{\text{QED}}^{\text{HFS}}$  disregards effects associated with the recoil of the proton and with its structure and polarizability) can be obtained within an effective field theory that describes baryon interaction with photons and leptons. In recent years, an experiment devoted to measuring the  $2P$ – $2S$  Lamb shift in muonic hydrogen ( $\mu p$ ) has been performed at the Paul Scherrer Institute (PSI) [7]. The objective of that experiment is to measure the Lamb shift in muonic hydrogen to a precision of  $30 \times 10^{-6}$ , which would make it possible to assess the proton charge radius to a relative

precision of  $10^{-3}$ , this being one order of magnitude higher than that which has so far been achieved on the basis of an analysis of elastic  $ep$  scattering and of the Lamb shift in ordinary hydrogen. Another important problem is associated with studying the hydrogen–deuterium isotopic shift in the  $1S$ – $2S$  splitting [8–10]. The main distinctions between the energy levels of the isotopes stem from their different masses and nuclear-charge distributions. Finer effects are determined by the spins of the nuclei and their magnetic and quadrupole moments. The experimental value of the H–D isotopic shift ( $\delta$  is the relative experimental error),

$$\Delta E_{\text{H-D}}(1S-2S) = 670\,994\,334.64(15) \text{ kHz}, \quad (1)$$
$$\delta = 2.2 \times 10^{-10},$$

was obtained to a precision that requires taking into account effects of the nuclear structure and polarizability in theoretically calculating this quantity. Using the result in (1), one can deduce the difference of the squares of the proton and deuteron charge radii [11]:

$$r_d^2 - r_p^2 = 3.8213(11.7) \text{ fm}^2. \quad (2)$$

Therefore, measurement of the Lamb shift in ( $\mu p$ ) to a precision of  $30 \times 10^{-6}$  would make it possible to derive  $r_d$  from expression (2) to a relative precision of  $10^{-3}$ . A different possibility of determining the deuteron charge radius more precisely is associated with measuring the isotopic shift between muonic hydrogen and deuterium in the  $1S$ – $2S$  splitting. In order to implement this possibility, the precision of the corresponding experiment must be commensurate with that in (1). Bearing in mind that the relative error in the Lamb shift for the ( $\mu p$ ) system will be

<sup>1)</sup>Scientific Council for the Interdisciplinary Problem Cybernetics, Russian Academy of Sciences, ul. Vavilova 40, Moscow, 117967 Russia.

\* e-mail: mart@info.ssu.samara.ru

\*\* e-mail: faustov@theory.sinp.msu.ru

$10^{-5}$  in the PSI experiment, the possibility of the corresponding measurement of the  $(\mu p)$ – $(\mu d)$  isotopic shift in the  $1S$ – $2S$  splitting seems quite realistic. For this, it is of course necessary to calculate all possible corrections to the Lamb shift in muonic hydrogen and deuterium to the same accuracy. The Lamb shift is determined by the sum of the QED contribution (one-, two-, and three-loop corrections, as well as recoil corrections and radiative corrections featuring recoil) and nuclear corrections. While the QED corrections are presently known to a relative accuracy of  $10^{-7}$  [11], the contribution of nuclear effects is more uncertain. The accuracy in calculating this contribution (nuclear structure and polarizability) depends both on the experimentally measured distributions of the charge, the magnetic moment, and other relevant quantities in nuclei and on the theoretical models used. Experiments measuring the isotopic shift (1) and the hyperfine structure of the hydrogen atom may discriminate between numerous nuclear models.

The hyperfine splitting of the deuterium ground state is yet another quantity of importance where nuclear-structure corrections can be tested experimentally. The experimental value of the hyperfine splitting was previously obtained to a high precision [11, 12],

$$\Delta E_{\text{expt}}^{\text{HFS}}(\text{D}) = 327\,384.352\,521\,9(17)(3) \text{ kHz}, \quad (3)$$

$$\delta = 5.2 \times 10^{-12}.$$

The discrepancy between the experimental value in (3) and the theoretical value obtained for the hyperfine splitting in deuterium with allowance for only the QCD corrections is 45 kHz. A significant contribution to this value comes first of all from corrections induced by the nuclear structure. The nucleus of the deuterium atom is a spin-1 object, and its structure is determined by three electromagnetic form factors.

The objective of the present study is to take consistently into account, both for the Lamb shift in the ordinary- and the muonic-deuterium atom and for the hyperfine structure, all effects of order  $(Z\alpha)^5$  that are associated with the deuteron structure. In contrast to the previous investigations of these problems in [13–16], the electromagnetic interaction of the spin-1 deuteron with a  $1/2$ -spin lepton is constructed by employing a manifestly covariant approach to describe the quasipotential of two-photon interaction. In addition, we take into account up-to-date experimental data on the deuteron electromagnetic form factors, including the charge, the magnetic, and the quadrupole form factor.

## 2. CORRECTIONS OF ORDER $(Z\alpha)^5$ TO THE LAMB SHIFT IN DEUTERIUM

The main nuclear-structure-induced contribution of order  $(Z\alpha)^4$  to the Lamb shift in the hydrogen atom is determined by one-photon interaction. The amplitude of the elastic-scattering process  $ed \rightarrow ed$  can be represented as the convolution of the electron and deuteron electromagnetic currents. The deuteron electromagnetic current can be parametrized as [17, 18]

$$J_d^\mu(p_2, q_2) = \varepsilon_\rho^*(q_2) \left\{ \frac{(p_2 + q_2)_\mu}{2m_2} g_{\rho\sigma} F_1(k^2) \right. \quad (4)$$

$$\left. - \frac{(p_2 + q_2)_\mu k_\rho k_\sigma}{2m_2} F_2(k^2) - \Sigma_{\rho\sigma}^{\mu\nu} \frac{k^\nu}{2m_2} F_3(k^2) \right\} \varepsilon_\sigma(p_2),$$

where  $p_2$  and  $q_2$  are the deuteron 4-momenta in, respectively, the initial and the final state;  $k = q_2 - p_2$ ; and  $m_2$  is the deuteron mass. The polarization vectors of a spin-1 particle satisfy the relations

$$\varepsilon_\mu^*(\mathbf{k}, \lambda) \varepsilon^\mu(\mathbf{k}, \lambda') = -\delta_{\lambda\lambda'}, \quad k_\mu \varepsilon^\mu(\mathbf{k}, \lambda) = 0, \quad (5)$$

$$\sum_\lambda \varepsilon_\mu^*(\mathbf{k}, \lambda) \varepsilon_\nu(\mathbf{k}, \lambda) = -g_{\mu\nu} + \frac{k_\mu k_\nu}{m_2^2}.$$

The generator of infinitesimal Lorentz transformations is given by

$$\Sigma_{\rho\sigma}^{\mu\nu} = g_\rho^\mu g_\sigma^\nu - g_\sigma^\mu g_\rho^\nu. \quad (6)$$

The deuteron electromagnetic form factors  $F_i(k^2)$  are functions of the square of the photon 4-momentum. They are related to the electric, magnetic, and quadrupole form factors for the deuteron by the equations

$$F_C = F_1 + \frac{2}{3}\eta [F_1 + (1 + \eta)F_2 - F_3], \quad (7)$$

$$F_M = F_3, \quad F_Q = F_1 + (1 + \eta)F_2 - F_3,$$

$$\eta = -\frac{k^2}{4m_2^2}.$$

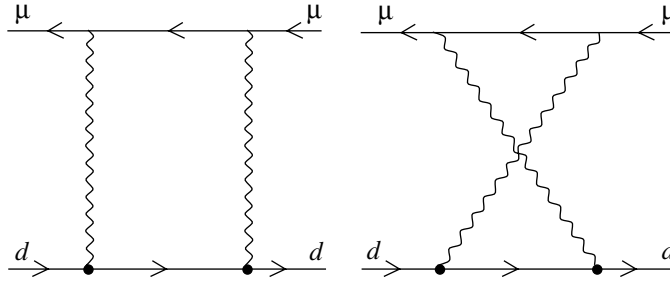
The lepton electromagnetic current has the form

$$J_l^\mu(p_1, q_1) \quad (8)$$

$$= \bar{u}(q_1) \left[ \frac{(p_1 + q_1)^\mu}{2m_1} - (1 + \kappa_l) \sigma^{\mu\nu} \frac{k_\nu}{2m_1} \right] u(p_1),$$

where  $p_1$  and  $q_1$  are the electron (muon) 4-momenta in, respectively, the initial and the final state;  $\sigma^{\mu\nu} = (\gamma^\mu \gamma^\nu - \gamma^\nu \gamma^\mu)/2$ ;  $\kappa_l$  is the lepton anomalous magnetic moment; and  $u(p)$  is a Dirac bispinor.

In order to derive the contribution of one-photon interaction to the Lamb shift, it is necessary to average the currents in (4) and (8) over the electron and



Nuclear-structure-induced corrections of order  $(Z\alpha)^5$ . Closed circles represent deuteron vertex operators.

deuteron spins. As a result, the contribution of order  $(Z\alpha)^4$  to the Lamb shift is expressed in terms of the deuteron charge radius as

$$E^{\text{Ls}} = \frac{2\mu^3}{3n^3} (Z\alpha)^4 [r_d^2 + F_M(0) - F_C(0)], \quad (9)$$

$$r_d^2 = \frac{6}{F_C(0)} \left. \frac{dF_C(k^2)}{dk^2} \right|_{k^2=0}.$$

For muonic deuterium at  $r_d = 2.094$  fm, the numerical value of this expression in the  $1S-2S$  splitting is  $-186.74$  meV. The contribution of the quadrupole magnetic term in (9)—it is proportional to  $[F_M(0) - F_C(0)] = 2\mu_d - 1$  ( $\mu_d$  is the deuteron magnetic moment) and coincides with that which was obtained in [19]—is 0.2%. We now consider two-photon-exchange amplitudes shown in the figure, which lead to corrections of order  $(Z\alpha)^5$  to the Lamb shift in deuterium. In processes of virtual Compton scattering, the intermediate state involves a spin-1 particle, a deuteron. The amplitudes describing the virtual Compton scattering of a lepton and a deuteron can be represented as

$$M_{\mu\nu}^{(l)} = \bar{u}(q_1) \left[ \gamma_\mu \frac{\hat{p}_1 + \hat{k} + m_1}{(p_1 + k)^2 - m_1^2} \gamma_\nu \right. \quad (10)$$

$$\left. + \gamma_\nu \frac{\hat{p}_1 - \hat{k} + m_1}{(p_1 - k)^2 - m_1^2} \gamma_\mu \right] u(p_1),$$

$$M_{\mu\nu}^{(d)} = \varepsilon_\rho^*(q_2) \left[ \frac{(q_2 + p_2 - k)_\mu}{2m_2} g_{\rho\lambda} F_1 \right. \quad (11)$$

$$- \frac{(q_2 + p_2 - k)_\mu}{2m_2} \frac{k_\rho k_\lambda}{2m_2^2} F_2$$

$$- \left. \Sigma_{\rho\lambda}^{\mu\alpha} \frac{k_\alpha}{2m_2} F_3 \right] \frac{-g_{\lambda\omega} + \frac{(p_2 - k)_\lambda (p_2 - k)_\omega}{m_2^2}}{(p_2 - k)^2 - m_2^2}$$

$$\times \left[ \frac{(p_2 + q_2 - k)_\nu}{2m_2} g_{\omega\sigma} F_1 \right.$$

$$\left. - \frac{(p_2 + q_2 - k)_\nu}{2m_2} \frac{k_\omega k_\sigma}{2m_2^2} F_2 + \Sigma_{\omega\sigma}^{\nu\beta} \frac{k_\beta}{2m_2} F_3 \right] \varepsilon_\sigma(p_2).$$

In order to single out the contribution of the  $2\gamma$  amplitudes to the Lamb shift, we average the amplitudes in (10) and (11) over the lepton and deuteron spins. Multiplying the resulting expressions, we represent the required quasipotential in the form (we use the FORM system of codes [20] for calculating the arising traces of the products of Dirac  $\gamma$  matrices and the contraction over Lorentz indices)

$$V_{2\gamma}^{\text{Ls}}(ed) = \frac{2m_1(Z\alpha)^2}{3m_2^2} \quad (12)$$

$$\times \int \frac{id^4k}{\pi^2} \frac{1}{(k^2)^2(k^4 - 4k_0^2m_1^2)(k^2 - 4k_0^2m_2^2)}$$

$$\times \left\{ 4F_1^2 m_2^2 k^2 (k^2 - k_0^2) [3m_2^2 - k^2 + k_0^2] \right.$$

$$+ 4F_1 F_2 (k^2 - k_0^2)^2 [k^4 - m_2^2 (k^2 + 2k_0^2)]$$

$$+ 4F_1 F_3 m_2^2 k^2 (k^2 - k_0^2) (k^2 - 2k_0^2)$$

$$- F_2^2 \frac{k^2 (k^2 - k_0^2)^2}{m_2^2} [k^4 - m_2^2 (k^2 + 3k_0^2)]$$

$$- 2F_1 F_3 k^4 (k^2 - k_0^2)^2$$

$$\left. + F_3^2 k^2 k_0^2 [-3k^4 + 4m_2^2 (2k^2 + k_0^2)] \right\}.$$

We now proceed to perform integration over four-dimensional Euclidean space with the aid of the relations

$$\int d^4k = 4\pi \int_0^\infty k^3 dk \int_0^\pi \sin^2 \phi \cdot d\phi, \quad k_0 = k \cos \phi. \quad (13)$$

Integration with respect to the angle  $\phi$  in (12) can then be performed analytically. Upon averaging, with Coulomb wave functions, the quasipotential obtained from (12), we obtain the respective contribution to the

Nuclear-structure-induced corrections of orders  $(Z\alpha)^4$  and  $(Z\alpha)^5$  to the Lamb shift in ordinary and muonic deuterium

$E^{Ls}$	$1S (Z\alpha)^4$	$1S (Z\alpha)^5$	$2S (Z\alpha)^4$	$2S (Z\alpha)^5$	$2S-1S (Z\alpha)^4$	$2S-1S (Z\alpha)^5$
( $ed$ ), kHz	$6.875 \times 10^3$	-0.603	$0.859 \times 10^3$	-0.075	$-6.016 \times 10^3$	0.527
( $\mu d$ ), meV	213.42	-2.94	26.68	-0.37	-186.74	2.57

energy spectrum in the form

$$\begin{aligned}
 E_{2\gamma}^{Ls} = & -\frac{\mu^3(Z\alpha)^5}{6m_1^3m_2^5(m_1^2 - m_2^2)\pi n^3} \quad (14) \\
 & \times \int_0^\infty \frac{dk}{k} \left\{ F_1^2 \left[ \frac{12m_1^2m_2^4}{k^3} (m_2^2h_1^3 - m_1^2h_2^3) \right. \right. \\
 & \left. \left. + \frac{1}{k} (m_2^4h_1^5 - m_1^4h_2^5) + (m_1^2 - m_2^2) \right] \right. \\
 & \times (10k^2m_1^2m_2^2 + 12m_1^2m_2^4 + k^4(m_1^2 + m_2^2)) \left. \right] \\
 & + \frac{F_1F_2}{2m_1^2m_2^2} \left[ \frac{1}{k} m_2^4h_1^5 (2m_1^2m_2^2 + k^2(2m_1^2 - m_2^2)) \right. \\
 & \left. - \frac{1}{k} m_1^6h_2^5 (k^2 + 2m_2^2) + k^2(m_1^2 - m_2^2) \right. \\
 & \left. \times (-10m_1^4m_2^4 + k^4(m_1^4 + m_1^2m_2^2 - m_2^4) \right. \\
 & \left. + 4k^2(3m_1^4m_2^2 - 2m_1^2m_2^4)) \right] \\
 & + \frac{F_2^2}{16m_1^2m_2^4} \left[ -h_2^7km_1^6 + h_1^5km_2^4(4m_1^2m_2^2 \right. \\
 & \left. + k^2(4m_1^2 - 3m_2^2)) + k^4(m_1^2 - m_2^2) \right. \\
 & \left. \times (-50m_1^4m_2^4 + k^4(m_1^4 + m_1^2m_2^2 - 3m_2^4) \right. \\
 & \left. + 2k^2(7m_1^4m_2^2 - 13m_1^2m_2^4)) \right] \\
 & + F_1F_3 \left[ \frac{4m_1^2m_2^2}{k} (m_1^2h_2^3 - m_2^2h_1^3) \right. \\
 & \left. - 2k(m_2^4h_1^3 - m_1^4h_2^3) - 2k^2(m_1^2 - m_2^2) \right. \\
 & \left. \times (8m_1^2m_2^2 + k^2(m_1^2 + m_2^2)) \right] \\
 & + \frac{F_2F_3}{2m_2^2} [h_2^5km_1^4 - h_1^5km_2^4 \\
 & - k^4(10m_1^2m_2^2 + k^2(m_1^2 + m_2^2))(m_1^2 - m_2^2)]
 \end{aligned}$$

$$\begin{aligned}
 & + F_3^2 \left[ -2h_2^3km_1^4 + h_1km_2^2(8m_1^2m_2^2 \right. \\
 & \left. + k^2(3m_1^2 - m_2^2)) + k^2(m_1^2 - m_2^2) \right. \\
 & \left. \times (6m_1^2m_2^2 + k^2(2m_1^2 - m_2^2)) \right] \left. \right\},
 \end{aligned}$$

where  $h_i = \sqrt{k^2 + 4m_i^2}$ . An analysis of the coefficients of the deuteron form factors in expression (14) reveals that, in the region of low  $k$ , there exist three terms involving an infrared divergence, which are proportional to  $F_1^2$ ,  $F_1F_2$ , and  $F_1F_3$ . In order to regularize these terms, the quasipotential in (12) must be supplemented, first of all, with an iteration term whose contribution to the Lamb shift of  $S$  energy levels can be represented as

$$\begin{aligned}
 \Delta E_{\text{iter}}^{Ls} \quad (15) \\
 = \langle [V_{1\gamma} \times G^f \times V_{1\gamma}]^{Ls} \rangle = -\frac{16\mu^4(Z\alpha)^5}{\pi n^3} \int_0^\infty \frac{dk}{k^4} \\
 \times \left[ F_1^2(0) + 2F_1(0)F_1'(0)k^2 + \frac{k^2}{3m_2^2} F_1(0)F_2(0) \right],
 \end{aligned}$$

where  $[G^f]^{-1} = (b^2 - \mathbf{p}^2)/2\mu_R$  is the inverse free two-particle Green's function [21],  $V_{1\gamma}$  is the quasipotential corresponding to one-photon interaction, and angular brackets denote averaging with Coulomb wave functions. In order to eliminate the divergence in the term proportional to  $F_1(k^2)F_3(k^2)$ , we additionally subtract from it the corresponding contribution for the pointlike deuteron [it is proportional to  $F_1(0)F_3(0)$ ]; of course, the corrections of order  $(Z\alpha)^5$  to the Lamb shift for the pointlike deuteron must be studied separately [22]. In order to perform numerical calculations with the aid of expression (14), we invoked up-to-date experimental data on the deuteron electromagnetic form factors [23]. In the region  $0 \leq k \leq 1.4$  GeV, there exist several parametrizations for these form factors. We relied on the parametrization [24]

$$\begin{pmatrix} F_C \\ F_Q \\ F_M \end{pmatrix} = F_D^2 \left( \frac{k^2}{4} \right) M(\eta) \begin{pmatrix} f_0 \\ f_1 \\ f_2 \end{pmatrix}, \quad (16)$$

where  $F_D$  is the nucleon dipole form factor,  $M(\eta)$  is a matrix that is formed by the coefficients of the variable  $\eta = k^2/4m_2^2$ , and

$$f_m = k^m \sum_{i=1}^4 \frac{a_{mi}}{\alpha_{mi}^2 + k^2}. \quad (17)$$

For each electromagnetic form factor, the parameters  $a_{mi}$  and  $\alpha_{mi}$  can be found in [24] (see also <http://www.daphnia.cea.fr/Sphn/T20/Parametrizations>). It should be noted that the parametrization in (16) leads to the deuteron charge radius of  $r_d = 2.094$  fm [23], a value that is 2.6% less than the value of  $r_d = 2.148$  fm, which is obtained from (2) by using the value of  $r_p$  from [11]. The results of our numerical calculations are given in the table. The momenta of integration that determine the main contribution in expression (14) have a specific nuclear scale. The value of 0.527 kHz that we obtained for the correction of order  $(Z\alpha)^5$  to the  $2S-1S$  splitting in ordinary deuterium is in agreement with the result obtained in [16], 0.49 kHz. In the case of muonic deuterium, the analogous contribution is 2.57 meV; in performing a comparison with future experimental data, one must take into account the total nuclear-structure-induced correction to the isotopic shift in muonic (ordinary) hydrogen [25, 26]; that is,

$$\Delta E_{\text{str}}^{\text{IS}}(1S-2S) = \begin{cases} (\mu p) - (\mu d) & 1.41 \text{ meV}, \\ (ep) - (ed) & 0.497 \text{ kHz}. \end{cases} \quad (18)$$

### 3. CORRECTIONS OF ORDER $(Z\alpha)^5$ TO THE HYPERFINE STRUCTURE IN DEUTERIUM

In constructing a quasipotential that describes the hyperfine splitting of the deuterium ground state, it is necessary to retain not only the terms in the operator  $\Sigma_{ij} = 2i\varepsilon_{ijk}S_2^k$  (6) that are proportional to the deuteron spin  $\mathbf{S}_2$  but also the terms in  $\Sigma_{0n}$  that are associated with the generator  $\Sigma$  of the Lorentz translations for a spin-1 particle. There exist two possibilities for determining the hyperfine part of the particle-interaction operator: (i) that of taking consistently into account, in calculating the contraction of amplitudes (10) and (11) in Lorentz indices, all terms that are associated with the operator  $(\mathbf{S}_1 \cdot \mathbf{S}_2)$  representing spin-spin interaction and (ii) that of employing special operators of projection onto the lepton and deuteron states characterized by the total spin of 3/2 and 1/2.

In the present study, we construct a quasipotential for the hyperfine structure in a covariant way by introducing, for particles in the initial and in the final state, the projection operators  $\hat{\pi}_{\mu,3/2}$  and  $\hat{\pi}_{\mu,1/2}$  as

$$\hat{\pi}_{\mu,3/2} = [u(p_1)\varepsilon_\mu(p_2)]_{3/2} = \Psi_\mu(P), \quad (19)$$

$$\sum_\lambda \Psi_\mu^\lambda \bar{\Psi}_\nu^\lambda = \frac{(\hat{P} + M)}{2M} \quad (20)$$

$$\times \left( g_{\mu\nu} - \frac{1}{3}\gamma_\mu\gamma_\nu - \frac{2P_\mu P_\nu}{3M^2} + \frac{P_\mu\gamma_\nu - P_\nu\gamma_\mu}{3M} \right),$$

$$\hat{\pi}_{\mu,1/2} = [u(p_1)\varepsilon_\mu(p_2)]_{1/2} \quad (21)$$

$$= \frac{i}{\sqrt{3}}\gamma_5 \left( \gamma_\mu - \frac{P_\mu}{M} \right) \Psi(P),$$

where the spin vector  $\Psi_\mu(P)$  and spinor  $\Psi(P)$  describe, respectively, spin-3/2 and spin-1/2 lepton-deuteron states;  $M = m_1 + m_2$  is the bound-state mass; and  $P = p_1 + p_2$ . Multiplying the amplitudes in (10) and (11) and taking into account relations (19)–(21), we can represent the sought hyperfine-structure quasipotential as

$$V_{2\gamma}^{\text{HFS}} = (Z\alpha)^2 \quad (22)$$

$$\times \int \frac{d^4k}{\pi^2} \frac{1}{(k^2)^2} \frac{1}{k^4 - 4k_0^2 m_1^2} \frac{1}{k^4 - 4k_0^2 m_2^2}$$

$$\times \left\{ 4F_1 F_3 \left[ 2(k_0^2 + k^2) - \frac{k^4}{m_2^2} \right] k^2 \mathbf{k}^2 \right.$$

$$+ 2F_2 F_3 \frac{k^4 \mathbf{k}^2}{m_2^2} \left( \frac{k^4}{m_2^2} - 4k_0^2 + \mathbf{k}^2 \right)$$

$$\left. + 2F_3^2 k^2 \mathbf{k}^2 \left( k_0^2 + \frac{k^4}{m_2^2} \right) \right\}.$$

The number of the form-factor terms decreased by a factor of 2 with respect to expression (14), since the spin-dependent terms associated with the second particle are proportional to  $F_3$ . Expression (22) appears to be less singular than the operator in (14). The only infrared divergence in (22) for  $k \rightarrow 0$  is due to the term proportional to  $F_1 F_3 k^2$ . This divergence can be completely removed with the aid of the iteration term of the quasipotential. By using Eqs. (4) and (8), this iteration term can be obtained in the form

$$\Delta V_{\text{iter}}^{\text{HFS}} = [V_{1\gamma} \times G^f \times V_{1\gamma}]^{\text{HFS}} \quad (23)$$

$$= \frac{32\mu(Z\alpha)^2}{3m_1 m_2} (\mathbf{S}_1 \cdot \mathbf{S}_2) \int_0^\infty \frac{dk}{k^2} F_1 F_3.$$

Upon subtracting the iteration term (23) from the quasipotential in (22), we calculate integrals with respect to angular variables in Euclidean momentum space and average the resulting expression with the Coulomb wave functions. As a result, the contribution of the  $2\gamma$  amplitudes to the hyperfine structure of

deuterium takes the form

$$\begin{aligned}
 E_{2\gamma}^{\text{HFS}} = E_{\text{D}}^{\text{F}} \frac{2(Z\alpha)}{\pi n^3} \int_0^\infty \frac{dk}{k^2} \quad (24) \\
 \times \left\{ \frac{F_3}{F_3(0)} \left[ 4F_1 + \frac{k^2}{m_2^2} (2F_1 - F_2 - F_3) + \frac{k^4}{m_2^4} F_2 \right] \right. \\
 \times \left[ \frac{m_1^2 m_2}{m_1^2 - m_2^2} \left( 1 + \frac{k^2}{4m_1^2} \right)^{3/2} \right. \\
 \left. - \frac{m_1 m_2^2}{m_1^2 - m_2^2} \left( 1 + \frac{k^2}{4m_2^2} \right)^{3/2} + \frac{k^3}{8m_1 m_2} \right] \\
 - \frac{F_3 k^2}{F_3(0)} \left( F_1 + \frac{F_3}{4} + \frac{3}{4} F_2 \frac{k^2}{m_2^2} \right) \\
 \times \left[ \frac{m_2}{m_1^2 - m_2^2} \left( 1 + \frac{k^2}{4m_1^2} \right)^{3/2} \right. \\
 \left. - \frac{m_1}{m_1^2 - m_2^2} \left( 1 + \frac{k^2}{4m_2^2} \right)^{3/2} \right. \\
 \left. + \frac{k^3 (m_1^2 + m_2^2)}{8m_1^3 m_2^3} + \frac{3k}{4m_1 m_2} \right] - 4\mu \left. \right\},
 \end{aligned}$$

where the Fermi energy of hyperfine splitting in the deuterium atom is

$$E_{\text{D}}^{\text{F}} = 2\mu_d \alpha^4 \frac{\mu^3}{m_e m_p} = 326\,967.678(4) \text{ kHz}. \quad (25)$$

Here,  $\mu_d = 0.857\,438\,228\,4(94)$  is the deuteron magnetic moment in nuclear-magneton units,  $\mu$  is the reduced mass of the deuterium atom, and  $m_p$  is the proton mass. A numerical integration in (24) was also performed with the aid of the deuteron form factors (16). As a result, the contribution of (24) to the hyperfine structure of ordinary deuterium is found to be

$$E_{2\gamma}^{\text{HFS}}(ed) = -34.72 \text{ kHz}. \quad (26)$$

Previously, the hyperfine splitting of the deuterium ground state was calculated analytically in [15] by using the zero-range approximation for the deuteron form factors. In this approximation, one disregards the wave function for the  $D$ -wave state of the deuteron and employs the asymptotic form  $Be^{-\beta r}$  for the  $S$ -state wave function. The result obtained in [15] for the respective contribution to the hyperfine structure has the form

$$\begin{aligned}
 \Delta E^{\text{HFS}}(ed) = -E_{\text{D}}^{\text{F}} \quad (27) \\
 \times \left[ \alpha \frac{m_e}{3\kappa} (1 + 2 \ln 2) - \frac{3\alpha m_e}{8\pi m_p} \ln \frac{\kappa}{m_e} \right.
 \end{aligned}$$

$$\begin{aligned}
 & \times \left( \mu_d - 2 - \frac{3}{\mu_d} \right) + \frac{3\alpha m_e}{4\pi m_p} \\
 & \times \ln \frac{\kappa}{m_p \mu_d} (\mu_p^2 - 2\mu_p - 3 + \mu_n^2) \left. \right] = -21.31 \text{ kHz},
 \end{aligned}$$

where  $\kappa = 45.7$  MeV is the inverse deuteron radius. The fact that the nuclear-structure-induced correction of order  $(Z\alpha)^5$  to the deuterium hyperfine structure in our case is significantly greater than the result obtained in [15] is due both to including all three of the deuteron form factors and to going beyond the zero-range approximation. The value that we obtained for  $E_{2\gamma}^{\text{HFS}}$  considerably increases the discrepancy between the theoretical and experimental results, which was 45 kHz without corrections coming from the deuteron structure and polarizability. In the case of muonic deuterium, the analogous contribution is

$$E_{2\gamma}^{\text{HFS}}(\mu d) = -0.925 \text{ meV}. \quad (28)$$

The error in the theoretical results (18), (26), and (28), as well as in those given in the table, is determined by errors in experimentally measuring the deuteron form factors, these errors amounting to 5% in the most significant range  $0 \leq k \leq 0.5$  GeV. Therefore, the theoretical error in the results obtained in the present study is about 10%. It is useful to compare the relative contribution of the nuclear-structure-induced corrections to the energy spectra of light and heavy hydrogen. For ordinary (muonic) hydrogen, the main one-loop contribution to the hyperfine structure is given by (Zemach correction) [27, 28]

$$\begin{aligned}
 \Delta E = E_{\text{F}} \frac{2\alpha\mu}{\pi^2} \int \frac{d\mathbf{p}}{(p^2 + b^2)^2} \quad (29) \\
 \times \left[ \frac{G_E(-\mathbf{p}^2) G_M(-\mathbf{p}^2)}{1 + \kappa} - 1 \right] \\
 = E_{\text{F}} (-2\mu\alpha) R_p, \quad b = \alpha\mu,
 \end{aligned}$$

where  $R_p$  is the Zemach radius. By using the parametrizations proposed for the proton electric and magnetic form factors in Mainz more than 20 years ago on the basis of an analysis of elastic electron scattering by protons [29], we obtain the following results:

$$\text{for ordinary hydrogen, } R_p = 1.067 \text{ fm}, \quad (30)$$

$$\delta_Z = -40.3 \times 10^{-6};$$

$$\text{for muonic hydrogen, } R_p = 1.064 \text{ fm}, \quad (31)$$

$$\delta_Z = -74.7 \times 10^{-4}.$$

The relative contribution of the nuclear-structure-induced corrections to the deuterium hyperfine structure that were obtained in the present study can be

written as follows:

$$\text{for ordinary deuterium, } \delta_{\text{crp}}^{\text{HFS}} = -106.19 \times 10^{-6}; \quad (32)$$

$$\text{for muonic deuterium, } \delta_{\text{crp}}^{\text{HFS}} = -188.37 \times 10^{-4}. \quad (33)$$

A threefold increase in the contributions given in (32) and (33) with respect to those in (30) and (31) is explained by the fact that the sizes of the region over which the deuteron charge and magnetic moment are distributed are considerably larger. The numerical values obtained for the muonic deuterium must be taken into account both in extracting the deuteron charge radius in future experiments devoted to determining the  $(\mu p)$ – $(\mu d)$  isotopic shift and in measuring the hyperfine structure.

### ACKNOWLEDGMENTS

We are grateful to I.B. Khriplovich and R.A. Sen'kov for enlightening discussions and to J. Ball and J. Jourdan for sending the numerical values of the parameters for the deuteron form factors.

This work was financially supported by the program Universities of Russia—Basic Research (project no. UR.01.02.016) and the Ministry for Higher Education of the Russian Federation (project no. EOO-3.3-45).

### REFERENCES

1. E. Borie and G. A. Rinker, *Rev. Mod. Phys.* **54**, 67 (1982).
2. J. Bernabeu and T. E. O. Ericson, *Z. Phys. A* **309**, 213 (1983).
3. S. G. Karshenboim, *Phys. Lett. A* **225**, 97 (1997).
4. E. V. Cherednikova, R. N. Faustov, and A. P. Martynenko, *Nucl. Phys. A* **703**, 365 (2002).
5. J. L. Friar, *Can. J. Phys.* **80**, 1337 (2002).
6. A. Pineda, *Phys. Rev. C* **67**, 025201 (2003).
7. F. Kottmann, F. Biraben, C. A. N. Conde, *et al.*, in *Proceedings of the Second Workshop on Quantum Electrodynamics and Physics of the Vacuum, QED 2000*, Ed. by G. Cantatore (2000), Vol. 564, p. 13.
8. G. Breit, *Rev. Mod. Phys.* **30**, 507 (1958).
9. A. Huber, Th. Udem, B. Gross, *et al.*, *Phys. Rev. Lett.* **80**, 468 (1998).
10. K. Pachucki, D. Leibfried, M. Weitz, *et al.*, *J. Phys. B* **29**, 177 (1996).
11. M. I. Eides, H. Grotch, and V. A. Shelyuto, *Phys. Rep.* **342**, 62 (2001).
12. D. J. Wineland and N. F. Ramsey, *Phys. Rev. A* **5**, 821 (1972).
13. F. E. Low and E. E. Salpeter, *Phys. Rev.* **83**, 478 (1951).
14. E. E. Salpeter, *Phys. Rev.* **89**, 92 (1953).
15. A. I. Mil'shtein, S. S. Petrosyan, and I. B. Khriplovich, *Zh. Éksp. Teor. Fiz.* **109**, 1146 (1996) [*JETP* **82**, 616 (1996)].
16. J. L. Friar and G. L. Payne, *Phys. Rev. A* **56**, 5173 (1997).
17. S. J. Brodsky and R. G. Parsons, *Phys. Rev.* **163**, 134 (1967).
18. S. J. Brodsky and J. R. Hiller, *Phys. Rev. D* **46**, 2141 (1992).
19. I. B. Khriplovich, A. I. Milstein, and R. A. Sen'kov, *Phys. Lett. A* **221**, 370 (1996).
20. J. A. M. Vermaseren, math-ph/0010025.
21. A. P. Martynenko and R. N. Faustov, *Teor. Mat. Fiz.* **64**, 179 (1985).
22. J. R. Sapirstein and D. R. Yennie, in *Quantum Electrodynamics*, Ed. by T. Kinoshita (World Sci., Singapore, 1990), p. 560.
23. D. Abbott *et al.*, *Eur. Phys. J. A* **7**, 421 (2000).
24. A. P. Kobushkin and A. I. Syamtomov, *Yad. Fiz.* **58**, 1565 (1995) [*Phys. At. Nucl.* **58**, 1477 (1995)].
25. K. Pachucki, *Phys. Rev. A* **53**, 2092 (1996).
26. A. P. Martynenko and R. N. Faustov, *Yad. Fiz.* **63**, 915 (2000) [*Phys. At. Nucl.* **63**, 845 (2000)].
27. A. C. Zemach, *Phys. Rev.* **104**, 1771 (1956).
28. G. T. Bodwin and D. R. Yennie, *Phys. Rev. D* **37**, 498 (1988).
29. G. G. Simon, Ch. Schmitt, F. Borkowski, and V. H. Walther, *Nucl. Phys. A* **333**, 381 (1980).

*Translated by A. Isaakyan*

## Atomic Effects in Tritium Beta Decay and Their Role in Determining the Ratio $G_A/G_V$ and the Lifetime of the Free Neutron

Yu. A. Akulov\* and B. A. Mamyrin

*Ioffe Institute for Physics and Technology, Russian Academy of Sciences,  
Politekhnicheskaya ul. 26, St. Petersburg, 194021 Russia*

Received March 26, 2003

**Abstract**—The helium-isotope mass-spectroscopy method for measuring the triton decay constant for various cases of the electron environment was used to determine the tritium half-life without allowance for decay to beta-electron bound states and to calculate the respective reduced half-life, which proved to be  $(fT_{1/2})_t = 1129.6 \pm 3.0$  s. The equations relating  $fT_{1/2}$  to  $G_A/G_V$  made it possible to obtain the value of  $(G_A/G_V)_t = -1.2646 \pm 0.0035$  and to estimate the neutron lifetime at  $\tau_n = 890.3 \pm 3.9(\text{stat.}) \pm 1.4(\text{syst.})$  s. © 2004 MAIK “Nauka/Interperiodica”.

### 1. INTRODUCTION

Since the tritium nucleus (triton) has a rather simple structure, it appears to be a convenient object of investigations aimed at determining constants that characterize beta processes. Until recently, however, attempts at analyzing theoretical models and at evaluating their parameters on the basis of data on triton beta decay did not lead to positive results, since the experimental values of the decay constant ( $\lambda$ ) and of the endpoint energy of the beta spectrum involved systematic uncertainties associated with final-state beta-electron interaction. According to the Fermi theory of beta decay, the probability of electron emission by nuclei and the spectrum of emitted electrons depend on the structure of that part of the electron phase space in the atomic or molecular system including a beta-active nucleus which is accessible to the nascent beta electron. In view of this, values determined experimentally for the decay constant and for the endpoint energy of the beta spectrum are sensitive to the electron environment of the nucleus being studied. The development of isotopic mass-spectroscopy methods for measuring the chemical shifts of the triton decay constant and the implementation of experiments devoted to measuring the difference of the half-lives for atomic and molecular tritium made it possible to determine the absolute value of the half-life ( $T_{1/2} = \ln 2/\lambda$ ) for atomic tritium. The availability of an experimental value of the half-life for atomic tritium permitted employing theoretical data on the chemical shifts of the half-life upon going over from the atom to the positively charged ion  ${}^3\text{H}^+$  (triton), whereby it was possible to determine the

absolute value of the free-triton half-life both for the case where only electrons of the continuous spectrum are formed and for the case where the decay to bound states in the  ${}^3\text{He}^+$  ion (this is an additional reaction channel) is taken into account. The determination of the triton half-life without allowing for decay to bound states enabled one to use, in calculating the reduced half-life, the mass difference between the tritium and  ${}^3\text{He}$  nuclei, which is known to a fairly high precision. This in turn made it possible to calculate the reduced (comparative) half-life of the triton with a small error and paved the way to deriving independent estimates for the free-neutron lifetime and for the ratio of the axial-vector and vector coupling constants for weak interaction.

### 2. DETERMINATION OF THE FREE-TRITON HALF-LIFE

In considering the process of beta-electron formation in the phase space of atomic or molecular systems containing tritium, one distinguishes three reaction channels: (i) a direct formation of a continuous-spectrum electron; (ii) the formation of a continuous-spectrum electron owing to the replacement of an orbital electron by a beta electron; and (iii) decay into bound states—that is, the formation of a beta electron in one of the shells of the daughter atom. For  ${}^3\text{H}^+$ , the value obtained by averaging the results of the calculations from [1–3] for the ratio of the probabilities of decay to bound states and decay to the continuous spectrum is  $\Delta\lambda_{bt}/\lambda = (1.07 \pm 0.04)\%$ . For the  ${}^3\text{H}$  atom, the relative enhancement of the decay rate due to the decay to bound states was calculated in [1, 3–5]; the result was

\* e-mail: akulov.mass@mail.ioffe.ru

$\Delta\lambda_{ba}/\lambda = (0.62 \pm 0.07)\%$ . Final-state beta-electron interaction with an orbital electron must lead to an enhancement of the triton decay rate in the  ${}^3\text{H}$  atom by  $\Delta\lambda_{ch}/\lambda \approx 0.15\%$  owing to the transition of this orbital electron to continuous-spectrum states [3, 6]. For tritium-containing systems where the phase space accessible to a beta electron is deformed in the vicinity of the triton by molecular orbitals, the results of the calculation of exchange corrections to the probability of beta decay are only qualitative.

In the case where beta decay leads to a direct formation of a continuous-spectrum electron in the Coulomb field of a nucleus, the effect of the electron environment on the phase-space factor ( $f$ ) is described by introducing a parameter that takes into account the screening of the nuclear charge by orbital electrons and a parameter that takes into account the reduction of the observed endpoint energy due to the formation of excited orbital-electron states upon the increase in the nuclear charge by unity [7]. Transitions triggered by the decay from the ground state end in the formation of the  $1s$  state of the  ${}^3\text{He}^+$  ion in about 70% of cases, the  $2s$  state in about 25% of cases, the  $3s$  state in about 1.3% of cases, and so on [6, 8]. This leads to an increase of  $\Delta\lambda_{ex}/\lambda \approx 0.50\%$  in the rate of triton decay in the atom [2, 3] in relation to the rate of free-triton decay. A detailed theoretical investigation of the screening effect was performed only for triton decay in the  ${}^3\text{H}$  atom and in the  ${}^3\text{H}^-$  ion [3], where the screening potential is formed by simple electron configurations ( $ns^1$  in the  ${}^3\text{He}^+$  ion and  $1s^2$ ,  $2s^2$ , and  $ns^1ms^1$  in the neutral helium atom). For the  ${}^3\text{H}$  atom, this leads to a decrease of  $\Delta\lambda_s/\lambda \approx 0.41\%$  in the decay constant  $\lambda$  in relation to its value for a free triton.

Thus, the total set of theoretical values of the corrections to the half-life for four possible atomic effects in beta decay—decay to bound states, the exchange effect, the screening of the nuclear charge by orbital electrons, and the excitation of orbital electrons—was obtained only for the free tritium atom. This means that the absolute value of the free-triton half-life can be calculated only by using the absolute value of the tritium-atom half-life, provided that the latter is determined experimentally. A method for determining the difference of the triton decay constants by comparing the rates of growth of the ratios of the content of radiogenic  ${}^3\text{He}$  and reference  ${}^4\text{He}$  in samples was proposed in [9]. The method was used to measure the difference of beta-decay constants for atomic and molecular tritium. The experimental scheme assumed the creation of two identical samples of a gaseous mixture that contained  ${}^4\text{He}$  and molecular tritium, one of the samples then being subjected to an external effect with the aim of

causing a transition of tritium to an atomic state. In order to obtain thermalized free atoms of tritium, use was made of resonance dissociation triggered by the mechanism where the energy necessary for breaking the interatomic bond in  ${}^3\text{H}_2$  molecules came from an impact of the second kind in the interaction with mercury atoms that were excited in a high-frequency discharge. On the basis of data from five series of mass-spectroscopy measurements of helium isotopic ratios—test amounts of a helium mixture from a molecular and an atomic sample were alternately supplied to the chamber in each of these series—the relative change in the beta-decay constant in going over from molecular to atomic tritium was determined to be  $(\lambda_a - \lambda_m)/\lambda_m = 0.00257 \pm 0.00045$  [10], where the error corresponded to one standard deviation and was due primarily to the scatter between the series in determining helium isotopic ratios.

The above result makes it possible to determine the absolute value of the atomic-tritium half-life, since the half-life of molecular tritium was measured in direct experiments. The weighted mean value of the two estimates of the molecular-tritium half-life that were published most recently and which are in good agreement with each other—one was obtained by the helium-isotope method [11], while the other was derived from the decay curve constructed by recording beta-electron bremsstrahlung [12]—is  $\langle(T_{1/2})_m\rangle = 12.296 \pm 0.017$  yr. Considering that  $\Delta T_{1/2}/T_{1/2} = -\Delta\lambda/\lambda$  for  $\Delta\lambda/\lambda \ll 1$ , we obtain  $(\Delta T_{1/2})_{ma} = (T_{1/2})_m - (T_{1/2})_a = 0.0316 \pm 0.0055$  yr. Therefore, the absolute value of the atomic-tritium half-life is  $(T_{1/2})_a = 12.264 \pm 0.018$  yr, the error in this value being almost completely determined by the uncertainty in  $\langle(T_{1/2})_m\rangle$ . Since  $\langle(T_{1/2})_m\rangle$  and  $(\Delta T_{1/2})_{ma}$  were determined by using experimental procedures that make it possible to allow for all beta-decay channels, the value obtained for  $(T_{1/2})_a$  corresponds to the total probability of atomic-tritium decay (that is, it takes into account both processes producing continuous-spectrum electrons and decay into bound states). In this case, all four corrections for atomic effects in the free tritium atom must be taken into account in going over from  $(T_{1/2})_a$  to the triton half-life  $(T_{1/2})_t$ . Considering that the atomic corrections are much less than unity,  $(T_{1/2})_t$  can be determined from the relation

$$\begin{aligned} (T_{1/2})_a &= \left(1 + \frac{\Delta\lambda_{ba} + \Delta\lambda_{ch} + \Delta\lambda_{ex} - \Delta\lambda_s}{\lambda}\right) \\ &= (T_{1/2})_t \left(1 + \frac{\Delta\lambda_{bt}}{\lambda}\right), \end{aligned} \quad (1)$$

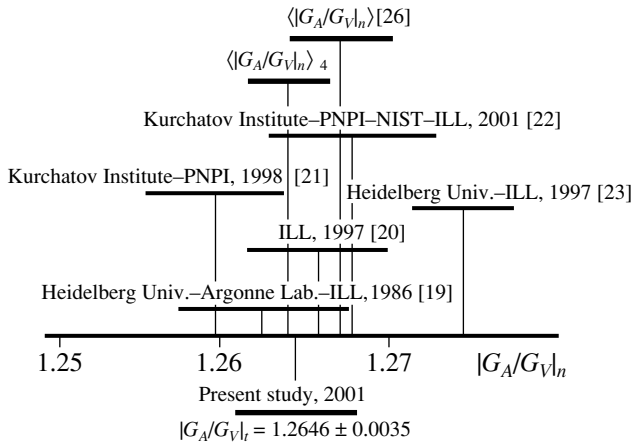


Fig. 1. Results of studies devoted to determining  $G_A/G_V$ .

where the second term in the parenthetical expression on the right-hand side of this equality is due to the change in  $(T_{1/2})_t$  because of decay to the bound states in the  ${}^3\text{He}^+$  ion. Making use of the above theoretical values of the atomic corrections and of the experimental value of  $(T_{1/2})_a$ , we find from relation (1) that the triton half-life is  $(T_{1/2})_t = 12.238 \pm 0.020$  yr.

In the case where one only takes into account the effect of the Coulomb field of the nucleus on the beta spectrum (that is, one calculates the phase-space factor with the standard Fermi function and disregards decay to bound states), the half-life assumes the value of  $(T_{1/2})_t^{\text{cont}} = 12.369 \pm 0.020$  yr. The value  $(T_{1/2})_t^{\text{cont}}$  must also be used in calculating the reduced triton half-life  $fT_{1/2}$  if the upper boundary of the energy interval of integration of the beta spectrum is set to the quantity obtained by subtracting the recoil energy of the helium nucleus from the nuclear mass difference between tritium and  ${}^3\text{He}$ —that is, if the difference of the orbital-electron binding energies in the initial and final atomic and molecular systems is disregarded.

### 3. DETERMINATION OF THE RATIO OF THE AXIAL-VECTOR AND VECTOR COUPLING CONSTANTS FOR WEAK INTERACTIONS IN HADRON-LEPTON PROCESSES

The nuclear mass difference between tritium and  ${}^3\text{He}$  that is determined from the weighted mean value according to the results of 11 independent experiments [13, 14] is  $(18\,529 \pm 2)$  eV +  $m_e c^2$ . The recoil energy of the helium atom is 3.4 eV, in which case  $E = (18\,525.6 \pm 2)$  eV +  $m_e c^2$ . By employing

the procedure according to which the phase-space factor is calculated with allowance for the Coulomb interaction of the beta electron with a nucleus of finite size and mass and for processes involving virtual photons and charged particles originating from beta decay (radiative corrections being included to terms of order  $\alpha^2$ ) [15], it can be found for the above value of  $E$  that  $f = (2.894 \pm 0.006) \times 10^{-6}$ , in which case  $(fT_{1/2})_t = 1129.6 \pm 3.0$  s.

For allowed beta transitions, including triton beta decay, the quantity  $fT_{1/2}$  is related to the vector and the axial-vector matrix element ( $M_V$  and  $M_A$ , respectively) of the beta-decay Hamiltonian by the equation [16]

$$fT_{1/2} = \frac{k/G_V^2}{|M_V|^2 + (G_A/G_V)^2|M_A|^2}, \quad (2)$$

where  $G_V$  and  $G_A$  are, respectively, the vector and the axial-vector coupling constant for weak hadron-lepton interaction and  $k$  is a constant coefficient. Since the relations  $|M_V| = \sqrt{2}$  and  $|M_A| = 0$  hold for  $0^+ \rightarrow 0^+$  transitions within isospin multiplets characterized by the total isospin  $T = 1$  and the final-state isospin projection  $T_z = 0$  and since  $|M_V|_t = 1$  for triton beta decay, the application of Eq. (2) to the case of the triton and  $0^+ \rightarrow 0^+$  transitions leads to the relation

$$(1 + (G_A/G_V)_t^2|M_A|_t^2)(fT_{1/2})_t = 2(fT_{1/2})_{0^+ \rightarrow 0^+}. \quad (3)$$

The result obtained for  $(fT_{1/2})_{0^+ \rightarrow 0^+}$  by using data on eight purely Fermi transitions is  $3072.3 \pm 0.9(\text{stat.}) \pm 1.1(\text{syst.})$  s [17]. The value of  $|M_A|_t = \sqrt{3} \times (0.962 \pm 0.002)$  was calculated by Saito *et al.* [18], who considered five modifications of the intranuclear potential and showed that, for wide variations of the potential shape and of the structure of the wave functions for the tritium and  ${}^3\text{He}$  nuclei, the axial-vector matrix element exhibits a relatively low sensitivity to the existence of delta isobars and exchange currents. Using relation (3), we find at the above values of  $(fT_{1/2})_t$ ,  $(fT_{1/2})_{0^+ \rightarrow 0^+}$ , and  $|M_A|_t$  that  $(G_A/G_V)_t = -1.2646 \pm 0.0035$ .

For the mixed transition  $n \rightarrow p + e^- + \bar{\nu}$ , the ratio of the axial-vector and vector coupling constants for weak interaction,  $(G_A/G_V)_n$ , is determined from data obtained by measuring a coefficient that characterizes the asymmetry of beta-electron emission with respect to the decaying-neutron spin. The results of four such experiments— $(G_A/G_V)_n = -1.262 \pm 0.005$  [19],  $(G_A/G_V)_n = -1.266 \pm 0.004$  [20],  $(G_A/G_V)_n = -1.2594 \pm 0.0038$  [21], and  $(G_A/G_V)_n = -1.2686 \pm 0.0046 \pm$

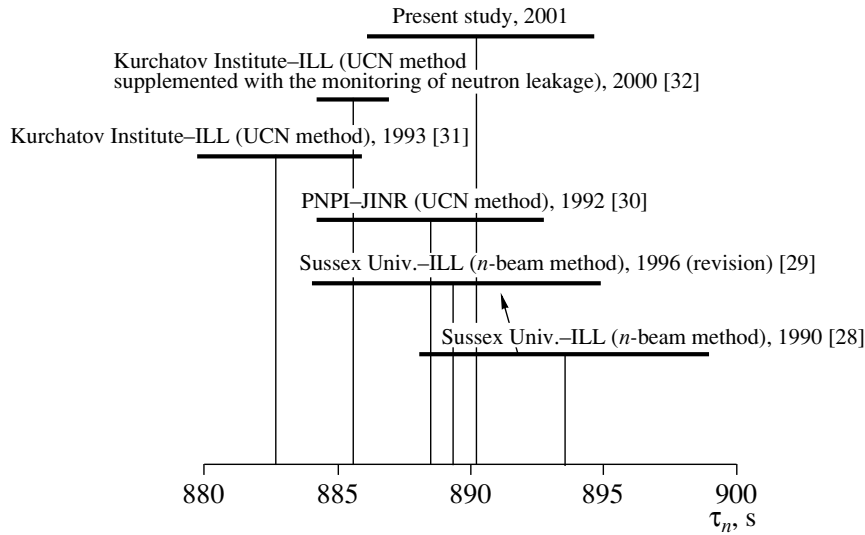


Fig. 2. Results of studies devoted to determining the neutron lifetime.

0.0007 [22]—agree within the quoted errors, the respective weighted mean value being  $\langle(G_A/G_V)_n\rangle_4 = -1.2637 \pm 0.0023$ , which complies well with the value of  $(G_A/G_V)_t$  (Fig. 1), whence we conclude that the ratio  $G_A/G_V$  can be viewed as a universal fundamental constant that characterizes beta processes. At the same time, it is worthy of note that, for the ratio of the axial-vector and vector coupling constants, Abele *et al.* [23] obtained the value of  $(G_A/G_V)_n = -1.274 \pm 0.003$ , which differs sizably from  $(G_A/G_V)_t$ . Should this result be confirmed, there will arise the question of whether axial-vector interaction can be partly suppressed in the presence of pion exchange in the triton.

#### 4. DETERMINATION OF THE FREE-NEUTRON LIFETIME

Neutron decay, as well as triton decay, belongs to the class of allowed transitions; that is, the use of relation (2) makes it possible to represent the free-neutron half-life  $(T_{1/2})_n$  in the form

$$(T_{1/2})_n = \frac{k/G_V^2}{f_n [|M_V|_n^2 + (G_A/G_V)_n^2 |M_A|_n^2]}, \quad (4)$$

where  $f_n$  is the phase-space factor and  $(M_V)_n$  and  $(M_A)_n$  are, respectively, the vector and the axial-vector matrix element of the neutron-beta-decay Hamiltonian. Owing to the fact that the values of these matrix elements are known exactly,  $|M_V|_n = 1$  and  $|M_A|_n = \sqrt{3}$ , the neutron half-life can be expressed as follows by taking the ratio of relation (2)

for the case of triton beta decay and relation (4):

$$(T_{1/2})_n = \frac{(fT_{1/2})_t [1 + |M_A|_t^2 (G_A/G_V)_t^2]}{f_n [1 + 3(G_A/G_V)_n^2]}. \quad (5)$$

Upon taking into account the proton recoil energy, the energy of the  $n \rightarrow p$  transition—it is given by  $m_n c^2 - m_p c^2 = (782\,333 \pm 6) \text{ eV} + m_e c^2$  [24]—takes the value of  $(E_{\text{max}})_n = 781\,582 \pm 6 \text{ eV}$ , the phase-space integral determined according to the procedure developed in [25] and with allowance for radiative corrections of order  $\alpha$  and for the finiteness of the nuclear size and mass being  $f_n = 1.71487 \pm 0.00015$ .

Assuming that the ratio of the coupling constants for weak interaction is universal,  $(G_A/G_V)_n = (G_A/G_V)_t = G_A/G_V = -1.2641$ , we find for the above values of  $f_n$ ,  $|M_A|_t$ , and  $(fT_{1/2})_t$  that  $(T_{1/2})_n = 618.1 \pm 2.7 \text{ s}$ , which corresponds to the average free-neutron lifetime of  $\tau_n = 891.7 \pm 3.9 \text{ s}$  with respect to beta decay. Since the parameter determining the sensitivity of  $(T_{1/2})_n$  to variations of  $G_A/G_V$  in expression (5) is small,  $[1/(T_{1/2})_n][d(T_{1/2})_n/d(G_A/G_V)] = 0.018$ , an error of about 0.01 in determining  $G_A/G_V$  would lead to an uncertainty in  $(T_{1/2})_n$  below 0.1 s.

Upon taking into account the value of  $(G_A/G_V)_n$  from [23], the calculation of the average ratio of the axial-vector and the vector coupling constant for weak interaction in neutron beta decay yields  $\langle(G_A/G_V)_n\rangle = -1.2670 \pm 0.0030$  [26], which differs from  $(G_A/G_V)_t$ . Under the assumption that the distinction between  $(G_A/G_V)_t$  and  $(G_A/G_V)_n$  is

significant, the value determined for the neutron half-life from relation (5) is  $(T_{1/2})_n = 616.1$  s; that is,  $\tau_n = 888.9$  s. Considering the shift of  $\tau_n$  due to the possible distinction between  $(G_A/G_V)_t$  and  $(G_A/G_V)_n$  as the systematic component of the error in the method used to determine  $\tau_n$ , one can propose the following interval of possible values of the neutron lifetime with respect to beta decay:  $\tau_n = (890.3 \pm 3.9(\text{stat.}) \pm 1.4(\text{syst.}))$  s [27].

Figure 2 shows the latest experimental results for the free-neutron lifetime, which were obtained by counting decay events in a calibrated neutron beam [28, 29] or by determining the parameters of the decay exponent for an ensemble of ultracold neutrons (UCN) [30–32]. From the displayed data, it can be seen that the average free-neutron lifetime obtained with allowance for the results of measurements by the helium-isotope mass-spectroscopy method supports high values of the neutron lifetime. In this connection, it should be noted that measurements of  $\tau_n$  in experiments with ultracold neutrons are plagued by a poorly controllable systematic uncertainty that stems from the escape of neutrons from gravitational traps and which must result in the reduction of the observed values of  $\tau_n$ .

## 5. CONCLUSION

A new helium-isotope method for measuring the triton decay constant in various tritium-containing compounds has been developed. By using data from the elaborate theory of atomic effects accompanying the decay of a free triton and the decay of the triton in a tritium atom, the value of the free-triton half-life has been extracted from the results of helium-isotope measurements both with and without allowance for decay to bound states. This has enabled us to obtain a precise estimate of the reduced triton half-life. For the first time, the ratio of the axial-vector and the vector coupling constant for weak interaction has been obtained for the three-nucleon nucleus of tritium. Good agreement between the resulting value and the value of this ratio for the neutron leads to the conclusion that the ratio  $G_A/G_V$  is invariant with respect to the presence of strong interaction in the form of pion exchange in beta-active nuclei, and this gives sufficient grounds to consider the ratio  $G_A/G_V$  as a universal fundamental constant that characterizes beta processes. By using data on triton beta decay, we have determined the free-neutron lifetime with respect to beta decay. A comparison of this neutron-lifetime value with the results obtained for  $\tau_n$  by measuring the parameters of the decay exponent for an ensemble of ultracold neutrons and by counting decay events in a calibrated neutron beam supports high values of  $\tau_n$ .

## ACKNOWLEDGMENTS

This work was supported by the Russian Foundation for Basic Research (project no. 01-03-32777), the State Research and Technological Program Fundamental Metrology (project no. 4.06), and the Program of the Russian Academy of Sciences Neutron Physics and Standard Model.

## REFERENCES

1. V. N. Tikhonov and F. E. Chukreev, *Vopr. At. Nauki Tekh., Ser.: At. Metalloved.*, No. 1(4), 12 (1980).
2. B. Budick, *Phys. Rev. Lett.* **51**, 1034 (1983).
3. M. R. Harston and N. C. Pyper, *Phys. Rev. A* **48**, 268 (1993).
4. P. M. Sherk, *Phys. Rev.* **75**, 789 (1949).
5. J. N. Bahcall, *Phys. Rev.* **124**, 495 (1961).
6. W. S. Haxton, *Phys. Rev. Lett.* **55**, 807 (1985).
7. K.-E. Bergkvist, *Phys. Scr.* **4**, 23 (1971).
8. E. G. Drukarev, *Phys. Rev. C* **54**, 3277 (1996).
9. Yu. A. Akulov, B. A. Mamyrin, and P. M. Shikhaliev, *Pis'ma Zh. Tekh. Fiz.* **19**, 72 (1993).
10. Yu. B. Akulov and B. A. Mamyrin, *Pis'ma Zh. Éksp. Teor. Fiz.* **68**, 167 (1998).
11. Yu. A. Akulov, B. A. Mamyrin, L. V. Khabarin, *et al.*, *Pis'ma Zh. Tekh. Fiz.* **14**, 940 (1988).
12. B. Budick, J. Chen, and H. Lin, *Phys. Rev. Lett.* **67**, 2630 (1991).
13. B. Budick, J. Chen, and H. Lin, *Phys. Rev. Lett.* **67**, 2626 (1991).
14. H. Kawakami, S. Kato, T. Ohshima, *et al.*, *Phys. Lett. B* **256**, 105 (1991).
15. D. H. Wilkinson and B. E. F. Macefield, *Nucl. Phys. A* **232**, 58 (1974).
16. R. J. Blin-Stoyle, *Fundamental Interactions and the Nucleus* (North-Holland, Amsterdam, 1973; Mir, Moscow, 1976).
17. Yu. V. Gaponov and Yu. A. Mostovoi, *Yad. Fiz.* **63**, 1432 (2000) [*Phys. At. Nucl.* **63**, 1356 (2000)].
18. T.-Y. Saito, Y. Wu, S. Ishikawa, and T. Sasakawa, *Phys. Lett. B* **242**, 12 (1990).
19. P. Bopp, D. Dubbers, L. Hornig, *et al.*, *Phys. Rev. Lett.* **56**, 919 (1986).
20. P. Liaud *et al.*, *Nucl. Phys. A* **612**, 53 (1997).
21. B. G. Yerozolimsky, I. A. Kuznetsov, Yu. A. Mostovoi, and I. V. Stepanenko, *Yad. Fiz.* **61**, 572 (1998) [*Phys. At. Nucl.* **61**, 507 (1998)].
22. Yu. A. Mostovoi, I. A. Kuznetsov, V. A. Solovei, *et al.*, *Yad. Fiz.* **64**, 2040 (2001) [*Phys. At. Nucl.* **64**, 1955 (2001)].
23. H. Abele, S. Baebler, D. Dubbers, *et al.*, *Phys. Lett. B* **407**, 212 (1997).
24. P. J. Mohr and B. N. Taylor, *J. Phys. Chem. Ref. Data* **28**, 1713 (1999).
25. D. H. Wilkinson, *Nucl. Phys. A* **377**, 474 (1982).
26. Particle Data Group (K. Hagiwara *et al.*), *Phys. Rev. D* **66**, 010001 (2002).

27. Yu. A. Akulov and B. A. Mamyrin, *Proc. XXXV St. Petersburg Nucl. Phys. Inst. Winter School on Physics of the Atomic Nucleus and Elementary Particles* (PIYaF, St. Petersburg, 2001), p. 81.
28. J. Byrne *et al.*, *Phys. Rev. Lett.* **65**, 289 (1990).
29. J. Byrne, *Europhys. Lett.* **33**, 187 (1996).
30. V. P. Alfimenkov, V. V. Nesvizhevskii, A. P. Serebrov, *et al.*, *Zh. Éksp. Teor. Fiz.* **102**, 740 (1992) [*Sov. Phys. JETP* **75**, 405 (1992)].
31. L. N. Bondarenko, V. I. Morozov, Yu. N. Panin, and A. I. Fomin, *Pis'ma Zh. Éksp. Teor. Fiz.* **64**, 382 (1996) [*JETP Lett.* **64**, 416 (1996)]; V. Mampe, L. N. Bondarenko, V. I. Morozov, *et al.*, *Pis'ma Zh. Éksp. Teor. Fiz.* **57**, 77 (1993) [*JETP Lett.* **57**, 82 (1993)].
32. S. Arzumanov, L. Bondarenko, S. Chernyavsky, *et al.*, *Nucl. Instrum. Methods Phys. Res. A* **440**, 511 (2000).

*Translated by A. Isaakyan*

## Microscopics of Mesonic Degrees of Freedom in Nucleons and Mesons in Nuclei: Quasielastic Meson Knockout by High-Energy Electrons

V. G. Neudatchin, I. T. Obukhovskiy, L. L. Sviridova, and N. P. Yudin\*

*Institute of Nuclear Physics, Moscow State University, Vorob'evy gory, Moscow, 119899 Russia*

Received February 3, 2003; in final form, August 26, 2003

**Abstract**—The following questions are considered: (i) that of what quasielastic-knockout reactions are; (ii) that of what experience has been gained in measuring, in various channels, the momentum distributions and spectroscopic factors of nucleons and clusters in nuclei and of electrons in atoms, molecules, and solid-state bodies; (iii) that of how it is possible to introduce the concept of quasielastic knockout in the theory of meson-electroproduction processes  $p(e, e'm)B$  at beam energies of a few GeV and at moderate values of the square of the virtual-photon 4-momentum,  $Q^2 = 2-4$  (GeV/c)<sup>2</sup>; and (iv) that of how the momentum distributions of mesons in various channels of virtual proton decay,  $p \rightarrow B + \pi$ ,  $p \rightarrow B + \rho$ , and  $p \rightarrow Y + K$ , are predicted on the basis of the microscopic model of a fluctuation of the QCD vacuum in a nucleon. Proposals for relevant experiments are formulated. It is indicated that quasielastic-knockout processes like  $(e, e'\pi)$  provide the best way to study the problem of a scalar pion condensate in nuclei. In conclusion, it is emphasized that quasielastic processes  ${}^2H(e, e'p)B$  involving various spectator baryons  $B$  are of great value for determining the composition of multi-quark configurations in nucleon–nucleon systems. © 2004 MAIK “Nauka/Interperiodica”.

### 1. INTRODUCTORY COMMENTS: CONCEPT OF QUASIELASTIC PARTICLE KNOCKOUT AND ITS GENERALIZATION TO THE CASE OF MESON KNOCKOUT

The idea of employing quasielastic nucleon knockout from a nucleus by high-energy protons,  $(p, 2p)$  and  $(p, pn)$ , was formulated by the famous theorists Chew, Low, and Goldberger as far back as the 1950s [1]. The essence of this idea is that it is necessary to record, in coincidence, such events in which the projectile particle transfers a considerable part of its primary energy to the knock-on particle, the process—in particular, its kinematics—being close to free scattering: the final spectator nucleus,  $A - x$ , has a relatively low recoil momentum. By exploring, for example, the angular correlation between the scattered and the knock-on particle, we then obtain [2], instead of a delta function of angles (as in the case of free scattering), a rather narrow peak, whose height and shape characterize the momentum distribution of knock-on particles  $x$  in the irradiated nucleus in a specific channel,  $A_i \rightarrow (A - x)_f + x$ . This channel is singled out with the aid of the energy-conservation law. The smallness of the width of the angular peak in question is due to the fact that the momentum of the particle  $x$  in the nucleus,  $|\mathbf{k}|$ , is much lower than its momentum in the final state of the knockout

process,  $|\mathbf{k}'|$ . Accordingly, the binding energy of the particle  $x$  in the nucleus must also be much lower than its final-state energy. It is important to note that the shape of the momentum distribution of a knock-on particle makes it possible to determine its orbital angular momentum in the nucleus unambiguously. This physical situation of quasielastic knockout corresponds to the pole diagram in Fig. 1a. It is obvious that, if we do not consider exotic systems possessing some incomprehensible properties, the concept being discussed can be used to analyze any system experimentally—only the values of the projectile energy and of the momentum transfer are of importance here. Among numerous experimental results concerning  $(p, 2p)$  processes, we would like to highlight those that were obtained at the Petersburg Nuclear Physics Institute (PNPI, Gatchina) by investigating, in a 1-GeV proton beam, the momentum distributions of nucleons in the lowest  $0s$  shell of medium-mass and heavy nuclei (there, the nucleon binding energy lies in the range 60–70 MeV) [3]. Also, the quasielastic knockout of clusters in  $(p, p\alpha)$  processes in  $1p$ -shell nuclei was studied by using 200-MeV protons [4]. A feature peculiar to such moderate energies is that the quasielastic-knockout process is diagonal in the internal state of the alpha particle involved:  $p + \alpha_0 \rightarrow p' + \alpha_0$ . Here, the theory that admits the clustering of nucleons in nuclei and which relies on the multiparticle shell model [5]

\* e-mail: yudin@helena.sinp.msu.ru

was well confirmed. This theory, which, in the 1960s, was the subject of lively discussions in Moscow, produced the following interesting result: if, in the reaction  $^{16}\text{O}(p, p\alpha)^{12}\text{C}^*$ , for example, summation is performed over all levels of the spectator nucleus  $^{12}\text{C}$  that are excited upon alpha-particle emission, the sum of all spectroscopic factors—that is, the total probability of finding, in this process, an alpha particle in the  $^{16}\text{O}$  target nucleus—will be approximately equal to 13, which is due to a combinatorial factor that reflects the identity of nucleons.

Later on, it was shown [6, 7] that, if the proton-beam energy is increased to values in the range 600–1000 MeV, in which case processes of multiple proton rescattering already play a significant role, the reaction of quasielastic cluster knockout acquires a qualitatively new character—namely, amplitudes for processes in which a virtually excited cluster  $\alpha^*$  of nonzero intrinsic orbital angular momentum goes over to the ground state under the effect of a proton impact ( $\alpha^* \rightarrow \alpha_0$ ) and leaves the nucleus (the energies of knock-on particles are then about 100 MeV) become dominant. In this way, there arise pronounced anisotropies of momentum distributions in what is concerned with the orientation of the recoil momentum  $\mathbf{p}'$  of the final-state nucleus  $A - 4$  with respect to the beam axis and with respect to the plane of fast-proton scattering (Treiman–Yang anisotropy) [6, 7]. Unfortunately, such an exclusive  $(p, p\alpha)$  experiment has yet to be performed.

To conclude this brief survey of the potential of the quasielastic-knockout method (which has not yet become a popular tool among specialists in elementary-particle physics), we would like to note that, in the 1960s, it was proposed to study multielectron systems in atoms, molecules, and solid-state bodies by means of quasielastic processes of the  $(e, 2e)$  type at beam energies of a few keV [8]. An implementation of this proposal yielded highly seminal results [9, 10]. For example, a direct visualization of the hybridization of  $s$  and  $p$  orbitals in carbon atoms was obtained for various organic molecules ( $\text{CH}_4$  and so on). Further, the effect of Coulomb short-range correlations in atoms and molecules was revealed most comprehensively. By way of example, we indicate that, in the quasielastic-knockout reaction  $\text{He}(e, 2e)\text{He}^+$ , the satellite excited state  $\text{He}^+(2p)$ , with the momentum distribution of knock-on electrons being characteristic of precisely the  $2p$  state, was observed in addition to the main, most probable, transition to the  $\text{He}^+(1s)$  level. This corresponds to a relatively small  $(2p)^2$  admixture to the dominant electron configuration  $(1s)^2$  in the wave function for the ground-state helium atom. Such an experiment could be of use for nuclear physics as well, where the short-range

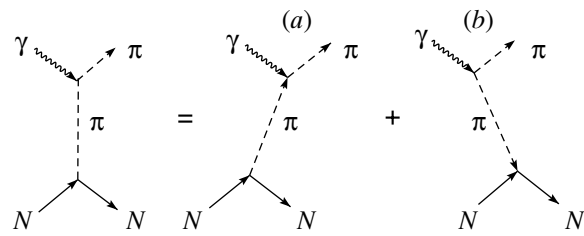


**Fig. 1.** Pole diagram for quasielastic pion knockout from a nucleon.

part of the nucleon–nucleon interaction also leads to small admixtures of higher configurations in the wave functions for ground-state nuclei.

Let us now proceed to consider directly  $(e, e\pi)$  processes on nucleons and nuclei at electron energies of a few GeV and knock-on-pion energies of about 1 GeV. First of all, we note that, in relation to the nonrelativistic approach outlined above, a new point arises here in a similar consideration in the laboratory frame—namely, there appears yet another pole diagram, the  $z$  diagram in Fig. 1b (it involves the production of a virtual  $\pi^+\pi^-$  pair). The amplitudes associated by the diagrams in Figs. 1a and 1b differ only by the pole denominators. If the contribution of more complicated diagrams is suppressed owing to the choice of quasielastic kinematics, the inclusion of two diagrams instead of one does not present any problem.

Second, we note that, although the theory of meson electroproduction in  $p(e, e'\pi^+)n$  processes has not yet been discussed in terms of quasielastic knockout, the problem of the pole diagram has already arisen. For example, the following important circumstance was noticed: in the limit of an indefinitely great square  $Q^2$  of the virtual-photon 4-momentum, the meson pole is dominant [11], if we digress from the fact that, at the values of  $Q^2 = 1-3 (\text{GeV}/c)^2$  and  $Q^2 \geq 10 (\text{GeV}/c)^2$ , which are of importance for us, the process is governed by totally different mechanisms (see below). Further, the differential cross section for the reaction  $p(e, e'\pi^+)n$  as a function of  $Q^2$  was studied experimentally in the range between 0.3 and 4  $(\text{GeV}/c)^2$  [12]. Below, we will see that, by and large, the data obtained in this way correspond to quasielastic kinematics and provide strong evidence in support of the pole approximation. The point is that the quantity  $Q^2$  is roughly proportional to the final momentum of the knock-on pion, so that the kinematics of quasielastic knockout arises at not overly high values of this quantity,  $Q^2 \simeq 1-3 (\text{GeV}/c)^2$ . As  $Q^2$  grows further, the mechanism of the process of course changes, and quark degrees of freedom, which have nothing to do with the projection onto

soft meson–baryon channels, come into play for  $Q^2 \geq 10$  (GeV/c)<sup>2</sup>. On the other hand, pion photoproduction ( $Q^2 = 0$ ), for which the fact that the pion is bound in a nucleon plays a fundamental role, receives commensurate contributions from two diagrams, the  $t$ -pole and the  $s$ -pole one [13].

All of these issues are discussed in Section 2. In Section 3, we consider the projection of the quark wave function describing a nucleon and involving an admixture of a scalar  $^3P_0$  quark–antiquark fluctuation of the QCD vacuum onto pion–baryon channels of  $N \rightarrow B + \pi$  virtual decays, where  $B = N, \Delta, N^*, N^{**}$ . These channels can be efficiently investigated precisely in quasielastic processes belonging to the  $p(e, e'\pi^+)B$  type and involving longitudinal virtual photons, the spectroscopic factors and the momentum distributions of pions being substantially different in these channels. The channels  $N \rightarrow Y + K, Y = \Lambda, \Sigma$  are considered in a similar way.

In Section 4, we show that the quasielastic process in question on a nucleus,  $A(e, e'\pi)A^*$ , is likely to be the most efficient tool for studying the problem of a pion condensate in nuclei. In Section 5, we discuss some prospects for the application of the method of quasielastic pion knockout.

## 2. PROBLEMS ASSOCIATED WITH THE DOMINANCE OF THE $t$ -POLE DIAGRAM

The question of whether it is possible to describe pion electroproduction on nucleons at high energies of a knock-on pion in terms of the pion-pole mechanism in the  $t$  channel (see Fig. 1) has been repeatedly discussed in the literature [11, 14]. Here, the fact that, in relation to the cross section for the pole mechanism in the  $t$  channel, the cross section associated with the main competing mechanism of the nucleon pole in the  $s$  channel dies out in proportion to  $Q^{-4}$  with increasing virtual-photon 4-momentum  $q_\mu$  ( $Q^2 = -q^2$ ) [11] is a compelling argument in support of this. The calculation of the pole mechanism (Fig. 1) in [11, 14] was performed within light-front dynamics.

In contrast to [15], the analysis of the pion-electroproduction process  $p(e, e'\pi)n$  in [11, 14] was performed in the laboratory frame by employing experience gained in calculating quasielastic particle knockout from atoms and nuclei [5–8]. In the laboratory frame, the kinematical region of low momenta of final-baryon recoil and high energies of the knock-on meson—that is, the region of quasielastic knockout—is singled out in a natural way. The quasielastic knockout of electrons from atomic orbitals or of nucleons and clusters from nuclei is a

nonrelativistic process, which can adequately be described in terms of the diagram in Fig. 1a exclusively. Quasielastic pion knockout from a nucleon is a relativistic process; therefore, it is necessary to include in the consideration the  $z$  diagram in Fig. 1b—that is, the diagram representing the process in which the production of a  $\pi^+\pi^-$  pair is followed by the absorption of one of the pions by a nucleon. The amplitudes corresponding to these two diagrams differ only by their pole denominators (crossing symmetry); therefore, the inclusion of one additional diagram does not complicate the calculation. The sum of the diagrams in Figs. 1a and 1b will correspond to introducing the relativistic propagator

$$\frac{1}{k^2 - m_\pi^2} \sim \frac{1}{E_\pi(\mathbf{k}) - k_0} + \frac{1}{E_\pi(\mathbf{k}) + k_0},$$

where  $k = (k_0, \mathbf{k})$  is the virtual-pion 4-momentum and  $E_\pi(\mathbf{k}) = \sqrt{\mathbf{k}^2 + m_\pi^2}$ .

In [15], the pion, rho-meson, and omega-meson wave functions in a nucleon were obtained on the basis of general principles of field theory. The respective calculations relied on the assumption that, in the case of quasielastic kinematics, the pole diagrams in Fig. 1 are dominant. In [16], the role of competing diagrams—in particular, the  $s$ -pole diagram—was analyzed under various kinematical conditions.

The role of the pole diagram in the  $t$  and  $s$  channels was compared at various values of  $Q^2$  (the actual values of  $Q^2$  in the experiment reported in [12] were in the range 1–3 (GeV/c)<sup>2</sup>). This analysis was performed both for longitudinal virtual and for transverse photons, a comparison with the case of photoproduction being performed in the latter case. (As was shown previously in [15], reactions featuring longitudinal virtual photons furnish information about the pion cloud of a nucleon, while reactions involving transverse photons probe its rho-meson cloud).

It was found that, at sufficiently high values of the virtual-photon mass ( $Q^2 \geq 2$  (GeV/c)<sup>2</sup>), the  $s$ -pole diagram is immaterial both for the longitudinal and for the transverse cross section. Here, the situation is dominated by the  $t$ -pole diagram involving a virtual pion in the case of longitudinal photons and a rho meson in the case of transverse photons. At  $Q^2 = 0.7$  (GeV/c)<sup>2</sup>, the interference between the pion-pole amplitudes in the  $t$  and  $s$  channels still makes a non-trivial contribution to the longitudinal cross section.

A few diagrams are significant in the case of photoproduction. A fundamental difference between the cases of electro- and photoproduction is that, in photoproduction, quasielastic knockout is impossible since a real photon cannot be absorbed by a free meson—that the process does in fact occur is entirely due to the fact that mesons are bound in nucleons.

Therefore, the pole diagrams in Fig. 1 are not dominant here.

In analyzing experimental data on pion electroproduction at  $Q^2 = 0.7\text{--}3.3$  (GeV/c)<sup>2</sup> and the total c.m. energy of about 2 GeV [12], three pieces of evidence were found in support of the statement that the  $t$ -pole mechanism is dominant in this region (that is, that the relative contribution of the  $s$ -pole diagram is small).

First, it was found that, in the case of quasielastic kinematics and the energies of the knock-on pion that vary within a rather broad range, experimental data from [12] lead to the same momentum distribution, as this must be for the pole mechanism (see Fig. 2).

Second, a direct calculation of the pole diagram in the  $s$  channel revealed that its contribution is very small [16].

Third, the result that we extracted, from pion-electroproduction experiments, for the momentum distribution of pions in a nucleon is in excellent agreement with that which we obtained on the basis of the separable pion–nucleon potential introduced by Saito and Afnan [17]. This potential in turn was determined by using phase shifts of pion–nucleon scattering, which are totally independent data. The separate potential proposed in [18] leads to a somewhat different wave function (see Fig. 2).

The scheme for calculating the momentum distribution of pions in a nucleon is briefly as follows. An element of the cross section for the quasielastic knockout of particle  $a$  from a composite system  $T$  by an incident particle  $x$  ( $T + x \rightarrow R + a + x'$ ) has the form

$$d^9\sigma_{\text{quasi-elastic}} = A^2 T^2 \frac{d\mathbf{p}'_x}{E_x} \frac{d\mathbf{p}_a}{E_a} \frac{d\mathbf{p}_R}{E_R} \quad (1)$$

$$\times \delta^4(p_T + p_x - p'_x - p_a - p_R),$$

where  $p_R$  is the 4-momentum of the  $R = T - a$  system;  $A$  is the amplitude of the virtual decay  $T \rightarrow R + a$ , and  $T$  is the amplitude of the quasifree scattering  $x + a^* \rightarrow x' + a$  of the incident particle  $x$  by constituent  $a$ . An element of the cross section for this quasifree scattering is given by

$$d^6\sigma_{\text{elastic}}^{\text{free}} = T^2 \frac{d\mathbf{p}'_x}{E_x} \frac{d\mathbf{p}_a}{E_a} \delta^4(p_{a^*} + p_x - p'_x - p_a). \quad (2)$$

Upon integration with respect to the absolute values of  $p'_x$  and  $p_a$ , the cross section for free scattering reduces to the form

$$d^2\sigma_{\text{elastic}}^{\text{free}} = T^2 \frac{p_a}{p'_x} d\Omega_a \left[ 1 - \frac{E_a}{p_a} \cos(\mathbf{p}_a, \mathbf{p}'_x) \right]. \quad (3)$$

Integrating the cross-section element in (1) with respect to  $\mathbf{p}_R$  and  $p_a$  and using Eq. (3), we obtain

$$\frac{d^5\sigma}{dE'_x d\Omega'_x d\Omega_a} \quad (4)$$

$$= A^2 \frac{E'_x{}^2}{E_T} \left[ 1 - \frac{E_a}{p_a} \cos(\mathbf{p}_a, \mathbf{p}'_x) \right] \frac{d^2\sigma_{\text{elastic}}^{\text{free}}}{d\Omega_a}.$$

Apart from kinematical factors, the amplitude  $A$  is proportional to the wave function for particle  $a$  in the virtual-decay channel  $T \rightarrow a + R$   $\Psi_T^{Ra}(\mathbf{k})$  ( $\mathbf{k}$  is the momentum of particle  $a$ ). Thus, we eventually have

$$\frac{d^5\sigma}{dE'_x d\Omega'_x d\Omega_a} = E_x^2 |\Psi_T^{Ra}(\mathbf{k})|^2 \quad (5)$$

$$\times \left[ 1 - \frac{E_a}{p_a} \cos(\mathbf{p}_a, \mathbf{p}'_x) \right] \frac{d^2\sigma_{\text{elastic}}^{\text{free}}}{d\Omega_a}.$$

These formulas are quite general in the sense that they are applicable to the quasielastic knockout of any constituents from a composite system, including the knockout of electrons from an atom and nucleons from a nucleus. We will now consider the specific problem of quasielastic pion knockout from nucleons by electrons of energy about a few GeV:  $p + e \rightarrow n + \pi^+ + e'$ . In the present case, quasielastic kinematics is realized if the square of the virtual-photon 4-momentum and the total c.m. energy take values in, respectively, the region  $Q^2 > 1$  (GeV/c)<sup>2</sup> and the interval  $W = 2\text{--}3$  GeV. We denote the kinematical variables by  $p_T = p_N = p$ ,  $p_R = p'$ , and  $p_a = k'$ .

As was shown in [15], the momentum distribution of virtual pions in a nucleon can be extracted from experimental data on the longitudinal cross section for pion electroproduction (that is, from the cross section corresponding to longitudinal virtual photons). As to the transverse cross section, it provides information about the momentum distribution of virtual rho mesons.

Figure 2 shows the results that we obtained by extracting, from experimental data reported in [12], the momentum distribution of pions in a nucleon. The fact that experimental data at different  $Q^2$  values fit in the same curve is a strong indication of a quasidelectric character of the process in question and of the suppression of all diagrams, other than those in Fig. 1. Also illustrated in this figure is the Yukawa asymptotic behavior for the pion–nucleon vertex:  $k^2/(k^2 - m_\pi^2)$ .

The quantity obtained by integrating the square of the wave function with respect to the momentum  $k$  is equal to the spectroscopic factor  $S_p^{n\pi}$ , which is equal to the effective number of pions in a nucleon. For this, our result is  $S_p^{n\pi} \simeq 0.25$ .

From experimental data on the transverse cross section for pion electroproduction on nucleons at  $Q^2 = 3.3$  (GeV/c)<sup>2</sup>, we have determined the rho-meson wave function in the region of momenta that

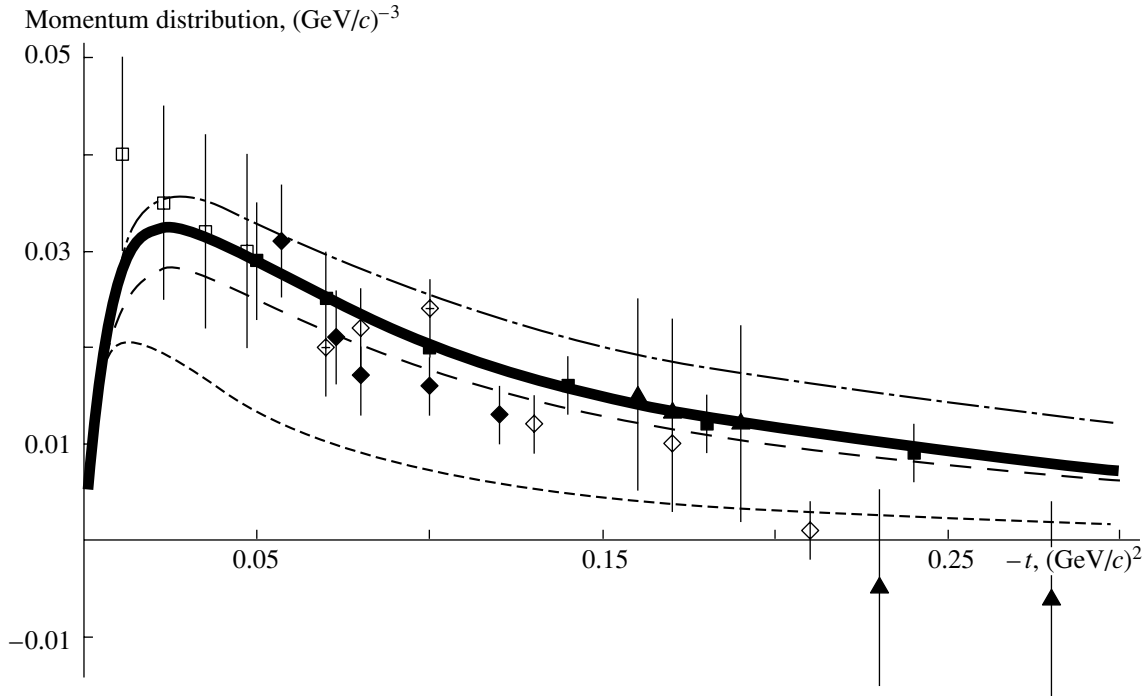


**Fig. 2.** Momentum distribution of pions in a nucleon,  $|\Psi_p^\pi(k^2)|^2$ , as a function of  $t = k^2$ : (solid curve) results of the calculation from [15], (long dashes) wave function obtained for the Afnan pion–nucleon potential, (short dashes) wave function obtained from the Lee potential, and (dash-dotted curve, which corresponds to the Yukawa asymptotic behavior) approximation of the vertex form factor  $g_{\pi NN}(k^2)$  by unity. The experimental data from [12] are presented for the following values of  $Q^2$  [(GeV/c) $^2$ ]: (open boxes) 0.35, (closed boxes) 0.70, (closed diamonds) 1.19, (open diamonds) 2.00, and (closed triangles) 3.32.

are low in relation to the meson mass. These experimental data cover an overly narrow interval of virtual-rho-meson momenta. In view of this, it was proposed in [16] to make use of data on photoproduction. However, it turned out that the result derived for the cutoff parameter  $\Lambda_\rho$  in the vertex function  $g_{\rho NN}(\mathbf{k}^2)$  from photoproduction data differs significantly from the  $\Lambda_\rho$  value extracted from electroproduction data. Moreover, problems associated with gauge invariance become nontrivial in calculating photoproduction. At low virtual-meson momenta, these problems are immaterial, and the value that was deduced from photoproduction data for the cutoff parameter in the pion vertex function  $g_{\pi NN}(\mathbf{k}^2)$  is  $\Lambda_\rho = 0.7$  GeV/c, which complies with that which was obtained from electroproduction data.

A transition from plane waves to taking into account final-state interaction between the knock-on pion and a spectator nucleon must be the next step in the theoretical analysis of electro- and photoproduction.

### 3. PION AND KAON WAVE FUNCTIONS IN A NUCLEON IN VARIOUS CHANNELS WITHIN THE MODEL OF A $^3P_0$ SCALAR QUARK–ANTIQUARK FLUCTUATION OF A QCD VACUUM

In [15], the analysis of quasielastic pion knockout was phenomenological and was based on the simplest effective Lagrangians that describe the interaction between pion and nucleon fields. Valuable possibilities that the concept of quasielastic pion knockout provides in solving fundamental problems of hadron physics were considered in [19]. Here, we mean the quark microscopics of meson–baryon degrees of freedom as a whole. At the present time, these issues are being discussed within a phenomenological concept of effective fields [20] with allowance for only hadron degrees of freedom, within a semimicroscopic model that describes the interaction of quarks directly with mesons [21], and within the microscopic model of a  $^3P_0$  scalar quark–antiquark fluctuation of the QCD vacuum [22]. In the present study, we consider two possibilities within the scheme of a  $^3P_0$  quark fluctuation. A possible connection between this scheme and a global quark condensate, which has the same quantum numbers as the  $^3P_0$  fluctuation, is an additional argument in favor of analyzing the scheme in

question first of all. This model was used previously to obtain the decay widths of dibaryon resonances [23], but our group was the first to disclose its potential for analyzing quasielastic meson knockout. The  $N \rightarrow B + \pi$  and  $N \rightarrow Y + K$  channels have not yet been considered within this model. Also, the concepts of wave functions, momentum distributions, and spectroscopic factors were introduced for the first time within the model being discussed.

An appropriate formalism was developed for calculating meson momentum distributions and spectroscopic factors microscopically. This formalism involves the following ingredients. First, these are models that describe the structure of nucleons, baryons, and mesons. Second, there is a rearrangement of quark coordinates between the nucleon ( $qqq$ ) and the fluctuation ( $q\bar{q}$ ) subsystem in the formation of mesons (a pion and a kaon) and final spectator baryons (since, these mesons, for example, do not feature a spin of  $S = 1$ , which is peculiar to the fluctuation in question). Third, the above rearrangement is used to project the macroscopic wave function for the  $q^4\bar{q}$  system onto the virtual-decay channels  $N \rightarrow B + \pi$  and  $N \rightarrow Y + K$  with the aid of known quark wave functions for final-state particles. By way of example, we indicate that, in the  $qqq + q\bar{q}$  system, one determines the wave functions describing the relative motion of the  $B-\pi$  and  $Y-K$  subsystems—that is, the respective momentum distributions. This approach is an analog of the well-known theory of cluster degrees of freedom in nuclei [24], which is based on the formalism of the multiparticle shell model.

Let us now consider some details of the method used. In the momentum representation, a  ${}^3P_0$  scalar quark–antiquark fluctuation of the QCD vacuum is described in terms of the particle-creation operator  $T$ ,

$$T = -\nu \sum_{\alpha, \bar{\beta}} d\mathbf{p}_q d\mathbf{p}_{\bar{q}} \delta(\mathbf{p}_q + \mathbf{p}_{\bar{q}}) C_{\alpha, \bar{\beta}} F_{\alpha, \bar{\beta}} \quad (6)$$

$$\times Z(\mathbf{p}_q \mathbf{p}_{\bar{q}}) \sum_m (1m1 - m|00) X_{\alpha, \bar{\beta}}^m Y_1^{-m}(\mathbf{p}_q - \mathbf{p}_{\bar{q}})$$

$$\times b_{\alpha}^+(\mathbf{p}_q) d_{\bar{\beta}}^+(\mathbf{p}_{\bar{q}}),$$

where  $b_{\alpha}^+$  and  $d_{\bar{\beta}}^+$ , with  $\alpha = \{s_{\alpha}, f_{\alpha}, c_{\alpha}\}$  and  $\bar{\beta} = \{s_{\bar{\beta}}, f_{\bar{\beta}}, c_{\bar{\beta}}\}$  being the spin, flavor, and charm indices of the quark and antiquark, respectively, are relevant creation operators;  $C_{\alpha, \bar{\beta}}$  and  $F_{\alpha, \bar{\beta}}$  are, respectively, the color-singlet and the flavor-singlet wave function;  $X_{\alpha, \bar{\beta}}^m$  is the spin-triplet wave function; and  $Y_1^{-m}(\mathbf{p}_q - \mathbf{p}_{\bar{q}})$  is a spherical harmonic. The phenomenological constant  $\nu$  specifies the degree of polarization of the QCD vacuum. It is normalized to the pion–nucleon

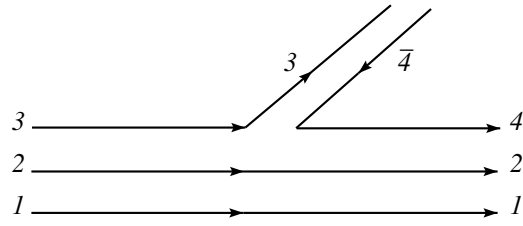


Fig. 3. Quark pattern of pion production.

coupling constant  $G_{\pi NN} \left( \nu = -\frac{3}{5} G_{\pi NN} (2\pi)^{3/2} \right)$ .

The function  $Z(\mathbf{p}_q \mathbf{p}_{\bar{q}})$  describes the spatial characteristics of the  $q\bar{q}$  fluctuation—in particular, its shape and dimensions. Usually, this function is approximated by unity,  $Z(\mathbf{p}_q \mathbf{p}_{\bar{q}}) = 1$ ; concurrently, it is assumed that the phenomenological nucleon-radius parameter  $b$  also reflects the degree of the spatial localization of the  ${}^3P_0$  fluctuation.

The amplitude of the virtual decay  $N \rightarrow B + \pi^{\lambda}$ ,  $\lambda = 0, \pm 1$ , is given by

$$M(N \rightarrow B + \pi^{\lambda}) = \langle B \pi^{\lambda} | T | N \rangle, \quad (7)$$

where  $T|N$  characterizes  $(1234\bar{4})$  quark system,  $B$  characterizes the  $(124)$  system, and  $\pi$  stands for the  $(3\bar{4})$  system (see Fig. 3).

This expression can be recast into the form

$$M(N \rightarrow B + \pi^{\lambda}) = \langle B | 3H_{\lambda} | N \rangle, \quad (8)$$

where the factor of 3 reflects the identity of three quarks and the operator  $H_{\lambda}$  is defined as

$$H_{\lambda}(\boldsymbol{\rho}'_2, \boldsymbol{\rho}_2) = \nu \exp \left\{ i \frac{2}{3} \mathbf{k} \cdot \boldsymbol{\rho}'_2 \right\} \tau_{-\lambda}^{(3)} \hat{O}(\boldsymbol{\rho}'_2, \boldsymbol{\rho}_2) \quad (9)$$

$$\times \boldsymbol{\sigma}^{(3)} \cdot \left[ \frac{E_{\pi}(\mathbf{k})}{2m_q} \left( \frac{2}{i} \nabla_{\boldsymbol{\rho}_2} + \frac{2}{3} \mathbf{k} \right) + \left( 1 + \frac{E_{\pi}(\mathbf{k})}{6m_q} \right) \mathbf{k} \right].$$

Here,  $\boldsymbol{\rho}_2 = (\mathbf{r}_1 + \mathbf{r}_2)/2 - \mathbf{r}_3$ ;  $\boldsymbol{\rho}'_2 = (\mathbf{r}_1 + \mathbf{r}_2)/2 - \mathbf{r}_4$ ;  $\mathbf{r}_i$  is the coordinate of the  $i$ th quark;  $\mathbf{k}$  is the virtual-pion momentum;  $E_{\pi}(\mathbf{k}) = \sqrt{\mathbf{k}^2 + m_{\pi}^2}$ ;  $\boldsymbol{\sigma}^{(3)}$  and  $\boldsymbol{\tau}^{(3)}$  are, respectively, the spin and isospin Pauli matrices for the third quark;  $\lambda = 0, \pm 1$  are the indices of the spherical components of the vector  $\boldsymbol{\tau}^{(3)}$  that correspond to the pion  $\pi^{\lambda}$ ; and  $m_q = 313$  MeV is the constituent quark mass. The nonlocal kernel  $\hat{O}(\boldsymbol{\rho}'_2, \boldsymbol{\rho}_2)$  has the form

$$\hat{O}(\boldsymbol{\rho}'_2, \boldsymbol{\rho}_2) = \exp \left( i \frac{1}{2} \mathbf{k} \cdot (\boldsymbol{\rho}'_2 - \boldsymbol{\rho}_2) \right) \quad (10)$$

$$\times \frac{1}{(4\pi b_{\pi})^{3/2}} \exp \left( \frac{1}{4\pi b_{\pi}^2} (\boldsymbol{\rho}'_2 - \boldsymbol{\rho}_2)^2 \right),$$

which involves the wave function for the pion as a  $q\bar{q}$  system. This wave function is chosen in the Gaussian

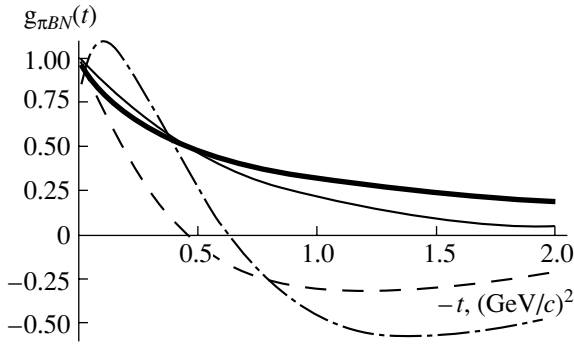


**Fig. 4.** Form factors in  $\pi BN$  vertices: (thin solid curve)  $g_{\pi NN}(k^2)$ , (dashed curve)  $g_{\pi N^*N}(k^2)$ , (dash-dotted curve)  $g_{\pi N^{**}N}(k^2)$ , and (thick solid curve)  $g_{\pi NN}(k^2) = (\Lambda_\pi^2 - m_\pi^2)/(\Lambda_\pi^2 + |k^2|)$  with  $\Lambda_\pi = 0.7$  (GeV/c) $^2$ .

form  $\Psi_\pi(\rho^2) \sim \exp(-\rho^2/4b_\pi^2)$ , where  $b_\pi$  is the pion radius.

In (8),  $|N\rangle$  and  $|B\rangle$  are baryon wave functions; that is,

$$\begin{aligned}
 |N\rangle &= |s^3[3]_x L=0\rangle_{\text{TISM}} & (11) \\
 &\times |[1^3]_c([21]_S \circ [21]_T)[3]_{ST} : [1^3]_{CST}\rangle, \\
 |\Delta\rangle &= |s^3[3]_x L=0\rangle_{\text{TISM}} \\
 &\times |[1^3]_c([3]_S \circ [3]_T)[3]_{ST} : [1^3]_{CST}\rangle, \\
 |N^*(1535)\rangle &= |s^2p[21]_x L=1\rangle_{\text{TISM}} \\
 &\times |[1^3]_c([21]_S \circ [21]_T)[21]_{ST} : [21]_{CST}\rangle_{[1^3]_x CST}^{J=1}, \\
 |N^{**}(1440)\rangle &= |sp^2[3]_x L=0\rangle_{\text{TISM}} \\
 &\times |[1^3]_c([21]_S \circ [21]_T)[3]_{ST} : [1^3]_{CST}\rangle,
 \end{aligned}$$

where  $[f]$  are Young diagrams in various subspaces and the abbreviation TISM stands for the translation-invariant shell model.

Upon averaging the squares of the amplitudes for  $N \rightarrow B + \pi$  subprocesses over the initial spin projections and performing summation of the result over the final spin projections, we obtain

$$|M^{qm}(N \rightarrow N\pi)|^2 = G_{\pi NN}^2 g_{\pi NN}^2 \cdot 2\mathbf{k}^2, \quad (12)$$

$$|M^{qm}(N \rightarrow \Delta\pi)|^2 = G_{\pi \Delta N}^2 g_{\pi \Delta N}^2 \cdot 2\mathbf{k}^2,$$

$$|M^{qm}(N \rightarrow N^*\pi)|^2 = G_{\pi N^*N}^2 g_{\pi N^*N}^2 \cdot 2E_\pi^2(\mathbf{k}),$$

$$|M^{qm}(N \rightarrow N^{**}\pi)|^2 = G_{\pi N^{**}N}^2 g_{\pi N^{**}N}^2 \cdot 2\mathbf{k}^2,$$

where the vertex constants are

$$G_{\pi NN} = 5 \frac{1}{N} \left(1 + \frac{m_\pi}{6m_q}\right) G_{\pi qq}, \quad (13)$$

$$G_{\pi \Delta N} = \frac{4\sqrt{2}}{5} G_{\pi NN},$$

$$G_{\pi N^*N} = \frac{2\sqrt{2}}{5\sqrt{3}} \frac{3-2a}{3m_q b(1+m_\pi/6m_q)} G_{\pi NN},$$

$$\begin{aligned}
 G_{\pi N^{**}N} &= \frac{1}{3\sqrt{3}} \left[ 3a + \frac{m_\pi}{m_q} \frac{1}{1+m_\pi/6m_q} \right. \\
 &\quad \left. \times \left(1 - \frac{1}{3}a + \frac{5}{9}a\right) \right] G_{\pi NN}.
 \end{aligned}$$

Here,  $a = x^2(1+2x^2/3)^{-1}$ ,  $x = b_\pi/b$ ,  $N = (1+2x^2/3)^{3/2}$ , and  $G_{\pi NN}^2/4\pi \simeq 14$ .

The form factors in the respective meson–baryon vertices are given by

$$g_{\pi NN}(\mathbf{k}^2) = g_{\pi \Delta N}(\mathbf{k}^2) = \exp\left\{-\frac{1}{6}\mathbf{k}^2 b^2 \left(1 + \frac{a}{6}\right)\right\}, \quad (14)$$

$$g_{\pi N^*N}(\mathbf{k}^2) = \left[1 - \frac{\mathbf{k}^2 b^2}{6} \frac{3+a}{3-2a}\right.$$

$$\left. \times \left(1 + \frac{E_\pi(\mathbf{k})}{6m_q} - \frac{4a}{9}\right)\right] g_{\pi NN}(\mathbf{k}^2),$$

$$g_{\pi N^{**}N}(\mathbf{k}^2) = \left[\frac{m_\pi}{m_q} \frac{1}{1-m_\pi/6m_q}\right.$$

$$\left. \times \left(1 - \frac{a}{3} + \frac{5a^2}{9}\right) + 3a\right]^{-1} \frac{1 + E_\pi(\mathbf{k})/6m_q}{1 + m_\pi/m_q}$$

$$\times \left[\frac{E_\pi(\mathbf{k})}{m_q} \frac{1}{1 + E_\pi(\mathbf{k})/6m_q} \left(1 - \frac{a}{3} + \frac{5a^2}{9}\right)\right.$$

$$\left. - \frac{\mathbf{k}^2 b^2}{18} a \left(1 + \frac{a}{3}\right)^2\right] + 3a$$

$$\left. - \frac{\mathbf{k}^2 b^2}{2} \left(1 + \frac{a}{3}\right)^2\right] g_{\pi NN}(\mathbf{k}^2).$$

With the aid of these expressions, the wave function is calculated by the formula

$$|\overline{\Psi}_p^{n\pi}(\mathbf{k})|^2 = \frac{|M(p \rightarrow n + \pi)|^2}{(k_0 - E_\pi(\mathbf{k}))^2}. \quad (15)$$

Figure 4 shows the form factors  $g_{\pi BN}(\mathbf{k}^2)$  in the respective meson–baryon vertices. It can be seen that all three curves representing  $g_{\pi BN}(\mathbf{k}^2)$  for  $B = N$ ,  $N^*$ , and  $N^{**}$  differ from one another strongly, which will make it possible to test our model in experiments easily. The expression for  $g_{KY N}(\mathbf{k}^2)$  is similar to that in (14).

The momentum distribution calculated for the  $p \rightarrow n + \pi$  channel is in fairly good agreement with that which was extracted in [15] from the experimental data reported in [12]. For other channels, where  $B = \Delta$ ,  $N^*(3/2^-, 1/2^-)$ , and  $N^{**}(1/2^+, \text{Roper})$  and  $Y = \Lambda$  and  $\Sigma$ , our results are predictions, which,

as we hope, will give impetus to performing relevant exclusive experiments, the more so as a group of experimentalists from the Institute of Nuclear Physics (Moscow State University) is permanently working at the Thomas Jefferson Laboratory, where the implementation of such experiments is quite feasible.

At low virtual-pion momenta, the momentum distribution in the  $B = N^*(3/2^-, 1/2^-)$  channel differs significantly from the momentum distributions in other channels, since, in this channel, the orbital angular momentum  $l$  of the pion is equal to zero ( $s$  state), while, in other channels,  $l = 1$  ( $p$  state). The spectroscopic factor in this channel is about 1% of the spectroscopic factor in the  $B = N$  channel. In the  $B = N^{**}$  channel, the spectroscopic factor is also small, but it is quite measurable.

The model used here also makes it possible to obtain numerical values for the coupling constants in meson–baryon vertices if we assume that the constant  $G_{\pi NN}^2/4\pi$  is known to be equal to 14, this constant specifying the only parameter of the model,  $\nu$ . We have obtained the following values:  $G_{\pi\Delta N}^2/4\pi = 57$ ,  $G_{\pi N^*N}^2/4\pi = 1.4$ , and  $G_{\pi N^{**}N}^2/4\pi = 0.02$ .

For the  $N \rightarrow Y + K$  channel, the model yields only the ratio  $G_{K\Lambda N}/G_{K\Sigma N}$ , since, in general, the constant  $G_{\pi qq}$ , which is determined by the parameter  $\nu$  and which is fitted to the known value of  $G_{\pi NN}^2/4\pi = 14$ , is not equal to  $G_{Kqq}$ . We have obtained the value of  $|G_{K\Lambda N}/G_{K\Sigma N}| = 3\sqrt{3}$ . As to the absolute values of the constants appearing in this ratio, it is necessary to set  $G_{Kqq}^2 = (6-10)G_{\pi qq}$  in order to reproduce experimental data from [25].

In the future, we are going to extend this model to the case of vector-meson knockout, but, for this, it is necessary to develop its relativistic version. We also plan to explore the potential of the quasielastic-knockout mechanism for a comparison with the microscopic models of the other aforementioned theoretical concepts of the origin of meson–baryon interaction—namely, the concept of an effective field and the concept of quark–meson interaction.

#### 4. PIONS IN NUCLEI

Processes of quasielastic pion knockout will contribute to solving many problems of meson dynamics in nuclei. Starting from the studies of Migdal and his disciples [26], theorists discuss the question of whether pions are present in the ground state of a nucleus. Within Migdal's concept, a condensate of pions is that of configurations formed by a delta particle and a nucleon hole, the interaction of these configurations being mediated by pion exchange. According to the

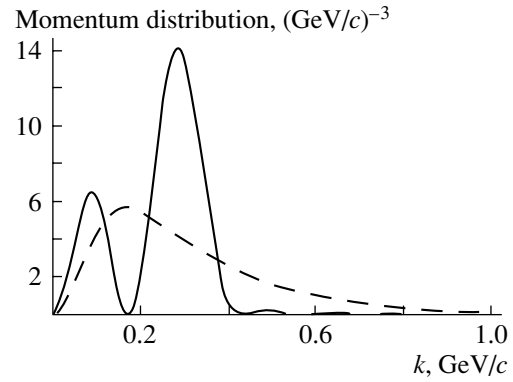


**Fig. 5.** Momentum distribution of pions in nuclei: (solid curve) momentum distribution of collective pions in  $A = 70-80$  nuclei versus  $|k|$  according to the Preparata model and (dashed curve) momentum distribution of pions in a free nucleon.

theoretical estimates presented in [27], the actual nucleon density in nuclei is, however, two to three times lower than that which is required for the formation of a real condensate, and it is presently believed that there is no pion condensate in nuclei. This, however, does not exhaust the question of pionic degrees of freedom in nuclei. As a development of the above line of investigations, Preparata and his coauthors [28] found in the 1990s yet another mechanism of pumping the ground state with pions. This mechanism is associated with the phenomenon of Dicke's superradiance [29]. Superradiance is based on coherent photon emission from atoms. It turns out that, in a system of identical atoms, the probability of photon emission increases as the atoms undergo deexcitation, reaching a maximum when the number of deexcited atoms becomes equal to  $N/2$ , where  $N$  is the total number of atoms in the system. This corresponds to the enhancement of the transition probability by the factor  $N^2/4$ . Therefore, there arises a superstrong photon-field interaction with atoms, which is absent at the level of individual atoms. The authors of [28] extended this concept to the system of nucleons and studied the effect of a similar superstrong interaction on nuclear dynamics. In this case,  $N$  and  $\Delta$  play the role of, respectively, ground and the excited state of atoms, while the pion field plays the role of the photon field. From their estimates, it follows that, although an enormous amount of energy is required for exciting a delta isobar (300 MeV), the intense interaction arising between the nucleon, delta-isobar, and pion subsystems leads to an effective increase of about 10 MeV/nucleon in the binding energy. The coherence region where such an interaction occurs involves approximately 70 nucleons. This new mechanism of the generation of a pion field in a nucleus results in that, even at an actual nucleon density, a

nucleus does indeed occur in a superradiance state with respect to the pion mode, the corresponding pion momentum being  $q \simeq 0.3 \text{ GeV}/c$ , as is suggested by the relation

$$\sqrt{\mathbf{q}^2 + m_\pi^2} = M_\Delta - M_N. \quad (16)$$

The number of collective pions of one type  $i$  ( $\pi^+$ ,  $\pi^-$ ,  $\pi^0$ ) per nucleon that have the above momentum  $\mathbf{q}$  in an  $N = Z$  nucleus,  $n_{i,\text{coll}}/A$ , is about 0.1. This number is greater than the corresponding number of pions in the meson skin of an individual nucleon that have momenta, for example, in the range  $\mathbf{k} = (1 \pm 0.2)\mathbf{q}$ .

Some other facets of the presence of pions in nuclei have also been revealed in recent years. We would like to highlight one of these. The point is that, in nuclei, a global quark–antiquark condensate transforms substantially, appearing to be less in magnitude by about 30% [30]. Further, the forms of realization of the condensate may change significantly in nuclei. According to the estimates presented in [31], up to half of the quark condensate can assume the form of a pion condensate. The method of quasielastic pion knockout will be of use in solving this question of great importance. In the present study, we will briefly consider the possibility of experimentally verifying the existence of the Preparata mechanism in nuclei. It turns out that the momentum distributions of pions knocked out from individual nucleons and from a nucleus (Preparata mechanism) differ significantly.

Figure 5 displays the momentum distribution of pions per nucleon in a nucleus according to the calculations from [32]. In those calculations, it was assumed that the coherence region for collective pions corresponds to the entire nucleus and that the pion radial wave function has the simplest standing-wave form  $\Phi(\mathbf{r}) = c \cdot j_1(\mathbf{q} \cdot \mathbf{r})$  for  $r \leq R$  and is  $\Phi(\mathbf{r}) = 0$  for  $r > R$ , where  $R$  is the nuclear radius corresponding to  $A = 70$  at  $N = Z$  and where the constant  $c$  is determined by the normalization of the wave function to the above value of  $n_{i,\text{coll}}/A$ .

A distinct dominant maximum of the momentum distribution at  $k \simeq 0.3 \text{ GeV}/c$  will be the main signature of the presence of collective pions in a nucleus. The dashed curve corresponds to the momentum distribution of pions in the skin of an isolated nucleon.

In the knockout of collective pions, it is the final spectator nucleus as a discrete unit that undergoes recoil, the respective recoil energy  $E \simeq \mathbf{q}^2/2AM_N$  being very low in view of the fact that  $A = 70\text{--}80$ . At the same time, the knockout of a virtual pion belonging to the individual meson skin of a nucleon and having a momentum  $q$  that is rather high in magnitude (the main maximum of the dashed curve in Fig. 5) corresponds to the case where a single

nucleon undergoes recoil, with the energy transferred to it being  $E \simeq q^2/2M_N \simeq 50 \text{ MeV}$  (here, we mean numerous loosely bound nucleons of the outer shell). In a double-coincidence experiment, this event will be seen as that in which the final spectator nucleus, which received the recoil momentum  $|\mathbf{q}| = q$ , also receives the internal excitation energy, which is approximately equal to 50 MeV. It follows that, at an energy resolution of 10 MeV, it would be quite feasible to discriminate between the knockout of a collective pion and the knockout of an individual pion both by the shape of the resulting momentum distribution and by the character of recoil (compare with the Mössbauer effect).

## 5. SOME PROSPECTS

Having discussed in Section 2 the problem of quasielastic rho-meson knockout on the basis of Rosenbluth's separation and the use of the spin-flip subprocess  $\rho^+ + \gamma_T^* \rightarrow \pi$ , we can develop this idea with allowance for the experience of the theory of quasielastic cluster knockout from nuclei bombarded with intermediate-energy protons [6, 7], in which case processes involving the flip of the intrinsic orbital angular momentum  $L^*$  of a virtually excited cluster  $\alpha^*$  undergoing quasielastic knockout induced by protons were seen to play a significant role:  $\alpha^*(L^* \neq 0) + p \rightarrow \alpha_0(L = 0) + p'$ . Owing to this, the respective differential cross section appears to be strongly dependent on the orientation of the recoil momentum  $-\mathbf{k}$  of the  $(A - 4)$  spectator nucleus with respect to the beam axis (anisotropy in the polar angle  $\theta$ ) and with respect to the proton-scattering plane (Treiman–Yang anisotropy in the azimuthal angle  $\phi$ ) [6, 7]. In the analogous knockout of clusters by high-energy electrons, the anisotropies in question must be less pronounced, but this issue has not yet received adequate study. On the basis of this experience, we formulate the problem of microscopically considering in a nucleon positive-parity virtual mesons—that is, those whose intrinsic orbital angular momentum is  $l = 1$  (this is compatible, in particular, with the  ${}^3P_0$  scalar fluctuation, which was discussed above). If their internal structure is rather simple and corresponds to the  $q\bar{q}$  configuration, an electron impact will transform, with a reasonably high probability, such a meson into a pion; if the spectroscopic factor of this meson is quite great, the process being considered can be observed by studying the above two types of anisotropy of the differential cross sections.

As to more complicated structures in a nucleon that belong to the  $q^2\bar{q}^2$  type [33] and which may have large spectroscopic factors for virtual decay to, for example, a  $\pi^+\pi^-$  pair, it is possible to investigate

them by borrowing, from the physics of electron collisions, the idea of a high-energy ( $e, 3e$ ) process in which there is a hierarchy of the momenta of three final electrons [10] (this process is used to explore short-range Coulomb electron–electron correlations in multielectron systems). Specifically, we mean the following: for mesons that are characterized by a more complicated structure of the above type and, at the same time, by a rather large spectroscopic factor for a virtual decay to a  $\pi^+\pi^-$  pair (in particular, scalar mesons [33]), it would be reasonable to explore the process  $p(e, e'\pi^+\pi^-)B$  [with the aid of the triple-coincidence technique, which can be applied here since the cross sections under discussion in the range  $Q^2 \sim 2-4$  (GeV/c) $^2$  are quite sufficient for this], where, in the final state, there appear a quasielastic  $e'\pi^+$  pair (the momenta of the particles forming this pair are high in the case of quasielastic kinematics) and a negatively charged pion, which is a “first-order spectator” in the knockout of a positively charged pion from the “complex” meson being discussed, and where, concurrently, the recoil momentum of the negatively charged pion must be intermediate between very high momenta of the  $e'$  and  $\pi^+$  particles and a low recoil momentum of the final baryon  $B$ , which is a “second-order spectator.” The respective experiment is intended to solve two problems: a determination of the momentum distribution of the “complex” meson  $m$  in the virtual-decay channel  $p \rightarrow m + B$  and a determination of the momentum distribution for the relative motion of the positively and the negatively charged pion in the “complex” meson  $m$ . Here, the main difficulty consists in that, in general, the contributions of different mesons  $m$  are summed; however, these contributions can be separated by using Rosenbluth’s separation, the separation of the momentum distributions in each channel with respect to orbital angular momenta, and a set of a few states of  $B$ .

We would like to dwell on yet another interesting issue associated with mesonic degrees of freedom. In principle, the relativistic generalization of quasielastic-knockout theory by including the  $z$  diagram in Fig. 1b and the virtual production of a  $\pi^+\pi^-$  pair in the nucleon field paves the way for studying, with the aid of ( $e, e'\pi$ ) processes, the currently popular problem of the formation in heavy nuclei of a bound  $1s$  state of a negatively charged pion originating from ( $d, {}^3\text{He}$ ) reactions at rather high deuteron energies of  $E_d \simeq 500$  MeV [34]. Namely, the two diagrams in Fig. 1 will correspond, in this case, to the production of a virtual  $\pi^+\pi^-$  pair, with the capture of the negatively charged pion into a bound  $1s$  state prior to the electron impact in one of these diagrams and after it in the other. According to the aforesaid, an

$A(e, e'\pi^+)A_{1s}(\pi^-)$  experiment would furnish information both about the momentum distribution of pions captured by the target nucleus in the  $1s$  state and about the binding energy in the nucleus. The energy and the angular resolution of the ( $e, e'\pi$ ) experiments being discussed are quite sufficient for reliably separating the states of the spectator baryon  $B$  and for measuring the momentum distributions of mesons in respective channels, but, for pions in nuclei, there arise, however, methodological problems (see above). The problem of studying pion atoms by means of ( $e, e'\pi$ ) reactions, which is discussed here, is beyond the reach of the present experimental potential.

Finally, much attention should be given to quasi-elastic proton knockout from a deuteron by electrons of energy equal to a few GeV in the process  ${}^2\text{H}(e, e'p)B$  leading to the formation of a final spectator baryon  $B$ , whose energy is also to be determined [35]. This is of importance for revealing the form of six-quark configurations in the nucleon–nucleon system in the region of nucleon overlap. For example, the Moscow potential of nucleon–nucleon interaction [36]—it leads to a node of the wave function at the repulsive-core position (this is typical of commonly accepted meson potentials)—corresponds to the  $s^4p^2$ [42] $_x$ [42] $_{CS}$  six-quark configuration ([42] $_x$  is the Young diagram in coordinate space, while [42] $_{CS}$  is the Young diagram in color–spin space) [37]. Only this potential makes it possible to explain (at a semiquantitative level) data on nucleon–nucleon scattering (differential cross sections and polarizations) up to energies of  $E_{\text{lab}} = 5-6$  GeV. A feature peculiar to this six-quark configuration is that a rich spectrum of excited baryon–baryon states arises upon projecting the respective six-quark wave function onto these baryon channels [35]. One of the components is  $N(1p)N^*(3/2^-, 1/2^-)$ , its weight being predicted at a level of 1% [35] ( $1p$  means the  $1p$  state of relative motion). The existence of this component was confirmed by its strong specific effect (because of the aforementioned  $p$  wave with respect to relative motion) on polarization features in elastic  $\mathbf{d} + p$  scattering accompanied by polarization transfer and, similarly, in the inclusive process  $\mathbf{d} + {}^{12}\text{C} \rightarrow \mathbf{p} + X$  [38]. If the momentum distribution of protons in the virtual-decay channel  ${}^2\text{H} \rightarrow N + N^*(3/2^-, 1/2^-)$  was measured in the quasielastic-knockout reaction  ${}^2\text{H}(e, e'p)N^*(3/2^-, 1/2^-)$  examined in studying the process  ${}^2\text{H}(e, e'p)B$  and if the  $p$ -wave character of the relative motion of  $N$  and  $N^*(3/2^-, 1/2^-)$  was confirmed on the basis of this momentum-distribution measurement, this would provide an independent, quite a spectacular piece of evidence in favor of the existence of this component. There

is yet another interesting detail: the  $6q$  configuration  $s^4 p^2 [42]_x [42]_{CS}$  does not involve a  $\Delta\Delta$  component in the deuteron [35], while the alternative configuration  $s^6 [6]_x [2^3]_{CS}$ , which corresponds to a repulsive core [39], contains it with a high probability (of about 3%). It is of importance that the most detailed experiment devoted to this issue was unable to reveal a  $\Delta\Delta$  configuration [40]. Measurement of the cross section for the quasielastic process  ${}^2H(e, e'p)\Delta$  would be an important independent investigation, the  $e + \Delta \rightarrow e' + p$  inelastic amplitude, which is well known in inverse kinematics [41], being implied here.

## REFERENCES

- G. F. Chew and M. L. Goldberger, *Phys. Rev.* **87**, 788 (1952); G. F. Chew and F. F. Low, *Phys. Rev.* **113**, 1640 (1959).
- H. Tyren, P. Hillman, and Th. A. Maris, *Nucl. Phys.* **7**, 10 (1958); *Phys. Rev. Lett.* **5**, 107 (1960).
- S. S. Volkov, A. A. Vorob'ev, O. A. Domchenkov, *et al.*, *Yad. Fiz.* **52**, 1339 (1990) [*Sov. J. Nucl. Phys.* **52**, 848 (1990)]; A. A. Vorob'ev, Yu. V. Dotsenko, A. A. Lobodenko, *et al.*, *Yad. Fiz.* **58**, 1923 (1995) [*Phys. At. Nucl.* **58**, 1817 (1995)].
- P. G. Roos, N. S. Chant, A. A. Cowley, *et al.*, *Phys. Rev. C* **15**, 69 (1977); A. A. Cowley *et al.*, *Phys. Rev. C* **50**, 2449 (1994).
- V. G. Neudachin and Yu. F. Smirnov, *Nucleon Clusters in Light Nuclei* (Nauka, Moscow, 1969) [in Russian].
- V. G. Neudatchin, Yu. F. Smirnov, and N. F. Golovanova, *Adv. Nucl. Phys.* **11**, 1 (1979).
- V. G. Neudatchin, A. A. Sakharuk, V. V. Kurovsky, and Yu. M. Chuvil'sky, *Phys. Rev. C* **50**, 148 (1994); **51**, 784 (1995); V. G. Neudatchin, A. A. Sakharuk, W. W. Kurovsky, and Yu. M. Tchuvil'sky, *Yad. Fiz.* **58**, 1234 (1995) [*Phys. At. Nucl.* **58**, 1155 (1995)].
- Yu. F. Smirnov and V. G. Neudachin, *Pis'ma Zh. Éksp. Teor. Fiz.* **3**, 298 (1966) [*JETP Lett.* **3**, 192 (1966)]; V. G. Neudachin, G. A. Novoskol'tseva, and Yu. F. Smirnov, *Zh. Éksp. Teor. Fiz.* **55**, 1039 (1968) [*Sov. Phys. JETP* **28**, 540 (1968)].
- E. Weigold and I. McCarthy, *Electron Momentum Spectroscopy* (Plenum Publ., New York, 1999).
- V. G. Neudachin, Yu. V. Popov, Yu. F. Smirnov, *Usp. Fiz. Nauk* **169**, 1111 (1999).
- J. Speth and V. R. Zoller, *Phys. Lett. B* **351**, 533 (1995).
- P. Brauel, T. Canzler, D. Cords, *et al.*, *Z. Phys. C* **3**, 101 (1979); C. J. Bebek, C. N. Brown, S. D. Holmes, *et al.*, *Phys. Rev. D* **17**, 1693 (1978).
- M. Guidal, J.-M. Laget, and M. Vanderhaeghen, *Nucl. Phys. A* **627**, 645 (1997).
- J. Speth and A. W. Thomas, *Adv. Nucl. Phys.* **24**, 83 (1997); N. N. Nikolaev, J. Speth, and G. T. Garvey, *Z. Phys. A* **349**, 59 (1994); A. Szczurek and J. Speth, *Nucl. Phys. A* **570**, 765 (1994); **555**, 249 (1993); H. Holtmann, A. Szczurek, and J. Speth, *Nucl. Phys. A* **596**, 631 (1996).
- V. G. Neudatchin, N. P. Yudin, and L. L. Sviridova, *Yad. Fiz.* **60**, 2020 (1997) [*Phys. At. Nucl.* **60**, 1848 (1997)]; N. P. Yudin, L. L. Sviridova, and V. G. Neudatchin, *Yad. Fiz.* **61**, 1689 (1998) [*Phys. At. Nucl.* **61**, 1577 (1998)]; N. P. Yudin, V. G. Neudatchin, and L. L. Sviridova, *Yad. Fiz.* **62**, 694 (1999) [*Phys. At. Nucl.* **62**, 645 (1999)].
- N. P. Yudin, V. G. Neudatchin, and L. L. Sviridova, *Yad. Fiz.* **65**, 594 (2002) [*Phys. At. Nucl.* **65**, 567 (2002)].
- T.-Y. Saito and I. R. Afnan, *Few-Body Systems* **18**, 101 (1995).
- S. Nozawa, B. Blankleider, and T.-S. H. Lee, *Nucl. Phys. A* **513**, 459 (1990).
- I. T. Obukhovskiy, V. G. Neudachin, L. L. Sviridova, and N. P. Yudin, *Yad. Fiz.* **66**, 338 (2003) [*Phys. At. Nucl.* **66**, 313 (2003)]; I. T. Obukhovskiy, L. L. Sviridova, and V. G. Neudachin, *Yad. Fiz.* **66**, 2233 (2003) [*Phys. At. Nucl.* **66**, 2183 (2003)].
- D. V. Kaplan, *nucl-th/9506035*.
- D. O. Riska and G. E. Brown, *Nucl. Phys. A* **679**, 577 (2001).
- B. Desplanques, C. Gignoux, B. Silvestre-Brac, *et al.*, *Z. Phys. A* **343**, 331 (1992); F. Cano, P. Gonzalez, S. Noguera, and B. Desplanques, *Nucl. Phys. A* **603**, 257 (1996); P. J. A. Bicudo, L. S. Ferreira, C. M. Placido, and J. Ribeiro, *Phys. Rev. C* **56**, 670 (1997).
- I. T. Obukhovskiy and A. I. Obukhovskiy, *Yad. Fiz.* **63**, 324 (2000) [*Phys. At. Nucl.* **63**, 264 (2000)].
- O. F. Nemets, V. G. Neudatchin, A. T. Rudchik, *et al.*, *Nucleons Clusters in Nuclei and Nuclear Multinucleon-Transfer Reactions* (Naukova Dumka, Kiev, 1988) [in Russian].
- R. A. Adelseck and B. Saghai, *Phys. Rev. C* **42**, 108 (1990); R. A. Williams *et al.*, *Phys. Rev. C* **46**, 1617 (1992); J. de Swart, *Rev. Mod. Phys.* **35**, 916 (1963).
- A. B. Migdal, *Zh. Éksp. Teor. Fiz.* **61**, 2209 (1971) [*Sov. Phys. JETP* **34**, 1184 (1971)]; *Rev. Mod. Phys.* **50**, 107 (1978); A. B. Migdal, D. N. Voskresensky, E. E. Sapershtein, and M. A. Troitsky, *Pion Degrees of Freedom in Nuclear Matter* (Nauka, Moscow, 1991) [in Russian].
- Yu. B. Ivanov, J. Knoll, H. Van Hees, and D. N. Voskresensky, *Yad. Fiz.* **64**, 711 (2001) [*Phys. At. Nucl.* **64**, 652 (2001)].
- R. Alzetta, G. Liberti, and G. Preparata, *Nucl. Phys. A* **585**, 307c (1995); R. Alzetta, T. Bubba, R. LePerra, *et al.*, *Nuovo Cimento A* **112**, 762 (1999); R. Alzetta, G. Liberti, and G. Preparata, *Nuovo Cimento A* **112**, 1609 (1999).
- A. V. Andreev, V. I. Emel'yanov, and Yu. A. Il'inskiĭ, *Coherent Phenomena in Optics* (Nauka, Moscow, 1988) [in Russian].
- E. G. Drukarev, M. G. Ryskin, and V. A. Sadovnikova, *Prog. Part. Nucl. Phys.* **47**, 73 (2001).
- G. Chanfray, M. Ericson, and P. A. M. Guichon, *Phys. Rev. C* **63**, 055202 (2001).
- V. G. Neudachin, N. P. Yudin, L. L. Sviridova, *Yad. Fiz.* **65**, 1598 (2002) [*Phys. At. Nucl.* **65**, 1560 (2002)].

33. K. Ayat and A. Watt, Nucl. Phys. A **535**, 592 (1991); F. E. Close, Nucl. Phys. A **622**, 255 (1997); E. Marco, E. Oset, and H. Toki, Phys. Rev. C **60**, 015202 (1999); D. Ebert, M. Nagy, M. K. Volkov, and V. L. Yudichev, Eur. Phys. J. A **8**, 567 (2000).
34. A. Gillitzer, Nucl. Phys. A **639**, 525c (1998); Y. Umemoto, S. Herenzaki, K. Kume, *et al.*, Nucl. Phys. A **679**, 549 (2001); R. S. Hayano, Nucl. Phys. A **680**, 125c (2001).
35. Ya. L. Glozman, V. G. Neudatchin, and I. T. Obukhovskiy, Phys. Rev. C **48**, 389 (1993); Ya. L. Glozman and A. Faessler, Phys. Lett. B **348**, 270 (1995).
36. I. T. Obukhovskiy, V. G. Neudatchin, Yu. F. Smirnov, and Yu. M. Chuvilsky, Phys. Lett. B **88**, 231 (1979); V. G. Neudachin, I. T. Obukhovskiy, Yu. F. Smirnov, Fiz. Élem. Chastits At. Yadra **15**, 1165 (1984); A. M. Kusainov, V. G. Neudatchin, and I. T. Obukhovskiy, Phys. Rev. C **44**, 2343 (1991).
37. V. G. Neudatchin, N. P. Yudin, Yu. L. Dorodnikh, and I. T. Obukhovskiy, Phys. Rev. C **43**, 2499 (1991).
38. M. P. Rekalov and I. M. Sitnik, Phys. Lett. B **356**, 434 (1995); B. Kuehn, Ch. Perdrisat, and E. A. Strokovsky, Yad. Fiz. **58**, 1898 (1995) [Phys. At. Nucl. **58**, 1795 (1995)]; A. P. Kobushkin, A. P. Kostyuk, and A. Faessler, Few-Body System. Suppl. **10**, 447 (1999); L. S. Azhgirey and N. P. Yudin, Yad. Fiz. **63**, 2280 (2000) [Phys. At. Nucl. **63**, 2184 (2000)].
39. Z.-Y. Zhang, A. Faessler, U. Straub, and Ya. L. Glozman, Nucl. Phys. A **587**, 573 (1994); D. R. Entem, A. I. Machavariani, A. Valcarce, *et al.*, Nucl. Phys. A **602**, 308 (1996).
40. D. Allasia, C. Angelini, A. Baldini, *et al.*, Phys. Lett. B **174**, 450 (1986).
41. Y. B. Dong, K. Shimizu, and A. Faessler, Nucl. Phys. A **689**, 784 (2001).

*Translated by A. Isaakyan*

---

---

## ELEMENTARY PARTICLES AND FIELDS

### Experiment

---

---

# VEPP-2000 Project: Collider, Detectors, and Physics Program

S. I. Serebnyakov

*Budker Institute of Nuclear Physics, Siberian Division, Russian Academy of Sciences,  
pr. Akademika Lavrent'eva 11, Novosibirsk, 630090 Russia  
Novosibirsk State University, ul. Pirogova 2, Novosibirsk, 630090 Russia*

Received March 26, 2003; in final form, August 12, 2003

**Abstract**—The new VEPP-2000  $e^+e^-$  collider of maximum energy 2000 MeV, which is under construction at the Budker Institute of Nuclear Physics (Siberian Division, Russian Academy of Sciences, Novosibirsk), is briefly described. Experiments at VEPP-2000 will be performed with two upgraded detectors, CMD-2M and SND. A precise measurement of the total cross section for the process  $e^+e^- \rightarrow$  hadrons and of the partial cross sections for its exclusive hadronic channels is the main point of the physics program for this machine. These measurements will be aimed at testing QCD and the VMD and CVC models, as well as at refining the hadron contribution to fundamental constants such as the muon anomalous magnetic moment  $a_\mu = \frac{g-2}{2}$  and the fine-structure constant  $\alpha_{em}(M_Z^2)$ . Measurements of the nucleon form factors in the reactions  $e^+e^- \rightarrow p\bar{p}, n\bar{n}$  at their threshold will also be of great importance.  
© 2004 MAIK “Nauka/Interperiodica”.

## 1. VEPP-2000 COLLIDER

The project of VEPP-2000 was proposed to extend the physics program of the VEPP-2M collider [1] toward higher energies up to 2.0 GeV in the c.m. frame. In the new accelerator complex, the VEPP-2M collider will be replaced by VEPP-2000. Figure 1 shows the layout of the VEPP-2000 accelerator complex. It should be noted that the injection part of the complex (linear accelerator, electron synchrotron, booster) will not undergo significant changes.

The main parameters of VEPP-2000 are the following [2, 3]:

(a) The operating energy (in the c.m. frame) will range between 0.4 and 2.0 GeV.

(b) The luminosity will be  $L = 10^{31} \text{cm}^{-2}\text{s}^{-1}$  and  $L = 10^{32} \text{cm}^{-2}\text{s}^{-1}$  at  $2E = 1.0$  GeV and  $2E = 2.0$  GeV, respectively.

(c) The perimeter will be 24.5 m.

(d) The current will be 200 mA ( $E = 0.9$  GeV).

(e) The size of the beam along the orbit will be 3.4 cm ( $E = 0.9$  GeV).

(f) The energy scatter will be 0.7 MeV ( $E = 0.9$  GeV).

Although the VEPP-2000 luminosity is lower than the luminosities of  $e^+e^-$  factories, however, it is two to three orders of magnitude higher than that of colliders that operated earlier at energies of  $2E > 1.4$  GeV, such as DCI (Orsay) and ADONE (Frascati). The expected integrated luminosity of

VEPP-2000 will be about  $3 \text{fb}^{-1}$  over a 5-year period of experiments.

A feature peculiar to VEPP-2000 is an unusual focusing system that involves both traditional quadrupole lenses and a radically new element, superconducting solenoids creating a magnetic field of strength 8 T. As electrons traverse a solenoid, the plane of betatron oscillations is rotated through  $90^\circ$ , whereby there occurs the mixing of the vertical and horizontal betatron oscillations, with the result that the beam cross section becomes circular. The current producing the maximum effect of the intersection of beams increases, which leads to an increase in the collider luminosity. This scheme of increasing the luminosity will be tested at VEPP-2000.

Presently, the collider elements are being manufactured and mounted in the experimental hall.

## 2. SND DETECTOR

Experiments with the spherical neutral detector (SND) [4] were carried out at the VEPP-2M  $e^+e^-$  collider of integrated luminosity about  $30 \text{pb}^{-1}$  over the period from 1995 to 2000.

An electromagnetic calorimeter based on 1632 NaI(Tl) crystals is the main part of the SND detector; it is manufactured in the form of three spherical layers (Fig. 2). The total weight of the NaI(Tl) crystals is 3.6 t, and the solid angle of the calorimeter is about 90% of  $4\pi$ . The energy resolution for photons is

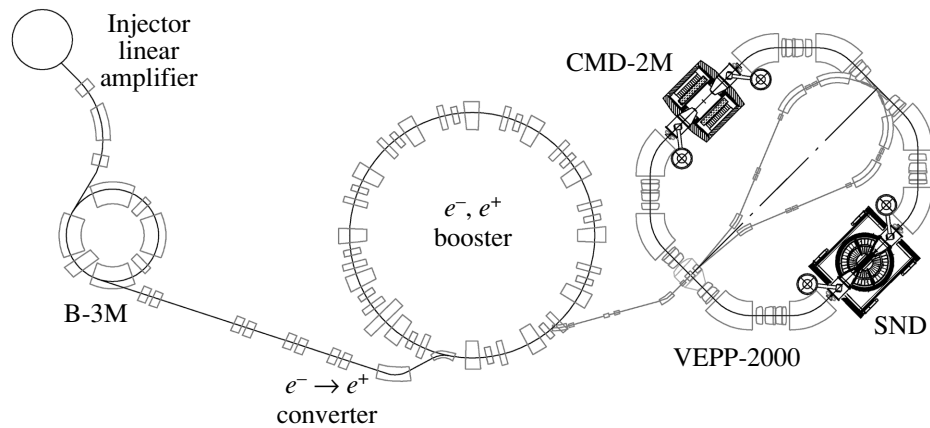


**Fig. 1.** Layout of the VEPP-2000 accelerator complex. The SND and CMD-2M detectors are shown in the right part of the figure along with the VEPP-2000 collider.

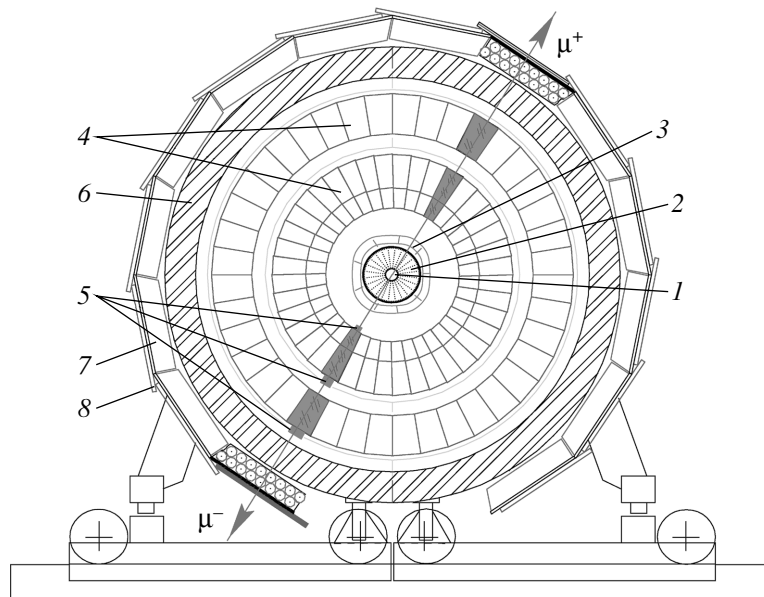


**Fig. 2.** SND detector view in the plane transverse to the beam direction: (1) vacuum chamber, (2) drift chambers, (3) aerogel Cherenkov counters, (4) NaI(Tl) counters, (5) phototriodes, (6) iron absorber, (7) streamer tubes, and (8) scintillation counters.

$\sigma_E/E = 4.2\%/\sqrt[4]{E(\text{GeV})}$  [5], and the angular resolution is about  $1.5^\circ$ . The photon-energy threshold is set at a level of 20 MeV. A system of two cylindrical drift chambers with a solid angle of 95% of  $4\pi$  is used to measure the emission angle of charged particles. The measurement accuracy is  $0.4^\circ$  for the azimuthal angle and about  $2^\circ$  for the polar angle. A muon detector consisting of streamer tubes [6] is placed outside the calorimeter.

An upgrade of SND is presently being performed [7]. A new drift chamber is being manufactured to be used as a track detector. An aerogel Cherenkov counter (with the refractive index being  $n = 1.13$ ) will be an additional element of SND. It will permit

separating  $\pi^-$  and  $K$  mesons of momentum up to 900 MeV/c. In the new SND detector, electronics and the system of data readout and data processing will also be upgraded.

### 3. CMD-2M DETECTOR

Figure 3 shows layout of the CMD-2M detector [8], which is a superconducting solenoid  $0.15X_0$  thick generating a magnetic field of strength 1.5 T; it encloses a drift chamber that ensures measurement of the emission angles and momenta of charged particles. The angular accuracy is about 5 mrad; the momentum resolution is about 3% for a momentum

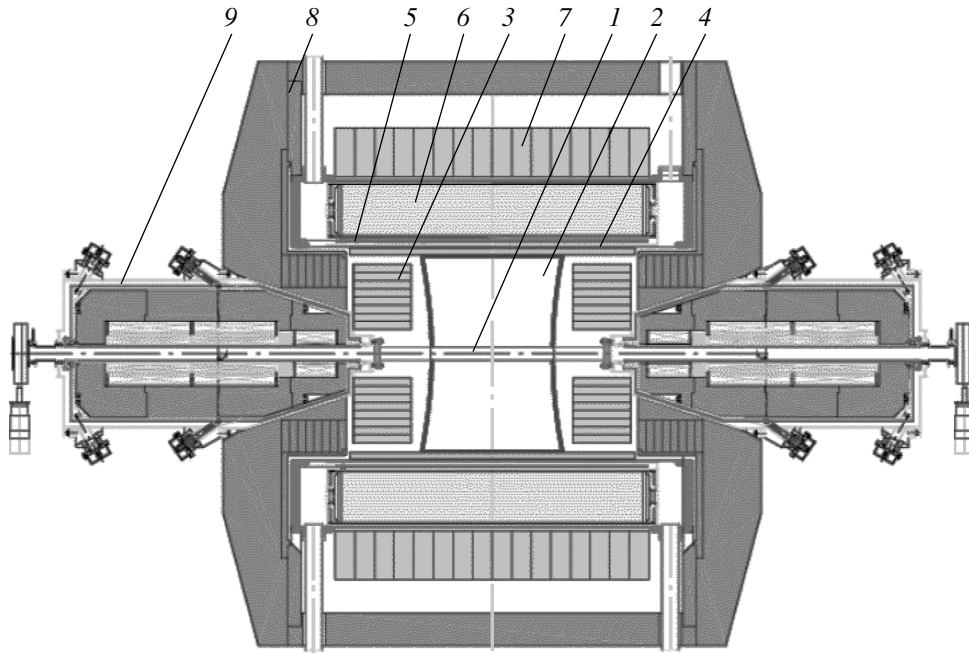


**Fig. 3.** CMD-2M detector view along the beam direction: (1) vacuum chamber, (2) drift chambers, (3) BGO calorimeter, (4) Z chamber, (5) superconducting solenoid, (6) LXe calorimeter, (7) CsI calorimeter, (8) magnet yoke, and (9) superconducting focusing solenoids.

of 1 GeV; the mean number of wires along a track is 19.

The CMD-2M calorimeter is combined. Its endcap part is formed by BGO crystals with readout based on silicon photodiodes. The barrel part of the calorimeter incorporates liquid krypton ( $8X_0$ ) and CsI(Tl) crystals ( $5X_0$ ) along the particle path. The CMD-2M calorimeter has a very high solid-angle granularity, this permitting an efficient detection of events featuring a high multiplicity or closely outgoing particles. The energy resolution of the calorimeter for 0.1- to 1-GeV photons is expected to be in the range 3–6%. The angular resolution ranges from  $0.3^\circ$  (in the barrel part) to  $1^\circ$  (in the endcap part).

In order to improve the separation of  $\pi^-$  and  $K$  mesons and to suppress the cosmic-ray background, a time-of-flight system based on plane scintillation counters is placed outside the calorimeter.

## 4. PHYSICS PROGRAM

### 4.1. Total Cross Section for $e^+e^-$ Annihilation into Hadrons

The ratio  $R = \frac{\sigma(e^+e^- \rightarrow \text{hadrons})}{\sigma(e^+e^- \rightarrow \mu^+\mu^-)}$  is a fundamental constant within the quark model and QCD. To a first approximation,  $R = 3 \sum_q e_q^2$ ; for the first three quarks  $u$ ,  $d$ , and  $s$ , we then have  $R \simeq 2$ . The calculated value of  $R$  with allowance for QCD corrections

is in agreement with experimental data in the energy region  $2E > 1.5$  GeV. The VEPP-2000 range  $2E = 1.4$ – $2.0$  GeV is the resonance or transition energy region, where the cross sections for the main processes making a dominant contribution to  $R$  change abruptly with energy. The experimental uncertainties in these cross sections are still large and result in an uncertainty of  $\Delta R/R \simeq 10\%$ . The challenge of VEPP-2000 is to reduce this uncertainty to 2–3%.

### 4.2. Contribution of $R$ to the Muon Anomalous

$$\text{Magnetic Moment } a_\mu = \frac{g-2}{2}$$

The muon anomalous magnetic moment is one of the fundamental constants in elementary-particle physics. It is about  $10^{-3}$  of the total magnetic moment of the muon; this small value was measured to a precision of  $0.7 \text{ ppm}^1$  in the E821 experiment (BNL) [9]. The accuracy of the calculated muon anomalous magnetic moment is nearly identical to the experimental one: 0.9 ppm [10]. However, there are some problems in the calculation. The point is that the leading contribution to the calculated accuracy comes from the hadronic vacuum polarization, which cannot be obtained from basic QCD concepts at present. To calculate the hadronic vacuum polarization, use is made of experimental data on the total cross section

<sup>1</sup>1 ppm =  $10^{-6}$ .

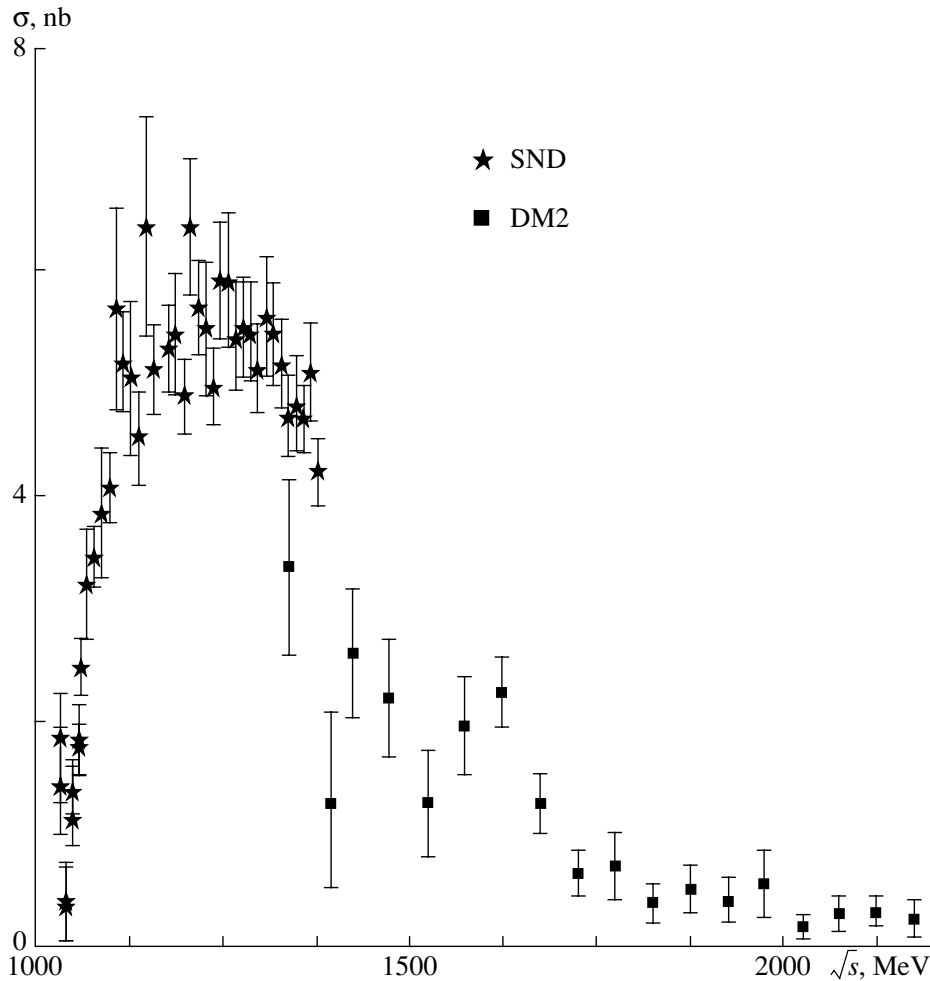


Fig. 4. Experimental cross sections for the process  $e^+e^- \rightarrow \pi^+\pi^-\pi^0$ .

for the process  $e^+e^- \rightarrow \text{hadrons}$ . Lower energies (the  $\rho$ -meson region) make the greatest contribution to  $R$ , which is actually measured at VEPP-2M and VEPP-2000.

The most accurate measurements of  $R$  were performed by the CMD-2 Collaboration (Novosibirsk) [11]. The muon anomalous magnetic moment calculated with the data of these measurements is less than the result of the E821 experiment by three standard deviations (2.9 ppm). The respective value from  $\tau$ -lepton decays is also less than the E821 result, but, in this case, the difference is less ( $1.5\sigma$ ). New measurements of  $R$  at VEPP-2000 are absolutely necessary, because a reliably established discrepancy between the experimental and the theoretical results for the muon anomalous magnetic moment would mean a breakdown of the Standard Model.

#### 4.3. Contribution of $R$ to the Fine-Structure Constant $\alpha_{\text{em}}(M_Z^2)$

As is well known, the fine-structure constant  $\alpha_{\text{em}}$  grows slowly with increasing energy, and its value is  $1/129$  at the  $Z_0$ -boson peak (instead of the usual value, which is equal to  $1/137$  in the zero-energy limit). However, the accuracy of  $\alpha_{\text{em}}(0)$  is  $4 \times 10^{-8}$  [12], but the accuracy of  $\alpha_{\text{em}}(M_Z^2)$  is substantially poorer ( $\sim 10^{-3}$ ).

In order to test the electroweak model precisely, it is of great importance to improve the accuracy of  $\alpha_{\text{em}}(M_Z^2)$ . For instance, verification of the relation

$$\sin^2 \theta_W (1 - \sin^2 \theta_W) = \frac{\pi \alpha_{\text{em}}(M_Z^2)}{\sqrt{2} G_F M_Z^2}$$

is hindered by the accuracy of  $\alpha_{\text{em}}(M_Z^2)$  (the dependence on  $M_t$  and  $M_H$  is not taken into account). The uncertainties in the other quantities appearing in this relation are considerably smaller:

$$\delta G_F \sim 10^{-5}; \quad \delta M_Z \sim 10^{-4}.$$

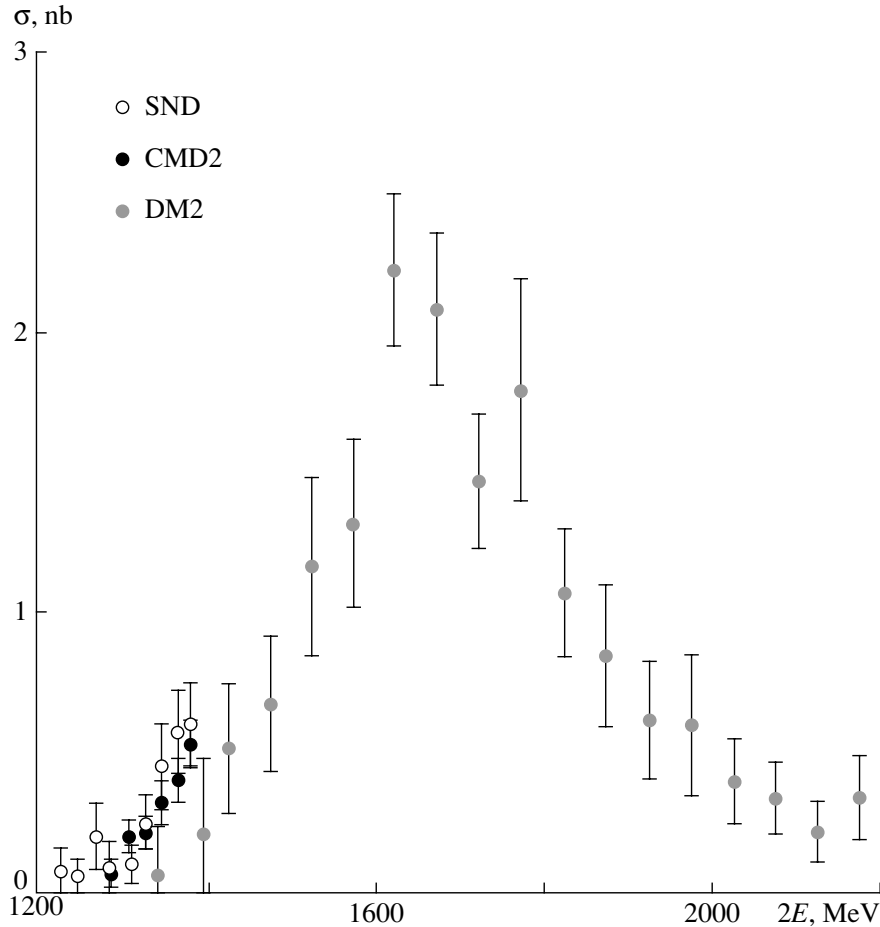


Fig. 5. Experimental cross sections for the process  $e^+e^- \rightarrow \omega\pi^+\pi^-$ .

As in the case of the muon anomalous magnetic moment, the experimental cross section for the process  $e^+e^- \rightarrow \text{hadrons}$  is employed in the QED calculation of the constant  $\alpha_{\text{em}}(M_Z^2)$ . However, higher energies make the most significant contribution to the hadronic vacuum polarization here. According to the 1999 data, however, the energy region  $2E < 2 \text{ GeV}$  makes a contribution of above 30% to the uncertainty in  $\alpha_{\text{em}}(M_Z^2)$ . It follows that, if an improved precision at higher energies is achieved, for example, with VEPP-4M, new, more precise measurements of  $R$  at VEPP-2000 (that is, with an accuracy higher than 1% in the  $\rho$ -meson region and higher than 2 to 3% between 1 and 2 GeV) will make it possible to improve the accuracy of testing electroweak theory in the future considerably.

#### 4.4. Individual Processes of $e^+e^-$ Annihilation into Hadrons and Spectroscopy of Excited Vector Mesons

The value of  $R$  is determined by the sum of the cross sections for all hadronic processes, for example,

$$e^+e^- \rightarrow 2\pi, 3\pi, 4\pi, 5\pi, K\bar{K}, K\bar{K}\pi, N\bar{N}, \dots$$

These processes are dominant at VEPP-2000. In the region  $2E < 1 \text{ GeV}$ , the processes  $e^+e^- \rightarrow 2\pi, 3\pi$  have the largest cross section; at higher energies, these cross sections decrease, so that the process  $e^+e^- \rightarrow 4\pi$  appears to be dominant. For each individual process, the cross section is described rather well by the vector-meson-dominance (VMD) model with some corrections, including the energy dependence of the resonance width. In addition to the well-known resonances  $\rho(770)$ ,  $\omega(782)$ , and  $\phi(1020)$ , the existence of heavier and wider resonances (excited quarkonia) has been established experimentally [12]:

$$\rho(1450): M = 1465 \pm 25; \Gamma = 310 \pm 60; 4\pi;$$

$$\rho(1700): M = 1700 \pm 20; \Gamma = 240 \pm 60; 4\pi;$$

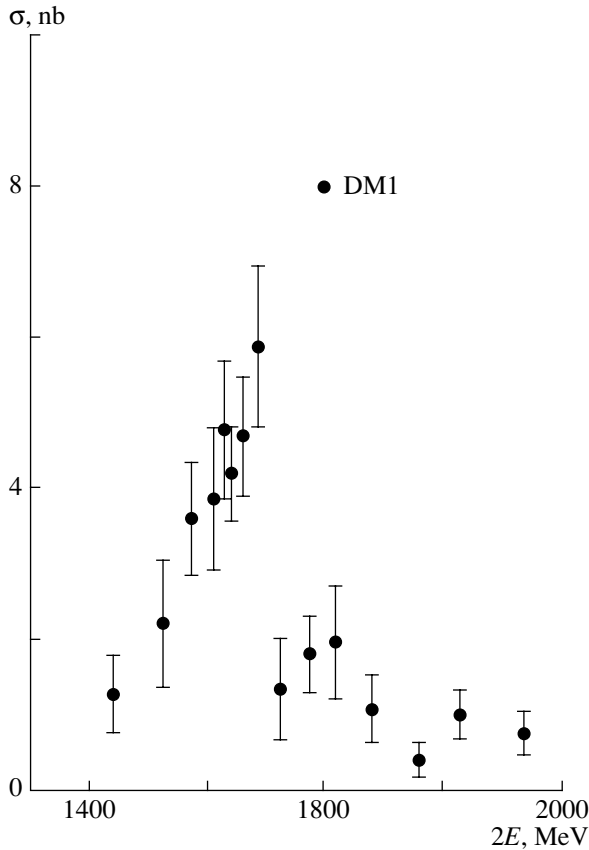


Fig. 6. Experimental cross sections for the process  $e^+e^- \rightarrow K_S K^+ \pi^-$ .

$\rho(2150)$ :  $M = 2149 \pm 17$ ;  $\Gamma = 363 \pm 50$ ;  $K^+ K^-$ ;  
 $\omega(1420)$ :  $M = 1419 \pm 31$ ;  $\Gamma = 174 \pm 60$ ;  $3\pi$ ;  
 $\omega(1650)$ :  $M = 1649 \pm 24$ ;  $\Gamma = 220 \pm 35$ ;  $\omega\pi^+\pi^-$ ;  
 $\phi(1680)$ :  $M = 1680 \pm 20$ ;  $\Gamma = 150 \pm 50$ ;  $K^* K$ .

(Here  $M$  and  $\Gamma$  are given in MeV.)

The parameters of excited resonances, especially their decay modes, have not yet been determined properly (large systematic uncertainties of about 20%, very large energy step between the measurements, poor statistical accuracy). For some processes, Figs. 4–6 display experimental data obtained over 30 years in the experiments performed at the VEPP-2, VEPP-2M, ACO, ADONE, and DCI colliders.

The experimental accuracy achieved in studying these processes is far from required values of 3 to 5%. This is due to a low integrated luminosity of about  $5 \text{ pb}^{-1}$  in the energy range  $1.4 < 2E < 2 \text{ GeV}$  and insufficient quality of the detectors used previously. The integrated luminosity expected at VEPP-2000 is about  $3 \text{ fb}^{-1}$ , which is three orders of magnitude

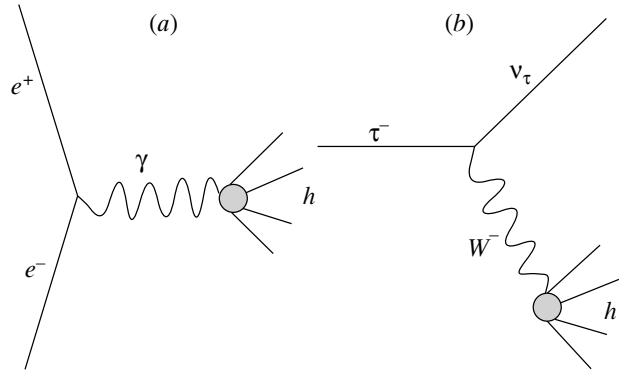


Fig. 7. Diagrams illustrating the CVC hypothesis: (a) diagram representing the process  $e^+e^- \rightarrow \text{hadrons}$  and (b) diagram representing  $\tau$  decay.

higher than that which is available at present. Additionally, the VEPP-2000 detectors (SND, CMD-2M) are modern detectors that cover a large solid angle and a high potential for identifying particles; therefore, a considerable improvement of accuracy is quite feasible.

#### 4.5. Testing of the Hypothesis of the Conservation of the Vector Current

The hypothesis of the conservation of the vector current (CVC) relates the  $\tau$ -leptonic-decay mass spectra of  $J^{PG} = 1^{-+}$  hadrons to the isovector part of the cross section for  $e^+e^-$  annihilation into hadrons as a function of energy (Fig. 7). For example, the spectrum of hadron masses  $M_h$  in the decay  $\tau^+ \rightarrow \omega\pi^+\nu$  is related to the cross section  $\sigma_{e^+e^-}^{I=1}$  for the process  $e^+e^- \rightarrow \omega\pi^0$  by the equation

$$\frac{dM_h}{dq^2} = \frac{G_F^2 \cos^2 \theta_c (1 + \delta_{EW})}{32\pi^2 \alpha^2 m_\tau^3} \times (m_\tau^2 - q^2)(m_\tau^2 + 2q^2)v_1(q^2),$$

$$v_1(q^2) = \frac{q^2 \sigma_{e^+e^-}^{I=1}(q^2)}{4\pi\alpha^2}.$$

Presently, this expression is being experimentally verified for many isovector processes of  $e^+e^-$  annihilation and this serves as a test of the electroweak model. On the other hand, there appears the possibility of cross-checking data on  $e^+e^-$  annihilation and  $\tau$  lepton under the assumption that the CVC hypothesis is valid.

In Fig. 8, the cross section measured with the SND detector at VEPP-2M [13] for the process  $e^+e^- \rightarrow \omega\pi^0$  is contrasted against the CVC prediction based on  $\tau$ -lepton decays in the CLEO experiment. This is one of the best examples of testing the CVC hypothesis. Another example has already

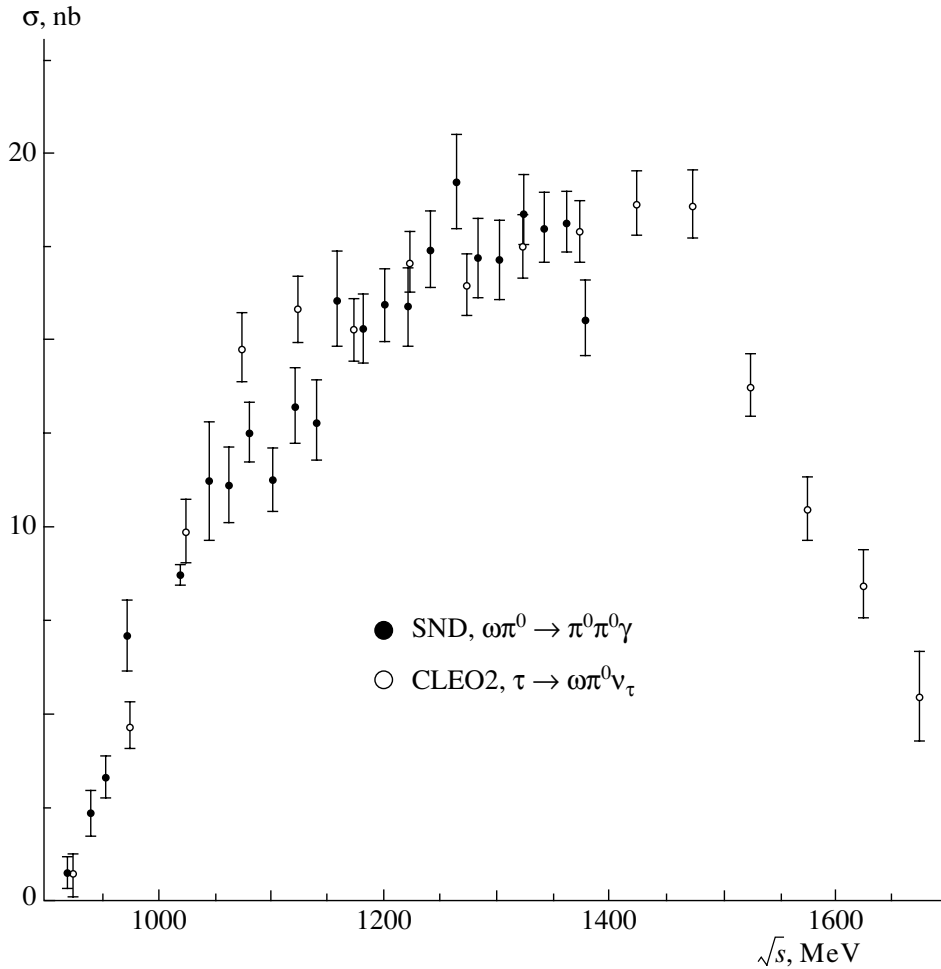


**Fig. 8.** Comparison of the cross section for the process  $e^+e^- \rightarrow \omega\pi^0$  (SND) and the CVC prediction on the basis of  $\tau$  decays (CLEO).

been given above in discussing the muon anomalous magnetic moment. In the latter case, the process  $e^+e^- \rightarrow \pi^+\pi^-$  makes the main contribution to the muon anomalous magnetic moment, with result that the data on  $e^+e^-$  annihilation appear to be 1.5% lower than those on the  $\tau$  lepton.

In summary, we can say that the next step in testing the CVC hypothesis for the main isovector processes to a precision of about 1% can be made at VEPP-2000.

#### 4.6. Threshold Production of Nucleon Pairs

At VEPP-2000, the production of nucleon pairs in the processes  $e^+e^- \rightarrow p\bar{p}, n\bar{n}$  becomes possible, which will permit extracting data on the electromagnetic form factors for the proton and the neutron in the timelike region of momentum transfer at the nucleon-production threshold. It should be noted that the timelike form factors for meson pairs ( $\pi^+\pi^-, K\bar{K}$ )

were measured adequately, and strong resonances [such as  $\rho(770)$  and  $\phi(1020)$ ] were observed.

The situation is somewhat different for nucleon pairs. In the threshold region  $2E < 2$  GeV, available data are very scanty, and there are no data at all on nucleons of kinetic energy in the region  $T < 10$  MeV. The neutron yield was measured in a single experiment (FENICE, ADONE) [14]. Figures 9 and 10 illustrate the available experimental results for the form factors.

The DM2 and FENICE experiments at  $\sqrt{s} \simeq 2$  GeV yielded  $\sigma_{p\bar{p}} \simeq \sigma_{n\bar{n}} \simeq 1$  nb and  $|G^p| \simeq |G^n| \simeq 0.4$ .

For the cross-section ratio  $r = \frac{\sigma(e^+e^- \rightarrow n\bar{n})}{\sigma(e^+e^- \rightarrow p\bar{p})}$ , various models of the nucleon form factors (perturbative QCD, extended VMD model, Skyrme model) give a wide range of values:  $r = 1/4-100$ .

The following problems will be studied at VEPP-2000. Is the neutron form factor indeed greater than

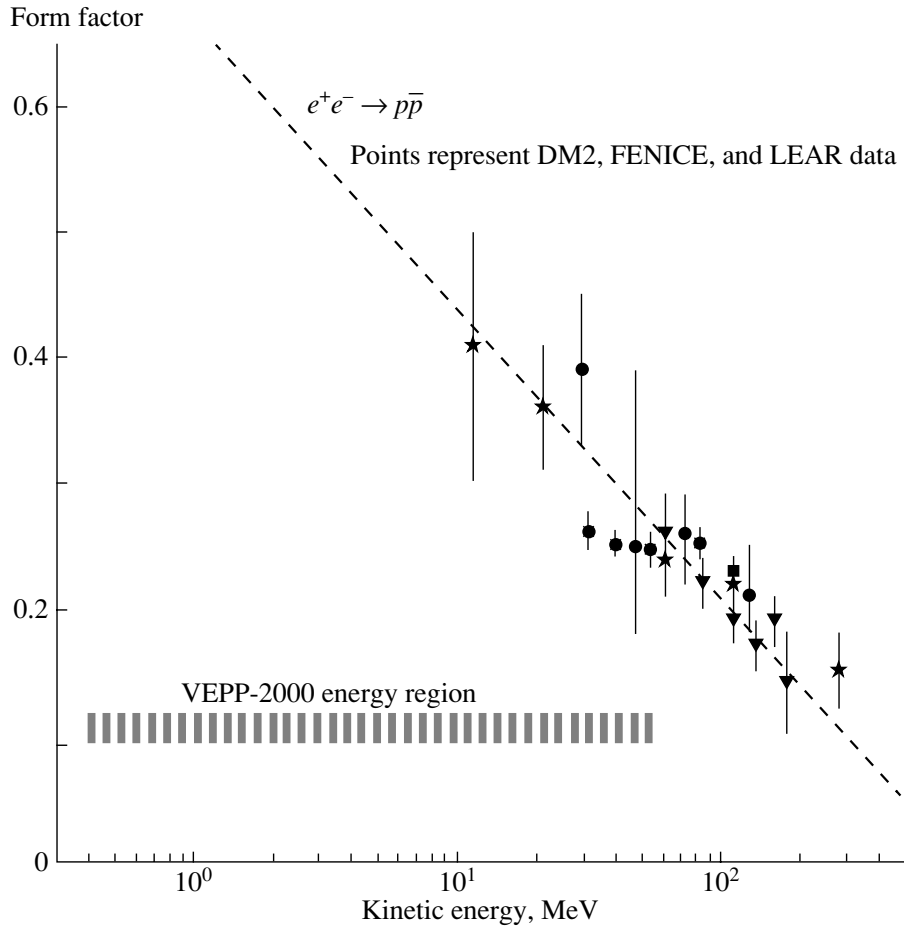


Fig. 9. Experimental data on the proton form factor.

the proton form factor? Will it be confirmed that the form factor grows as the energy decreases down to the very threshold? Will it be possible to measure the electric and magnetic form factors separately? Are there  $N\bar{N}$  bound states in the vicinity of the threshold?

In particular, the DM2 data on the process  $e^+e^- \rightarrow 3\pi^+3\pi^-$  (Fig. 11) [15] favor the existence of  $N\bar{N}$  bound states. Specifically, these data suggest a resonance structure in the cross section precisely at the nucleon-production threshold. We can add that, if an  $N\bar{N}$  bound state is an above-threshold one, it can be observed distinctly in the processes  $e^+e^- \rightarrow p\bar{p}, n\bar{n}$  in the form of an irregularity in the threshold cross section.

At an integrated luminosity of  $\Delta L \sim 1 \text{ fb}^{-1}$  and a detection efficiency of  $\epsilon \sim 0.1$ , the number of events involving nucleon-antinucleon pairs can be estimated at  $N_{p\bar{p}} \sim N_{n\bar{n}} \sim 10^4$  on the basis of the threshold cross section of  $\sigma_{p\bar{p}} \simeq \sigma_{n\bar{n}} \simeq 10^{-34} \text{ cm}^2$  at  $T \sim 1 \text{ MeV}$  (the energy scatter being  $\sigma E \simeq 0.7 \text{ MeV}$ ). This is two orders of magnitude greater than the

statistics of such events in previous experiments. This is the reason why one can hope that experiments at VEPP-2000 will provide answers to many of the questions formulated above.

The cross sections for proton-pair production at the threshold has the characteristic form of a step at  $2E = 2M_p$ , this enabling calibration of the collider energy scale. An estimation shows that, within a measurement period of about one day, the energy can be calibrated to a precision of  $\Delta E \simeq 0.1 \text{ MeV}$ . This value is an order of magnitude less than the energy scatter of  $\sigma E \simeq 0.7 \text{ MeV}$ .

A very narrow ( $\Gamma \sim 10^{-2} \text{ eV}$ )  $p\bar{p}$  Coulomb-like bound state of binding energy about  $-12.5 \text{ keV}$  can be formed at the threshold for proton-pair production. Unfortunately, the energy scatter leads to a decrease in the cross section for the production of this resonance by many orders of magnitude to a level of 1% of the cross section for the process  $e^+e^- \rightarrow \text{hadrons}$ . At a high statistical accuracy, there is, however, a chance to observe this phenomenon if the cross section for the process  $e^+e^- \rightarrow \text{hadrons}$  behaves smoothly in the vicinity of the threshold for proton-pair production.

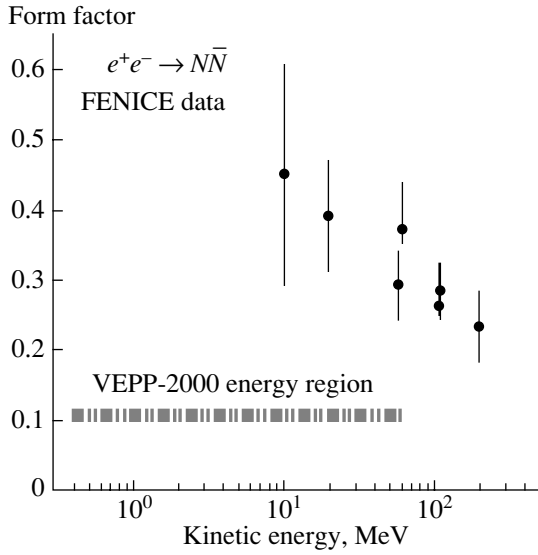


Fig. 10. Experimental data on the neutron form factor.

4.7. Hadron Production in Processes of “Radiative Return to a Resonance” (Fig. 12)

The production of hadrons of effective mass in the region  $M < \sqrt{s}$  is also possible in processes involving the emission of a photon of energy  $\omega = \frac{s - M^2}{2\sqrt{s}}$  [16].

Sometimes, such processes are referred to as those of the initial-state-radiation (ISR) type. Although the cross sections for ISR processes is considerably smaller than those for direct hadron production, these processes have a number of special features that make their experimental study worthwhile. First, the integrated luminosity of colliders usually grows fast with increasing energy; therefore, the number of  $\rho, \omega,$  and  $\phi$  mesons produced at  $B$  factories, for example, is quite commensurate with the number of these particles produced directly at VEPP-2M. Second, hadrons from ISR processes are tagged, since they are accompanied by a recoil photon, this simplifying the analysis of respective events. Third, the entire mass spectrum of hadrons is accessible, so that normalization to the calibration process  $e^+e^- \rightarrow \mu^+\mu^-\gamma$  is possible.

A simple ISR process such as  $e^+e^- \rightarrow \omega\gamma \rightarrow \pi^0\pi^0\gamma$  was clearly seen even at VEPP-2M with SND (Fig. 13). At an integrated luminosity of  $\Delta L \sim 3 \text{ fb}^{-1}$ , about  $10^7$   $\rho$  mesons and  $10^6$   $\omega$  mesons are expected at VEPP-2000; this will make it possible to perform independent measurements of hadron cross sections and the parameters of vector mesons.

4.8. Two-Photon Physics

The production of  $C$ -even mesons ( $C^+$ ) at an  $e^+e^-$  collider is possible in processes of two types:

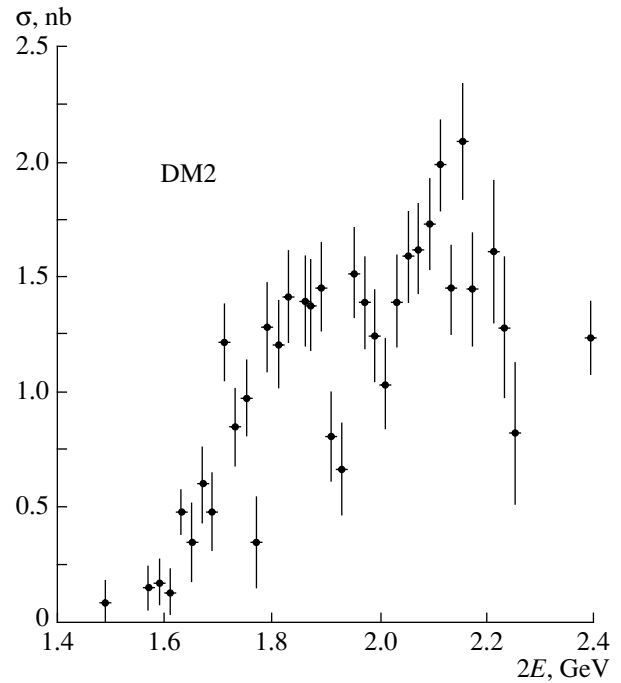


Fig. 11. Cross section for the process  $e^+e^- \rightarrow 3\pi^+3\pi^-$  in the vicinity of the hadron-production threshold according to data from [15].

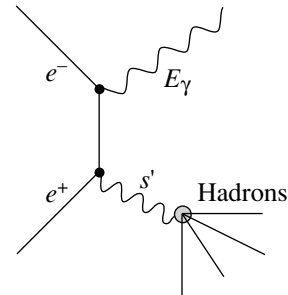
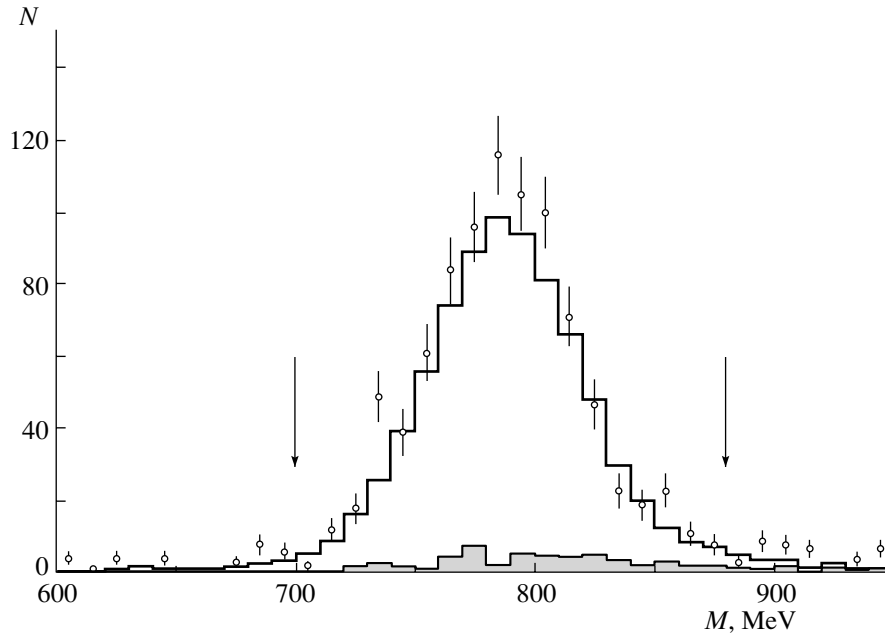


Fig. 12. Diagram representing hadron production in a process of radiative reversion to a resonance.

$e^+e^- \rightarrow e^+e^- + C^+$  and  $e^+e^- \rightarrow C^+$ . Processes of the first type have long since been studied in  $e^+e^-$  experiments. This made it possible to measure the widths  $\Gamma(C^+ \rightarrow 2\gamma)$  for many  $C$ -even mesons and the cross sections for the processes  $\gamma\gamma \rightarrow$  hadrons.

It is of interest to measure the two-photon widths of the  $f_0(980)$  and  $a_0(980)$  mesons at VEPP-2000. These scalar mesons have an anomalously small two-photon width of about 0.3 keV in relation to their nearest pseudoscalar neighbor  $\eta'(960)$  (its width is 4.4 keV). Therefore, a new and more precise measurement of  $\Gamma_{2\gamma}$  at VEPP-2000 will be useful. It will also be possible to measure anew the cross section for the processes  $\gamma\gamma \rightarrow \pi\pi, \eta\pi, \dots$  in the region  $\sqrt{s} < 1 \text{ GeV}$ , where available experimental data are scanty.



**Fig. 13.** Mass spectrum of  $\omega$  mesons in the process  $e^+e^- \rightarrow \omega\gamma$ : (points) SND experimental results and (histogram) results of a simulation of the process. The arrows show the cuts used in calculating the total cross section. The shaded histogram corresponds to the background contribution.

The statistics of events produced in these processes will be about  $10^3$ – $10^4$ .

Previously,  $C$ -even processes of the second type,  $e^+e^- \rightarrow C^+$ , were studied only at VEPP-2M [17], where upper limits on the electron widths of the  $f_2(1270)$  and  $a_2(1320)$  mesons were established at a level close to the results of respective calculations. We hope to observe the direct production of these mesons in the process  $e^+e^- \rightarrow f_2(1270), a_2(1320)$  at VEPP-2000 with a high integrated luminosity.

#### 4.9. Test of QED in Processes with a High Multiplicity in the Final State

There are many QED processes producing at large angles a great number of final-state particles ( $\theta \sim 1$ ), for example,

$$e^+e^- \rightarrow \gamma\gamma\gamma\gamma, \quad e^+e^-e^+e^-, \quad e^+e^-\gamma\gamma\gamma, \dots$$

The cross sections for these processes range between  $10^{-36}$  and  $10^{-34}$  cm<sup>2</sup> (within the solid angle of the detector); therefore, the number of respective events amounts to hundreds or thousands even with allowance for the detection efficiency. For instance, the process  $e^+e^- \rightarrow \gamma\gamma\gamma\gamma$  was first found at VEPP-2M with the ND detector [18] (87 events were observed), while the process of annihilation into five photons can be observed at VEPP-2000.

Interest in such QED processes is due to two reasons:

(1) Advances in experimental techniques give impetus to the development of methods for calculating the cross sections of these processes.

(2) These are background processes in searches for rare hadron reactions—such as  $e^+e^- \rightarrow \omega\pi^0 \rightarrow \pi^0\pi^0\gamma \rightarrow 5\gamma$  or  $e^+e^- \rightarrow \phi \rightarrow \pi^0e^+e^- \rightarrow e^+e^-\gamma\gamma$ ; therefore, it is necessary to perform precise calculations for these processes.

## 5. CONCLUSION

The proposed physics program for VEPP-2000 is quite extensive. Despite a relatively small increase in energy—from 1.4 GeV at VEPP-2M to 2.0 GeV at VEPP-2000—there arise new possibilities in the new energy range that were not available at VEPP-2M:

(1) The uncertainty in measuring the fundamental ratio  $R$  will be reduced owing to experiments at VEPP-2000.

(2) It will be possible to perform a thorough investigation of the parameters of the excited vector mesons  $\rho'$ ,  $\omega'$ , and  $\phi'$ , their masses lying precisely in the range  $2E = 1.4$ – $2.0$  GeV.

(3) Since the VEPP-2000 energy is higher than the  $\tau$ -lepton mass,  $2E > m_\tau$ , the CVC hypothesis can be tested throughout the whole range of the  $\tau$ -lepton-decay spectra.

(4) Since the VEPP-2000 energy is above the threshold for nucleon-pair production, it will be possible to measure the nucleon form factors in the timelike region and to clarify the problem of  $NN$  bound states.

## ACKNOWLEDGMENTS

I am grateful to V.B. Golubev, Yu.M. Shatunov, B.I. Khazin, and S.I. Eidelman for enlightening discussions on many aspects of this study.

This work was supported by the Russian Foundation for Basic Research (project nos. 02-02-16269-a, 03-02-16581) and by the Program for the Promotion of Scientific Schools (grant no. 1335.2003.2).

## REFERENCES

1. G. M. Tumaikin, in *Proceedings of the 10th International Conference on High-Energy Particle Accelerators, Serpukhov, 1977*, Vol. 1, p. 443.
2. I. A. Koop *et al.*, Frascati Physics Series **XVI**, 393 (1999).
3. Yu. M. Shatunov *et al.*, in *Proceedings of the 7th European Particle Accelerators Conference EPAC2000, Vienna, Austria, 2000*, p. 439.
4. M. N. Achasov *et al.*, Nucl. Instrum. Methods Phys. Res. A **449**, 125 (2000).
5. M. N. Achasov *et al.*, Nucl. Instrum. Methods Phys. Res. A **441**, 337 (1998); **401**, 179 (1997).
6. V. M. Aulchenko *et al.*, Preprint Budker INP 85-122 (Novosibirsk, 1985).
7. G. N. Abramov *et al.*, Preprint Budker INP 2001-29 (Novosibirsk, 2001).
8. R. R. Akhmetshin *et al.*, Preprint Budker INP 2001-45 (Novosibirsk, 2001).
9. Muon g-2 Collab. (G. W. Benaett *et al.*), hep-ex/0208001.
10. M. Davier *et al.*, Preprint LAL 02-81, Orsay; hep-ex/0208177.
11. R. R. Akhmetshin *et al.*, Phys. Lett. B **527**, 161 (2002).
12. Particle Data Group, Eur. Phys. J. **15** (2000).
13. M. N. Achasov *et al.*, Phys. Lett. B **486**, 29 (2000).
14. A. Antonelli *et al.*, Nucl. Phys. B **517**, 3 (1998).
15. A. B. Clegg and A. Donnache, Z. Phys. C **34**, 257 (1987).
16. V. Benayoun *et al.*, Mod. Phys. Lett. A **14**, 2605 (1999).
17. M. N. Achasov *et al.*, Phys. Lett. B **492**, 8 (2000).
18. S. I. Dolinsky *et al.*, Phys. Rep. **202**, 99 (1991).

*Translated by E. Kozlovsky*

---

---

**ELEMENTARY PARTICLES AND FIELDS**  
**Experiment**

---

---

## Measurement of Differential Cross Sections for Charge-Exchange $\pi^-p$ Scattering in the Region of Small Scattering Angles

**D. E. Bayadilov\***, Yu. A. Beloglazov, M. R. Kan, N. G. Kozlenko, S. P. Kruglov,  
I. V. Lopatin, D. V. Novinsky, A. K. Radkov, V. V. Sumachev, and E. A. Filimonov

*Petersburg Nuclear Physics Institute, Russian Academy of Sciences, Gatchina, 188350 Russia*

Received April 3, 2003

**Abstract**—Differential cross sections for the reaction  $\pi^-p \rightarrow \pi^0n$  were measured for nearly forward scattering angles. The experiment was performed at the pion channel of the synchrocyclotron installed at the Petersburg Nuclear Physics Institute (PNPI, Gatchina), the incident-pion momenta ranging between 417 and 710 MeV/c. The measurements, which involved recording both photons from the decay process  $\pi^0 \rightarrow 2\gamma$ , employed the neutral-pion spectrometer developed at the PNPI. A description of the experimental facility is given, and the results of the measurements are presented. © 2004 MAIK “Nauka/Interperiodica”.

### 1. INTRODUCTION

Measurement of differential cross sections for charge-exchange  $\pi^-p$  scattering is part of the program Spectroscopy of Nonstrange Baryons with 300- to 2000-MeV Pion Beams, which has been implemented by experimentalists from the Petersburg Nuclear Physics Institute (PNPI, Gatchina) since 1970.

At the present time, the accuracy in determining the properties of excited nonstrange baryons (that is, pion–nucleon resonances) is bounded primarily by the absence of high-quality experimental data on differential cross sections for charge-exchange  $\pi^-p$  scattering,<sup>1)</sup> especially in the region of low-lying  $\pi N$  resonances. The only systematic set of such data was obtained in 1975 by Brown *et al.* [1] at the Rutherford Appleton Laboratory (UK). However, the opinion that the experimental data reported in [1] are plagued by large systematic uncertainties that are caused by an error in the absolute normalization of the momentum scale of the pion channel and which are difficult to estimate is widespread among physicists involved in constructing a compilation of  $\pi N$  data. An attempt at measuring differential cross sections for the charge-exchange reaction in question was made at the Los Alamos Meson Physics Facility (USA), but the results of that experiment [2] have not yet been published—probably, again because of problems concerning systematic uncertainties. Finally, differential

cross sections for the charge-exchange reaction in the region of low-lying  $\pi N$  resonances were measured at the Brookhaven National Laboratory (USA) by using the Crystal Ball detector; however, only preliminary results in a bounded momentum range between 147 and 322 MeV/c have been published so far [3, 4]. As before, a realistic estimation of systematic uncertainties presented the main difficulty there.

In order to fill the existing gap in the relevant database and to remove the discrepancies between scanty experimental data available to date, two experiments aimed at measuring differential cross sections for the charge-exchange reaction have been launched at PNPI. The measurements, which are being performed at the pion channel of the PNPI synchrocyclotron, cover the energy range from 300 to 585 MeV (the corresponding momentum range extends from 417 to 710 MeV/c).

In the first experiment, differential cross sections for the charge-exchange reaction were measured for the case of scattering into the backward hemisphere. The experiment, which was reported in [5, 6], was performed by detecting the recoil neutron in coincidence with one of the photons from the decay  $\pi^0 \rightarrow 2\gamma$ .

In the future, we are going to extend our measurements to the region of smaller scattering angles. However, the method based on detecting recoil neutrons becomes inadequate for angles in the region  $\theta^{c.m.} < 50^\circ$ , because, there, the energy of recoil neutrons falls below 50 MeV, in which case the efficiency of their detection is overly low.

---

\* e-mail: [dair@pnpi.spb.ru](mailto:dair@pnpi.spb.ru)

<sup>1)</sup>For the sake of brevity, we will henceforth refer to this process merely as a charge-exchange reaction.

## 2. NEUTRAL-PION SPECTROMETER

In order to sidestep this difficulty, we designed and manufactured at PNPI a new neutral-pion spectrometer [7] that makes it possible to measure differential cross sections for the charge-exchange reaction over an angular range extended to extremely small angles.

The construction of this instrument is based on the idea to determine the kinetic energy of a neutral pion,  $E_{\pi^0}$ , and its emission angle  $\theta_{\pi^0}$  by measuring the energies ( $E_{\gamma 1}, E_{\gamma 2}$ ) of two photons from its decay and the angles  $\theta_{\gamma 1}$  and  $\theta_{\gamma 2}$  at which these photons are emitted in the laboratory frame. Once the quantities  $E_{\gamma 1}, E_{\gamma 2}, \theta_{\gamma 1}$ , and  $\theta_{\gamma 2}$  have been measured, the energy  $E_{\pi^0}$  and the angle  $\theta_{\pi^0}$  can be calculated by the formulas

$$E_{\pi^0} = \left[ \frac{2M_{\pi^0}^2}{(1 - \cos \Psi_{\gamma\gamma})(1 - X^2)} \right]^{1/2} - M_{\pi^0}, \quad (1)$$

$$\cos \theta_{\pi^0} = \frac{E_{\gamma 1} \cos \theta_{\gamma 1} + E_{\gamma 2} \cos \theta_{\gamma 2}}{\sqrt{E_{\gamma 1}^2 + E_{\gamma 2}^2 + 2E_{\gamma 1}E_{\gamma 2} \cos \Psi_{\gamma\gamma}}}, \quad (2)$$

where  $M_{\pi^0}$  is the neutral-pion mass, the quantity  $X = (E_{\gamma 1} - E_{\gamma 2}) / (E_{\gamma 1} + E_{\gamma 2})$  characterizes the distribution of the neutral-pion energy between two product photons, and  $\Psi_{\gamma\gamma}$  is the angle of divergence of two photons.

The layout of the neutral-pion spectrometer is displayed in Fig. 1. This instrument consists of two full-absorption electromagnetic calorimeters intended for detecting both photons from neutral-pion decay. Each calorimeter involves a  $6 \times 4$  matrix of CsI(Na) crystals having dimensions of  $6 \times 6 \times 30$  cm<sup>3</sup>, the last dimension being a thickness that corresponds to 16.2 radiation-length units.

Each of the 48 crystals is equipped with a photomultiplier FEU-97, each photomultiplier having its own high-voltage source that is mounted directly on the photomultiplier link block and which ensures a good stabilization of high voltage. These independent sources of high voltage were developed and manufactured at PNPI.

The energy calibration of each of the 48 measuring channels [CsI(Na) crystal + photomultiplier + charge-code converter (CCC)] was performed by two methods:

- (i) with the aid of cosmic-ray muons traversing a crystal in the vertical direction;
- (ii) with the aid of electrons incident on the front end face of a crystal.

In the first case, the coincidence of the signals from the upper and the lower layer of CsI(Na) crystals served as a trigger. A typical spectrum (obtained after the subtraction of the CCC pedestal) is shown in

Fig. 2a. The observed peak corresponds to the ionization losses of cosmic-ray muons traversing a 6-cm crystal; our calculations reveal that the average value of these losses is 45 MeV. In performing the energy calibration with cosmic-ray muons, the values of the high voltage at various photomultiplier were selected in such a way that the cosmic-ray-muon peaks occurred in approximately the same CCC channel for all 48 crystals.

In the second case, we employed electrons that are always present in the beam of negatively charged particles that is formed by the pion channel. The separation of electrons from beam pions and muons was accomplished with the aid of a gaseous Cherenkov counter filled with carbon dioxide at a pressure of 3 atm; this counter was arranged on the beam axis in front of the target. The procedure of calibration consisted in directing a narrow electron beam<sup>2)</sup> at the center of the CsI(Na) crystal being studied and in measuring the spectrum from the corresponding CCC channel. The energy of electrons incident on the calorimeter was varied between 70 and 500 MeV [8]. By way of example, the spectrum obtained at the electron energy of 300 MeV is shown in Fig. 2b. Because of the transverse propagation of the respective electromagnetic shower, the energy of the electron incident on a crystal is not entirely deposited in it—part of this energy is carried away to the neighboring crystals. In order to obtain the total energy deposition (which must be equal to the incident-electron energy), it is therefore necessary to sum the CCC spectrum from the crystal being studied and the spectra from the eight crystals surrounding it. A typical contribution of the surrounding crystals to the total energy deposition is about 10%.

## 3. DESCRIPTION OF THE EXPERIMENT

At the first stage of the experiment, the calorimeters of the neutral-pion spectrometer were arranged in such a way (see Fig. 1) as to perform a measurement of the differential cross section for the charge-exchange reaction at nearly forward angles—that is, for the case of neutral-pion emission at angles close to zero.

The experiment employed a safe vacuum-type liquid-hydrogen target preliminarily cooled with the aid of a nitrogen reservoir. The angle open for detecting emitted particles was 270°. The hydrogen container had the shape of a vertical cylinder 12 cm in height and 10 cm in diameter, its aluminum walls being 100  $\mu$ m thick. The liquefaction of hydrogen was accomplished by cooling the container with

<sup>2)</sup>The beam size was determined by a small scintillation counter positioned immediately in front of the calorimeter.

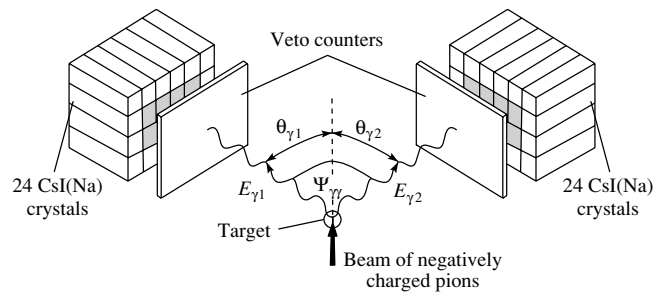


Fig. 1. Layout of the neutral-pion spectrometer (see explanations in the main body of the text).

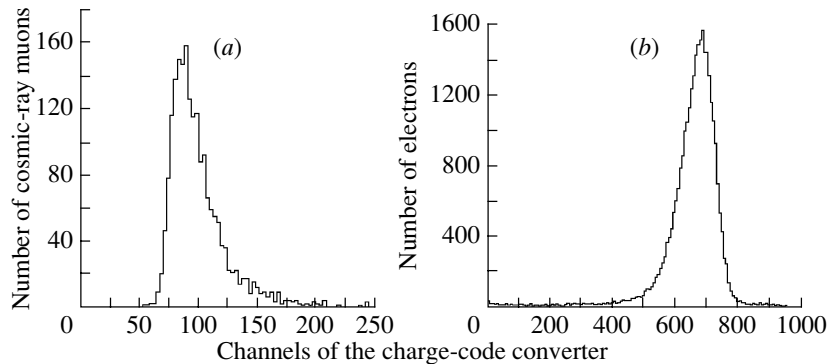


Fig. 2. Typical spectra obtained with the charge-code converter (upon pedestal subtraction) from a single CsI(Na) crystal in detecting (a) cosmic-ray muons traversing the crystal in the vertical direction and (b) 300-MeV electrons incident on the crystal in the horizontal direction.

cold gaseous helium. The external window of the vacuum casing was manufactured from Mylar of thickness  $200 \mu\text{m}$ . The temperature (and, hence, the density) of liquid hydrogen was monitored throughout the experiment by measuring the resistance of a calibrated germanium diode and the pressure of vapor above the liquid surface. The liquid-hydrogen density was  $0.0740 \pm 0.0004 \text{ g/cm}^3$ .

Two electromagnetic calorimeters were arranged symmetrically with respect to the beam axis, the angle between the axis of each of them and the beam axis being  $16^\circ$ . This arrangement of the calorimeters and the magnitude of the angle ( $16^\circ$ ) were dictated by the special features of the decay  $\pi^0 \rightarrow 2\gamma$ : for the most part, photons are emitted symmetrically in this decay with respect to the direction of the neutral-pion momentum, and the angle  $\Psi_{\gamma\gamma}$  between the photon-emission directions is minimal in such a symmetric case, ranging between  $\pm 11^\circ$  and  $\pm 18^\circ$ , its specific value being dependent on the momentum of incident negatively charged pions. The distance of  $L = 101 \text{ cm}$  from the inlet of the calorimeters to the target center was specified with allowance for the requirement that the edges of the calorimeters not be irradiated with beam pions. At the location of a calorimeter, the

beam, which diverges in horizontal directions, already has quite large dimensions.

Thin scintillation veto counters  $RV$  and  $LV$  (specifically, their thickness is  $5 \text{ mm}$ ) were placed in front of each of the calorimeters. These counters are intended for suppressing the trigger that could actuate the facility in the cases where charged particles emitted from the target rather than electrons hit the calorimeter.

The facility also includes two monitor counters  $C1$  and  $C2$  (not shown in Fig. 1)—of these, one is arranged immediately in front of the target, while the other is positioned at the outlet of the vacuum pipe of the pion channel—as well as the beam veto counter  $C3$ , which is placed on the beam axis immediately behind the calorimeters.

Schematically, the trigger actuating the facility can be represented in the coincidence form

$$T = C1 \cdot C2 \cdot R \cdot L \cdot \overline{C3} \cdot \overline{RV} \cdot \overline{LV}, \quad (3)$$

where  $C1$  and  $C2$  are signals from the monitor counters  $C1$  and  $C2$ , respectively;  $R$  and  $L$  are dynode signals from, respectively, the right ( $R$ ) and the left ( $L$ ) calorimeter, each of the dynode signals being formed if the energy deposited in eight internal crystals of the calorimeter exceeds a threshold level;  $C3$  is a signal

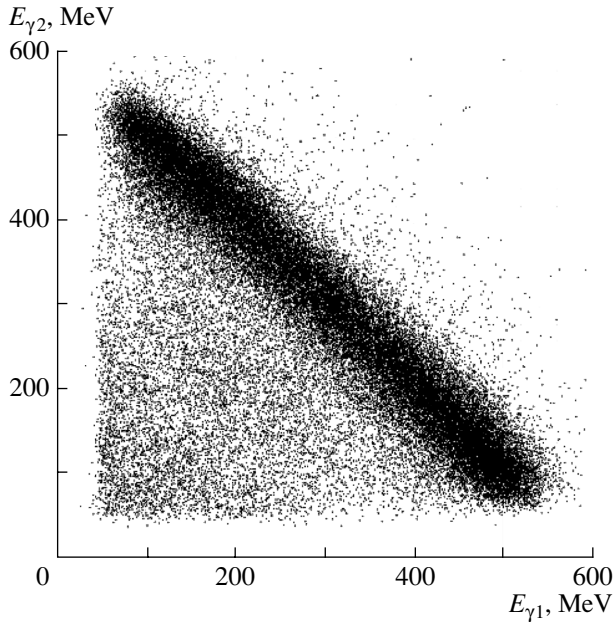


**Fig. 3.** Correlation matrix of energies that were deposited in the two calorimeters of the neutral-pion spectrometer.

from the beam veto counter *C3* placed on the beam axis behind the calorimeters; and *RV* and *LV* are signals from the veto counters arranged in front of each of the calorimeters.

As soon as the trigger *T* is formed, the following information is saved on the hard disk of a computer: the charge collected on each of 48 CCC, the time of particle flight over the base between the monitor counter *C2* and the calorimeter *R* or *L*, and the number of monitor counts  $C1 \cdot C2$  over the period between the current and the preceding trigger.

#### 4. DATA PROCESSING

The initial step of data processing consisted in the kinematical reconstruction of each event; by this, we mean the determination of the energies ( $E_{\gamma 1} \times E_{\gamma 2}$ ) and emission angles ( $\theta_{\gamma 1}, \theta_{\gamma 2}$ ) for both recorded photons. When a photon hits a specific CsI(Na) crystal, its energy can be deposited not only in this crystal but also partly in the surrounding crystals because of the transverse propagation of the respective electromagnetic shower. In order to evaluate the total photon energy  $E_{\gamma}$ , it is necessary to find the crystal where the energy deposition is maximal—we denote it by  $E_0$ —and to add, to this quantity, the sum of the energies  $E_i$  deposited in the eight surrounding crystals:

$$E_{\gamma} = \sum_{i=0}^8 E_i. \quad (4)$$

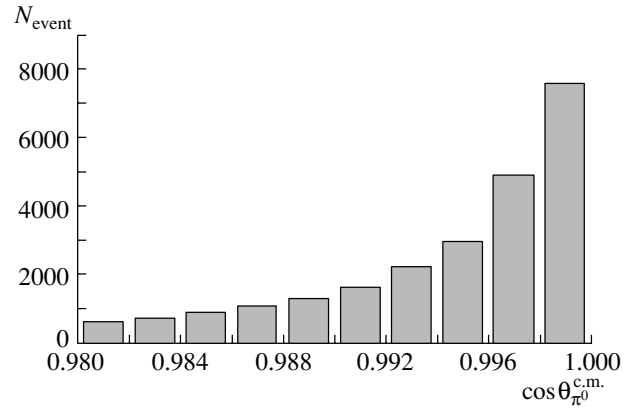


**Fig. 4.** Angular distribution of recorded photon-coincidence events.

By way of example, Fig. 3 shows the  $(E_{\gamma 1}, E_{\gamma 2})$  correlation matrix obtained at  $p_{\pi^-} = 614 \text{ MeV}/c$  by applying the procedure outlined above. It can be seen that the energy range of detected photons is quite wide, from 60 to 540 MeV. Since the energy resolution of an individual crystal becomes poorer at low photon energies, energy thresholds were usually introduced for  $E_{\gamma 1}$  and  $E_{\gamma 2}$  in the ensuing analysis.

As to the determination of the point at which a photon hits a calorimeter, this is, for a first approximation, the center of the crystal in which the energy deposition was maximal. A more realistic estimate can be obtained by means of a weighing procedure, where the weights used are proportional to  $\sqrt{E_i}$ .

Once the energies of both photons and the points at which they enter the calorimeter (and, hence, their entrance directions) have been determined, the emission angle of the neutral pion can be calculated by formula (2). For the ensuing analysis, the total set of processed events was broken down into several angular bins. An example of the resulting angular distribution is given in Fig. 4 ( $p_{\pi^-} = 614 \text{ MeV}/c$ ; the angular-bin size is  $\Delta \cos \theta_{\pi^0}^{c.m.} = 0.002$ ). It can be seen that the angular distribution is characterized by a fast growth of the number of events for  $\cos \theta_{\pi^0}^{c.m.} \rightarrow 1$  (that is, for  $\theta_{\pi^0}^{c.m.} \rightarrow 0^\circ$ ). This property of the angular distribution reflects the aforementioned special feature of the decay  $\pi^0 \rightarrow 2\gamma$ : the photon-emission probability is the highest in the case where the angle between the photon momenta is minimal and where the photons are emitted symmetrically with respect to the neutral-pion momentum. The angular acceptance for the detection of the photons decreases sharply if the photons are emitted in directions differing from those in the above case.

For each angular bin, the values of the differential cross section were calculated by the formula

$$\frac{d\sigma^{\text{c.m.}}}{d\Omega} = \frac{N_{\gamma\gamma}}{N_{\pi} \cdot N_p \cdot A \cdot \Delta\Omega^{\text{c.m.}}}, \quad (5)$$

where  $N_{\gamma\gamma}$  is the number of  $\gamma\gamma$  coincidences that was recorded throughout the experimental time,  $N_{\pi}$  is the number of negatively charged pions that hit the target throughout the experiment ( $N_{\pi}$  is determined from the total monitor number  $C1 \cdot C2$  after the introduction of corrections that take into account the admixture of electrons and muons in the beam),  $N_p$  is the number of protons in the target, and  $\Delta\Omega^{\text{c.m.}}$  is the covered solid angle ( $\Delta\Omega^{\text{c.m.}} = 2\pi \cdot 0.002$  at  $\Delta \cos \theta^{\text{c.m.}} = 0.002$ ). In order to calculate the angular acceptance  $A$ , we must first determine the number of neutral pions formed in the solid angle  $\Delta\Omega^{\text{c.m.}}$  and then find that fraction of all photons from the decay of these neutral pions which is recorded by the neutral-pion spectrometer. In order to perform such calculations, we simulated the experiment by the Monte Carlo method, taking into account the precise geometry of our experimental facility, all details of the structure of the liquid-hydrogen target used, and the spatial and momentum distribution of pions in the beam. The results are dependent on the momentum of incident negatively charged pions and on the angle  $\theta^{\text{c.m.}}$  of charge-exchange  $\pi^-p$  scattering.

Photon–photon coincidences recorded in the course of the experiment may feature not only photons from the reaction  $\pi^-p \rightarrow \pi^0n \rightarrow 2\gamma n$ , which is studied here, but also a physical background that is caused by the reaction  $\pi^-p \rightarrow \pi^0\pi^0n \rightarrow 4\gamma n$ , as well as by the charge-exchange reaction on the nuclei of the scintillator of the counter  $C2$  and by photon rescattering on the structural elements of the liquid-hydrogen target.

We have investigated the contribution from various background sources by analyzing various distributions. First of all, we have calculated, for each event, the invariant mass of two photons,  $M_{\text{inv}}$ ,

$$M_{\text{inv}} = \sqrt{2E_{\gamma 1}E_{\gamma 2}(1 - \cos \Psi_{\gamma\gamma})}, \quad (6)$$

and plotted the distribution of the number of events versus  $M_{\text{inv}}$  (see Fig. 5, which shows such a distribution for  $p_{\pi^-} = 614 \text{ MeV}/c$ ). We can see a distinct peak occurring at about  $M_{\text{inv}} = 130 \text{ MeV}$  and corresponding to photons produced in the reaction  $\pi^-p \rightarrow \pi^0n \rightarrow 2\gamma n$  on the protons of the liquid-hydrogen target. Events in the region  $M_{\text{inv}} < 100 \text{ MeV}$  can be explained by photon rescattering on the structural elements of the liquid-hydrogen target, while a slight excess in the range  $M_{\text{inv}} = 160\text{--}180 \text{ MeV}$  is due to photons produced in the charge-exchange reaction

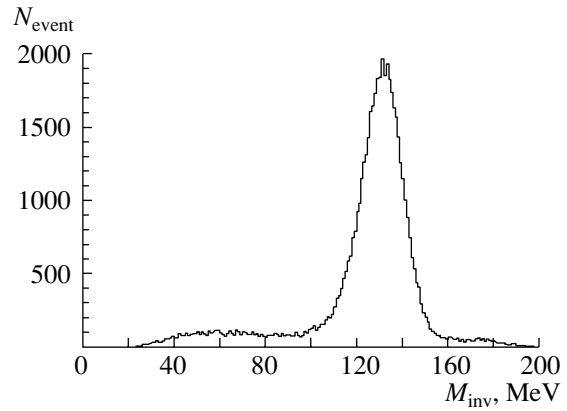


**Fig. 5.** Invariant-mass spectrum of the  $\gamma\gamma$  system at the momentum of incident negatively charged pions that is equal to  $614 \text{ MeV}/c$ .

on the nuclei of the  $C2$  scintillator. By extrapolating the left- and the right-hand background pedestal to the region under the main peak, one can in principle estimate the total contribution of the two background sources; however, the procedure of such an extrapolation is not quite unambiguous. In addition, there is a contribution from the reaction  $\pi^-p \rightarrow \pi^0\pi^0n \rightarrow 4\gamma n$ , and this contribution is indistinguishable from the main peak in the invariant-mass spectrum—this reaction proceeds predominantly as the two-step process  $\pi^-p \rightarrow R^0\pi^0$  followed by the intermediate-resonance decay  $R^0 \rightarrow \pi^0n \rightarrow 2\gamma n$ . This is clearly demonstrated by the two-dimensional graph in Fig. 6, where the missing mass and the invariant mass of the  $\gamma\gamma$  system are plotted along the abscissa and the ordinate, respectively. Events associated with the charge-exchange reaction on protons of the liquid-hydrogen target lie within the ellipse whose center has the coordinates of  $M_{\text{miss}} \simeq 900 \text{ MeV}$  and  $M_{\text{inv}} \simeq 130 \text{ MeV}$ , while events caused by the neutral-pion-production reaction  $\pi^-p \rightarrow \pi^0\pi^0n$  occur at higher values of  $M_{\text{miss}}$  and approximately the same values of  $M_{\text{inv}}$ . One can see that events associated with the reactions  $\pi^-p \rightarrow \pi^0n \rightarrow 2\gamma n$  and  $\pi^-p \rightarrow \pi^0R^0 \rightarrow \pi^0\pi^0n \rightarrow 4\gamma n$  are indeed indistinguishable if use is made only of the invariant-mass distribution.

Eventually, it was the number of events within the ellipses in two-dimensional plots similar to that in Fig. 6 that was used for  $N_{\gamma\gamma}$  in calculating the differential cross section for the charge-exchange reaction by formula (5). In order to estimate the systematic error introduced by uncertainties in the dimensions and shape of the ellipses being considered, special measurements with an empty target were performed at a few low momentum values ( $456, 490,$  and  $532 \text{ MeV}/c$ ), in which case the contribution of the

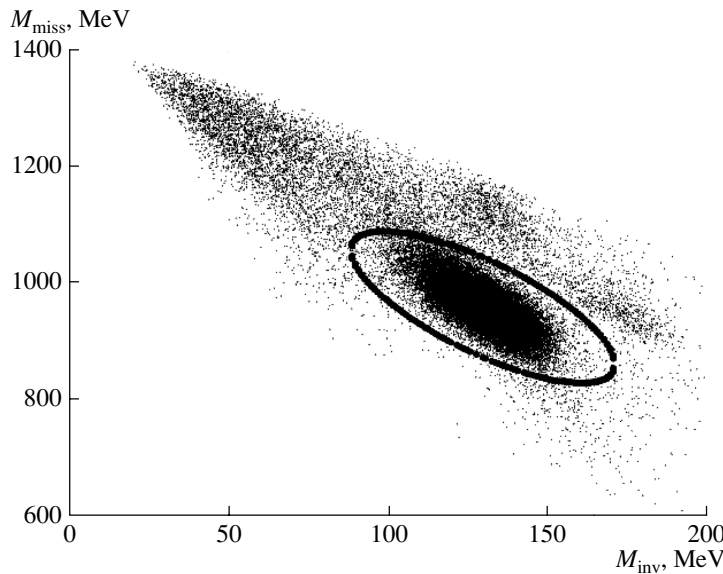


**Fig. 6.** Two-dimensional distribution where the missing mass  $M_{\text{miss}}$  is given as a function of the invariant mass  $M_{\text{inv}}$  for the momentum of incident negatively charged pions that is equal to  $614 \text{ MeV}/c$ .

reaction  $\pi^- p \rightarrow \pi^0 \pi^0 n$  is insignificant. In the subsequent analysis, the data obtained with the empty target were subtracted, after the relevant renormalization of the monitor numbers, from the data obtained with the liquid-hydrogen target, and the differential cross sections were then determined by using only the invariant-mass distributions. It turned out that, to within 3 to 5%, the results derived with this difference of the data agree with the results obtained on the basis of the data from the liquid-hydrogen data by using the  $M_{\text{miss}}$  vs.  $M_{\text{inv}}$  distributions with elliptic cuts. This gives sufficient grounds to state that the respective systematic error is about  $\pm 2\%$ .

Figure 7 illustrates the dependence of the resulting differential cross sections on the scattering angle in the c.m. frame. It can be seen that, in the region being considered, this angular dependence is very weak and can be approximated by a linear function. The extrap-

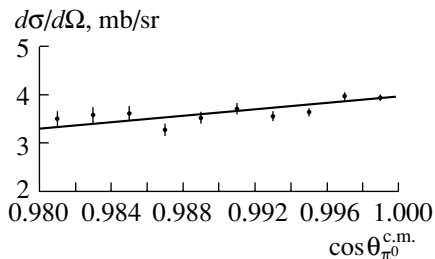


**Fig. 7.** Angular dependence of the differential cross section for the charge-exchange reaction at the momentum of incident negatively charged pions that is equal to  $614 \text{ MeV}/c$ .

olation to the point  $\cos \theta_{\pi^0}^{\text{c.m.}} = 1$  was performed by the least squares method.

## 5. RESULTS

In Fig. 8, the values obtained for  $\frac{d\sigma}{d\Omega}(0^\circ)$  are given versus the momentum of incident pions. For the sake of comparison, data from some fragmentary experiments reported previously [1, 9–11] are also displayed in this figure. It should be noted that, in [1, 9], the differential cross sections at zero angle were not measured directly—the values  $\frac{d\sigma}{d\Omega}(0^\circ)$  shown in Fig. 8 were derived with the aid of the expansions in terms of Legendre polynomials from those studies. It can be seen that the quality of preceding measurements was insufficient for getting a comprehensive and unambiguous pattern of the dependence of the cross section for the charge-exchange reaction at zero angle on the incident-pion momentum. The present results are much more precise; moreover, these results form a systematic set of data in a wide range of incident-pion momenta, since they were obtained at the same pion channel and with the same experimental facility.

The curves in Fig. 8 represent the momentum dependences of the differential cross section at zero angle that are predicted by the KH-80 and SM-02 partial-wave analyses. The first of these analyses [12] was performed in 1980 by Professor Höhler and his coauthors and is still used to extract the features that the Particle Data Group presents for pion–nucleon resonances in its Review of Particle Physics. The SM-02 analysis (see

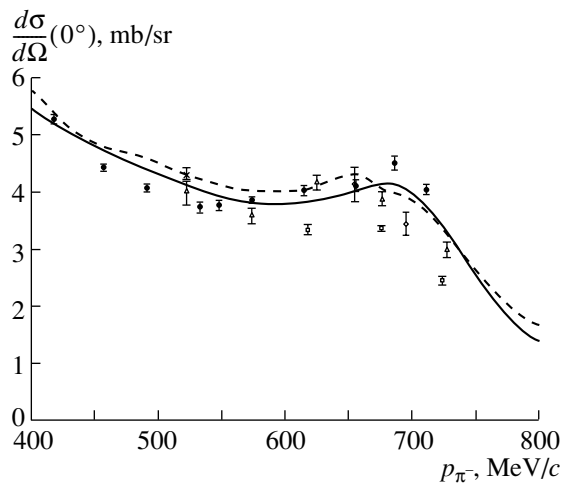


**Fig. 8.** Differential cross section for the charge-exchange reaction at  $\theta^{c.m.} = 0^\circ$  as a function of the momentum of incident negatively charged pions according to the present data (closed circles) along with the results reported by (open diamonds) Bulos *et al.* [9], (open boxes) Brown *et al.* [1], (open triangles) Kravtsov *et al.* [10], and (crosses) Gaille *et al.* [11]. The predictions of the KH-80 and SM-02 partial-wave analyses are represented by the dashed and the solid curve, respectively.

[http://gwdac.gwu.edu/analysis/pin\\_analysis.html](http://gwdac.gwu.edu/analysis/pin_analysis.html)) was performed in 2002 by a group of physicists that is headed by Professor Arndt (George Washington University, USA);<sup>3)</sup> in contrast to the former, the latter analysis relied on the entire set of data obtained for pion-nucleon scattering by the summer of 2002 inclusive. As can be seen, there is a significant discrepancy between our experimental results and the predictions of both partial-wave analyses, especially in the region of low momenta.

## ACKNOWLEDGMENTS

The participants of the present experiment are grateful to the Accelerator Division of PNPI for ensuring a stable long-term operation of the accelerator. We are indebted to L.D. Malakhov, A.V. Shvedchikov, and N.A. Semenova for assistance in servicing the liquid-hydrogen target.

This work was supported by the Russian Foundation for Basic Research.

## REFERENCES

1. R. M. Brown *et al.*, Nucl. Phys. B **117**, 12 (1976).
2. F. O. Borchering, PhD Thesis (University of California, Los Angeles, 1982).
3. The Crystal Ball Collab. (A. Koulbardi *et al.*), in *Proceedings of the 9th International Conference on Hadron Spectroscopy, Protvino, Russia, 2001*, Ed. by D. Amelin and A. M. Zaitsev; AIP Conf. Proc. **619**, 701 (2002).
4. M. E. Sadler, A. A. Koulbardi, *et al.*, Preprint No. 2473, PNPI (Gatchina, 2002).
5. I. V. Lopatin *et al.*, Preprint No. 2363, Petersburg Inst. Nucl. Phys. (Gatchina, 2000).
6. I. V. Lopatin, Yad. Fiz. **65**, 260 (2002) [Phys. At. Nucl. **65**, 236 (2002)].
7. D. E. Bayadilov *et al.*, PNPI Research Report 1998–1999 (Gatchina, 2000), Part 1, p. 22.
8. I. V. Lopatin *et al.*, Preprint No. 2268 (Petersburg Inst. Nucl. Phys., Gatchina, 1998).
9. F. Bulos *et al.*, Phys. Rev. **187**, 1827 (1969).
10. A. V. Kravtsov *et al.*, Nucl. Phys. B **140**, 279 (1978).
11. F. C. Gaille *et al.*, Phys. Rev. D **30**, 2408 (1984).
12. G. Höhler, in *Landolt-Börnstein* (Springer-Verlag, 1980), Vol. 9b.
13. R. A. Arndt *et al.*, Phys. Rev. C **52**, 2120 (1995).

*Translated by A. Isaakyan*

<sup>3)</sup>Previously, Arndt's group worked at the Virginia Polytechnic Institute (USA); the procedure used in their partial-wave analysis and the results extracted from this analysis for the features of pion-nucleon resonances can be found in [13].

## ELEMENTARY PARTICLES AND FIELDS

### Experiment

# Measurement of Spin-Rotation Parameters in Elastic $\pi^+p$ Scattering at a Momentum of 1.62 GeV/c and Calibration of a Carbon Polarimeter

Yu. A. Beloglazov<sup>1)</sup>, A. I. Kovalev<sup>1)</sup>, S. P. Kruglov<sup>1)</sup>, D. V. Novinsky<sup>1)\*</sup>, V. V. Sumachev<sup>1)</sup>, V. Yu. Trautman<sup>1)</sup>, V. A. Shchedrov<sup>2)</sup>, I. G. Alekseev<sup>2)</sup>, P. E. Budkovsky<sup>2)</sup>, V. V. Zhurkin<sup>2)</sup>, V. P. Kanavets<sup>2)</sup>, L. I. Koroleva<sup>2)</sup>, B. V. Morozov<sup>2)</sup>, V. M. Nesterov<sup>2)</sup>, V. V. Ryltsov<sup>2)</sup>, D. N. Svirida<sup>2)</sup>, A. D. Sulimov<sup>2)</sup>, N. A. Bazhanov<sup>3)</sup>, and E. I. Bunyatova<sup>3)</sup>

Received April 3, 2003; in final form, July 14, 2003

**Abstract**—Experimental data on the spin-rotation parameters  $A$  and  $R$  in elastic  $\pi^+p$  interaction were obtained for the first time at a momentum of  $p_\pi = 1.62$  GeV/c. These data are necessary for unambiguously reconstructing the amplitude of pion–nucleon scattering and, hence, for deducing a correct spectrum of nonstrange baryon resonances. In order to obtain results for the polarization parameters  $A$  and  $R$  with the minimum possible systematic error, the carbon polarimeter used was preliminarily calibrated in a dedicated experiment; that is, the analyzing power was measured in proton–carbon scattering for incident-proton energies in the range  $T_p = 0.7$ – $1.3$  GeV. The experimental data reported in the present article were obtained by a collaboration of researchers from the Petersburg Nuclear Physics Institute and Institute of Theoretical and Experimental Physics (ITEP, Moscow) at the ITEP synchrotron. © 2004 MAIK “Nauka/Interperiodica”.

## 1. INTRODUCTION

The main objective of the present study is to reconstruct the amplitude of pion–nucleon scattering unambiguously by experimentally exploring the polarization spin-rotation parameters  $A$  and  $R$  ( $RA$  experiment) with the aim of deducing a correct spectrum of pion–nucleon resonances consisting of  $u$  and  $d$  quarks. Experiments devoted to measuring the spin-rotation parameters play a key role in studying pion–nucleon scattering, since, in the absence of data on the parameters  $A$  and  $R$ , attempts at reconstructing the amplitude of pion–nucleon interaction run into the problem of discrete ambiguities [1] even in the presence of vast experimental information about the total ( $\sigma_{\text{tot}}$ ) and differential ( $d\sigma/d\Omega$ ) cross sections and about the polarization parameter  $P$ . It is the situation that had been prevalent before 1995 in the second resonance region of  $\pi^\pm p$  scattering ( $p_\pi$  about 1 to 2 GeV/c), where, in view of the complete absence of data on the spin-rotation parameters in all channels of

pion–nucleon scattering, there had been serious disagreements between the predictions of global partial-wave analyses.

Indeed, the amplitude for pion–proton scattering can be represented in the form [2]

$$M = f - ig(\boldsymbol{\sigma} \cdot \mathbf{n}), \quad (1)$$

where  $f$  and  $g$  are the complex-valued spin-flip and non-spin-flip scattering amplitudes, respectively;  $\boldsymbol{\sigma}$  is the Pauli matrix; and  $\mathbf{n}$  is a unit vector orthogonal to the plane of elastic pion–proton scattering.

The observables of pion–nucleon scattering are defined in terms of the amplitudes  $f$  and  $g$  as [2]

$$d\sigma/d\Omega = |f|^2 + |g|^2, \quad (2)$$

$$P = \frac{2\text{Re}(f^*g)}{|f|^2 + |g|^2}, \quad (3)$$

$$A = \frac{-(|f|^2 - |g|^2) \sin \theta_{\text{c.m.}} + 2\text{Im}(f^*g) \cos \theta_{\text{c.m.}}}{|f|^2 + |g|^2}, \quad (4)$$

$$R = \frac{(|f|^2 - |g|^2) \cos \theta_{\text{c.m.}} + 2\text{Im}(f^*g) \sin \theta_{\text{c.m.}}}{|f|^2 + |g|^2}, \quad (5)$$

where  $\theta_{\text{c.m.}}$  is the scattering angle in the c.m. frame. By explicitly taking the sum of the squares of the quantities  $P$ ,  $A$ , and  $R$ , we obtain

$$P^2 + A^2 + R^2 = 1. \quad (6)$$

<sup>1)</sup>Petersburg Nuclear Physics Institute, Russian Academy of Sciences, Gatchina, 188350 Russia.

<sup>2)</sup>Institute of Theoretical and Experimental Physics, Bol'shaya Cheremushkinskaya ul. 25, Moscow, 117218 Russia.

<sup>3)</sup>Joint Institute for Nuclear Research, Dubna, Moscow oblast, 141980 Russia.

\* e-mail: dimanov@pnpi.spb.ru

**Table 1.** Features (masses and widths, the latter being given parenthetically) of  $I = 3/2$  resonances ( $I$  is the resonance isospin) according to the predictions of the SM90 [5], KH80 [6], CMB80 [7], and SM95 [8] partial-wave analyses

Resonance	$L_{3,2J}$	Status	KH80	CMB80	SM90	SM95
$\Delta(1900)$	$S_{31}$	**	1908(140)	1890(170)	No	No
$\Delta(1905)$	$F_{35}$	****	1905(260)	1910(400)	1794(230)	1850(294)
$\Delta(1910)$	$P_{31}$	****	1888(280)	1910(225)	1950(400)	2152(760)
$\Delta(1920)$	$P_{33}$	***	1868(220)	1920(300)	No	No
$\Delta(1930)$	$D_{35}$	***	1901(195)	1940(320)	2018(400)	2056(590)
$\Delta(1940)$	$D_{33}$	*	No	1940(200)	No	No
$\Delta(1950)$	$F_{37}$	****	1923(224)	1950(320)	1884(240)	1921(232)

Previously, it was shown [1, 3] that, if only the differential cross section and the parameter  $P$  are measured, it is impossible to determine the amplitudes  $f$  and  $g$  unambiguously, since different combinations of  $f$  and  $g$  may correspond to the same value of  $P$ . Only by experimentally investigating the spin-rotation parameters  $A$  and  $R$  it is possible to eliminate such ambiguities, which cannot be determined from the measurement of  $d\sigma/d\Omega$  and  $P$ ; therefore, these parameters provide radically new information about the amplitude of pion–proton scattering.

The first measurements of the spin-rotation parameters for elastic  $\pi^+p$  scattering at a momentum of  $p_\pi = 1.43$  GeV/ $c$  [4] revealed that the result for the parameter  $A$  was consistent with the prediction of the SM90 partial-wave analysis [5], which was performed at the Virginia Polytechnic Institute, but that this result was at odds (at the level of three standard deviations) with the predictions of the KH80 [6] and CMB80 [7] partial-wave analyses, which were reported by, respectively, the Karlsruhe–Helsinki group and the group from Carnegie Mellon University and Berkeley. These three partial-wave analyses predict different spectra and different features of delta resonances whose masses are equal to those of the  $\pi^+p$  system,  $M \equiv \sqrt{s} \sim 2$  GeV. The spectra and basic parameters of these resonances are given in Table 1. It can be seen that the partial-wave analyses of the Virginia group (SM90 [5], SM95 [8]) did not confirm the existence of the  $S_{31}(1900)$  and  $P_{33}(1920)$  resonances, which have a rather high rating in the other two analyses, whose predictions were not supported by the experimental data from [4]. Although the Particle Data Group lowered the rating of the  $S_{31}(1900)$  resonance in 1998 [9] from \*\*\* to \*\*, the table of delta resonances whose masses are  $M(\pi^+p) \sim 2$  GeV has so far been composed on the basis of precisely the KH80 and CMB80 partial-wave analyses.

In order to test the conclusions of the previous experiment reported in [4] that concern the correctness of the predictions of the partial-wave analysis performed at the Virginia Polytechnic Institute, it was necessary to perform new measurements of the spin-rotation parameters in  $\pi^+p$  scattering over the same region of kinematical variables. In planning the experiment, we decided on measuring the spin-rotation parameter  $A$ , since the distinction between the predictions of the partial-wave analyses is much greater for it than for the parameter  $R$ .

## 2. DESCRIPTION OF THE EXPERIMENT

Figure 1 displays the layout of the experiment devoted to measuring the spin-rotation parameters in so-called  $A$  geometry: a beam of  $\pi^+$  mesons is incident on a polarized proton target, the proton polarization vector being aligned with the pion-beam axis. The experimental facility used records the tracks of the scattered pion and of the recoil proton. The experiment (see Fig. 1) consists in measuring the polarization  $\mathbf{P}(p_{\text{recoil}}^+)$  of recoil protons by means of their rescattering on a carbon nucleus at a given degree of target-proton polarization,  $P_T$ .

The transverse component of the recoil-proton polarization vector in the scattering plane corresponds to the parameter  $A$ , while its longitudinal component corresponds to the parameter  $R$ . The component along the normal to the scattering plane is equal to the degree of normal polarization,  $P$ . The spin-rotation parameter  $A$  is determined from the asymmetry  $\varepsilon_1$  of proton–carbon ( $pC$ ) scattering in the vertical plane, while the polarization parameter  $P$  is deduced from the asymmetry  $\varepsilon_2$  in the horizontal plane (see Fig. 1).

Under the conditions of the present experiment, where the target-proton polarization vector is aligned with the primary momentum, only two parameters ( $A$ ,  $P$ ) are measured directly, as was shown in [10],

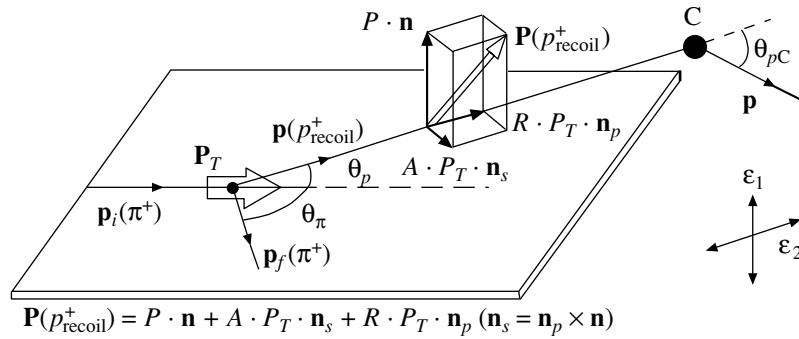


**Fig. 1.** Schematic representation of an experiment devoted to measuring the spin-rotation parameters in elastic  $\pi^+p$  scattering. A pion ( $\pi^+$ ) of momentum  $\mathbf{p}_i$  is incident on a polarized target having a horizontal proton polarization vector  $\mathbf{P}_T$ . Further, one selects the recoil proton and the pion elastically scattered at the angles  $\theta_p$  and  $\theta_\pi$ , respectively. The polarization of recoil protons is determined with the aid of a carbon polarimeter (C) by measuring the asymmetry of scattering in the vertical and horizontal planes,  $\theta_{pC}$  being the angle of scattering on the carbon analyzer.

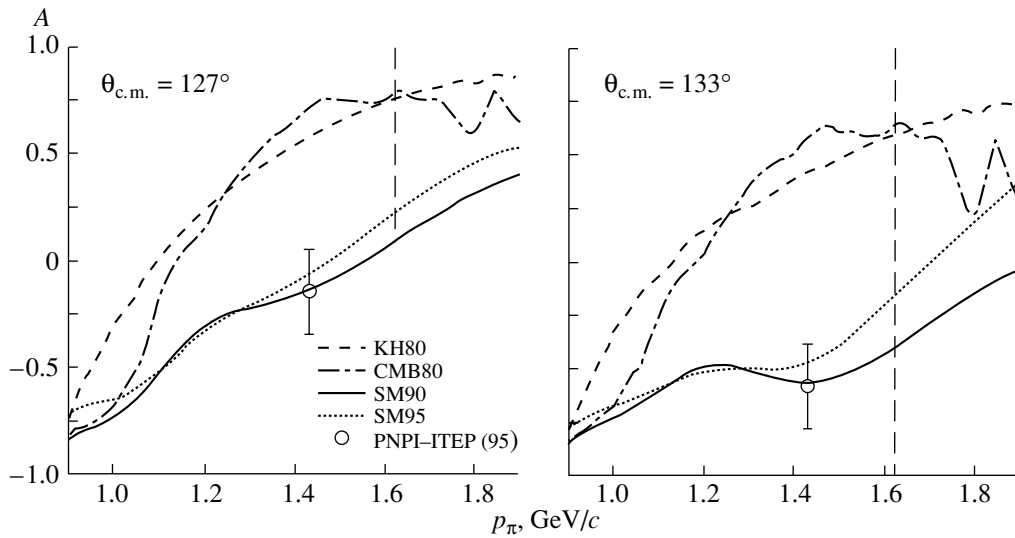


**Fig. 2.** Values of the spin-rotation parameter  $A$  in elastic  $\pi^+p$  scattering at momenta in the range  $p_\pi \sim 1\text{--}2$  GeV/ $c$  for angles of  $\theta_{\text{c.m.}} = 127^\circ$  and  $133^\circ$ . Also given in this figure are the predictions of the SM90 [5], KH80 [6], CMB80 [7], and SM95 [8] partial-wave analyses and the experimental results obtained by a collaboration of physicists from the Petersburg Nuclear Physics Institute (PNPI) and Institute of Theoretical and Experimental Physics (ITEP) at a momentum of  $p_\pi = 1.43$  GeV/ $c$  [4]. The vertical line corresponds to the momentum value of  $p_\pi = 1.62$  GeV/ $c$ .

the absolute value of  $R$  being determined from relation (6). This experiment, in which we are dealing with double scattering, is quite complicated, since it calls for the presence of a polarized proton target featuring a horizontally oriented proton spin and of a highly efficient carbon polarimeter measuring recoil-proton polarization in the required region of energies and angles of  $pC$  scattering. It is necessary to know the analyzing power of  $pC$  scattering to a precision that makes it possible to choose between the solutions of the partial-wave analyses at the level of three standard deviations ( $3\sigma$ ).

For elastic  $\pi^+p$  interaction, the momentum dependence of the predictions of three global partial-

wave analyses for the spin-rotation parameter  $A$  is displayed in Fig. 2 for two values of the pion scattering angle in the c.m. frame. Specifically, shown in the figure are the predictions of the SM90 [5], KH80 [6], CMB80 [7], and SM95 [8] partial-wave analyses and the result of the measurements at a momentum of  $p_\pi = 1.43$  GeV/ $c$  from [4]. It can be seen that the experimental data from [4] agree with the predictions of the SM90 and SM95 partial-wave analyses,<sup>4)</sup> but that it deviates strongly from the predictions of the KH80 and CMB80 partial-wave analyses. The

<sup>4)</sup>The results reported in [4] were included in the SM95 partial-wave analysis.

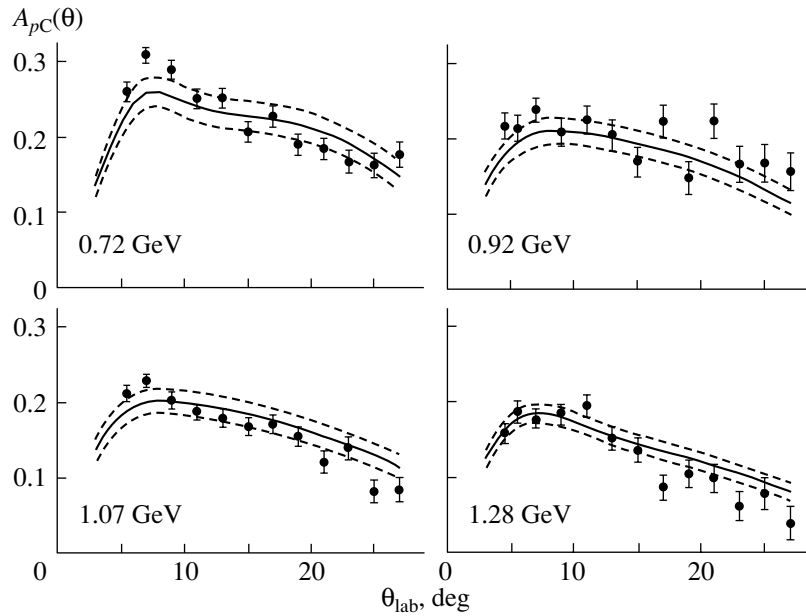


**Fig. 3.** Results of the measurements of the carbon analyzing power  $A_{pC}(\theta)$  that were performed by the PNPI–ITEP Collaboration for proton energies  $T_p = 0.72, 0.92, 1.07,$  and  $1.28$  GeV at an analyzer thickness of  $36.5$  g/cm $^2$ . The solid curve represents a fit to data, while the dashed curves bound the error corridor.

vertical line in Fig. 2 corresponds to the momentum of  $p_\pi = 1.62$  GeV/ $c$ , at which the present measurements have been performed. The reaction and the kinematical region of the measurements ( $p_\pi = 1.62$  GeV/ $c$ ,  $\Delta\theta_{c.m.} \sim 120^\circ$ – $140^\circ$ ) were chosen on the basis of the following considerations. In the second resonance region of pion–proton scattering, the spin-rotation parameters were previously measured at a single momentum value of  $p_\pi = 1.43$  GeV/ $c$ . In order to choose between the existing partial-wave analyses conclusively, it is necessary, however, to perform new measurements of the parameters  $A$  and  $R$ , since there were

(i) serious discrepancies between the predictions of the partial-wave analyses in the chosen region precisely for the parameter  $A$ ;

(ii) a pure isospin state (elastic  $\pi^+p$  scattering), this facilitating the physical interpretation of the result considerably;

(iii) a cross-section value (about  $0.7$  mb/sr in the middle of the scattering angle interval  $\theta_{c.m.} = 120^\circ$ – $140^\circ$ ) that is quite acceptable for a reasonably fast accumulation of the required number of events;

(iv) data in the literature for the normal polarization  $P$  in elastic  $\pi^+p$  scattering for estimating systematic uncertainties;

(v) the analyzing power measured by the present authors for carbon of thickness  $36.5$  g/cm $^2$  [11].

It was shown in [12] that, for reliably choosing, on the basis of experimental data, between the predictions of the partial-wave analyses performed by the Virginia group and those of the partial-wave analyses of the other two groups at a  $3\sigma$  level, it is necessary to know the analyzing power of proton–carbon scattering to a relative precision not poorer than 10%. We surveyed data available worldwide for the relevant analyzing power, and it turned out that the data from the literature do not ensure the required accuracy; for this reason, we performed a calibration of our carbon polarimeter in a dedicated experiment.

In order to measure the analyzing power of proton–carbon scattering, we created four versions of the facility that are characterized by different values of the graphite thickness. The scheme of the experiment and its results are described in detail elsewhere [11]. A carbon filter of thickness  $36.5$  g/cm $^2$  proved to be the most efficient for our purposes [12]. Figure 3 displays the results obtained by measuring the analyzing power  $A_{pC}(\theta)$  at the polarimeter thickness of  $36.5$  g/cm $^2$ . There, the solid curve represents a fit to data from [11], while the dashed curves bound the error corridor. It can be seen that, in the angular region extending up to  $20^\circ$ , the relative error in the approximation of data does not exceed the required value of 10%.

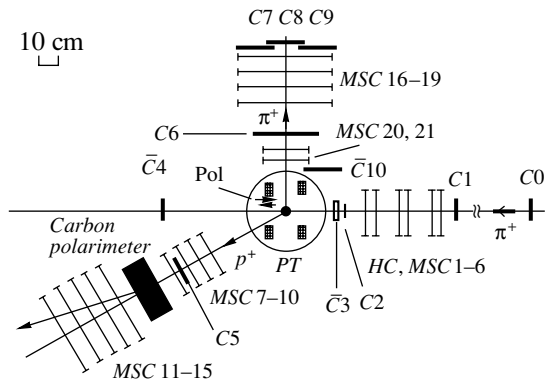


**Fig. 4.** Experimental facility for measuring the spin-rotation parameters at the pion-beam momentum of  $p_\pi = 1.62$  GeV/ $c$ : (*PT*) polarized proton target, (*C0–C10*) scintillation counters, (*HC, MSC*) beam track and magnetostrictive spark chambers, and (*carbon polarimeter*) carbon analyzer of thickness  $36.5$  g/cm $^2$  ( $23$  cm).

### 3. EXPERIMENTAL INVESTIGATION OF THE SPIN-ROTATION PARAMETERS

#### 3.1. Experimental Facility

The facility used to measure the parameters  $A$  and  $R$  contains the following basic elements (see Fig. 4):

- (i) a polarized proton target in a superconducting solenoid;
- (ii) a carbon polarimeter;
- (iii) two-coordinate spark chambers with a magnetostrictive readout, which are intended for reconstructing the trajectories of the incident and scattered pions and of recoil protons, as well as for measuring the angle of recoil-proton scattering on the carbon analyzer (*carbon polarimeter*);
- (iv) scintillation counters for developing a trigger.

The facility is arranged at the universal two-step magneto-optical channel of the ITEP accelerator, this channel ensuring the extraction of both negatively and positively charged pions and of protons in the momentum range  $0.9$ – $2.1$  GeV/ $c$  with a resolution of  $\Delta p/p(\text{FWHM}) = \pm 1.8\%$ . In the case of accelerator operation at an energy of  $T_p = 8$  GeV in the main ring, the intensity of a  $1.62$ -GeV/ $c$  pion beam was about  $4 \times 10^5$  positively charged pions per accelerator spill (one spill per approximately 4 s). In the region of the polarized target position, the horizontal and vertical sizes of the beam (width at half maximum) were about 30 mm. The arrangement of the facility corresponds to the geometry of the  $A$  experiment (see Fig. 1).

The experiment employs a polarized proton target (*PT*) featuring a horizontal orientation of the proton polarization vector. The construction and the features of the target are described in [13]. For the working

substance, we used propanediol ( $\text{C}_3\text{O}_2\text{H}_8$ ) supplemented with an addition of  $\text{Cr}^V$ . Its density is  $\rho \approx 1.1$  g/cm $^3$ , and it contains about 10% free hydrogen in mass. The container, which has the shape of a cylinder 30 mm in diameter and 30 mm in height, was filled with the working substance and was placed in a magnetic field of strength 2.5 T that was generated by a couple of superconducting Helmholtz coils. The nonuniformity of the field in the sample volume did not exceed 0.001 T. The cooling of the sample down to a temperature of 0.5 K was performed by evacuating  $^3\text{He}$  in the cryostat of the target. The pumping of polarization was accomplished by using a high-frequency source of frequency about 70 GHz. The degree of target polarization was  $P_T = 70$ – $75\%$  and was monitored in the course of the experiment, the relative error in measuring polarization being not greater than  $\pm 2\%$ .

In order to reconstruct events of elastic  $\pi^+p$  scattering, we employed two-coordinate spark wire chambers (*HC, MSC*). The tracks of an incident pion were reconstructed by an assembly of three packets of chambers (*HC, MSC 1–6*), each such packet containing one hybrid and one spark chamber; the dimensions of the sensitive volume were  $250 \times 250$  mm $^2$ . In order to determine the trajectory of the scattered pion, we employed an assembly that consists of two one-coordinate (of dimensions  $250 \times 250$  mm $^2$ ) and four two-coordinate (of dimensions  $420 \times 600$  mm $^2$ ) magnetostrictive spark chambers (*MSC 16–21*). For the above two assemblies, the error in measuring the coordinates  $x$  and  $y$  did not exceed  $\pm 0.5$  mm.

A one-layer analyzer based on two-coordinate wire magnetostrictive chambers (*MSC 7–15*) that features a graphite scatterer of thickness  $36.5$  g/cm $^2$  was used in the RA experiment. The choice of the polarimeter configuration and of the analyzer thickness was made upon thoroughly studying various versions of the polarimeter in a beam of polarized protons. For a conclusion in favor of one partial-wave analysis or another to be drawn on the basis of measurements of the spin-rotation parameters, it is necessary that the relative errors in determining the analyzing power not exceed a value of about 10%. The required accuracy in measuring the analyzing power was achieved in the scattering-angle range  $3^\circ$ – $20^\circ$ . The trajectory of the recoil proton in front of the analyzer was determined by the assembly of four magnetostrictive spark chambers whose sensitive volume has dimensions of  $250 \times 250$  mm $^2$ , while the trajectory of the proton scattered by the analyzer was determined by an assembly consisting of five similar chambers (the dimensions of their sensitive volume are  $420 \times 600$  mm $^2$ ). The coordinate accuracy of a

**Table 2.** Values of the polarization parameters at the momentum of 1.62 GeV/c

$\theta_{c.m.}, \text{deg}$		$P$	$A$	$ R $
range	average value			
118–123.5	121.7	$0.24 \pm 0.12$	$0.27 \pm 0.18$	$0.93 \pm 0.06$
123.5–127	125.2	$0.30 \pm 0.12$	$0.36 \pm 0.20$	$0.88 \pm 0.09$
127–131	128.8	$0.40 \pm 0.13$	$-0.32 \pm 0.20$	$0.86 \pm 0.10$
131–140	133.6	$0.29 \pm 0.13$	$-0.40 \pm 0.21$	$0.87 \pm 0.11$

spark chamber was at a level of  $\pm 0.5$  mm, which ensured an angular resolution not poorer than  $0.5^\circ$ .

The triggering pulse that actuates the readout of information from the chambers (in all 40 coordinates) was formed in the presence of the coincidence of pulses from scintillation counters:

$$C0 \cdot C1 \cdot C2 \cdot \bar{C}3 \cdot \bar{C}4 \cdot C5 \cdot C6 \cdot (C7 + C8 + C9) \cdot \bar{C}10; \quad (7)$$

that is, the simultaneous presence of signals from the incident pion, the scattered pion, and the recoil proton was required.

### 3.2. Data Processing

In the course of the experiment devoted to measuring the spin-rotation parameters  $A$  and  $R$ , about  $1.4 \times 10^6$  events of scattering on the target were accumulated and logged in a beam of positively charged pions throughout the accelerator-operation time of about 400 hours. The processing of accumulated information involved

(i) separating events of elastic  $\pi^+p$  interaction in the operating region of the target according to the coplanarity criteria and the angular correlations of the scattered pion and the recoil pion and estimating the fraction of background events;

(ii) selecting single-track events in the polarimeter for proton scattering angles in the region  $\theta > 3^\circ$ ;

(iii) evaluating the spin-rotation parameters.

In order to separate events of elastic  $\pi^+p$  scattering, we employed the  $\chi^2$  method that takes simultaneously into account the coplanarity criteria and angular correlations between the scattered pion and the recoil proton; that is, we chose the functional  $\chi^2$  in the form

$$\chi^2 = (\Delta\theta/\sigma_\theta)^2 + (\Delta\varphi/\sigma_\varphi)^2, \quad (8)$$

where  $\Delta\varphi$  and  $\Delta\theta$  are the deviations of the azimuthal and polar scattering angles from elastic kinematics, while  $\sigma_\varphi$  and  $\sigma_\theta$  correspond to the widths of the distributions of the numbers of events with respect

to the coplanarity and angular correlations according to a Monte Carlo simulation. For the polarized target and for an imitating carbon target, Fig. 5a displays the distributions of the numbers of events with respect to  $\chi^2$  for two degrees of freedom [calculation by formula (8)]. In a separate experiment, the imitating carbon target that had the shape of a cylinder 30 mm in diameter and 30 mm in height was placed in the cryostat. The distribution obtained for it was normalized in accordance with the number of protons in nuclei contained in the carbon target and in complex nuclei of the polarized target ( $C_3O_2H_8$ ). Upon the subtraction of the quasielastic background, the distribution of elastic events was compared with the results of the simulation that we performed (Fig. 5b). The agreement between the experimental data (his-

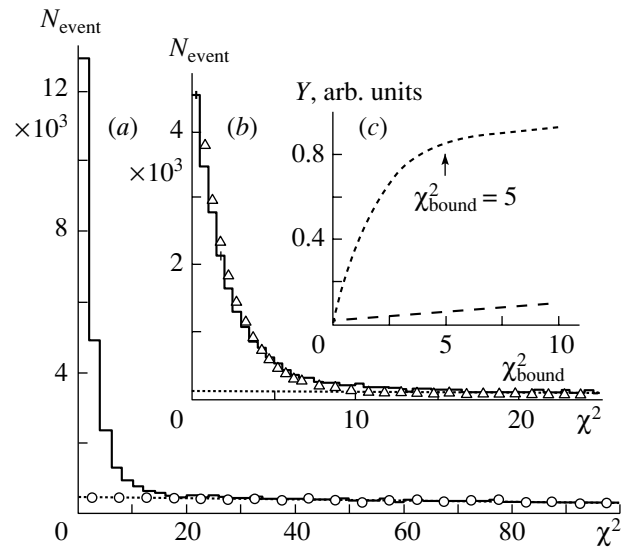


**Fig. 5.** (a, b)  $\chi^2$  distribution (on an enlarged scale in Fig. 5b) of (histograms) elastic-scattering events induced by  $\pi^+p$  in the polarized target and (open circles in Fig. 5a) events of quasielastic scattering on the carbon target, as well as (triangles in Fig. 5b) the expected  $\chi^2$  distribution according to the results of a Monte Carlo simulation. The dotted lines represent the quasielastic background. (c) Yield of useful events (long dashes) and relative background (short dashes) versus the cutoff level  $\chi^2_{\text{bound}}$ .

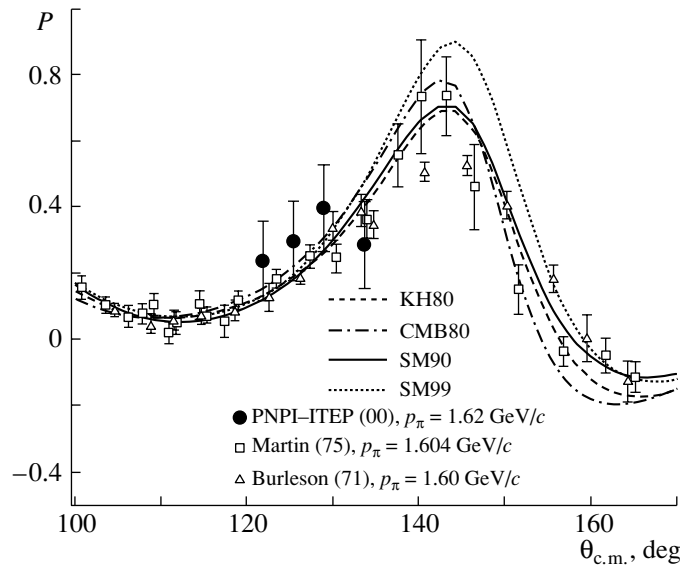


**Fig. 6.** Results obtained by measuring the polarization  $P$  in elastic  $\pi^+p$  scattering at a momentum of  $p_\pi \sim 1.6$  GeV/ $c$ : (closed circles) our present results, (open boxes) data from [15], and (open triangles) data from [16]. The curves represent the predictions of the SM90 [5], KH80 [6], CMB80 [7], and SM99 [8] partial-wave analyses.

togram) and the results of the calculations (triangles) proved to be satisfactory. If the cutoff criterion is chosen at the level of  $\chi^2 = 5$ , about 15% of useful events are lost, the fraction of the background to the selected events being about 7% (see Fig. 5c).

For events selected according to the criteria for the first pion–proton scattering, single-track events of recoil-proton scattering on carbon nuclei were sought

in the polarimeter. Specifically, we determined the coordinates of the interaction vertex within the target analyzer and the polar and azimuthal scattering angles ( $\theta$  and  $\varphi$ , respectively) and rejected events on the basis of the discrepancy between the tracks of the incident and the scattered proton. Events were selected in the range  $\theta = 3^\circ$ – $20^\circ$ , the azimuthal-angle coverage  $\varphi = 0^\circ$ – $360^\circ$  being ensured.

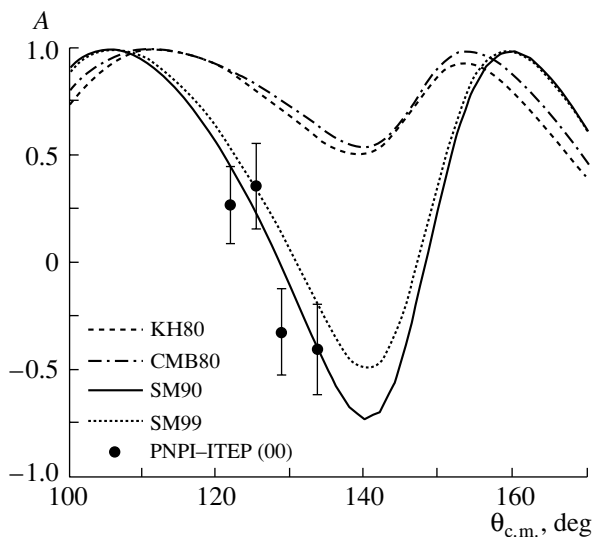


**Fig. 7.** Results obtained by measuring the spin-rotation parameter  $A$  in elastic  $\pi^+p$  scattering at a momentum of 1.62 GeV/ $c$  for the scattering angles of  $\theta_{c.m.} = 121.7^\circ$ ,  $125.2^\circ$ ,  $128.8^\circ$ , and  $133.6^\circ$  along with the predictions of the partial-wave analyses reported in [5–8].

In all, about  $16.5 \times 10^3$  events of the second proton–carbon scattering were selected for a further analysis. The studied range of the angles of  $\pi^+p$  scattering was broken down into four angular bins, and the spin-rotation parameters were calculated by the maximum-likelihood method (in the same way as in [4, 14]) for each of these bins, the parameters  $P$ ,  $A$ , and  $|R|$  being determined simultaneously. In the probability distributions for the observables, we found two maxima corresponding to opposite signs of the spin-rotation parameter  $R$  ( $\pm|R|$ ). At these two values ( $\pm|R|$ ), the parameters  $A$  and  $P$  took values within a margin that is much less than the respective systematic errors.

### 3.3. Results of the RA Experiment

The spin-rotation parameters were determined for the first time in the studied region of the momenta of the incident positively charged pion and the angles of  $\pi^+p$  scattering. These experimental results confirm the conclusion drawn in [4], where, at masses

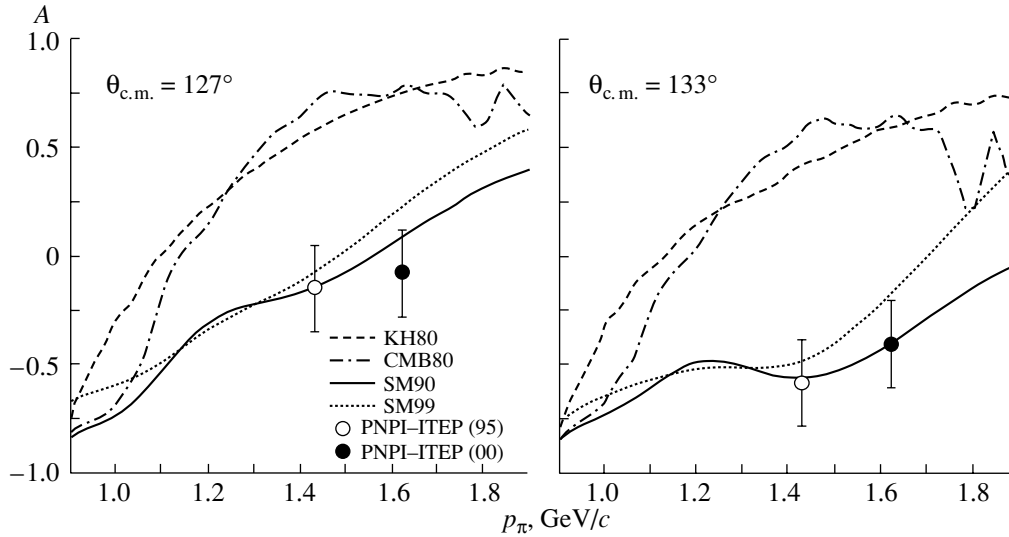


**Fig. 8.** Results obtained by measuring the spin-rotation parameter  $A$  in elastic  $\pi^+p$  scattering at the momenta of (closed circles) 1.62 and (open circles) 1.43 GeV/c [4] for the scattering angles of  $\theta_{\text{c.m.}} = 127^\circ$  and  $133^\circ$  along with the predictions of the partial-wave analyses reported in [5–8].

of the pion–nucleon system in the range  $M \approx 1.9$ – $2.0$  GeV, the results were in accord with the predictions of the partial-wave analysis performed by the group from Virginia Polytechnic Institute.

Table 2 displays the values obtained for the polarization  $P$  and for the spin-rotation parameters  $A$  and  $|R|$ . The errors quoted there are purely statistical. Since the parameters  $A$  and  $R$  were measured for the first time ever at the momentum of 1.62 GeV/c, the systematic errors were estimated on the basis of a comparison with other experiments that measured the parameter  $P$ , which, in our case, was determined simultaneously with the spin-rotation parameters  $A$  and  $R$ . In Fig. 6, the results of our measurements are contrasted against the results previously reported in [15, 16]. The predictions of all partial-wave analyses for the parameter  $P$  do not show significant distinctions in the angular range  $118^\circ$ – $140^\circ$ . It can be seen that, within the errors, the results of our measurements agree with data from other experiments. This indicates that the systematic errors in the parameter  $P$  do not exceed statistical errors.

As is well known, the main contribution to the systematic errors in the parameters  $P$ ,  $A$ , and  $R$  comes from the uncertainty in the analyzing power, and its relative value proved to be not higher than 8% in our case, this being obviously below the preset uncertainty of about 10% in our estimates. The other sources of the systematic error are the following:

(i) the contribution of the instrumental asymmetry of the polarimeter (it is suppressed by periodically reversing the target polarization);

(ii) the uncertainty in estimating the polarization of the quasielastic-scattering background;

(iii) the uncertainty in the degree of target polarization.

The total systematic error in the measured spin-rotation parameters  $A$  and  $R$  can be estimated as

$$\Delta_{\text{sys}}(A, R) \leq \Delta_{\text{stat}}(A, R)/3. \quad (9)$$

The results obtained by measuring the parameter  $A$  at the momentum of 1.62 GeV/c are given in Fig. 7 for four values of the scattering angle in the c.m. frame. It can be seen that, within the errors, the new data obtained for the spin-rotation parameter  $A$  are in agreement with the predictions of the SM90 [5] and SM99 [8] partial-wave analyses, these experimental data confirming, in the angular interval being studied, the angular dependence predicted by the SM90 and SM99 partial-wave analyses.

Over the entire resonance region  $p_\pi \sim 1$ – $2$  GeV/c, our results are contrasted in Fig. 8 against the predictions of the partial-wave analyses at the scattering-angle values of  $\theta_{\text{c.m.}} = 127^\circ$  and  $133^\circ$ . Also shown in the same figure are the results of the preceding PNPI–ITEP measurements at the momentum of  $p_\pi = 1.43$  GeV/c [4]. It can be seen that, for the above two values of the scattering angle, the characteristic distinction between the predictions of the SM90 and SM99 partial-wave analyses, on one hand, and the predictions of the KH80 [6] and CMB80 [7] partial-wave analyses, on the other hand, persists over a broader momentum interval,  $p_\pi = 1.2$ – $1.7$  GeV/c.

From a comparison of the results obtained by measuring the spin-rotation parameter  $A$  with the predictions of the partial-wave analyses, it can be concluded that the experimental results in question agree well with the predictions of the SM90 [5] and SM99 [8] partial-wave analyses, but that they disagree with the predictions of the KH80 [6] and CMB80 [7] partial-wave analyses. Thus, our measurements of the spin-rotation parameters  $A$  and  $R$  disproved the predictions of the KH80 and CMB80 partial-wave analyses in the momentum range  $p_\pi = 1.2\text{--}1.7$  GeV/ $c$ . It follows that there appears the possibility of unambiguously reconstructing the amplitude of  $\pi^+p$  scattering and that the table of baryon resonances needs a more substantial correction for masses of the  $\pi^+p$  system around  $M \approx 2$  GeV than that which was done previously.

#### 4. CONCLUSIONS

The main results of this study are the following:

(i) The spin-rotation parameter  $A$  in elastic pion–nucleon scattering has been measured for the first time at a momentum of  $p_\pi = 1.62$  GeV/ $c$ .

(ii) From a comparison of the results of our measurements for the parameter  $A$  with the predictions of partial-wave analyses, it follows that, within the errors, these results comply with the predictions of the partial-wave analyses performed at Virginia Polytechnic Institute (SM90, SM99), but that they disagree with the predictions of the KH80 and CMB80 partial-wave analyses at the level of four to five standard deviations.

(iii) For a few thicknesses of carbon targets playing the role of an analyzer, the analyzing power of proton–carbon scattering has been determined to a precision not poorer than 10% in the proton-energy range  $T_p = 0.7\text{--}1.3$  GeV. The uncertainties in determining the analyzing power do not make a significant contribution to the error in the spin-rotation parameter  $A$ .

(iv) From the agreement of our present results for the spin-rotation parameters with the predictions of the partial-wave analyses of the Virginia group, it follows that the tables of baryon resonances whose masses are around  $M(\pi^+p) \sim 2$  GeV must be corrected, since these tables are based primarily on the old partial-wave analyses KH80 and CMB80.

In order to establish the features of delta resonances conclusively, a new partial-wave analysis is required. Such an analysis is being presently planned at the University of Helsinki (Finland). As a matter of fact, this is a continuation of Höhler studies where data that have been collected since 1980 will be included. The completion of a new partial-wave analysis with allowance for the data obtained by the

PNPI–ITEP group for the parameters  $A$  and  $R$  in elastic pion–nucleon scattering will solve the problem of whether resonances of low rating exist.

#### ACKNOWLEDGMENTS

We are grateful to the ITEP accelerator service for ensuring excellent conditions for work with the beam and to the staff of the ITEP Cryogenic Laboratory for the uninterrupted supply of liquid helium and nitrogen. Special thanks are also due to our colleagues from George Washington University (USA) for composing the SAID code for the case of nucleon–nucleon and pion–nucleon scattering and for providing the possibility of using it in the present study.

This work was supported in part by the Russian Foundation for Basic Research (project no. 99-09-16635) and by the Russian State Scientific and Technological Project Fundamental Nuclear Physics.

#### REFERENCES

1. E. Barrellet, *Nuovo Cimento A* **8**, 331 (1972).
2. R. J. Cence, *Pion–Nucleon Scattering* (Princeton University Press, Princeton, 1969), p. 138.
3. S. M. Bilen'kiĭ and R. M. Ryndin, *Yad. Fiz.* **4**, 646 (1966) [*Sov. J. Nucl. Phys.* **4**, 457 (1967)].
4. V. V. Abaev *et al.*, *Yad. Fiz.* **58**, 1635 (1995) [*Phys. At. Nucl.* **58**, 1542 (1995)]; I. G. Alekseev *et al.*, *Phys. Lett. B* **351**, 585 (1995).
5. R. A. Arndt *et al.*, *Phys. Rev. D* **43**, 2131 (1991).
6. G. Hoehler, *Handbook of Pion–Nucleon Scattering, Physics Data* (Fachinformationzentrum, Karlsruhe, 1979), No. 12–1.
7. R. E. Cutkosky *et al.*, *Phys. Rev. D* **20**, 2804 (1979).
8. R. A. Arndt *et al.*, *Phys. Rev. C* **52**, 2120 (1995); nucl-th/9807087; [http://gwdac.phys.gwu.edu/analysis/pin\\_analysis.html](http://gwdac.phys.gwu.edu/analysis/pin_analysis.html)
9. Particle Data Group, *Eur. Phys. J. C* **15** (1) (2000).
10. R. L. Kelly, J. C. Sandusky, and R. E. Cutkosky, *Phys. Rev. D* **10**, 2309 (1974).
11. I. G. Alekseev *et al.*, *Nucl. Instrum. Methods Phys. Res. A* **434**, 254 (1999); I. G. Alekseev *et al.*, *Yad. Fiz.* **62**, 2194 (1999) [*Phys. At. Nucl.* **62**, 2024 (1999)].
12. D. V. Novinsky, Candidate's Dissertation in Physics and Mathematics (Petersburg Nucl. Phys. Inst., Gatchina, 2002).
13. É. I. Bunyatova *et al.*, Preprint No. 1191 (Petersburg Nucl. Phys. Inst., Gatchina, 1986).
14. R. Amblard, Thèses de l'Université de Paris (Paris, 1971).
15. J. E. Martin *et al.*, *Nucl. Phys. B* **89**, 253 (1975).
16. G. Burlison *et al.*, *Phys. Rev. Lett.* **26**, 338 (1971).

*Translated by A. Isaakyan*

## Transverse-Momentum Distribution of $J/\psi$ Mesons Produced in Proton–Nucleus and Lead–Lead Interactions

N. S. Topilskaya\*  
(NA50 Collaboration)

*Institute for Nuclear Research, Russian Academy of Sciences,  
pr. Shestidesyatiletiya Oktyabrya 7a, Moscow, 117312 Russia*

Received February 27, 2003

**Abstract**—The transverse-momentum and transverse-mass distributions of  $J/\psi$  mesons produced in proton–nucleus and lead–lead interactions at 400 GeV and 158 GeV/nucleon, respectively, were measured in the NA50 experiment. The change in these distributions with increasing centrality is studied for various interaction energies. Data obtained in the NA38 experiment for collisions of light nuclei at 200 GeV per nucleon is also used in the present analysis. Investigation of the transverse-momentum and transverse-mass distributions of  $J/\psi$  particles can provide additional information about the properties of the phase transition of ordinary nuclear matter to quark–gluon plasma. © 2004 MAIK “Nauka/Interperiodica”.

### 1. INTRODUCTION

A phase transition from ordinary nuclear matter to the state where quarks and gluons are deconfined (quark–gluon plasma) is predicted by nonperturbative QCD to occur at fairly high temperatures and densities [1]. Such conditions are expected to be reached in collisions of heavy-ion beams at the CERN accelerator. The NA50 experiment is aimed primarily at studying a special signal of the phase transition of nuclear matter to quark–gluon plasma—namely, the predicted suppression of the production of charmonium states [2]. Indeed, the NA50 experiment observed an anomalous absorption of  $J/\psi$  mesons [3], which is indicative of the deconfinement of quarks and gluons in central lead–lead interactions at an impact parameter below 8 fm. Investigation of the transverse-momentum and transverse-mass distributions of  $J/\psi$  mesons can provide new information about the properties of this phase transition.

### 2. EXPERIMENTAL SETUP

The cross section for dimuon-pair production was measured at the NA50 setup as a function of interaction centrality. Dimuons were recorded within the kinematical region specified by the inequalities  $2.92 < y_{\text{lab}} < 3.92$  and  $-0.5 < \cos \theta_{\text{CS}} < 0.5$ , where  $y_{\text{lab}}$  is the dimuon rapidity in the laboratory frame and  $\theta_{\text{CS}}$  is the muon angle with respect to the beam axis in the muon-pair rest frame (the Collins–Soper reference

frame). The interaction centrality can be determined with the aid of three detectors: an electromagnetic calorimeter, a detector of multiplicity, and a zero-angle calorimeter. In our analysis, the interaction centrality was determined by the neutral energy  $E_T$  carried away in a transverse direction and measured with the electromagnetic calorimeter.

The conditions of data acquisition in PbPb collisions were identical throughout all measurements.

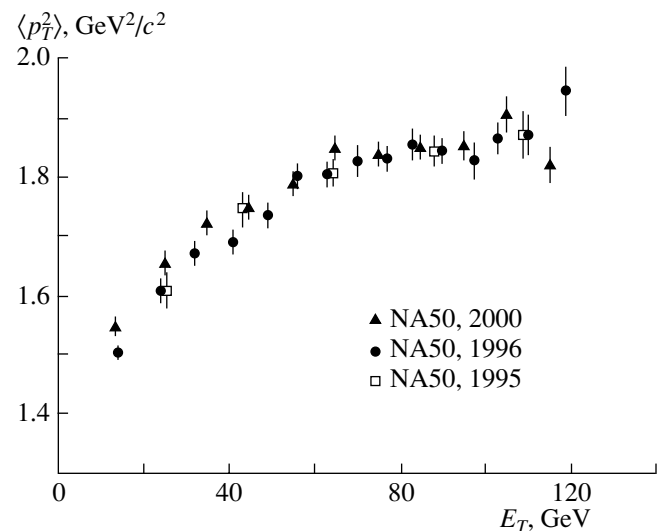


**Fig. 1.** Values obtained within various periods of measurements for the mean square of the transverse momentum of  $J/\psi$  mesons as a function of transverse energy in PbPb interactions at 158 GeV per nucleon.

\* e-mail: topilaska@al20.inr.troitsk.ru

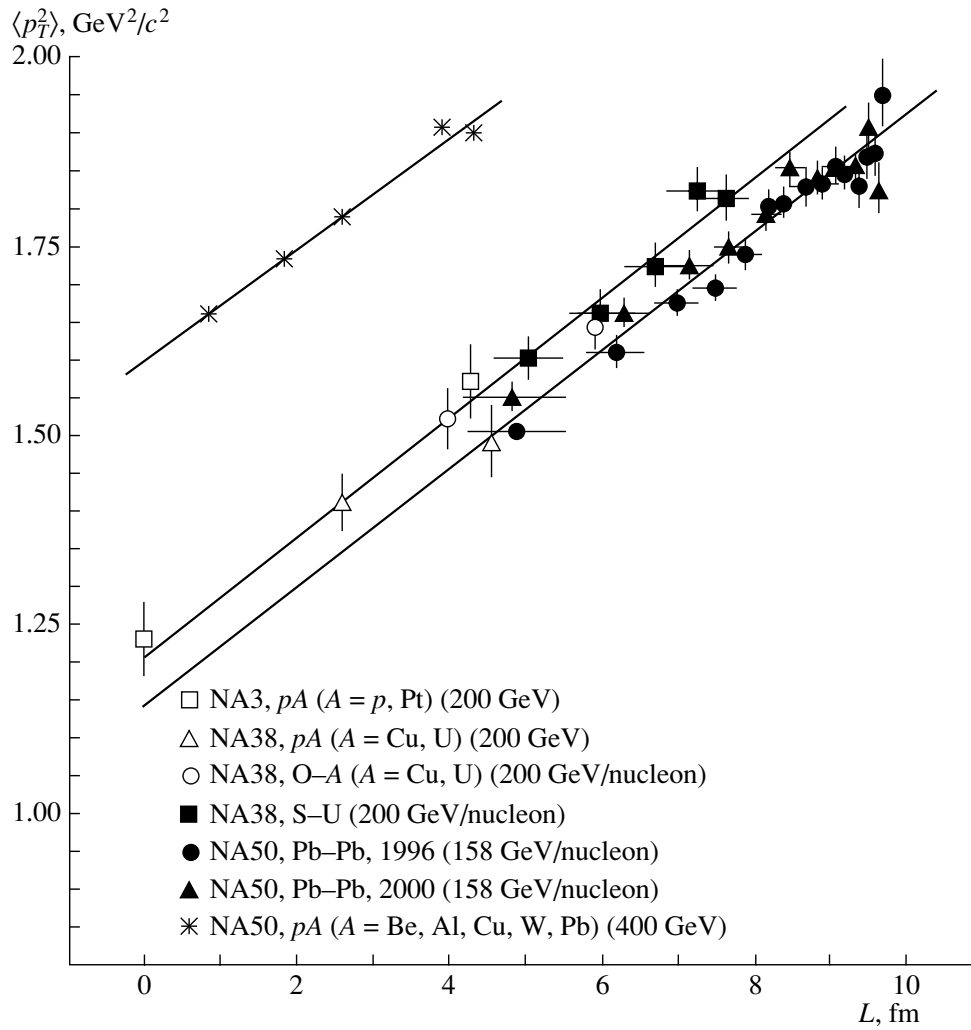


**Fig. 2.** Mean square of the transverse momentum of  $J/\psi$  mesons as a function of the distance traveled by  $J/\psi$  mesons in the nucleus for three different energies of the incident beam.

However, the thicknesses of the targets used were different. In the 1996 (1995) measurement runs, the total thickness of the target was 12 mm (7 mm), which is 30% (17%) of the interaction length. In the 2000 run, a target 4 mm thick (9.33% of the interaction length) was placed into a vacuum, whereby the contribution from the interactions of lead nuclei with air in peripheral PbPb collisions was removed. The total number of  $J/\psi$  mesons recorded in 1995, 1996, and 2000 was 50 000, 190 000, and 110 000, respectively. In 2000, data on proton–nucleus interactions were obtained for Be, Al, Cu, W, and Pb in a high-intensity proton beam at 400 GeV. The number of recorded  $J/\psi$  mesons was 40 000, 50 000, 47 000, 51 000, and 71 000, respectively.

### 3. DATA ANALYSIS

The invariant-mass spectrum of dimuons receives contributions from four known physical processes:

the decay of  $J/\psi$  and  $\psi'$  resonances, the Drell–Yan (DY) process, and the semileptonic decay of pairs of charmed mesons ( $D$  and  $\bar{D}$  mesons). The spectrum also includes the contribution of the combinatorial background caused by uncorrelated  $\pi$  and  $K$  decays. The magnitude of the combinatorial background is determined by measuring pairs of like-charged muons.

To subtract the dimuon-background contribution under the  $J/\psi$  peak, we describe the invariant-mass spectrum as a superposition of the contributions of the four physical processes and the combinatorial background. In the  $J/\psi$ -resonance-mass region  $2.9 < M < 3.3$  GeV, the background contribution is below 8%, the physical background being about 3% and being caused primarily by the Drell–Yan process.

To obtain the transverse-momentum distributions of  $J/\psi$  mesons, the  $p_T$  distribution of background dimuons was subtracted from that of muon pairs

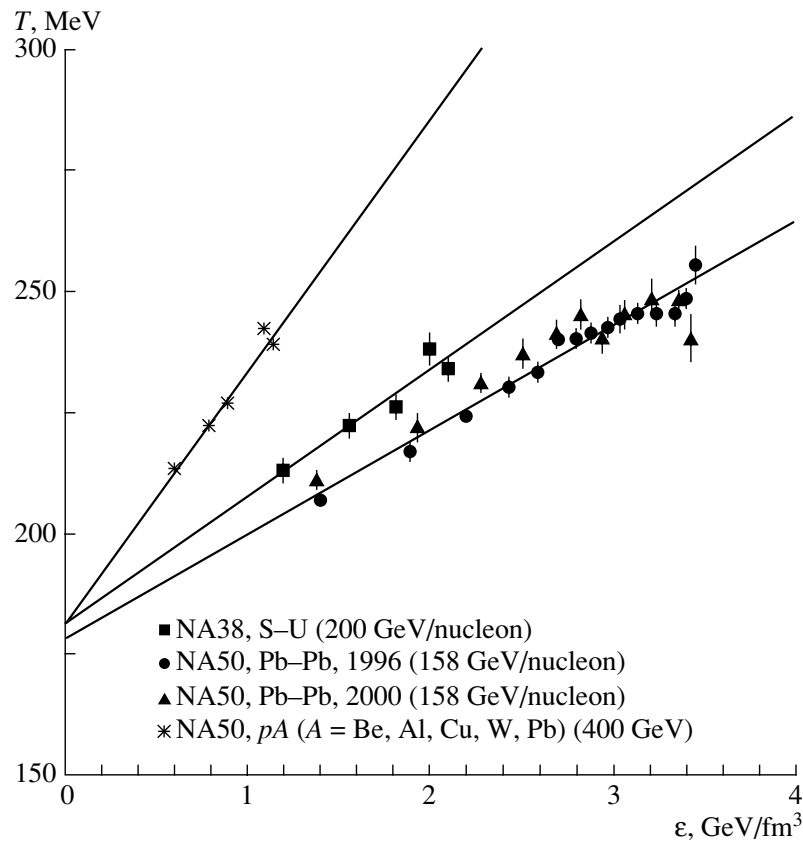


Fig. 3. Inverse-slope parameter  $T$  for  $J/\psi$  mesons as a function of the energy density reached in a collision event. The lines represent fits to data in terms of linear functions at three energies of the incident beam.

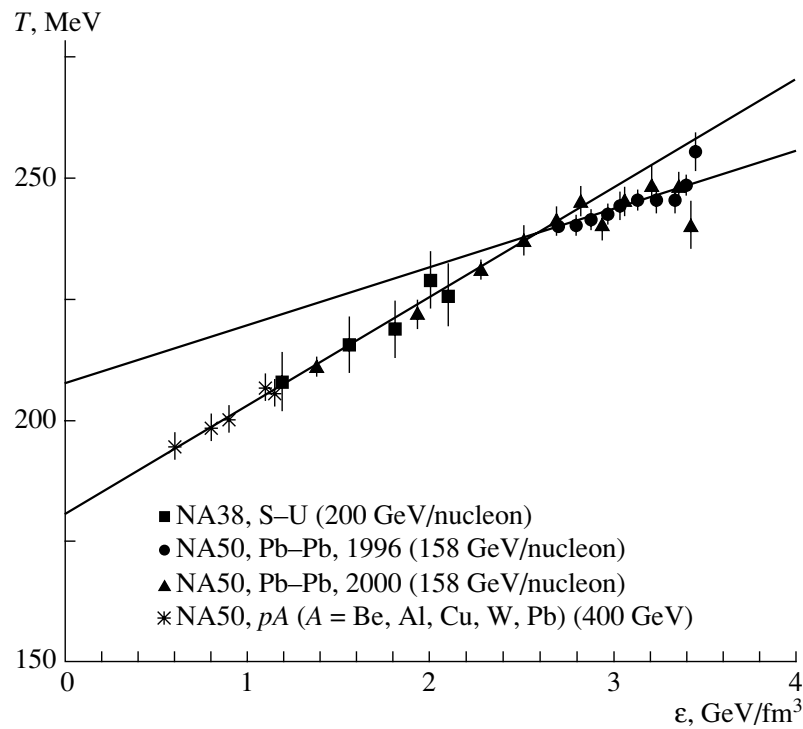


Fig. 4. As in Fig. 3, but upon rescaling all of the data to the energy value of 158 GeV/nucleon.

within the resonance-mass region. The  $p_T$  distribution of background dimuons was experimentally measured for dimuons of mass above and below that of the  $J/\psi$  resonance. A detailed description of the method used in the present analysis is given in [4].

#### 4. TRANSVERSE-MOMENTUM DISTRIBUTION

Figure 1 shows the mean square of the transverse momentum,  $\langle p_T^2 \rangle$ , as a function of transverse energy according to data obtained for PbPb collisions in 1995, 1996, and 2000. These data sets behave identically: a fast rise gives way to a slower increase for the most central events. The  $\langle p_T^2 \rangle$  values obtained in 1995 and 1996 are in good agreement with each other over the whole range of transverse energy; for peripheral events, the 2000 data display a slight ( $<4\%$ ) but steady excess over the data obtained in 1995 and 1996. This effect is probably due to the contribution from the interaction of Pb nuclei with air in the 1995 and 1996 data. The  $\langle p_T^2 \rangle$  values for  $J/\psi$  mesons produced in the interaction of light incident particles ( $p$ , O, S) with nuclei [5, 6] were successfully described within the model of the multiple parton interaction in the initial state [7, 8]. In order to study the effects of initial-state interaction in more detail, the  $\langle p_T^2 \rangle$  values obtained in  $pA$  interactions at 200 and 400 GeV and in OCu, OU, and SU interactions at 200 GeV/nucleon are presented along with the data on PbPb interaction at 158 GeV/nucleon in Fig. 2, where these data are plotted versus  $L$ , the distance traveled by partons in the initial state prior to  $J/\psi$  production. Within the model of multiple parton rescattering in the initial state [8], the mean square of the transverse momentum of product  $J/\psi$  mesons has two components—that is, the contribution from  $J/\psi$  produced in  $pp$  interaction and the contribution caused by multiple rescattering of gluons prior to the stage of parton fusion and  $J/\psi$  production, the fraction of the former mechanism being proportional to  $L$ . The experimental data were approximated by the function  $\langle p_T^2 \rangle = \langle p_T^2 \rangle_{pp} + a_{gN}L$  [8]. All three slopes are in agreement within their uncertainties, and  $\langle p_T^2 \rangle_{pp}$  increases with increasing beam energy. A simultaneous description of all data in terms of linear functions having the same slope yielded  $a_{gN} = 0.077 \pm 0.002 \text{ (GeV}/c)^2 \text{ fm}^{-1}$ .

It is evident that  $\langle p_T^2 \rangle_{pp}$  increases linearly with total energy in the nucleon–nucleon c.m. frame,  $\sqrt{s}$ , in just the same way as this occurs in the data of the NA3 experiment with a pion beam [5]. The observed dependence of  $\langle p_T^2 \rangle$  of  $J/\psi$  mesons on the interaction centrality can be explained within the model of multiple parton interactions in the initial state.

#### 5. TRANSVERSE-MASS DISTRIBUTION

We also studied the transverse-mass distributions of  $J/\psi$  mesons, describing them by the analytic function  $(1/T)M_T^2 K_1(M_T/T)$ , where  $K_1$  is a modified Bessel function. The inverse-slope parameter  $T$  in the transverse-mass distribution can be related to the effective temperature of the system within the thermal model of particle production [9]. Figure 3 displays the values obtained for the inverse slopes as a function of the energy density  $\varepsilon$  reached in a collision event and calculated within the Bjorken model [10]. For all colliding systems, the effective temperature increases almost linearly with energy density at close initial values of  $T$  at  $\varepsilon = 0$ . A simultaneous description of all data at three energies with a common initial value of  $T$  yields  $T(\varepsilon = 0) = 178 \pm 2 \text{ MeV}$  and a slope that increases linearly with increasing  $\sqrt{s}$ .

Figure 4 shows  $T$  versus  $\varepsilon$  after rescaling all of the data to the same energy value of 158 GeV per nucleon. For peripheral PbPb collisions, use was made of the 2000 data, which are not distorted by the contribution from the interaction of lead ions with air. It is evident that the linear growth of  $T$  with increasing energy density  $\varepsilon$  becomes more gently sloping for the most central PbPb collisions, in which case the slope value changes from  $(22 \pm 1) \times 10^{-3}$  to  $(12 \pm 3) \times 10^{-3} \text{ fm}^{-3}$ .

#### 6. CONCLUSION

The results obtained in PbPb interactions within three different periods of measurements under different experimental conditions are indicative of the same behavior of  $\langle p_T^2 \rangle$  and  $T$  versus the interaction centrality—that is, the initial fast growth gives way to a flatter behavior. The observed growth of  $\langle p_T^2 \rangle$  can be explained within the theory of multiple parton rescattering in the initial state, at least for collisions of light ions and for peripheral PbPb collisions.

For all colliding systems, a linear growth of the effective temperature  $T$  with increasing energy density is observed, the values of  $T$  being identical at  $\varepsilon = 0$ . However, a decrease in the slope of the energy-density dependence of  $T$  is observed for the most central PbPb collisions.

#### REFERENCES

1. C. Bernard *et al.*, Phys. Rev. D **54**, 4585 (1996).
2. T. Matsui and H. Satz, Phys. Lett. B **178**, 416 (1986).
3. NA50 Collab. (M. C. Abreu *et al.*), Phys. Lett. B **410**, 337 (1997); **450**, 456 (1999); **477**, 28 (2000).
4. NA50 Collab. (M. C. Abreu *et al.*), Phys. Lett. B **499**, 85 (2001).
5. NA3 Collab. (J. Badier *et al.*), Z. Phys. C **20**, 101 (1983).

6. NA38 Collab. (C. Baglin *et al.*), Phys. Lett. B **262**, 362 (1991); NA38 Collab. (M. C. Abreu *et al.*), Phys. Lett. B **423**, 207 (1998).
7. S. Gavin and M. Gyulassy, Phys. Lett. B **214**, 241 (1988); J. P. Blaizot and J. Y. Ollitrault, Phys. Lett. B **217**, 392 (1989).
8. J. Hufner, Y. Kurihara, and H. J. Pirner, Phys. Lett. B **215**, 218 (1988).
9. R. Hagedorn, Riv. Nuovo Cimento **6**, 1 (1983).
10. J. D. Bjorken, Phys. Rev. D **27**, 140 (1983).

*Translated by S. Slabospitsky*

---

---

**ELEMENTARY PARTICLES AND FIELDS**  
**Experiment**

---

---

## Investigation of Clustering in Light Nuclei by Means of Relativistic-Multifragmentation Processes

**M. I. Adamovich<sup>†1)</sup>, V. Bradnova<sup>2)</sup>, S. Vokal<sup>2),3)</sup>, S. G. Gerasimov<sup>1)</sup>, V. A. Dronov<sup>1)</sup>,  
P. I. Zarubin<sup>2)\*</sup>, A. D. Kovalenko<sup>2)</sup>, K. A. Kotel'nikov<sup>1)</sup>, V. A. Krasnov<sup>2)</sup>,  
V. G. Larionova<sup>1)</sup>, F. G. Lepekhin<sup>4)</sup>, A. I. Malakhov<sup>2)</sup>, G. I. Orlova<sup>1)</sup>, N. G. Peresadko<sup>1)</sup>,  
N. G. Polukhina<sup>1)</sup>, P. A. Rukoyatkin<sup>2)</sup>, V. V. Rusakova<sup>2)</sup>, N. A. Salmanova<sup>1)</sup>,  
B. B. Simonov<sup>4)</sup>, M. M. Chernyavsky<sup>1)</sup>, M. Haiduc<sup>5)</sup>, S. P. Kharlamov<sup>1)</sup>, and L. Just<sup>6)</sup>**  
**BECQUEREL Collaboration**

Received March 26, 2003

**Abstract**—New results concerning the topology of the fragmentation of relativistic nuclei  ${}^7\text{Li}$  and  ${}^{10}\text{B}$  are presented. A program is proposed for studying the cluster structure of stable and radioactive nuclei. The use of emulsions in the investigation of nuclear clustering in the fragmentation of light nuclei at energies are in excess of 1 GeV per nucleon is discussed. © 2004 MAIK “Nauka/Interperiodica”.

Advances in experiments with relativistic nuclear beams gives impetus to developing new approaches in solving some nuclear-structure problems of great importance. In this connection, we would like to indicate investigation of collective degrees of freedom in excited nuclei, where individual groups of nucleons behave as constituent clusters. Such clustering in excited nuclei is especially pronounced in light nuclei, where the possible number of cluster configurations is relatively small. Few-nucleon systems having no intrinsic excitations are natural components of such a pattern. First of all, these are alpha particles, as well as deuterons, tritons, and  ${}^3\text{He}$  nuclei, but paired states of protons and neutrons can also play this role. Perhaps, investigation of the fragmentation of stable and radioactive nuclei into clusters at relativistic energies would reveal some new special features of

the origin of clusters and their role in nucleosynthesis processes.

The use of nuclear beams of energy above 1 GeV per nucleon in solving the problem being discussed is based on the known effect of limiting nuclear fragmentation. In the present case, this implies that the isotopic composition of projectile fragments is independent of the target-nucleus type. This gives sufficient grounds to employ, for a target and a detector of relativistic-fragmentation products, a nuclear emulsion, which is a material of rather complicated composition. The absence of an energy threshold for detecting a fragmentation process is one of the advantages of the emulsion method. Emulsions ensure the detection of multiparticle relativistic-fragmentation processes, which enables one to reveal the most probable charge channels of such processes. Measurement of multiple-scattering angles makes it possible to determine the total momentum of the relativistic fragments of hydrogen and helium, whereby one can estimate their mass. Owing to a record angular resolution, the emulsion technique permits reconstructing the invariant mass (that is, the excitation energy) of the fragmenting system.

Interactions of relativistic nuclei that lead to minimal mutual excitations of colliding nuclei and which do not involve charged-meson production are the most advantageous in studying the cluster structure of nuclei. In this case, projectile- and target-fragmentation products can be clearly separated in momentum. The requirement that the electric charge and the mass number of the projectile nucleus be

---

<sup>†</sup>Deceased.

<sup>1)</sup>Lebedev Institute of Physics, Russian Academy of Sciences, Leninskii pr. 53, Moscow, 117924 Russia.

<sup>2)</sup>Joint Institute for Nuclear Research, Dubna, Moscow oblast, 141980 Russia.

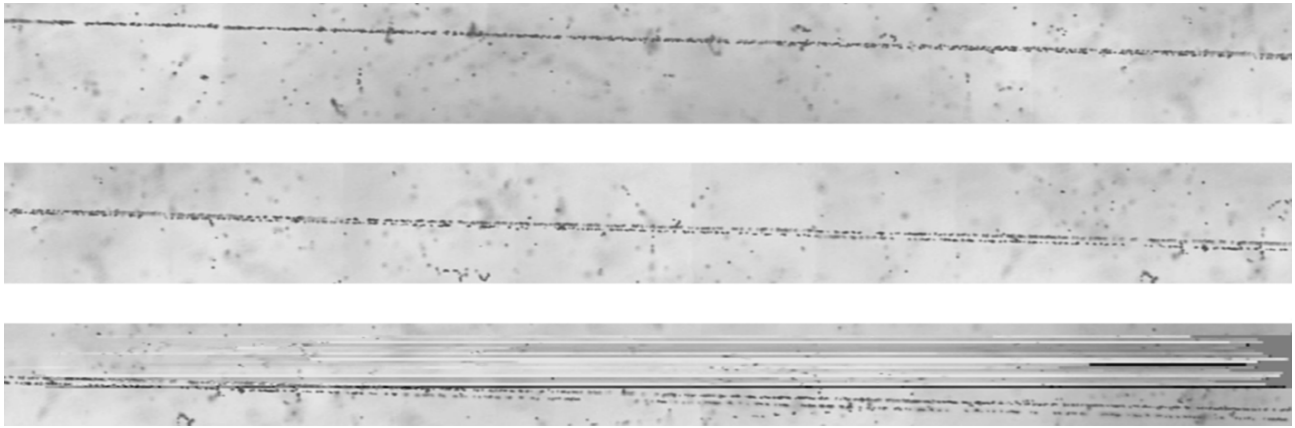
<sup>3)</sup>University of P.J. Šafárik, Jesenná 5, SK-041 54 Košice, Slovak Republic.

<sup>4)</sup>Institute of Nuclear Physics, Russian Academy of Sciences, Gatchina, 188350 Russia.

<sup>5)</sup>Institute of Space Sciences, Bucharest-Magurele, Romania.

<sup>6)</sup>Institute of Experimental Physics, Slovak Academy of Sciences, Watsonova 47, SK-043 53 Košice, Slovak Republic.

\* e-mail: zarubin@ihe.jinr.ru



Event of the coherent dissociation of a  $^{10}\text{B}$  nucleus to triply charged (top) and doubly charged (bottom) fragments on three consecutive sections of the tracks. A three-dimensional image of the event was reconstructed as a plane projection by means of an automated microscope (Lebedev Institute of Physics, Moscow) of the PAVIKOM complex.

conserved within a narrow angular cone of fragmentation is the main criterion for selecting such events. The application of this criterion leads to a sharp decrease in the mean multiplicity of target-fragmentation products.

These considerations formed a basis for our experimental program (BECQUEREL project [1]) aimed at systematically studying the channels of fragmentation of stable and radioactive nuclei in beams from the nuclotron at the Joint Institute of Nuclear Research (JINR, Dubna) by employing the emulsion technique. The investigation of the cluster fragmentation of  $^6\text{Li}$  ( $\alpha$ -d) [2–5],  $^{12}\text{C}$  ( $3\alpha$ ) [6–9], and  $^{16}\text{O}$  ( $4\alpha$ ) [10] nuclei by means of the emulsion technique served as a guideline for our project. Below, we discuss the results obtained by studying the cluster structure of the  $^{10}\text{B}$  and  $^7\text{Li}$  nuclei. These results provide a basis for the development of investigations into the clustering in light neutron-deficit nuclei and heavier stable nuclei.

**Clustering in the  $^{10}\text{B}$  nucleus.** Nuclei of  $^{10}\text{B}$  were accelerated at the JINR nuclotron, and their beam of energy 1 GeV per nucleon was formed. This beam was used to irradiate stacks of layers of BR-2 emulsion, the layer thickness and dimensions being, respectively,  $550\ \mu\text{m}$  and  $10 \times 20\ \text{cm}^2$ . The emulsions used were sensitive even to singly charged relativistic particles. The exposed emulsion layers were parallel to the beam axis. Nucleus–nucleus interaction was sought by viewing the particle tracks by means of microscopes with a magnification of 900. Over the viewed-track length of 138.1 m, we found 960 events of inelastic interactions of  $^{10}\text{B}$  nuclei. The mean range of  $^{10}\text{B}$  nuclei to an inelastic interaction in the nuclear emulsion was  $14.4 \pm 0.5\ \text{cm}$ . This value agrees well with the dependence of the mean range on the projectile atomic number for light nuclei having a uniform nucleon density.

We obtained information about the charge composition of charged fragments and about the channels of  $^{10}\text{B}$  fragmentation in peripheral interactions. Those events were associated with peripheral interactions in which the total charge of relativistic fragments was equal to the charge of the primary nucleus  $^{10}\text{B}$  and in which charged mesons were not produced, but slow fragments of emulsion nuclei could be formed. In order to separate these events, we estimated the charge of relativistic particles (mainly singly and doubly charged ones) emitted at angles smaller than  $15^\circ$  with respect to the momentum of  $^{10}\text{B}$  nuclei. For a primary-beam energy of 1 GeV per nucleon, this value of the emission angle corresponds to the proton transverse momentum of  $0.44\ \text{GeV}/c$ . The mass of singly charged fragments was estimated by the method of multiple-scattering measurement.

The number of detected events in which the total charge of fragments is equal to five and in which charged mesons are not observed is 93 (10% of the total number of events); of these, 41 feature no fragments originating from target-nucleus breakup. An analysis revealed that the presence (absence) of the target fragmentation has virtually no effect on the distribution in the projectile-fragment charge.

In 65% of peripheral interactions, a  $^{10}\text{B}$  nucleus decays to two doubly charged particles and one singly charged particle, with the latter being a deuteron in 40% of these events. In 10% of events, triply and doubly charged fragments (isotopes of Li and He) appear simultaneously. The production of a  $^6\text{Li}$  nucleus accompanied by an alpha particle can be treated as an already established correlation of the alpha-particle and deuteron clusters. In 2% of events, there are fragments of charge equal to four and unity ( $^9\text{Be}$  and proton, respectively). The photograph shows an

example of a two-body decay to a lithium and a helium fragment. The fraction of the fragmentation channel involving one doubly charged fragment and three singly charged fragments (products originating from the breakup of one of the alpha-particle clusters) is 15%.

A channel-fraction ratio of  $(2\text{He} + d)/(2\text{He} + p) \approx 1$  is indicative of an analogy with  ${}^6\text{Li}$  fragmentation, where  $(\text{He} + d)/(\text{He} + p) \approx 1$ , and of an abundant yield of deuterons in the  ${}^{10}\text{B}$  case as well [2, 3]. A low value of the mean transverse momentum of deuterons ( $\langle P_t^d \rangle = 0.14 \pm 0.01$  GeV/ $c$ ) in these events, in just the same way as in the case of  ${}^6\text{Li}$  fragmentation, where  $\langle P_t^d \rangle = 0.13 \pm 0.02$  GeV/ $c$ , is yet another indication of deuteron clustering.

It should be noted that, along with the deuteron and the  ${}^6\text{Li}$  and  ${}^{14}\text{N}$  nuclei, the  ${}^{10}\text{B}$  nucleus belongs to the rare class of odd-odd stable nuclei. Therefore, it would be of interest to reveal signals from deuteron clustering in the fragmentation of relativistic  ${}^{14}\text{N}$  nuclei.

**Clustering in the  ${}^7\text{Li}$  nucleus.** In the nuclear photoemulsion exposed to a beam of  ${}^7\text{Li}$  nuclei accelerated to a momentum of 3 GeV/ $c$  per nucleon at the JINR Synchrophasotron, 1274 events of inelastic interaction were found over a viewed-track length of 185 m. The mean range of  ${}^7\text{Li}$  nuclei to an inelastic interaction in the emulsion was  $14.5 \pm 0.4$  cm, which agrees within the errors with the mean range of  ${}^6\text{Li}$  [2, 3]. Close values of the mean range and of the total cross sections for the inelastic interactions of  ${}^6\text{Li}$  and  ${}^7\text{Li}$  nuclei suggest close effective interaction ranges.

Peripheral interactions (92 events), which involve only charged fragments of the relativistic nucleus and no other charged secondaries and in which the total charge of the fragments is equal to the charge of the fragmenting nucleus, constitute about 7% of all the inelastic interactions of  ${}^7\text{Li}$  nuclei. Of these, 80 events are the two-body decays of a  ${}^7\text{Li}$  nucleus to one doubly and one singly charged fragment. The reconstruction of the mass of relativistic fragments revealed that half of these events are due to  ${}^7\text{Li}$  decay to an alpha particle and a triton (40 events). The fraction of decays to an alpha particle, a deuteron, and a neutron is equal to 30%, while the fraction of decays to an alpha particle, a proton, and two neutrons constitutes 20%. The isotopic composition of decay fragments implies that these events are associated with the structure in the form of alpha-particle and triton clusters. A greater fraction of tritons in the isotopic composition of singly charged fragments suggests the dominance of the triton cluster in the fragmentation of a  ${}^7\text{Li}$  nucleus in extremely peripheral interactions with emulsion nuclei.

Earlier, similar two-body decays of  ${}^6\text{Li}$  nuclei to an alpha particle and a deuteron, which reflect a loosely bound two-cluster structure of the nucleus, were detected in inelastic peripheral interactions of  ${}^6\text{Li}$  nuclei of momentum 4.5 GeV/ $c$  per nucleon in photoemulsions. Therefore, the structure formed by an alpha-particle core and superficial nucleons bound into a cluster is typical not only of the  ${}^6\text{Li}$  but also of the  ${}^7\text{Li}$  nucleus. The value obtained for the cross section describing the coherent decay of a  ${}^7\text{Li}$  nucleus to an alpha particle and a triton ( $27 \pm 4$  mb) appeared to be nearly identical to that given in [2] for the decay of a  ${}^6\text{Li}$  nucleus to an alpha particle and a deuteron ( $22 \pm 4$  mb). This can be treated as an indication of the fact that the mechanisms of the decays under consideration are of the same nature.

It is of interest to pursue further the investigation of the possible role of tritons as cluster elements in dissociation of the  ${}^{11}\text{B}$ ,  ${}^{15}\text{N}$  and  ${}^{19}\text{F}$  nuclei.

**Clustering that involves a  ${}^4\text{He}$  nucleus.** Within the present study, we have launched anew the investigation of emulsions exposed to beams of  ${}^{22}\text{Ne}$ ,  ${}^{24}\text{Mg}$ ,  ${}^{28}\text{Si}$ , and  ${}^{32}\text{S}$  nuclei accelerated to a momentum of 4.5 GeV/ $c$  per nucleon. It is planned to seek and explore the fragmentation of these nuclei by observing final states that involve a few alpha particles. Searches for states that can be interpreted as nuclear molecules are of particular interest. Our approach will enable us to decide whether this resonance is a configuration formed by a few bound alpha particles or we have a resonance arising only in nuclear scattering. We can expect that the applicability range of the pattern where alpha-particle clustering in a nuclear core is combined with peripheral clustering in the form of deuterons, tritons,  ${}^3\text{He}$ , and nucleon pairs would become still wider. A further investigation of relativistic multiparticle fragmentation will provide an experimental basis for cluster models of light nuclei.

**Clustering that involves a  ${}^3\text{He}$  nucleus.** The  ${}^3\text{He}$  nucleus is a natural element of the cluster pattern of excitations of light neutron-deficit nuclei like  ${}^6\text{Be}$ ,  ${}^7\text{Be}$ ,  ${}^8\text{B}$ ,  ${}^9\text{C}$ ,  ${}^{10}\text{C}$ ,  ${}^{11}\text{C}$ , and  ${}^{12}\text{N}$ , as well as heavier ones. Going over from alpha particles to  ${}^3\text{He}$  nuclei, one can obtain similar cluster states of the  ${}^8\text{Be}$ ,  ${}^9\text{Be}$ ,  ${}^{10}\text{B}$ ,  ${}^{12}\text{C}$ , and  ${}^{14}\text{N}$  nuclei. Within this approach, the  ${}^6\text{Be}$  nucleus is a loosely bound  ${}^3\text{He}$ - ${}^3\text{He}$  resonance whose properties are similar to those of the  $\alpha$ - $\alpha$  system in the  ${}^8\text{Be}$  nucleus.

By analogy with the  ${}^9\text{Be}$  nucleus,  ${}^7\text{Be}$  can have the  $n$ - ${}^6\text{Be}$  and  ${}^3\text{He}$ - $n$ - ${}^3\text{He}$  excitations in addition to the  $\alpha$ - ${}^3\text{He}$  state. In the case of the  ${}^8\text{B}$  nucleus, the  ${}^3\text{He}$ - $d$ - ${}^3\text{He}$  cluster excitation is possible in addition to the  $p$ - ${}^7\text{Be}$  and  $p$ - $\alpha$ - ${}^3\text{He}$  states. It is of interest to

reveal the  ${}^3\text{He}-{}^3\text{He}-{}^3\text{He}$  state in the  ${}^9\text{C}$  nucleus as an analog of the  $\alpha-\alpha-\alpha$  state in  ${}^{12}\text{C}$  and to compare the intensity of its excitation with that of the  $p-{}^8\text{B}$  and  $p-p-\alpha-{}^3\text{He}$  states.

We would like to indicate some other interesting states like  $pp-\alpha-\alpha$  and  $\alpha-{}^3\text{He}-{}^3\text{He}$  in the  ${}^{10}\text{C}$  nucleus,  $\alpha-\alpha-{}^3\text{He}$  in  ${}^{11}\text{C}$ , and  $\alpha-{}^8\text{B}$  in  ${}^{12}\text{N}$ . The existence of such molecular quantum states formed by nuclei may imply that there are alternative scenarios of the nucleosynthesis of light nuclei via the formation of intermediate radioactive nuclei in the burning of complex isotopic mixtures of hydrogen and helium nuclei owing to fusion reactions, including the simultaneous fusion of a few particles belonging to an intermediate bound state.

As a first step along these lines, we exposed emulsions at the JINR nuclotron to a secondary beam containing a considerable fraction of  ${}^7\text{Be}$  nuclei. The beam was formed by tuning the magneto-optical channel to optimally choosing the products of the charge-exchange reaction involving accelerated  ${}^7\text{Li}$  and  ${}^7\text{Be}$  nuclei. The cross section for this reaction is about  $10^{-4}$  of the inelastic cross section. The results of this exposure are presently being analyzed.

We hope that the charge-exchange reactions  ${}^{10}\text{B} \rightarrow {}^{10}\text{C}$ ,  ${}^{11}\text{B} \rightarrow {}^{11}\text{C}$ , and  ${}^{12}\text{C} \rightarrow {}^{12}\text{N}$  will make it possible to form secondary beams. We propose to form a  ${}^8\text{B}$  beam via the fragmentation reaction  ${}^{10}\text{B} \rightarrow {}^8\text{B}$ . In the case of the observation of two events of boron-nucleus scattering accompanied by a high-momentum recoil of target fragments, the probability of obtaining a  ${}^8\text{B}$  beam at the available nuclotron energy can be estimated at about  $10^{-3}$  of the inelastic cross section. This method of the beam formation requires a careful verification by means of spectrometric measurements. An exposure involving  ${}^9\text{C}$  nuclei presents the most serious problem because, in this case, accompanying  ${}^3\text{He}$  nuclei, which have the same magnetic rigidity, generate an irremovable background.

We believe that the use of emulsions in experiments where they are exposed to beams of relativistic radioactive nuclei is the most reasonable in the case of light neutron-deficit isotopes. Owing to the possibility of completely observing the results of the interaction, the most significant channels of decay of excited

nuclei can be determined by analyzing the charge in the final state. For these channels, one can study the mass and angular spectra, reveal correlations, and estimate characteristic excitation energies.

#### ACKNOWLEDGMENTS

The work was supported by the Russian Foundation for Basic Research [project nos. 96-15-96423 (Scientific School of Academician A.M. Baldin) and 02-02-164 12a], VEGA 1/9036/02 Grant from the Agency for Science of the Ministry for Education of the Slovak Republic and the Slovak Academy of Sciences, and grants from the JINR Plenipotentiaries of the Slovak Republic and Romania in 2002.

#### REFERENCES

1. V. Bradnova *et al.*, Few-Body Systems Suppl. **14**, 241 (2003).
2. M. I. Adamovich *et al.*, Yad. Fiz. **62**, 1461 (1999) [Phys. At. Nucl. **62**, 1378 (1999)].
3. F. G. Lepekhin, D. M. Seliverstov, and B. B. Simonov, Pis'ma Zh. Éksp. Teor. Fiz. **59**, 312 (1994) [JETP Lett. **59**, 332 (1994)].
4. F. G. Lepekhin, D. M. Seliverstov, and B. B. Simonov, Yad. Fiz. **58**, 881 (1995) [Phys. At. Nucl. **58**, 816 (1995)].
5. F. G. Lepekhin, D. M. Seliverstov, and B. B. Simonov, Eur. Phys. J. A **1**, 137 (1998).
6. V. V. Belaga *et al.*, Yad. Fiz. **58**, 2014 (1995) [Phys. At. Nucl. **58**, 1905 (1995)].
7. V. V. Belaga *et al.*, Nucl. Tracks Radiat. Meas. **25**, 271 (1995).
8. V. V. Belaga, M. M. Muminov, and G. M. Chernov, Zh. Éksp. Teor. Fiz. **62**, 285 (1995) [JETP Lett. **62**, 395 (1995)].
9. V. V. Belaga, G. M. Chernov, and M. M. Muminov, Jr., Yad. Fiz. **60**, 885 (1997) [Phys. At. Nucl. **60**, 791 (1997)].
10. Almaty–Bucharest–Dubna–Dushanbe–Yerevan–Košice–Moscow–St. Petersburg–Tashkent–Tbilisi Collab. (N. P. Andreeva *et al.*), Yad. Fiz. **59**, 110 (1996) [Phys. At. Nucl. **59**, 102 (1996)].

*Translated by O. Chernavskaya*

---

---

**ELEMENTARY PARTICLES AND FIELDS**  
**Experiment**

---

---

## Azimuthal Anisotropy of the Emission of Fragments and Relativistic Particles in Collisions between Iron Nuclei of Momentum 2.5 GeV/c per Nucleon and Photoemulsion Nuclei

V. V. Dubinina, N. P. Egorenkova, V. I. Krotkova, E. A. Pozharova, and V. A. Smirnitsky

*Institute of Theoretical and Experimental Physics,  
Bol'shaya Cheremushkinskaya ul. 25, Moscow, 117259 Russia*

Received February 28, 2003; in final form, July 2, 2003

**Abstract**—The azimuthal anisotropy of the emission of fragments and relativistic particles in collisions between  $^{56}\text{Fe}$  nuclei of momentum 2.5 GeV/c per nucleon and photoemulsion nuclei is measured. For semicentral collisions at impact-parameter values in the range  $0.12 \leq b/b_{\text{max}} \leq 0.70$ , charged fragments and relativistic particles are predominantly emitted in the direction orthogonal to the nuclear-reaction plane. The azimuthal-asymmetry parameter  $P_2$  for fragments whose charge numbers are  $Z = 1, 2$  and  $Z \geq 3$  takes values of, respectively,  $-0.192 \pm 0.057$ ,  $-0.28 \pm 0.07$ , and  $-0.39 \pm 0.12$ . Evaporated  $b$  particles have an isotropic azimuthal distribution. © 2004 MAIK “Nauka/Interperiodica”.

### 1. INTRODUCTION

Collisions of relativistic nuclei create conditions for the production of strongly compressed nuclear matter ( $\rho/\rho_0 = 2-5$ ) at high temperatures ( $T = 50-100$  MeV). Experimental data obtained under such conditions furnish information about nuclear viscosity and possible phase transitions. Also, they can be used to obtain estimates relevant to astrophysical investigations. Moreover, collisions of relativistic nuclei open the possibility of studying similar phenomena under controlled laboratory conditions. The hydrodynamic model [1] predicts that part of the compression energy is released in the form of the collective emission of nuclear matter. In some experiments, projectile fragments undergo collective side bounce-off and side splash [2–4], these effects being due to transverse momentum. Investigation of a new component of the collective flux, the so-called squeeze-out of nuclear matter in the direction orthogonal to the nuclear-reaction plane [5–7], is of particular interest. The emission of fragments and particles in this direction is the only case where, during the interaction, they may avoid undergoing collisions or rescattering within the projectile and target nuclei.

We use two methods to determine the nuclear-reaction plane. The first [8, 9] is based on calculating the kinetic-energy flux carried by fragments and particles produced in collisions of nuclei. The flux is described in space by a three-dimensional ellipsoid, whose orientation depends on the impact parameter. The major axis of the ellipsoid and, hence, the direction of the main energy flux, together with the projectile momentum vector  $\mathbf{P}_{\text{pr}}$ , determine the reaction

plane. The second [6, 9–11] is based on measuring the vector  $\mathbf{Q}$  defined as the sum of the fragment-momentum projections  $\mathbf{P}_{\text{fr}}(i)$  onto the plane orthogonal to the projectile trajectory:  $\mathbf{Q} = \sum \mathbf{P}_{\text{fr}}(i)$ . In this case, the reaction plane is determined as the plane spanned by the vectors  $\mathbf{Q}$  and  $\mathbf{P}_{\text{pr}}$ ; in other words, the total transverse momentum with respect to this plane is equal to zero. A careful test [6] of the two methods for determining the reaction plane revealed their complete identity. The majority of experiments aimed at determining the reaction plane rely on the method of transverse momenta.

The preferred emission of  $Z \geq 2$  fragments (as usual,  $Z$  is their charge number) in the direction orthogonal to the reaction plane was observed at energies up to about 1 GeV per nucleon [6]. At higher energies, either this effect is nonexistent, or its contribution is negligible. In the interaction between iron nuclei of momentum  $\mathbf{P}_{\text{pr}} = 2.5$  GeV/c per nucleon and photoemulsion nuclei, we measured, in our experiment, the anisotropy of the emission of multiply charged and singly charged fragments and relativistic singly charged particles in the plane orthogonal to the vector  $\mathbf{P}_{\text{pr}}$ .

### 2. DESCRIPTION OF THE EXPERIMENT

An emulsion chamber formed by layers of BR-2 nuclear photoemulsion 450  $\mu\text{m}$  thick was irradiated with a beam of  $^{56}\text{Fe}$  accelerated to a momentum of 2.5 GeV/c per nucleon at the accelerator of Lawrence Berkeley National Laboratory (Berkeley, USA), the

angle of beam incidence with respect to the emulsion plane being small. Searches for nuclear interactions were performed by viewing tracks of projectile nuclei. As a result, 400 events were found. Some of these events were not employed in subsequent measurements and analysis. In order to rule out edge effects (effect of a planar chamber), we rejected events that occurred in the vicinity of (within  $30 \mu\text{m}$ ) the upper and the lower surface of the emulsion layer. Previous experiments showed that it is advisable to use semi-central interactions to determine the reaction plane. Peripheral interactions at an energy of a few GeV are inappropriate for this purpose because of a low multiplicity, which results in a large error in determining the reaction plane. Central interactions have a high multiplicity, but a small impact parameter, the latter leading to an uncertainty in determining the position of the reaction plane. We estimated the impact parameter on the basis of the ratio  $\beta = M_i/M_{\text{max}}$ , where  $M_i$  is the multiplicity of the  $i$ th event and  $M_{\text{max}}$  is the maximum multiplicity in a collision at a given energy. In [12, 13], it was shown that it is reasonable to treat  $\beta_p \leq 0.15$ – $0.20$  events as peripheral ones and  $\beta_c \geq 0.75$ – $0.80$  events as central ones. For subsequent measurements and analysis, we selected events in the multiplicity interval  $\beta_p < \beta < \beta_c$ , which involve three or more  $Z \geq 2$  fragments. In these events, the impact parameter was within the interval  $0.12 \leq b/b_{\text{max}} \leq 0.70$ . This selection criteria left 138 events for measurements.

The particle charges and emission angles were determined by means of a measuring microscope KSM supplemented with an on-line computer. The fragment charges were determined by measuring the lengths of track gaps and by calibrating the results of these measurements with aid of those for singly charged relativistic particles. On the basis of these measurements, we partitioned all fragments into three groups for a further analysis, these groups containing singly charged, doubly charged, and multiply charged ( $Z \geq 3$ ) fragments. The measurement of the fragment emission angles and the direction of the projectile nucleus was reduced to the measurement of the grain coordinates on the corresponding tracks. These measurements made it possible to calculate the angles in the microscope reference frame. The maintenance code supported the required dialog between the operator and the computer, whereby the monitoring of the results of the measurement was ensured. The angles were measured to within 2 to 3 mrad for multiply charged fragments and to within 1 mrad for singly and doubly charged fragments. In order to determine the nuclear-reaction plane, it is necessary to transform all angular measurements to the reference frame associated with the direction of projectile motion, because the angular distributions

are analyzed with respect to the projectile trajectory. In measuring the angles, the operator determined the projectile track along the  $x$  axis of the microscope to a precision of about 1 mrad. The required transformation of the coordinate frame was performed by means of a rotation about the  $y$  axis through an angle such that the azimuthal plane  $yz$  became orthogonal to the projectile trajectory. Upon the rotation of the coordinate frame, the  $x^*$  axis coincides with the projectile trajectory, while the  $z^*$  axis lies in the azimuthal plane. The angle between a track and the projectile trajectory is referred to as a polar angle ( $\theta$ ), while the angle between the track projection onto the  $yz^*$  plane and the projectile trajectory is the azimuthal angle ( $\varphi$ ).

We determined the nuclear-reaction plane according to the procedure described in [10, 11], employing singly and doubly charged fragments within the angular interval  $10 \leq \theta \leq 100$  mrad. We rejected fragments from a narrow cone having a polar angle  $\theta$  less than 10 mrad because of large errors in calculating azimuthal angles from the results of measurements.

Fragments produced upon the interaction-induced breakup of the projectile nucleus conserve the projectile longitudinal momentum; that is,  $\mathbf{P}_{\text{flong}}(i) = (\mathbf{P}_{\text{pr}}/A)n(i)$ , where  $n(i)$  is the number of nucleons in the  $i$ th fragment (we assumed that all doubly charged fragments are alpha particles). For each fragment, the momentum projection onto the azimuthal plane is then  $\mathbf{P}_{\text{ftr}}(i) = \mathbf{P}_{\text{flong}}(i) \tan \theta(i)$ , where  $\theta(i)$  is the polar angle of the  $i$ th fragment; the total transverse momentum of all fragments in an event is  $\mathbf{Q} = \sum \mathbf{P}_{\text{ftr}}(i)$ . For each event, we determined the azimuthal angle  $\varphi_q$  of the vector  $\mathbf{Q}$ , this angle specifying the angular position of the nuclear-reaction plane. The mean scatter  $\sigma_q$  in determining the angle  $\varphi_q$  is about  $30^\circ$  for semicentral collision [3, 6, 7, 11]; the azimuthal distribution within the interval  $0^\circ \leq \varphi_q \leq 360^\circ$  proved to be isotropic. Each event was then rotated in space to make the respective reaction planes coincident (that is, to make the angles and the directions of the vectors  $\mathbf{Q}$  coincident). After that, we summed all azimuthal angular spectra of fragments and particles from all interaction events selected for the analysis. The resulting total spectrum was used to analyze the azimuthal anisotropy of particle emission in nucleus–nucleus collisions (Fe Em).

### 3. RESULTS OF THE MEASUREMENTS

Summation of the azimuthal distributions from all events without bringing the nuclear-reaction planes into coincidence must produce a uniform azimuthal distribution, and this is precisely what was observed in numerous previous experiments. This statement

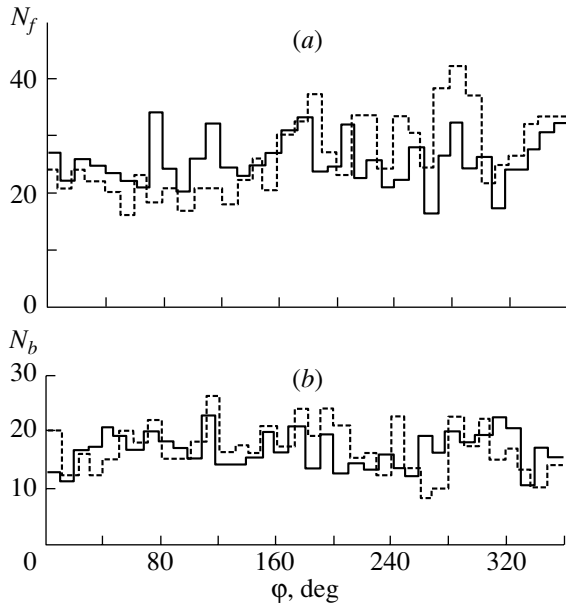


**Fig. 1.** Azimuthal distributions in the measuring-microscope coordinate frame (dashed-line histogram) and in the coordinate frame associated with the projectile momentum (solid-line histogram) for (a)  $0.5^\circ \leq \theta \leq 6^\circ$  fragments and (b) evaporated particles.

is valid only if the coordinate frame of the measuring microscope coincides with the projectile coordinate frame. As was indicated above, the projectile-momentum direction in our emulsion chamber has a small incidence angle with respect to the emulsion plane and, hence, with respect to the  $xy$  plane of the microscope coordinate frame. According to our measurements, this angle is  $\langle \text{dip} \rangle \sim 6$  mrad. In this case, the azimuthal distribution is shifted toward the incidence of the projectile-track direction. Indeed, Fig. 1a shows the experimental distribution of the fragment azimuthal angles, the dashed-line and the solid-line histogram corresponding, respectively, to the microscope coordinate frame and to the coordinate frame associated with the projectile-trajectory direction. It is clear that the solid-line histogram represents an isotropic distribution. The data show that, in order to study the anisotropy of the azimuthal angular distribution, it is necessary to transform the angular measurements to the coordinate frame associated with the projectile-momentum direction. This rotation of the coordinate frame affects the azimuthal distribution if the emitted fragments and particles “remember” the projectile-momentum direction, this being so if their emission is caused by processes that occur at the instant of the nucleus–nucleus interaction. If one considers evaporated particles, which appear upon the “heating” of the residual nucleus to the evaporation temperature, their multiplicity and their angular distribution do not depend on the projectile energy

and type over a rather broad region [4]. The dashed-line and the solid-line histogram in Fig. 1b represent the azimuthal angular distribution of the evaporation particles in, respectively, the measuring-microscope and the projectile coordinate frame. Both histograms provide similar descriptions of a uniform azimuthal angular distribution. A small longitudinal velocity of the residual nucleus does not affect the azimuthal distribution because it is associated with the plane orthogonal to the projectile velocity. This reference-frame independence of the angular distribution of evaporated particles was used to verify the absence of systematic errors in rotating events to bring the positions of their reaction planes into coincidence.

For selected events, we partitioned all tracks into six different arrays, measured angular azimuthal distributions for each array, and approximated the results by a second-order Legendre polynomial as [6, 13]

$$N_{az}(\varphi) = a(1 + P_1 \cos(\varphi) + P_2 \cos(2\varphi)), \quad (1)$$

where  $\varphi$  is the track azimuthal angle upon bringing the nuclear-reaction planes into coincidence. The parameter  $P_1$  characterizes the forward–backward asymmetry in the azimuthal plane with respect to the vector  $\mathbf{Q}$  (the vector  $\mathbf{Q}$  is directed from  $180^\circ$  to  $0^\circ$ )—it represents a so-called direct flux;  $P_2$  is the azimuthal-anisotropy parameter, which determines particle emission in the direction orthogonal to the reaction plane, an elliptic flux. The ratio of the probability of particle emission in the orthogonal direction to that of particle emission in the reaction plane is given by

$$R = [N(90^\circ) + N(270^\circ)]/[N(0^\circ) + N(180^\circ)] \quad (2) \\ = (1 - P_2)/(1 + P_2).$$

If  $P_2 < 0$ , then  $R > 1$ , and we observe the preferred emission (squeeze-out) of fragments and particles in the direction orthogonal to the reaction plane. If  $P_2 > 0$ , then  $R < 1$ , and the main flux is directed in the reaction plane. Figure 2 shows the spectra of azimuthal angles for six different arrays of experimental data, while Table 1 presents the main features of these arrays, the results of approximating them by expression (1), and the fitted values of the parameters  $P_1$  and  $P_2$ .

#### 4. DISCUSSION OF THE RESULTS OF THE MEASUREMENTS

It is clear from the data in Table 1 that the squeeze-out of fragments in the direction orthogonal to the nuclear-reaction plane (elliptic flux) increases with the fragment charge (arrays 4–6 in Table 1). Table 2 presents available experimental data on the elliptic flux of heavy fragments ( $Z \geq 2$ ) [4, 6, 10, 13–15]. According to data from [14], the elliptic flux (at

**Table 1.** Results of the measurements of the azimuthal anisotropy

Array	Features of an array	$P_1$	$P_2$
1	Evaporated $b$ particles (slow fragments of the residue of the target nucleus, $R \leq 3$ mm of photoemulsion)	$0.04 \pm 0.05$	$0.01 \pm 0.05$
2	$g$ particles in the angular interval $6^\circ < \theta \leq 70^\circ$ (mainly, fast particles from the target nucleus, $R > 3$ mm of photoemulsion, $\beta \leq 0.7$ )	$-0.04 \pm 0.07$	$-0.18 \pm 0.07$
3	$s$ particles (protons and $\pi$ mesons, $\beta > 0.7$ , $6^\circ < \theta \leq 30^\circ$ )	$0.061 \pm 0.041$	$-0.180 \pm 0.043$
4	$Z = 1$ fragments, $0.5^\circ \leq \theta \leq 6^\circ$	$-0.032 \pm 0.054$	$-0.192 \pm 0.057$
5	$Z = 2$ fragments, $0.5^\circ \leq \theta \leq 6^\circ$	$0.11 \pm 0.06$	$-0.28 \pm 0.07$
6	$Z \geq 3$ fragments, $0.5^\circ \leq \theta \leq 6^\circ$	$0.12 \pm 0.11$	$-0.39 \pm 0.12$

**Table 2.** Azimuthal anisotropy of the emission of  $Z \geq 2$  fragments

Projectile $A$	Target	Energy per nucleon, GeV	Charge $Z$	$P_1$	$P_2$	References
Au	Au	0.4	2	—	$-0.38 \pm 0.06$	[6]
Au	Au	0.4	2*	—	$-0.34 \pm 0.02$	[14]
Kr	Em	0.95	$\geq 2$	$0.453 \pm 0.043$	$-0.012 \pm 0.045$	[10]
Bi	Pb	1.0	2	0.76	0.01	[15]
Fe	Em	1.88	2	$0.11 \pm 0.06$	$-0.28 \pm 0.07$	This paper
Fe	Em	1.88	$\geq 3$	$0.12 \pm 0.11$	$-0.39 \pm 0.12$	This paper
Au	Em	10.6	2	$0.086 \pm 0.030$	$0.143 \pm 0.0040$	[13]
Au	Em	10.6	$\geq 2$	$0.444 \pm 0.026$	$0.054 \pm 0.026$	[4]

\* In [14], the result is given for  $A = 4$  rather than for  $Z = 2$ , but this is likely to be equivalent.

the projectile energy of 0.4 GeV per nucleon) depends strongly on the mass number  $A$  of fragments and on their transverse momenta  $\mathbf{P}_{tr}$ . By way of example, we indicate that, for  $A = 2$ , the azimuthal anisotropy increases ( $P_2$  is negative); with respect to the anisotropy at  $A = 1$ ,  $|P_2|$  grows by a factor of 2 to 3 at this value of  $A$ , by a factor of 3 to 4 for  $A = 3$ , and by a factor of 4 to 5 for  $A = 4$ . At the same time, the squeeze-out of heavy fragments is expected to be suppressed within hydrodynamic model [6] if nuclear viscosity is high. This statement contradicts experimental data quoted in [14] and in Table 2. With increasing projectile energy, the parameter  $P_2$  changes sign, which corresponds to a change in the character of the azimuthal asymmetry—a transition from an elliptic to a direct flux. A similar picture is observed for the emission of protons and pions [4, 7]. The equation of state for nuclear matter,  $E(n, T)$ , depends on the nuclear-matter density and tempera-

ture, which, in nucleus–nucleus collisions, are determined by the projectile energy [16, 17]. The nuclear-matter compressibility  $K \approx \partial^2 E(n, T)/\partial n^2$  changes from about 380 MeV for negative  $P_2$  (rigid nucleus) to about 200 MeV for positive  $P_2$  (soft nucleus). The reversal of the sign of  $P_2$  and the respective change in the nuclear-matter state make it possible to determine the projectile energy  $E_{tran}$  corresponding to this phenomenon. The change in the nuclear-matter state (compressibility) versus the temperature and density may be indicative of the occurrence of a phase transition. An experimental measurement of  $E_{tran}$  offers the possibility of improving the equation of state for nuclear matter under extreme conditions. It is more straightforward to observe the reversal of the sign of the azimuthal anisotropy parameter  $P_2$  in an experiment with multiply charged fragments, where the magnitude of  $P_2$  is severalfold greater than the anisotropy of the emission of singly charged particles.

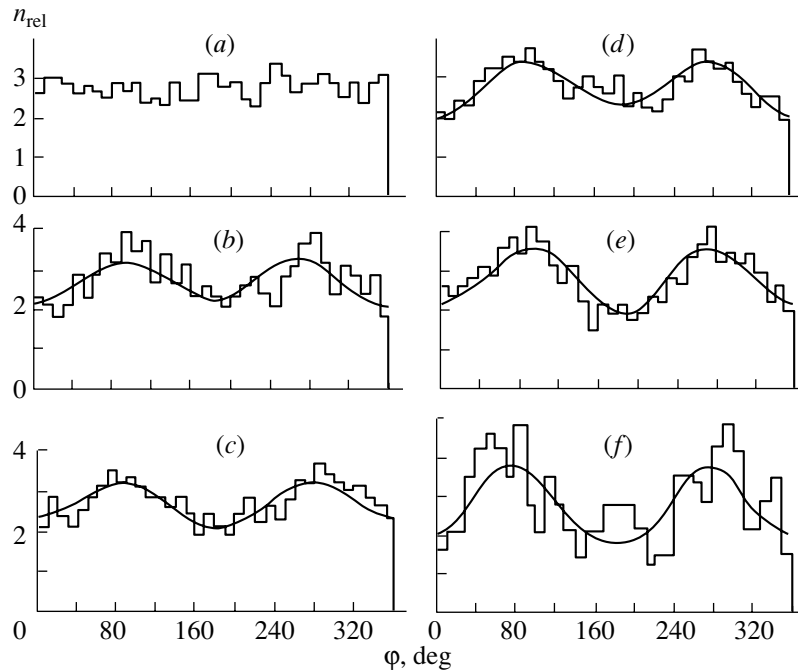


**Fig. 2.** Results obtained by measuring the azimuthal anisotropy (histogram) and fit to the data in terms of expression (1) (solid curve): (a) 826 tracks of  $b$  particles, which are slow fragments of the residue of the target nucleus ( $R \leq 3$  mm of photoemulsion); (b) 381 tracks of  $g$  particles, which are mainly fast particles from the target nucleus ( $R > 3$  mm of photoemulsion,  $\beta \leq 0.7$ ,  $6^\circ < \theta \leq 70^\circ$ ); (c) 1046 tracks of  $s$  particles, which are protons and pions ( $\beta > 0.7$ ,  $6^\circ < \theta \leq 30^\circ$ ); (d) 626 tracks of  $Z = 1$  fragments ( $0.5^\circ \leq \theta \leq 6^\circ$ ); (e) 425 tracks of  $Z = 2$  fragments ( $0.5^\circ \leq \theta \leq 6^\circ$ ); and (f) 146 tracks of  $Z \geq 3$  fragments ( $0.5^\circ \leq \theta \leq 6^\circ$ ).

## 5. CONCLUSION

The main result of our measurement of azimuthal anisotropy in collisions between iron and photoemulsion nuclei is the observation of a preferred emission of fragments in the direction orthogonal to the nuclear-reaction plane, the degree of this anisotropy being dependent on the fragment charge (see arrays 4–6 of the Table 1) as  $P_2 \approx -0.1(0.9 + Z)$ . The entire body of available experimental data (see Table 2) gives no way to determine the projectile energy  $E_{\text{tran}}$  at which the asymmetry parameter  $P_2$  changes sign for multiply charged fragments. It is necessary to perform experiments that are similar to the present one, but in which the projectile energy is varied over a broader region extending up to 4 or 5 GeV.

The anisotropy of the emission of  $s$  particles produced in FeEm collisions corresponds to  $P_2 < 0$  and agrees with other experimental data. A similar analysis for evaporated  $b$  particles leads to an isotropic distribution, this indicating that there are significant methodological errors in our measurements.

## ACKNOWLEDGMENTS

We are grateful to V.A. Sheinkman for assistance in exposing test samples of nuclear photoemulsion

at the accelerator of the Institute of Experimental and Theoretical Physics (ITEP, Moscow), to V.V. Shamanov for his help in computer-aided data processing, and to R. Kholynskii for providing us with layers of photoemulsion irradiated with Fe ions.

## REFERENCES

1. S. Z. Belenkij and L. D. Landau, *Nuovo Cimento Suppl.* **3**, 15 (1956); W. Scheid, H. Müller, and W. Greiner, *Phys. Rev. Lett.* **32**, 741 (1974); M. Sano *et al.*, *Phys. Lett. B* **156B**, 27 (1985).
2. H. A. Gustafsson, H. H. Gutbrod, B. Kolb, *et al.*, *Phys. Rev. Lett.* **52**, 1590 (1984); D. Beavis, S. Y. Fung, W. Gorn, *et al.*, *Phys. Rev. Lett.* **54**, 1652 (1985); J. Gosset, *Phys. Lett. B* **247**, 233 (1990); M. I. Adamovich, E. S. Basova, M. M. Chernyavsky, *et al.*, *Yad. Fiz.* **60**, 1580 (1997) [*Phys. At. Nucl.* **60**, 1435 (1997)].
3. M. I. Adamovich, M. M. Aggarwal, Y. A. Alexandrov, *et al.*, *Eur. Phys. J. A* **2**, 61 (1998).
4. S. Vokal, Doctoral Dissertation in Mathematics and Physics (Joint Inst. Nucl. Res., Dubna, 2001).
5. H. H. Gutbrod, K. H. Kampert, B. Kolb, *et al.*, *Phys. Lett. B* **216**, 267 (1989).
6. H. H. Gutbrod, K. H. Kampert, B. Kolb, *et al.*, *Phys. Rev. C* **42**, 640 (1990).
7. P. L. Jain and G. Singh, *Mod. Phys. Lett. A* **9**, 1445 (1994).

8. M. Gyulassy, K. A. Frankel, and H. Stöker, Phys. Lett. B **110B**, 185 (1982); Jean-Yves Ollitrault, Phys. Rev. D **48**, 1132 (1993).
9. P. Danielewicz, H. Strobele, G. Odyniec, *et al.*, Phys. Rev. C **38**, 120 (1988).
10. M. I. Adamovich, E. S. Basova, M. M. Chernyavsky, *et al.*, Eur. Phys. J. A **6**, 427 (1999).
11. P. Danielewicz and G. Odyniec, Phys. Lett. B **157B**, 146 (1985).
12. C. A. Ogilvie, J. C. Adloff, M. Begemann-Blaich, *et al.*, Phys. Rev. Lett. **67**, 1214 (1991); M. Tsang *et al.*, Phys. Rev. C **40**, 1685 (1989); C. Cavata *et al.*, Phys. Rev. C **42**, 1760 (1990); D. Brill, W. Ahner, P. Baltes, *et al.*, Phys. Rev. Lett. **71**, 336 (1993).
13. P. L. Jain, G. Singh, and A. Mukhopadhyay, Phys. Rev. Lett. **74**, 1534 (1995).
14. FOPI Collab. (A. Andronic *et al.*), Nucl. Phys. A **661**, 333 (1999).
15. A. Kugler, V. Wagner, M. Pachr, *et al.*, Phys. Lett. B **335**, 319 (1994).
16. P. Danielewicz, R. A. Lacey, P. B. Gossiaux, *et al.*, Phys. Rev. Lett. **81**, 2438 (1998); C. Pinkenburg, N. N. Ajitanand, J. M. Alexander, *et al.*, Phys. Rev. Lett. **83**, 1295 (1999).
17. G. Rai, Nucl. Phys. A **661**, 162 (1999); E. V. Shuryak, Nucl. Phys. A **661**, 119 (1999).

*Translated by M. Kobrinsky*

## ELEMENTARY PARTICLES AND FIELDS

### Theory

# Familon $\rightarrow$ Photon Transition in a Magnetized Plasma

N. V. Mikheev\* and E. N. Narynskaya\*\*

Yaroslavl State University, Sovetskaya ul. 14, Yaroslavl, 150000 Russia

Received March 26, 2003

**Abstract**—The external-magnetic-field-induced interaction of a pseudoscalar particle with a photon is investigated in  $e^-e^+$  plasma. The familon arising upon the breakdown of a horizontal symmetry between fermion generations is considered for a pseudoscalar particle. The expressions for the plasma and the field contribution to the effective familon–photon coupling are derived in the limit of strongly magnetized plasma and the limit where the plasma being considered occurs in a relatively weak magnetic field.

© 2004 MAIK “Nauka/Interperiodica”.

## 1. INTRODUCTION

At the present time, physics beyond the Standard Model is a subject of great interest. In particular, special attention has been given to light and even strictly massless Goldstone and pseudo-Goldstone bosons that could arise upon the breakdown of a new symmetry at some energy scale. Particles of such kind include the familon that arises upon the spontaneous breakdown of a horizontal symmetry between fermion generations [1]. Since Goldstone particles interact with matter very weakly, investigation of physical corollaries of their existence can be of interest for astrophysics and cosmology [2].

In studying quantum processes in astrophysical objects such as neutron stars, white dwarfs, and supernovae, it is necessary to take into account the effect of active external media, including an electron–positron plasma and a strong magnetic field. Magnetic fields whose strength considerably exceeds the critical (so-called Schwinger) value of  $B_e = m_e^2/e = 4.41 \times 10^{14} \text{ G}^1$  are of particular interest for possible astrophysical applications. Under laboratory conditions, such fields cannot be generated at the moment. According to currently prevalent concepts, fields of such or even greater scale could exist in astrophysical objects. For example, the observation of pulsars indicates the possible existence of magnetic fields of strength  $10^{12}$ – $10^{13} \text{ G}$  at their surface [3]. In astrophysical cataclysms such as a supernova explosion, the strength of the magnetic field developed in the collapse of the star core reaches strengths of  $10^{13}$ – $10^{14} \text{ G}$ ; allowance for star rotation can increase

the strength of this magnetic field by a factor of  $10^3$  to  $10^4$  [4, 5]. At the present time, the mechanisms of the generation of such fields whose strength is as large as  $10^{15}$ – $10^{17} \text{ G}$  are being widely discussed [6–11].

In the present study, we analyze the familon  $\rightarrow$  photon transition in a magnetized plasma. The electromagnetic-field-induced effective interaction of a pseudoscalar particle with a photon is described by the Lagrangian

$$L_{\phi\gamma} = g_{\phi\gamma} \tilde{F}^{\alpha\beta} (\partial_\beta A_\alpha) \Phi, \quad (1)$$

where  $A_\mu$  is the 4-potential of a quantized electromagnetic field;  $F_{\alpha\beta}$  and  $\tilde{F}_{\alpha\beta} = \frac{1}{2} \varepsilon_{\alpha\beta\rho\sigma} F_{\rho\sigma}$  are, respectively, the strength tensor of the external magnetic field and its dual counterpart;  $\Phi$  is the familon wave function; and  $g_{\phi\gamma}$  is the effective coupling constant for familon–photon interaction in a magnetized plasma.

The Lagrangian in (1) directly leads to the  $\phi \rightarrow \gamma$  transition amplitude in the form

$$M_{\phi \rightarrow \gamma} = ig_{\phi\gamma} (\varepsilon^* \tilde{F} q), \quad (2)$$

where  $q^\mu = (\omega, \mathbf{k})$  is the photon (familon) 4-momentum and  $\varepsilon_\mu$  is the photon-polarization 4-vector. It should be noted, however, that, in the presence of a magnetic field, to say nothing of a plasma, expression (2) does not completely describe the amplitude for the transition  $\phi \rightarrow \gamma$ . In general, the conversion process  $\phi \rightarrow \gamma$  in a magnetized plasma is affected both by the magnetic field and by the plasma; therefore, the  $\phi \rightarrow \gamma$  transition amplitude can be represented as the sum of two contributions:

$$M_{\phi \rightarrow \gamma} = M_{\phi \rightarrow \gamma}^{\text{field}} + M_{\phi \rightarrow \gamma}^{\text{plasma}}. \quad (3)$$

\* e-mail: mikheev@uniyar.ac.ru

\*\* e-mail: elenan@uniyar.ac.ru

<sup>1</sup> Here, use is made of a natural system of units where  $c = \hbar = 1$ , and  $e > 0$  is an elementary charge.

The first term in (3) is associated with the contribution induced by an external magnetic field and is represented by the loop-diagram in Fig. 1, where summation is performed over fermions  $f$ . The second term describes the plasma contribution, which comes from Compton-like processes of familon → photon transitions occurring on plasma electrons and positrons. Figure 2 displays the diagrams that represent the  $\phi \rightarrow \gamma$  transition on plasma electrons. The positron contribution is described by the analogous diagrams where  $e^-(p)$  is replaced by  $e^+(p)$ , with  $p^\mu = (E, \mathbf{p})$  being the electron (positron) 4-momentum.

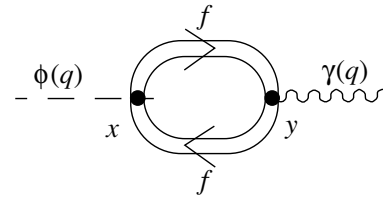


Fig. 1. Diagram representing the external-magnetic-field contribution to the amplitude for the familon → photon transition. The double line corresponds to the exact fermion propagator in a magnetic field.

In the present study, we consider the  $\phi \rightarrow \gamma$  transition in a plasma in the presence of an external magnetic field and derive an expression for the effective familon–photon coupling in two limiting cases that are of interest for some astrophysical applications.

where the index  $\parallel$  corresponds to the longitudinal components of 4-vectors—if the magnetic field is directed along the  $z$  axis, then  $q_{\parallel}^2 = \omega^2 - k_z^2$  and  $(pq)_{\parallel} = E\omega - k_z p_z$ ;  $E = \sqrt{p_z^2 + m_e^2}$  is the electron or the positron energy in the first Landau level; and  $f(E, \mu)$  and  $f(E, -\mu)$  are the distributions of plasma electrons and positrons, respectively. In the plasma rest frame, these distributions have the form

2. STRONGLY MAGNETIZED  $e^-e^+$  PLASMA

For astrophysical objects such as the envelope of an exploding supernova, the physical situation is typical where the magnetic field specifies the maximum energy scale of the problem; that is,

$$eB \gg \mu^2, T^2 \gg m_e^2, \tag{4}$$

where  $\mu$  and  $T$  are the plasma chemical potential and temperature, respectively. Under the conditions in (4), the limit of a strong magnetic field is realized, where plasma electrons occupy only the first Landau level. Since the motion of such electrons in the direction orthogonal to the magnetic-field direction becomes unobservable, the calculations are considerably simplified.

$$f(E, \mu) = \frac{1}{e^{(E-\mu)/T} + 1},$$

$$f(E, -\mu) = \frac{1}{e^{(E+\mu)/T} + 1}.$$

The plasma contribution to the  $\phi \rightarrow \gamma$  transition amplitude can be directly obtained from the Lagrangian

By using the amplitude in (6), the contribution of a strongly magnetized plasma to the effective coupling constant  $g_{\phi\gamma}$  can be reduced to the form

$$L = \frac{c_e}{F} (\bar{\Psi}_e \gamma_\alpha \gamma_5 \Psi_e) \partial^\alpha \Phi + e (\bar{\Psi}_e \gamma_\alpha \Psi_e) A^\alpha, \tag{5}$$

where  $F$  is the scale of horizontal-symmetry breaking;  $c_e$  is a dimensionless parameter that is on the order of unity and which depends on the choice of model; and  $\Phi$  and  $\Psi_e$  are, respectively, the familon and the electron–positron field.

$$g_{\phi\gamma}^{\text{plasma}} = \frac{c_e e^2 m_e^2}{\pi^2 F} q_{\parallel}^2 \int_{-\infty}^{+\infty} \frac{dp_z}{E} \frac{f(E, \mu) + f(E, -\mu)}{4(pq)_{\parallel}^2 - q_{\parallel}^4}. \tag{7}$$

The result obtained by calculating the plasma contribution to the amplitude in (3) with allowance for coherent scattering on all of the plasma electrons and positrons can be expressed in terms of a single integral as

The field contribution to the  $\phi \rightarrow \gamma$  transition amplitude is represented by the diagram in Fig. 1. In the following, we assume conditions under which the magnetic field is much greater than the critical field for electrons,  $B \gg B_e$ , but it is considerably less than the critical magnetic field for all other fermions ( $B \ll B_f, f \neq e$ ). The electron is the most sensitive to the effect of an external field since it is a particle that carries the maximum specific charge. It follows that, owing to the hierarchy of the fermion masses, the main contribution to the sum comes from electrons—under the conditions being considered, the contribution of other fermions is negligible.

In the limit of a strong magnetic field, the expression for the field contribution to the transition amplitude (3) can be borrowed from [12], where the one-loop field-induced contributions to the generalized amplitude for the  $j \rightarrow f\bar{f} \rightarrow j'$  transition in an external electromagnetic field were calculated for arbitrary combinations of the scalar, pseudoscalar, vector, and

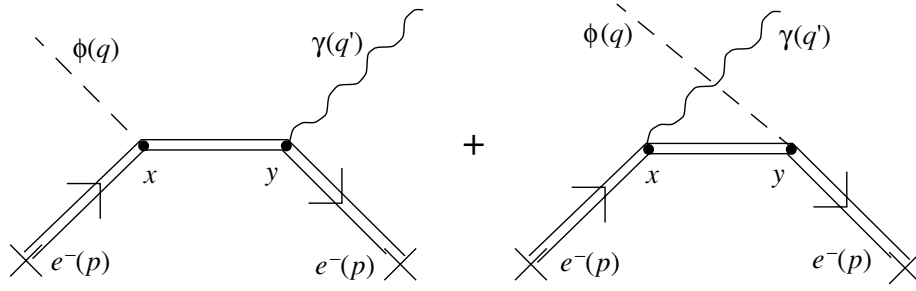


Fig. 2. Contribution of plasma electrons to the familon → photon transition.

pseudovector interactions of the currents  $j$  and  $j'$  with fermions. In particular, the external-magnetic-field-induced contribution to the amplitude of the *pseudoscalar particle* → *vector particle* transition is described by formula (2.14) in (12). Making the substitutions  $j_P \rightarrow -i2m_e/F$  and  $j_{V\mu} \rightarrow e\epsilon_\mu^*$  in that formula and setting  $q^2 = 0$ , we find in the limit of a strong magnetic field that

$$M_{\phi \rightarrow \gamma}^{\text{field}} = \frac{-ic_e e^2}{2\pi^2 F} (\epsilon^* \tilde{F} q) \int_0^1 \frac{m_e^2 du}{m_e^2 - q_{\parallel}^2 (1 - u^2)/4}. \quad (8)$$

If the interaction of the pseudoscalar particle being considered is free from the Adler anomaly (as is the case for the familon) or if the Adler anomaly is entirely absorbed in a vacuum term (as is the case for the axion), expression (8) can be recast into the form

$$M_{\phi \rightarrow \gamma}^{\text{field}} = \frac{-ic_e e^2}{2\pi^2 F} (\epsilon^* \tilde{F} q) \times \left( \int_0^1 \frac{m_e^2 du}{m_e^2 - q_{\parallel}^2 (1 - u^2)/4} - 1 \right), \quad (9)$$

which clearly demonstrates that the transition amplitude does not involve a term that is linear in the field. Comparing the result in (9) with the amplitude in (2), we find that, in the limit of a strong magnetic field, the external-magnetic-field-induced contribution to the effective coupling constant  $g_{\phi\gamma}$  is

$$g_{\phi\gamma}^{\text{field}} = \frac{-c_e e^2}{2\pi^2 F} H(z), \quad (10)$$

where  $z = 4m_e^2/q_{\parallel}^2$  and the function  $H(z)$  is given by

$$H(z) = \frac{z}{\sqrt{z-1}} \arctan \frac{1}{\sqrt{z-1}} - 1, \quad z > 1,$$

$$H(z) = -\frac{1}{2} \left( \frac{z}{\sqrt{1-z}} \ln \frac{1 + \sqrt{1-z}}{1 - \sqrt{1-z}} - \frac{i\pi z}{\sqrt{1-z}} + 2 \right), \quad z < 1.$$

Taking into account (7) and (10), we can write the effective familon–photon coupling constant in a strongly magnetized plasma in the form

$$g_{\phi\gamma} = \frac{-c_e e^2}{2\pi^2 F} \times \left( H(z) - 2m_e^2 q_{\parallel}^2 \int_{-\infty}^{+\infty} \frac{dp_z}{E} \frac{f(E, \mu) + f(E, -\mu)}{4(pq_{\parallel}^2 - q_{\parallel}^4)} \right). \quad (11)$$

The expression for the effective coupling constant (11) is significantly simplified in the limiting cases of soft and hard familons.

(i) Let us consider the case of soft familons ( $\omega \ll m_e$ ). In this limit, the argument of the function  $H(z)$ , which determines the external-field-induced contribution, satisfies the condition  $z = 4m_e^2/q_{\parallel}^2 \gg 1$ , while the function itself becomes

$$H(z)|_{z \gg 1} \simeq \frac{2}{3z} \ll 1.$$

Therefore, the effective coupling constant  $g_{\phi\gamma}$  is then dominated by the plasma contribution, which can be reduced to the form

$$g_{\phi\gamma} \simeq g_{\phi\gamma}^{\text{plasma}} \simeq \frac{c_e e^2}{2\pi^2 F} \times \int_0^{\infty} dp_z \frac{d}{dE} (f(E, \mu) + f(E, -\mu)).$$

In an ultrarelativistic plasma, the integral with respect to  $p_z$  can easily be calculated. Eventually, we obtain

$$g_{\phi\gamma} \simeq g_{\phi\gamma}^{\text{plasma}} \simeq -\frac{c_e e^2}{2\pi^2 F}. \quad (12)$$

(ii) Let us consider the case of hard familons ( $\omega \gg m_e$ ). In this limit, the plasma contribution to the coupling constant  $g_{\phi\gamma}$  involves a suppression associated with the electron mass, its square  $m_e^2$  being the smallest parameter in the problem. Thus, the effective familon–photon coupling is determined, in the case

of hard familons, by the field contribution exclusively; that is,

$$g_{\phi\gamma} \simeq g_{\phi\gamma}^{\text{field}} \simeq \frac{c_e e^2}{2\pi^2 F}. \quad (13)$$

It can be seen from (12) and (13) that, at high ( $\omega \gg m_e$ ) and at low ( $\omega \ll m_e$ ) familon energies, the familon–photon coupling appears to be independent of the familon (photon) momentum—that is, it is a constant.

### 3. WEAKLY MAGNETIZED ELECTRON–POSITRON PLASMA

In this section, we consider the physical situation where, of the two components of the active medium, the plasma component is much more significant than the field one; that is,

$$\mu^2, T^2 \gg eB \gg m_e^2. \quad (14)$$

Under the physical conditions specified by (14), a large number of Landau levels are excited. As a matter of fact, the result in the leading approximation then depends on only one dynamical invariant,  $[e^2(qFFq)]^{1/2}$ . This means that investigation of quantum processes under these conditions effectively reduces to calculations in a constant crossed field ( $\mathbf{B} \perp \mathbf{E}, |\mathbf{B}| = |\mathbf{E}|$ ), the technique of such calculations being well known [13, 14]. It should be noted that, although the magnetic field is weak on the scale of plasma–electron energies [see Eq. (14)], it can at the same time be quite strong in relation to the Schwinger value  $B_e$ . By way of example, we indicate that, under the conditions prevalent in the core of a supernova after the collapse, where, according to present-day concepts, the plasma chemical potential is  $\mu \sim 500 m_e$  and the plasma temperature is  $T \sim 70m_e$  [2], we find from (14) that

$$\frac{\mu^2}{m_e^2} \sim 10^5 \gg \frac{B}{B_e} \gg 1. \quad (15)$$

Relation (15) demonstrates that even magnetic fields of strength up to  $B \sim 10^{17}$  G satisfy the conditions in (14); therefore, they can be considered to be relatively weak.

The calculation of the plasma contribution to the  $\phi \rightarrow \gamma$  transition amplitude yields

$$M_{\phi \rightarrow \gamma}^{\text{plasma}} = \frac{ic_e e^2}{2\pi^2 F} (\varepsilon^* \tilde{F} q) \times \int_0^\infty dv (z_1 f(z_1) - z_2 f^*(z_2)) (f(v, \mu) + f(v, -\mu)), \quad (16)$$

where  $f(z)$  is a Hardy–Stokes function, its arguments being

$$z_{1,2} = (\chi_q v (1 \mp v))^{-2/3}, \quad \chi_q^2 = \frac{e^2 (qFFq)}{m_e^6},$$

while  $f(v, \mu)$  and  $f(v, -\mu)$  are the distributions of, respectively, plasma electrons and plasma positrons. These distributions can be represented in the form

$$f(v, \mu) = \frac{1}{e^{v\chi_q/\chi_0 - \mu/T} + 1}, \quad \chi_0 = \frac{eBT}{m_e^3}.$$

The transition amplitude (16) leads to the following expression for the plasma contribution to the coupling constant  $g_{\phi\gamma}$ :

$$g_{\phi\gamma}^{\text{plasma}} = \frac{c_e e^2}{2\pi^2 F} \int_0^\infty dv (z_1 f(z_1) - z_2 f^*(z_2)) \times (f(v, \mu) + f(v, -\mu)). \quad (17)$$

Under the physical conditions (14), a typical familon energy is  $\omega \sim T \gg m_e$ ; therefore, the dynamical parameter satisfies the condition  $\chi_q \gg 1$ . In this case, the integral with respect to the variable  $v$  can easily be calculated, and the plasma contribution to the effective coupling constant  $g_{\phi\gamma}$  can be rewritten in the simpler form

$$g_{\phi\gamma}^{\text{plasma}} = \frac{3^{1/3} e^2 c_e}{4\pi^3 F} \Gamma\left(\frac{1}{3}\right)^4 \frac{1}{\chi_q^{2/3}}. \quad (18)$$

In the amplitude for the  $\phi \rightarrow \gamma$  transition, the one-loop contribution induced by a relatively weak external magnetic field can be derived, for example, from formula (3.5) in [12]. The result is

$$M_{\phi \rightarrow \gamma}^{\text{field}} = \frac{i(q\tilde{F}\varepsilon^*)}{2\pi^2 F} \sum_f c_f e_f^2 (J - 1), \quad (19)$$

where  $c_f$  is a dimensionless factor that is on the order of unity and which depends on the choice of model and  $e_f$  is the electric charge of a virtual fermion  $f$  in the loop. In expression (19), we have subtracted the contribution corresponding to the Adler anomaly and have introduced a field form factor  $J$  that, in general, depends both on the magnetic-field strength and on the 4-vector  $q_\mu$ . In the crossed-field limit,  $J$  depends only on the combination  $(qFFq)$  and takes the form

$$J(\chi_f) = \int_0^1 \eta f(\eta) dt, \quad (20)$$

$$f(\eta) = i \int_0^\infty dz \exp \left[ -i \left( \eta z + \frac{1}{3} z^3 \right) \right],$$

$$\eta = \left[ \frac{4}{\chi_f(1-t^2)} \right]^{2/3},$$

where  $f(\eta)$  is a Hardy–Stokes function and  $\chi_f^2 = e_f^2(qFFq)/m_f^6$  is the dimensionless ratio of the familon dynamical parameter to the virtual-fermion ( $f$ ) mass.

At small and large values of the dynamical parameter  $\chi_f$ , the asymptotic behavior of the integral  $J$  in (20) can be represented as

$$\begin{aligned} J &\simeq -1 + O(\chi_f^2), & \chi_f &\ll 1, \\ J &\simeq O(\chi_f^{-2/3}), & \chi_f &\gg 1. \end{aligned} \quad (21)$$

By virtue of the asymptotic expressions in (21), the contribution to the transition amplitude (19) comes only from relatively light fermions characterized by  $\chi_f \gg 1$ . Because of the fermion-mass hierarchy, the main contribution comes, under the conditions being considered, from a virtual electron, in which case we have

$$M_{\phi \rightarrow \gamma}^{\text{field}} = \frac{ic_e e^2}{2\pi^2 F} (\varepsilon^* \tilde{F} q). \quad (22)$$

Comparing expressions (22) and (2), we obtain the contribution of the external magnetic field to the effective coupling constant  $g_{\phi\gamma}$ :

$$g_{\phi\gamma}^{\text{field}} = \frac{c_e e^2}{2\pi^2 F}. \quad (23)$$

With the aid of the results presented in (18) and (23), the effective familon–photon coupling in a plasma occurring in a relatively weak magnetic field can be written in the form

$$\begin{aligned} g_{\phi\gamma} &= \frac{2c_e \alpha}{\pi F} \left( 1 + \frac{3^{1/3}}{\pi} \Gamma\left(\frac{1}{3}\right)^4 \frac{1}{\chi_q^{2/3}} \right) \\ &\simeq \frac{2c_e \alpha}{\pi F} \left( 1 + \frac{23.65}{\chi_q^{2/3}} \right). \end{aligned}$$

Under the conditions being considered ( $T \sim 70m_e$ ,  $B \sim 10^{17}$  G), the dynamical familon parameter is

$$\chi_q = \frac{eB\omega \sin \theta}{m_e^3} \sim \left( \frac{B}{B_e} \right) \left( \frac{\omega}{m_e} \right) \sim 10^5.$$

It follows that, under physical conditions corresponding to the core of a supernova, the field contribution to the effective coupling constant  $g_{\phi\gamma}$  is much greater than the respective plasma contribution.

#### 4. CONCLUSION

The effective external-magnetic-field-induced interaction of the familon with a photon in a magnetized electron–positron plasma has been explored in this study. Expressions for the effective coupling constant characterizing familon–photon interaction have been obtained for two cases that are the most realistic for astrophysics—namely, the case of a strongly magnetized plasma, where plasma electrons and positrons occupy only the first Landau level, and the case where the plasma being considered occurs in a relatively weak magnetic field, so that a large number of Landau levels are excited. It has been shown that, in the physical situation where, of two components of the active medium being considered, the plasma component is dominant, the plasma contribution to the coupling constant  $g_{\phi\gamma}$  is considerably less than the field contribution. In the limit of a strongly magnetized plasma, it has been found that the effective familon–photon coupling is dominated by the field contribution in the case of hard familons ( $\omega \gg m_e$ ) and by the plasma contribution in the case of soft familons ( $\omega \ll m_e$ ).

The results obtained in this study can be useful in analyzing processes in an active external medium that involve pseudoscalar particles.

#### ACKNOWLEDGMENTS

This work was supported in part by the Ministry for Higher Education of the Russian Federation (project no. E02-11.0-48); by the Russian Foundation for Basic Research (project nos. 01-02-17334, 03-02-06215); and by the Ministry for Industry, Sciences, and Technologies of the Russian Federation [a presidential grant (no. NSh-1916.2003.2) for support of leading scientific schools].

#### REFERENCES

1. A. A. Ansel'm and N. G. Ural'tsev, Zh. Éksp. Teor. Fiz. **84**, 1961 (1983) [Sov. Phys. JETP **57**, 1142 (1983)].
2. G. G. Raffelt, *Stars as Laboratories for Fundamental Physics* (University of Chicago Press, Chicago, 1996).
3. V. M. Lipunov, *Astrophysics of Neutron Stars* (Nauka, Moscow, 1987; Springer-Verlag, Heidelberg, 1991) [in Russian].
4. G. S. Bisnovatyĭ-Kogan, Astron. Zh. **47**, 813 (1970) [Sov. Astron. **14**, 652 (1970)].
5. G. S. Bisnovatyĭ-Kogan, *Physical Problems of the Star Evolution Theory* (Nauka, Moscow, 1989) [in Russian].

6. M. Ruderman, in *Neutron Stars: Theory and Observation*, Ed. by J. Ventura and D. Pines (Kluwer Academic Publ., Dordrecht, 1991).
7. R. C. Duncan and C. Thompson, *Astrophys. J.* **392**, 9 (1992).
8. C. Thompson and R. C. Duncan, *Astrophys. J.* **408**, 194 (1993).
9. G. S. Bisnovatyi-Kogan, *Astron. Astrophys. Trans.* **3**, 287 (1993).
10. M. Bocquet *et al.*, *Astron. Astrophys.* **301**, 757 (1995).
11. G. J. Mathews, J. R. Wilson, and J. Salmonson, astro-ph/9710229.
12. M. Yu. Borovkov, A. V. Kuznetsov, and N. V. Mikheev, *Yad. Fiz.* **62**, 1714 (1999) [*Phys. At. Nucl.* **62**, 1601 (1999)].
13. A. I. Nikishov and V. I. Ritus, *Zh. Éksp. Teor. Fiz.* **46**, 776 (1964) [*Sov. Phys. JETP* **19**, 529 (1964)].
14. V. I. Ritus, *Tr. Fiz. Inst. Akad. Nauk SSSR* **111**, 5 (1979).

*Translated by A. Isaakyan*

## Logarithmic Contributions in the Particle-Mass Ratio to the Fine Shift of $S$ Energy Levels of Hydrogen-Like Atoms in the Fifth Order in the Fine-Structure Constant

N. A. Boikova\*, S. V. Kleshchevskaya, Yu. N. Tyukhtyaev, and R. N. Faustov<sup>1)</sup>

*Saratov State University, Astrakhanskaya ul. 83, Saratov, 490071 Russia*

Received December 6, 2002; in final form, May 27, 2003

**Abstract**—A high-precision investigation of a logarithmic contribution in the particle-mass ratio to the fine shift of the  $S$  energy levels of hydrogen-like atoms from the exchange of a Coulomb photon is performed. It is shown that diagrams describing the exchange of one transverse photon and two Coulomb photons do not make such contributions. © 2004 MAIK “Nauka/Interperiodica”.

In recent years, it has become clear that attempts at improving the accuracy in measuring the shifts of energy levels in hydrogen-like atoms by means of radiofrequency methods run into serious difficulties. Methods of Doppler-free two-photon laser spectroscopy open new prospects for reducing experimental errors.

The  $1S_{1/2}-2S_{1/2}$  interval has been measured at present [1, 2] in the hydrogen atom to a precision of a few tens of kHz,

$$\nu_{1S-2S}^L = 2\,466\,061\,413\,187.34(84) \text{ kHz (1997)}, \quad (1)$$

$$\nu_{1S-2S}^L = 2\,466\,061\,413\,187.103(46) \text{ Hz (2000)}. \quad (2)$$

Advances made in the most recent experimental studies have given impetus to the development of theoretical methods for precisely determining corrections to known values of energy-level shifts. The considerable number of review articles devoted to the theory of the spectra of hydrogen-like atoms and published within a relatively short time interval is indicative of the growth of interest in investigations along these lines [3–11]. Recoil corrections calculated by the time at which the review article of Eides *et al.* [11] was written are compiled in Table VIII of that article. An extensive list of respective data involves only one contribution that is logarithmic in the parameter  $\beta = m_1/m_2$  (where  $m_1$  and  $m_2$  are the masses of, respectively, the light and the heavy particle) and which

was obtained by Fulton and Martin [12] as far back as 1954. The problem of other similar contributions was first formulated and partly solved in [13] nearly 50 years later.

We begin applying the quasipotential approach to the fine-shift problem in the case of one-photon exchange, following the same lines of reasoning as in [14]. We consider the equation

$$\begin{aligned} \left( E - \sqrt{\mathbf{p}^2 + m_1^2} - \sqrt{\mathbf{p}^2 + m_2^2} \right) \Psi(\mathbf{p}) & \quad (3) \\ & = (2\pi)^{-3} \int V(\mathbf{p}, \mathbf{q}; E) \Psi(\mathbf{q}) d^3q, \end{aligned}$$

where  $E$  is the total energy of the system,  $\Psi(\mathbf{p})$  is the wave function, and  $V(\mathbf{p}, \mathbf{q}; E)$  is the quasipotential.

Using the expansion

$$\begin{aligned} \varepsilon_{ip} = \sqrt{\mathbf{p}^2 + m_i^2} & \approx m_i \left( 1 + \frac{\mathbf{p}^2}{2m_i^2} - \frac{\mathbf{p}^4}{8m_i^4} + \dots \right), \\ & \quad i = 1, 2, \end{aligned}$$

we obtain

$$\varepsilon_{1p} + \varepsilon_{2p} \cong m_1 + m_2 + \frac{\mathbf{p}^2}{2\mu} - \frac{\mathbf{p}^4}{8\mu^3} + \frac{3\mathbf{p}^4}{8\mu m_1 m_2}, \quad (4)$$

where  $\mu = m_1 m_2 / (m_1 + m_2)$  is the reduced mass.

Equation (3) takes the form

$$\begin{aligned} \left( W - \frac{\mathbf{p}^2}{2\mu} \right) \Psi(\mathbf{p}) & = (2\pi)^{-3} \int (v_C(\mathbf{p}, \mathbf{q}) \\ & + \Delta V(\mathbf{p}, \mathbf{q}; E) + V_{\text{kin}}(\mathbf{p}, \mathbf{q}; E)) \Psi(\mathbf{q}) d^3q, \end{aligned} \quad (5)$$

where

$$W = E - m_1 - m_2$$

<sup>1)</sup>Scientific Council for the Interdisciplinary Problem Cybernetics, Russian Academy of Sciences, ul. Vavilova 40, Moscow, 117976 Russia.

\* e-mail: theorphys@sgu.ru

is the binding energy of the system,

$$V_{\text{kin}} = - \left( \frac{\mathbf{p}^4}{8\mu^3} - \frac{3\mathbf{p}^4}{8\mu m_1 m_2} \right) (2\pi)^3 \delta(\mathbf{p} - \mathbf{q}) \quad (6)$$

is a correction to the kinetic energy, and

$$\Delta V = V - v_C, \quad (7)$$

$$v_C(\mathbf{p}, \mathbf{q}) = - \frac{e^2}{(\mathbf{p} - \mathbf{q})^2}$$

is the Coulomb potential. In order to study the fine structure of energy levels, we set

$$\Delta V = V_B,$$

where  $V_B$  is the Breit kernel, and write

$$\left( \mathbf{p}^2 + \frac{\alpha^2 \mu^2}{n^2} \right) \Psi(\mathbf{p}) = - \frac{\mu}{4\pi^3} \int (v_C(\mathbf{p}, \mathbf{q}) + V_B(\mathbf{p}, \mathbf{q}; E) + V_{\text{kin}}(\mathbf{p}, \mathbf{q}; E)) \Psi(\mathbf{q}) d^3 q, \quad (8)$$

where  $\alpha$  is the fine-structure constant and  $n$  is the principal quantum number.

In the lowest approximation and in the Coulomb gauge, the quasipotential has the form

$$V = (T_2)_+ = (K_C)_+ + (K_T)_+ \quad (9)$$

$$= v_C + (K_C)_+ - v_C + (K_T)_+$$

and corresponds to the one-photon-exchange diagram. Here, the operation  $(\dots)_+ = u_1^* u_2^* \gamma_{10} \gamma_{20} (\dots) u_1 u_2$  means the projection onto the positive-energy states

$$u_i(\mathbf{p}) = N_{m_i p} \begin{pmatrix} w \\ \frac{\boldsymbol{\sigma} \cdot \mathbf{p}}{\varepsilon_{ip} + m_i} w \end{pmatrix} \quad N_{m_i p} = \sqrt{\frac{\varepsilon_{ip} + m_i}{2\varepsilon_{ip}}}. \quad (10)$$

Here,  $u_i(\mathbf{p})$  is a Dirac bispinor that is written in the two-component form,  $w$  is an ordinary spinor that satisfies the normalization condition  $w^* w = 1$ , and  $\boldsymbol{\sigma}$  is the vector whose components are equal to the Pauli matrices. In (9), the kernels can be represented as  $K_C = v_C \gamma_{10} \gamma_{20}$  and

$$K_T = - \frac{4\pi\alpha}{k_0^2 - \mathbf{k}^2 + i0} \left( \gamma_1 \cdot \gamma_2 - \frac{(\gamma_1 \cdot \mathbf{k})(\gamma_2 \cdot \mathbf{k})}{\mathbf{k}^2} \right),$$

where  $\gamma_{i0}$  and  $\boldsymbol{\gamma}_i$  are the Dirac matrices,  $i = 1, 2$ . The indices ‘‘C’’ and ‘‘T’’ symbolize the exchange of a Coulomb photon and a transverse photon, respectively.

According to [14], the Breit interaction kernel can be derived by expanding the quasipotential (9) in powers of the quantities  $\mathbf{p}^2/m_i^2$  and is given by

$$V_B = V_\mu + V_{p\mu}, \quad (11)$$

$$V_\mu = (K_C)_+ - v_C = \frac{e^2}{8} \left( \frac{1}{m_1^2} + \frac{1}{m_2^2} \right), \quad (12)$$

$$V_{p\mu} = (K_T)_+ \quad (13)$$

$$= - \frac{e^2}{4m_1 m_2} \left[ \frac{4(\mathbf{p} \cdot \mathbf{q})}{(\mathbf{p} - \mathbf{q})^2} + 1 - \frac{(p^2 - q^2)^2}{(\mathbf{p} - \mathbf{q})^4} \right].$$

Solving Eq. (8) with the quasipotential

$$V_{\text{is}} = V_{\text{kin}} + V_\mu + V_{p\mu},$$

we arrive at the known expression for the fine structure of energy levels [11]; that is,

$$E_{nj} = (m_1 + m_2) - \frac{\mu(Z\alpha)^2}{2n^2}$$

$$- \frac{\mu(Z\alpha)^4}{2n^3} \left( \frac{1}{j + 1/2} - \frac{3}{4n} + \frac{\mu}{4n(m_1 + m_2)} \right),$$

where  $Z$  is the charge of an atom and  $j$  is an internal quantum number.

Thus, the quasipotential approach reproduces the result obtained for the fine structure of the energy levels in hydrogen-like atoms by exactly solving the Dirac equation with the Coulomb potential and by subsequently taking into account recoil effects.

In order to study the fine shift of energy levels, we must pursue further an analysis of the expression for the quasipotential describing the one-photon interaction of particles. We first consider the Coulomb part of the interaction, discarding terms that are responsible for a hyperfine shift. We have

$$\Delta \tilde{E}_C = \langle \varphi_C(\mathbf{p}) | (K_C)_+ - v_C | \varphi_C(\mathbf{q}) \rangle \quad (14)$$

$$= \langle \varphi_C(\mathbf{p}) | v_C N_p N_q \left( 1 + \frac{\mathbf{p} \cdot \mathbf{q}}{M_{1p} M_{1q}} + \frac{\mathbf{p} \cdot \mathbf{q}}{M_{2p} M_{2q}} \right. \right.$$

$$\left. \left. + \frac{(\mathbf{p} \cdot \mathbf{q})^2}{M_{1p} M_{1q} M_{2p} M_{2q}} \right) - v_C | \varphi_C(\mathbf{q}) \rangle,$$

where  $M_{ir} = \varepsilon_{ir} + m_i$ ;

$$N_r = N_{m_{1r}} N_{m_{2r}}$$

$$= \sqrt{\frac{\sqrt{\mathbf{r}^2 + m_1^2} + m_1}{2\sqrt{\mathbf{r}^2 + m_1^2}}} \sqrt{\frac{\sqrt{\mathbf{r}^2 + m_2^2} + m_2}{2\sqrt{\mathbf{r}^2 + m_2^2}}}$$

is the product of the normalization factors of the Dirac bispinors (1); and  $\mathbf{r} = \mathbf{p}, \mathbf{q}$ .

For the sake of simplicity, we represent the Coulomb wave function  $\varphi_C(\mathbf{p})$  corresponding to the  $1S$  state in the form

$$\varphi_C(\mathbf{p}) = \frac{8\pi\alpha\mu\varphi_C(0)}{(\mathbf{p}^2 + \alpha^2\mu^2)^2} (2\pi)^{-3/2},$$

$$|\varphi_C(0)|^2 = \frac{\alpha^3\mu^3}{\pi};$$

for  $nS$  states, the fine shift decreases by the factor  $n^3$ .

In order to investigate the first and the last term in (14) in more detail, we represent them in the form

$$\begin{aligned} & \langle \varphi_C(\mathbf{p}) | v_C N_p N_q - v_C | \varphi_C(\mathbf{q}) \rangle \quad (15) \\ &= \langle \varphi_C(\mathbf{p}) | v_C [1 - (1 - N_p)] [1 - (1 - N_q)] \\ & \quad - v_C | \varphi_C(\mathbf{q}) \rangle = \langle \varphi_C(\mathbf{p}) | - v_C (1 - N_p) \\ & \quad - v_C (1 - N_q) + v_C (1 - N_p)(1 - N_q) | \varphi_C(\mathbf{q}) \rangle. \end{aligned}$$

Estimating the last term that appears in (15) and which has the form

$$\langle \varphi_C(\mathbf{p}) | v_C (1 - N_p)(1 - N_q) | \varphi_C(\mathbf{q}) \rangle \quad (16)$$

leads to the standard integral [15]

$$\begin{aligned} I_{st} &= \int \frac{d^3 p}{\varepsilon_{1p} \varepsilon_{2p} (p^2 + \alpha^2 \mu^2)} \\ &\times \int \frac{d^3 q}{(q^2 + \alpha^2 \mu^2) (\mathbf{p} - \mathbf{q})^2} = \frac{4\pi^4}{m_1 m_2} \ln \alpha^{-1}. \end{aligned}$$

According to the most recent data, such corrections are canceled in the sum of relevant diagrams, so that this term can be excluded from the ensuing consideration. Further, we can use symmetry with respect to the variables  $\mathbf{p}$  and  $\mathbf{q}$  in expression (15); that is,

$$\begin{aligned} & \langle \varphi_C(\mathbf{p}) | v_C N_p N_q - v_C | \varphi_C(\mathbf{q}) \rangle \quad (17) \\ & \cong \langle \varphi_C(\mathbf{p}) | - 2v_C (1 - N_p) | \varphi_C(\mathbf{q}) \rangle. \end{aligned}$$

In order to calculate the second term in (17), we use a trivial algebraic transformation,

$$\begin{aligned} & v_C (1 - N_p) \quad (18) \\ &= v_C [1 - (1 - (1 - N_{m_1 p})) (1 - (1 - N_{m_2 p}))] \\ &= v_C [(1 - N_{m_1 p}) + (1 - N_{m_2 p}) \\ & \quad - (1 - N_{m_1 p})(1 - N_{m_2 p})]. \end{aligned}$$

The applicability of an expansion of the type

$$N_{m_i p} \approx 1 - \frac{p^2}{8m_i^2} + \frac{p^4}{128m_i^4} - \dots \quad (19)$$

is restricted because, at some stage, there arise divergences at high momentum values. In view of this, it is necessary to study the possibilities of transforming the integrands more thoroughly.

Using the change of variables  $p = p' m_2$  and  $q = q' m_2$ , we go over to dimensionless quantities in the expression being considered. We then have

$$\begin{aligned} & -2 \langle \varphi_C(\mathbf{p}) | v_C (1 - N_p) | \varphi_C(\mathbf{q}) \rangle \quad (20) \\ &= \frac{8}{\pi^4} \frac{\alpha^6 \mu^5}{m_2^4} \int \frac{d^3 q}{(q^2 + \gamma^2)^2} \int \frac{d^3 p}{(p^2 + \gamma^2)^2 (\mathbf{p} - \mathbf{q})^2} \\ &\times [(1 - N_{1p}) + (1 - N_{\beta p}) - (1 - N_{1p})(1 - N_{\beta p})] \\ &= \frac{32}{\pi} \frac{\alpha^5 \mu^3}{m_1 m_2} \frac{\beta^2}{1 + \beta} \int_0^\infty \frac{dp p^2}{(p^2 + \gamma^2)^3} \end{aligned}$$

$$\times [(1 - N_{1p}) + (1 - N_{\beta p}) - (1 - N_{1p})(1 - N_{\beta p})],$$

where  $\gamma = \alpha\beta/(1 + \beta)$ ,

$$N_{\beta p} = \sqrt{\frac{\sqrt{p^2 + \beta^2} + \beta}{2\sqrt{p^2 + \beta^2}}}, \quad N_{1p} = \sqrt{\frac{\sqrt{p^2 + 1} + 1}{2\sqrt{p^2 + 1}}}.$$

In expression (20), the primes on the variables  $p'$  and  $q'$  are omitted.

Upon transforming the integrand with the aid of the identity

$$\begin{aligned} 1 - N_{1p} &= \frac{p^2}{4\sqrt{p^2 + 1}(\sqrt{p^2 + 1} + 1)} \quad (21) \\ &+ \frac{p^4}{32(p^2 + 1)(\sqrt{p^2 + 1} + 1)^2} \\ &+ \frac{p^6(3 + N_{1p})}{64(p^2 + 1)^{3/2}(\sqrt{p^2 + 1} + 1)^3(1 + N_{1p})^3}, \end{aligned}$$

we readily arrive at the following conclusions. The first two terms in (20) are of the leading order  $\alpha^4$  and do not make contributions to the fine shift that involve  $\ln \beta^{-1}$ .

Calculating the correction  $\Delta \tilde{E}_C$  by expression (14) to the fourth-order terms in the fine-structure constant  $\alpha$  inclusive and using an expansion of the type in (19), we arrive at

$$\begin{aligned} \Delta \tilde{E}_C(\alpha^4) &= \langle \varphi_C(\mathbf{p}) | (K_C)_+ - v_C | \varphi_C(\mathbf{q}) \rangle \\ &= \langle \varphi_C(\mathbf{p}) | \frac{e^2}{8} \left( \frac{1}{m_1^2} + \frac{1}{m_2^2} \right) | \varphi_C(\mathbf{q}) \rangle \\ &= \frac{\alpha^4 \mu^3}{2} \left( \frac{1}{m_1^2} + \frac{1}{m_2^2} \right), \end{aligned}$$

which corresponds to the result obtained in [14]. We only note that, if use is made of the exact expressions for these terms, there arise additional corrections involving integral degrees of the parameters  $\alpha$  and  $\beta$ .

We now derive the logarithmic corrections in the particle-mass ratio ( $\ln(m_2/m_1)$ ) to the fine structure of the energy levels:

$$\begin{aligned} \Delta \tilde{E}_C^{\ln} &= \langle \varphi_C(\mathbf{p}) | 2v_C (1 - N_{m_1 p})(1 - N_{m_2 p}) | \varphi_C(\mathbf{q}) \rangle \quad (22) \\ &= -\frac{32}{\pi} \frac{\alpha^5 \mu^3}{m_1 m_2} \frac{\beta^2}{1 + \beta} \\ &\times \int_0^\infty \frac{dp p^2}{(p^2 + \gamma^2)^3} (1 - N_{\beta p})(1 - N_{1p}). \end{aligned}$$

Instead of the quantity  $1 - N_{1p}$ , we substitute its representation in the form (21); that is,

$$\begin{aligned} \Delta \tilde{E}_C^{\ln} = & -\frac{32}{\pi} \frac{\alpha^5 \mu^3}{m_1 m_2} \frac{\beta^2}{1 + \beta} \int_0^\infty \frac{dp p^2}{(p^2 + \gamma^2)^3} (1 - N_{\beta p}) \\ & \times \left\{ \frac{p^2}{4\sqrt{p^2 + 1}(\sqrt{p^2 + 1} + 1)} \right. \\ & + \frac{p^4}{32(p^2 + 1)(\sqrt{p^2 + 1} + 1)^2} \\ & \left. + \frac{p^6(3 + N_{1p})}{64(p^2 + 1)^{3/2}(\sqrt{p^2 + 1} + 1)^3(1 + N_{1p})^3} \right\} \\ & = I_1 + I_2 + I_3. \end{aligned} \tag{23}$$

Since the leading contribution of the integral  $I_3$  is

$$\begin{aligned} I_3 \approx & \frac{\alpha^5 \mu^3}{m_1 m_2} \beta^2 \int_0^\infty \frac{dpp^8}{(p^2 + \gamma^2)^3(p^2 + 1)^3} \\ & \times \left( N_{\beta p} - \frac{1}{\sqrt{2}} \right) \sim \frac{\alpha^5 \mu^3}{m_1 m_2} \beta^3, \end{aligned} \tag{24}$$

there is no need for taking into account the last term in (23) in the calculations to terms of order  $\alpha^5[\mu^3/(m_1 m_2)]\beta^3 \ln \beta^{-1}$ .

To the above accuracy, the contribution from the second term to the integral appearing in the expression for  $\Delta \tilde{E}_C^{\ln}$  exists. With the aid of the estimate in (24), it can be represented as

$$\begin{aligned} I_2 = & -\frac{1}{4\pi} \frac{\alpha^5 \mu^3}{m_1 m_2} \frac{\beta^2}{1 + \beta} \int_0^\infty \frac{dp}{p^2 + 1} (1 - N_{\beta p}) \\ = & -\frac{1}{4\pi} \frac{\alpha^5 \mu^3}{m_1 m_2} \frac{\beta^3}{1 + \beta} \int_0^\infty \frac{dp}{p^2 + \beta^2} \\ & \times \left( 1 - \sqrt{\frac{\sqrt{p^2 + 1} + p}{2\sqrt{p^2 + 1}}} \right). \end{aligned}$$

Using the expansion of the radical in  $p/\sqrt{p^2 + 1} < 1$  in calculating  $I_2$ , we find that the leading logarithmic contribution in the particle-mass ratio is

$$I_2(\ln \beta^{-1}) = \frac{1}{8\sqrt{2}\pi} \frac{\alpha^5 \mu^3}{m_1 m_2} \frac{\beta^3}{1 + \beta} \ln \beta^{-1}.$$

The calculation of the logarithmic contribution from the first term in (23) reduces to the calculation of the quantity

$$I_1 = -\frac{8}{\pi} \frac{\alpha^5 \mu^3}{m_1 m_2} \frac{\beta^2}{1 + \beta}$$

$$\begin{aligned} & \times \int_0^\infty \frac{dpp^4}{(p^2 + \gamma^2)^3 \sqrt{p^2 + 1}(\sqrt{p^2 + 1} + 1)} (1 - N_{\beta p}) \\ & \sim \frac{3}{\pi} \frac{\alpha^5 \mu^3}{m_1 m_2} \frac{\beta^2}{1 + \beta} \int_0^\infty \frac{dp}{p^2 + 1} (1 - N_{\beta p}), \end{aligned}$$

whence we obtain

$$I_1(\ln \beta^{-1}) = -\frac{3}{2\sqrt{2}\pi} \frac{\alpha^5 \mu^3}{m_1 m_2} \frac{\beta^3}{1 + \beta} \ln \beta^{-1}.$$

Thus, a new logarithmic contribution in the particle-mass ratio from the exchange of a Coulomb photon is given by

$$\Delta \tilde{E}_C^{\ln} = -\frac{11}{8\sqrt{2}\pi} \frac{\alpha^5 \mu^3}{m_1 m_2} \frac{\beta^3}{1 + \beta} \ln \beta^{-1}. \tag{25}$$

In clarifying the question of whether there are other logarithmic contributions in the parameter  $\beta$ , we note that the expansion

$$\sqrt{1 + x} = 1 + \frac{x}{2} - \frac{x^2}{8} + \dots \tag{26}$$

is valid in the closed interval  $0 \leq x \leq 1$ .

It follows that, in the integration interval  $0 \leq p \leq 1$ , the factor  $N_{1p}$  can be expanded in a series in powers of  $p^2$ ; that is,

$$\begin{aligned} N_{1p} = & \sqrt{1 - \frac{p^2}{2\sqrt{p^2 + 1}(\sqrt{p^2 + 1} + 1)}} \\ = & 1 - \frac{p^2}{4\sqrt{p^2 + 1}(\sqrt{p^2 + 1} + 1)} \\ & - \frac{p^4}{32(p^2 + 1)(\sqrt{p^2 + 1} + 1)^2} - \dots \end{aligned}$$

In this interval, we also have

$$\begin{aligned} N_{\beta p} = & \sqrt{\frac{\sqrt{p^2 + \beta^2} + \beta}{2\sqrt{p^2 + \beta^2}}} \cong \frac{1}{\sqrt{2}} \left( 1 + \frac{\beta}{2\sqrt{p^2 + \beta^2}} \right. \\ & \left. - \frac{\beta^2}{8(p^2 + \beta^2)} + \frac{\beta^3}{16(p^2 + \beta^2)^{3/2}} - \dots \right). \end{aligned}$$

We note that, within the integration interval  $1 \leq p < \infty$ , the integral in (22) does not involve logarithmic contributions in the particle-mass ratio. It was mentioned above that, in the interval  $0 \leq p \leq 1$ , there must arise integrals of the type

$$i_n = \int_0^1 \frac{dpp^{2n} \beta^{2n+1}}{(\sqrt{p^2 + \beta^2})^{2n+1}}.$$

Considering that, at all integral values of  $n$ , with the exception of  $n = 1$ , the integrals

$$\int_0^1 \frac{dp}{(\sqrt{p^2 + \beta^2})^{2n+1}}$$

make contributions in the form of integral powers of  $\beta$ , we obtain

$$i_n = \beta^{2n+1} \ln \beta^{-1};$$

that is, the integral  $I_1$  involves contributions proportional to  $\beta \ln \beta^{-1}$ ,  $\beta^3 \ln \beta^{-1}$ ,  $\beta^5 \ln \beta^{-1}$ , etc.

In order to analyze the distinction between the conditions for the emergence of contributions involving the quantities  $\ln \alpha^{-1}$  and  $\ln \beta^{-1}$ , we consider the integral

$$J = \int \frac{d^3p}{\varepsilon_{1p}\varepsilon_{2p}(p^2 + \alpha^2\mu^2)} \times \int \frac{d^3q}{(q^2 + \alpha^2\mu^2)^2(\mathbf{p} - \mathbf{q})^2} \times (m_2(q^2 + \alpha^2\mu^2) + \alpha\mu(\mathbf{p} - \mathbf{q})^2).$$

Upon performing integration with respect to  $\mathbf{q}$ , going over to a dimensionless variable of integration by means of the substitution  $p = p'm_2$ , and breaking down the interval of integration into the segments  $0 \leq p \leq \beta$ ,  $\beta \leq p \leq 1$ , and  $1 \leq p \leq \infty$ , we obtain

$$J = \frac{4\pi^3}{m_2} \left\{ \int_0^\beta \frac{dpp^2}{\sqrt{p^2 + \beta^2}\sqrt{p^2 + 1}(p^2 + \gamma^2)} \times \left[ \frac{2}{p} \arctan \frac{p}{\gamma} + 1 \right] + \int_\beta^1 \frac{dpp^2}{\sqrt{p^2 + \beta^2}\sqrt{p^2 + 1}(p^2 + \gamma^2)} \left[ \frac{2}{p} \arctan \frac{p}{\gamma} + 1 \right] + \int_1^\infty \frac{dpp^2}{\sqrt{p^2 + \beta^2}\sqrt{p^2 + 1}(p^2 + \gamma^2)} \left[ \frac{2}{p} \arctan \frac{p}{\gamma} + 1 \right] \right\}. \quad (27)$$

Upon expanding the integrand in powers of  $1/p$ , one can see that the last term in (27) involves no logarithmic contributions in the parameters  $\alpha$  and  $\beta$ .

Employing the expansion in (26) for the first term in (27) and retaining lowest order terms in  $\beta$  and  $\alpha$ , we obtain

$$J_1 = \frac{4\pi^3}{m_2} \int_0^\beta \frac{dpp^2}{\sqrt{p^2 + \beta^2}\sqrt{p^2 + 1}(p^2 + \gamma^2)}$$

$$\times \left[ \frac{2}{p} \arctan \frac{p}{\gamma} + 1 \right] \sim \frac{8\pi^3}{m_2\beta} \int_0^1 \frac{dpp}{p^2 + \delta^2} \arctan \frac{p}{\delta} \sim \frac{4\pi^4}{m_1} \ln \alpha^{-1},$$

where  $\delta = \alpha/(1 + \beta)$ .

By consistently expanding the integrand, we find for the second term in (27) that

$$J_2 = \frac{4\pi^3}{m_2} \int_\beta^1 \frac{dpp^2}{\sqrt{p^2 + \beta^2}\sqrt{p^2 + 1}(p^2 + \gamma^2)} \times \left[ \frac{2}{p} \arctan \frac{p}{\gamma} + 1 \right] \sim \frac{4\pi^3}{m_2} \int_\beta^1 dp \left( 1 - \frac{\gamma^2}{p^2} \right) \times \left( \frac{1}{p} - \frac{\beta^2}{2p^3} \right) \left( 1 - \frac{p^2}{2} \right) \left[ \frac{2}{p} \arctan \frac{p}{\gamma} + 1 \right] \sim \frac{4\pi^3}{m_2} \int_\beta^1 \frac{dp}{p} \sim \frac{4\pi^3}{m_2} \ln \beta^{-1}.$$

Thus, contributions involving  $\ln \alpha^{-1}$  arise within the integration interval  $0 \leq p \leq m_1$ , while the contributions involving  $\ln \beta^{-1}$  arise within the integration interval  $m_1 \leq p \leq m_2$ .

Let us consider cases where the cancellation of the correction in (25), which was obtained in the present study, is the most probable. It was indicated in [12] that the kernel  $J_C$  corresponds to the interaction of the particles of a hydrogen-like atom via the exchange of two Coulomb photons. The contribution to the shift of energy levels in a hydrogen-like atom due to this interaction can be expressed in terms of an integral of the type

$$\Delta E_C = \frac{\alpha^2 |\varphi(0)|^2}{2\pi} \int \frac{d^3k}{k^4 \varepsilon_{1k} \varepsilon_{2k}} \times \left[ \frac{(\varepsilon_{1k} + m_1)(\varepsilon_{2k} - m_2)}{\varepsilon_{1k} - (\varepsilon_{2k} + m_2 + m_1)} + \frac{(\varepsilon_{1k} - m_1)(\varepsilon_{2k} + m_2)}{\varepsilon_{2k} - (\varepsilon_{1k} + m_2 + m_1)} - \frac{2(\varepsilon_{1k} - m_1)(\varepsilon_{2k} - m_2)}{\varepsilon_{1k} + \varepsilon_{2k} + m_2 + m_1} \right], \quad (28)$$

where

$$|\varphi(0)|^2 = \frac{Z^3 \alpha^3 \mu^3}{\pi n^3}.$$

The statement that this integral can be exactly calculated means that the integrand in (28) must not

involve the radical expressions  $\sqrt{k^2 + m_1^2}\sqrt{k^2 + m_2^2}$ . It can easily be shown that the integral

$$\int_0^\infty \frac{dk}{\sqrt{k^2 + m_1^2}\sqrt{k^2 + m_2^2}} \quad (29)$$

reduces to a complete elliptic integral of the first kind, which cannot be calculated in terms of elementary functions.

Let us analyze this statement in more detail in view of its importance: the absence of integrals belonging to the type in (29) means that the Coulomb kernel  $J_C$  corresponding to the exchange of two Coulomb photons does not make logarithmic contributions in the particle-mass ratio  $[\ln(m_2/m_1)]$  to the shift of energy levels. The radical expressions  $\sqrt{k^2 + m_1^2}\sqrt{k^2 + m_2^2}$  appear in each term of the integrand in (28); that is,

$$\begin{aligned} & \frac{1}{\varepsilon_{1k}\varepsilon_{2k}} \frac{(\varepsilon_{1k} + m_1)(\varepsilon_{2k} - m_2)}{\varepsilon_{1k} - (\varepsilon_{2k} + m_2 + m_1)} \\ \rightarrow & \frac{\mu}{2\varepsilon_{1k}\varepsilon_{2k}} - \frac{2m_1^2}{(m_1 + m_2)\varepsilon_{1k}(\varepsilon_{2k} + m_2)} \\ & + \frac{m_1 - m_2}{\varepsilon_{1k}\varepsilon_{2k}} - \frac{k^2}{2(m_1 + m_2)\varepsilon_{1k}\varepsilon_{2k}}, \\ & \frac{1}{\varepsilon_{1k}\varepsilon_{2k}} \frac{(\varepsilon_{1k} - m_1)(\varepsilon_{2k} + m_2)}{\varepsilon_{2k} - (\varepsilon_{1k} + m_2 + m_1)} \\ \rightarrow & \frac{\mu}{2\varepsilon_{1k}\varepsilon_{2k}} - \frac{2m_2^2}{(m_1 + m_2)\varepsilon_{2k}(\varepsilon_{1k} + m_1)} \\ & + \frac{m_2 - m_1}{\varepsilon_{1k}\varepsilon_{2k}} - \frac{k^2}{2(m_1 + m_2)\varepsilon_{1k}\varepsilon_{2k}}, \\ & - \frac{2}{\varepsilon_{1k}\varepsilon_{2k}} \frac{(\varepsilon_{1k} - m_1)(\varepsilon_{2k} - m_2)}{\varepsilon_{1k} + \varepsilon_{2k} + m_2 + m_1} \\ \rightarrow & - \frac{\mu}{\varepsilon_{1k}\varepsilon_{2k}} + \frac{2m_1^2}{(m_1 + m_2)\varepsilon_{1k}(\varepsilon_{2k} + m_2)} \\ & + \frac{2m_2^2}{(m_1 + m_2)\varepsilon_{2k}(\varepsilon_{1k} + m_1)} + \frac{k^2}{(m_1 + m_2)\varepsilon_{1k}\varepsilon_{2k}}. \end{aligned}$$

It follows that the total integrand in (28) does not involve the above product of radical expressions. Thus, we have proven that, in considering the total contribution of Coulomb interactions, the correction

$$\frac{\alpha^5 \mu^3}{m_1 m_2} \frac{\beta^3}{1 + \beta} \ln \beta^{-1}$$

[see Eq. (25)] remains valid to terms of order  $\alpha^5$ .

Another possibility of a probable cancellation of this correction is associated with an analysis of the exchange of one transverse photon. The corresponding shift can be represented in the form

$$\Delta E_T = \frac{1}{(2\pi)^3} \alpha \pi \quad (30)$$

$$\begin{aligned} & \times \int d^3 p d^3 q \varphi_C^*(\mathbf{p}) N_p \varphi_C(\mathbf{q}) N_q \frac{1}{(\mathbf{p} - \mathbf{q})^2} \\ & \times \left[ -(\mathbf{p} + \mathbf{q})^2 \left( \frac{1}{M_{1p}} + \frac{1}{M_{1q}} \right) \left( \frac{1}{M_{2p}} + \frac{1}{M_{2q}} \right) \right. \\ & \quad + \frac{1}{(\mathbf{p} - \mathbf{q})^2} \frac{1}{(\varepsilon_{1p} + \varepsilon_{1q})(\varepsilon_{2p} + \varepsilon_{2q})} \\ & \quad \times \left\{ 4 + 2(p^2 + q^2) \left( \frac{1}{M_{1p}M_{1q}} + \frac{1}{M_{2p}M_{2q}} \right) \right. \\ & \quad \left. \left. + \frac{(p^2 + q^2)^2}{M_{1p}M_{2p}M_{1q}M_{2q}} \right\} \right]. \end{aligned}$$

Setting  $\varepsilon_{ip} \approx m_i$ , we find that the leading contribution of the fourth order in the fine-structure constant [14] generates the quasipotential

$$V_{p\mu} = -\frac{e^2}{4m_1 m_2} \left[ \frac{4(\mathbf{p} \cdot \mathbf{q})}{(\mathbf{p} - \mathbf{q})^2} + 1 - \frac{(p^2 - q^2)^2}{(\mathbf{p} - \mathbf{q})^4} \right]. \quad (31)$$

Thus, it becomes possible to eliminate terms from expression (30) that lead to a correction proportional to  $\alpha^4 \mu^3 / (m_1 m_2)$ .

Moreover, there is the property that, if functions  $\varphi$  and  $\psi$  are bounded and integrable on a set  $\Omega$  and if  $\varphi(x) \leq \psi(x)$  ( $x \in \Omega$ ), the integrals of these functions over this set satisfy the inequality

$$\int_\Omega \varphi(x) dx \leq \int_\Omega \psi(x) dx. \quad (32)$$

With the aid of (32), one can isolate terms in (30) that are explicitly proportional to  $\alpha^6 \mu^3 / (m_1 m_2)$ . As a result, the shift in (30) takes the form

$$\begin{aligned} \Delta \tilde{E}_T = & \frac{1}{(2\pi)^3} \alpha \pi \int d^3 p d^3 q \varphi_C^*(\mathbf{p}) N_p \varphi_C(\mathbf{q}) N_q \quad (33) \\ & \times \left\{ -\frac{1}{m_1 m_2} \frac{4(\mathbf{p} \cdot \mathbf{q})}{(\mathbf{p} - \mathbf{q})^2} - \frac{3}{2m_1 m_2} \frac{p^2}{M_{1p}^2} \right. \\ & + \frac{1}{m_1 m_2} \frac{p^2}{M_{2p}^2} + \frac{3}{m_1} \frac{p^2}{M_{1p}^2 M_{2p}} - \frac{2}{m_2} \frac{p^2}{M_{1p} M_{2p}^2} \\ & \left. + \frac{1}{2m_1 m_2} \frac{p^4}{M_{1p}^2 M_{2p}^2} \right\}. \end{aligned}$$

Terms that do not involve angular variables mutually cancel, and, to terms of order

$$\frac{\alpha^5 \mu^3}{m_1 m_2} \frac{\beta^3}{1 + \beta} \ln \beta^{-1},$$

we obtain

$$\Delta \tilde{E}_T = -\frac{4}{\pi^4} \frac{\alpha^6 \mu^5}{m_1 m_2} \int \frac{d^3 p N_p}{(p^2 + \alpha^2 \mu^2)^2} \quad (34)$$

$$\begin{aligned} & \times \int \frac{d^3q N_q}{(q^2 + \alpha^2 \mu^2)^2} \frac{(\mathbf{p} \cdot \mathbf{q})}{(\mathbf{p} - \mathbf{q})^2} = -\frac{2}{\pi^4} \frac{\alpha^6 \mu^5}{m_1 m_2} \\ & \times \int \frac{d^3p N_p}{(p^2 + \alpha^2 \mu^2)^2} \int \frac{d^3q N_q}{(q^2 + \alpha^2 \mu^2)^2} \\ & \times \left( \frac{2p^2}{(\mathbf{p} - \mathbf{q})^2} - 1 \right) \cong -\frac{2}{\pi^4} \frac{\alpha^6 \mu^5}{m_1 m_2} \\ & \times \left\{ \frac{2\pi^2}{\alpha\mu} \int \frac{d^3p p^2 N_p}{(p^2 + \alpha^2 \mu^2)^3} \right. \\ & \left. - \int \frac{d^3p N_p}{(p^2 + \alpha^2 \mu^2)^2} \int \frac{d^3q N_q}{(q^2 + \alpha^2 \mu^2)^2} \right\}. \end{aligned}$$

An analysis of the respective integral yields

$$\begin{aligned} & \int \frac{d^3q N_q}{(q^2 + \alpha^2 \mu^2)^2} \cong \frac{4\pi}{m_2} \left\{ \int_0^\beta \frac{dq q^2}{(q^2 + \gamma^2)^2} \right. \\ & \left. + \frac{1}{\sqrt{2}} \int_\beta^1 \frac{dq}{q^2} (1 + C_1 q^2 + C_2 q^4) \right. \\ & \left. \times \left( 1 + C_3 \frac{\beta}{q} + C_4 \frac{\beta^3}{q^3} \right) + \int_1^\infty \frac{dq N_{1q}}{q^2} \right\} \\ & \approx \frac{\pi^2}{\alpha\mu} + \frac{2\sqrt{2}\pi}{m_2} C_1 C_3 \beta \ln \beta^{-1}. \end{aligned} \quad (35)$$

Similarly, we can obtain

$$\int \frac{d^3p p^2 N_p}{(p^2 + \alpha^2 \mu^2)^3} \approx \frac{3\pi^2}{4\alpha\mu} + \frac{2\sqrt{2}\pi}{m_2} C_1 C_3 \beta \ln \beta^{-1}. \quad (36)$$

To the fifth order in the fine-structure constant, we then arrive at

$$\Delta \tilde{E}_T \approx -\frac{2}{\pi} \frac{\alpha^5 \mu^4}{m_1 m_2} \left( \frac{3\pi}{2\alpha\mu} + \frac{4\sqrt{2}}{m_2} C_1 C_3 \beta \ln \beta^{-1} \right. \\ \left. - \frac{\pi}{\alpha\mu} - \frac{4\sqrt{2}}{m_2} C_1 C_3 \beta \ln \beta^{-1} \right) \approx -\frac{\alpha^4 \mu^3}{m_1 m_2}. \quad (37)$$

Thus, expression (30) involves no logarithmic corrections in the particle-mass ratio that are of order  $\alpha^5$ .

Our calculations indicate that the expression

$$\Delta \tilde{E}_C^{\ln} \sim \frac{\alpha^5 \mu^3}{m_1 m_2} \frac{\beta^3}{1 + \beta} \ln \beta^{-1},$$

which was obtained in the present study for the shift of energy levels, is the final result.

As was mentioned above, the recoil-effect-induced contribution to the fine shift of  $S$  energy levels in a hydrogen-like atom was already analyzed at an early

stage of investigations into the problem of bound states of two particles [12, 16]. That analysis yielded

$$\begin{aligned} \Delta E = & \frac{(Z\alpha)^5 \mu^3}{\pi m_1 m_2} \frac{1}{n^3} \left\{ A + \frac{2}{3} \delta_{l0} \ln(Z\alpha)^{-1} \right. \\ & \left. - \frac{8}{3} \ln[k_0(n)] + 2 \frac{\beta^2}{1 - \beta^2} \delta_{l0} \ln \beta^{-1} \right\}, \end{aligned} \quad (38)$$

where

$$\begin{aligned} A = & -\frac{1}{9} \delta_{l0} + \frac{14}{3} \\ & \times \left\{ \left[ \ln \frac{2}{n} + \left( 1 + \frac{1}{2} + \dots + \frac{1}{n} \right) + 1 - \frac{1}{2n} \right] \delta_{l0} \right. \\ & \left. + \frac{1 - \delta_{l0}}{l(l+1)(2l+1)} \right\} + \frac{2}{1 - \beta^2} \ln(1 + \beta) \delta_{l0}, \end{aligned}$$

$\ln[k_0(n)]$  is the Bethe logarithm, and  $l$  is the orbital angular momentum.

Taking into account the new contribution  $\ln(m_2/m_1)$ , which was obtained in the present study, and the results presented in [17–20], we can recast expression (38) into the form

$$\begin{aligned} \Delta \tilde{E} = & \frac{(Z\alpha)^5 \mu^3}{\pi m_1 m_2} \frac{1}{n^3} \left\{ A + \frac{2}{3} \delta_{l0} \ln(Z\alpha)^{-1} \right. \\ & - \frac{8}{3} \ln[k_0(n)] + \beta \ln \beta^{-1} \left[ \beta C_\beta + \beta^2 C_{\beta^2} + \frac{\alpha}{\beta} C_{\alpha/\beta} \right. \\ & \left. \left. + \alpha C_\alpha + \alpha C_{\alpha\beta} \ln \beta^{-1} + \alpha\beta C_{\alpha\beta^2} \ln \beta^{-1} \right] \right\}, \end{aligned} \quad (39)$$

where

$$C_\beta = 2 - \frac{\sqrt{2}}{4} \approx 1.646, \quad (40)$$

$$C_{\beta^2} = -\frac{11}{8\sqrt{2}} \approx -0.972, \quad (41)$$

$$C_{\alpha/\beta} = -\frac{2\sqrt{2}}{\pi} \left[ \ln(1 + \sqrt{2}) - \sqrt{2} \right] \approx 0.480, \quad (42)$$

$$C_\alpha = \frac{1}{\pi} \left[ 1 + \frac{\sqrt{2}}{2} \right] \quad (43)$$

$$- \frac{3}{2} (1 + 2\sqrt{2}) \ln(1 + \sqrt{2}) + 6 \ln 2 \approx 0.256,$$

$$C_{\alpha\beta} = \frac{1}{\sqrt{2}\pi} \frac{2 + \sqrt{2}}{1 + \sqrt{2}} \approx 0.318, \quad (44)$$

$$C_{\alpha\beta^2} = -\frac{1}{8\sqrt{2}\pi} \approx -0.028. \quad (45)$$

The correction in (41) was calculated in the present study; the contribution in (42), which is written here with allowance for iterations, was obtained in [18]; the correction in (43) was calculated in [20]; the contribution in (44) was considered in [13, 20]; moreover, there have recently appeared new values of the corrections in (40) and (45).

Going over to numerical estimates, we have [21]

$$\beta_H = 0.0005446170232(12),$$

$$\beta_\mu = 0.00483633210(15).$$

Therefore, the numerical values found here for the logarithmic corrections in the particle-mass ratio for the hydrogen and muonium atoms at  $n = 1$  are

$$\Delta\tilde{E}_H - \Delta E_H \approx 11.69 \text{ kHz},$$

$$\Delta\tilde{E}_\mu - \Delta E_\mu \approx 73.74 \text{ kHz}.$$

#### ACKNOWLEDGMENTS

We are grateful to S.N. Bagaev, V.I. Savrin, and O.A. Khrustalev for attention to this study.

#### REFERENCES

1. Th. Udem, A. Huber, B. Gross, *et al.*, Phys. Rev. Lett. **79**, 2646 (1997).
2. M. Niering, R. Holzwarth, J. Reichert, *et al.*, Phys. Rev. Lett. **84**, 5496 (2000).
3. H. Grotch, Found. Phys. **24**, 249 (1994).
4. V. V. Dvoeglazov, Yu. N. Tyukhtyaev, and R. N. Faustov, Fiz. Élem. Chastits At. Yadra **25**, 144 (1994) [Phys. Part. Nucl. **25**, 58 (1994)].
5. M. I. Eides, in *Proceedings of the Paris Workshop on Quantum Infrared Physics, 1994*, Ed. by H. M. Fried and B. M. Mueller (World Sci., Singapore, 1995), p. 262.
6. T. Kinoshita, Rep. Prog. Phys. **59**, 3803 (1996).
7. J. Sapirstein, in *Atomic, Molecular, and Optical Physics Handbook*, Ed. by G. W. Drake (AIP Press, 1996), p. 327.
8. P. J. Mohr, in *Atomic, Molecular, and Optical Physics Handbook*, Ed. by G. W. Drake (AIP Press, 1996), p. 341.
9. K. Pachuki, D. Leibfried, M. Weitz, *et al.*, J. Phys. B **29**, 177 (1996).
10. T. Kinoshita, hep-ph/9808351.
11. M. I. Eides, H. Grotch, and V. A. Shelyuto, hep-ph/0002158.
12. T. Fulton and P. C. Martin, Phys. Rev. **95**, 811 (1954).
13. N. A. Boikova, Yu. N. Tyukhtyaev, and R. N. Faustov, Yad. Fiz. **61**, 866 (1998) [Phys. At. Nucl. **61**, 781 (1998)].
14. R. N. Faustov, Fiz. Élem. Chastits At. Yadra **3**, 238 (1972) [Sov. J. Part. Nucl. **3**(1), 119 (1972)].
15. N. A. Boikova, Yu. N. Tyukhtyaev, and R. N. Faustov, in *Proceedings of the IV Int. Seminar on Problems in High Energy Physics and Quantum Field Theory, Protvino, Russia, 1983*, Ed. by M. L. Folomeshkina (Inst. Fiz. Vys. Energiï, Protvino, 1983), Vol. 1, p. 116.
16. E. E. Salpeter and H. A. Bethe, Phys. Rev. **84**, 1232 (1951).
17. N. A. Boikova, N. E. Nyun'ko, Yu. N. Tyukhtyaev, and R. N. Faustov, Teor. Mat. Fiz. **126**, 475 (2001).
18. N. A. Boikova, Yu. N. Tyukhtyaev, and R. N. Faustov, Yad. Fiz. **64**, 986 (2001) [Phys. At. Nucl. **64**, 917 (2001)].
19. N. A. Boikova, S. V. Kleshchevskaya, Yu. N. Tyukhtyaev, and R. N. Faustov, Yad. Fiz. **64**, 1437 (2001) [Phys. At. Nucl. **64**, 1359 (2001)].
20. N. A. Boikova, S. V. Kleshchevskaya, and Yu. N. Tyukhtyaev, *Problems in Optical Physics: Proc. 5th Int. School in Optics, Laser Physics, and Biophysics for Young Scientists, Saratov, Russia, 2001*, Ed. by L. M. Babkov (GosUNTs Kolledzh, Saratov, 2002), p. 98.
21. P. J. Mohr and B. N. Taylor, Rev. Mod. Phys. **72**, 351 (2000).

*Translated by A. Isaakyan*

## Adiabatic Potentials and Spectra of Heavy Hybrid Mesons\*

Yu. S. Kalashnikova\*\* and D. S. Kuzmenko\*\*\*

*Institute of Theoretical and Experimental Physics,  
Bol'shaya Cheremushkinskaya ul. 25, Moscow, 117259 Russia*

Received March 20, 2003

**Abstract**—Using the QCD string approach, adiabatic potentials and spectra of  $b\bar{b}$  hybrid mesons are calculated. The results are compared with lattice studies. © 2004 MAIK “Nauka/Interperiodica”.

1. An assumption about the existence of hybrid mesons consisting of a valence quark and antiquark and valence gluon was made for the first time by Okun and Vainshtein [1] just after QCD appeared. The last decade was a time of intensive studies of hybrid mesons both in experimental and in theoretical frameworks.

In this paper, we study the system of a static quark and antiquark and a dynamical gluon joined to the former by an infinitely thin string of a background gluon field in the analytic QCD string approach [2, 3] based on background perturbation theory [4]. In other words, we study the spectrum of vibrations of the confining string or the spectrum of adiabatic potentials. We will pay our attention to small and intermediate quark–antiquark separations, which are directly related to the spectrum of heavy hybrid mesons. Using adiabatic potentials, we will calculate the spectra of  $b\bar{b}$  hybrid mesons.

2. In the background perturbation theory framework, we start from the propagator of the valence gluon in the background field  $B$  [4],

$$G_{\mu\nu} = (D^2(B)\delta_{\mu\nu} + 2igF_{\mu\nu}(B))^{-1}, \quad (1)$$

where  $D(B)$  is the covariant derivative depending on the field  $B$ , and  $F_{\mu\nu}(B)$  is the background field strength tensor, which is related to spin effects and will be considered below. A Green's function of the hybrid meson with the static quark and antiquark in the Fock–Feynman–Schwinger representation reduces to the form (see [3] and references therein)

$$G_h(\bar{X}, X) = \int_0^\infty ds \int (\mathcal{D}z_g)_{x_g y_g} \exp(-K) \langle \mathcal{W}_h \rangle_B, \quad (2)$$

where  $\mathcal{W}_h$  is the hybrid Wilson loop, consisting of the trajectories  $\Gamma_Q$ ,  $\Gamma_{\bar{Q}}$ , and  $\Gamma_g$  of a valence quark, antiquark, and gluon (see Fig. 1), and  $K$  is the kinetic energy of the gluon.

In what follows, we will use the Wilson loop area law, which is confirmed by lattice QCD (see, e.g., [5]). The area law for hybrid mesons takes the form

$$\langle \mathcal{W}_h \rangle_B = \frac{N_c^2 - 1}{2} \exp(-\sigma(S_1 + S_2)), \quad (3)$$

where  $S_1(S_2)$  is an area of the minimal surface bounded by the valence quark (antiquark) and gluon trajectories, and  $\sigma$  is the string tension. We parametrize minimal surfaces introducing parameters  $0 \leq \tau \leq T$  and  $0 \leq \beta_{1,2} \leq 1$ . It is also convenient to introduce einbein fields  $\mu(\tau)$ ,  $\nu_{1,2}(\tau, \beta_{1,2})$  and write the hybrid Green's function in the form

$$G_h(\bar{X}, X) = \int (\mathcal{D}^3 z_g)_{x_g y_g} \mathcal{D}\mu \mathcal{D}\nu_1 \mathcal{D}\nu_2 \quad (4)$$

$$\times \exp\left(-\int_0^T d\tau L\right),$$

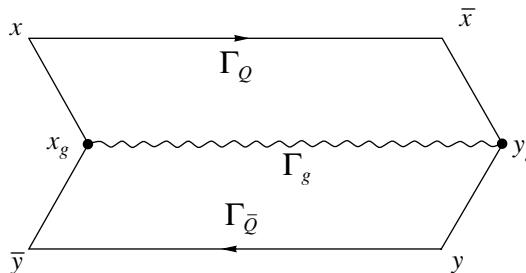


Fig. 1. A Wilson loop for hybrid meson.

\* This article was submitted by the authors in English.

\*\* e-mail: yulia@vxitep.itep.ru

\*\*\* e-mail: kuzmenko@heron.itep.ru

where  $L$  is the Lagrangian, which defines the following string Hamiltonian [3]:

$$H = \mathbf{p} \cdot \dot{\mathbf{r}} - L = H_0 + \frac{\mu}{2} + \int_0^1 d\beta_1 \frac{\sigma^2 r_1^2}{2\nu_1} \quad (5)$$

$$+ \int_0^1 d\beta_2 \frac{\sigma^2 r_2^2}{2\nu_2} + \int_0^1 d\beta_1 \frac{\nu_1}{2} + \int_0^1 d\beta_2 \frac{\nu_2}{2}.$$

Here,

$$H_0 = \frac{p^2}{2(\mu + J_1 + J_2)} + \frac{1}{2\Delta(\mu + J_1 + J_2)} \quad (6)$$

$$\times \left\{ \frac{(\mathbf{p} \cdot \mathbf{r}_1)^2}{r_1^2} J_1(\mu + J_1) + \frac{(\mathbf{p} \cdot \mathbf{r}_2)^2}{r_2^2} J_2(\mu + J_2) \right.$$

$$\left. + \frac{2J_1 J_2}{r_1^2 r_2^2} (\mathbf{r}_1 \cdot \mathbf{r}_2)(\mathbf{p} \cdot \mathbf{r}_1)(\mathbf{p} \cdot \mathbf{r}_2) \right\},$$

$$\Delta = (\mu + J_1)(\mu + J_2) - J_1 J_2 \frac{(\mathbf{r}_1 \cdot \mathbf{r}_2)^2}{r_1^2 r_2^2},$$

$$J_i = \int_0^1 d\beta_i \beta_i^2 \nu_i(\beta_i), \quad i = 1, 2,$$

$\mathbf{r}$  and  $\mathbf{p}$  are the valence gluon coordinate and momentum,  $\mathbf{r}_{1,2} = \mathbf{r} \pm \mathbf{R}/2$ ,  $\pm \mathbf{R}/2$  are static quark and antiquark locations. Einbein fields are to be excluded from the Hamiltonian by the conditions

$$\frac{\partial H}{\partial \mu} = 0, \quad \frac{\delta H}{\delta \nu_i(\beta_i)} = 0. \quad (7)$$

One can show that einbein  $\mu$  plays the role of the gluon constituent mass,  $\nu_i(\beta)$  plays the role of the background field energy density along the string, and  $J_i$  is the string inertia.

**3.** We proceed now to calculations of the string Hamiltonian spectrum at small and intermediate quark–antiquark separations,  $R \lesssim 1$  fm. In this region, the string inertia  $J_i$  is much smaller than the gluon constituent mass,  $J_i \ll \mu$ . Neglecting  $J_i$  and calculating the extremum over  $\mu$  in the initial Hamiltonian, we arrive at the Hamiltonian of the potential model,

$$H = \sqrt{\mathbf{p}^2} + \sigma r_1 + \sigma r_2. \quad (8)$$

However, it is more convenient to calculate eigenvalues  $E(\mu)$  of the Hamiltonian keeping the einbein  $\mu$  and then minimize them with respect to the einbein, according to

$$\frac{\partial E(\mu)}{\partial \mu} = 0. \quad (9)$$

This procedure is commonly used in the QCD string approach and, for ordinary mesons, is justified with an accuracy better than 5% (see, e.g., [2]).

Besides the nonperturbative string part considered above, the hybrid Hamiltonian should contain the perturbative part  $V_c$ , which is dominated by one-gluon exchange,

$$V_c = -\frac{3\alpha_s}{2r_1} - \frac{3\alpha_s}{2r_2} + \frac{\alpha_s}{6R}. \quad (10)$$

Therefore, the Hamiltonian with the string inertia neglected takes the form

$$H = \frac{\mu}{2} + \frac{p^2}{2\mu} + \sigma r_1 + \sigma r_2 + V_c. \quad (11)$$

Despite its nonrelativistic appearance, this Hamiltonian is essentially relativistic due to condition (9).

The Hamiltonian of the string correction of the order of  $J/\mu$  derived from (5), (6) has a transparent form,

$$H^{\text{string}} = -\frac{\sigma}{6\mu^2} \left( \frac{1}{r_1} L_1^2 + \frac{1}{r_2} L_2^2 \right), \quad (12)$$

where  $\mathbf{L}_i = \mathbf{r}_i \times \mathbf{p}$ .

A spin interaction of heavy quarks with mass  $m$  in ordinary mesons has been expressed through the number of universal unknown potentials of order  $1/m^2$  using the Wilson loop in [6]. These potentials were calculated in the QCD string approach, using the method of field correlators (see [2] and references therein). Although no expansion in  $1/m$  is performed in the approach, the results have the same appearance with  $m$  replaced by the einbein  $\mu$  and are applicable to both light and heavy quarks.

A spin interaction of the valence gluon with the quark and antiquark in hybrid mesons is generated by the strength tensor term in propagator (1), which can be rewritten as  $F_{ik} = i(\mathbf{S} \cdot \mathbf{B})_{ik}$ , where the spin operator  $\mathbf{S}$  acts on the gluon wave function  $\Psi$  according to  $(S_i \Psi)_j = -i\epsilon_{ijk} \Psi_k$ . Performing calculations similar to [2], we derive the following relations in the Eichten–Feinberg notation:

$$V_1^{(p)} = 0, \quad V_2^{(p)} = \epsilon^{(p)}, \quad \epsilon^{(p)} = -\frac{3\alpha_s}{2r_1} - \frac{3\alpha_s}{2r_2}, \quad (13)$$

and

$$V_1^{(np)} = -\epsilon^{(np)}, \quad V_2^{(np)} = 0, \quad (14)$$

$$\epsilon^{(np)} = \sigma r_1 + \sigma r_2.$$

**Table 1.** Quantum numbers of adiabatic levels of Fig. 2

(a)	$\Sigma_u^-, \Pi_u$
(b)	$\Sigma_g^+, \Pi_g$
(c)	$\Sigma_g^-, \Pi_g, \Delta_g$
(d)	$\Sigma_u^+, \Pi_u, \Delta_u$

**Table 2.** The masses of the lowest  $b\bar{b}$  exotic states in our approach

State	$l$	$l_{Q\bar{Q}}$	$M^{b\bar{b}g}$ , GeV
GE	1	0	10.83
QE	0	1	10.92

One can verify that Gromes relation  $\epsilon + V_1 - V_2 = 0$  is justified for both perturbative and nonperturbative potentials. The corresponding Hamiltonian consists of the following perturbative and nonperturbative parts [3]:

$$H^{LS(p)} = \frac{3\alpha_s}{4\mu^2} \left( \frac{\mathbf{L}_1 \cdot \mathbf{S}}{r_1^3} + \frac{\mathbf{L}_2 \cdot \mathbf{S}}{r_2^3} \right), \quad (15)$$

$$H^{LS(np)} = -\frac{\sigma}{2\mu^2} \left( \frac{\mathbf{L}_1 \cdot \mathbf{S}}{r_1} + \frac{\mathbf{L}_2 \cdot \mathbf{S}}{r_2} \right). \quad (16)$$

We calculate the energy levels of the initial Hamiltonian (11) variationally, using Gaussian wave functions of the gluon

$$\Psi_{j\lambda\Lambda}(\mathbf{r}) = \phi_l(r) \sum_{\mu_1\mu_2} C_{l\mu_1\mu_2}^{j\Lambda} Y_{l\mu_1} \left( \frac{\mathbf{r}}{r} \right) \chi_{1\mu_2}, \quad (17)$$

$$\phi_l(r) \sim \exp(-\beta^2 r^2/2).$$

Corrections (12)–(16) amount to a 70–150 MeV decrease in total energy, depending on the level.

The resulting adiabatic potentials are shown in Fig. 2 in comparison with lattice ones [7]. Quantum numbers of levels in diatomic molecule notation are listed at Table 1. Potentials are normalized to the ground  $Q\bar{Q}$  level shown in the bottom right corner of Fig. 2a. We can see the overall correspondence with the lattice. The curves tend to form three multiplets with different values of the gluon angular momentum, which is a good quantum number at short distances. When  $R$  goes to zero, the potentials increase rapidly due to the color-Coulomb repulsion of quark and antiquark, which are in a color octet state. Note that the wrong bend of the  $\Pi_g$  lattice level in Fig. 2b and the absence of a  $\Pi_g$  lattice level in Fig. 2c mean that these two  $\Pi_g$  levels are not properly resolved

on the lattice. The order of levels in our approach corresponds to the lattice one, with the exception of Fig. 2c. A difference of separations between levels of Fig. 2a in our and the lattice approaches is presumably related to the influence of the Coulomb gluon–quark and gluon–antiquark interaction on the gluon wave function. Variational calculations using Coulomb-modified wave functions are needed to verify this assumption.

The lowest level with quantum numbers  $\Sigma_g^-, \Pi_g$  is absent on the lattice and therefore is not shown in Fig. 2. Comparative analysis of adiabatic potentials in other approaches can be found in [3].

4. Let us calculate the spectra of masses of the heavy hybrid mesons in the Born–Oppenheimer approximation assuming that the motion of the valence quark and antiquark is slow compared to the motion of the valence gluon and using the adiabatic potentials. In this case, an essential region is the one near the minimum of the potential, where the adiabatic potential can be replaced by the oscillatory one. Therefore, the problem reduces to the calculation of the spectrum of a three-dimensional oscillator.

We tune the values of parameters  $\alpha_s = 0.225$ ,  $\sigma = 0.18 \text{ GeV}^2$ ,  $m_b = 4.56 \text{ GeV}$  to reproduce the experimental value of the ground state of the  $b\bar{b}$  meson,  $M_{\text{exp}}^{\Upsilon(1S)} = 9.4 \text{ GeV}$ , from the Cornell potential,

$$V^{b\bar{b}} = 2m_b - \frac{4}{3} \frac{\alpha_s}{R} + \sigma R. \quad (18)$$

Then, we calculate the masses of  $b\bar{b}$  hybrid mesons through the equation

$$M^{b\bar{b}g} = 2m_b + E^{\text{osc}}, \quad (19)$$

where  $E^{\text{osc}}$  is the energy of  $b$  quarks in the adiabatic potential, approximated in the vicinity of its minimum by the oscillatory one.

The lowest exotic hybrid states have quantum numbers  $J^{PC} = 1^{-+}$  and may be of two different kinds, a gluon-excited (GE) one, with the gluon angular momentum  $l = 1$  and quark–antiquark relative angular momentum  $l_{Q\bar{Q}} = 0$ , and quark-excited (QE) one, with  $l = 0$  and  $l_{Q\bar{Q}} = 1$ . Their masses are given in Table 2. One can calculate the energy of the gluon excitation using the mass of the GE state from the table:

$$\Delta M = M_{\text{GE}}^{b\bar{b}g} - M^{\Upsilon(1S)} = 1.43 \text{ GeV}. \quad (20)$$

One can see that  $\Delta M \ll m_b$ , so that the adiabatic approximation for  $b\bar{b}$  hybrid mesons is justified. The mass of the  $c$  quark is close to the energy of gluon excitation, so that the adiabatic approximation for  $c\bar{c}$  hybrid mesons is invalid.

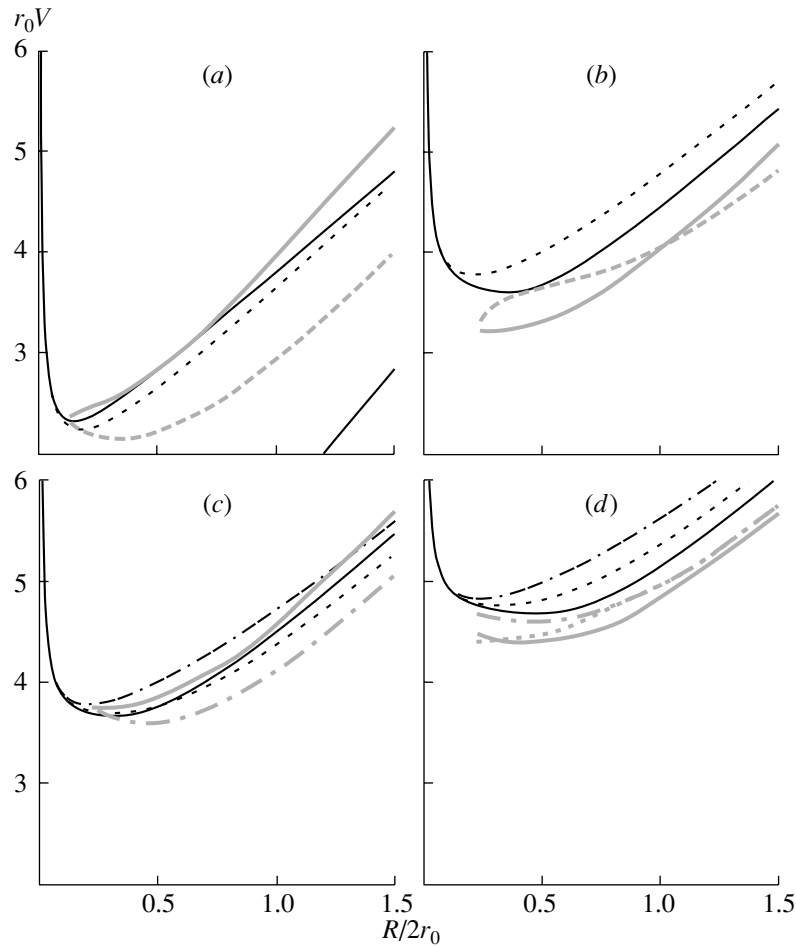


**Fig. 2.** Hybrid potentials with corrections included (black curves) compared to lattice ones (gray curves) in units  $1/r_0 = 400 \text{ MeV}$  ( $r_0 = 2.5 \text{ GeV}^{-1}$ ). On the horizontal axis,  $Q\bar{Q}$  distance  $R$  is presented in units  $2r_0 \approx 1 \text{ fm}$ . States (a)–(d) are given in Table 1. Solid, dashed, and dash-dotted curves correspond to  $\Lambda = 0, 1,$  and  $2$ . Solid line in the bottom right corner of Fig. 2a represents the Coulomb + linear potential with  $\alpha_s = 0.4$  and  $\sigma = 0.21 \text{ GeV}^2$ .

The mass of the lowest exotic state of the  $b\bar{b}$  hybrid meson was calculated on the lattice [7], as well as in the constituent gluon model [8]. The results are shown in Table 3. In lattice QCD, the lowest quark-excited state is absent, as was already noted above. One can see from Tables 2 and 3 that the mass of the gluon-excited state computed in the adiabatic approximation is almost the same as ours. Note that, in both cases, the quenched approximation was used. One can guess that a proper account of the sea quarks will not change the result significantly.

The results of [8] were obtained using the Hamiltonian (11) and the einbein field method and agree with the results of this work within the accuracy of approximation. The main difference is due to the constant subtracted in [8]. The adiabatic Born–Oppenheimer approximation was not used in [8] and string and spin corrections to the Hamiltonian were not considered.

Note also that ITEP sum rules and the flux-tube model predict the lowest exotic  $b\bar{b}$  hybrid mass with large error bars, which include both our numbers, and the bag model seems to underestimate the mass.

In conclusion, we have implemented the QCD string approach to calculate the adiabatic potentials and masses of heavy hybrid mesons. The background field method for valent glue and the Feynman–Schwinger representation of the hybrid meson Green’s function were used to reduce the latter to the background vacuum average of the Wilson loop

**Table 3.** The masses of lowest  $b\bar{b}$  exotic states with  $J^{PC} = 1^{-+}$  in other works

	$M^{b\bar{b}g}, \text{ GeV}$
Lattice QCD [7]	10.8
Constituent gluon model [8]	10.64

in the spinless case with static quark and antiquark. Using the minimal area law for the Wilson loop at large distances and color Coulomb potential at small ones, as well as the einbein field method for the valent gluon kinetic energy, the string Hamiltonian was extracted. The Hamiltonian spectrum was calculated using the probe wave functions of vector particle for valent gluon. It was shown that the levels with corresponding quantum numbers are in agreement with lattice QCD ones within the accuracy of the method ( $\sim 5\%$ ). However, extra levels are present due to the longitudinal components of the vector wave function. Further variational calculations are called for to discriminate appropriate degrees of freedom of constituent glue.

#### ACKNOWLEDGMENTS

This work was supported by the Russian Foundation for Basic Research (project nos. 00-02-17836, 00-15-96786) and INTAS (grant nos. 00-00110, 00-00366).

#### REFERENCES

1. A. I. Vainstein and L. B. Okun, *Yad. Fiz.* **23**, 1347 (1976) [*Sov. J. Nucl. Phys.* **23**, 716 (1976)].
2. Yu. A. Simonov, in *Lectures at the XVII International School of Physics, Lisbon, 1999*; hep-ph/9911237.
3. Yu. S. Kalashnikova and D. S. Kuzmenko, *Yad. Fiz.* **66**, 988 (2003) [*Phys. At. Nucl.* **66**, 955 (2003)]; D. S. Kuzmenko, Candidate's Dissertation (Moscow, 2002).
4. Yu. A. Simonov, *Lecture Notes in Physics* (Springer-Verlag, Berlin, 1996), Vol. 479, p. 139; *Yad. Fiz.* **58**, 113 (1995) [*Phys. At. Nucl.* **58**, 107 (1995)].
5. A. M. Badalian and D. S. Kuzmenko, *Yad. Fiz.* **67**, 579 (2004) [*Phys. At. Nucl.* **67**, 561 (2004)]; hep-ph/0302072.
6. E. Eichten and F. Feinberg, *Phys. Rev. D* **23**, 2724 (1981); D. Gromes, *Z. Phys. C* **26**, 401 (1984).
7. K. J. Juge, J. Kuti, and C. Morningstar, *Nucl. Phys. B (Proc. Suppl.)* **73**, 590 (1999).
8. Yu. S. Kalashnikova and Yu. B. Yufryakov, *Yad. Fiz.* **60**, 374 (1997) [*Phys. At. Nucl.* **60**, 307 (1997)].

## Triangular and Y-Shaped Hadrons with Static Sources\*

D. S. Kuzmenko\*\* and Yu. A. Simonov\*\*\*

*Institute of Theoretical and Experimental Physics,  
Bol'shaya Cheremushkinskaya ul. 25, Moscow, 117259 Russia*

Received March 20, 2003

**Abstract**—The structure of hadrons consisting of three static color sources in fundamental (baryons) or adjoint (three-gluon glueballs) representations is studied. The static potentials of glueballs, as well as gluon field distributions in glueballs and baryons, are calculated in the framework of the field correlator method.

© 2004 MAIK “Nauka/Interperiodica”.

1. The study of the gluon field structure in hadrons is important for the deep understanding of strong-interaction physics. We demonstrate below how to perform such studies in a gauge-invariant way using the field correlator method, which relies directly on QCD.

The static potential in a baryon was considered in detail in [1] and we will extensively refer to this paper in what follows. We start with the calculations of static potentials in three-gluon glueballs. This part of the paper presents the results from [2]. In the rest of the paper, the gluon field distributions in hadrons are discussed on the basis of [3–5].

In contrast to baryons, the gauge-invariant extended wave function of glueballs may have both Y-type and triangular structure. In the former case, it may be written as

$$G_Y^{(f)}(x, y, z, Y) = f^{abc} g_a(x, Y) g_b(y, Y) g_c(z, Y) \quad (1)$$

or

$$G_Y^{(g)}(x, y, z, Y) = d^{abc} g_a(x, Y) g_b(y, Y) g_c(z, Y). \quad (2)$$

Here,  $g_a(x, Y) = g_a(x) \Phi^{ab}(x, Y)$  denotes the extended gluon operator,  $g_a(x)$  is the valence gluon operator, and  $\Phi^{ab}(x, Y) = [P \exp(ig \int_Y^x A_\mu dz_\mu)]^{ab}$  is the parallel transporter or Schwinger line in the adjoint representation. The coordinates  $x, y, z$ , and  $Y$  in (1) apply to the valence gluons and string junction positions, respectively, and  $f^{abc}$  and  $d^{abc}$  denote adjoint antisymmetric and symmetric symbols.

The wave function of a triangular glueball has the form

$$G_\Delta(x, y, z) = G_\alpha^\beta(x) \Phi_\beta^\gamma(x, y) G_\gamma^\delta(y) \quad (3) \\ \times \Phi_\delta^\epsilon(y, z) G_\epsilon^\rho(z) \Phi_\rho^\alpha(z, x),$$

where  $G_\alpha^\beta(x) = g^a(x) (t^a)_\alpha^\beta$ ,  $t$  is the generator of  $SU(3)$ , and  $\Phi_\alpha^\beta$  is the parallel transporter in the fundamental representation.

According to (1), (2), the Wilson loop of a Y-type glueball has the same structure as in the case of a baryon {see Eq. (2) and Fig. 1 of [1]}. The difference is that the adjoint transporters should be substituted for the fundamental ones and symbols  $f^{abc}$  or  $d^{abc}$  for  $\epsilon_{\alpha\beta\gamma}$ .

The Wilson loop of a triangular glueball, induced by (3) in the limit of large  $N_c$ , is shown in Fig. 1. The

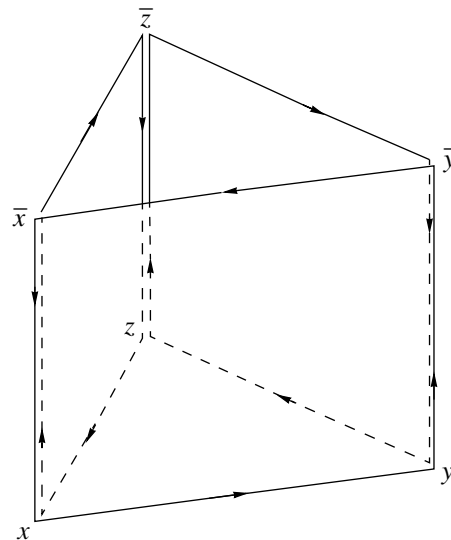
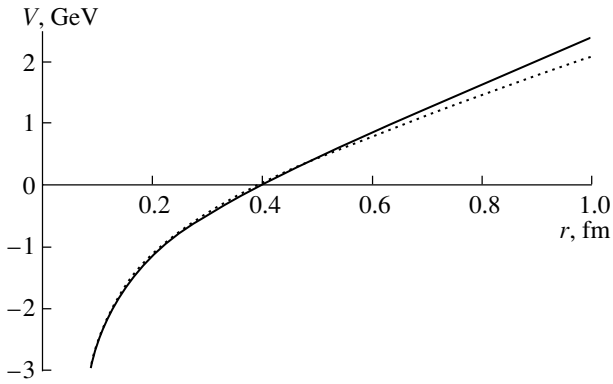


Fig. 1.  $\Delta$ -type Wilson loop.

\*This article was submitted by the authors in English.

\*\* e-mail: kuzmenko@heron.itep.ru

\*\*\* e-mail: simonov@heron.itep.ru



**Fig. 2.** Glueball potentials  $V_Y^{(G)}(r) + V_{(adj)}^{pert}(r)$  (solid curve) and  $V_{\Delta}^{(G)}(r) + V_{(adj)}^{pert}(r)$  (dotted curve) in an equilateral triangle with the quark separations  $r$  for  $\alpha_s = 0.3$ ,  $\sigma = 0.18 \text{ GeV}^2$ , and  $T_g = 0.12 \text{ fm}$ . The nondiagonal terms are neglected.

trajectories of valence gluons are replaced here with two fundamental (quark) trajectories and the Wilson loop is reduced to three disconnected rectangular meson loops.

The static potential in a baryon calculated in the field correlator method (MFC) is proportional to the two-point gluon field strength correlators in the fundamental representation [see, e.g., (5), (6) from [1]]. Therefore, it is proportional to the fundamental Casimir operator,  $C_F = 4/3$ , and the ratio of  $Y$ -type glueball and baryon potentials is equal to the ratio of corresponding Casimir operators,

$$\frac{V_Y^{(G)}}{V_Y^{(B)}} = \frac{C_A}{C_F} = \frac{9}{4}, \quad (4)$$

where  $C_A = 3$  is the adjoint Casimir operator and nondiagonal (interference) terms are neglected. The diagonal part of the baryon potential in an equilateral triangle has the form [2]

$$V_Y^{(B)}(R) = \frac{6\sigma}{\pi} \left\{ R \int_0^{R/T_g} dx x K_1(x) \right. \quad (5)$$

$$F_{\mu\nu}^H(x) = \frac{\langle \mathcal{W}_{\beta}^{\mathcal{H}\alpha}(x_0) \Phi_{\gamma}^{\beta}(x_0, x) (-igF_{\mu\nu}^a(x) t^a)_{\delta}^{\gamma} (\Phi^+)_{\alpha}^{\delta}(x, x_0) \rangle}{\langle \mathcal{W}^{\mathcal{H}} \rangle}. \quad (8)$$

The following expression is valid in the bilocal approximation of MFC in the case of mesons [4]:

$$F_{\mu\nu}^M(x) = \int_S d\sigma_{\rho\sigma}(x') \mathcal{D}_{\rho\sigma, \mu\nu}(x' - x), \quad (9)$$

$$\left. - T_g \left( 2 - \frac{R^2}{T_g^2} K_2 \left( \frac{R}{T_g} \right) \right) \right\} \equiv 3V^{(M)}(R),$$

where  $R$  is the distance from quarks to string junction,  $K_1$  and  $K_2$  are McDonald functions,  $\sigma = 0.18 \text{ GeV}^2$  and  $T_g = 0.12\text{--}0.2 \text{ fm}$  are the string tension and the gluon field correlation length, and  $V^{(M)}(R)$  is the static potential in a meson.

Now we turn to the triangular glueball, whose Wilson loop, according to Fig. 1, is the product of three meson loops. Therefore, the potential  $V_{\Delta}^{(G)}$ , which is the logarithm of the Wilson loop, is the sum of three meson potentials. In the case of an equilateral triangle with the side  $r = \sqrt{3}R$ ,

$$V_{\Delta}^{(G)}(r) = 3V^{(M)}(r). \quad (6)$$

The perturbative potential for three-gluon glueballs reads

$$V_{(adj)}^{pert}(r) = -\frac{3}{2} \frac{C_2(\text{adj})\alpha_s}{r}. \quad (7)$$

The behavior of total potentials in  $Y$ -type and triangular glueballs is shown in Fig. 2. One can see that they are very close up to distances  $r \approx 0.6 \text{ fm}$ . Note that the interference terms will change this picture. They will be considered in subsequent publications.

**2.** We proceed now to the study of the gluon field structure using the connected probe [6, 7]. The connected probe consists of the probe plaquette joined to the Wilson loop by parallel transporters and forms the frame with the current in four-dimensional Euclidean space (see Fig. 3). When the plaquette size is small enough, the connected probe allows one to calculate the color-integrated gluon field in a hadron, using the Wilson loop  $\mathcal{W}^{\mathcal{H}}$  of the latter,

where the integration is taken over the minimal surface of the Wilson loop,  $x' \in S$ , and  $\mathcal{D}$  denotes the gauge-invariant bilocal gluon field strength correlator [see, e.g., (5) of [1] for details]. Using the MFC parametrization of correlators [1], we determine that

the electric component of the  $F^M$  has the form [5]

$$\mathbf{E}^M(\mathbf{x}, \mathbf{R}) = \mathbf{n} \frac{2\sigma}{\pi} \int_0^{R/T_g} dl \left| \mathbf{l}\mathbf{n} - \frac{\mathbf{x}}{T_g} \right| \quad (10)$$

$$\times K_1 \left( \left| \mathbf{l}\mathbf{n} - \frac{\mathbf{x}}{T_g} \right| \right),$$

while the magnetic one is absent.

The field  $\mathbf{E}^M(\mathbf{x}, \mathbf{R})$  (10), which we call the non-perturbative background gluon field in a meson, is the force acting on the probe located at the point  $\mathbf{x}$  while the quark is located at zero and the antiquark at the point  $\mathbf{R}$ . It is related to the field acting on the quark as follows.

The force  $\mathbf{F}^M$  acting on the quark in a meson is defined by the static potential  $V^{(M)}$  (5),

$$\mathbf{F}^M(\mathbf{r}) = -\nabla V^{(M)}(\mathbf{r}). \quad (11)$$

One can verify using (5), (10), and (11) that the following relations are valid [5]:

$$\mathbf{E}^M(0, \mathbf{R}) = \mathbf{E}^M(\mathbf{R}, \mathbf{R}) = \mathbf{F}^M(\mathbf{R}), \quad (12)$$

$$\mathbf{E}^M(\mathbf{R}, 2\mathbf{R}) = \mathbf{E}^M(0, \mathbf{R}) + \mathbf{E}^M(\mathbf{R}, \mathbf{R}) \quad (13)$$

$$= 2\mathbf{F}^M(\mathbf{R}).$$

Relation (12) means that when the locations of the probe and quark (antiquark) coincide, the probe recombines with the latter, and that is why it is affected by the same force  $\mathbf{F}^M$ . One can conclude from relation (13) that, when the probe is located in the middle of two sources, it interacts with both the quark and the antiquark, and the total field becomes twice as big. If the point  $\mathbf{x}$  is located on the line connecting the quark and antiquark, it is easy to check using (5), (10) that the generalization of (12), (13) has the form

$$\mathbf{E}^M(\mathbf{x}, \mathbf{R}) = \mathbf{F}^M(\mathbf{x}) - \mathbf{F}^M(\mathbf{x} - \mathbf{R}). \quad (14)$$

According to (11), the force  $\mathbf{F}^M(\mathbf{R})$  acting on the quark increases linearly with the slope  $2\sigma/(\pi T_g)$  at small distances  $R \lesssim T_g$  and saturates with the value  $\sigma$  at  $R \gtrsim 0.7$  fm.

The field  $\mathbf{E}^M$  in the saturated regime acquires the universal profile  $E^{\text{string}}$ , which does not depend on the quark–antiquark separation,

$$E^{\text{string}}(\rho) = 2\sigma \left( 1 + \frac{\rho}{T_g} \right) \exp \left( -\frac{\rho}{T_g} \right), \quad (15)$$

where  $\rho$  is the distance from the quark–antiquark axis. We apply now the Gauss law in the form

$$\int \mathbf{E} d\mathbf{S} = 4\pi C_F \alpha_s \quad (16)$$

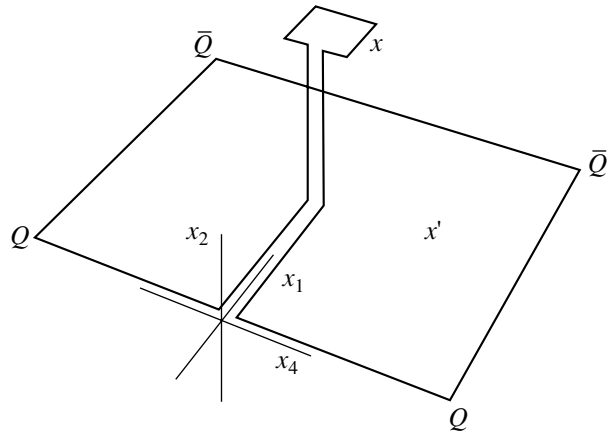


Fig. 3. A connected probe in the case of meson.

to the saturated field (15) and get the parameter relation

$$3\sigma T_g = C_F \alpha_s. \quad (17)$$

Taking the freezing value of the strong coupling  $\alpha_s \approx 0.4$  [8] and the phenomenological value of the string tension  $\sigma = 0.18 \text{ GeV}^2$ , we determine from (17) the reasonable gluon correlation length value  $T_g \approx 0.2$  fm (see [1]).

Using the Maxwell equation with magnetic currents,

$$\text{curl} \mathbf{E}^M = \mathbf{j}_{\text{magn}}, \quad (18)$$

we find that currents corresponding to the saturated field (15) form closed circles around the quark–antiquark axis, with the density

$$j_{\text{magn}}(\rho) = \frac{\partial E^{\text{string}}(\rho)}{\partial \rho} = \frac{2\sigma\rho}{T_g^2} \exp \left( -\frac{\rho}{T_g} \right). \quad (19)$$

One can verify using (9), (18), and the non-Abelian Bianchi identity that magnetic currents arise due to the three-point field strength correlator, which describes the emission of the color-magnetic gluon field by the color-electric one.

The detailed study of these and other properties of the field  $\mathbf{E}^M$  will be given elsewhere.

3. When the field distribution of the quark–antiquark pair is known, it is straightforward to calculate the field of a triangular glueball (see Fig. 1). We join the connected probe to each of the quark–antiquark loops and arrive at the expression

$$\mathbf{E}_{\Delta}^{(G)}(\mathbf{x}, \mathbf{r}^{(1)}, \mathbf{r}^{(2)}, \mathbf{r}^{(3)}) = \sum_{i=1}^3 \mathbf{E}^M(\mathbf{x} - \mathbf{r}^{(i)}, \mathbf{R}^{(i)}), \quad (20)$$

where  $\mathbf{r}^{(i)}$  is the position of the  $i$ th valence gluon and  $\mathbf{R}^{(i)} = \mathbf{r}^{(i+1)\text{mod}3} - \mathbf{r}^{(i)}$ . The surface defined by

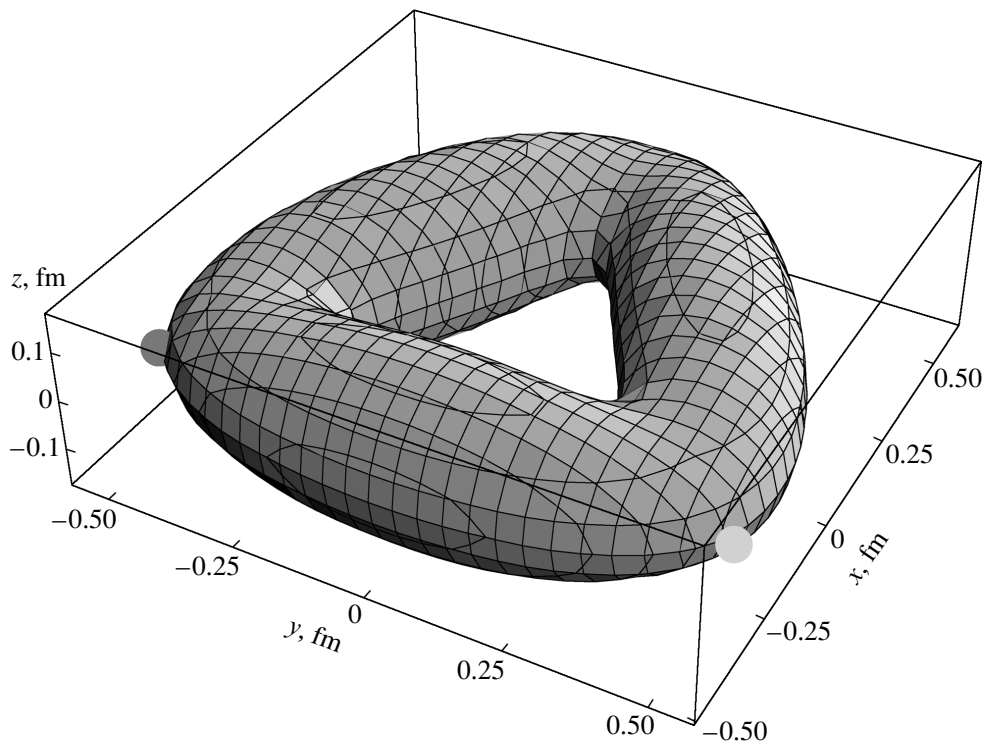


**Fig. 4.** A contour plot of the surface  $|\mathbf{E}_{\Delta}^{(G)}(\mathbf{x})| = \sigma$  of the field in the  $\Delta$ -type three-gluon glueball. Valence gluon separations are 1 fm,  $\sigma = 0.18 \text{ GeV}^2$ , and  $T_g = 0.12 \text{ fm}$ .

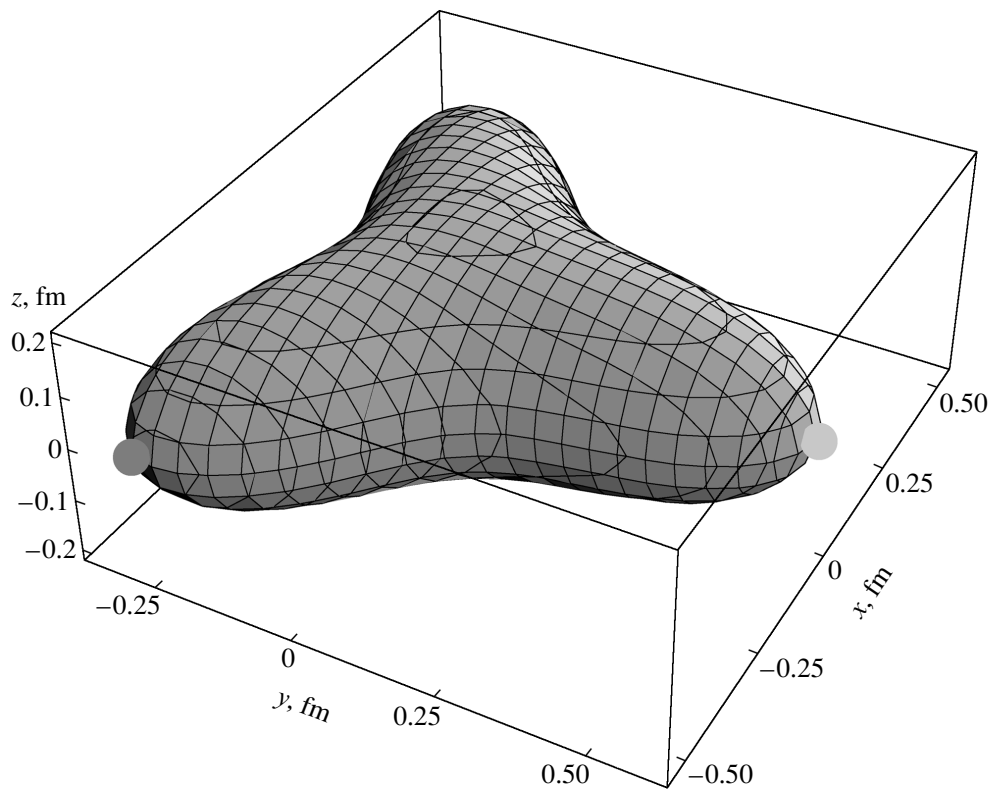


**Fig. 5.** A contour plot of the surface  $|\mathbf{E}^{(B)}(\mathbf{x})| = \sigma$  of the field in the baryon. Quark separations are 1 fm,  $\sigma = 0.18 \text{ GeV}^2$ , and  $T_g = 0.12 \text{ fm}$ .

the condition  $|\mathbf{E}_{\Delta}^{(G)}(\mathbf{x})| = \sigma$  at gluon separations of 1 fm is shown in Fig. 4. The values of parameters  $\sigma = 0.18 \text{ GeV}^2$  and  $T_g = 0.12 \text{ fm}$  are used. The surface shown in the figure goes through the valence gluon locations. Indeed, one can verify using (20) that two forces of the value  $\sigma$  having the angle  $2\pi/3$  between them add to give the resulting force of the value  $\sigma$ .

The same procedure can be applied to the system of an arbitrary number of mesons to obtain the field distributions in the leading order of  $1/N_c$ . The next-order corrections can also be considered within the approach.

4. The problem of baryon (or Y-type glueball) field calculations is more complicated. When we join the probe plaquette to the trajectory of the first quark and calculate the field distribution (8) using the bilocal approximation of MFC, we arrive at the following relation for the electric field:

$$\mathbf{E}_{(1)}^B(\mathbf{x}, \mathbf{R}^{(1)}, \mathbf{R}^{(2)}, \mathbf{R}^{(3)}) = \mathbf{E}^M(\mathbf{x}, \mathbf{R}^{(1)}) - \frac{1}{2}\mathbf{E}^M(\mathbf{x}, \mathbf{R}^{(2)}) - \frac{1}{2}\mathbf{E}^M(\mathbf{x}, \mathbf{R}^{(3)}) \quad (21)$$

(the magnetic field is absent just as in the meson case). The vector  $\mathbf{R}^{(i)}$  here is directed from the string junction to the  $i$ th quark, and  $\mathbf{E}^M$  is defined in (10). When we join the probe to the second and third quark trajectories, we will get analogous formulas with the corresponding index transpositions.

To obtain symmetric field distributions, we must sum squares  $(\mathbf{E}_{(i)}^B)^2$ ,

$$(\mathbf{E}^{(B)})^2 = \frac{2}{3} \left( (\mathbf{E}_{(1)}^B)^2 + (\mathbf{E}_{(2)}^B)^2 + (\mathbf{E}_{(3)}^B)^2 \right). \quad (22)$$

The surface given by the condition  $|\mathbf{E}^{(B)}(\mathbf{x})| = \sigma$  at quark separations of 1 fm is shown in Fig. 5. It goes through the quark positions and has a small convexity near the string junction.

The ratio of the energy density at the string junction position,  $w_{sj}$ , to the density in the middle of the string with the saturated profile,  $w_{string}$ , has to be equal to the corresponding field squares, and, according to (22), (15),

$$\frac{w_{sj}}{w_{string}} = \frac{(\mathbf{E}^{(B)}(0))^2}{(\mathbf{E}^{string}(0))^2} = \frac{9}{8}. \quad (23)$$

In conclusion, hadron static potentials and the gluon field distributions, which ensure the confinement of color sources, were calculated using the field correlator method. It is stressed that the mechanism of confinement is the process of emission of the color-magnetic gluon field by the color-electric one in non-perturbative vacuum. The static potentials of three-gluon glueballs were reduced in the first approximation to the appropriate sum of quark–antiquark potentials. The nonperturbative gluon field induced by the static quark–antiquark pair was calculated using the connected probe, and its classical Abelian properties were considered. Triangular gluon field distributions were calculated for glueballs and Y-type ones for baryons.

An extension of the method to an arbitrary number of colors is straightforward. It is also applicable to the study of nuclear structure.

### ACKNOWLEDGMENTS

This work was supported by the Russian Foundation for Basic Research (project nos. 00-02-17836, 00-15-96786) and INTAS (grant nos. 00-00110, 00-00366).

### REFERENCES

1. D. S. Kuzmenko, *Yad. Fiz.* **67** (3), 561 (2004); hep-ph/0302067.
2. D. S. Kuzmenko and Yu. A. Simonov, *Yad. Fiz.* **66**, 983 (2003) [*Phys. At. Nucl.* **66**, 950 (2003)]; hep-ph/0202277.
3. D. S. Kuzmenko and Yu. A. Simonov, *Phys. Lett. B* **494**, 81 (2000).
4. D. S. Kuzmenko and Yu. A. Simonov, *Yad. Fiz.* **64**, 110 (2001) [*Phys. At. Nucl.* **64**, 107 (2001)]; hep-ph/0010114.
5. D. S. Kuzmenko, Preprint ITEP-2002-06 (Moscow, 2002); Candidate's Dissertation (Moscow, 2002).
6. A. Di Giacomo, M. Maggiore, and S. Olejnik, *Phys. Lett. B* **236**, 199 (1990); *Nucl. Phys. B* **347**, 441 (1990).
7. L. Del Debbio, A. Di Giacomo, and Yu. A. Simonov, *Phys. Lett. B* **332**, 111 (1994).
8. A. M. Badalian and D. S. Kuzmenko, *Phys. Rev. D* **65**, 016004 (2002).

## ELEMENTARY PARTICLES AND FIELDS

### Theory

## Static Potential in Baryon\*

D. S. Kuzmenko\*\*

*Institute of Theoretical and Experimental Physics,  
Bol'shaya Cheremushkinskaya ul. 25, Moscow, 117259 Russia*

Received March 20, 2003

**Abstract**—The baryon static potential is calculated in the framework of the field correlator method and is shown to match the recent lattice results. The effects of the nonzero value of the gluon correlation length are emphasized. © 2004 MAIK “Nauka/Interperiodica”.

1. The static potential is a key quantity in the calculations of spectra and wave functions of baryons in the potential models [1], as well as in the QCD string approach [2]. On the other hand, the static potential is generated by the gluon forces of QCD and therefore sheds light on the profound properties of strong interactions. Accurate numerical calculations of the static potential in a baryon performed in lattice QCD in recent years [3, 4] induced a new significant growth of interest in the structure of the gluon forces in a baryon.

The results of calculations of the baryon potential in the framework of the method of field correlators (MFC) [5] are presented in this paper. We set the correspondence of this potential to the lattice one and emphasize the fundamental effects of strong interactions—the confinement of color charges and definite value of the correlation length of the gluon fields, which reveal themselves in the behavior of the baryon potential.

2. The static potential is expressed through the Wilson loop  $\mathcal{W}_B$  according to the relation

$$V_B = - \lim_{T \rightarrow \infty} \frac{1}{T} \ln \mathcal{W}_B, \quad (1)$$

and that is why we proceed now to the calculation of the Wilson loop. The baryon Wilson loop is shown in Fig. 1 and is defined as follows:

$$\mathcal{W}_B = \left\langle \frac{1}{6} \epsilon_{\alpha\beta\gamma} \epsilon^{\alpha'\beta'\gamma'} \Phi_{\alpha'}^{\alpha}(C_1) \Phi_{\beta'}^{\beta}(C_2) \Phi_{\gamma'}^{\gamma}(C_3) \right\rangle, \quad (2)$$

where the parallel transporter or Schwinger line  $\Phi$  is given as

$$\Phi_{\beta}^{\alpha}(x, y, C) = \left( P \exp \left( ig \int_C A_{\mu} dz_{\mu} \right) \right)_{\beta}^{\alpha}. \quad (3)$$

The average of the Wilson loop over the vacuum fields using the non-Abelian Stokes theorem and bilocal (two-point) approximation is performed in [5], and the result reads

$$\begin{aligned} \mathcal{W}_B = \exp \left\{ - \sum_{i=1}^3 \frac{1}{2} \int_{S_i} \int_{S_i} d\sigma_{\mu_1\nu_1}(x) \right. & (4) \\ & \times d\sigma_{\mu_2\nu_2}(x') \mathcal{D}_{\mu_1\nu_1, \mu_2\nu_2}(x - x') \\ & + \sum_{i < j} \frac{1}{2} \int_{S_i} \int_{S_j} d\sigma_{\mu_1\nu_1}(x) d\sigma_{\mu_2\nu_2}(x') \\ & \left. \times \mathcal{D}_{\mu_1\nu_1, \mu_2\nu_2}(x - x') \right\}, \end{aligned}$$

where  $\mathcal{D}$  designates the bilocal field strength correlators,

$$\begin{aligned} & \mathcal{D}_{\mu_1\nu_1, \mu_2\nu_2}(x - x') & (5) \\ \equiv & \frac{g^2}{N_c} \text{tr} \langle F_{\mu_1\nu_1}(x) \Phi(x, x') F_{\mu_2\nu_2}(x') \Phi(x', x) \rangle, \end{aligned}$$

and it is assumed that the straight-line trajectories for parallel transporters are chosen. Integrations in (4) are taken over the surfaces  $S_i$  of the Wilson loop, which are formed by the trajectories of the corresponding quark,  $C_i$ , and that of the string junction (see Fig. 1). The trajectory of the string junction is shown in the figure by the dotted line.

Relying on the phenomena of the Casimir scaling [6], which is confirmed in lattice simulations, one

\*This article was submitted by the author in English.

\*\* e-mail: kuzmenko@heron.itep.ru

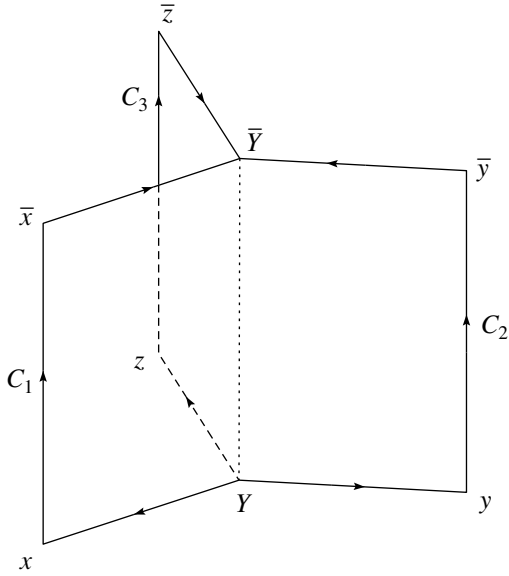


Fig. 1. The baryon Wilson loop.

can expect that the bilocal approximation (4) is valid within an accuracy of 1%.

Performing the surface integration in (4) and substituting the result into (1), we arrive at the expression for the baryon potential in the bilocal approximation,

$$V_B(R_1, R_2, R_3) = \left( \sum_{a=b} - \sum_{a<b} \right) n_i^{(a)} n_j^{(b)} \quad (6)$$

$$\times \int_0^{R_a} \int_0^{R_b} dl dl' \int_0^\infty dt \mathcal{D}_{i4, j4}(z_{ab}),$$

where  $R_a$  is a separation of the string junction and corresponding ( $a$ th) quark,  $\mathbf{n}^{(a)}$  is the unity vector directed from the string junction to this quark, and  $z_{ab} = (l\mathbf{n}^{(a)} - l'\mathbf{n}^{(b)}, t)$ .

According to MFC [7], the bilocal correlators are written in the general form containing two scalar form factors  $D(z)$  and  $D_1(z)$ ,

$$\begin{aligned} & \mathcal{D}_{\mu_1\nu_1, \mu_2\nu_2}(z) \quad (7) \\ &= (\delta_{\mu_1\mu_2} \delta_{\nu_1\nu_2} - \delta_{\mu_1\nu_2} \delta_{\mu_2\nu_1}) D(z) \\ &+ \frac{1}{2} \left( \frac{\partial}{\partial z_{\mu_1}} (z_{\mu_2} \delta_{\nu_1\nu_2} - z_{\nu_2} \delta_{\nu_1\mu_2}) \right. \\ &\left. + \frac{\partial}{\partial z_{\nu_1}} (z_{\nu_2} \delta_{\mu_1\mu_2} - z_{\mu_2} \delta_{\mu_1\nu_2}) \right) D_1(z). \end{aligned}$$

The form factor  $D(z)$  decreases exponentially,

$$D(z) = D(0) \exp\left(-\frac{|z|}{T_g}\right), \quad (8)$$

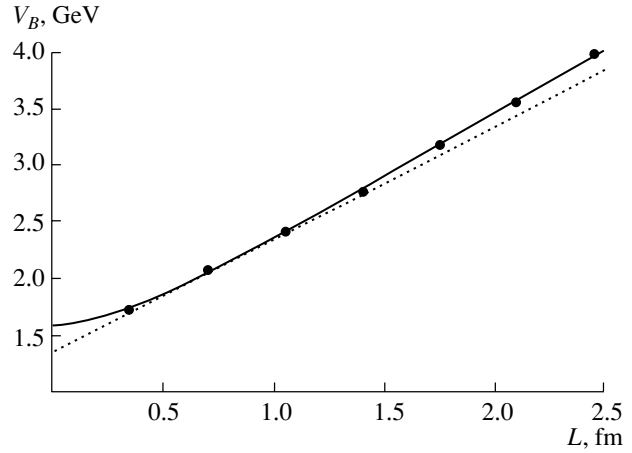


Fig. 2. The lattice nonperturbative baryon potential from [3] (points) for lattice parameter  $\beta = 5.8$  and MFC potential  $V^{(B)}$  (solid curve) with parameters  $\sigma = 0.22 \text{ GeV}^2$  and  $T_g = 0.12 \text{ fm}$  vs. the minimal length of the string  $L$ . The dotted line is a tangent at  $L = 0.7 \text{ fm}$ .

which reflects the stochastic properties of the non-perturbative background gluon fields and is justified by the lattice computations [8]. This behavior leads to the asymptotic area law for the Wilson loop, where the string tension  $\sigma$  is expressed through  $D(z)$  as follows:

$$\sigma = \frac{\pi}{2} \int_0^\infty dz^2 D(z) = \pi D(0) T_g^2 = 0.18 \text{ GeV}^2. \quad (9)$$

The string tension is the main nonperturbative parameter of MFC. Its value is defined phenomenologically by the slope of the meson Regge trajectories [9] and is directly related to the radius of confinement.

There is another parameter in (8), the correlation length of the background gluon field  $T_g$ . However, it is not an independent parameter. Its value is extracted from the energy of the gluon excitation of the hadron spectra [10] and may be calculated in the QCD string approach [10, 11] using the only parameter  $\sigma$ . The energy of the gluon excitation is large,  $\sim 1.5 \text{ GeV}$  [11], and therefore the gluon correlation scale is significantly less than the confinement scale.

The form factor  $D_1(z)$  is dominated by the contribution of one-gluon exchange from perturbation theory, which gives rise to the static color-Coulomb potential. In the case of a baryon with the quarks forming an equilateral triangle with the side  $r$ , the perturbative potential reads

$$V_{\text{pert}}(r) = -\frac{3 C_F \alpha_s}{2 r}, \quad (10)$$

where  $C_F = 4/3$ .

3. We now proceed to the comparison of the potential (6)–(10) with the lattice results [3, 4]. In Fig. 2,

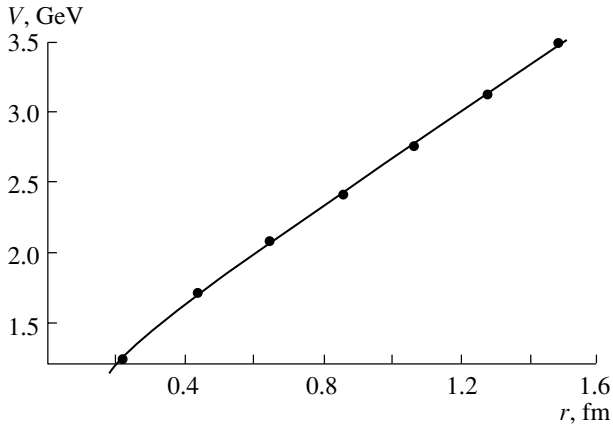


**Fig. 3.** The lattice baryon potential in the equilateral triangle with quark separations  $r$  from [4] (points) at  $\beta = 5.8$  and the MFC potential  $V^{(B)} + V_{\text{pert}}$  (solid curve) at  $\alpha_s = 0.18$ ,  $\sigma = 0.18 \text{ GeV}^2$ , and  $T_g = 0.12 \text{ fm}$ .

the results of the lattice simulations [3] of the baryon potential with the perturbative part subtracted are shown by points as a function of the length of the string,  $L = R_1 + R_2 + R_3$ . The solid curve in the figure shows the behavior of the nonperturbative potential calculated in MFC for the configurations of an equilateral triangle. When  $L \gtrsim 1 \text{ fm}$ , the potential grows linearly, having the slope  $\sigma$ . When the length of the string gets smaller, the slope of the potential diminishes. The dotted line is the tangent to the MFC potential at  $L = 0.7 \text{ fm}$ . The slope of the tangent is  $\sim 0.9\sigma$ . A linear phenomenological potential with the same slope was used in the constituent model for the description of the spectra of baryons a long time ago [1]. One can see from the figure that our curve goes through all lattice points well. The configurations of quarks forming triangles with the angles in the region  $[\pi/20, \pi/2]$ , which were used in lattice work [3], do not allow one to establish any dependence of the potential on the configuration with the accuracy given. The study of the MFC potential on quark configurations will be performed in what follows (see below Fig. 4).

In Fig. 3, the results of lattice computations of the potential in an equilateral triangle [4] are presented (points) vs. the quark separations  $r$ . The MFC potential with the perturbative part included is shown by the solid curve. One can see that all the lattice data are completely described by the MFC potential.

Computations in [3, 4] are performed in the quenched approximation. In the MFC calculations, sea quarks are not considered either. The studies of the effects of light dynamical quarks on the  $Q\bar{Q}$  static potential in a lattice were recently performed in [12]. No clear evidence for a flattening of the potential was found up to distances of 2.5 fm. One can therefore

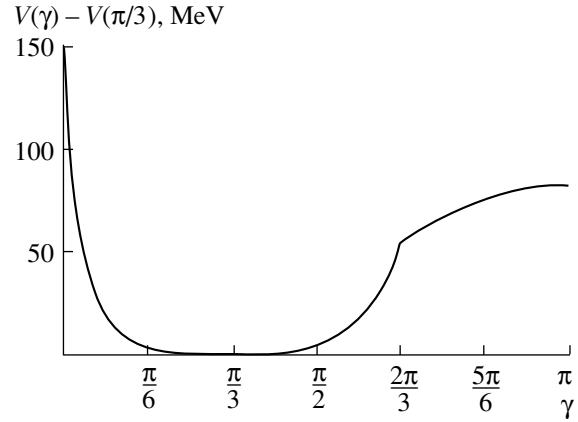


**Fig. 4.** The baryon potential in an isosceles triangle with the length of the string  $L = 1.8 \text{ fm}$  vs. the vertex  $\gamma$  for  $\sigma = 0.18 \text{ GeV}^2$  and  $T_g = 0.12 \text{ fm}$ .

expect that the sea quarks would not change the baryon potential significantly at typical hadron sizes.

It is also interesting to study the dependence of the potential in a baryon on the quark locations at fixed length of the string  $L$ . Let us consider isosceles triangles with the full length of the string  $L$  and vertex  $\gamma$  and use  $V^L(\gamma)$  to denote the nonperturbative potential in these triangles. At large enough sizes,  $L \gtrsim 1 \text{ fm} \gg T_g$ , asymptotic relations follow from (6)–(9). When  $\gamma = 0$  and the locations of two quarks coincide, these quarks combine in antitriplet. The string consists of one line and

$$V_1 \equiv V^L(\gamma = 0) = \sigma L - \frac{4}{\pi} \sigma T_g. \quad (11)$$

When  $0 < \gamma < 2\pi/3$ , the string consists of three lines and potential

$$\begin{aligned} V_2 &\equiv V^L(0 < \gamma < 2\pi/3) \\ &= \sigma L + \left( -\frac{12}{\pi} + \frac{2}{\sqrt{3}} \right) \sigma T_g. \end{aligned} \quad (12)$$

When  $\gamma \geq 2\pi/3$ , the string consists of two lines. In this case,

$$\begin{aligned} V^L(\gamma \geq 2\pi/3) \\ = \sigma L + \left( -\frac{8}{\pi} + \frac{2}{\pi}(\pi - \gamma) \cot(\pi - \gamma) \right) \sigma T_g. \end{aligned} \quad (13)$$

It is not difficult to calculate the difference between the potentials in different configurations (we use  $\sigma = 0.18 \text{ GeV}^2$ ,  $T_g = 0.12 \text{ fm}$ ),

$$\begin{aligned} \Delta V_1 &\equiv V_1 - V_2 = \left( \frac{8}{\pi} - \frac{2}{\sqrt{3}} \right) \sigma T_g \\ &\approx 150 \text{ MeV}, \end{aligned} \quad (14)$$

$$\begin{aligned} \Delta V_2 &\equiv V^L \left( \frac{2\pi}{3} \right) - V_2 & (15) \\ &= \left( \frac{4}{\pi} - \frac{4}{3\sqrt{3}} \right) \sigma T_g \approx 55 \text{ MeV}, \end{aligned}$$

$$\begin{aligned} \Delta V_3 &\equiv V^L(\gamma \rightarrow \pi) - V^L \left( \frac{2\pi}{3} \right) & (16) \\ &= \left( \frac{2}{\pi} - \frac{2}{3\sqrt{3}} \right) \sigma T_g \approx 30 \text{ MeV}. \end{aligned}$$

In Fig. 4, the dependence of the baryon potential in an isosceles triangle on the angle  $\gamma$  at  $L = 1.8$  fm is shown. One can verify that, for the curve shown in the figure, relations (13)–(16) are justified (taking  $\gamma = \pi/3$  for  $V_2$ ).

The nonperturbative potential in the configurations under consideration has a peak near  $\gamma = 0$ . However, in this region, the perturbative part of the total potential dominates. Indeed, the effect reveals itself when the quark separation  $r_{qq}$  becomes less than the background correlation length. But at separation  $r_{qq} \approx 0.1$  fm, the color-Coulomb interaction of quarks attains 300 MeV and grows rapidly when  $r_{qq}$  diminishes. That is why, to answer the question about the relevance of quark–diquark configurations, we have to consider the motion of two quarks in their perturbative potential. In particular, the radius of a diquark may be estimated using the Bohr formula,  $r_{qq} = 2/(m_q C_F \alpha_s)$ , which yields  $r_{bb} \approx 0.3$  fm and  $r_{cc} \approx 1.0$  fm. More accurate values were obtained in the relativistic quark model [13], where relativistic corrections to the perturbative potential as well as the linear nonperturbative potential were accounted for. The radii of diquarks calculated in [13] for the ground states are  $r_{bb} = 0.37$  fm,  $r_{cc} = 0.56$  fm. We should state that the radii of diquarks are comparable to the size of a baryon, which perhaps signals that the formation of a quark–diquark configuration is improbable. Nevertheless, the quark–diquark approximation turns out to be useful for the computations of the baryon spectra (see, e.g., [13]). Account of the nonperturbative effects considered in (11)–(16) and Fig. 4 would spoil this approximation only a little.

4. To summarize, we have calculated nonperturbatively the static potential in a baryon and demonstrated that it completely describes recent lattice results. The latter means in particular that the problem of the form of the potential is resolved. The potential in our approach has an apparent  $Y$ -type structure; i.e., it depends only on the distances from the quarks to the string junction, the location of the latter being determined by the condition of the minimal total length of the string. The formal answer to the problem of the potential law is that the slope of the nonperturbative potential as a function of the length of the string  $L$

grows from zero to  $\sigma$  when  $L$  changes from zero to  $\sim 1.5$  fm. Therefore, the effective slope at typical hadronic sizes may be chosen to be  $\sim 0.9 \sigma$ .

The behavior of the baryon potential considered is a consequence of two profound properties of the strong interaction, the confinement of quarks and the definite value of the correlation length of nonperturbative gluon fields. The latter is directly related to the energy scale of the gluon excitations of the hadron spectra. It is the correlation length that induces the change in the slope of the potential in a baryon. Note that, for mesons, the situation differs. The slope of the nonperturbative static potential in mesons hardly changes at small distances due to the interference with the perturbative fields [14].

Apart from the change in the slope of the potential in a baryon, another related effect was studied, namely, the behavior of the potential when the length of the string is fixed. It was demonstrated in particular that the difference of the potentials in configurations with the string consisting of different (one, two, or three) numbers of lines turns out to be proportional to  $\sigma T_g$ . The combination of the parameters directs immediately that the effect is induced by both the scale of confinement and correlations of gluon fields. The influence of the effect on the creation of the quark–diquark configuration is shown to be small. Last but not least, it would be interesting to study this effect in devoted lattice calculations.

#### ACKNOWLEDGMENTS

I am grateful to Yu.A. Simonov for many fruitful discussions.

This work was supported by the Russian Foundation for Basic Research (project nos. 00-02-17836, 00-15-96786) and INTAS (grant nos. 00-00110, 00-00366).

#### REFERENCES

1. S. Capstick and N. Isgur, Phys. Rev. D **34**, 2809 (1986).
2. Yu. A. Simonov, hep-ph/0205334.
3. T. T. Takahashi *et al.*, Phys. Rev. D **65**, 114509 (2002).
4. C. Alexandrou, Ph. de Forcrand, and O. Jahn, hep-lat/0209062; *Talk Presented at 20th International Symposium on Lattice Field Theory (LATTICE 2002), Boston, Massachusetts, 2002* (in press).
5. D. S. Kuzmenko, hep-ph/0204250; submitted to Yad. Fiz.
6. G. S. Bali, Nucl. Phys. B (Proc. Suppl.) **83**, 422 (2000); Yu. A. Simonov, Pis'ma Zh. Éksp. Teor. Fiz. **71**, 187 (2000) [JETP Lett. **71**, 127 (2000)]; hep-ph/0001244; V. I. Shevchenko and Yu. A. Simonov, Phys. Rev. Lett. **85**, 1811 (2000).

7. H. G. Dosch, Phys. Lett. B **190**, 177 (1987); H. G. Dosch and Yu. A. Simonov, Phys. Lett. B **205**, 399 (1988); Yu. A. Simonov, Nucl. Phys. B **307**, 512 (1988); A. Di Giacomo, H. G. Dosch, V. I. Shevchenko, and Yu. A. Simonov, Phys. Rep. **372**, 319 (2002).
8. M. Campostrini, A. Di Giacomo, and G. Mussardo, Z. Phys. C **25**, 173 (1984); A. Di Giacomo and H. Panagopoulos, Phys. Lett. B **285**, 133 (1992); A. Di Giacomo, E. Meggiolaro, and H. Panagopoulos, Nucl. Phys. B **483**, 371 (1997); G. S. Bali, N. Brambilla, and A. Vairo, Phys. Lett. B **421**, 265 (1998).
9. A. Yu. Dubin, A. B. Kaidalov, and Yu. A. Simonov, Phys. Lett. B **323**, 41 (1994); Phys. Lett. B **343**, 310 (1995); Yu. S. Kalashnikova, A. V. Nefediev, and Yu. A. Simonov, Phys. Rev. D **64**, 014037 (2001).
10. Yu. A. Simonov, Nucl. Phys. B **592**, 350 (2000).
11. Yu. S. Kalashnikova and D. S. Kuzmenko, Yad. Fiz. **67**, 556 (2004) [Phys. At. Nucl. **67**, 538 (2004)]; hep-ph/0302070.
12. MILC Collab. (C. Bernard *et al.*), in *Proceedings of 20th International Symposium on Lattice Field Theory (LATTICE 2002), Boston, Massachusetts, 2002*; hep-lat/0209051; A. Duncan, E. Eichten, and J. Yoo, hep-lat/0209123.
13. D. Ebert, R. N. Faustov, V. O. Galkin, and A. P. Martynenko, Phys. Rev. D **66**, 014008 (2002).
14. A. M. Badalian and D. S. Kuzmenko, Yad. Fiz. **67**, 579 (2004) [Phys. At. Nucl. **67**, 561 (2004)]; hep-ph/0302072.

---

---

**ELEMENTARY PARTICLES AND FIELDS**  
**Theory**

---

---

**The QCD Spectrum: Mixing, Strong Decays,  
and the Role of Sea Quarks\***

Yu. A. Simonov\*\*

*Institute of Theoretical and Experimental Physics,  
Bol'shaya Cheremushkinskaya ul. 25, Moscow, 117259 Russia*

Received April 16, 2003

**Abstract**—The light hadron spectrum as computed in nonperturbative QCD is reviewed and compared to lattice data and experiment. The mixing of mesons, hybrids, and glueballs is calculated in the field correlator method. The strong decay mechanisms are found in the method and compared to the known phenomenological models. The role of sea quarks (unquenched approximation) is studied analytically, using radially excited mesons as an example, and compared to experiment. © 2004 MAIK “Nauka/Interperiodica”.

## 1. INTRODUCTION

In the last decade, there has been substantial progress in understanding the QCD spectrum, both in analytical methods [1] and in lattice calculations [2]. On the analytic side, the most economical and promising turns out to be the field correlator method (FCM) [3], which starts from the basic principles and correct description of the QCD vacuum with the help of gauge-invariant field correlators. It was proved [4] that confinement can be described by the lowest, quadratic correlator  $\langle F_{\mu\nu}(x)F_{\lambda\sigma}(y) \rangle$  which contains two scalar form factors  $D(x-y)$  and  $D_1(x-y)$ . Lattice data [5] show that  $D$  and  $D_1$  describe the  $Q\bar{Q}$  static potential with a few percent accuracy, and the string tension  $\sigma$  is obtained directly from  $D(x)$ :  $\sigma = \frac{1}{2} \int D(x) d^2x$ .

In addition,  $D(x) \equiv D(x/T_g)$  contains another important parameter—the gluon correlation length  $T_g$ , which was found on the lattice [6] and analytically [7] to be very small,  $T_g \leq 0.2$  fm.

This circumstance allows one to develop the local Hamiltonian and Lagrangian methods for the description of the  $q\bar{q}$  and  $3q$  bound states, which will be discussed in the next section.

However, this is not the whole story since there are valence gluons which can also form bound states by themselves (glueballs) and with the  $q\bar{q}$  (hybrids). To introduce these states, one should define the valence gluons in contrast to the nonperturbative background, and one can do it unambiguously in the framework of background perturbation theory [8]. In

this way, one gets the local Hamiltonian also for hybrids [9, 10] and for glueballs [11] and calculations of the corresponding spectra in good agreement with lattice data. In doing so, one realizes that a gluon excitation “costs” around 1 GeV, which allows one to disregard these states in the first approximation when computing the lowest meson or baryon states.

However, the exact treatment requires the introduction of Fock tower of states and consideration of mixing between meson and hybrid states, which is done in Section 3. The effects of sea quarks on the spectrum and strong decays are considered in Section 4, while Section 5 is devoted to conclusions.

## 2. HAMILTONIAN

There are two possible approaches to incorporating nonperturbative field correlators in quark–antiquark (or  $3q$ ) dynamics. The first has to deal with the effective nonlocal quark Lagrangian containing field correlators [12]. From this, one obtains first-order Dirac-type integro-differential equations for heavy-light mesons [12, 13] and light mesons and baryons [14]. These equations contain the effect of chiral symmetry breaking [12], which is directly connected to confinement.

The second approach is based on the effective Hamiltonian for any gauge-invariant quark–gluon system. In the limit  $T_g \rightarrow 0$ , this Hamiltonian is simple and local, and in most cases when spin interaction can be considered as a perturbation, one obtains results for the spectra in an analytic form, which is transparent.

For this reason, we choose below the second, Hamiltonian, approach [15, 16]. We start with the exact Fock–Feynman–Schwinger representation for

---

\*This article was submitted by the author in English.

\*\* e-mail: [simonov@heron.itep.ru](mailto:simonov@heron.itep.ru)

the  $q\bar{q}$  Green's function (for a review, see [17]), taking for simplicity the nonzero flavor case

$$G_{q\bar{q}}(x, y) = \int_0^\infty ds_1 \int_0^\infty ds_2 (Dz)_{xy} (D\bar{z})_{xy} e^{-K_1 - K_2} \quad (1)$$

$$\times \langle \text{tr} \Gamma_{\text{in}}(m_1 - \hat{D}_1) W_\sigma(C) \Gamma_{\text{out}}(m_2 - \hat{D}_2) \rangle_A,$$

where  $K_i = \int_0^{s_i} d\tau_i (m_i + \frac{1}{4}(\dot{z}_\mu^{(i)})^2)$ ;  $\Gamma_{\text{in,out}} = 1, \gamma_5, \dots$  are meson vertices; and  $W_\sigma(C)$  is the Wilson loop with spin insertions, taken along the contour  $C$  formed by paths  $(Dz)_{xy}$  and  $(D\bar{z})_{xy}$ ,

$$W_\sigma(C) = P_F P_A \exp \left( ig \int_C A_\mu dz_\mu \right) \quad (2)$$

$$\times \exp \left( g \int_0^{s_1} \sigma_{\mu\nu}^{(1)} F_{\mu\nu} d\tau_1 - g \int_0^{s_2} \sigma_{\mu\nu}^{(2)} F_{\mu\nu} d\tau_2 \right).$$

The last factor in (2) defines the spin interaction of quark and antiquark. The average  $\langle W_\sigma \rangle_A$  in (1) can be computed exactly through field correlators  $\langle F(1) \dots F(n) \rangle_A$ , and keeping only the lowest one,  $\langle F(1)F(2) \rangle$ , which yields according to a lattice calculation [5] an accuracy around 1% [4], one obtains

$$\langle W_\sigma(C) \rangle_A \simeq \exp \left( -\frac{1}{2} \left[ \int_{S_{\text{min}}} ds_{\mu\nu}(1) \int_{S_{\text{min}}} ds_{\lambda\sigma}(2) \right. \right. \quad (3)$$

$$\left. \left. + \sum_{i,j=1}^2 \int_0^{s_i} \sigma_{\mu\nu}^{(i)} d\tau_i \int_0^{s_j} \sigma_{\lambda\sigma}^{(j)} d\tau_j \right] \langle F_{\mu\nu}(1) F_{\lambda\sigma}(2) \rangle \right).$$

Here,  $ds_{\mu\nu}(i)$  is the surface element,  $i = 1, 2$ , and the double integration in (3) is performed over the minimal area surface  $S_{\text{min}}$  inside the contour  $C$ .

The Gaussian correlator  $\langle F_{\mu\nu}(1) F_{\lambda\sigma}(2) \rangle \equiv D_{\mu\nu, \lambda\sigma}(1, 2)$  can be rewritten identically in terms of two scalar functions  $D(x)$  and  $D_1(x)$  [3], which have been computed on the lattice [6] to have the exponential form  $D(x), D_1(x) \sim \exp(-|x|/T_g)$  with the gluon correlation length  $T_g \approx 0.2$  fm.

As the next step, one introduces the einbein variables  $\mu_i$  and  $\nu$ , the first one to transform the proper times  $s_i, \tau_i$  into the actual (Euclidean) times  $t_i \equiv z_4^{(i)}$ . One has [16]

$$2\mu_i(t_i) = \frac{dt_i}{d\tau_i}, \quad (4)$$

$$\int_0^\infty ds_i (D^4 z^{(i)})_{xy} = \text{const} \int D\mu_i(t_i) (D^3 z^{(i)})_{xy}.$$

The variable  $\nu$  enters in the Gaussian representation of the Nambu–Goto form for  $S_{\text{min}}$  and its stationary value  $\nu_0$  has the physical meaning of the energy density along the string. In the case of several strings, as in the baryon case or the hybrid case, each piece of string has its own parameter  $\nu^{(i)}$ .

To get rid of the path integration in (1), one can go over to the effective Hamiltonian using the identity

$$G_{q\bar{q}}(x, y) = \langle x | \exp(-HT) | y \rangle, \quad (5)$$

where  $T$  is the evolution parameter corresponding to the hypersurface chosen for the Hamiltonian: it is the hyperplane  $z_4 = \text{const}$  in the c.m. case [16].

The final form of the c.m. Hamiltonian (apart from the spin and perturbative terms to be discussed later) for the  $q\bar{q}$  case is [16, 18]

$$H_0 = \sum_{i=1}^2 \left( \frac{m_i^2 + \mathbf{p}_i^2}{2\mu_i} + \frac{\mu_i}{2} \right) \quad (6)$$

$$+ \frac{\hat{L}^2/r^2}{2[\mu_1(1-\zeta)^2 + \mu_2\zeta^2 + \int_0^1 d\beta(\beta-\zeta)^2\nu(\beta)]}$$

$$+ \frac{\sigma^2 r^2}{2} \int_0^1 \frac{d\beta}{\nu(\beta)} + \int_0^1 \frac{\nu(\beta)}{2} d\beta.$$

Here,  $\zeta = (\mu_1 + \int_0^1 \beta\nu d\beta) / (\mu_1 + \mu_2 + \int_0^1 \beta\nu d\beta)$  and  $\mu_i$  and  $\nu(\beta)$  are found from the stationary point of the Hamiltonian

$$\frac{\partial H_0}{\partial \mu_i} \Big|_{\mu_i=\mu_i^{(0)}} = 0, \quad \frac{\partial H_0}{\partial \nu} \Big|_{\nu=\nu^{(0)}} = 0. \quad (7)$$

Note that  $H_0$  contains as input only  $m_1, m_2$ , and  $\sigma$ , where  $m_i$  are current masses defined at the scale 1 GeV. The further analysis is simplified by the observation that, for  $L = 0$ , one finds  $\nu^{(0)} = \sigma r$  from (7) and  $\mu_i = \sqrt{m_i^2 + \mathbf{p}^2}$ ; hence,  $H_0$  becomes the usual relativistic quark model Hamiltonian

$$H_0(L = 0) = \sum_{i=1}^2 \sqrt{m_i^2 + \mathbf{p}^2} + \sigma r. \quad (8)$$

But  $H_0$  is not the whole story; one should take into account three additional terms  $H_{\text{self}}, H_{\text{spin}}$ , and  $H_{\text{Coul}}$ , namely, spin terms in (3) which produce two types of contributions: self-energy correction [19]

$$H_{\text{self}} = \sum_{i=1}^2 \frac{\Delta m_q^2(i)}{2\mu_i}, \quad \Delta m_q^2 = -\frac{4\sigma}{\pi} \eta(m_i), \quad (9)$$

$$\eta(0) \cong 0.9-1,$$

where  $\eta(m_i)$  is a known function of current mass  $m_i$  [19], and spin-dependent interaction between quark and antiquark  $H_{\text{spin}}$  [1, 20], which is entirely described by the field correlators  $D(x)$  and  $D_1(x)$ , including also the one-gluon-exchange part present in  $D_1(x)$ .

Finally, one should take into account gluon-exchange contributions [8], which can be divided into the Coulomb part  $H_{\text{Coul}} = -\frac{4}{3} \frac{\alpha_s(r)}{r}$  and  $H_{\text{rad}}$  including spacelike gluon exchanges and perturbative self-energy corrections (we shall systematically omit these corrections since they are small for light quarks to be discussed below). In addition, there are gluon contributions which are nondiagonal in number of gluons  $n_g$  and quarks (until now only the sector  $n_g = 0$  was considered) and therefore mixing meson states with hybrids and glueballs [21]; we call these terms  $H_{\text{mix}}$  and refer the reader to [21] and the references cited therein for more discussion. Assembling all terms together, one has the following total Hamiltonian in the limit of large  $N_c$  and small  $T_g$ :

$$H = H_0 + H_{\text{self}} + H_{\text{spin}} + H_{\text{Coul}} + H_{\text{rad}} + H_{\text{mix}}. \tag{10}$$

We start with  $H_0 = H_R + H_{\text{string}}$ , where  $H_{\text{string}}$  is the term proportional to  $\hat{L}^2$  in (6) and  $H_R$  is all the remaining terms in (6). The eigenvalues  $M_0$  of  $H_R$  can be given with 1% accuracy by [22]

$$M_0^2 \approx 8\sigma L + 4\pi\sigma \left( n + \frac{3}{4} \right), \tag{11}$$

where  $n$  is the radial quantum number,  $n = 0, 1, 2, \dots$ . Remarkably,  $M_0 \approx 4\mu_0$ , and for  $L = n = 0$ , one has  $\mu_0(0, 0) = 0.35$  GeV for  $\sigma = 0.18$  GeV<sup>2</sup>, and  $\mu_0$  is fast increasing with growing  $n$  and  $L$ . This fact partly explains that spin interactions become unimportant beyond  $L = 0, 1, 2$  since they are proportional to  $d\tau_1 d\tau_2 \sim dt_1 dt_2 / (4\mu_1 \mu_2)$  {see (3) and [1, 22]}. Thus, constituent mass (which is actually “constituent energy”)  $\mu_0$  is “running.” The validity of  $\mu_0$  as a socially accepted “constituent mass” is confirmed by its numerical value given above, by the spin splittings of light and heavy mesons [23], and by baryon magnetic moments expressed directly through  $\mu_0$  and being in agreement with experimental values [24].

We now come to the gluon-containing systems, hybrids and glueballs. Referring the reader to the original papers [9–11], one can recapitulate the main results for the spectrum. In both cases the total Hamiltonian has the same form as in (10); however, the contribution of corrections differs.

For glueballs, it was argued in [11] that  $H_0$  (6) has the same form, but with  $m_i = 0$  and  $\sigma \rightarrow \sigma_{\text{adj}} = (9/4)\sigma$ , while  $H_{\text{self}} = 0$  due to gauge invariance.

We now come to the next topic of this talk: hybrids and their role in hadron dynamics. We start with the hybrid Hamiltonian and spectrum. This topic in the framework of FCM was considered in [9, 10]. The Hamiltonian  $H_0$  for the hybrid looks like [1]

$$H_0^{(h)} = \frac{m_1^2}{2\mu_1} + \frac{m_2^2}{2\mu_2} + \frac{\mu_1 + \mu_2 + \mu_g}{2} \tag{12}$$

$$+ \frac{\mathbf{p}_\xi^2 + \mathbf{p}_\eta^2}{2\mu} + \sigma \sum_{i=1}^2 |\mathbf{r}_g - \mathbf{r}_i| + H_{\text{str}}.$$

Here,  $\mathbf{p}_\xi, \mathbf{p}_\eta$  are Jacobi momenta of the three-body system;  $H_{\text{self}}$  is the same as for a meson, while  $H_{\text{spin}}$  and  $H_{\text{Coul}}$  have different structure [10];  $H_{\text{str}}$  is the string term similar to  $H_{\text{string}}$  in (10).

The main feature of the present approach based on background perturbation theory is that the valence gluon in the hybrid is situated at some point on the string connecting the quark and antiquark, and the gluon creates a kink on the string so that two pieces of the string move independently (however, connected at the point of the gluon). This differs strongly from the flux-tube model, where the hybrid is associated with the string excitation as a whole.

Results for light and heavy exotic  $1^{-+}$  hybrids also given in [1] and are in agreement with lattice calculations. Typically, an additional gluon in the exotic ( $L = 1$ ) state “weights” 1.2–1.5 GeV for light to heavy quarks, while a nonexotic gluon ( $L = 0$ ) brings about 1 GeV to the mass of the total  $q\bar{q}g$  system.

### 3. HAMILTONIAN AND FOCK STATES

As was mentioned above, the QCD Hamiltonian is introduced in correspondence with the chosen hypersurface, which defines internal coordinates  $\{\xi_k\}$  lying inside the hypersurface, and the evolution parameter, perpendicular to it. Two extreme choices are frequently used: (1) the c.m. coordinate system with the hypersurface  $x_4 = \text{const}$ , which implies that all hadron constituents have the same (Euclidean) time coordinates  $x_4^{(i)} = \text{const}, i = 1, \dots, n$ ; (2) the light-cone coordinate system, where the role of  $x_4$  and  $x_4^{(i)}$  is played by the  $x_+, x_+^{(i)}$  components,  $x_+ = (x_0 + x_3)/\sqrt{2}$ .

To describe the structure of the Hamiltonian in general terms, we first assume that bound valence states exist for mesons, glueballs, and baryons consisting of a minimal number of constituents. To form the Fock tower of states starting with the given valence state, one can add gluons and  $q\bar{q}$  pairs keeping

the  $J^{PC}$  assignment intact. At this point, we make the basic simplifying approximation assuming that the number of colors  $N_c$  tends to infinity, so that one can do for any physical quantity an expansion in powers of  $1/N_c$ . Recent lattice data confirm a good convergence of this expansion for  $N_c = 3, 4, 6$  and all quantities considered [25] (glueball mass, critical temperature, topological susceptibility, etc.).

Then, the construction of the Fock tower is greatly simplified since any additional  $q\bar{q}$  pair enters with the coefficient  $1/N_c$  and any additional white (e.g., glueball) component brings in the coefficient  $1/N_c^2$ . In view of this, in the leading order of  $1/N_c$ , the Fock tower is formed only by creating additional gluons in the system, i.e., by the hybrid excitation of the original (valence) system. Thus, all of the Fock tower consists of the valence component and its hybrid equivalents, and each line of this tower is characterized by the number  $n$  of added gluons. Then, the internal coordinates  $\{\xi\}_n$  describe coordinates and polarizations of  $n$  gluons in addition to those of valence constituents.

We turn now to the Hamiltonian  $H$ , assuming it to be either the total QCD Hamiltonian  $H_{\text{QCD}}$  or the effective Hamiltonian  $H^{(\text{eff})}$ , obtained from  $H_{\text{QCD}}$  by integrating out short-range degrees of freedom. We shall denote the diagonal elements of  $H$ , describing the dynamics of the  $n$ th hybrid excitation of the  $s$ th valence state ( $s = m\{f\bar{f}\}, gg, 3g, b\{f_1 f_2 f_3\}$  for mesons, two-gluon and three-gluon glueballs, and baryons, respectively, with  $f_i$  denoting flavor of quarks), as  $H_{nn}^{(s)}$ . For nondiagonal elements, we need only the lowest order operators  $H_{n,n+1}^{(s)}$  and  $H_{n-1,n}^{(s)}$  describing creation or annihilation of one additional gluon, viz.,

$$H_{\bar{q}qg} = g \int \bar{q}(\mathbf{x}, 0) \hat{a}(\mathbf{x}, 0) q(\mathbf{x}, 0) d^3x, \quad (13)$$

$$H_{g2g} = \frac{g}{2} f^{abc} \int (\partial_\mu a_\nu^a - \partial_\nu a_\mu^a) a_\mu^b a_\nu^c d^3x. \quad (14)$$

As it is clear from (13), (14), the first operator refers to the gluon creation from the quark line, while the second refers to the creation of two gluons from the gluon line. In what follows, we shall be mostly interested in the first operator, which yields a dominant contribution at large energies and physically describes addition of one last crosspiece to the ladder of gluon exchanges between quark lines, while (14) corresponds in the same ladder to the  $\alpha_s$  renormalization graphs.

The effective Hamiltonian in the one-hadron sector can be written as follows:

$$\hat{H} = \hat{H}^{(0)} + \hat{V}, \quad (15)$$

where  $H^{(0)}$  is the diagonal matrix of operators,

$$H^{(0)} = \{H_{00}^{(s)}, H_{11}^{(s)}, H_{22}^{(s)}, \dots\}, \quad (16)$$

while  $\hat{V}$  is the sum of operators (13) and (14), creating and annihilating one gluon. In (16),  $H_{nn}^{(s)}$  is the Hamiltonian operator for what we call the “ $n$  hybrid,” i.e., a bound state of the system, consisting of  $n$  gluons together with the particles of the valence component. In this way, the  $n$  hybrid for the valence  $\rho$  meson is the system consisting of  $q\bar{q}$  plus  $n$  gluons “sitting” on the string connecting  $q$  and  $\bar{q}$ .

Before applying the stationary perturbation theory in  $\hat{V}$  to the Hamiltonian (15), one should have in mind that there are two types of excitations of the ground-state valence Fock component: (1) Each of the operators  $H_{nn}^{(s)}, n = 0, 1, \dots$ , has an infinite number of excited states, when radial or orbital motion of any degree of freedom is excited. (2) In addition, one can add a gluon, which means exciting the string and these excitations due to the operator  $\hat{V}$  transform the  $n$ th Fock component  $\psi_n^{(s)}$  into  $\psi_{n+1}^{(s)}$ .

The wave equation for the Fock tower  $\Psi_N\{P, \xi\}$  has the standard form

$$\hat{H}\Psi_N = (\hat{H}^{(0)} + \hat{V})\Psi_N = E_N\Psi_N, \quad (17)$$

where  $N$  numerates energy eigenvalues, and  $\xi$  is a set of internal quantum numbers in the  $n$  hybrid or in the integral form

$$\Psi_N = \Psi_N^{(0)} - G^{(0)}\hat{V}\Psi_N. \quad (18)$$

Here,  $G^{(0)}$  is diagonal in Fock components,

$$G^{(0)}(E) = \frac{1}{\hat{H}^{(0)} - E}, \quad G_{nm}^{(0)}(E) = \delta_{nm} \frac{1}{H_{nn}^{(s)} - E}, \quad (19)$$

and  $\Psi_N^{(0)}$  is the eigenfunction of  $\hat{H}^{(0)}$ ,

$$\hat{H}^{(0)}\Psi_N^{(0)} = E_N^{(0)}\Psi_N^{(0)}, \quad (20)$$

and, since  $\hat{H}^{(0)}$  is diagonal,  $\Psi_N^{(0)}$  has only one Fock component,  $\Psi_N^{(0)} = \psi_n(P, \{\xi\}_n), n = 0, 1, 2, \dots$ , and the eigenvalues  $E_N^{(0)}$  contain all possible excitation energies of the  $n$  hybrid, with the number  $n$  of gluons in the system fixed,

$$E_N^{(0)} = E_n^{(0)}(P) = \sqrt{\mathbf{P}^2 + M_{n\{k\}}^2}, \quad (21)$$

where  $\{k\}$  denotes the set of quantum numbers of the excited  $n$  hybrid.

From (18), one obtains in the standard way corrections to the eigenvalues and eigenfunctions.

As a first step, one should specify the unperturbed functions  $\Psi_N^{(0)}$ , introducing the set of quantum numbers  $\{k\}$  defining the excited hybrid state for each  $n$ -hybrid Fock component  $\psi_n(P\{\xi\}_n)$ ; therefore, we shall denote

$$\Psi_N^{(0)} = \psi_{n\{k\}}(P, \{\xi\}_n), \quad n = 0, 1, 2, \dots \quad (22)$$

The set of functions  $\psi_{n\{k\}}$  with all possible  $n$  and  $\{k\}$  is a complete set to be used in the expansion of the exact wave function (Fock tower)  $\Psi_N$ :

$$\Psi_N = \sum_{m\{k\}} c_{m\{k\}}^N \psi_{m\{k\}}. \quad (23)$$

Using the orthonormality condition

$$\int \psi_{m\{k\}}^+ \psi_{n\{p\}} d\Gamma = \delta_{mn} \delta_{\{k\}\{p\}}, \quad (24)$$

where  $d\Gamma$  implies integration over all internal coordinates and summation over all indices, one obtains from (17) an equation for  $c_{m\{k\}}^N$  and  $E_N$ ,

$$c_{n\{p\}}^N (E_N - E_{n\{p\}}^{(0)}) = \sum_{m\{k\}} c_{m\{k\}}^N V_{n\{p\},m\{k\}}, \quad (25)$$

where we have defined

$$V_{n\{p\},m\{k\}} = \int \psi_{n\{p\}}^+ \hat{V} \psi_{m\{k\}} d\Gamma, \quad (26)$$

and  $E_{n\{p\}}^{(0)}$  is the eigenvalue of the wave-function component  $\psi_{n\{p\}}$ .

Consider now the Fock tower built on the valence component  $\psi_{\nu\{\kappa\}}$ , where  $\nu$  can be any integer. For  $\nu\{\kappa\} = 0\{0\}$ , this valence component corresponds to an unperturbed hadron with a minimal number of valence particles. For higher values of  $\nu\{\kappa\}$ , the Fock component  $\psi_{\nu\{\kappa\}}$  corresponds to the hybrid with  $\nu$  gluons, which after taking into account the interaction is “dressed up” and acquires all other Fock components, so that the number  $N$  in (23) contains the “bare number”  $\nu\{\kappa\}$  as its part  $N = \nu\{\kappa\}, \dots$  (at least for small perturbation  $\hat{V}$ ).

One can impose on  $\Psi_N$  the orthonormality condition

$$\int \Psi_N^+ \Psi_M d\Gamma = \sum_{m\{k\}} c_{m\{k\}}^N c_{m\{k\}}^M = \delta_{NM}. \quad (27)$$

Expanding in powers of  $\hat{V}$ , one has

$$c_{m\{k\}}^{N(\nu\{\kappa\})} = \delta_{m\nu} \delta_{\{k\}\{\kappa\}} + c_{m\{k\}}^{N(1)} + c_{m\{k\}}^{N(2)} + \dots, \quad (28)$$

$$E_{N(\nu\{\kappa\})} = E_{\nu\{\kappa\}}^{(0)} + E_N^{(1)} + E_N^{(2)} + \dots \quad (29)$$

It is easy to see that  $E_N^{(1)} \equiv 0$ , while for  $c^{(1)}$  one obtains from (25) the standard expression

$$c_{n\{p\}}^{N(1)} = \frac{V_{n\{p\},\nu\{\kappa\}}}{E_{\nu\{\kappa\}}^{(0)} - E_{n\{p\}}^{(0)}}. \quad (30)$$

In what follows, we shall be interested in the high Fock components,  $\nu + l, \{k\}$ , obtained by adding  $l$  gluons to the valence component  $\nu\{\kappa\}$ . Using (25) and (28), one obtains

$$c_{\nu+l,\{k\}}^{N(\nu\{\kappa\})} = \sum_{\{k_1\} \dots \{k_l\}} \frac{V_{\nu+l\{k\},\nu+l-1\{k_1\}}}{E_{\nu\{\kappa\}}^{(0)} - E_{\nu+l\{k\}}^{(0)}} \times \frac{V_{\nu+l-1\{k_1\},\nu+l-2\{k_2\}}}{E_{\nu\{\kappa\}}^{(0)} - E_{\nu+l-1\{k_1\}}^{(0)}} \dots \frac{V_{\nu+1\{k_l\},\nu\{\kappa\}}}{E_{\nu\{\kappa\}}^{(0)} - E_{\nu+1\{k_l\}}^{(0)}} \times O(V^{l+2}). \quad (31)$$

Since  $\hat{V}$  is proportional to  $g$ , one obtains in (28) the perturbation series in powers of  $\alpha_s$  for  $c^N$  and, hence, for  $\Psi_N$  (23). One should note that  $\alpha_s(Q^2)$  is the background coupling constant, having the property of saturation for positive  $Q^2$  [8, 26], and the background perturbation series has no Landau ghost pole and is defined in all of the Euclidean region of  $Q^2$ .

The estimate of the mixing between meson and hybrid was done earlier in the framework of the potential model for the meson in [27]. In [21], the mixing between hybrid, meson, and glueball states was calculated in the framework of the present formalism and we briefly summarize the results. One must estimate the matrix element (26) between meson and hybrid wave functions taking the operator  $\hat{V}$  in the form of (13), where the operator of gluon emission at the point  $(\mathbf{x}, 0)$  can be approximated as

$$a_\mu(\mathbf{x}, t) = \sum_{\mathbf{k}, \lambda} \frac{1}{\sqrt{2\mu(\mathbf{k})V}} \times [\exp(i\mathbf{k} \cdot \mathbf{x} - i\mu t) e_\mu^{(\lambda)} c_\lambda(\mathbf{k}) + e_\mu^{(\lambda)} c_\lambda^+(\mathbf{k}) \exp(-i\mathbf{k} \cdot \mathbf{x} + i\mu t)]. \quad (32)$$

Omitting for simplicity all polarization vectors and spin-coupling coefficients which are of the order of unity, one has the matrix element

$$V_{Mh} = \frac{g}{\sqrt{2\mu_g}} \int \varphi_M(\mathbf{r})^\mu \psi_h^+(0, \mathbf{r}) d^3r, \quad (33)$$

where  $\varphi_M(\mathbf{r})$  and  ${}^\mu\psi_h(\mathbf{r}_1, \mathbf{r}_2)$  are meson and hybrid wave functions, respectively, and in (33) it is taken into account that the gluon is emitted (absorbed) from the quark position.

Using a realistic Gaussian approximation for the wave functions in (33), one obtains the estimate [21]

$$V_{Mh} \approx g \cdot 0.08 \text{ GeV}. \quad (34)$$

A similar estimate is obtained in [21] for the hybrid–glueball mixing matrix element, while the meson–glueball mixing is second-order in (34).

Hence, the first-order hybrid admixture coefficient (30) for the meson is

$$C_{Mh} = \frac{V_{Mh}}{E_M^{(0)} - E_h^{(0)}} = \frac{V_{Mh}}{\Delta M_{Mh}}, \quad (35)$$

and for the ground-state low-lying mesons when  $\Delta M_{Mh} \sim 1$  GeV, it is small,  $C_{Mh} \sim 0.1$ – $0.15$ , yielding a 1–2% probability. However, for higher states in the region  $M_M \gtrsim 1.5$  GeV, the mass difference  $\Delta M_{Mh}$  of mesons and hybrids with the same quantum numbers can be around 200 MeV, and the mixing becomes extremely important, also for meson–glueball mixing, which can be written as

$$C_{MG} = \sum_h \frac{V_{Mh} V_{hG}}{\Delta M_{Mh} \Delta M_{hG}}, \quad (36)$$

and  $V_{Mh} \sim V_{hG}$ . A good example is given by the three  $f_0$  mesons,  $f_0(1390)$ ,  $f_0(1500)$ , and  $f_0(1710)$ , studied on the lattice in [28].

The authors [28] arrive at the following result of careful lattice studies:

$$\begin{aligned} |f_0(1710)\rangle &= 0.859|g\rangle + 0.302|s\bar{s}\rangle + 0.413|n\bar{n}\rangle, \\ |f_0(1500)\rangle &= -0.128|g\rangle + 0.908|s\bar{s}\rangle - 0.399|n\bar{n}\rangle, \\ |f_0(1390)\rangle &= -0.495|g\rangle + 0.290|s\bar{s}\rangle + 0.819|n\bar{n}\rangle. \end{aligned} \quad (37)$$

From (37), it is clear that a strong mixing occurs between states in the region 1.4–1.7 GeV; however, the dominant valence component in all three cases is clearly visible: it is  $(n\bar{n})$  for  $f_0(1390)$ ,  $(s\bar{s})$  for  $f_0(1500)$ , and the two-gluon glueball ( $g$ ) for  $f_0(1710)$ .

#### 4. SEA QUARKS IN THE SPECTRUM AND STRONG DECAYS

In all the discussion above, the dynamics in the  $q\bar{q}$  system was described by the Wilson loop  $W_\sigma(C)$  in (1). However, the formalism in (1)–(3) is correct only in the large- $N_c$  limit, which holds for the lower part of the spectrum with accuracy of the order of 10%. For higher excited states with the radius exceeding 1.3–1.4 fm, one should take into account the admixture of quark pairs. This can be accomplished formally replacing  $W_\sigma(C)$  in (1) by the product  $W_\sigma(C) \prod_f \det(m_f + \hat{D})$ . Using the heat kernel (Fock–Feynman–Schwinger) representation for the determinant, one has

$$\text{Re}[\ln \det(m + \hat{D})] = \frac{1}{2} \ln \det(m^2 + \hat{D}^2) \quad (38)$$

$$\begin{aligned} &= \int d^4x \int_0^\infty \frac{ds}{s} \exp(-m^2 s) \\ &\times (Dz)_{xx} \exp(-K) W(C_x), \end{aligned}$$

where  $W(C)$  is the Wilson loop without spin factors, present in (2), and  $C_x$  is the closed contour beginning and ending at the point  $x$ . In this way, the determinant can be expanded in a series in powers of number of sea-quark loops and the averaging of the product above yields

$$\begin{aligned} &\langle W_\sigma(C) \det(m + \hat{D}) \rangle \\ &= \langle W_\sigma(C) \rangle \langle \det(m + \hat{D}) \rangle + \frac{a_1}{N_c} W_1(C, C_x) + \dots, \end{aligned} \quad (39)$$

where

$$W_1(C, C_x) \equiv \langle W_\sigma(C) W(C_x) \rangle - \langle W_\sigma(C) \rangle \langle W(C_x) \rangle. \quad (40)$$

It was shown in [29] that the interaction of Wilson loops given by (40) effectively produces holes in the original world sheet of the string in  $W_\sigma(C)$ . It was argued in [30] that, for unstable states with a lifetime  $T \sim 1$  fm and average radius larger than 1.4 fm, the holes due to the  $q\bar{q}$  pairs can be in metastable equilibrium, which can be called the “predecay state.” In this state, the linear potential between quarks starts to saturate, and the resulting meson masses calculated in [30] are strongly decreased by 200–500 MeV, which is in good agreement with experimental data. The resulting radial Regge trajectories are of surprisingly good linear form and are given in [31].

Another phenomenon, where sea quarks play the crucial role, is the strong decay process. As was shown in [32], one can distinguish three possible mechanisms of strong decays, where nonperturbative QCD is involved: (1) chiral mechanism, which appears after bosonization [33, 34]; (2) string-breaking mechanism; and (3) pair creation via the intermediate hybrid or glueball formation.

Taking into account the valence (perturbative) gluon field  $a_\mu(x)$ , one has after averaging over the background gluon field and bosonization the following effective quark–meson Lagrangian [32–34]:

$$\begin{aligned} L_{\text{QML}} &= \int d^4x \int d^4y \{ {}^f \psi_{a\alpha}^+(x) \\ &\times [i(\hat{\partial} - ig\hat{a}) + im_f]_{\alpha\beta} \delta^{(4)}(x-y) \delta_{fg} \\ &+ iM_S \hat{U}_{\alpha\beta}^{(fg)}(x, y) {}^g \psi_{a\beta}(y) \\ &- 2n_f [J(x, y)]^{-1} M_S^2(x, y) \}, \end{aligned} \quad (41)$$

where  $\hat{U} = \exp(i\hat{\phi}(x, y)\gamma_5)$ ,  $\hat{\phi} = t^a \phi_a / f_\pi$  being the pionic field;  $n_f$  is number of flavors;  $J(x, y)$  is the kernel proportional to the integral of the field correlator;

$f, g$  are flavor indices; and  $M_S(x, y)$  is the effective quark mass operator containing the string connecting the quark to the closest antiquark position (for details and notation, see [32–34]).

All decay mechanisms listed above are contained in the Lagrangian (41); e.g., the chiral mechanism is obtained by expanding  $\hat{U}(\phi)$  in powers of  $\phi_a$  (as for the details and comparison with experiment, see [33] and the references cited therein).

The nonperturbative string breaking mechanism is described in (41) by the term  $\psi^+ M_S \psi$ , where it is essential that the mass operator  $M_S(x, y) = M_S^{(\text{br})}$  enters at the vertex of the quark–antiquark formation (rather than the string mass operator in the quark propagation). The explicit computation of  $M_S^{(\text{br})}$  in the string-breaking term was done in [32] and yields

$$\Delta L^{(\text{br})} = \frac{2T_g \sigma}{\sqrt{\pi}} \int d^4x \bar{\psi}(x) \psi(x). \quad (42)$$

As is clear from (42), one obtains the  ${}^3P_0$  mechanism with the predicted coefficient, which agrees with the generic phenomenologically fitted value.

Finally, mechanism 3 is given by the combination of the  $q\bar{q}$  generation by the perturbative gluon, due to the term  $\psi^+ \hat{a} \psi$ , with the subsequent string world sheet envelopment of the gluon and quark trajectories. In this way, one obtains hybrid-mediated decay and—for the OZI-violating processes—glueball-mediated decay, suggested in [32]. The relative role and theoretical estimates of all three mechanisms were not elaborated in [32].

## 5. CONCLUSIONS

It was shown above that the field correlator method is a powerful tool for the investigation of all effects in the QCD spectrum. In particular, the low-lying part of the spectrum, where the string breaking is not essential, is well described by the Hamiltonian (10) containing the minimum number of input parameters: current quark masses, string tension, and  $\alpha_s$ . Here, effects of mixing and decay are inessential (less than 10%) and the leading large  $N_c$  approximation is valid. However, for higher masses (and for high-energy processes), one should take into account the Fock tower structure of hadrons, where, in particular, hybrids contribute significantly. Superficially, these Fock towers are similar to the light-cone Fock states considered in [35]; however, the (essential) difference is that, in our case, all Fock components are bound states (mesons or hybrids in the leading large- $N_c$  limit), while in [35] only perturbative dynamics is present.

It was demonstrated above that also the  $1/N_c$  effects, namely, the glueball admixture in mesons and decay amplitudes, are easily computed in the framework of the FCM, and moreover no new parameters are introduced. However, only the first step is done in [32] for the construction of decay and production amplitudes.

## ACKNOWLEDGMENTS

The partial support of INTAS (grant nos. 00-110 and 00-366) is gratefully acknowledged.

## REFERENCES

1. Yu. A. Simonov, in *QCD: Perturbative or Non-perturbative*, Ed. by L. Ferreira, P. Nogueira, and J. I. Silva-Marcos (World Sci., Singapore, 2001); hep-ph/9911237.
2. C. Michael, hep-lat/0302001.
3. H. G. Dosch, Phys. Lett. B **190**, 177 (1987); H. G. Dosch and Yu. A. Simonov, Phys. Lett. B **205**, 339 (1988); Yu. A. Simonov, Nucl. Phys. B **307**, 512 (1988); for a review see A. Di Giacomo, H. G. Dosch, V. I. Shevchenko, and Yu. A. Simonov, Phys. Rep. **372**, 319 (2002); hep-ph/0007223.
4. Yu. A. Simonov, Pis'ma Zh. Éksp. Teor. Fiz. **71**, 187 (2000) [JETP Lett. **71**, 127 (2000)]; V. I. Shevchenko and Yu. A. Simonov, Phys. Rev. Lett. **85**, 1811 (2000).
5. G. S. Bali, Phys. Rev. D **62**, 114503 (2000); S. Deldar, Phys. Rev. D **62**, 034509 (2000).
6. A. Di Giacomo and H. Panagopoulos, Phys. Lett. B **285**, 133 (1992); A. Di Giacomo, E. Meggiolaro, and H. Panagopoulos, Nucl. Phys. B **483**, 371 (1997); A. Di Giacomo and E. Meggiolaro, hep-lat/0203012; G. S. Bali, N. Brambilla, and A. Vairo, Phys. Lett. B **421**, 265 (1998).
7. Yu. A. Simonov, Nucl. Phys. B **592**, 350 (2001); M. Eidemüller, H. G. Dosch, and M. Jamin, Nucl. Phys. B (Proc. Suppl.) **86**, 421 (2000).
8. Yu. A. Simonov, Yad. Fiz. **58**, 113 (1995) [Phys. At. Nucl. **58**, 107 (1995)]; Pis'ma Zh. Éksp. Teor. Fiz. **57**, 525 (1993) [JETP Lett. **75**, 525 (1993)]; in *Lecture Notes in Physics*, Ed. by H. Latal and W. Schweiger (Springer, Berlin-Heidelberg, 1996), Vol. 479, p. 139.
9. Yu. A. Simonov, in *Proceedings of the Workshop on Physics and Detectors for DAΦNE, Frascati, 1991*; Nucl. Phys. B (Proc. Suppl.) **23**, 283 (1991); Nuovo Cimento A **107**, 2629 (1994); Yu. S. Kalashnikova and Yu. B. Yufryakov, Phys. Lett. B **359**, 175 (1995); Yu. Yufryakov, hep-ph/9510358.
10. Yu. S. Kalashnikova and D. S. Kuzmenko, hep-ph/0203128.
11. Yu. A. Simonov, Phys. Lett. B **249**, 514 (1990); A. B. Kaidalov and Yu. A. Simonov, Phys. Lett. B **477**, 163 (2000); Yad. Fiz. **63**, 1507 (2000) [Phys. At. Nucl. **63**, 1428 (2000)].

12. Yu. A. Simonov, *Yad. Fiz.* **60**, 2252 (1997) [*Phys. At. Nucl.* **60**, 2069 (1997)]; hep-ph/9704301; Yu. A. Simonov and J. A. Tjon, *Phys. Rev. D* **62**, 014501 (2000); **62**, 094511 (2000).
13. Yu. A. Simonov, *Yad. Fiz.* **63**, 106 (2000) [*Phys. At. Nucl.* **63**, 94 (2000)].
14. Yu. A. Simonov, *Yad. Fiz.* **62**, 2087 (1999) [*Phys. At. Nucl.* **62**, 1932 (1999)]; hep-ph/9912383; Yu. A. Simonov, J. A. Tjon, and J. Weda, *Phys. Rev. D* **65**, 094013 (2002).
15. Yu. A. Simonov, *Phys. Lett. B* **226**, 151 (1989); **228**, 413 (1989).
16. A. Yu. Dubin, A. B. Kaidalov, and Yu. A. Simonov, *Phys. Lett. B* **323**, 41 (1994); *Yad. Fiz.* **56** (11), 213 (1993) [*Phys. At. Nucl.* **56**, 1745 (1993)].
17. Yu. A. Simonov and J. A. Tjon, *Ann. Phys. (N.Y.)* **300**, 54 (2002).
18. E. L. Gubankova and A. Yu. Dubin, *Phys. Lett. B* **334**, 180 (1994).
19. Yu. A. Simonov, *Phys. Lett. B* **515**, 137 (2001).
20. Yu. A. Simonov, *Nucl. Phys. B* **324**, 67 (1989); A. M. Badalian and Yu. A. Simonov, *Yad. Fiz.* **59**, 2247 (1996) [*Phys. At. Nucl.* **59**, 2164 (1996)].
21. Yu. A. Simonov, *Yad. Fiz.* **64**, 1956 (2001) [*Phys. At. Nucl.* **64**, 1876 (2001)].
22. T. J. Allen, G. Goebel, M. G. Olsson, and S. Veseli, *Phys. Rev. D* **64**, 094011 (2001).
23. A. M. Badalian, B. L. G. Bakker, and V. L. Morgunov, *Yad. Fiz.* **63**, 1722 (2000) [*Phys. At. Nucl.* **63**, 1635 (2000)]; A. M. Badalian and B. L. G. Bakker, *Phys. Rev. D* **64**, 114010 (2001).
24. B. O. Kerbikov and Yu. A. Simonov, *Phys. Rev. D* **62**, 093016 (2000).
25. M. Teper, hep-ph/0203203.
26. A. M. Badalian and D. S. Kuzmenko, *Phys. Rev. D* **65**, 016004 (2002).
27. A. Le Yaouanc, L. Oliver, O. Pène, *et al.*, *Z. Phys. C* **28**, 309 (1985); F. Iddir, S. Saïr, and O. Pène, *Phys. Lett. B* **433**, 125 (1998).
28. W. Lee and D. Weingarten, *Nucl. Phys. B (Proc. Suppl.)* **53**, 232 (1997); **63**, 194 (1998); **73**, 249 (1999); hep-lat/9910008; hep-lat/9811005.
29. V. Shevchenko and Yu. A. Simonov, *Phys. Rev. D* **66**, 056012 (2002).
30. A. M. Badalian, B. L. G. Bakker, and Yu. A. Simonov, *Phys. Rev. D* **66**, 034026 (2002).
31. Yu. A. Simonov, *Yad. Fiz.* **66**, 2088 (2003) [*Phys. At. Nucl.* **66**, 2038 (2003)].
32. Yu. A. Simonov, *Yad. Fiz.* **66**, 2095 (2003) [*Phys. At. Nucl.* **66**, 2045 (2003)].
33. Yu. A. Simonov, *Phys. Rev. D* **65**, 094018 (2002).
34. Yu. A. Simonov, hep-ph/0302090.
35. S. J. Brodsky and G. P. Lepage, in *Perturbative Quantum Chromodynamics*, Ed. by A. H. Mueller (World Sci., Singapore, 1989).

## ELEMENTARY PARTICLES AND FIELDS

### Theory

# A Short-Distance Quark–Antiquark Potential\*

A. M. Badalian\*\* and D. S. Kuzmenko\*\*\*

*Institute of Theoretical and Experimental Physics,  
Bol'shaya Cheremushkinskaya ul. 25, Moscow, 117259 Russia*

Received March 20, 2003

**Abstract**—Leading terms of the static quark–antiquark potential in background perturbation theory are reviewed, including perturbative, nonperturbative, and interference ones. The potential is shown to describe lattice data at short quark–antiquark separations with a good accuracy. © 2004 MAIK “Nauka/Interperiodica”.

1. The static quark–antiquark potential was calculated with high accuracy in lattice QCD some years ago [1]. It was shown to be well described by the phenomenological Coulomb plus linear Cornell potential at sufficiently large quark–antiquark separations,  $R \gtrsim 0.2$  fm. At smaller distances, the Cornell potential is not applicable. The region  $0.03 \leq R \leq 0.22$  fm was studied in quenched lattice theory in detail [2], and the conclusion was made that the standard perturbative theory expansion in coupling constant does not yield an appropriate description of lattice results, at least in one- and two-loop approximations. As is known, the succeeding terms of the asymptotic coupling expansion depend on the renormalization scheme, and so does the corresponding static potential. One can argue that the standard perturbative theory fails because this region is close to the unphysical Landau pole of the strong coupling.

There is a wealth of literature on the short-distance potential behavior (see [3–6] and references therein). In this paper, we consider the static quark–antiquark potential in background perturbation theory (BPT) [7]. This potential incorporates both the features of the standard perturbative potential at tiny distances,  $R \lesssim 0.05$  fm, and of the Cornell potential at  $R \gtrsim 0.4$  fm due to taking nonperturbative background field effects into account. After a brief review of leading background potential terms, we present our results concerning the behavior of the potential at short distances and its comparison with the lattice [5].

2. The gluon field  $A_\mu$  in BPT is divided into the dynamical perturbative part  $a_\mu$  and the background nonperturbative field  $B_\mu$ :

$$A_\mu = a_\mu + B_\mu. \quad (1)$$

The background field, in which perturbative valence gluons propagate, results in the creation of a vacuum condensate.

The static potential has to be calculated using the vacuum averaged Wilson loop for the quark–antiquark pair. The BPT Wilson loop expansion in the field  $a_\mu$  has the form [7]

$$W(B + a) = W(B) + \sum_{n=1}^{\infty} (ig)^n \quad (2)$$

$$\times W^{(n)}(B; x(1) \cdots x(n)) a_{\mu_1} \cdots a_{\mu_n} dx_{\mu_1}(1) \cdots dx_{\mu_n}(n).$$

To perform the averaging of the expression (2), we take into account that the linear in  $a_\mu$  term vanishes,

$$\langle W(B + a) \rangle_{B,a} \quad (3)$$

$$= \langle W(B) \rangle_B - g^2 \langle W^{(2)}(B; x, y) \rangle_B dx dy + \dots,$$

where

$$-g^2 W^{(2)} dx dy = -g^2 \int \Phi^{\alpha\beta}(x, y, B) t_{\delta\alpha}^a t_{\beta\gamma}^b \quad (4)$$

$$\times G_{\mu\nu}^{ab}(x, y, B) \Phi^{\gamma\delta}(y, x) dx_\mu dy_\nu.$$

The Green's function of the valence gluon in the background gauge takes the form [7]

$$G_{\mu\nu}(x, y) = \langle a_\mu(x) a_\nu(y) \rangle_B \quad (5)$$

$$= \langle x | (\hat{D}^2 \delta_{\mu\nu} - 2ig \hat{F}_{\mu\nu})^{-1} | y \rangle,$$

where  $\hat{D}^2$  is the covariant derivative depending on the field  $B$ , and  $\hat{F}_{\mu\nu}$  is the background field strength. The operator  $\hat{F}_{\mu\nu}$  has to be considered as a correction [7]. The Green's function expansion in  $\hat{F}_{\mu\nu}$  takes the form

$$G(x, y) = \langle x | D^{-2} | y \rangle - \langle x | D^{-2} 2ig \hat{F} D^{-2} | y \rangle \quad (6)$$

$$+ \langle x | D^{-2} 2ig \hat{F} D^{-2} 2ig \hat{F} D^{-2} | y \rangle + \dots$$

The terms of odd powers in the field  $B$  vanish. Let us confine ourselves to the third term in expansion (6)

\*This article was submitted by the authors in English.

\*\* e-mail: badalian@heron.itep.ru

\*\*\* e-mail: kuzmenko@heron.itep.ru

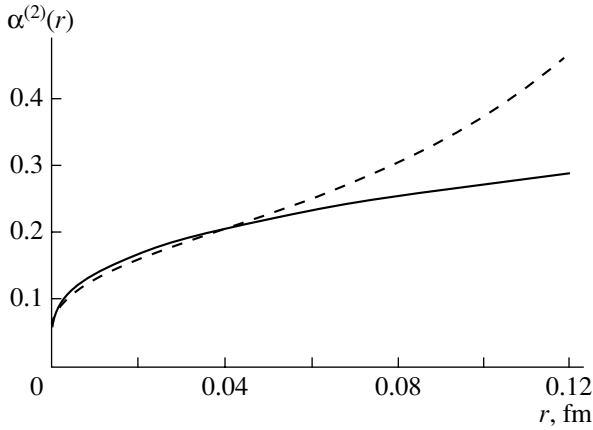


**Fig. 1.** The background coupling  $\alpha_B^{(2)}(r)$  with  $\Lambda = 385$  MeV and  $m_B = 1.0$  GeV (solid curve) compared to the perturbative  $\alpha_s^{(2)}(r)$  with  $\Lambda_R = 686$  MeV (dashed curve) at short distances. A rigorous definition of  $\alpha_s(r)$  and  $\Lambda_R$  is given in [5].

and quadratic term in (3) and write the Wilson loop in the form

$$\begin{aligned} \langle W(B+a) \rangle_{B,a} & \quad (7) \\ & \simeq \langle W(B) \rangle_B + \langle W(B) \rangle_B \left( \tilde{W}_1^{(2)} + \tilde{W}_3^{(2)} \right). \end{aligned}$$

One can verify using the Fock–Feynman–Schwinger representation [8] for the Green’s function expansion (6) that the factorization of the second term in (7) is valid. Terms proportional to  $\tilde{W}_1^{(2)}$  and  $\tilde{W}_3^{(2)}$  come from the first and third terms in (6). The following approximate expression is valid within the accuracy considered:

$$\langle W(B+a) \rangle_{B,a} \simeq \langle W(B) \rangle_B \exp \left( \tilde{W}_1^{(2)} + \tilde{W}_3^{(2)} \right). \quad (8)$$

Taking the logarithm, we arrive at three corresponding terms in the static potential:

$$\begin{aligned} V_{Q\bar{Q}}(r) &= - \lim_{T \rightarrow \infty} \frac{1}{T} \ln \langle W(B+a) \rangle_{B,a} \quad (9) \\ &= V_{\text{NP}}(r) + V_P(r) + V_{\text{int}}(r), \end{aligned}$$

where  $r$  is the quark–antiquark separation, the non-perturbative potential  $V_{\text{NP}}$  is given by the average of the Wilson loop  $\langle W(B) \rangle_B$ , the background perturbative potential  $V_P$  comes from the first term in expansion (6), and the interference potential  $V_{\text{int}}$  comes from the third one. The nonperturbative potential rises linearly at distances  $r \gtrsim T_g$ , where  $T_g = 0.12\text{--}0.2$  fm is the background field correlation length, and is quadratic at short distances (see, e.g., [9]):

$$V_{\text{NP}}(r) \simeq \frac{2}{\pi} \frac{r}{T_g} \sigma r. \quad (10)$$

One can see that, at short distances,  $V_{\text{NP}}(r) \ll \sigma r$ .

The interference potential was calculated in [3] and shown to be close to the linear one at short distances,

$$V_{\text{int}}(r) \simeq \sigma R. \quad (11)$$

The background perturbative potential has the form [7]

$$V_P(r) = - \frac{C_F \alpha_B(r)}{r}, \quad (12)$$

where  $C_F = 4/3$  and the background coupling  $\alpha_B(r)$  saturates with some critical, or freezing, value at large  $r$ .

**3.** We proceed now to a comparison between background and standard couplings at short distances. The Callan–Symanzik equation yields the following expressions for the running coupling constant in one- and two-loop approximations:

$$\alpha_s^{(1)}(q) = \frac{4\pi}{\beta_0 \ln(q^2/\Lambda^2)}, \quad (13)$$

$$\alpha_s^{(2)}(q) = \alpha_s^{(1)}(q) \left( 1 - \frac{\beta_1 \ln \ln(q^2/\Lambda^2)}{\beta_0^2 \ln(q^2/\Lambda^2)} \right), \quad (14)$$

where  $\beta_0 = 11 - \frac{2}{3}n_f$ ,  $\beta_1 = 102 - \frac{38}{3}n_f$ ,  $q^2 \equiv \mathbf{q}^2$ , and  $\Lambda \approx 385$  MeV is the QCD constant (for the discussion of its value see [5]).

The modified Callan–Symanzik equation is used in BPT [7] for the background coupling  $\alpha_B$ , which takes into account the background field contribution and leads to the substitution  $q^2 \rightarrow q^2 + m_B^2$  in (13), (14), where  $m_B = 1$  GeV [5]. One can see that the background coupling saturates with the freezing value in infrared region  $q^2 \ll m_B^2$  and turns to standard  $\alpha_s$  in ultraviolet one.

The background coupling in the coordinate representation can be calculated using the Fourier transform, and in two-loop approximation takes the form

$$\begin{aligned} \alpha_B^{(2)}(r) &= \frac{8}{\beta_0} \int_0^\infty \frac{dq}{q} \frac{\sin(qr)}{\ln[(q^2 + m_B^2)/\Lambda^2]} \quad (15) \\ &\times \left( 1 - \frac{\beta_1 \ln \ln[(q^2 + m_B^2)/\Lambda^2]}{\beta_0^2 \ln[(q^2 + m_B^2)/\Lambda^2]} \right). \end{aligned}$$

It is shown in comparison with the standard coupling in Fig. 1. One can see from the figure a considerable difference between two curves at  $r > 0.05$  fm. The coupling  $\alpha_s^{(2)}(r)$  grows rapidly in this region due to the influence of the pole, which is situated at  $r \simeq 0.3$  fm.

Let us compare now the background static potential behavior at short distances with the lattice one.

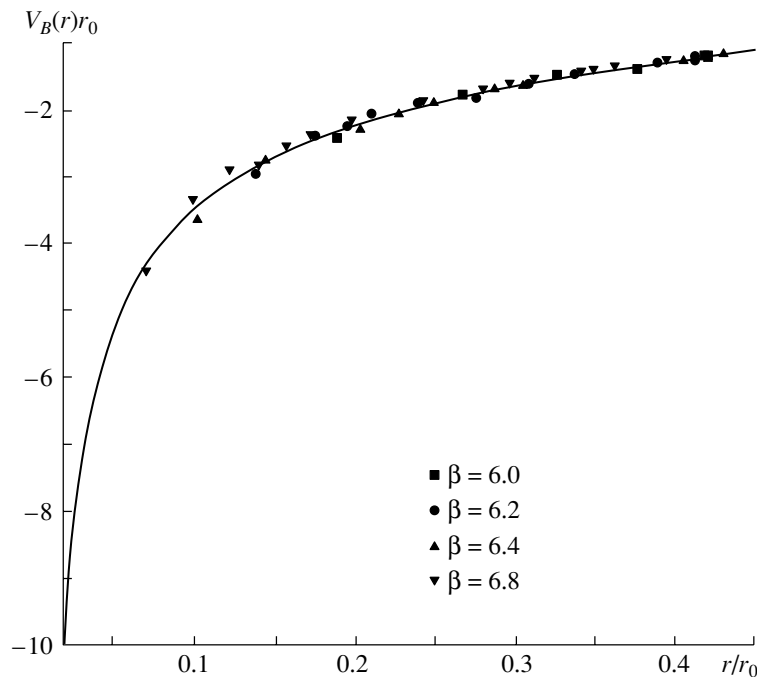


**Fig. 2.** The background potential  $V_B(r)$  (solid curve) compared to the lattice one from [2] (points) in units of  $r_0 = 2.5 \text{ GeV}^{-1}$ . The curve with points is taken from [5].

Relying on the relations (9)–(12), (15), we approximate the potential in this region by the sum [5]

$$V_B(r) \approx -\frac{4}{3} \frac{\alpha_B^{(2)}(r)}{r} + \sigma r. \quad (16)$$

The behavior of  $V_B(r)$  at  $r < 0.22 \text{ fm}$  is shown in Fig. 2 in comparison with lattice points from [2]. The values of  $\sigma = 0.2 \text{ GeV}^2$  and overall shift  $C = -253 \text{ MeV}$  were taken from the fit, which provided agreement between background and lattice potentials with an accuracy of  $\lesssim 50 \text{ MeV}$  of the latter.

**4.** In summary we enumerate some properties of the short distance static quark–antiquark potential.

(1) The potential at  $r \ll T_g$  consists mainly of perturbative and interference parts. The purely non-perturbative potential is small in this region.

(2) The background running coupling constant saturates with the freezing value in the infrared region and goes over to the standard coupling in the ultraviolet region.

(3) A considerable difference between standard and background couplings in the two-loop approximation already appears at distances  $r \gtrsim 0.05 \text{ fm}$ .

(4) The background potential, approximated as a sum of the two-loop background perturbative potential and linear potential with the slope  $\sigma$ , yields a good description of lattice simulations at short distances. This in turn means that the short-distance area law for the Wilson loop, used, in particular, in the QCD string approach (see, e.g., [10]), is justified.

## ACKNOWLEDGMENTS

This work was supported by the Russian Foundation for Basic Research (project nos. 00-02-17836, 00-15-96786) and INTAS (grant nos. 00-00110, 00-00366).

## REFERENCES

1. G. S. Bali, Phys. Rep. **343**, 1 (2001).
2. G. S. Bali, Phys. Lett. B **460**, 170 (1999).
3. Yu. A. Simonov, Phys. Rep. **320**, 265 (1999).
4. F. V. Gubarev, M. I. Polikarpov, and V. I. Zakharov, Mod. Phys. Lett. A **14**, 2039 (1999); M. N. Chernodub, F. V. Gubarev, M. I. Polikarpov, and V. I. Zakharov, Phys. Lett. B **475**, 303 (2000).
5. A. M. Badalian and D. S. Kuzmenko, Phys. Rev. D **65**, 016004 (2002).
6. V. I. Shevchenko, hep-ph/0301280.
7. Yu. A. Simonov, *Lecture Notes in Physics* (Springer-Verlag, Berlin, 1996), Vol. 479, p. 139; Phys. At. Nucl. **58**, 107 (1995).
8. Yu. A. Simonov and J. A. Tjon, Ann. Phys. (N.Y.) **300**, 54 (2002).
9. D. S. Kuzmenko, Yad. Fiz. **67**, 566 (2004) [Phys. At. Nucl. **67**, 548 (2004)]; hep-ph/0302067.
10. Yu. S. Kalashnikova and D. S. Kuzmenko, Yad. Fiz. **67**, 556 (2004) [Phys. At. Nucl. **67**, 538 (2004)]; hep-ph/0302070.

---

---

**ELEMENTARY PARTICLES AND FIELDS**  
**Theory**

---

---

## **$z$ -Scaling and High- $p_T$ Particle Production in Hadron–Hadron and Hadron–Nucleus Collisions at High Energies\***

**M. V. Tokarev\*\* , G. L. Efimov, and D. E. Toivonen**

*Joint Institute for Nuclear Research, Dubna, Moscow oblast, 141980 Russia*

Received April 15, 2003

**Abstract**—The general features of particle production in hadron–hadron and hadron–nucleus collisions at high energy and transverse momentum using the concept of  $z$ -scaling are reviewed.  $z$ -Presentation of experimental data on the inclusive cross sections obtained at ISR, SPS, and Tevatron is presented and its properties are discussed. It is argued that the properties reflect the fundamental symmetries such as self-similarity, locality, and fractality.  $z$ -Scaling is used to predict particle yields in hadron–hadron and hadron–nucleus collisions at RHIC and LHC energies. The violation of  $z$ -scaling is considered as a signature of new physics phenomena. © 2004 MAIK “Nauka/Interperiodica”.

### 1. INTRODUCTION

Properties of particle formation are believed to reveal themselves more clearly at high energy  $\sqrt{s}$  and transverse momenta. It is considered also that partons produced in hard scattering retain information about the primary collision during hadronization. It is known that the mechanism of particle formation is modified by the nuclear medium and can be sensitive to the phase transition of nuclear matter. Therefore, the features of high- $p_T$  single inclusive particle spectra of hadron–hadron and hadron–nucleus collisions are of interest to search for new physics phenomena (a phase transition of nuclear matter, new types of interactions, quark compositeness, a fractal structure of spacetime, etc.).

One of the methods to study the properties of particle formation in nuclear matter is to search for the violation of known regularities, e.g., the Bjorken and Feynman scaling laws and quark counting rules [1, 2], established in elementary collisions.

In the paper, the general concept of a new scaling,  $z$ -scaling [3–11], is reviewed and the results of high- $p_T$  data analysis for hadron–hadron and hadron–nucleus collisions are presented.

### 2. $z$ -SCALING

The idea of  $z$ -scaling [3] is based on the assumptions that the inclusive particle distribution of the process

$$P_1 + P_2 \rightarrow p + X \quad (1)$$

at high energies can be described in terms of the corresponding kinematic characteristics of the exclusive subprocess [12] written in the symbolic form

$$(x_1 M_1) + (x_2 M_2) \rightarrow m_1 + (x_1 M_1 + x_2 M_2 + m_2), \quad (2)$$

and that the scaling function depending on a single variable exists and is expressed via the dynamic quantities, the invariant inclusive cross section  $Ed^3\sigma/dp^3$  and the charged particle multiplicity density  $\rho(s, \eta)$ , of the process (1). The kinematic quantities of the process (1)  $P_1, P_2, p$  and  $M_1, M_2, m_1$  are the momenta and the masses of colliding objects (hadrons, nuclei) and inclusive particles. The energy of the process and pseudorapidity are defined by the formulas  $s = (P_1 + P_2)^2$  and  $\eta = -\ln(\tan(\theta/2))$ , where  $\theta$  is an angle of a produced particle.

The parameter  $m_2$  is introduced to satisfy the internal conservation laws (for isospin, baryon number, and strangeness). The terms  $x_1$  and  $x_2$  are the scale-invariant fractions of the incoming four-momenta  $P_1$  and  $P_2$ . They determine the minimum energy that is necessary for the production of a secondary particle with mass  $m_1$  and four-momentum  $p$ .

#### 2.1. Fractions $x_1$ and $x_2$

The elementary parton–parton collision is considered as a binary subprocess that satisfies the condition

$$(x_1 P_1 + x_2 P_2 - p)^2 = (x_1 M_1 + x_2 M_2 + m_2)^2. \quad (3)$$

The equation reflects the minimum recoil mass hypothesis in the elementary subprocess. To connect the

---

\*This article was submitted by the authors in English.

\*\* e-mail: tokarev@sunhe.jinr.ru

kinematic and structural characteristics of the interaction, the coefficient  $\Omega$  is introduced. It is chosen in the form

$$\Omega(x_1, x_2) = (1 - x_1)^{\delta_1} (1 - x_2)^{\delta_2}, \quad (4)$$

where  $\delta_1$  and  $\delta_2$  are the factors relating to the fractal structure of the colliding objects [4]. The fractions  $x_1$  and  $x_2$  are determined to maximize the value of  $\Omega(x_1, x_2)$ , simultaneously fulfilling condition (3):

$$d\Omega(x_1, x_2)/dx_1|_{x_2=x_2(x_1)} = 0. \quad (5)$$

The variables  $x_{1,2}$  are equal to unity along the phase-space limit and cover the full phase space accessible at any energy.

### 2.2. Scaling Function $\psi(z)$ and Variable $z$

The scaling function  $\psi(z)$  depends on a single scaling variable  $z$  and is written in the form [4]

$$\psi(z) = -\frac{\pi s_A}{\rho_A(s, \eta) \sigma_{\text{inel}}} J^{-1} E \frac{d^3\sigma}{dp^3}. \quad (6)$$

Here,  $\sigma_{\text{inel}}$  is the inelastic cross section,  $s_A \simeq sA$  and  $s$  are the c.m. energies squared of the corresponding  $h-A$  and  $h-N$  systems,  $A$  is the atomic weight, and  $\rho_A(s, \eta)$  is the average particle multiplicity density. The factor  $J$  is a known function of the kinematic variables, the momenta and masses of the colliding and produced particles.

Expression (6) relates the differential cross section for the production of the inclusive particle  $m_1$  and the average particle multiplicity density  $\rho_A(s, \eta)$  with the scaling function  $\psi(z)$ .

In accordance with the ansatz suggested in [4], the variable  $z$  is taken in the form

$$z = \frac{\sqrt{\hat{s}_\perp}}{\Omega \rho_A(s) m} \quad (7)$$

as a simple physically meaningful variable reflecting self-similarity and fractality as the general pattern of hadron production at high energies. Here,  $\sqrt{\hat{s}_\perp}$  is the minimum transverse energy of colliding constituents necessary to produce a real hadron in the reaction (1). The factor  $\Omega$  is given by (4), the multiplicity particle density  $\rho_A(s)$  is taken at  $\eta = 0$  in the corresponding c.m. nucleon–nucleon system, and  $m$  is the mass constant. The transverse energy consists of two parts which represent the transverse energy of the inclusive particle and its recoil. The form of  $z$  determines its range of variation ( $z_{\text{min}}, \infty$ ). Here,  $z_{\text{min}}$  is the value of  $z$  for the corresponding exclusive process.

The function is normalized as

$$\int_{z_{\text{min}}}^{\infty} \psi(z) dz = 1. \quad (8)$$

This equation allows us to give the physical meaning of the function  $\psi$  as a probability density to form a particle with the corresponding value of the variable  $z$ .

### 2.3. Fractality

The principle of fractality states that variables used in the description of the process diverge in terms of resolution [4, 13, 14]. This property is characteristic for the scaling variable

$$z = z_0 \Omega^{-1}. \quad (9)$$

The variable  $z$  has the character of a fractal measure. For the given production process (1), the finite part  $z_0$  is the ratio of transverse energy released in the binary collision of constituents (2) and the average multiplicity density  $\rho_A(s)$ . The divergent part  $\Omega^{-1}$  describes the resolution at which the collision of the constituents can be singled out of this process.  $\Omega(x_1, x_2)$  represents the relative number of all initial configurations containing the constituents, which carry fractions  $x_1$  and  $x_2$  of the incoming momenta.  $\delta_1$  and  $\delta_2$  are the anomalous fractal dimensions of the colliding objects (hadrons or nuclei). The momentum fractions  $x_1$  and  $x_2$  are determined in a way to minimize the resolution  $\Omega^{-1}(x_1, x_2)$  of the fractal measure  $z$  with respect to all possible subprocesses (2) subjected to the condition (3). The variable  $z$  was interpreted as a particle formation length.

## 3. PROPERTIES OF *z*-SCALING

In this section, we discuss properties of the  $z$ -scaling for the particles ( $\pi^{\pm,0}, K^{\pm}, \bar{p}, \gamma$ ) produced in hadron–hadron and hadron–nucleus collisions. They are the energy and angular independence of data  $z$ -presentation, the power law of the scaling function at high  $p_T$ , and  $A$  and  $F$  dependence of  $z$ -scaling. Numerous experimental data on inclusive cross sections at high  $p_T$  obtained at U-70 [15, 16], ISR [17–22], SPS [23–27], and Tevatron [28–33] were used in the analysis.

### 3.1. Energy Independence

The energy independence of data  $z$ -presentation means that the scaling function  $\psi(z)$  has the same shape for different  $\sqrt{s}$  over a wide  $p_T$  range.

Figures 1a–3a show the dependence of the cross section of the  $\pi^-$ ,  $K^+$ , and  $\pi^0$  mesons produced in  $pp$  collisions on transverse momentum  $p_T$  at the angle  $\theta_{\text{c.m.s.}} \simeq 90^\circ$ . The data cover a wide transverse momentum range,  $p_T = 1-14 \text{ GeV}/c$ .

As seen from Figs. 1a–3a, the spectra demonstrate a strong dependence on the energy  $\sqrt{s} =$

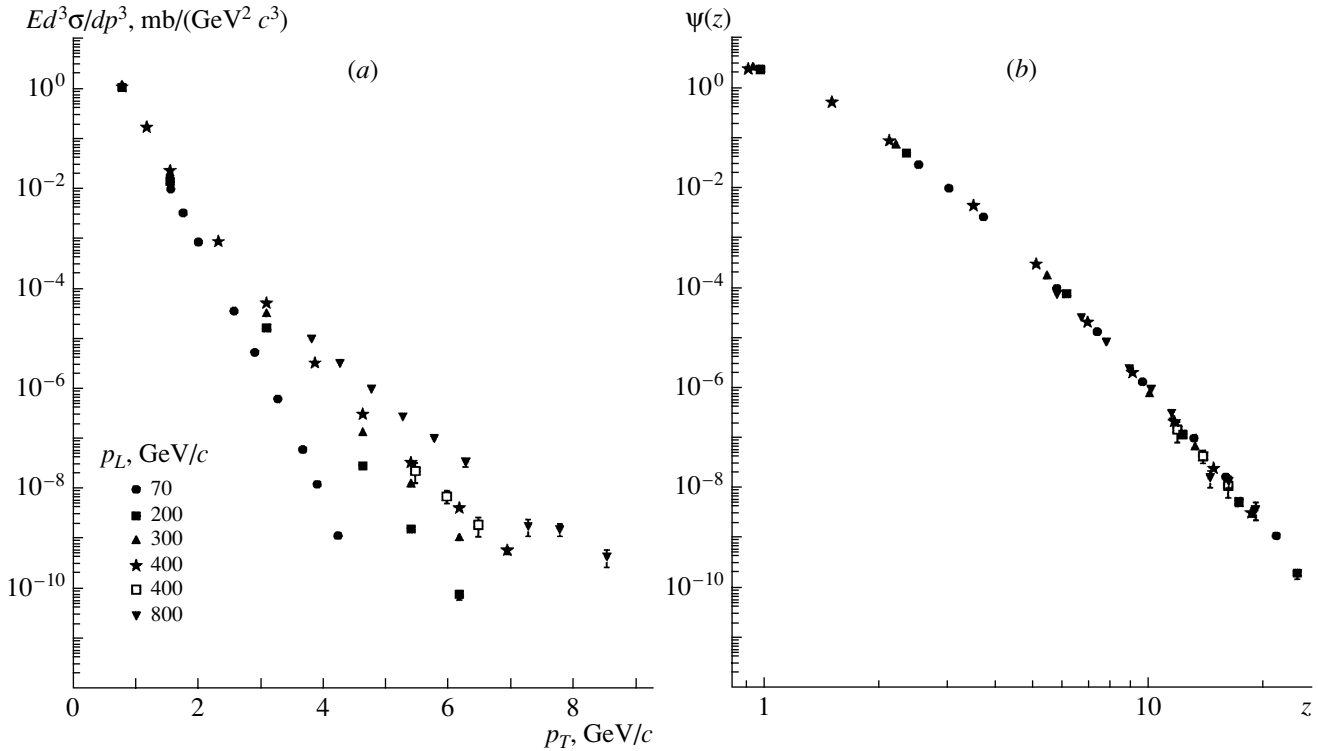


**Fig. 1.** (a) The inclusive cross section for the  $\pi^-$  mesons produced in  $pp$  collisions at  $p_L = 70, 200, 300, 400,$  and  $800 \text{ GeV}/c$  and  $\theta_{\text{c.m.s.}} \simeq 90^\circ$  as functions of the transverse momentum. Experimental data are taken from [15, 28, 29]. (b) The corresponding scaling function  $\psi(z)$ .

$\left[2m^2 + 2m\sqrt{m^2 + p_L^2}\right]^{1/2}$ . The difference between hadron yields increases with the transverse momentum and the energy  $\sqrt{s}$ . A nonexponential behavior of the spectra at  $p_T > 1 \text{ GeV}/c$  is observed.

Figures 1b–3b show  $z$ -presentation of the same data sets. We would like to note that the larger value of  $p_T$  corresponds to the larger value of  $z$  at the given energy  $\sqrt{s}$ . Taking into account the experimental errors, we can conclude that the scaling function  $\psi(z)$  demonstrates energy independence over a wide energy and transverse momentum range at  $\theta_{\text{c.m.s.}} \simeq 90^\circ$  for particles with different flavor content. We would like to note that new data obtained at Tevatron [29] and RHIC [34] involved in the present analysis give no indications of  $z$ -scaling violation.

Figures 4a, 5a and 4b, 5b show the energy dependence of data  $p_T$ - and  $z$ -presentation for direct  $\gamma$  production in  $\bar{p}p$  and  $pp$  collisions. The experimental data on cross sections were obtained at Tevatron, SPS, and ISR. One can see that all data sets reveal the property of the energy independence of  $\psi(z)$  in  $z$ -presentation.

### 3.2. Angular Independence

The angular independence of data  $z$ -presentation means that the scaling function  $\psi(z)$  has the same shape for different values of angle  $\theta$  of produced particle over a wide  $p_T$  and  $\sqrt{s}$  range. Taking into account the energy independence of  $\psi(z)$ , it will be enough to verify the property at some  $\sqrt{s}$ .

As seen in Fig. 6a, the D0 data [32] for direct  $\gamma$  produced in  $\bar{p}p$  collisions at  $\sqrt{s} = 1800 \text{ GeV}$  demonstrate a strong angular dependence of the cross section. The data  $z$ -presentation show that the function  $\psi(z)$  is independent of the angle  $\theta$  over a wide  $p_T$  range. This is the experimental confirmation of the angular scaling of data  $z$ -presentation.

### 3.3. Power Law

Here, we discuss a new feature of data  $z$ -presentation for particle production at high  $p_T$ . This is the power law of the scaling function,  $\psi(z) \sim z^{-\beta}$ .

As seen from Figs. 1b–3b, a linear  $z$  dependence of  $\psi(z)$  on a log–log scale at  $z > 4$  for different types of particles is observed. This feature occurs for the direct photon production in  $\bar{p}p$  (Figs. 4b, 6b) and  $pp$  (Fig. 5b) collisions as well. The value of the slope

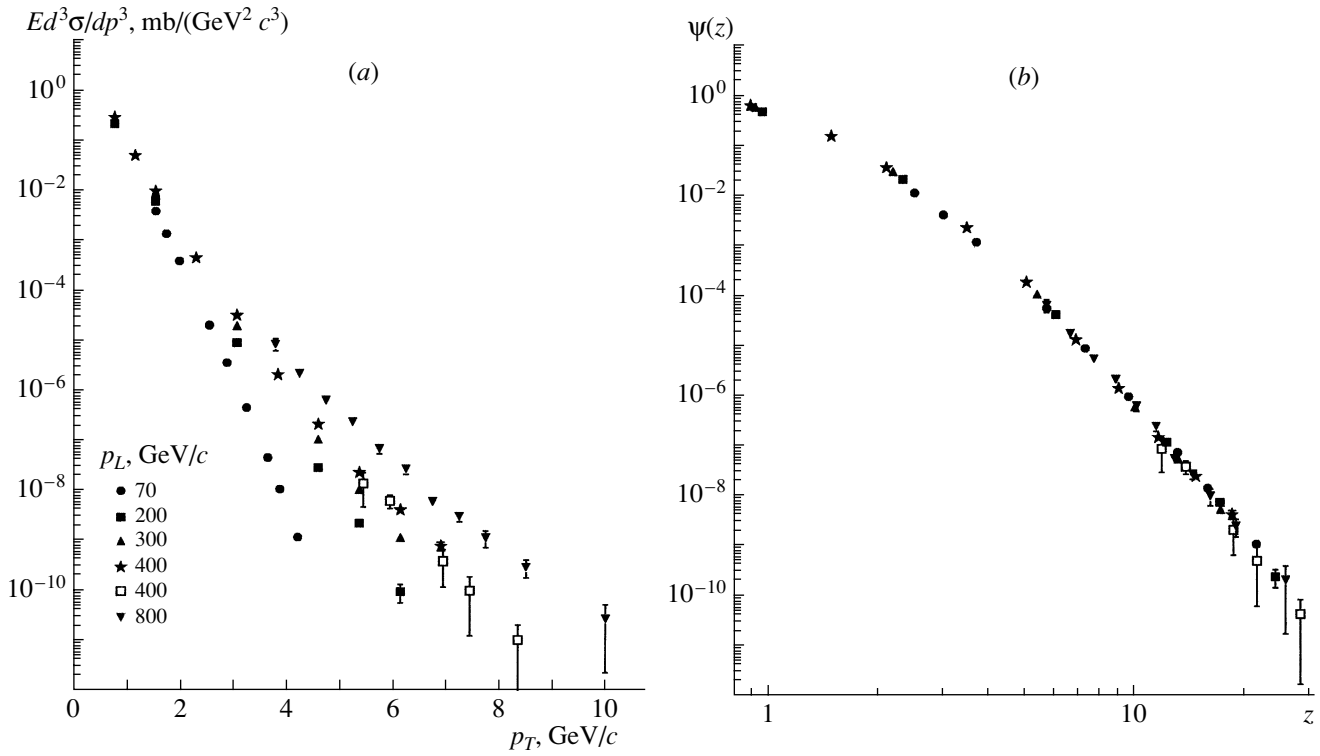


**Fig. 2.** (a) The inclusive cross section for  $K^+$  mesons produced in  $pp$  collisions at  $p_L = 70, 200, 300, 400,$  and  $800 \text{ GeV}/c$  and  $\theta_{\text{c.m.s.}} \simeq 90^\circ$  as functions of the transverse momentum. Experimental data are taken from [15, 28, 29]. (b) The corresponding scaling function  $\psi(z)$ .

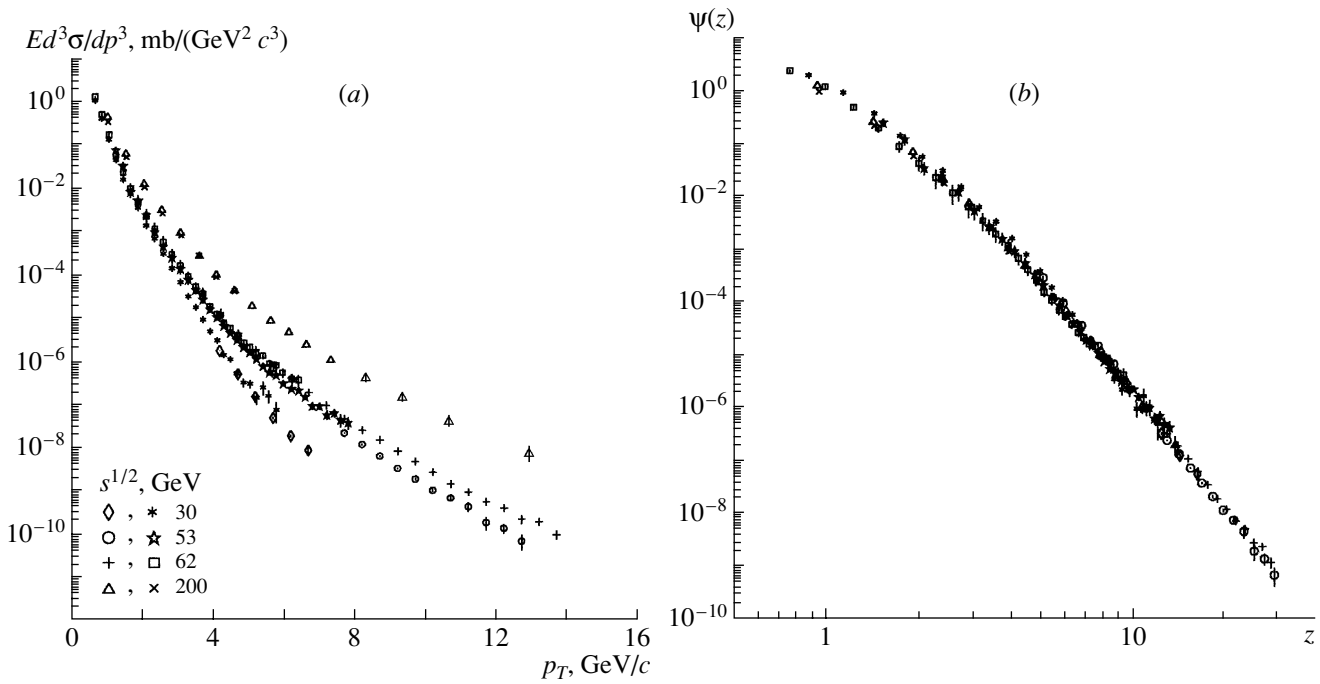


**Fig. 3.** (a) The dependence of the inclusive cross section of  $\pi^0$ -meson production on transverse momentum in  $pp$  collisions at  $\sqrt{s} = 30, 53, 62,$  and  $200 \text{ GeV}$  and an angle  $\theta_{\text{c.m.s.}} \simeq 90^\circ$ . The experimental data are taken from [17–21, 34]. (b) The corresponding scaling function  $\psi(z)$ .

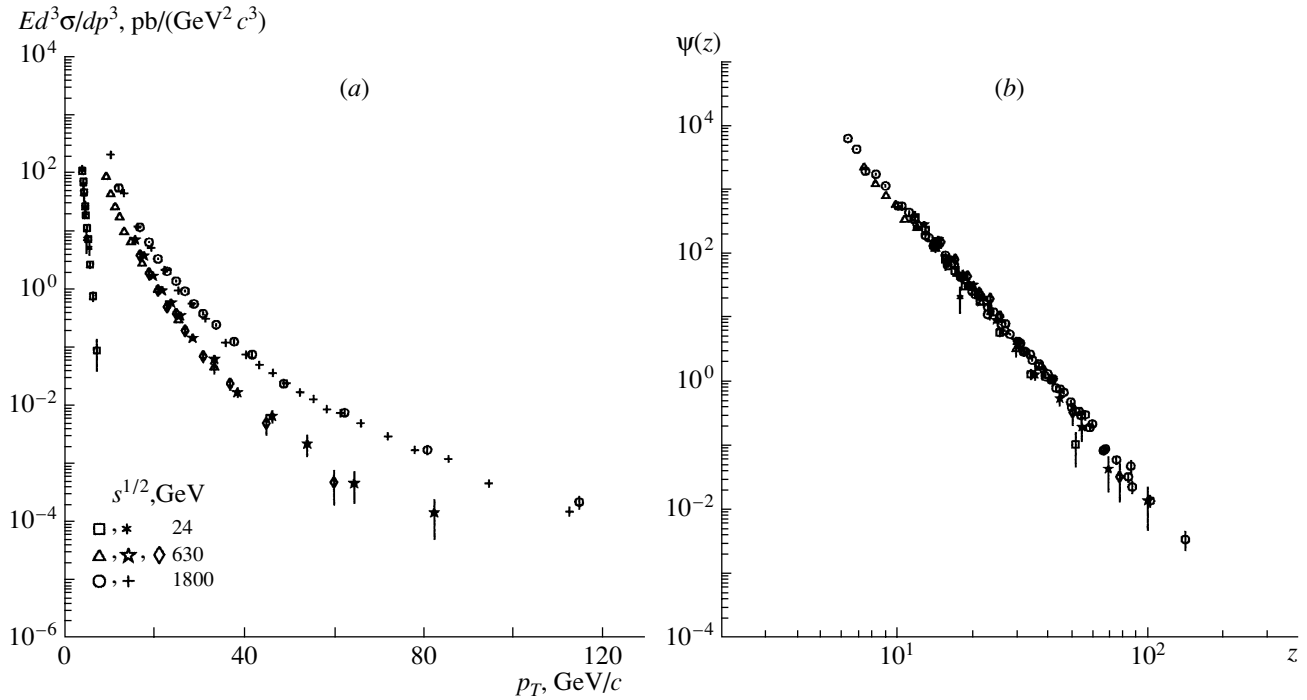


**Fig. 4.** (a) The dependence of the inclusive cross section of direct photon production on transverse momentum in  $\bar{p}p$  collisions at  $\sqrt{s} = 24$ –1800 GeV. Experimental data obtained by the UA1, UA2, UA6, CDF, and D0 Collaborations are taken from [23–27, 31, 32]. (b) The corresponding scaling functions.

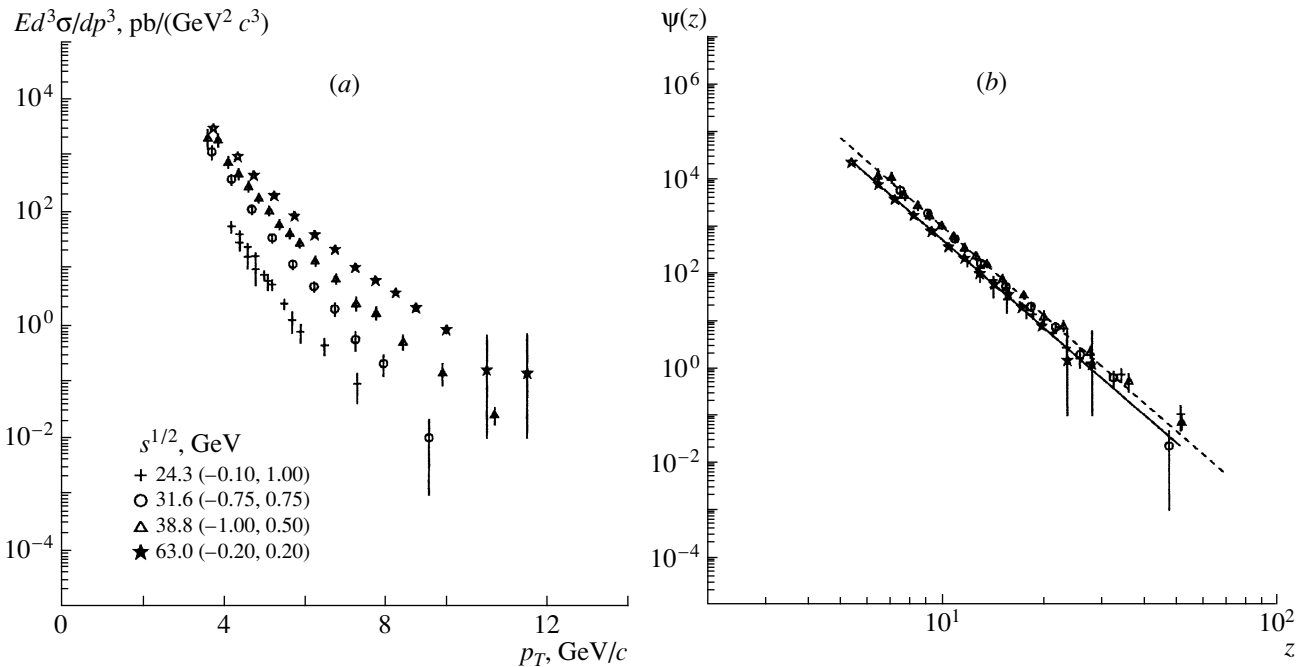


**Fig. 5.** (a) The dependence of the inclusive cross section of direct photon production on transverse momentum in  $pp$  collisions at  $\sqrt{s} = 24.3, 31.6, 38.8,$  and  $63.0$  GeV and the rapidity intervals  $(-0.10, 1.00)$ ,  $(-0.75, 0.75)$ ,  $(-1.00, 0.50)$ , and  $(-0.20, 0.20)$ , respectively. Experimental data (+, \*) and (o,  $\Delta$ ) are taken from [22, 27] and [33]. (b) The corresponding scaling function  $\psi(z)$ . The solid and dashed lines are obtained by fitting of  $\psi(z)$  corresponding to the data [22, 27] and [33].

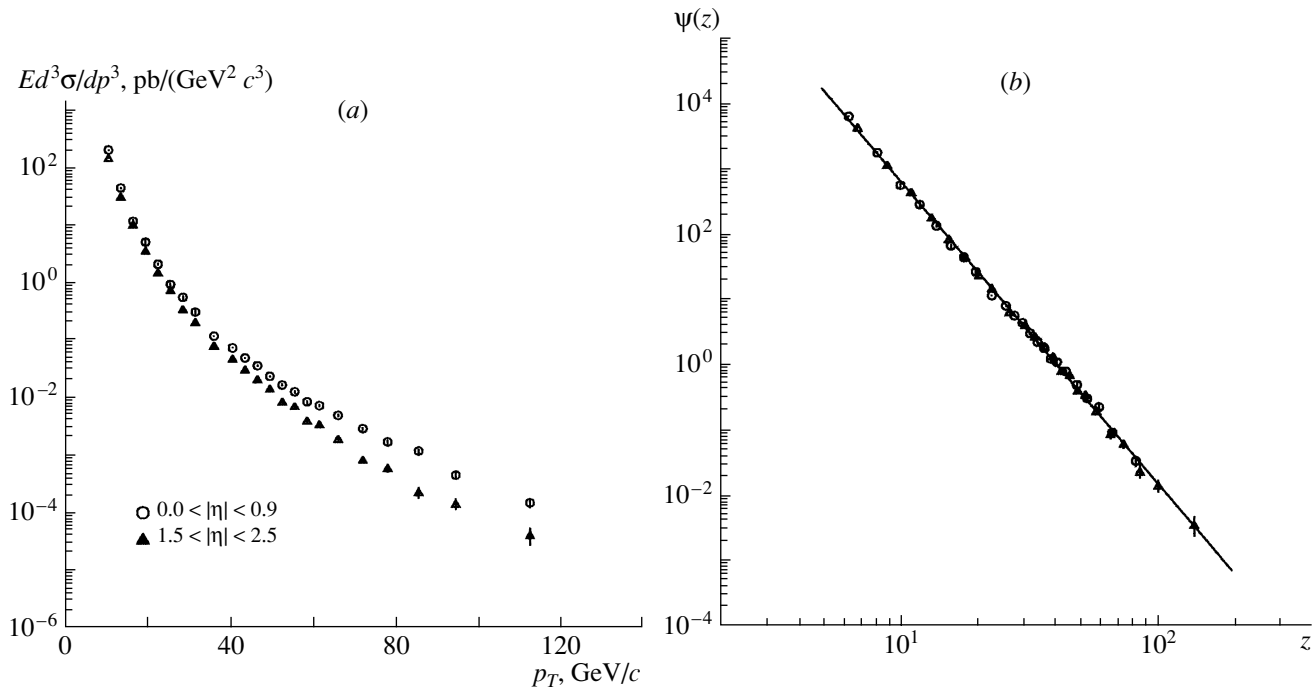


**Fig. 6.** (a) The dependence of the inclusive cross section of direct photon production in  $\bar{p}p$  collisions on transverse momentum for different pseudorapidity intervals ( $0.0 < |\eta| < 0.9$ ;  $1.6 < |\eta| < 2.5$ ) at  $\sqrt{s} = 1800$  GeV. Experimental data on the cross sections obtained by the D0 Collaboration are taken from [32]. (b) The corresponding scaling function  $\psi(z)$ . The solid line is obtained by fitting of  $\psi(z)$ .

parameter  $\beta$  is independent of the energy  $\sqrt{s}$  over a wide range of high transverse momentum. The mean values of the slope parameter for particle production in  $pp$  and  $\bar{p}p$  collisions were found to be different, so that  $\beta_{pp} > \beta_{\bar{p}p}$ . The result reflects the difference between elementary subprocesses initiating the mechanism of particle formation at the different scales. The existence of the power law,  $\psi(z) \sim z^{-\beta}$ , means, from our point of view, that the mechanism of particle formation reveals self-similar and fractal properties.

### 3.4. $A$ Dependence

A study of  $A$  dependence of particle production in  $hA$  and  $AA$  collisions is traditionally connected with the influence of nuclear matter on particle formation. The difference between the cross sections of particle production on free and bound nucleons is normally considered as an indication of unusual physics phenomena like the EMC effect,  $J/\psi$  suppression, and Cronin effect [28].

The  $A$  dependence of  $z$ -scaling for particle production in  $pA$  collisions was studied in [5]. The scaling properties for every nuclei ( $A = d$ -Pb) and type of produced particles ( $\pi^{\pm,0}$ ,  $K^{\pm}$ ,  $\bar{p}$ ) were established. The symmetry transformation of the scaling function  $\psi(z)$  and variable  $z$  under the scale transformation

$z \rightarrow \alpha_A z$ ,  $\psi \rightarrow \alpha_A^{-1} \psi$  was used to compare the scaling function for different nuclei. It was found that  $\alpha_A$  depends only on the atomic number and can be parametrized by the formula  $\alpha_A = 0.9A^{0.15}$  [5]. Data  $p_T$ - and  $z$ -presentation for  $\pi^+$  mesons produced in  $pA$  collisions are shown in Fig. 7. As can be seen from Figs. 7a and 7b, the mechanism of particle formation in the high- $p_T$  range is modified by nuclear medium self-similar manner for light ( $d$ ) and heavy (Pb) nuclei. Therefore, the  $A$  dependence of  $z$ -scaling can be used for searching for  $z$ -scaling violation. The results presented in Fig. 8 give no indications of the scaling violation for  $\pi^+$ -meson production in  $pd$  collisions at  $p_L = 70$  and  $400$   $\text{GeV}/c$  in the range  $p_T = 1$ - $8.5$   $\text{GeV}/c$  [15, 28, 29]. Similar results have been obtained for  $\pi^0$  mesons produced in  $pA$  [9] and  $\pi^{\pm,0}$ ,  $K^{\pm}$ ,  $\bar{p}$  production in  $\pi^- A$  collisions [10] as well. Data on inclusive cross sections [10] in  $p_T$ - and  $z$ -presentations for the  $\pi^- + A \rightarrow K^- + X$  process are shown in Figs. 9a and 9b, respectively. It was found that the fractal dimensions  $\delta_\pi$ ,  $\delta_N$ ,  $\delta_A$  and the slope parameter of  $\psi(z)$  are independent of  $\sqrt{s}$  and transverse momentum  $p_T$  over a wide kinematical range.

It is suggested that the change in the fractal dimension (“ $\delta$  jump”) be considered as a signature of nuclear matter transition. Therefore, it is of interest to

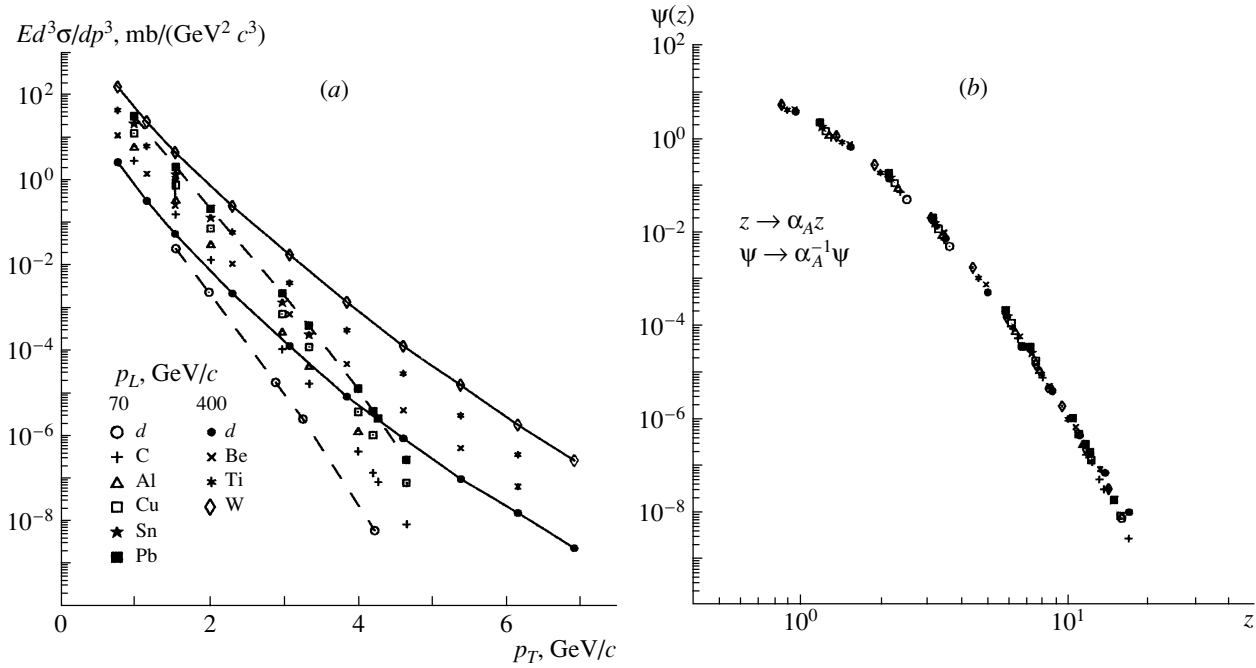


**Fig. 7.** (a) The inclusive cross section for  $\pi^+$  mesons produced in  $pA$  interactions at  $p_L = 70, 400 \text{ GeV}/c$  and  $\theta_{c.m.s.} \simeq 90^\circ$  in the proton–proton c.m. system as a function of the transverse momentum. Experimental data are taken from [15, 28]. Solid and dashed lines are obtained by fitting of the data for  $d, W$  [28] and  $d, Pb$  [15], respectively. (b) The corresponding scaling function  $\psi(z)$ .

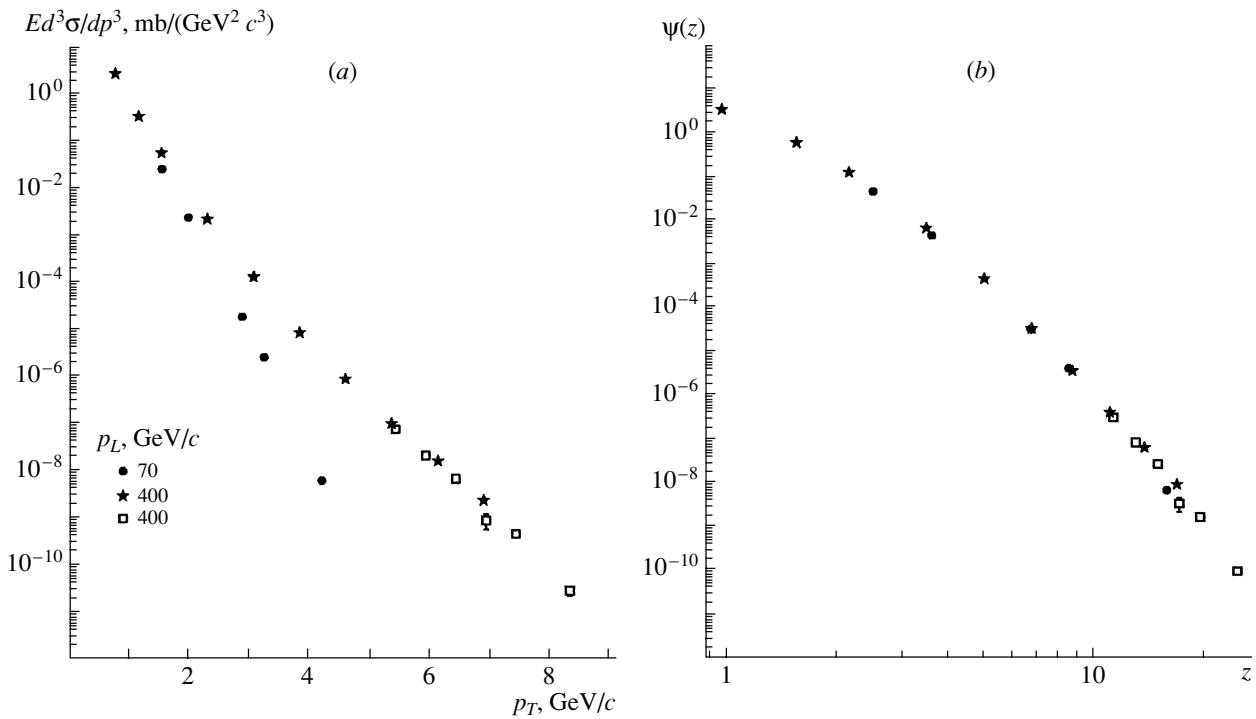


**Fig. 8.** (a) The inclusive differential cross section for  $\pi^+$  mesons produced in  $pd$  collisions at  $p_L = 70, 400 \text{ GeV}/c$  and  $\theta_{c.m.s.} \simeq 90^\circ$  in the nucleon–nucleon c.m. system as a function of the transverse momentum. Experimental data are taken from [15, 28, 29]. (b) The corresponding scaling function  $\psi(z)$ .

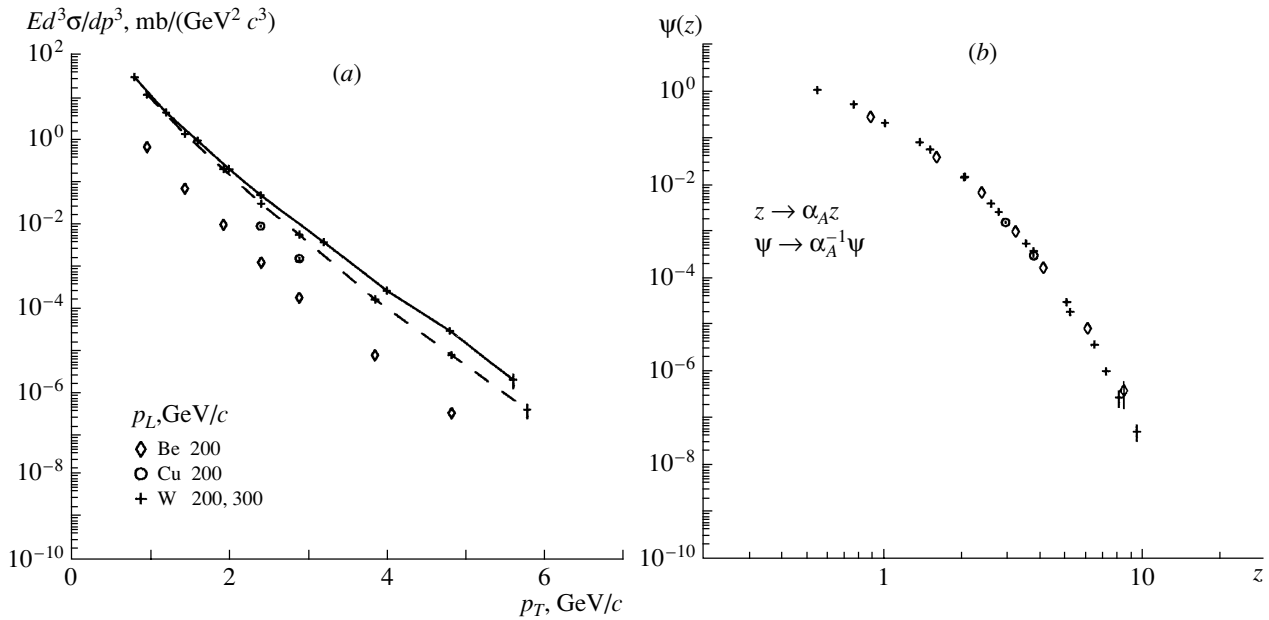


**Fig. 9.** (a) The dependence of the inclusive cross section of  $K^-$ -meson production on transverse momentum in  $\pi^- A$  collisions at  $p_L = 200, 300$   $\text{GeV}/c$ . Experimental data are taken from [30]. Solid and dashed lines are obtained by fitting of data for the nucleus W at  $p_L = 300$  and  $200$   $\text{GeV}/c$ , respectively. (b) The corresponding scaling function  $\psi(z)$ .

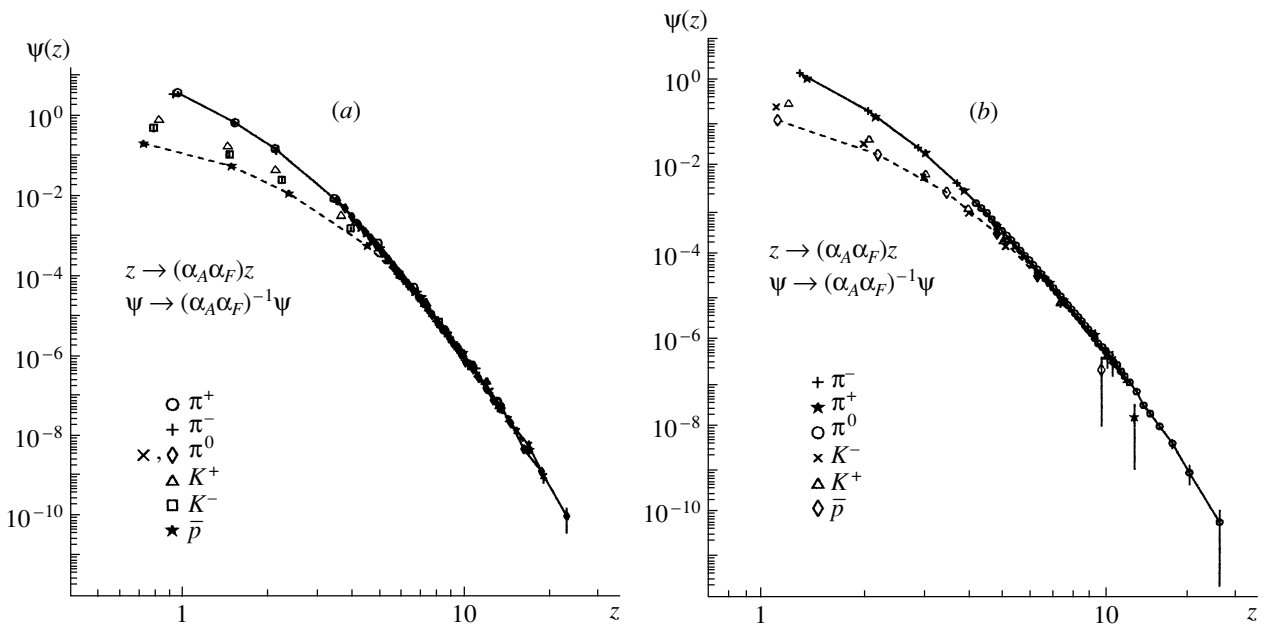


**Fig. 10.** The scaling functions  $\psi(z)$  for  $\pi^{\pm,0}, K^{\pm}, \bar{p}$  particles produced in (a)  $p\text{Be}$  at  $p_L = 400, 530,$  and  $800$   $\text{GeV}/c$  and (b)  $\pi^- \text{Be}$  collisions at  $p_L = 200$  and  $515$   $\text{GeV}/c$ , respectively. Experimental data on the inclusive cross sections are taken from [28, 33]. Solid and dashed lines are obtained by fitting of  $\psi(z)$  corresponding to  $\pi$  meson and  $\bar{p}$ , respectively.

investigate the energy and  $A$  dependence of the fractal dimension  $\delta(s)$  in the high- $p_T$  momentum range.

### 3.5. $F$ Dependence

The physical meaning of the scaling function  $\psi(z)$  is the probability density to produce a particle with

formation length  $z$ . The existence of the scaling is a confirmation of self-similarity at different scales, regulated by the energy  $\sqrt{s}$  and transverse momentum  $p_T$ . The power law,  $\psi(z) \sim z^{-\beta}$ , observed in the very high  $p_T$  range, is characterized by the slope parameter

$\beta$ . It was found that the parameter is independent of  $\sqrt{s}$  over a wide transverse momentum range. Therefore, it is of interest to compare the shape of the scaling function of produced particles with different flavor content. This dependence is called the  $F$  dependence of  $z$ -scaling.

Figures 10a and 10b show the scaling functions for particles produced in  $p$ Be and  $\pi^-$ Be collisions, respectively. The symmetry transformation of the scaling function  $\psi \rightarrow (\alpha_A \alpha_F)^{-1} \psi$  and the variable  $z \rightarrow (\alpha_A \alpha_F) z$  was used to compare the scaling function for different types of produced particles. The results give us an indication of the existence of universal asymptotics of  $\psi(z)$  at high  $z$  for different types of particles,  $\pi^{\pm,0}$ ,  $K^{\pm}$ ,  $\bar{p}$ . The property of data  $z$ -presentation reflects a new feature of particle formation, the flavor independence of the scaling function in the asymptotic region. The verification of this property for other particles ( $J/\psi$ ,  $\Upsilon$ ,  $D$ ,  $B$ ,  $W^{\pm}$ , and  $Z^0$ ) will be possible at RHIC and LHC and is important for understanding the mechanism of particle formation in hadron-hadron and hadron-nucleus collisions.

#### 4. CONCLUSIONS

Analysis of numerous experimental data on high- $p_T$  particle production in hadron-hadron and hadron-nucleus collisions obtained at ISR, SPS, and Tevatron in the framework of the  $z$ -scaling concept was presented. The general scheme of data  $z$ -presentation for different processes was formulated.

The scaling function  $\psi(z)$  and scaling variable  $z$  are expressed via the experimental quantities, the invariant inclusive cross section  $Ed^3\sigma/dp^3$  and the multiplicity density of charged particles  $\rho_A(s, \eta)$ . The physical interpretation of the scaling function  $\psi$  as a probability density to produce a particle with the formation length  $z$  is argued. The quantity  $z$  has the property of the fractal measure, and  $\delta$  is the fractal dimension describing the intrinsic structure of the interacting constituents revealed at high energies.

The fractal dimensions of nucleon  $\delta_N$ , pion  $\delta_\pi$ , and nuclei  $\delta_A$  satisfy the relation  $\delta_\pi < \delta_N \ll \delta_A$ .

It was shown that the properties of  $z$ -scaling, the energy and angular independence, the power law  $\psi(z) \sim z^{-\beta}$ , and the  $A$  and  $F$  dependence are confirmed by the numerous experimental data obtained by different collaborations at ISR, SPS, and Tevatron.

The violation of  $z$ -scaling is suggested for searching for new physics phenomena such as quark compositeness, new type of interactions, nuclear phase transition, and fractal structure of spacetime in hadron-hadron and hadron-nucleus collisions at SPS, RHIC, Tevatron, HERA, and LHC.

#### ACKNOWLEDGMENTS

Some results presented in the report were obtained in collaboration with I. Zborovský, Yu. Panebratsev, G. Škoro, E. Potrebenikova, T. Dedovich, and O. Rogachevski. We would like to thank them for collaboration and many useful and stimulating discussions on the problem.

#### REFERENCES

1. V. A. Matveev, R. M. Muradyan, and A. N. Tavkhelidze, *Fiz. Élem. Chastits At. Yadra* **1**, 7 (1971) [*Phys. Part. Nucl.* **1**, 2 (1971)]; *Lett. Nuovo Cimento* **5**, 907 (1972); **7**, 719 (1973).
2. S. Brodsky and G. Farrar, *Phys. Rev. Lett.* **31**, 1153 (1973); *Phys. Rev. D* **11**, 1309 (1975).
3. I. Zborovský, Yu. A. Panebratsev, M. V. Tokarev, and G. P. Škoro, *Phys. Rev. D* **54**, 5548 (1996).
4. I. Zborovský, M. V. Tokarev, Yu. A. Panebratsev, and G. P. Škoro, *Phys. Rev. C* **59**, 2227 (1999).
5. M. V. Tokarev, I. Zborovský, Yu. A. Panebratsev, and G. P. Škoro, *Int. J. Mod. Phys. A* **16**, 1281 (2001).
6. M. V. Tokarev and E. V. Potrebenikova, Preprint No. E2-98-64, JINR (Dubna, 1998); *Comput. Phys. Commun.* **117**, 229 (1999).
7. M. V. Tokarev and T. G. Dedovich, *Int. J. Mod. Phys. A* **15**, 3495 (2000).
8. M. V. Tokarev, O. V. Rogachevski, and T. G. Dedovich, *J. Phys. G* **26**, 1671 (2000).
9. M. V. Tokarev, O. V. Rogachevski, and T. G. Dedovich, Preprint No. E2-2000-90, JINR (Dubna, 2000).
10. M. V. Tokarev, I. Zborovský, Yu. A. Panebratsev, and G. P. Škoro, Preprint No. E2-2001-282, JINR (Dubna, 2001).
11. I. Zborovský, M. V. Tokarev, Yu. A. Panebratsev, and G. P. Škoro, Preprint No. E2-2001-41, JINR (Dubna, 2001).
12. V. S. Stavinsky, *Fiz. Élem. Chastits At. Yadra* **10**, 373 (1979) [*Sov. J. Part. Nucl.* **10**, 949 (1979)].
13. L. Nottale, *Fractal Space-Time and Microphysics* (World Sci., Singapore, 1993).
14. B. Mandelbrot, *The Fractal Geometry of Nature* (Freeman, San Francisco, 1982).
15. V. V. Abramov *et al.*, *Sov. J. Nucl. Phys.* **41**, 227 (1985).
16. L. K. Turchanovich *et al.*, *Yad. Fiz.* **56** (10), 116 (1993) [*Phys. At. Nucl.* **56**, 1367 (1993)].
17. A. L. S. Angelis *et al.*, *Phys. Lett. B* **79B**, 505 (1978).
18. C. Kourkoumelis *et al.*, *Phys. Lett. B* **83B**, 257 (1979).
19. C. Kourkoumelis *et al.*, *Z. Phys. C* **5**, 95 (1980).
20. D. Lloyd Owen *et al.*, *Phys. Rev. Lett.* **45**, 89 (1980).
21. K. Eggert *et al.*, *Nucl. Phys. B* **98**, 49 (1975).
22. E. Anassontzis *et al.*, *Z. Phys. C* **13**, 277 (1982).
23. GLMR Collab. (G. Balocchi *et al.*), *Yad. Fiz.* **57**, 1694 (1994).
24. C. Albajar *et al.*, *Phys. Lett. B* **209**, 385 (1988).

25. J. A. Appel *et al.*, Phys. Lett. B **176**, 239 (1986); J. Alitti *et al.*, Phys. Lett. B **263**, 544 (1991); R. Ansari *et al.*, Z. Phys. C **41**, 395 (1988).
26. J. Povlis *et al.*, Phys. Rev. Lett. **51**, 967 (1983).
27. G. Balocchi *et al.*, Phys. Lett. B **317**, 250 (1993); G. Balocchi *et al.*, Phys. Lett. B **436**, 222 (1998).
28. J. W. Cronin *et al.*, Phys. Rev. D **11**, 3105 (1975); D. Antreasyan *et al.*, Phys. Rev. D **19**, 764 (1979).
29. D. Jaffe *et al.*, Phys. Rev. D **40**, 2777 (1989).
30. N. D. Giokaris *et al.*, Phys. Rev. Lett. **47**, 1690 (1981); H. J. Frisch *et al.*, Phys. Rev. D **27**, 1001 (1983).
31. F. Abe *et al.*, Phys. Rev. Lett. **68**, 2734 (1992); F. Abe *et al.*, Phys. Rev. D **48**, 2998 (1993); F. Abe *et al.*, Phys. Rev. Lett. **73**, 2662 (1994); L. Nodulman, in *Proceedings of the 28th International Conference on High-Energy Physics, Warsaw, Poland, 1996*, PA04-76; FERMILAB-Conf-96/337-E.
32. A. Abachi *et al.*, Phys. Rev. Lett. **77**, 5011 (1996); FERMILAB-Pub-96/072-E; S. Fahey, PhD Thesis (Michigan State Univ., 1995); Y.-C. Liu, PhD Thesis (Northwestern Univ., 1996).
33. G. Alverson *et al.*, Phys. Rev. D **48**, 5 (1993); L. Apanasevich *et al.*, Phys. Rev. Lett. **81**, 2642 (1998); hep-ex/9711017; M. Begel *et al.*, in *Proceedings of the Workshop on the High- $p_T$  Phenomena at RHIC, BNL, 2001*.
34. PHENIX Collab. (H. Torii *et al.*), in *Proceedings of the Quark Matter 2002, Nantes, France*; <http://alice-france.in2p3.fr/qm2002>.

---

---

**ELEMENTARY PARTICLES AND FIELDS**  
**Theory**

---

---

## Intermittency in the Ginzburg–Landau Model for Parton–Hadron Phase Transitions

L. F. Babichev\*, A. A. Bukach, V. I. Kuvshinov\*\*, and V. A. Shaparau\*\*\*

*Institute of Physics, National Academy of Sciences of Belarus, pr. F. Skaryna 68, Minsk, 220072 Belarus*

Received March 20, 2003; in final form, August 21, 2003

**Abstract**—The formalism of squeezed states within Ginzburg–Landau theory is used to describe parton–hadron phase transitions in processes involving the production of rather high energy densities. Normalized factorial moments are studied as functions of a bin width of phase space at various squeezing parameters. The intermittency effect and scaling behavior of the moments under consideration are revealed. The values obtained for the scaling exponent agree with experimental data at small values of the squeezing parameter.

© 2004 MAIK “Nauka/Interperiodica”.

### 1. INTRODUCTION

As the collision energy is increased in modern experiments, the role of collective effects in the interactions of high-energy particles becomes more pronounced. Despite successes achieved in describing these processes within perturbative QCD [1–4], perturbation theory cannot reproduce all properties of quark–gluon interactions—in particular, collective aspects of the behavior of a parton system [5]. In view of confinement, the problem of adequately comparing the parton features obtained within perturbative QCD with hadron ones remains open.

The hypothesis of local parton–hadron duality gives grounds to consider functional dependences of inclusive distributions to be identical for partons and hadrons. However, this cannot be stated definitively for correlation features [6], whose behavior displays the effect of intermittency. Intermittency is highly sensitive to a specific description of the soft stage [7, 8], whose role is enhanced for processes leading to the generation of rather high energy densities—for example, in heavy-ion collisions. Along with calculations performed within perturbative QCD, use is therefore made of various models that take into account a nonperturbative evolution. Such models are intensively employed in describing experimental data on heavy-ion collisions (at RHIC) in view of the possible formation of quark–gluon plasma.

An approach where the parton–hadron transition is considered as a phase transition—this is corroborated by lattice calculations [9–12]—may be one of the possible ways to include nonperturbative effects.

It is well known that fluctuations of the multiplicity of hadrons generated in heavy-ion collisions at high energies can serve as a criterion of a phase transition in a quark–gluon system [13]. Such fluctuations were studied in nonlinear optics [14], where the instability of nonequilibrium photon states was related to a second-order phase transition near the generation threshold. An idea to use, in investigating multiparticle-production processes, methods of optics, where the number of photons is great, consisted in employing the coherent-state representation [15, 16]. This representation was used in studying fluctuations of hadron multiplicities within the Ginzburg–Landau model [17–21]. This resulted in discovering the effect of intermittency and the scaling behavior of factorial moments. In the case where the quark–gluon system underwent a second-order phase transition, the scaling exponent  $\nu$  was 1.305 [18]; for a first-order phase transition investigated within the generalized Ginzburg–Landau model, it lay between 1.32 and 1.33 [21]. The calculated data were at odds with experimental results. Indeed, the value obtained for the scaling exponent was  $\nu = 1.45 \pm 0.04$  in the production of particles in hadron collisions [8] and  $\nu = 1.55 \pm 0.12$  [8, 17] and  $\nu = 1.459 \pm 0.021$  [22] in heavy-ion collisions. This discrepancy between the theoretical and experimental results indicates that the use of the coherent-state representation is insufficient for explaining the entire body of experimental data. In view of this, one can attempt to use the formalism of squeezed states, which include coherent states as a particular case [15, 23–25]. Depending on the parameter determining the direction of maximum squeezing, squeezed states possess various characteristic features—in particular, oscillations of cumulant moments [26] and sub-Poisson and super-

---

\* e-mail: [babichev@dragon.bas-net.by](mailto:babichev@dragon.bas-net.by)

\*\* e-mail: [kuvshino@dragon.bas-net.by](mailto:kuvshino@dragon.bas-net.by)

\*\*\* e-mail: [shaporov@dragon.bas-net.by](mailto:shaporov@dragon.bas-net.by)

Poisson distributions. Owing to these properties, the states in question were successfully applied in phenomenological approaches to describing multiplicity distributions [27–31]. The investigation of the dynamics of gluon states at the nonperturbative stage of the evolution of QCD jets revealed that the formation of squeezed gluon states is possible [32–35], which leads to a multiplicity distribution different from the negative binomial distribution, and this is indeed confirmed by experimental data [36–38].

2. MULTIPLICITY DISTRIBUTION OF SQUEEZED HADRON STATES IN A PHASE TRANSITION

In quantum optics, use is made of two basic forms of ideal squeezed states—that is, coherent and scaling states that are defined as

$$\left. \begin{aligned} |\psi, \eta\rangle &= \hat{D}(\psi)\hat{S}(\eta)|0\rangle \text{ (coherent squeezed state),} \\ |\psi, \eta\rangle &= \hat{S}(\eta)\hat{D}(\psi)|0\rangle \text{ (scaling squeezed state),} \end{aligned} \right\} \quad (1)$$

where  $\hat{D}(\psi) = \exp\{\psi a^+ - \psi^* a\}$  is the amplitude-displacement operator;  $\hat{S}(\eta) = \exp\left\{\frac{\eta^*}{2}a^2 - \frac{\eta}{2}(a^+)^2\right\}$  is the squeezing operator;  $\psi = |\psi|e^{i\gamma}$  is an eigenvalue of the annihilation operator  $a$ ;  $|\psi|$  and  $\gamma$  are, respectively, the amplitude and the phase of a coherent state; and  $\eta = re^{i\theta}$  is an arbitrary complex-valued number, with  $r$  and  $\theta$  being, respectively, a squeeze factor and a phase that determines the direction of squeezing [24]. From an expression for the multiplicity distribution of two-photon coherent states [39], one can obtain the corresponding expressions for the distributions of coherent squeezed and scaling states; that is,

$$P_n^0 = \frac{1}{\cosh(r)n!} \left(\frac{\tanh(r)}{2}\right)^n |H_n(\xi_1)|^2 e^{\xi_2}, \quad (2)$$

where  $H_n(\xi_1)$  is a Hermitian polynomials and the quantities  $\xi_1$  and  $\xi_2$  can be represented as

$$\left. \begin{aligned} \xi_1 &= \sqrt{\frac{\langle n \rangle - \sinh^2(r)}{\sinh(2r)}} \left[ \cosh(r)e^{i(\gamma-\theta/2)} + \sinh(r)e^{-i(\gamma-\theta/2)} \right], \\ \xi_2 &= [\langle n \rangle - \sinh^2(r)] \times \left( \cosh(2r)[\tanh(r) \cos(2\gamma - \theta) - 1] \right. \\ &\quad \left. + \sinh(2r)[\tanh(r) - \cos(2\gamma - \theta)] \right) \end{aligned} \right\} \quad (3)$$

for coherent squeezed states and as

$$\left. \begin{aligned} \xi_1 &= \sqrt{\frac{\langle n \rangle - \sinh^2(r)}{\sinh(2r)}} e^{i(\gamma-\theta/2)} \left[ \cosh(2r) - \sinh(2r) \cos(2\gamma - \theta) \right]^{-1/2}, \\ \xi_2 &= \frac{[\langle n \rangle - \sinh^2(r)][\tanh(r) \cos(2\gamma - \theta) - 1]}{\cosh(2r) - \sinh(2r) \cos(2\gamma - \theta)} \end{aligned} \right\} \quad (4)$$

for scaling squeezed states. Here,  $\langle n \rangle$  is the mean number of hadrons in squeezed states. In the particular case of  $\gamma = \theta = 0$ , expression (2) coincides with the analogous expressions presented in [27, 28] and used in describing multiplicity distributions in  $e^+e^-$  and  $p\bar{p}$  processes.

Since, in quantum field theory, the mean number of particles in a volume  $V$  is defined, according to [40],

as

$$\langle n \rangle = \left\langle \int_V dz a^+(z)a(z) \right\rangle, \quad (5)$$

this quantity in the case of coherent and scaling squeezed states has the form

$$\left. \begin{aligned} \langle n \rangle &= \int_V |\psi(z)|^2 dz + \sinh^2(r) && \text{(coherent squeezed state),} \\ \langle n \rangle &= \left( \int_V |\psi(z)|^2 dz \right) \left[ \cosh(2r) - \sinh(2r) \cos(2\gamma - \theta) \right] + \sinh^2(r) && \text{(scaling squeezed states).} \end{aligned} \right\} \quad (6)$$

Here,  $z$  stands for the following set of kinematical variables:  $(y, \varphi, p_\perp)$ , where  $y$  is a rapidity,  $\varphi$  is an azimuthal angle ( $0 \leq \varphi \leq 2\pi$ ), and  $p_\perp$  is a transverse momentum; the ranges of the rapidity and transverse momentum depend on the specific type of the processes being considered. For the sake of simplicity, we assume here that the phase of a coherent state and squeeze factors are constant over the entire phase space—that is,  $\gamma$ ,  $r$ , and  $\theta$  are parameters. Substituting expressions (6) for the mean multiplicity into formulas (3) and (4) and using expression (2), one can determine the probability density for finding  $n$  particles in the squeezed state,  $|\langle n|\psi(z), \eta \rangle|^2 = P_n^0$ . We have

$$\begin{aligned} P_n^0 &= \frac{1}{\cosh(r)n!} \left( \frac{\tanh(r)}{2} \right)^n && (7) \\ &\times \left| H_n \left( \left[ \int_V |\psi(z)|^2 dz \right]^{1/2} F_1(r, \gamma, \theta) \right) \right|^2 \\ &\times \exp \left\{ \int_V |\psi(z)|^2 dz F_2(r, \gamma, \theta) \right\}, \end{aligned}$$

where  $F_1(r, \gamma, \theta)$  and  $F_2(r, \gamma, \theta)$  are functions of the parameters  $r$ ,  $\gamma$ , and  $\theta$ . These functions are written as

$$F_1(r, \gamma, \theta) = \frac{\cosh(r)e^{i(\gamma-\theta/2)} + \sinh(r)e^{-i(\gamma-\theta/2)}}{\sqrt{\sinh(2r)}}, \quad (8)$$

$$F_2(r, \gamma, \theta) = \cosh(2r)[\tanh(r) \cos(2\gamma - \theta) - 1] + \sinh(2r)[\tanh(r) - \cos(2\gamma - \theta)]$$

for coherent squeezed states and as

$$F_1(r, \gamma, \theta) = \frac{e^{i(\gamma-\theta/2)}}{\sqrt{\sinh(2r)}}, \quad (9)$$

$$F_2(r, \gamma, \theta) = \tanh(r) \cos(2\gamma - \theta) - 1$$

for scaling squeezed states. The expression that we obtained for the distributions of squeezed hadron states reflects the known properties inherent in the distributions of analogous photon states: depending on the parameter  $\theta$ , it can be either a sub-Poisson distribution (for example, at  $\theta = 0$ ) or a super-Poisson

distribution ( $\theta = \pi$ ); also, it can develop oscillations at  $r \geq 1$ , irrespective of the value of  $\theta$  (Fig. 1). It is obvious that, in the limit  $r \rightarrow 0$ , where there is no squeezing effect, we arrive at the Poisson distribution of hadrons

$$P_n^0 = \frac{1}{n!} \exp \left\{ - \int_V |\psi(z)|^2 dz \right\} \left( \int_V |\psi(z)|^2 dz \right)^n. \quad (10)$$

In general, the system being considered can be in a mixed state defined as a set of pure states  $|\psi(z), \eta \rangle$  with different weights. In this case, the multiplicity distribution is defined as a path integral of the type [41]

$$P_n = Z^{-1} \int D\psi P_n^0 e^{-F[\psi]}, \quad (11)$$

where  $Z = \int D\psi e^{-F[\psi]}$  is a normalization factor and  $F[\psi]$  is an arbitrary functional, a free energy being its analog in statistical physics. Since there is no full dynamical theory that would make it possible to calculate  $F[\psi]$ , it is natural to invoke a phenomenological ansatz. The evolution of the quark–gluon system that is formed at high collision-energy densities can be considered as a process in which the hydrodynamic expansion of a nuclear-matter bunch is followed by a phase transition to hadrons as soon as the decreasing temperature  $T$  reaches a certain value (critical temperature  $T_c$ ). By analogy with the phenomenological Ginzburg–Landau theory of superconductivity, the functional  $F[\psi]$  can be taken in the form

$$F[\psi] = \int dz \{ a|\psi(z)|^2 + b|\psi(z)|^4 + c|\partial\psi/\partial z|^2 \}, \quad (12)$$

where  $\psi(z)$  is a complex-valued order parameter,  $|\psi(z)|^2$  being the local hadron density. The phase-transition point corresponds to the vanishing of the parameter  $a = a_1(T - T_c)$ , where  $a_1 > 0$ ; for the hadronic phase,  $a < 0$ . The parameters  $b$  and  $c$  are positive [18].

Expression (11) reflects fluctuations of the hadron multiplicity, their magnitude being determined by the

Boltzmann thermodynamic factor  $e^{-F[\psi]}$ . By using expression (7), we can recast (11) into the form

$$P_n = \frac{1}{2Z \cosh(r)} \int D\psi \frac{\tanh^n(r)}{2^{n!}} \quad (13)$$

$$\times \exp \left\{ -F[\psi] + \int_V |\psi(z)|^2 dz F_2(r, \gamma, \theta) \right\}$$

$$\times \left| H_n \left( \left[ \int_V |\psi(z)|^2 dz \right]^{1/2} F_1(r, \gamma, \theta) \right) \right|^2.$$

In order to investigate the above expression, we make simplifications used in [17, 18] to analyze intermittency: specifically, we break down phase space into bins of identical width  $\delta$  ( $V = \delta^d$ , where  $d$  is the space dimensionality) and assume that  $|\psi(z)|$  is constant over each bin. In this case, the multiplicity distribution with allowance for a second-order phase transition can be represented as

$$P_n = \frac{1}{2\pi \cosh(r)} D_{-1}^{-1} \left( -|a| \sqrt{\frac{\delta^d}{2b}} \right) \quad (14)$$

$$\times \int_0^{2\pi} d\gamma \tanh^n(r)$$

$$\times \exp \left\{ \frac{\delta^d F_2(r, \gamma, \theta) (F_2(r, \gamma, \theta) + 2|a|)}{8b} \right\}$$

$$\times \sum_{k=0}^{n/2} \sum_{l=0}^{n/2} (-1)^{k+l} \left( \frac{2\delta^d}{b} \right)^{1/2(n-k-l)}$$

$$\times \frac{(2k-1)!!(2l-1)!!n!(n-k-l)!}{(2k)!(2l)!(n-2k)!(n-2l)!}$$

$$\times F_1^{n-2k}(r, \gamma, \theta) (F_1^*)^{n-2l}(r, \gamma, \theta)$$

$$\times D_{-(n-k-l+1)} \left( -[|a| + F_2(r, \gamma, \theta)] \sqrt{\frac{\delta^d}{2b}} \right),$$

where  $D_{-f}(w)$  is a parabolical cylinder function. It should be noted that the expression obtained for  $P_n$  depends on the parameters  $a$  and  $b$  of the Ginzburg–Landau potential, on the parameter  $r$  characterizing the degree of squeezing, and on the bin width  $\delta$ , but it is independent of the phase  $\theta$  characterizing the direction of maximum squeezing. In contrast to what was obtained in [17, 18], it is the emergence of an additional parameter  $r$  in the explicit form of the multiplicity distributions  $P_n$  [see Eqs. (13), (14)] that will play an important role in analyzing intermittency.

### 3. INTERMITTENCY

One of the efficient ways to reveal multiplicity fluctuations is to investigate the dependence of the

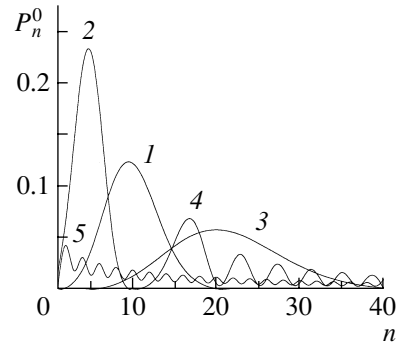


**Fig. 1.** Multiplicity distributions before phase transition: (1) Poisson distribution; (2, 3) distributions of scaling squeezed states at  $r = 0.38758$  for  $\theta = 0$  and  $\pi$ , respectively; and (4, 5) coherent squeezed states at  $r = 2.48$  for  $\theta = 0$  and  $\pi$ , respectively.

normalized factorial moments  $F_q$  [8, 42],

$$F_q = \frac{\langle n(n-1) \cdots (n-q+1) \rangle}{\langle n \rangle^q} = \frac{f_q}{f_1^q}, \quad (15)$$

on the rapidity-bin width  $\delta$ . Here,  $f_q = \langle n(n-1) \cdots (n-q+1) \rangle$  stands for unnormalized factorial moments,  $\langle \cdots \rangle$  denotes averaging over the entire ensemble of events, and  $n$  is the number of hadrons detected within the bin width  $\delta$  in a single event. If, with decreasing bin width, the moments in question increase according to a power law,

$$F_q \propto \delta^{-\varphi_q}, \quad (16)$$

the intermittency effect is present [8], its degree being determined by the intermittency exponent  $\varphi_q$  ( $\varphi_q > 0$ ). Multiplicity fluctuations will be absent if the behavior of the normalized factorial moments is independent of the bin width. Therefore, the presence of intermittency can serve as an indirect indication of the fact that the system has undergone a phase transition [42].

Let us investigate the behavior of factorial moments of the type  $f_q = \sum_{n=q}^{\infty} \frac{n!}{(n-q)!} P_n$ . By using (13), they can be written in the form

$$f_q = \frac{1}{2Z \cosh(r)} \int D\psi e^{-F[\psi]} \quad (17)$$

$$\times \exp \left\{ \int_V |\psi(z)|^2 dz F_2(r, \gamma, \theta) \right\}$$

$$\times \sum_{n=q}^{\infty} \frac{1}{(n-q)!} \left( \frac{\tanh(r)}{2} \right)^n$$

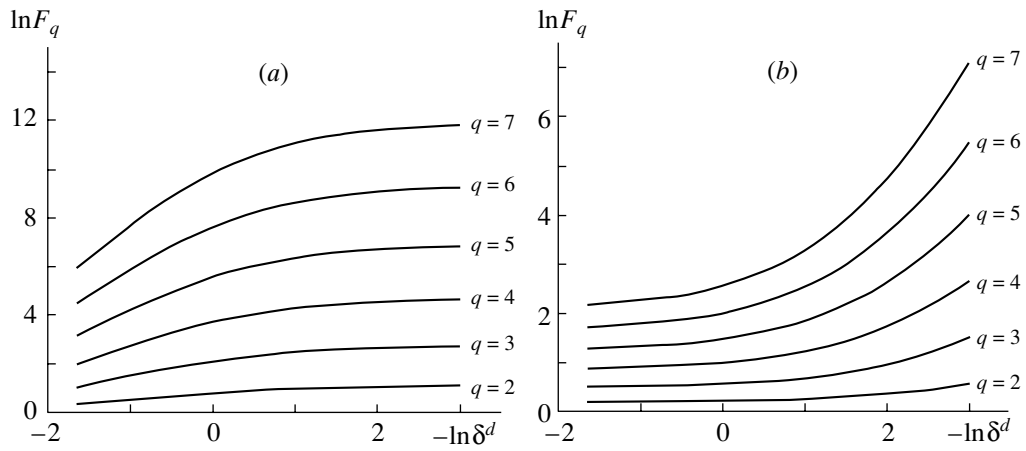


**Fig. 2.** Dependence of  $\ln F_q$  on  $(-\ln \delta^d)$  for (a) coherent squeezed states ( $r = 2.48$ ) and (b) scaling squeezed states ( $r = 0.38758$ ) of hadrons at  $a = -10$  and  $b = 0.20055$ .

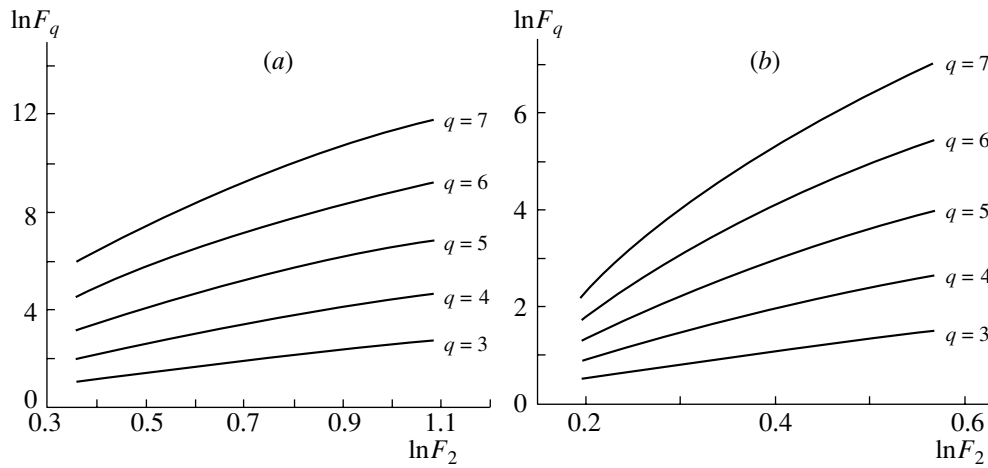


**Fig. 3.** Dependence of  $\ln F_q$  on  $\ln F_2$  for (a) coherent squeezed states and (b) scaling squeezed states of hadrons at the same values of the parameters  $a, b$ , and  $r$  as in Fig. 2.

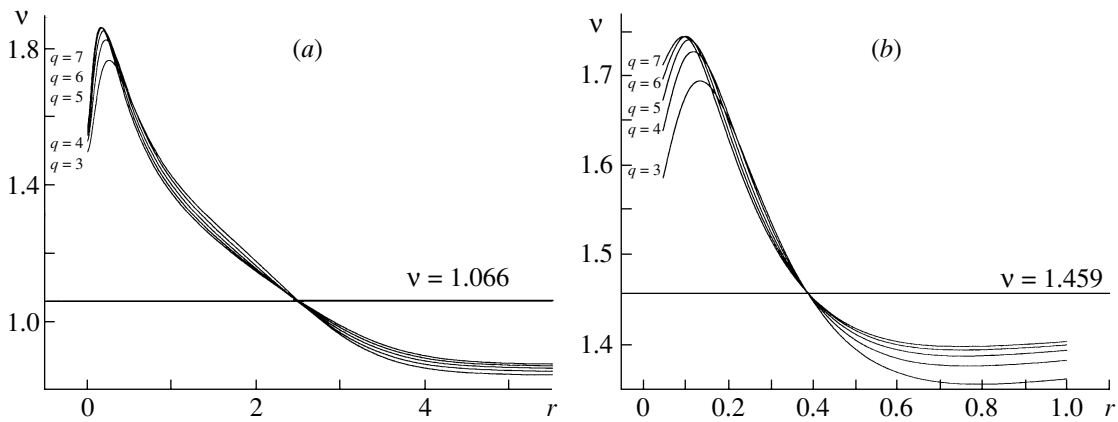


**Fig. 4.** Dependence of the scaling exponent  $\nu$  on the squeeze factor  $r$  for (a) coherent squeezed states and (b) scaling squeezed states of hadrons at the same values of the parameters  $a$  and  $b$  as in Fig. 2.

Parameters at which the values of the scaling exponent (in the case of scaling squeezed states) agree with experimental data

$a$	$\nu = 1.450$		$\nu = 1.459$		$\nu = 1.550$	
	$b$	$r$	$b$	$r$	$b$	$r$
-1	0.00663	0.32363	0.00592	0.32663	0.00220	0.34375
-2	0.02761	0.31312	0.02455	0.31826	0.00992	0.32266
-3	0.05217	0.32917	0.04988	0.32216	0.02275	0.31387
-4	0.07313	0.35251	0.06956	0.34795	0.03760	0.31758
-5	0.09535	0.36548	0.09052	0.36190	0.05582	0.31572
-6	0.11815	0.37385	0.11213	0.37079	0.07140	0.32305
-7	0.14138	0.37970	0.13398	0.37693	0.08570	0.33040
-8	0.16472	0.38401	0.15609	0.38144	0.09871	0.33740
-9	0.18819	0.38730	0.17834	0.38489	0.11190	0.34261
-10	0.21187	0.38983	0.20055	0.38758	0.12518	0.34664

$$\times \left| H_n \left( \left[ \int_V |\psi(z)|^2 dz \right]^{1/2} F_1(r, \gamma, \theta) \right) \right|^2, \quad \times \left| H_n \left( \sqrt{\frac{|\psi|^2 \delta^d}{\sinh(2r)}} e^{i(\gamma-\theta/2)} \right) \right|^2$$

where  $V$  is the volume of the cell in which  $f_q$  is measured. Taking into account the formula [43]

$$\sum_{k=0}^{\infty} \frac{t^k}{k!} H_{k+m}(x) H_{k+n}(y) = (1 - 4t^2)^{-(m+n+1)/2} \tag{18}$$

$$\times \exp \left[ \frac{4xyt - 4t^2(x^2 + y^2)}{1 - 4t^2} \right] \times \sum_{k=0}^{\min(m,n)} 2^{2k} k! \binom{m}{k} \binom{n}{k} t^k \times H_{m-k} \left( \frac{x - 2ty}{\sqrt{1 - 4t^2}} \right) H_{n-k} \left( \frac{y - 2tx}{\sqrt{1 - 4t^2}} \right)$$

and using known simplifications applied in analyzing intermittency [17, 18] and the explicit expressions for functions  $F_1(r, \gamma, \theta)$  and  $F_2(r, \gamma, \theta)$  [that is, expression (8) for coherent squeezed states and expression (9) for scaling squeezed states], we recast (17) into the form

$$f_q = (2Z)^{-1} \sinh^{2q}(r) \int_0^{2\pi} d\gamma \int_0^{\infty} d|\psi|^2 e^{-F[\psi]} \tag{19} \times \sum_{n=0}^q \frac{(q!)^2}{(n!)^2} \frac{1}{(q-n)!(2 \tanh(r))^n}$$

for coherent squeezed state and into the form

$$f_q = (2Z)^{-1} \sinh^{2q}(r) \int_0^{2\pi} d\gamma \int_0^{\infty} d|\psi|^2 e^{-F[\psi]} \tag{20} \times \sum_{n=0}^q \frac{(q!)^2}{(n!)^2} \frac{1}{(q-n)!(2 \tanh(r))^n} \times \left| H_n \left( \sqrt{\frac{|\psi|^2 \delta^d}{\sinh(2r)}} \left[ \cosh(r) e^{i(\gamma-\frac{\theta}{2})} - \sinh(r) e^{-i(\gamma-\frac{\theta}{2})} \right] \right) \right|^2$$

for scaling squeezed states. Upon integration, the resulting expressions can be represented as

$$f_q = \frac{J_q}{J_0}, \tag{21}$$

where

$$J_q = \frac{\pi}{\sqrt{2b\delta^d}} \exp \left\{ \frac{|a|^2 \delta^d}{8b} \right\} \sinh^{2q}(r) \tag{22} \times \sum_{n=0}^q \frac{(q!)^2}{(q-n)!} \tanh^{-n}(r) \sum_{k=0}^{n/2} \left( \frac{(2k-1)!!}{(2k)!} \right)^2 \times \frac{(\sinh(2r))^{2k-n}}{(n-2k)!} \left( \frac{2\delta^d}{b} \right)^{(1/2)(n-2k)}$$

$$\times D_{-(n-2k+1)} \left( -|a| \sqrt{\frac{\delta^d}{2b}} \right)$$

in the case of coherent squeezed states and

$$J_q = \frac{\pi}{\sqrt{2b\delta^d}} \exp \left\{ \frac{|a|^2 \delta^d}{8b} \right\} \sinh^{2q}(r) \quad (23)$$

$$\times \sum_{n=0}^q \frac{(q!)^2}{(q-n)!} \tanh^{-n}(r)$$

$$\times \sum_{k=0}^{n/2} \sum_{l=0}^{n/2} \frac{(2k-1)!!(2l-1)!!}{(2k)!(2l)!}$$

$$\times (\sinh(2r))^{k+l-n} (n-k-l)! \left( \frac{2\delta^d}{b} \right)^{(1/2)(n-k-l)}$$

$$\times D_{-(n-k-l+1)} \left( -|a| \sqrt{\frac{\delta^d}{2b}} \right) \sum_{j=0}^{n-2l}$$

$$\times \frac{(\sinh(r))^{l-k+2j} (\cosh(r))^{2n-k-2l-2j}}{j!(l-k+j)!(n-k-l-j)!(n-2l-j)!}$$

for scaling squeezed states. With allowance for (15), the normalized factorial moments  $F_q$  can also be expressed in terms of the function  $J_q$ ; that is,

$$F_q = J_q J_1^{-q} J_0^{q-1}. \quad (24)$$

An analysis of the graph of  $\ln F_q$  as a function of  $(-\ln \delta^d)$  at the squeeze-factor values of  $r = 2.48$  (coherent squeezed states) and  $r = 0.38758$  (scaling squeezed states) for the parameters of the Ginzburg–Landau model that are set to  $a = -10$  and  $b = 0.20055$  (Fig. 2) indicates the presence of multiplicity fluctuations. It should be noted that, for coherent squeezed states, the fluctuations of hadron multiplicities are the most pronounced for  $-\ln \delta^d < 0$ , while, for scaling squeezed states, the pattern is totally different—the fluctuations in question become significant for  $-\ln \delta^d > 1$ .

On the other hand, we note that, if the intermittency effect is peculiar to the system being considered, the scaling behavior of the normalized factorial moments is possible [42]; in this case, the slope of the curve representing the dependence  $\ln F_q(\ln F_2)$  is constant [44]:

$$F_q \propto F_2^{\beta_q}. \quad (25)$$

It can be seen from Fig. 3 that, in the case of squeezed states, the moments  $F_q$  manifest a scaling behavior at the same values of the parameters as in the analysis of  $\ln F_q$  as a function of  $(-\ln \delta^d)$ .

The slope coefficients  $\beta_q$  are approximated by the formula [17]

$$\beta_q = (q-1)^\nu, \quad (26)$$

where  $\nu$  is the scaling exponent. The dependence of  $\nu$  on the squeeze factor  $r$  in Fig. 4 at the same values of the parameters  $a$  and  $b$  of the Ginzburg–Landau model indicates the presence of scaling in the behavior of normalized factorial moments: in the case of coherent squeezed states,  $\nu = 1.066$  at  $r = 2.48$ , while, in the case of scaling squeezed states,  $\nu = 1.459$  at  $r = 0.38758$ . In the case of scaling squeezed states, the value of the scaling exponent is in agreement with NA22 experimental data on heavy-ion collisions [22]. The parameter values at which our results for the scaling exponent in the case of scaling squeezed states are in accord with various experimental data [8] are given in the table.

#### 4. CONCLUSION

By generalizing the concept of coherent states to the case of squeezed hadron states, we have studied fluctuations of hadron multiplicities within the Ginzburg–Landau model. The presence of such fluctuations suggests the possibility of a phase transition from partons to hadrons in processes where the collision-energy density is high. The behavior of the normalized factorial moments obtained here is indicative of the intermittency effect, which was discovered in various experiments that studied  $e^+e^-$ ,  $\mu p$ ,  $pp$ ,  $pA$ , and  $AA$  collisions [8]. At specific values of the squeeze factor  $r$  and of the parameters  $a$  and  $b$  of the Ginzburg–Landau functional, scaling has been found in the behavior of the normalized factorial moments being investigated. In contrast to what was done in [17, 18], the use of squeezed states has enabled us to obtain, by varying the squeeze factor, which is an additional parameter of our model, a scaling-exponent ( $\nu$ ) value that is in agreement with experimental data from [8, 22]. By way of example, we indicate that, for scaling squeezed states, the value of  $\nu = 1.459$  obtained at  $a = -10$ ,  $b = 0.20055$ , and  $r = 0.38758$  is in agreement with the respective experimental result for heavy-ion collisions [22].

We hope that the application of squeezed states will be of use in describing multiplicity fluctuations and in seeking the intermittency effect in processes leading to the formation of a quark–gluon plasma—for example, in heavy-ion collisions at high energies.

#### REFERENCES

1. Yu. L. Dokshitzer, V. A. Khoze, A. H. Mueller, and S. I. Troian, *Basics of Perturbative QCD* (Frontières, Gif-sur-Yvette, 1991).
2. T. Hebbeker, Phys. Rep. **217**, 69 (1992).
3. Yu. L. Dokshitzer *et al.*, J. Phys. G **17**, 1481 (1991).
4. I. M. Dremin and R. C. Hwa, Phys. Rev. D **49**, 5805 (1994).

5. I. M. Dremin and A. V. Leonidov, *Usp. Fiz. Nauk* **165**, 759 (1995).
6. I. M. Dremin, *Usp. Fiz. Nauk* **164**, 785 (1994).
7. E. A. De Wolf, I. M. Dremin, and W. Kittel, *Usp. Fiz. Nauk* **163**, 3 (1993).
8. E. A. De Wolf, I. M. Dremin, and W. Kittel, *Phys. Rep.* **270**, 1 (1996).
9. A. Ukawa, *Nucl. Phys. A* **498**, 227 (1989).
10. H. Gausterer and S. Sanielevici, *Phys. Lett. B* **209**, 533 (1988).
11. F. Wilzcek, *Int. J. Mod. Phys. A* **7**, 3911 (1992).
12. M. I. Polikarpov, *Usp. Fiz. Nauk* **165**, 6 (1995).
13. A. Bialas and R. C. Hwa, *Phys. Lett. B* **253**, 436 (1991).
14. R. Graham, *Quantum Statistics in Optics and Solid State Physics* (Springer-Verlag, Berlin, 1973).
15. D. F. Walls and G. J. Milburn, *Quantum Optics* (Springer-Verlag, New York, 1995).
16. J. C. Botke, D. J. Scalapino, and R. L. Sugar, *Phys. Rev. D* **9**, 813 (1974).
17. R. C. Hwa and M. T. Nazirov, *Phys. Rev. Lett.* **69**, 741 (1992).
18. R. C. Hwa, *Phys. Rev. D* **47**, 2773 (1993).
19. L. F. Babichev, D. V. Klenitsky, and V. I. Kuvshinov, in *Proceedings of the 3rd International Seminar on Nonlinear Phenomena in Complex Systems, 1994, Polatsk, Belarus* (Institute Phys., Minsk, 1995), p. 149.
20. R. C. Hwa, *Phys. Rev. C* **50**, 383 (1994).
21. L. F. Babichev, D. V. Klenitsky, and V. I. Kuvshinov, *Phys. Lett. B* **345**, 269 (1995).
22. P. L. Jain *et al.*, *Phys. Lett. B* **236**, 219 (1990); *Phys. Rev. C* **44**, 854 (1991); **48**, 517 (1993).
23. O. Hirota, *Squeezed Light* (Tokyo, 1992).
24. M. O. Scully and M. S. Zubairy, *Quantum Optics* (Cambridge Univ. Press, Cambridge, 1997).
25. S. Ya. Kilin, *Quantum Optics: Fields and Their Detection* (Nauka i Tekhnika, Minsk, 1990) [in Russian].
26. V. V. Dodonov, I. M. Dremin, P. G. Polynkin, and V. I. Man'ko, *Phys. Lett. A* **193**, 209 (1994).
27. B. A. Bambah and M. V. Satyanarayana, *Phys. Rev. D* **38**, 2202 (1988).
28. A. Vourdas and R. M. Weiner, *Phys. Rev. D* **38**, 2209 (1988).
29. C. C. Shih, *Phys. Rev. D* **34**, 2720 (1986).
30. P. Carruthers and C. C. Shih, *Int. J. Mod. Phys.* **2**, 1447 (1987).
31. I. M. Dremin and R. C. Hwa, *Phys. Rev. D* **53**, 1216 (1996).
32. S. Ya. Kilin, V. I. Kuvshinov, and S. A. Firago, in *Proceedings of the Workshop on Squeezed States and Uncertainty Relations, Moscow, Russia, 1992* (NASA, 1993), p. 301.
33. V. I. Kuvshinov and V. A. Shaporov, *Acta Phys. Pol. B* **30**, 59 (1999).
34. V. I. Kuvshinov and V. A. Shaparau, *Nonlinear Phenomena in Complex Systems* **3**, 28 (2000).
35. V. I. Kuvshinov and V. A. Shaparau, *Yad. Fiz.* **65**, 334 (2002) [*Phys. At. Nucl.* **65**, 309 (2002)].
36. UA-5 Collab. (G. J. Alner *et al.*), *Phys. Rep.* **154**, 247 (1987).
37. DELPHI Collab. (P. Abreu *et al.*), *Z. Phys. C* **50**, 185 (1991).
38. OPAL Collab. (P. D. Acton *et al.*), *Z. Phys. C* **53**, 539 (1992).
39. H. P. Yuen, *Phys. Rev. A* **13**, 2226 (1976).
40. C. Itzykson and J.-B. Zuber, *Introduction to Quantum Field Theory* (McGraw-Hill, New York, 1980; Mir, Moscow, 1984).
41. D. J. Scalapino and R. L. Sugar, *Phys. Rev. D* **8**, 2284 (1973).
42. A. Bialas and R. Peschanski, *Nucl. Phys. B* **273**, 703 (1986); **308**, 857 (1988).
43. A. P. Prudnikov, Yu. A. Brychkov, and O. I. Marichev, *Integrals and Series* (Nauka, Moscow, 1983; Gordon and Breach, New York, 1986), Vol. 2.
44. W. Ochs and J. Wosiek, *Phys. Lett. B* **214**, 617 (1988).

*Translated by A. Isaakyan*

---

---

**ELEMENTARY PARTICLES AND FIELDS**  
**Theory**

---

---

## Cosmological Constant in SUGRA Models and the Multiple-Point Principle\*

C. Froggatt<sup>1)\*\*</sup>, L. V. Laperashvili<sup>\*\*\*</sup>, R. B. Nevzorov<sup>\*\*\*\*</sup>, and H. B. Nielsen<sup>2)\*\*\*\*\*</sup>

*Institute of Theoretical and Experimental Physics,  
Bol'shaya Cheremushkinskaya ul. 25, Moscow, 117259 Russia*

Received February 18, 2003; in final form, October 3, 2003

**Abstract**—An attempt is made to explain the tiny order of magnitude of the cosmological constant in a model involving the following ingredients: supersymmetry breaking in  $N = 1$  supergravity and the multiple-point principle. We demonstrate the viability of this scenario in the minimal SUGRA model.

© 2004 MAIK “Nauka/Interperiodica”.

### 1. INTRODUCTION

As is well known, cosmology yields strong arguments against the Standard Model (SM). Although the SM describes perfectly the major part of all experimental data measured in Earth-based experiments, it does not provide any reliable candidate for dark matter. Another puzzle of modern cosmology is a tiny density of energy spread all over the Universe (the cosmological constant), which is responsible for its acceleration. At first glance, this energy density ( $\Lambda$ ) should be of the order of the Planck, or possibly the electroweak scale to the fourth power; however, a fit to recent data shows that  $\Lambda \sim 10^{-123} M_{\text{Pl}}^4 \sim 10^{-55} M_Z^4$  [1]. The smallness of the cosmological constant should be considered as a fine-tuning problem, for which new theoretical ideas must be employed to explain the enormous cancellations between the contributions of different condensates to the cosmological constant.

Unfortunately the cosmological constant problem cannot be resolved in any available generalization of the SM. An exact global supersymmetry (SUSY) ensures zero value for the energy density at the minimum of the potential of the scalar fields. But in the exact SUSY limit, bosons and fermions from one chiral multiplet get the same masses. Soft SUSY

breaking, which guarantees the absence of superpartners of observable fermions in the 100-GeV range, does not protect the cosmological constant from an electroweak scale mass and the fine-tuning problem is reintroduced.

In this article, we propose the multiple-point principle (MPP)[2] as a basic principle to explain the size of the cosmological constant. MPP postulates that, in nature, as many phases as possible, which are allowed by the underlying theory, should coexist. On the phase diagram of the theory, it corresponds to the special point—the multiple point—where many phases meet. The vacuum energy densities of these different phases are degenerate at the multiple point. In other words, nature should adjust all the couplings of the SM (or any other model) such that a number of degenerate vacua are realized. The MPP relations between coupling constants can arise dynamically. For example, a mild form of locality breaking in quantum gravity, due to baby universes [3] say, is expected to precisely fine-tune the couplings so that indeed several phases with degenerate vacua coexist. Another possible origin for the MPP could be a symmetry. Supersymmetry is the best candidate for this role because all global vacua in SUSY models are degenerate. Moreover, the SUSY scalar potential often contains a few flat directions with zero vacuum energy.

The idea of the MPP was applied to the pure SM, by postulating that the Higgs effective potential has two rings of minima in the Mexican hat with the same vacuum energy density [4] (the effective potential depends only on the Higgs field norm and has two minima in it). The radius of the little ring is at the electroweak vacuum expectation value of the Higgs field, while the radius of the big one was assumed to be near the Planck scale ( $M_{\text{Pl}} \approx 10^{19}$  GeV). These

---

\*This article was submitted by the authors in English.

<sup>1)</sup>Department of Physics and Astronomy, Glasgow University, Glasgow, Scotland.

<sup>2)</sup>The Niels Bohr Institute, Copenhagen, Denmark.

\*\* e-mail: c.froggatt@physics.gla.ac.uk

\*\*\* e-mail: laper@heron.itep.ru

\*\*\*\* e-mail: nevzorov@heron.itep.ru

\*\*\*\*\* e-mail: hbech@alf.nbi.dk

two assumptions lead to rather precise predictions for the top quark (pole) and Higgs boson masses [4],

$$M_t = 173 \pm 4 \text{ GeV}, \quad M_H = 135 \pm 9 \text{ GeV}. \quad (1)$$

In the present article, the MPP is used, in conjunction with SUSY models, to deduce a size for the cosmological constant to be compared with the value obtained by astrophysical observations. We shall do this by assuming a priori the existence of a supersymmetric phase in flat (Minkowski) space, in addition to the phase in which we live. Since the vacuum energy density (cosmological constant) of supersymmetric states in flat Minkowski space is just zero, the cosmological constant problem is thereby solved to a first approximation by assumption. Now, the strategy is to estimate the SUSY-breaking energy contribution in this most supersymmetric phase, which is the only contribution to the cosmological constant in this case, and, by virtue of the MPP, to assign the value found to all other phases and especially to the one in which we live.

However, such a procedure immediately raises the question as to why the most supersymmetric phase is taken, among all the various ones, to get its value for the cosmological constant transferred via the MPP to all the other phases. The suggested answer is that one should choose, for this purpose, the phase with the smallest SUSY breaking and thus lowest cosmological constant to be the decisive phase. It comes from the philosophy that it is easier for the MPP to tune some cancellation, in order to make a quantity small, than it is to get its value strongly enhanced.

Of course, we do not solve the cosmological constant problem entirely in this work. Indeed, there is a murky point in the suggested procedure. In order to have a tiny value of the cosmological constant in the phase where SUSY is broken severely, we must call upon supergravity (SUGRA). In this case, a hidden sector can give an additional contribution to the total energy density canceling ones from other sources (like electroweak symmetry breaking in our phase, for example). At the same time, even in vacuum, where local SUSY remains intact, the total energy density tends to be huge and negative. This makes our initial assumption concerning the existence of a phase with global SUSY in flat Minkowski space rather artificial. An extrafine-tuning is required to obtain a viable solution of this type and corresponds to searching for only a partial solution of the cosmological constant problem. The aim of this paper is to calculate the deviation from zero cosmological constant, once our initial assumption is accepted.

This article is organized as follows. In the next section, we describe the structure of  $N = 1$  SUGRA

models and discuss the mechanism of SUSY breaking. We formulate our MPP SUGRA model in Section 3 and present some numerical estimates of the vacuum energy density in Section 4. Our results are summarized in Section 5.

## 2. FROM SUGRA TO SM

SUSY models clear the way to the unification of gauge interactions with gravity. Such unification is carried out in the framework of SUGRA models. The simplest  $N = 1$  SUSY models correspond to  $N = 1$  SUGRA. The full  $N = 1$  SUGRA Lagrangian [5] is specified in terms of an analytic gauge kinetic function  $f_a(\phi_M)$  and a real gauge-invariant Kähler function  $G(\phi_M, \phi_M^*)$ , which depend on the chiral superfields  $\phi_M$ . The function  $f_a(\phi_M)$  determines the kinetic terms for the fields in the vector supermultiplets and the gauge coupling constants  $\text{Re}f_a(\phi_M) = 1/g_a^2$ , where the index  $a$  designates different gauge groups. The Kähler function is a combination of two functions:

$$G(\phi_M, \phi_M^*) = K(\phi_M, \phi_M^*) + \ln |W(\phi_M)|^2, \quad (2)$$

where  $K(\phi_M, \phi_M^*)$  is the Kähler potential whose second derivatives define the kinetic terms for the fields in the chiral supermultiplets.  $W(\phi_M)$  is the complete analytic superpotential of the considered SUSY model. In this article, standard SUGRA mass units are used:  $M_{\text{Pl}}/\sqrt{8\pi} = 1$ .

Experimentally, of course, SUSY cannot be an exact symmetry at low energies and has to be broken in such a way that quadratic divergences are not induced (so-called soft SUSY breaking). In SUGRA models, local SUSY breaking happens in a hidden sector, which contains singlet superfields ( $h_m$ ) under the SM  $SU(3) \times SU(2) \times U(1)$  gauge group. These hidden superfields are introduced by hand in the simplest models.

In theoretically reliable SUGRA models, the form of the Kähler function and the structure of the hidden sector are fixed by an underlying renormalizable or even finite theory. Nowadays, the best candidate for the ultimate theory is  $E_8 \times E_8$  (ten-dimensional) heterotic superstring theory [6]. The strong coupling limit in this theory can be described by eleven-dimensional SUGRA on a manifold with two ten-dimensional boundaries (M theory) [7]. Gauge multiplets of each  $E_8$  gauge group are localized on a separate boundary and interact with multiplets of the other  $E_8$  by virtue of gravitational forces. Compactification of the extra dimensions on a Calabi–Yau manifold leads to an effective SUGRA and results in the breaking of one  $E_8$  to  $E_6$  or its subgroups, which play the role of gauge symmetries in the observable sector. Multiplets of the remaining  $E_8$  belong to the

hidden part of the considered theory. Although all hidden sector multiplets can give rise to violation of SUSY, the minimal possible SUSY-breaking sector in string models involves dilaton ( $S$ ) and moduli ( $T_m$ ) superfields. The number of moduli varies from one string model to another. But dilaton and moduli fields are always present in four-dimensional heterotic superstrings, because  $S$  is related to the gravitational sector, while vacuum expectation values of  $T_m$  determine the size and shape of the compactified space.

After integration over hidden sector fields the superpotential of SUGRA models generally looks like (see, for example, [8])

$$W(\phi_M) = W^{(\text{tree})}(\phi_M) + W^{(\text{ind})}(\phi_M), \quad (3)$$

where

$$W^{(\text{tree})}(\phi_M) = \frac{1}{6} Y'_{\alpha\beta\gamma}(h_m) C^\alpha C^\beta C^\gamma + \dots \quad (4)$$

is a classical superpotential that depends on hidden  $h_m$  (dilaton and moduli) and observable  $C^\alpha$  superfields. Generally, supersymmetric mass terms are assumed to be absent in the classical part of the superpotential. They may be induced by nonperturbative corrections that summarize the effects of integrating out the hidden sector [8]:

$$W^{(\text{ind})}(\phi_M) = \hat{W}(h_m) + \frac{1}{2} \mu'_{\alpha\beta}(h_m) C^\alpha C^\beta + \dots \quad (5)$$

Expanding the full Kähler potential in powers of observable fields  $C^\alpha$ , we have [8, 9]

$$K = \hat{K}(h_m, h_m^*) + \tilde{K}_{\bar{\alpha}\beta}(h_m, h_m^*) C^{*\bar{\alpha}} C^\beta \quad (6) \\ + \left[ \frac{1}{2} Z_{\alpha\beta}(h_m, h_m^*) C^\alpha C^\beta + \text{h.c.} \right] + \dots$$

The ellipses in formulas (4)–(6) stand for higher order terms, whose coefficients are suppressed by negative powers of  $M_{\text{Pl}}$ .  $\hat{W}(h_m)$  and  $\hat{K}(h_m, h_m^*)$  are the superpotential and the Kähler potential of the hidden sector, respectively. Notice that the coefficients  $Y'_{\alpha\beta\gamma}$ ,  $\mu'_{\alpha\beta}$ ,  $\tilde{K}_{\bar{\alpha}\beta}$ , and  $Z_{\alpha\beta}$  in expansions (4)–(6) depend on the hidden sector fields in general. The bilinear terms associated with  $\mu'_{\alpha\beta}$  and  $Z_{\alpha\beta}$  are often forbidden by gauge invariance. However, their appearance destroys the  $Z_3$  discrete symmetry that leads to the domain wall problem [10] and provides a viable solution for the so-called  $\mu$ -problem, in the context of the minimal supersymmetric standard model (MSSM) [11].

The SUGRA scalar potential can be represented as a sum of  $F$  and  $D$  terms  $V_{\text{SUGRA}}(\phi_M, \phi_M^*) =$

$V_F(\phi_M, \phi_M^*) + V_D(\phi_M, \phi_M^*)$ , where the  $F$  part is given by [5, 12]

$$V_F(\phi_M, \phi_M^*) = e^G \left( G_M G^{M\bar{N}} G_{\bar{N}} - 3 \right), \quad (7)$$

$$G_M \equiv \partial_M G \equiv \partial G / \partial \phi_M, \quad G_{\bar{M}} \equiv \partial_{\bar{M}} G \equiv \partial G / \partial \phi_M^*, \\ G_{\bar{N}M} \equiv \partial_{\bar{N}} \partial_M G = \partial_{\bar{N}} \partial_M K \equiv K_{\bar{N}M}.$$

The matrix  $G^{M\bar{N}}$  is the inverse of the Kähler metric  $K_{\bar{N}M}$ . If, at the minimum of the scalar potential, hidden sector fields acquire vacuum expectation values such that at least one of their auxiliary fields

$$F^M = e^{G/2} G^{M\bar{P}} G_{\bar{P}} \quad (8)$$

is nonvanishing, then local SUSY is spontaneously broken. At the same time, a massless fermion with spin 1/2—the goldstino, which is a combination of the fermionic partners of the hidden sector fields giving rise to the breaking of SUGRA—is swallowed by a gravitino that becomes massive,

$$m_{3/2} = \langle e^{G/2} \rangle.$$

This phenomenon is called the super-Higgs effect [13].

Since the superfields of the hidden sector interact with the observable ones only by means of gravity, they are decoupled from the low-energy theory. The only signal that they produce is a set of terms that break the global SUSY of the low-energy effective Lagrangian of the observable sector in a soft way [14, 15]. The set of soft SUSY-breaking parameters includes gaugino masses  $M_a$ , masses of scalar components of observable superfields  $m_\alpha$ , trilinear  $A_{\alpha\beta\gamma}$  and bilinear  $B_{\alpha\beta}$  scalar couplings associated with Yukawa couplings, and  $\mu$  terms in the superpotential of the considered SUSY model [16]. Using the explicit form of the SUGRA scalar potential (7) and the expansion of the Kähler function in terms of observable superfields (4)–(6), one can compute soft SUSY-breaking terms at the Planck or Grand Unification scale. They are obtained by substituting vacuum expectation values for the hidden sector fields  $h_m$  and corresponding auxiliary fields  $F^m$ , and taking the flat limit [17], where  $M_{\text{Pl}} \rightarrow \infty$  but  $m_{3/2}$  is kept fixed. Then, one is left with a global SUSY Lagrangian plus the soft SUSY-breaking terms listed above. All nonrenormalizable terms can be omitted, since they are suppressed by inverse powers of  $M_{\text{Pl}}$ . Choosing the Kähler metric of the observable sector in the diagonal form  $\tilde{K}_{\bar{\alpha}\beta} = \tilde{K}_\alpha \delta_{\bar{\alpha}\beta}$  to avoid dangerous flavor-changing neutral current (FCNC) transitions and assuming that, at the minimum of the SUGRA scalar potential, the value of the cosmological constant equals zero  $\langle V(h_m) \rangle = 0$ , one finds [8, 9]

$$m_\alpha^2 = m_{3/2}^2 - F^{\bar{m}} F^n \partial_{\bar{m}} \partial_n \ln \tilde{K}_\alpha, \quad (9)$$

$$A_{\alpha\beta\gamma} = F^m \left[ \hat{K}_m + \partial_m \ln Y'_{\alpha\beta\gamma} - \partial_m \ln(\tilde{K}_\alpha \tilde{K}_\beta \tilde{K}_\gamma) \right],$$

$$M_a = \frac{1}{2} (\text{Re} f_a)^{-1} F^m \partial_m f_a.$$

As usual the  $D$ -term contributions to SUSY breaking are neglected. Explicit expressions for the bilinear scalar couplings  $B_{\alpha\beta}$  are not given here, because they depend significantly on the mechanism of  $\mu$ -term generation (see [9]).

The first term in the formula for  $m_\alpha^2$  gives a universal positive contribution to all soft scalar masses that, in general, allows us to make scalar particles heavier than their fermionic partners. The size of all soft SUSY-breaking terms is characterized by the gravitino mass scale. Therefore, the gravitino mass should not be very large, since the soft masses of the Higgs bosons have to be of the order of the electroweak scale to ensure a correct pattern for the  $SU(2) \times U(1)$  symmetry breaking. A huge mass hierarchy ( $m_{3/2} \ll M_{\text{Pl}}$ ) can appear due to a nonperturbative source of local SUSY breaking in the hidden sector gauge group [18].

### 3. MULTIPLE-POINT PRINCIPLE IN SUGRA MODELS

Let us now consider SUGRA models that obey the MPP. This means that there must be two or even more degenerate vacua in the considered models. In the SM and its renormalizable extensions, the MPP conditions are attained by adjusting arbitrary coupling constants. As mentioned in Section 2, in SUGRA models, there are two arbitrary functions that should be fixed via the MPP, in the same way as the coupling constants in renormalizable theories, resulting in a set of degenerate vacua.

As described above, a common paradigm implies that, at one minimum of the scalar potential (7), local SUSY is broken, leading to the appearance of soft terms in the effective Lagrangian of the observable sector. Further, we will treat this vacuum as the physical one, which is realized in nature, and denote the appropriate vacuum expectation values of hidden fields as  $h_m^{(1)}$ .

However, MPP inspired SUGRA models may have another minimum of the scalar potential with the same energy density, where the SUSY in the hidden sector is unbroken. Moreover, we assume that, in this second vacuum, the low-energy limit of the considered theory is described by a pure SUSY model in flat Minkowski space. As discussed in the introduction, the last requirement represents an extrafine-tuning because in general the cosmological constant in SUGRA models is huge and negative. To show this, let us suppose that the Kähler function has

a stationary point  $\phi_M = \phi_M^0$ , where  $G_M = 0$ . Then it is easy to check that this point is also an extremum of  $V_{\text{SUGRA}}(\phi_M, \phi_M^*)$ . Since, according to Eq. (8), the auxiliary fields  $F^M$  are “proportional” to the  $G_M$ , they vanish in its vicinity and local SUSY remains intact. At the same time, the energy density is huge and negative. While all  $D$  terms go to zero near the extremum point of  $G(\phi_M, \phi_M^*)$ , the last term in the brackets of Eq. (7) for  $V_F(\phi_M, \phi_M^*)$  gives a finite and negative contribution to the total density of energy. Thus, the cosmological constant in such SUGRA models is less than or equal to  $-3\text{exp}G(\phi_M^0, \phi_M^{0*})$ .

On the other hand, in flat Minkowski space, the energy density of any supersymmetric vacuum state is exactly zero. The effective description of the second vacuum, in terms of a supersymmetric one, is supposed to be valid down to very low energies ( $E \ll M_Z$ ) in the MPP inspired SUGRA model. Thus, all soft SUSY-breaking terms induced into the observable sector must vanish (with much higher accuracy than in the physical vacuum) and particles from a single supermultiplet will have the same mass. Since in the SUSY limit the graviton and gravitino are massless in the flat spacetime approximation, one obtains an additional constraint on the value of the superpotential of the hidden sector,

$$\langle \hat{W}(h_m^{(2)}) \rangle = 0, \tag{10}$$

where  $h_m^{(2)}$  denote vacuum expectation values of the hidden sector fields in the second vacuum. Equation (10) is nothing other than the extrafine-tuning in our model that corresponds to giving the complete solution of the cosmological constant problem.

If condition (10) is fulfilled, then the last term in the brackets of Eq. (7), which leads to a negative energy density, vanishes. Taking into account that the Kähler metric of the hidden sector is positive definite, one can prove in this case that the absolute minimum of the scalar potential (7) is achieved when

$$\left. \frac{\partial \hat{W}(h_m)}{\partial h_k} \right|_{h_m=h_m^{(2)}} = 0. \tag{11}$$

Together with the superpotential of the hidden sector and its derivatives, the energy density of the second vacuum and the auxiliary fields  $F^M$  go to zero, verifying that SUSY really is unbroken.

In order to demonstrate how the conditions (10) and (11) work, let us consider a particular example. For the sake of simplicity, we restrict our consideration to the minimal SUGRA model [14, 17, 19] with Kähler potential

$$K(\phi_M, \phi_M^*) = \sum_m h_m h_m^* + \sum_\alpha |C^\alpha|^2, \tag{12}$$

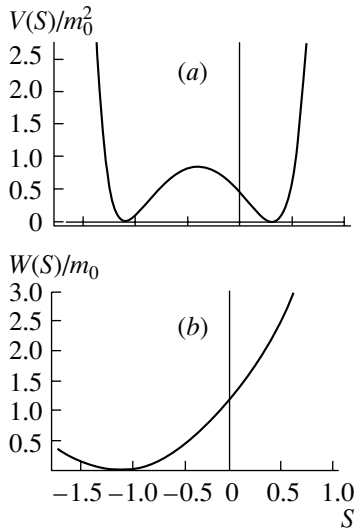


**Fig. 1.** (a) The scalar potential and (b) the superpotential for the simplest SUGRA model, where the MPP conditions are satisfied. The standard SUGRA mass units are used.

which results in canonical kinetic terms in the SUGRA Lagrangian. A canonical choice for the kinetic function  $f_a(h_m) = \text{const}$  corresponds to  $M_a = 0$ . Therefore, we assume a mild dependence of  $f_a(h_m)$  on the hidden fields, so that the gauge couplings in the physical and supersymmetric vacua do not differ by much, i.e.,  $|f_a(h_m^{(1)}) - f_a(h_m^{(2)})| \ll f_a(h_m^{(1)})$ .

Because the Kähler metric  $K_{\bar{N}M}$  and its inverse are diagonal, an explicit form for the SUGRA scalar potential of the hidden sector can be easily found:

$$V_F^{\text{hid}}(h_m, h_m^*) = e^{\hat{K}(h_m, h_m^*)} \times \left( \sum_k \left| \frac{\partial \hat{W}(h_m)}{\partial h_k} + h_k^* \hat{W}(h_m) \right|^2 - 3|\hat{W}(h_m)|^2 \right). \tag{13}$$

Although in principle the potential (13) takes positive as well as negative values near the second minimum, where SUSY is preserved, the energy density is always larger than or equal to zero:

$$\langle V_F^{\text{hid}}(h_m^{(2)}) \rangle_{\text{SUSY}} = e^{\hat{K}(h_m, h_m^*)} \left( \sum_k \left| \frac{\partial \hat{W}(h_m)}{\partial h_k} \right|^2 \right) \Big|_{h_m = h_m^{(2)}}, \tag{14}$$

while  $h_m^{(2)}$  satisfy equations for extrema

$$\sum_k \left( \frac{\partial \hat{W}(h_m)}{\partial h_k} \right)^* \times \left[ \frac{\partial^2 \hat{W}(h_m)}{\partial h_k \partial h_n} + h_n^* \frac{\partial \hat{W}(h_m)}{\partial h_k} + h_k^* \frac{\partial \hat{W}(h_m)}{\partial h_n} \right] = 0. \tag{15}$$

In the minimization conditions (15), we set  $\hat{W}(h_m) = 0$ . The index  $n$  varies from 1 to  $N$ , where  $N$  is the number of scalar fields in the hidden sector which acquire nonzero vacuum expectation values. From the equations that determine the position of the stationary point of the SUGRA scalar potential (15) and the expression for the energy density in the supersymmetric vacuum (14), it becomes clear that the deepest minimum is reached when the conditions (11) are satisfied and the value of the scalar potential (13) equals zero.

In the case where the hidden sector contains only one singlet superfield, the simplest superpotential that suits the MPP is

$$\hat{W}(S) = m_0(S + \beta)^2. \tag{16}$$

If the parameter  $\beta = -\sqrt{3} + 2\sqrt{2}$ , the SUGRA scalar potential possesses two degenerate minima with zero energy density at the classical level. The appropriate hidden scalar potential and superpotential as a function of the scalar component of the superfield  $S$  are shown in Figs. 1a and 1b. For large  $|S| \gtrsim 1$ , the SUGRA potential grows rapidly because of the exponential factor  $e^{|S|^2}$  that arises due to the first term in (12). There are three extremum points in the scalar potential. The left minimum coincides with the stationary point of the superpotential (16), where it vanishes, so that SUSY is unbroken. The right minimum is attained for  $\langle S \rangle = S_0 = \sqrt{3} - \sqrt{2}$ . In this vacuum, the gravitino gets a mass  $m_{3/2} = 1.487 \cdot m_0$  and the set of soft SUSY-breaking terms is generated:

$$m_\alpha^2 = m_{3/2}^2, \quad A_{\alpha\beta\gamma} = (3 - \sqrt{6})m_{3/2}. \tag{17}$$

To obtain these results, the explicit expressions for the Kähler potential (12) and superpotential (16) were substituted into formulas (2), (8), and (9), where the field  $S$  was replaced by its vacuum expectation value  $S_0$ . The predictions for the gaugino masses  $M_a$  are not given here, since we do not specify the dependence of the kinetic function on the hidden field  $S$ .

A more complex structure in the hidden sector superpotential can lead to a scalar potential that has a few vacua in which the SUSY of the full  $N = 1$  SUGRA Lagrangian is exact or only spontaneously broken. The MPP requires the degeneracy of all the vacua or at least the deepest physical and supersymmetric ones. If the hidden sector involves more than one superfield, SUGRA models may possess so-called vacuum valleys or flat directions. Then, the most preferable situation, from an MPP believer's point of view, arises when many vacua or flat directions that might or might not be supersymmetric have the same energy density. However, having one vacuum obeying the relations (10) and (11) means the existence of just one extra phase degenerate with our

own; this is only a beginning or a necessary condition for the MPP in the minimal SUGRA models. In general, the MPP means that there is a number of degenerate minima  $h_m^{(i)}$ :

$$V(h_m^{(1)}, h_m^{(1)*}) = V(h_m^{(i)}, h_m^{(i)*}), \quad (18)$$

$$\left. \frac{\partial V(h_m, h_m^*)}{\partial h_k} \right|_{h_m=h_m^{(1)}} = \left. \frac{\partial V(h_m, h_m^*)}{\partial h_k} \right|_{h_m=h_m^{(i)}} = 0.$$

Here,  $V(h_m, h_m^*)$  should be identified with the full SUGRA scalar potential  $V_{\text{SUGRA}}(h_m, h_m^*)$  or with its  $F$  part  $V_F(h_m, h_m^*)$  if all hidden sector fields are singlets.

#### 4. THE VALUE OF THE COSMOLOGICAL CONSTANT

In principle, the SUSY that remains intact in the second vacuum can be broken dynamically at low energies (for recent reviews, see [20, 21]). Indeed, even in the pure MSSM, the beta function of the strong gauge coupling constant exhibits asymptotically free behavior ( $b_3 = -3$ ). Since in the minimal SUGRA model the kinetic function does not depend on the hidden superfields ( $f_a(h_m) = \text{const}$ ), the values of the gauge couplings at the unification scale and their running down to the scale  $M_S \simeq m_{3/2}$  are the same in both vacua. Below the scale  $M_S$ , all superparticles in the physical vacuum decouple and the corresponding beta function changes ( $\tilde{b}_3 = -7$ ). Using the value of  $\alpha_3^{(1)}(M_Z) \approx 0.118 \pm 0.003$  [22] and matching condition  $\alpha_3^{(2)}(M_S) = \alpha_3^{(1)}(M_S)$ , one finds the strong coupling in the second vacuum

$$\frac{1}{\alpha_3^{(2)}(M_S)} = \frac{1}{\alpha_3^{(1)}(M_Z)} - \frac{\tilde{b}_3}{4\pi} \ln \frac{M_S^2}{M_Z^2}. \quad (19)$$

Here,  $\alpha_3^{(1)}$  and  $\alpha_3^{(2)}$  are the values of the strong gauge couplings in the physical and second minima of the SUGRA scalar potential.

At the scale  $\Lambda_{\text{SQCD}}$ , where the supersymmetric QCD interaction becomes strong in the second vacuum,

$$\Lambda_{\text{SQCD}} = M_S \exp \left[ \frac{2\pi}{b_3 \alpha_3^{(2)}(M_S)} \right], \quad (20)$$

the SUSY may be broken due to nonperturbative effects. If instantons generate a repulsive superpotential [20, 23] that lifts and stabilizes the vacuum valleys in the scalar potential, then a generalized O’Raifeartaigh mechanism can take place inducing a nonzero value for the cosmological constant

$$\Lambda \sim \Lambda_{\text{SQCD}}^4. \quad (21)$$

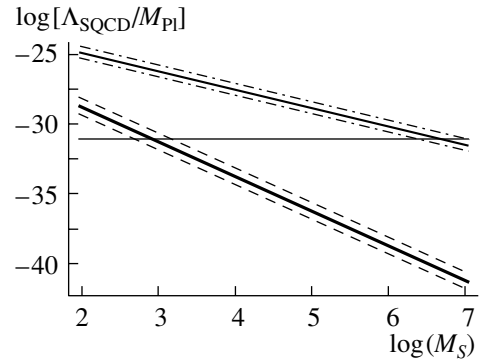


**Fig. 2.** The value of  $\log[\Lambda_{\text{SQCD}}/M_{\text{Pl}}]$  vs.  $\log(M_S)$ . The thin and thick solid lines correspond to the pure MSSM and the MSSM with an additional pair of  $5 + \bar{5}$  multiplets, respectively. The dashed and dash-dotted lines represent the uncertainty in  $\alpha_3(M_Z)$ . The upper dashed and dash-dotted lines are obtained for  $\alpha_3(M_Z) = 0.124$ , while the lower ones correspond to  $\alpha_3(M_Z) = 0.112$ . The horizontal line represents the measured value of  $\Lambda^{1/4}$ . The SUSY-breaking scale is given in GeV.

In Fig. 2, the dependence of  $\Lambda_{\text{SQCD}}$  on the SUSY-breaking scale  $M_S$  is examined. Because  $\tilde{b}_3 < b_3$ , the QCD gauge coupling below  $M_S$  is larger in the physical minimum than in the second one. Therefore, the value of  $\Lambda_{\text{SQCD}}$  is much lower than in the SM and diminishes with increasing  $M_S$ . For the pure MSSM, it varies from  $10^{-25} M_{\text{Pl}}$  to  $10^{-30} M_{\text{Pl}}$ , when  $M_S$  grows from 100 GeV to 1000 TeV. From rough estimates of the energy density (21), it can be easily seen that  $\Lambda_{\text{SQCD}} = 10^{-31} M_{\text{Pl}}$  gives the measured value of the cosmological constant. If MSSM is supplemented by an additional pair of  $5 + \bar{5}$  multiplets, then  $\Lambda_{\text{SQCD}}$  of the required size can be reproduced even for  $M_S = 100\text{--}1000$  GeV.

Achieving the SUSY-breaking at the scale  $\Lambda_{\text{SQCD}}$  is actually not at all easy. The discussion is different depending on whether the number of flavors  $N_f$  is larger or smaller than the number of colors  $N_c$ . In the MSSM and its simplest extensions where  $N_c = 3$  and  $N_f = 6$ , the generated superpotential has a polynomial form [21, 24]. The absolute minimum of the SUSY scalar potential is then achieved when all the superfields, including their  $F$  and  $D$  terms, acquire zero vacuum expectation values preserving SUSY. This result throws some doubt on our scenario for a tiny cosmological constant, which is based on Eq. (21).

Another method of breaking SUSY is by the appearance of gaugino condensation  $\bar{\lambda}_a \lambda_a$ . The gaugino condensation itself does not lead to the spontaneous breakdown of global SUSY [25]. But if a nontrivial dependence of the gauge kinetic function on the hidden sector fields is assumed, then the corresponding

auxiliary fields

$$F^i = e^{G/2} G^{i\bar{j}} G_{\bar{j}} - \frac{1}{4} G^{i\bar{j}} \frac{\partial f(h_m)}{\partial h_j} \bar{\lambda}_a \lambda_a + \dots \quad (22)$$

get an extra contribution that is proportional to  $\langle \bar{\lambda}_a \lambda_a \rangle \simeq \Lambda_{\text{SQCD}}^3$ , resulting in local SUSY breaking [18] and a nonzero vacuum energy density

$$\Lambda \sim \frac{\Lambda_{\text{SQCD}}^6}{M_{\text{Pl}}^2}. \quad (23)$$

Unfortunately, the gaugino condensation is not likely to occur if  $N_f > N_c$ .

However, the above disappointing facts concerning dynamical SUSY breaking were revealed in the framework of pure supersymmetric QCD, where all Yukawa couplings were supposed to be small or even absent. At the same time, the  $t$ -quark Yukawa coupling in the MSSM is of the same order of magnitude as the strong gauge coupling at the electroweak scale. Therefore, it can change the above results drastically. We plan to continue our investigations of SUSY breaking in the pure MSSM and its extensions.

## 5. CONCLUSIONS

In the present article, we have applied the multiple-point-principle assumption to  $N = 1$  supergravity. At first, we reviewed the structure of the  $N = 1$  SUGRA Lagrangian and local SUSY breaking via the hidden sector. Explicit expressions for the soft SUSY-breaking parameters in terms of the Kähler and gauge kinetic functions were also collected. The MPP-inspired SUGRA model that we considered implies that the corresponding scalar potential contains at least two degenerate minima. In one of them, local SUSY is broken in the hidden sector at the high-energy scale ( $\sim 10^{10} - 10^{12}$  GeV), inducing a set of soft SUSY-breaking terms for the observable fields. In the other vacuum, the low-energy limit of the considered theory is described by a pure SUSY model in flat Minkowski space. This second minimum is realized if the superpotential of the hidden sector has an extremum point where it goes to zero. The stationary point of the superpotential coincides with the position of the second minimum of the SUGRA scalar potential. The energy density and all auxiliary fields  $F^M$  of the hidden sector vanish in the second vacuum, preserving SUSY. The simplest SUGRA model, where the MPP conditions are satisfied, has been discussed and the predictions for the soft masses and trilinear scalar couplings have been obtained.

Nonperturbative effects in the observable sector can give rise to SUSY breakdown in the second

vacuum (phase). In this case, the value of the energy density is determined by the scale where the gauge interactions become strong. Numerical estimates have been carried out in the framework of the pure MSSM. They reveal that the corresponding scale is naturally low ( $\Lambda_{\text{SQCD}} \simeq 10^{-30} - 10^{-25} M_{\text{Pl}}$ ), providing a tiny energy density of the second phase. The crucial idea is then to use the MPP to transfer the energy density or cosmological constant from this second vacuum into all other vacua, especially into the physical one in which we live. In such a way, we have suggested an explanation of why the observed value of the cosmological constant has the tiny value it has.

The trouble with the considered approach is that the dynamical breakdown of SUSY looks rather questionable in models which involve QCD with more flavors than colors (as in the SM and its simplest SUSY extensions). However, the strong interaction between the Higgs and  $t$ -quark superfields in the superpotential, which has always been ignored in previous considerations, could play a decisive role. We intend to study this problem in more detail.

## ACKNOWLEDGMENTS

We are grateful to S. Bludman, D. Kazakov, O. Kancheli, V. Novikov, L. Okun, M. Shifman, K.A. Ter-Martirosyan, M. Vysotsky, and P. Zerwas for fruitful discussions and A. Anisimov and M. Trusov for useful comments. R. Nevzorov and H.B. Nielsen are indebted to the DESY Theory Group for hospitality extended to them in 2002, when this project was started. R. Nevzorov is also grateful to Alfred Toepfer Stiftung for the scholarship and for the favorable disposition during his stay in Hamburg (2001–2002). C. Froggatt and H.B. Nielsen would like to thank ITEP for inviting them to the XXXI ITEP Winter School, where this paper was completed, and L. Bergamin for interesting discussions.

This work was supported by the Russian Foundation for Basic Research, project nos. 00-15-96786, 00-15-96562, and 02-02-17379.

## REFERENCES

1. A. G. Riess *et al.*, *Astron. J.* **116**, 1009 (1998); S. Perlmutter *et al.*, *Astrophys. J.* **517**, 565 (1999); C. Bennett *et al.*, astro-ph/0302207; D. Spergel *et al.*, astro-ph/0302209.
2. D. L. Bennett and H. B. Nielsen, *Int. J. Mod. Phys. A* **9**, 5155 (1994); **14**, 3313 (1999); D. L. Bennett, C. D. Froggatt, and H. B. Nielsen, in *Proceedings of the 27th International Conference on High-Energy Physics, Glasgow, Scotland, 1994*, p. 557; *Perspectives in Particle Physics'94*, Ed. by D. Klabučar, I. Picek, and D. Tadić (World Sci., Singapore, 1995), p. 255; hep-ph/9504294.

3. S. W. Hawking, Phys. Rev. D **37**, 904 (1988); S. Coleman, Nucl. Phys. B **307**, 867 (1988); **310**, 643 (1988); T. Banks, Nucl. Phys. B **309**, 493 (1988).
4. C. D. Froggatt and H. B. Nielsen, Phys. Lett. B **368**, 96 (1996).
5. H. P. Nilles, Phys. Rep. **110**, 1 (1984); A. B. Lahanas and D. V. Nanopoulos, Phys. Rep. **145**, 1 (1987).
6. M. B. Green, J. H. Schwarz, and E. Witten, *Superstring Theory* (Cambridge Univ. Press, Cambridge, 1987).
7. P. Horava and E. Witten, Nucl. Phys. B **460**, 506 (1996); **475**, 94 (1996).
8. V. S. Kaplunovsky and J. Louis, Phys. Lett. B **306**, 269 (1993).
9. A. Brignole, L. E. Ibañez, and C. Muñoz, Nucl. Phys. B **422**, 125 (1994); **436**, 747(E) (1995); C. Muñoz, hep-th/9507108; A. Brignole, L. E. Ibañez, and C. Muñoz, hep-ph/9707209.
10. Ya. B. Zel'dovich, I. Yu. Kobzarev, and L. B. Okun, Zh. Éksp. Teor. Fiz. **67**, 3 (1975) [Sov. Phys. JETP **40**, 1 (1975)]; S. A. Abel, S. Sarkar, and P. L. White, Nucl. Phys. B **454**, 663 (1995).
11. J. E. Kim and H. P. Nilles, Phys. Lett. B **138B**, 150 (1984); **263**, 79 (1991); G. F. Giudice and A. Masiero, Phys. Lett. B **206**, 480 (1988); E. J. Chun, J. E. Kim, and H. P. Nilles, Nucl. Phys. B **370**, 105 (1992); J. A. Casas and C. Muñoz, Phys. Lett. B **306B**, 288 (1993).
12. E. Gremmer, S. Ferrara, L. Girardello, and A. Van Proeyen, Phys. Lett. B **116B**, 231 (1982); Nucl. Phys. B **212**, 413 (1983).
13. S. Deser and B. Zumino, Phys. Rev. Lett. **38**, 1433 (1977); E. Gremmer, B. Julia, J. Scherk, *et al.*, Phys. Lett. B **79B**, 231 (1978); Nucl. Phys. B **147**, 105 (1979).
14. H. P. Nilles, M. Srednicki, and D. Wyler, Phys. Lett. B **120B**, 345 (1983).
15. L. Hall, J. Lykken, and S. Weinberg, Phys. Rev. D **27**, 2359 (1983); S. K. Soni and H. A. Weldon, Phys. Lett. B **126B**, 215 (1983).
16. L. Girardello and M. T. Grisaru, Nucl. Phys. B **194**, 65 (1982).
17. R. Barbieri, S. Ferrara, and C. Savoy, Phys. Lett. B **119B**, 343 (1982).
18. H. P. Nilles, Int. J. Mod. Phys. A **5**, 4199 (1990).
19. A. H. Chamseddine, R. Arnowitt, and P. Nath, Phys. Rev. Lett. **49**, 970 (1982).
20. M. Shifman and A. Vainshtein, hep-th/9902018.
21. D. S. Gorbunov, S. L. Dubovskii, and S. V. Troitski, Usp. Fiz. Nauk **169**, 705 (1999).
22. Review of Particle Properties, Eur. Phys. J. C **3**, 1 (1998).
23. I. Affleck, M. Dine, and N. Seiberg, Nucl. Phys. B **241**, 493 (1984); **256**, 557 (1985); V. Novikov *et al.*, Nucl. Phys. B **260**, 157 (1985).
24. N. Seiberg, Nucl. Phys. B **435**, 129 (1995).
25. G. Veneziano and S. Yankielowicz, Phys. Lett. B **113B**, 231 (1982).

---

---

**ELEMENTARY PARTICLES AND FIELDS**  
**Theory**

---

---

## Vertex Functions for the Three-Particle Interaction of the Higgs Bosons $h^0$ and $H^0$ in the Minimal Supersymmetric Standard Model: One-Loop Analysis

**M. V. Dolgoplov\* and Yu. P. Philippov\*\***

*Samara State University, ul. Akademika Pavlova 1, Samara, 443011 Russia*

Received March 20, 2003; in final form, July 18, 2003

**Abstract**—Within the minimal supersymmetric standard model, two vertex functions for the three-particle interaction of the neutral Higgs bosons  $h^0$  and  $H^0$  are analyzed in the one-loop approximation with allowance for a complete set of one-loop diagrams. The analysis is performed in the c.m. frame under the assumption that one of the Higgs bosons is virtual. The results obtained in this way are compared with those that involve only leading corrections in the low-energy approximation. The vertex functions in question are presented graphically versus the mixing angle  $\beta$  and the energy  $\sqrt{s}$ . It is shown that corrections to these vertex functions may be significant in some domain of the model-parameter space, so that they must be taken into account in performing a detailed analysis of experimental data and theoretical predictions. The possibility of experimentally observing the dependences under study is explored.

© 2004 MAIK “Nauka/Interperiodica”.

### 1. INTRODUCTION

Among fundamental concepts underlying the construction of the Standard Model and its extension, a special role belongs to the mechanism responsible for the generation of elementary-particle masses. It involves two basic elements: a spontaneous breakdown of symmetry [1] and the Higgs mechanism [2]. Gauge bosons and fermions acquire masses via their interactions with Higgs fields possessing nonzero vacuum expectation values. Neither a spontaneous breakdown of symmetry nor the Higgs mechanism violates gauge invariance and the renormalizability of the theory.

However, the Higgs mechanism of mass generation has not yet been confirmed experimentally. To achieve this, experimentalists must solve the following problems [3]: (i) to discover a Higgs boson and to measure its mass; (ii) to prove that the couplings of the Higgs boson to quarks or leptons are proportional to the masses of respective fermions; and (iii) to determine the vertex functions for Higgs boson interactions.

The last problem is of particular interest in supersymmetric extensions of the Standard Model because the structure of these vertex functions is governed by the mechanism of a soft breakdown of supersymmetry.

At future high-luminosity colliders, some vertex functions for the three-particle interaction of the Higgs bosons in the minimal supersymmetric standard model (MSSM) can be measured to a fairly high precision [3–5]. Leading one-loop corrections caused by the neutral Higgs bosons are significant in some domain of the model-parameter space [6] and may affect an experimental determination of observables. However, nonleading contributions to the vertex functions in question were not taken into account in the studies quoted in [6].

Here, we calculate two vertex functions for three-particle Higgs boson interactions, taking into account the total one-loop contribution within the MSSM, whereupon we analyze the dependence of these results on the MSSM parameters. The main objective of our study is to find out how the interaction of Higgs bosons with other particles of the model modifies the Higgs potential (or vertex functions).

The present article is organized as follows. The Lagrangian describing the interaction of Higgs fields and explicit expressions for vertex functions in the lowest approximation are given in Section 2. In Sections 3 and 4, an approach to solving the problem on the basis of perturbation theory is proposed. In Section 5, our results are represented in the form of graphs versus the MSSM parameters and are compared with the results of other studies.

---

\* e-mail: [dolg@ssu.samara.ru](mailto:dolg@ssu.samara.ru)

\*\* e-mail: [yufilberg@pochtamt.ru](mailto:yufilberg@pochtamt.ru)

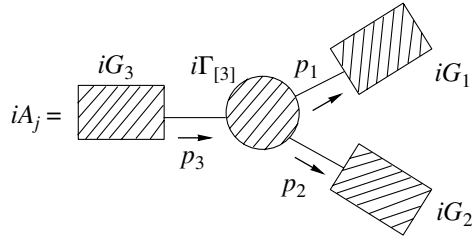


Fig. 1. Feynman diagram for the amplitude  $A_j$ .

## 2. LAGRANGIAN DESCRIBING THE INTERACTION OF HIGGS FIELDS

The Higgs sector in the MSSM involves five physical fields: (i) two neutral  $CP$ -even boson fields ( $h^0, H^0$ ); (ii) one neutral  $CP$ -odd boson field ( $A$ ); and (iii) two charged boson fields ( $H^\pm$ ).

The Lagrangian describing the interaction of the physical Higgs fields can be represented in the form

$$\mathcal{L}_{\text{Higgs}}^{\text{Int}} = \mathcal{L}_{3\text{-particle}}^{\text{Int}} + \mathcal{L}_{4\text{-particle}}^{\text{Int}}, \quad (1)$$

where

$$\begin{aligned} \mathcal{L}_{3\text{-particle}}^{\text{Int}} = & \frac{\lambda_{hhh}}{3!} hhh + \frac{\lambda_{hhH}}{2!} hhH \\ & + \frac{\lambda_{hHH}}{2!} hHH + \frac{\lambda_{HHH}}{3!} HHH \\ & + \frac{\lambda_{hAA}}{2!} hAA + \frac{\lambda_{HAA}}{2!} HAA \end{aligned} \quad (2)$$

$$+ \lambda_{hH^+H^-} hH^+H^- + \lambda_{HH^+H^-} HH^+H^-.$$

Here,  $\mathcal{L}_{3\text{-particle}}^{\text{Int}}$  is the Lagrangian for the three-particle interaction of the Higgs bosons. The four-particle interaction  $\mathcal{L}_{4\text{-particle}}^{\text{Int}}$  Lagrangian has a similar structure. In the lowest order approximation, the vertex functions for the above three-particle interaction, which appear in (2), depend on two free MSSM parameters  $M_A$  and  $\tan \beta$  as

$$\lambda_{hhh} = -3ia_0 \cos(2\alpha) \sin(\alpha + \beta), \quad (3)$$

$$\begin{aligned} \lambda_{hhH} = & -ia_0 [2 \sin(2\alpha) \sin(\alpha + \beta) \\ & - \cos(2\alpha) \cos(\alpha + \beta)], \end{aligned} \quad (4)$$

$$\begin{aligned} \lambda_{hHH} = & ia_0 [2 \sin(2\alpha) \cos(\alpha + \beta) \\ & + \cos(2\alpha) \sin(\alpha + \beta)], \end{aligned} \quad (5)$$

$$\lambda_{HHH} = -3ia_0 \cos(2\alpha) \cos(\alpha + \beta), \quad (6)$$

$$\lambda_{hAA} = -ia_0 \cos(2\beta) \sin(\alpha + \beta), \quad (7)$$

$$\lambda_{HAA} = ia_0 \cos(2\beta) \cos(\alpha + \beta), \quad (8)$$

$$\lambda_{hH^+H^-} = -igM_W \sin(\beta - \alpha) \quad (9)$$

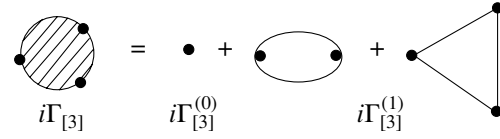


Fig. 2. Expansion of a vertex function: one-loop approximation.

$$- ia_0 \cos(2\beta) \sin(\alpha + \beta),$$

$$\lambda_{HH^+H^-} = -igM_W \cos(\beta - \alpha) \quad (10)$$

$$- ia_0 \cos(2\beta) \cos(\alpha + \beta),$$

where  $a_0 = \frac{igM_Z}{2 \cos \theta_W}$ ;  $M_W$  and  $M_Z$  are the masses of the gauge bosons  $W^\pm$  and  $Z^0$ , respectively;  $\theta_W$  is the Weinberg angle; and  $g$  is the  $SU_L(2)$  gauge coupling constant. In the tree approximation, the angles  $\alpha$  and  $\beta$  that characterize the mixing of the components of the original Higgs fields satisfy the relation

$$\tan(2\alpha) = \frac{M_A^2 + M_Z^2}{M_A^2 - M_Z^2} \tan(2\beta), \quad -\frac{\pi}{2} < \alpha < 0, \quad (11)$$

where  $M_A$  is the mass of the neutral  $CP$ -odd Higgs boson.

## 3. VERTEX FUNCTION

Our approach to solving the problem in question is based on perturbation theory for quantized fields. Particular attention is given here to the vertex function for the three-particle interaction of the Higgs bosons—that is, to the mathematical expression corresponding to that part of the Feynman diagram (as in Fig. 1) which describes the interaction of the Higgs fields. The contribution of this diagram to the amplitude can be represented in the form [7, 8]

$$-iA_j = -iG_1(p_1, \{a_1\}) \quad (12)$$

$$\times (i\Gamma_{[3]}(p_1, p_2, p_3, \{c\}))G_2(p_2, \{a_2\})G_3(p_3, \{a_3\}).$$

where  $G_i(p_i, \{a_i\})$  stands for the Green's functions associated with the remaining parts of the Feynman diagram,  $p_i$  is the momentum of the  $i$ th Higgs boson,  $\{a\}$  and  $\{c\}$  are additional parameters of the model that characterize this diagram, and  $\Gamma_{[3]}(p_1, p_2, p_3, \{c\})$  is the vertex function describing the interaction of three Higgs bosons. It can be expanded in a series as

$$\Gamma_{[3]}(p_1, p_2, p_3, \{c\}) = \sum_{l=0}^{\infty} \Gamma_{[3]}^{(l)}(p_1, p_2, p_3, \{c\}), \quad (13)$$

where the expansion is performed in the small parameter  $\alpha_e$ , each term there corresponding to the sum

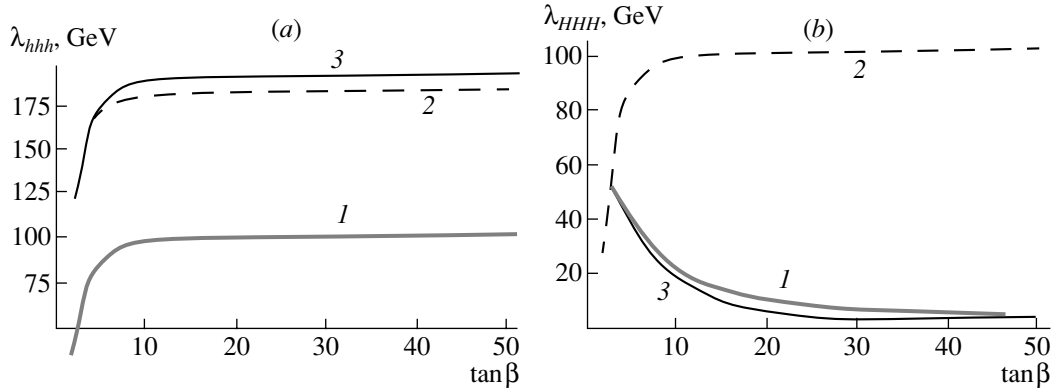


**Fig. 3.** Vertex functions for the three-particle interaction of the Higgs bosons  $h^0$  and  $H^0$  versus  $\tan\beta$  at  $\sqrt{s} = m_{H_{g_1}} + m_{H_{g_2}} + 10$  GeV,  $M_A = 500$  GeV,  $M_3 = \mu = 300$  GeV,  $M_{\tilde{Q}} = M_{\tilde{U}} = M_{\tilde{D}} = M_{\tilde{R}} = M_{\tilde{L}} = 1$  TeV, and  $A_f = 200$  GeV (in the tree and in the one-loop approximation): (curve 1)  $\lambda^0$ , (curve 2)  $\lambda^0 + \Delta\lambda^{\text{lead}}$ , and (curve 3)  $\lambda^0 + \Delta\lambda^{\text{full}}$ .

of one-particle-irreducible diagrams of the respective order in  $\alpha_e$ . In accordance with the conditions of the problem at hand, it is necessary to restrict our consideration to the approximation

$$\Gamma_{[3]}(p_1, p_2, p_3, \{c\}) \quad (14)$$

$$= \Gamma_{[3]}^{(0)}(p_1, p_2, p_3, \{c\}) + \Gamma_{[3]}^{(1)}(p_1, p_2, p_3, \{c\}).$$

The corresponding diagrammatic representation is given in Fig. 2. The vertex functions for Higgs boson interaction are functions of the model parameters. In terms of the parameters  $\lambda$ , Eq. (14) takes the form

$$\lambda_{H_{g_1}H_{g_2}H_{g_3}} = \lambda_{H_{g_1}H_{g_2}H_{g_3}}^{(0)} + \Delta\lambda_{H_{g_1}H_{g_2}H_{g_3}}^{(1)} \quad (15)$$

$$= \lambda_{H_{g_1}H_{g_2}H_{g_3}}^{(0)} (1 + \alpha_e \Delta\tilde{\lambda}_{H_{g_1}H_{g_2}H_{g_3}}^{(1)}).$$

The total one-loop correction in the Feynman gauge is governed by the contributions of both physical fields (fermions, sfermions, gauge bosons, charginos, neutralinos, Higgs bosons) and Goldstone modes and ghosts; that is,

$$\Delta\lambda_{H_{g_1}H_{g_2}H_{g_3}}^{(1)} = \Delta\lambda^{(1)}(f) \quad (16)$$

$$+ \Delta\lambda^{(1)}(\tilde{f}) + \Delta\lambda^{(1)}(Gb)$$

$$+ \Delta\lambda^{(1)}(Ch) + \Delta\lambda^{(1)}(\text{Neu}) + \Delta\lambda^{(1)}(Hg)$$

$$+ \Delta\lambda^{(1)}(Gs) + \Delta\lambda^{(1)}(Gh).$$

To solve the problem being considered, we have developed a new approach to calculating the above corrections. Specifically, we have obtained generalized formulas for calculating the two- and three-particle vertex function with allowance for the contributions of various virtual particles. On the basis of these results, we have written computer codes for calculating the corrections in question. The respective analytic results are not presented here because they are very cumbersome.

#### 4. A SCHEME FOR SOLVING THE PROBLEM OF THE THREE-PARTICLE HIGGS BOSON VERTEX FUNCTIONS

The following points were of importance in our procedure:

(i) We have used the c.m. frame and assumed that one of the Higgs bosons is virtual.

(ii) We have performed our calculations in the Feynman gauge.

(iii) For the gauge constants and the masses of third-generation quarks, we have taken solutions to the respective renormalization-group equations in order to allow for the energy dependence of the vertex functions [9].

(iv) We have calculated loop integrals by using tensor reduction.

(v) We have used the scheme of on-shell renormalization [10].

The values of the parameters used in our study were borrowed from [11].

#### 5. RESULTS OF THE CALCULATIONS AND THEIR ANALYSIS

Let us consider the results of our calculations. We have studied the vertex function in question versus the energy  $\sqrt{s}$  and versus the parameter  $\tan\beta$  (here, the energy of a process is taken to be 10 GeV greater than the sum of the physical masses of the Higgs bosons).

In Fig. 3, the results versus  $\tan\beta$  are given for the vertex function in the tree approximation ( $\lambda^0$ ), in the approximation where only the leading ( $t - \tilde{t}$ ) correction is additionally included ( $\lambda^0 + \Delta\lambda^{\text{lead}}$ ), and in the full one-loop approximation ( $\lambda^0 + \Delta\lambda^{\text{full}}$ ). The expressions for the vertex functions with allowance for leading one-loop corrections in the approximation of high masses of virtual particles are given in [6].

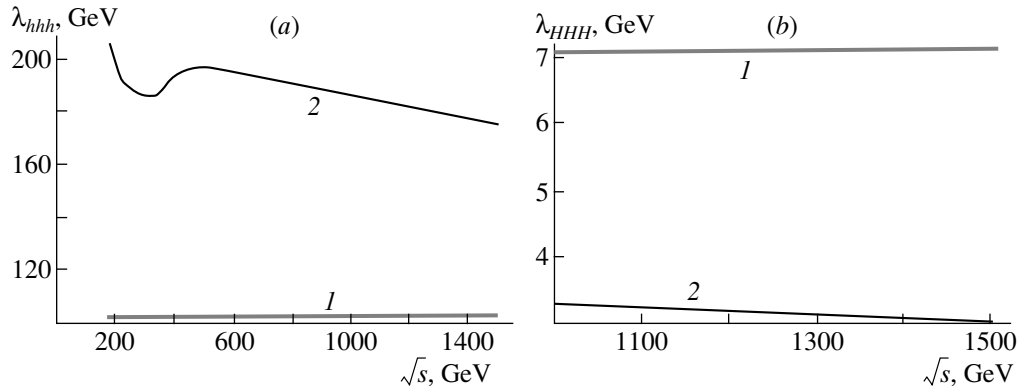


**Fig. 4.** Vertex functions for three-particle Higgs boson interaction versus  $\sqrt{s}$  at  $\tan\beta = 30$ ,  $M_A = 500$  GeV,  $M_3 = \mu = 300$  GeV,  $M_{\tilde{Q}} = M_{\tilde{U}} = M_{\tilde{D}} = M_{\tilde{R}} = M_{\tilde{L}} = 1$  TeV, and  $A_f = 200$  GeV (in the tree and in the one-loop approximation): (curve 1)  $\lambda^0$ , (curve 2)  $\lambda^0 + \Delta\lambda^{\text{full}}$ .

As can be seen from Fig. 3a, the vertex function  $\lambda_{hhh}$  in the full one-loop approximation differs only slightly from that which includes only the leading ( $t - \tilde{t}$ ) corrections, the difference amounting to 9.5% of the leading one-loop correction at  $\tan\beta = 45$ . It should be noted that a significant magnitude of the correction is consistent with the applicability of perturbation theory. It was shown in [12] that, in the noninteraction limit (the present case at  $M_A = 500$  GeV satisfies the conditions of this limit), the vertex function  $\lambda^0 + \Delta\lambda^{\text{lead}}$  can be expressed in terms of the  $h$ -boson mass and the leading one-loop correction to this mass. Upon redefining the tree vertex function and the one-loop correction to it, the correction becomes insignificant (it does not exceed 6%). Similar arguments lead to 11% for the full one-loop correction.

A completely different type of situation is observed in the case of the  $\lambda_{HHH}$  vertex function. Here, the curve corresponding to the vertex function including only the leading one-loop contribution is indicative of a huge value of this correction, but our value of the full one-loop correction is rather small. The reason is that the authors of the aforementioned results employed, in this case, the approximation of high masses of virtual particles, whereas we did not invoke any approximations in evaluating scalar integrals. The applicability of this approximation at the values taken for the free parameters is questionable (this not so only in the case of the  $hhh$  interaction vertex) in view of rather high masses of virtual Higgs bosons.

The dependences of the same vertex functions on the energy of a virtual Higgs boson are shown in Fig. 4. Our analysis revealed that the  $HHH$  vertex function is only slightly dependent on energy. At the values taken for the parameters of the model, this dependence can hardly be observed at next-generation

colliders. In analyzing experimental data, it is therefore reasonable to assume that the above vertex function is not a running parameter in the processes under study. The situation is completely different for the vertex function  $\lambda_{hhh}$ . At  $\sqrt{s} = 186$  GeV, this vertex function amounts to 205 GeV, but, at  $\sqrt{s} = 1500$  GeV, it is 175 GeV. It will be possible to observe the dependence of  $\lambda_{hhh}$  on  $\sqrt{s}$ , if the experimental resolution for  $\lambda_{hhh}$  is higher than 30 GeV over the range  $\sqrt{s} = 180\text{--}1500$  GeV. The error in determining vertex functions at a fixed value of  $M_A$  is governed by the error in determining the  $t$ -quark mass ( $\delta m_t = 5.1$  GeV) and the uncertainties in the parameters of a soft breakdown of supersymmetry. At  $M_A = 500$  GeV, the respective errors are 5 to 8 GeV for  $\lambda_{hhh}$  and do not exceed 1 to 2 GeV for  $\lambda_{HHH}$ .

## 6. CONCLUSION

We have performed a theoretical investigation of the behavior of two vertex functions for Higgs boson interaction, taking into account all one-loop quantum corrections within the MSSM. The dependences of the vertex functions  $\lambda_{hhh}$  and  $\lambda_{HHH}$  on energy and the mixing angle  $\beta$  are given in graphical form at typical values of other parameters under the assumption that one of the Higgs bosons is virtual. In contrast to the results obtained previously in [6], we have employed exact analytic expressions for scalar integrals. It has been shown that some loop corrections to the vertex functions under study can be significant in a certain domain of the model-parameter space; therefore, they must be taken into consideration in performing a detailed analysis of experimental data and theoretical predictions.

Our results are of importance since they can be used in performing a theoretical analysis of the MSSM and its modifications, in calculating various

features of the production and decay of Higgs bosons at high-luminosity colliders, and in determining the MSSM parameters (in particular, the parameters of the scalar potential, which is responsible for the generation of elementary-particle masses).

#### ACKNOWLEDGMENTS

We are grateful to E.E. Boos, M.N. Dubinin, and A.A. Biryukov for enlightening discussion on the results presented in this article and for critical comments at the stage of the preparation of the manuscript for publication.

#### REFERENCES

1. J. Goldstone, *Nuovo Cimento* **19**, 154 (1961); Y. Nambu and G. Jona-Lasinio, *Phys. Rev.* **122**, 345 (1961); J. Goldstone, A. Salam, and S. Weinberg, *Phys. Rev.* **127**, 965 (1962); N. N. Bogolyubov, *Selected Works on Statistical Physics* (Mosk. Gos. Univ., Moscow, 1979) [in Russian].
2. P. W. Higgs, *Phys. Lett.* **12**, 132 (1964); E. Englert and R. Brout, *Phys. Rev. Lett.* **13**, 321 (1964); P. W. Higgs, *Phys. Rev. Lett.* **13**, 508 (1964); G. S. Guralnik, C. R. Hagen, and T. W. B. Kibble, *Phys. Rev. Lett.* **13**, 585 (1964); P. W. Higgs, *Phys. Rev.* **145**, 1156 (1966); T. W. B. Kibble, *Phys. Rev.* **155**, 1554 (1967).
3. P. M. Zerwas, hep-ph/0003221.
4. A. Djouadi, W. Kilian, M. Muhlleitner, and P. M. Zerwas, hep-ph/0001169 (DESY 99/171).
5. S. Dawson, hep-ph/9912433.
6. H. E. Haber and R. Hempfling, *Phys. Rev. Lett.* **66**, 1815 (1991); Y. Okada, M. Yamaguchi, and T. Yanagida, *Prog. Theor. Phys.* **85**, 1 (1991); J. Ellis, G. Ridolfi, and F. Zwirner, *Phys. Lett. B* **257**, 83 (1991); V. Barger, M. S. Berger, A. L. Stange, and R. J. N. Phillips, *Phys. Rev. D* **45**, 4128 (1992); Z. Kunszt and F. Zwirner, *Nucl. Phys. B* **385**, 3 (1992); A. Djouadi, H. E. Haber, and P. M. Zerwas, *Phys. Lett. B* **375**, 203 (1996).
7. N. N. Bogoliubov and D. V. Shirkov, *Introduction to the Theory of Quantized Fields* (Nauka, Moscow, 1984, 4th ed.; Wiley, New York, 1980, transl. 3rd ed.).
8. V. B. Berestetskii, E. M. Lifshitz, and L. P. Pitaevskii, *Quantum Electrodynamics* (Nauka, Moscow, 1980; Pergamon, Oxford, 1982).
9. H. E. Haber, R. Hempfling, and A. H. Hoang, hep-ph/9609331.
10. P. H. Chankovski, S. Pokorski, and J. Rosiek, *Nucl. Phys. B* **423**, 437 (1994); hep-ph/9303309; A. Dabelstein, *Z. Phys. C* **67**, 495 (1995); hep-ph/9409375; *Nucl. Phys. B* **456**, 25 (1995); hep-ph/9503443.
11. LEP EWWG, <http://lepewwg.web.cern.ch/LEP-EWWG/plots/summer2000/>; D. E. Groom *et al.*, *Eur. Phys. J. C* **15**, 1 (2000); S. Bethke, *J. Phys. G* **26**, R27 (2000); hep-ex/0004021; A. D. Martin, J. Outhwaite, and M. C. Ryskin, *Phys. Lett. B* **492**, 69 (2000); hep-ph/0008078.
12. W. Hollik and S. Penaranda, hep-ph/0108245.

*Translated by R. Rogalyov*

## Generalized Model of Giant-Dipole-Resonance Splitting

B. S. Ishkhanov and V. N. Orlin

*Institute of Nuclear Physics, Moscow State University, Vorob'evy gory, Moscow, 119899 Russia*

Received October 10, 2002; in final form, January 22, 2003

**Abstract**—A simple semimicroscopic model that makes it possible to take into account the deformation, configuration, and isospin splitting of a giant dipole resonance is formulated and is used to describe the gross structure of the photoabsorption cross section in spherical, deformed, and transition nuclei over the mass range  $10 \lesssim A \lesssim 240$ . © 2004 MAIK “Nauka/Interperiodica”.

### 1. INTRODUCTION

Three types of giant-dipole-resonance splitting are known: that which is due to the deformation of a nucleus in the ground state (deformation splitting); that which is associated with the fact that the energies of single-particle  $E1$  transitions from the inner, filled, shell to the partly filled valence shell exceed the energies of single-particle transitions from the valence shell to free unfilled levels (configuration splitting); and, finally, that which is caused by the interaction of the isospins of a dipole excitation with a neutron excess (isospin splitting).

Different forms of giant-dipole-resonance splitting are dominant in different regions of the nuclear-mass spectrum. For example, the deformation splitting of giant dipole resonances is the most important in heavy nuclei—in the region of rare-earth elements ( $150 < A < 180$ ) and in the region of actinides ( $A > 230$ ). Configuration splitting is the most pronounced in light nuclei ( $A < 40$ ), while isospin splitting has the strongest effect on the shape of a giant dipole resonance in medium-mass nuclei ( $A \sim 40$ – $60$ ). In order to describe the gross structure of a giant resonance correctly, it is nevertheless necessary to take into account all three types of splitting, especially in the region of light and medium-mass nuclei, where there is a strong competition between the different types of splitting.

Individual types of giant-resonance splitting are rather well understood. Indeed, Danos [1] and Okamoto [2], who, in their studies that date back to the period between 1956 and 1958, relied on the hydrodynamic model, were able to provide a successful explanation of the deformation splitting of giant dipole resonances. Approximately ten years later, a number of studies were performed that were devoted to theoretically describing the spectrum of various isospin

$E1$  modes and which resulted in deriving simple analytic estimates for the isospin splitting of giant dipole resonances (see [3–6]). The configuration splitting of a giant resonance in light nonmagic nuclei was first considered in 1964 [7] and was then comprehensively studied in [8–10]. Despite all of these advances, the problem of theoretically describing the gross structure of giant resonances over a wide mass region has yet to be solved conclusively.

A semimicroscopic model that makes it possible to describe the deformation and configuration splitting of giant dipole resonances was formulated in [11]. This model was successfully used to describe the gross structure of giant dipole resonances in light self-conjugate nuclei.

In order to take into account the isospin splitting of dipole states, this model is supplemented with the analytic approach developed by Goulard and Faliellos [3]. In addition, a special semiempirical procedure is proposed for estimating the widths of such states. The generalized model obtained in this way for describing the splitting of giant dipole resonances is applied to a representative sample of various nuclei from the mass range  $10 \lesssim A \lesssim 240$ .

### 2. FUNDAMENTALS OF THE MODEL

#### *2.1. Allowance for the Deformation and Configuration Splitting of Giant Dipole Resonances*

Basic regularities in the behavior of nuclear dipole resonances can be explained by the interaction of single-particle nucleon excitations with the isovector dipole field that they generate and which is given by

$$F_s = \sum_{k=1}^A (2t_z x_s)_k = \sum_{\alpha > \beta} \langle \alpha | 2t_z x_s | \beta \rangle a_\alpha^+ a_\beta + \text{h.c.}, \quad (1)$$

where  $F_s$  and  $x_s$  ( $s = 1, 2, 3$ ) are the projections of, respectively, the dipole field  $\mathbf{F}$  and the nucleon radius vector  $\mathbf{r}$  onto the axes of the intrinsic coordinate frame;  $t_z = \pm 1/2$  is the nucleon isospin variable; and  $a_\alpha^+, a_\beta^+, \dots$  and  $a_\alpha, a_\beta, \dots$  are the operators of, respectively, nucleon creation and nucleon annihilation in the single-particle states  $|\alpha\rangle, |\beta\rangle, \dots$  (by these, we will henceforth mean the eigenstates of the Nilsson shell Hamiltonian [12]).

In a spherical nucleus, normal dipole vibrations in three mutually orthogonal directions are degenerate in energy. For this reason, it is sufficient to consider vibrations along only one coordinate axis. In a deformed spheroidal nucleus, this degeneracy is partly removed. In this case, it is necessary to distinguish between vibrations along the nuclear symmetry axis 3 and vibrations in a direction orthogonal to it (for example, along axis 1 or 2).

In order to allow for the configuration splitting of giant dipole resonances, it is necessary to take into account, for each direction  $s$  being considered, two types of collective vibrations, that which is associated with  $E1$  transitions between the valence shell and the outer shell (vibrations of type 1) and that which is associated with  $E1$  transitions between the inner shell and the valence shell (vibrations of type 2). For the quanta of such vibrations, the creation operators  $c_s^+(1)$  and  $c_s^+(2)$  and the annihilation operators  $c_s(1)$  and  $c_s(2)$  can be introduced by means of the relations [11]

$$F_s = \sum_{i=1}^2 F_s(i), \quad (2)$$

$$F_s(i) = \sum_{\alpha>\beta}^{(i)} \langle \alpha | 2t_z x_s | \beta \rangle a_\alpha^+ a_\beta + \text{h.c.} \quad (3)$$

$$= f_s(i) c_s^+(i) + f_s^*(i) c_s(i) \quad (i = 1, 2),$$

where the sum  $\sum_{\alpha>\beta}^{(i)}$  is taken over all single-particle  $E1$  transitions of type  $i$ ,

$$f_s(i) \approx \left[ \frac{\hbar\omega_s}{\varepsilon_s(i)} \sum_{\alpha>\beta}^{(i)} |\langle \alpha | 2t_z x_s | \beta \rangle|^2 \right]^{1/2} \quad (4)$$

is the amplitude of the probability for the excitation of the vibrations  $c_s^+(i)|0\rangle$  of energy  $\varepsilon_s(i)$  ( $|0\rangle$  is the physical vacuum),

$$\hbar\omega_s \approx 41A^{-1/3} \begin{cases} \sqrt{1 - \frac{4}{3}\delta'} & \text{for } s = 3 \\ \sqrt{1 + \frac{2}{3}\delta'} & \text{for } s = 1 \text{ or } 2 \end{cases} \quad (5)$$

stands for the energies (in MeV) of single-particle vibrations in the Nilsson potential [12] in the direction along ( $s = 3$ ) and in the direction orthogonal ( $s = 1$  or  $2$ ) to the nuclear symmetry axis, and  $\delta'$  is the parameter of the deformation of the Nilsson potential.

Exciting the isovector field  $F_s$ , vibrations of type 1 and 2 interact with each other. This circumstance can be taken into account by introducing, in the vibrational nuclear Hamiltonian, which describes normal vibrations along the  $s$  axis, dipole–dipole forces as [11]

$$H_s = \sum_{i=1}^2 \varepsilon_s(i) c_s^+(i) c_s(i) + \varkappa F_s(1) F_s(2). \quad (6)$$

The constant of dipole–dipole interaction can be expressed in terms of the symmetry potential  $V \approx 100$  MeV from the Weizsäcker mass formula as [13]

$$\varkappa = \frac{3V}{4A\langle r^2 \rangle} \approx 0.87V A^{-5/3} [\text{MeV fm}^{-2}], \quad (7)$$

where  $\langle r^2 \rangle \approx \frac{3}{5}(1.2A^{1/3})^2$  fm<sup>2</sup> is the mean distance between intranuclear nucleons and the center of the nucleus.

It should be borne in mind, however, that the actual value of the constant  $V$  may prove to be much less than 100 MeV because of the smallness of the spatial overlap of type-1 and type-2 particle–hole configurations generated by the operators  $c_s^+(1)$  and  $c_s^+(2)$ . Therefore, the quantity  $V$  is treated as a free parameter of the model.

The energies  $\varepsilon_s(1)$  and  $\varepsilon_s(2)$  are other adjustable parameters of the model. There is, however, a relationship between these two parameters. As was shown in [11], their ratio approximately satisfies the relation

$$\frac{\varepsilon_s(2)}{\varepsilon_s(1)} \approx \left( \frac{A}{A_{\text{cor}}} \right)^{1/3}, \quad (8)$$

where  $A_{\text{cor}}$  is the number of nucleons in the inner shells of the nucleus (that is, in the nuclear core).

For nuclei where  $N \neq Z$ , the quantity  $A_{\text{cor}}$  can be estimated as

$$A_{\text{cor}} \approx q(p)A_{\text{cor}}(p) + q(n)A_{\text{cor}}(n), \quad (9)$$

where  $A_{\text{cor}}(p)$  is the number of nucleons in the beta-stable nuclear core not containing valence protons (this quantity can be assessed, for example, on the basis of the Weizsäcker mass formula),  $A_{\text{cor}}(n)$  is the analogous feature of the core including only filled neutron shells, and the quantities  $q(p)$  and  $q(n)$  determine the contribution to the dipole sum  $\varepsilon_s(2)|f_s(2)|^2 = \hbar\omega_s \sum_{\alpha>\beta}^{(2)} |\langle \alpha | 2t_z x_s | \beta \rangle|^2$  [see

Eq. (4)] from protonic and neutronic transitions individually [ $q(p) + q(n) = 1$ ].

Relation (8) makes it possible to reduce the number of the parameters varied in describing the structure of a giant resonance in deformed nuclei to three; for these, we can take, for example, the energies  $\varepsilon_3(1)$  and  $\varepsilon_1(1)$  and the constant  $V$ .

The Hamiltonian in (6) can be diagonalized by means of the linear canonical transformation

$$\hat{c}_s^+(i) = \sum_{j=1}^2 (X_s(ij)c_s^+(j) - Y_s(ij)c_s(j)), \quad (10)$$

$$\hat{\varepsilon}_s(i) = \sqrt{\frac{\varepsilon_s^2(1) + \varepsilon_s^2(2)}{2} \mp \sqrt{\frac{(\varepsilon_s^2(1) - \varepsilon_s^2(2))^2}{4} + 4\kappa^2\varepsilon_s(1)\varepsilon_s(2)f_s^2(1)f_s^2(2)}}, \quad (12)$$

where  $i = 1, 2$  and  $\hat{\varepsilon}_s(1) \leq \hat{\varepsilon}_s(2)$ .

The dipole operator  $F_s$  can be recast into the form

$$F_s = \sum_{i=1}^2 (\hat{f}_s(i)\hat{c}_s^+(i) + \hat{f}_s^*(i)\hat{c}_s(i)), \quad (13)$$

where  $\hat{f}_s(i)$  stands for the amplitudes of the probability for the excitation of the normal vibrations  $\hat{c}_s^+(i)|0\rangle$ . These amplitudes can be found from the equation

$$\begin{aligned} \hat{\varepsilon}_s(i)\hat{f}_s^2(i) = & [\varepsilon_s(1)f_s^2(1)(\hat{\varepsilon}_s^2(i) - \varepsilon_s^2(2)) \\ & + \varepsilon_s(2)f_s^2(2)(\hat{\varepsilon}_s^2(i) - \varepsilon_s^2(1)) \\ & + 4\kappa\varepsilon_s(1)\varepsilon_s(2)f_s^2(1)f_s^2(2)] / (2\hat{\varepsilon}_s^2(i) - \varepsilon_s^2(1) - \varepsilon_s^2(2)) \end{aligned} \quad (14)$$

$(i = 1, 2).$

Finally, the relations

$$\begin{aligned} |X_s(i1)|^2 - |Y_s(i1)|^2 &= \frac{\hat{\varepsilon}_s^2(i) - \varepsilon_s^2(2)}{2\hat{\varepsilon}_s^2(i) - \varepsilon_s^2(1) - \varepsilon_s^2(2)}, \\ |X_s(i2)|^2 - |Y_s(i2)|^2 &= \frac{\hat{\varepsilon}_s^2(i) - \varepsilon_s^2(1)}{2\hat{\varepsilon}_s^2(i) - \varepsilon_s^2(1) - \varepsilon_s^2(2)} \end{aligned} \quad (15)$$

determine the contribution of type-1 and type-2 configurations to the dipole states  $\hat{c}_s^+(i)|0\rangle$  ( $i = 1, 2$ ).

## 2.2. Inclusion of the Isospin Splitting of Giant Dipole Resonances

The Hamiltonian in (6) takes into account the interaction of isovector dipole vibrations with the dynamical isovector nuclear field, but it does not describe their interaction with the static isovector field that exists in nuclei where  $N \neq Z$ . The latter interaction leads to the splitting of the states  $\hat{c}_s^+(i)|0\rangle$  into two components corresponding to two possible values of the dipole-state isospin:  $T_< = T_0$  and  $T_> =$

where the expansion coefficients  $X_s(ij)$  and  $Y_s(ij)$  satisfy the orthogonality conditions

$$\sum_{j=1}^2 (X_s(ij)X_s^*(kj) - Y_s(ij)Y_s^*(kj)) = \delta_{ik}, \quad (11)$$

$$\sum_{j=1}^2 (X_s(ij)Y_s(kj) - Y_s(ij)X_s(kj)) = 0.$$

The eigenenergies of the Hamiltonian  $H_s$  are given by

$T_0 + 1$  ( $T_0 = |N - Z|/2$  is the isospin of the nuclear ground state).

The energy positions  $\mathcal{E}_s(i, T_<)$  and  $\mathcal{E}_s(i, T_>)$  and the oscillator strengths  $\mathcal{F}_s(i, T_<)$  and  $\mathcal{F}_s(i, T_>)$  of the components into which the state  $\hat{c}_s^+(i)|0\rangle$  splits can be estimated by the formulas [3]

$$\mathcal{F}_s(i) = \mathcal{F}_s(i, T_<) + \mathcal{F}_s(i, T_>), \quad (16)$$

$$\frac{\mathcal{F}_s(i, T_>)}{\mathcal{F}_s(i, T_<)} \approx \frac{1}{T_0} \frac{1 - 1.5T_0A^{-2/3}}{1 + 1.5A^{-2/3}},$$

$$\mathcal{E}_s(i, T_<) = \hat{\varepsilon}_s(i) - \Delta\mathcal{E}_s(i, T_<),$$

$$\mathcal{E}_s(i, T_>) = \hat{\varepsilon}_s(i) + \Delta\mathcal{E}_s(i, T_>),$$

$$\Delta\mathcal{E}_s(i, T_<) + \Delta\mathcal{E}_s(i, T_>) \approx \frac{60}{A}(T_0 + 1) [\text{MeV}],$$

$$\frac{\Delta\mathcal{E}_s(i, T_>)}{\Delta\mathcal{E}_s(i, T_<)} = \frac{\mathcal{F}_s(i, T_<)}{\mathcal{F}_s(i, T_>)},$$

where  $\mathcal{F}_s(i) = \hat{\varepsilon}_s(i)\hat{f}_s^2(i)$  is the oscillator strength of the state  $\hat{c}_s^+(i)|0\rangle$ .

## 2.3. Estimating Dipole-State Widths

A collective dipole state  $|i\rangle$  can be treated as a coherent mixture of single-particle ( $1p1h$ ) nuclear excitations. The damping of dipole vibrations occurs either via the emission of a particle from a continuous spectrum or via the transfer of vibrational energy to other nuclear degrees of freedom. The first process is significant only in light and medium-mass nuclei. It leads to the formation of the emission dipole-state width  $\Gamma_i^\dagger$ . The second process is predominantly responsible for the damping of dipole vibrations in medium-mass and heavy nuclei. As a rule, it is realized owing to collisions between an excited particle or an excited hole with nucleons occupying levels below

the Fermi surface, whereby there occurs the production of yet another particle–hole pair. The dissipation of the energy of a collective dipole state over noncollective  $2p2h$  configurations interacting with it leads to the emergence of the so-called spreading width of this state,  $\Gamma_i^\downarrow$ . The total width of a dipole state,  $\Gamma_i$ , is approximately equal to the sum of the emission and spreading widths:

$$\Gamma_i = \Gamma_i^\uparrow + \Gamma_i^\downarrow. \quad (17)$$

The emission width can be approximated by the expression [14]

$$\Gamma_i^\uparrow = \sum_f 2k_f P_f |\gamma_{if}|^2. \quad (18)$$

Here,  $\gamma_{if} = (\hbar R / \sqrt{2\mu}) \int_{(S_{\mathcal{R}})} \Psi_i \Phi_f d\Omega$  is the reduced width of the state  $|i\rangle$  with respect to its nucleonic decay through the channel  $f$ , with  $\Psi_i$  and  $\Phi_f$  being, respectively, the wave function for the decaying state and the wave function that describes the angular part of the relative motion of reaction products and their internal state, so that this width is proportional (the quantity  $\mu$  appearing in the proportionality factor is the reduced nucleon mass) to the overlap integral of these wave functions over the surface of the nucleonic reaction channel ( $\mathcal{R}$  is its radius);  $P_f$  is the barrier penetrability; and  $k_f = \sqrt{2\mu\varepsilon_f}$  is the momentum of the outgoing nucleon, where  $\varepsilon_f = \mathcal{E}_i - \varepsilon_f^{-1} - B_{\text{nucl}}$  is its kinetic energy, with  $\mathcal{E}_i$ ,  $\varepsilon_f^{-1}$ , and  $B_{\text{nucl}}$  being, respectively, the energy of the state  $|i\rangle$ , the energy of

a hole in the state described by the wave function  $\Phi_f$ , and the nucleon-separation energy.

Normalizing the wave function  $\Psi_i$  to unity in the internal region of the reaction being considered and disregarding the contribution of particle–hole configurations of type 2 to the reduced widths  $\gamma_{if}$ , we obtain

$$\Gamma_i^\uparrow \approx q_i(1) \langle k_f P_f \rangle_i^{(1)} \left( \frac{\hbar^2 \mathcal{R}^2}{\mu} \right) \left\langle \frac{\varphi^2(\mathcal{R})}{\int_0^{\mathcal{R}} \varphi^2(r) r^2 dr} \right\rangle_i^{(1)}, \quad (19)$$

where the factor  $q_i(1)$  specifies the fraction of type-1 configurations in the dipole state  $|i\rangle$ ,  $\varphi(r)$  is the radial wave function describing the particle in question, and the symbol  $\langle \dots \rangle_i^{(1)}$  denotes averaging over type-1 configurations in the state  $|i\rangle$ .

In the nucleonic decay of a dipole state, the position chosen by convention for the boundary between the interior and the exterior region of the reaction is determined by the radial distribution of particles that are associated with particle–hole configurations of type 1. For the radius of the reaction channel, it is therefore reasonable to select, by analogy with the

nuclear radius  $R = \sqrt{\frac{5}{3}} \langle r^2 \rangle$ , the quantity

$$\mathcal{R} = \sqrt{\frac{5}{3}} \langle r^2 \rangle_1, \quad (20)$$

where

$$\langle r^2 \rangle_1 = \frac{\left[ \sum_{s=1}^3 \sum_{\alpha>\beta}^{(1)} \langle \alpha | r^2 | \alpha \rangle \langle \alpha | 2t_z x_s | \beta \rangle \right]^2}{\left[ \sum_{s=1}^3 \sum_{\alpha>\beta}^{(1)} |\langle \alpha | 2t_z x_s | \beta \rangle|^2 \right]}$$

is the mean square of the distance from the center of the nucleus to particles that are excited in  $E1$  transitions of type 1.

Calculations by formula (20) reveal that, with increasing mass number  $A$ , the quantity  $\mathcal{R}A^{-1/3}$  decreases smoothly from 1.6 fm at  $A \sim 10$  to 1.5 fm at  $A \sim 240$ .

The decay of the collective dipole state  $|i\rangle$  to one of the noncollective  $2p2h$  states is possible only under the following two conditions: (i) if there occurs a collision of an excited particle or an excited hole with a nonexcited nucleon of the nuclear medium and (ii) if this collision leads to the production of a new particle–hole pair.

The probability of the second event is in direct proportion to the number of ways in which excita-

tion energy can be transferred from the particle or the hole undergoing a collision to the component of the nascent pair (with allowance for the energy- and isospin-conservation laws). Evaluating this number within the model of equidistant single-particle levels [15], we find that the energy dependence of the spreading width has the form

$$\Gamma_i^\downarrow \propto (\mathcal{E}_i - \delta_{T_i T_\>} \Delta \mathcal{E}_\>)^2, \quad (21)$$

where  $\mathcal{E}_i$  the excitation energy of the dipole state  $|i\rangle$ ,  $T_i$  is its isospin, and  $\Delta \mathcal{E}_\>$  is the excitation energy of the lowest state of isospin  $T_\> = T_0 + 1$  in the nucleus being considered. [In (21), it is assumed that, owing to charge-exchange forces, the energy position of  $2p2h$  configurations having the isospin  $T_\>$  and appearing as final states in the decay of  $T_\>$  resonances

is shifted upward approximately by  $\Delta\mathcal{E}_>$  with respect to  $2p2h$  configurations having the isospin  $T_<$  and appearing as final states in the decay of  $T_<$  resonances.]

On the other hand, the spreading width  $\Gamma_i^\downarrow$  must depend on some mass factor  $I(A)$ , since the probability of a collision between an excited particle or an excited hole and a nonexcited nucleon is proportional to the mean nuclear-matter density at the collision point and since this density obviously decreases with decreasing mass number  $A$  owing to an increase in the fraction of nucleons occurring in a dilute surface layer of the nucleus as one goes over to lighter nuclei.

A specific form of the function  $I(A)$  depends on the character of the spatial distribution of particles and holes in the dipole state. If this distribution is identical to the distribution of nonexcited nucleons and can be described with the aid of the radial Fermi form factor, then this function is given by [16]

$$I(A) = \frac{1}{1 + \pi^2 \left(\frac{a}{R_0}\right)^2} \times \left[ 1 - 3\frac{a}{R_0} \frac{1 + \frac{\pi^2}{3} \left(\frac{a}{R_0}\right)^2}{1 + \pi^2 \left(\frac{a}{R_0}\right)^2} \right], \quad (22)$$

where  $R_0$  is the distance between the center of the nucleus and the locus where the nuclear-matter density  $\rho$  decreases by a factor of 2 and  $a$  is the diffuseness parameter of the nuclear surface. (From data on electron scattering, it follows that  $R_0 \approx 1.07A^{-1/3}$  fm and  $a = a_0 \approx 0.55$  fm.)

In fact, the particles and holes of the dipole state lie considerably farther from the center of the nucleus than nonexcited nucleons, and this leads to an additional decrease in the spreading width in the region of light nuclei. This effect can be taken into account by increasing, at a fixed value of the radius  $R_0$ , the diffuseness parameter  $a$  in relation to its value that follows from data on electron scattering.

There is yet another effect that is associated with the diffuseness of the nuclear surface: the probability of a collision of type-2 dipole particles and holes with a nonexcited nucleon is somewhat higher than the probability of such a collision for type-1 dipole particles and holes, which are concentrated somewhat farther from the center of the nucleus. The ratio of these probabilities,  $\eta(A)$ , that is averaged over all dipole transitions can easily be evaluated: the result of this averaging is about 1.4 for  $A \sim 10-40$  nuclei and about 1.2 for  $A \sim 140-240$  nuclei.

For the spreading width  $\Gamma_i^\downarrow$ , we eventually obtain

$$\Gamma_i^\downarrow = G[q_i(1) + (1 - q_i(1))\eta(A)] \quad (23)$$

$$\times I(A)(\mathcal{E}_i - \delta_{T_i T_>} \Delta\mathcal{E}_>)^2,$$

where  $G$  is a constant, the quantity  $q_i(1)$  is defined in (19), and the function  $I(A)$  is given by expression (22) with  $R_0 \approx 1.07A^{-1/3}$  fm and the free parameter  $a$ .

Expression (23) involves two free parameters,  $G$  and  $a$ . By varying them, we find that a semiempirical estimate of the widths of dipole states [see (17), (19), and (23)] provides the best fit to the experimental values of  $\Gamma_i$  over the mass range  $16 \lesssim A \lesssim 240$  at  $G = 0.0623 \text{ MeV}^{-1}$  and  $a = 1.407$  fm.

### 3. APPLICATION TO DESCRIBING THE GROSS STRUCTURE OF PHOTOABSORPTION CROSS SECTION

The model considered above was used to describe the gross structure of giant dipole resonances in 32 nuclei from the mass-number range  $10 \lesssim A \lesssim 240$  that possess different properties.

The following computational scheme was employed in the present analysis. First, the energies  $\mathcal{E}_s(i, T_<)$  and  $\mathcal{E}_s(i, T_>)$  and the oscillator strengths  $\mathcal{F}_s(i, T_<)$  and  $\mathcal{F}_s(i, T_>)$  of normal dipole vibrations were calculated on the basis of the formalism developed in Section 2. After that, the results found in this way for the dipole states, whose number ranged from one (in  $N = Z$  doubly magic nuclei) to eight (in  $N \neq Z$  deformed nuclei), were approximated by Lorentzian curves whose widths were estimated by formulas (17), (19), and (23).

In heavy nuclei, the energies calculated for some  $T_>$  resonances by formulas (16) prove to be close to  $\Delta\mathcal{E}_>$ ; according to (23), this leads to the emergence of very narrow peaks in the photoabsorption cross section in the region where the energy resolution of experimental data is usually low. Bearing this in mind, we set a lower limit of 1 MeV on the width  $\Gamma_i$ .

In order to take into account the effect of exchange forces, we have introduced a scale factor that ensures a normalization of the integrated photoabsorption cross section to

$$S_{\text{int}} = (1 + \alpha)60 \frac{NZ}{A} [\text{MeV mb}], \quad (24)$$

where  $\alpha = 0.2$  is an exchange parameter.

Below, we give a detailed account of our computational procedure.

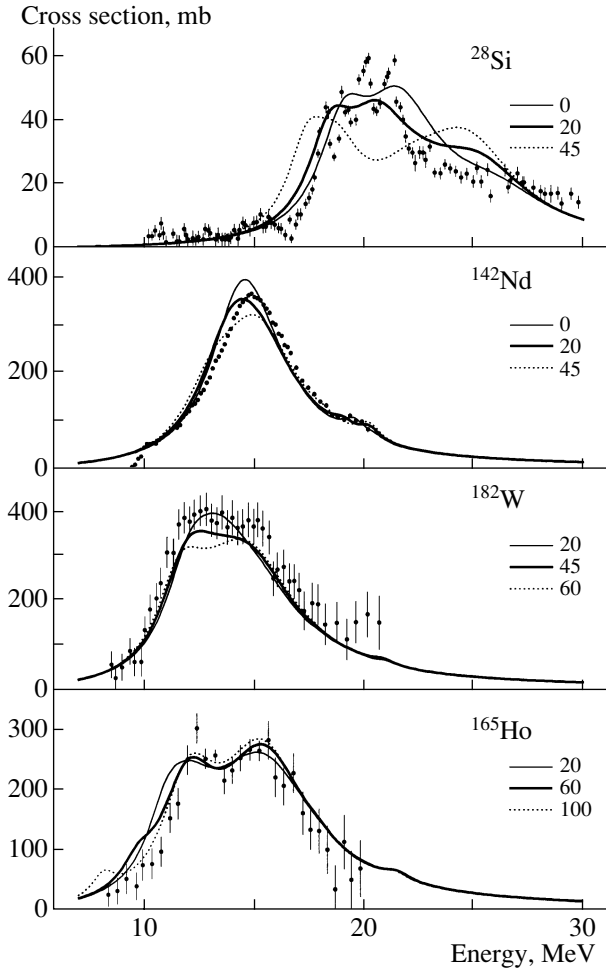


**Fig. 1.** Dependence of the results of our calculations on the choice of the parameter  $V$  for light, heavy spherical, heavy transition, and heavy deformed nuclei. Points represent the experimental photoabsorption cross sections from [19]. The thin solid, thick solid, and dotted curves correspond to the calculations with the values of  $V$  (in MeV) that are indicated to the right of the respective cross sections. The excitation energy of the nucleus being considered is plotted along the abscissa in each panel.

### 3.1. Selecting a Single-Particle Potential

In calculating the single-particle states  $|\alpha\rangle$  [see Eq. (1)], we employed the spheroidal Nilsson potential [17] with the parameters

$$\begin{aligned} \hbar\omega_3 &= 41A^{-1/3} \sqrt{1 - \frac{4}{3}\delta'}, & (25) \\ \hbar\omega_1 &= \hbar\omega_2 = 41A^{-1/3} \sqrt{1 + \frac{2}{3}\delta'}, \\ \delta' &= \delta / \left(1 + \frac{2}{3}\delta\right), \end{aligned}$$

where  $\delta$  is the parameter of the quadrupole deformation of the nucleus being considered,

$$\delta = \frac{3}{4} Q_0 / Z \langle r^2 \rangle. \quad (26)$$

Here,  $Q_0$  is the intrinsic quadrupole moment and  $\langle r^2 \rangle$  is the mean square of the radius of the nuclear-charge distribution.

For the nuclei being considered, the parameter  $\delta$  was calculated theoretically by means of the procedure described in [18]. For light nuclei, this procedure yields exaggerated values of  $\delta$  since it disregards the effect of nuclear-surface diffuseness on the quantities  $\langle x_1^2 \rangle$ ,  $\langle x_2^2 \rangle$ , and  $\langle x_3^2 \rangle$ . The values corrected with allowance for this point can be obtained by the formula

$$\delta_{\text{corr}} \approx \delta \frac{1 + 2\pi^2\xi^2 + \frac{2}{15}\pi^4\xi^4}{1 + \frac{10}{3}\pi^2\xi^2 + \frac{7}{3}\pi^4\xi^4}, \quad (27)$$

where  $\xi \equiv a_0/R_0$ ,  $a_0 \approx 0.55$  fm, and  $R_0 \approx 1.07A^{1/3}$  fm are the values that were extracted from data on electron scattering for the parameters of the Fermi form factor describing the charge distribution in the nucleus being considered.

### 3.2. Varying Model Parameters

We varied three parameters:  $\varepsilon_3(1)$ ,  $\varepsilon_1(1)$ , and  $V$  (see Section 2). First, we fixed a value of the parameter  $V$  and varied the energies  $\varepsilon_3(1)$  and  $\varepsilon_1(1)$  in such a way that the calculations reproduced the correct positions of the centroids of dipole states for the longitudinal and for the transverse mode of vibrations:

$$\begin{aligned} \frac{\sum_{T=T_<,T_>} \sum_i \mathcal{E}_3(i,T) \mathcal{F}_3(i,T)}{\sum_{T=T_<,T_>} \sum_s \sum_i \mathcal{F}_s(i,T)} &= \mathcal{E}_{\text{dip}}^{\parallel}, & (28) \\ \frac{\sum_{T=T_<,T_>} \sum_i \mathcal{E}_1(i,T) \mathcal{F}_1(i,T)}{\sum_{T=T_<,T_>} \sum_s \sum_i \mathcal{F}_s(i,T)} &= \mathcal{E}_{\text{dip}}^{\perp}. \end{aligned}$$

After that, the procedure was repeated for a different value of the parameter  $V$ .

The energies  $\mathcal{E}_{\text{dip}}^{\parallel}$  and  $\mathcal{E}_{\text{dip}}^{\perp}$  were calculated with the aid of the relations

$$\begin{aligned} \mathcal{E}_{\text{dip}} &= \frac{2\mathcal{E}_{\text{dip}}^{\perp} + \mathcal{E}_{\text{dip}}^{\parallel}}{3}, \\ \frac{\mathcal{E}_{\text{dip}}^{\perp}}{\mathcal{E}_{\text{dip}}^{\parallel}} &= \sqrt{\frac{\langle x_3^2 \rangle}{\langle x_1^2 \rangle}} = \sqrt{\frac{1 + \frac{2}{3}\delta'}{1 - \frac{4}{3}\delta'}}. & (29) \end{aligned}$$

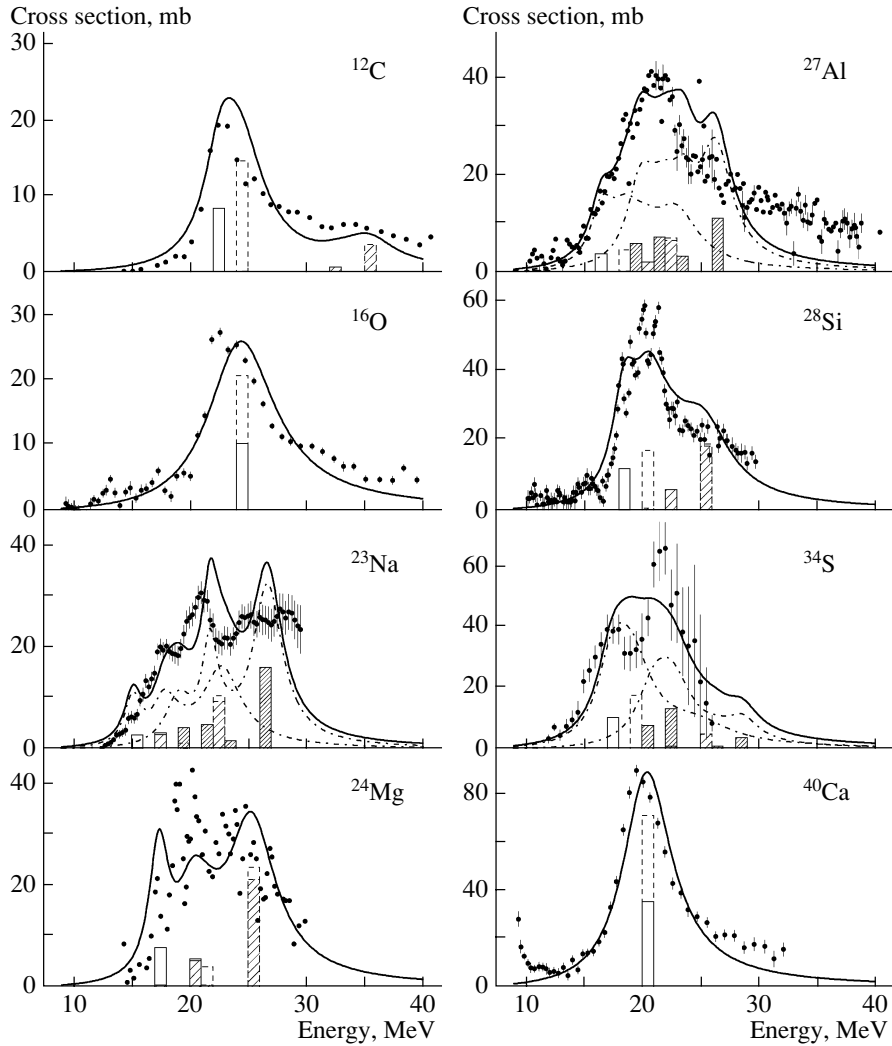


**Fig. 2.** Structure of giant dipole resonances in the mass range  $12 \leq A \leq 40$ : (points) experimental photoabsorption cross sections [19], (solid curves) theoretical cross sections, and (dash-dotted curves) two isospin components of these cross sections for  $N \neq Z$  nuclei. The histograms represent (in arbitrary units) the distribution of dipole strengths. For  $N = Z$  nuclei, solid-line (dashed-line) columns correspond to longitudinal (transverse) dipole vibrations. The unshaded (lightly shaded) parts of these columns represent the contribution of type-1 (type-2) configurations to the respective dipole state. For  $N \neq Z$  nuclei, the contributions associated with  $T_{<}$  states are depicted in similar way, while the contributions associated with  $T_{>}$  states are shown by thickly shaded columns enclosed by a solid-line contour.

The giant-resonance energy  $\mathcal{E}_{\text{dip}}$  appearing in the first of these relations was estimated by the formula [16]

$$\mathcal{E}_{\text{dip}} \approx 86A^{-1/3} \sqrt{\frac{1 + \pi^2 \xi^2}{1 + \frac{10}{3} \pi^2 \xi^2 + \frac{7}{3} \pi^4 \xi^4}} \quad [\text{MeV}], \quad (30)$$

where the quantity  $\xi$  is defined in (27).

In light and spherical nuclei, the interaction of type-1 and type-2 dipole configurations is weakened by the presence of a wide energy gap between the levels of the inner and the valence shell of the nucleus. For this reason, the best agreement between theoret-

ical and experimental results for such nuclei is obtained at a comparatively small value of the coupling constant  $V$  (see various versions of the calculation in Fig. 1 for the  $^{28}\text{Si}$  and  $^{142}\text{Nd}$  nuclei).

On the other hand, the single-particle levels of the valence and the inner shell in heavy deformed nuclei are mixed, which leads to the enhancement of the interaction between dipole configurations of two types. In this case, better agreement with experimental data is achieved if the coupling constant  $V$  is set to a value that is closer to the experimental value of the symmetry potential (see the results of the calculations in Fig. 1 for the  $^{165}\text{Ho}$  nucleus).

Transition nuclei occurring in the vicinity of the

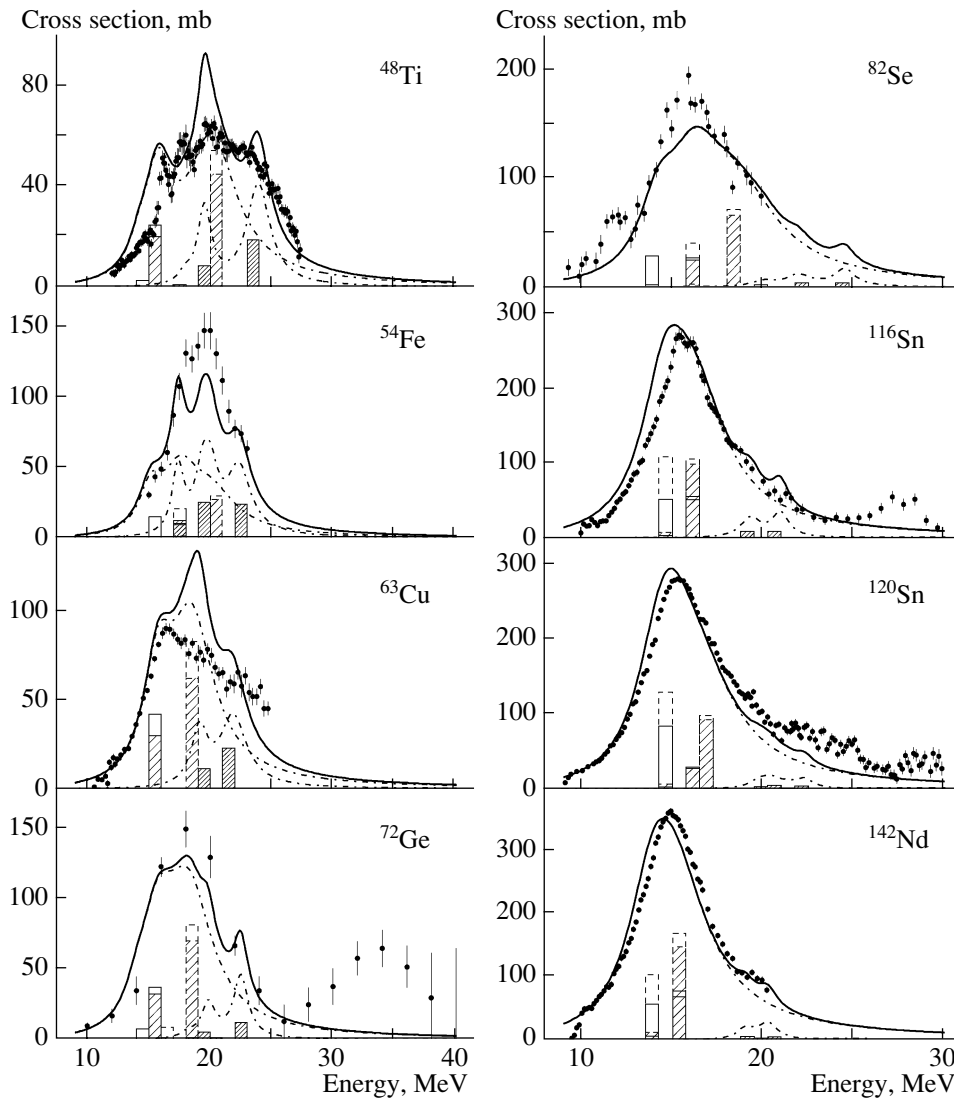


Fig. 3. Structure of giant dipole resonances in the mass range  $48 \leq A \leq 142$ . The notation is identical to that in Fig. 2.

boundaries of strong-deformation regions correspond to an intermediate situation (see the results of the calculations in Fig. 1 for the  $^{182}\text{W}$  nucleus).

In the calculations performed here, we have used the following values of the coupling constant:  $V = 20$  MeV for light, medium-mass, and heavy spherical nuclei;  $V = 45$  MeV for heavy transition nuclei ( $^{181}\text{Ta}$  and  $^{182}\text{W}$ ); and  $V = 60$  MeV for heavy deformed nuclei.

#### 4. DISCUSSION OF THE RESULTS

The main results of our calculations are displayed in Figs. 2–5.

In each of the figures, eight experimental values of the photoabsorption cross section from [19] (closed circles) are contrasted against the results of the calculations performed within the model described above

(curves and histogram). The solid curves represent the theoretical photoabsorption cross sections. Two dash-dotted curves (for  $N \neq Z$  nuclei) depict the contributions to these cross sections from the  $T_{<}$  and  $T_{>}$  components. The histograms represent the distributions of the oscillator strengths of the respective dipole states (in arbitrary units). For  $N = Z$  nuclei, columns corresponding to longitudinal and transverse dipole vibrations are enclosed by, respectively, solid and dashed lines. The unshaded (lightly shaded) part of these columns shows the contribution of type-1 (type-2) configurations to the dipole state being considered. For  $N \neq Z$  nuclei, the contribution of  $T_{<}$  states is depicted analogously, while the contribution of  $T_{>}$  states is shown by thickly shaded columns enclosed by solid lines.

As can be seen from Fig. 2, the gross structure of the photoabsorption cross sections in light nuclei

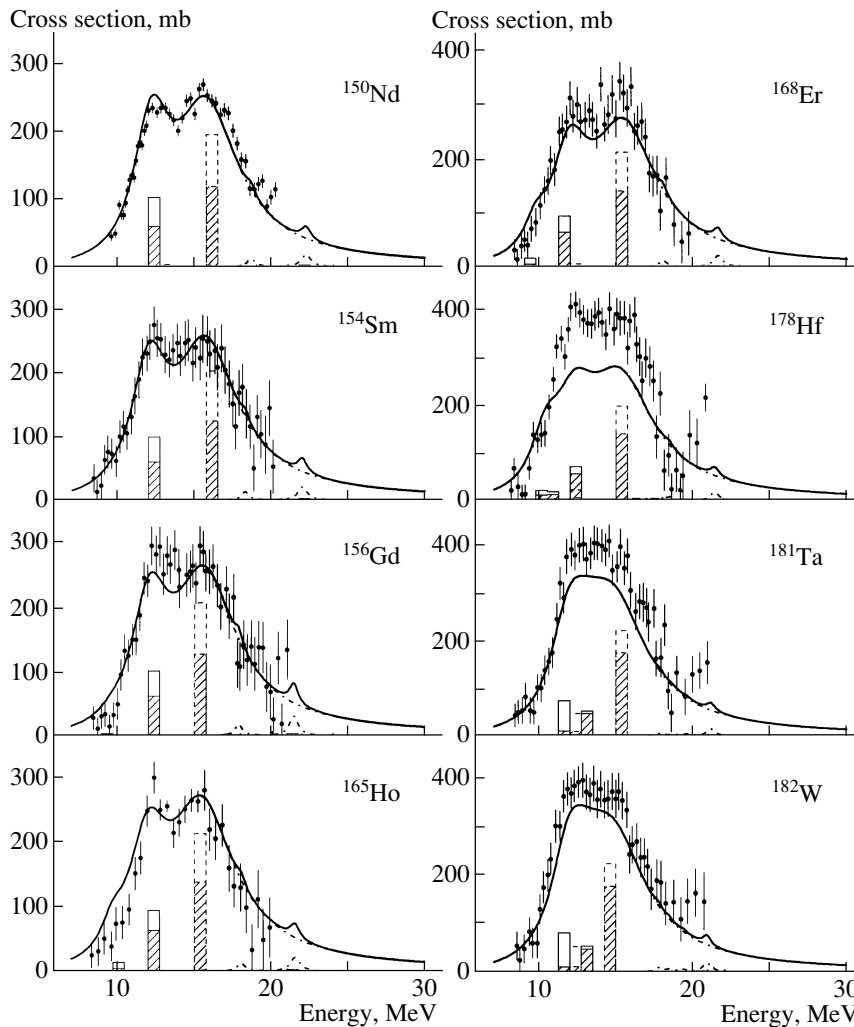


Fig. 4. Structure of giant dipole resonances in the mass range  $150 \leq A \leq 182$ . The notation is identical to that in Fig. 2.

is formed under the effect of all three types of giant-dipole-resonance splitting.

The configuration splitting is the most pronounced in nonmagic nuclei featuring but a small deformation, in  $^{12}\text{C}$  and  $^{28}\text{Si}$ ; however, it can easily be singled out in the structure of the cross section for photoabsorption on the deformed nuclei  $^{23}\text{Na}$  and  $^{24}\text{Mg}$  as well. From the histograms in Fig. 2, it can be seen that, in light nuclei, type-1 and type-2 dipole configurations are weakly mixed, which implies that the formation of normal modes is due primarily to the interaction of configurations belonging to the same type. It should also be noted that the main part of the strength of dipole transitions from an inner to the valence shell (that is, transitions of type 2) is associated with the transverse mode of dipole vibrations.

In  $1p$ - and  $2d2s$ -shell nonmagic nuclei, the strongest manifestations of the deformation splitting of a giant dipole resonance are observed in the vicinity of the mass number of  $A \sim 24$ . However, this type

of splitting also has a sizable effect on the shape of the cross sections for photoabsorption in slightly deformed nuclei such as  $^{12}\text{C}$  and  $^{28}\text{Si}$  (compare the positions of the histogram columns with the special features of the cross sections in the region of the main maximum).

In  $N \neq Z$  nuclei ( $^{23}\text{Na}$ ,  $^{27}\text{Al}$ , and  $^{34}\text{S}$ ), the formation of the gross structure of the photoabsorption cross sections is greatly affected by the isospin splitting of a giant dipole resonance. As can be seen from Fig. 2, the manifestation of this type of splitting is significantly facilitated by a decrease in the spreading widths of  $T_>$  states, which is due to the fact that  $2p2h$  configurations to which such states decay are shifted upward in energy by  $\Delta\mathcal{E}_>$  [see Eq. (21), (23)].

In comparing the theoretical and experimental data displayed in Fig. 2, it should be borne in mind that, in light nuclei, the structure of giant dipole resonances is significantly affected by shell effects, which

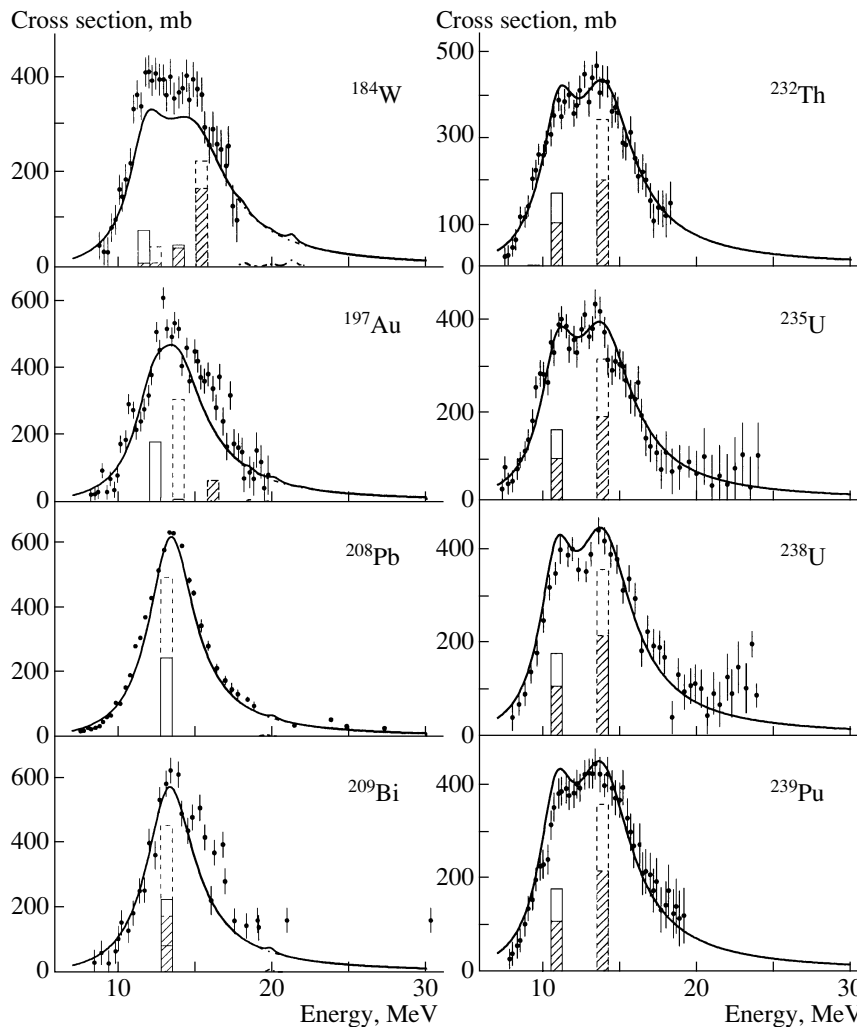


Fig. 5. Structure of giant dipole resonances in the mass range  $184 \leq A \leq 239$ . The notation is identical to that in Fig. 2.

are disregarded in the model underlying the present analysis.

Therefore, one cannot hope to achieve a detailed description of all features of experimental photoabsorption cross sections within this conceptual framework. The model is only aimed at describing the gross structure of giant dipole resonances. For the same reason, there may be (and there do indeed occur) discrepancies between the predicted and the actual values of the widths of some individual resonances.

By and large, the agreement between the theoretical and experimental results for light nuclei is quite satisfactory everywhere, with the exception of the range 30–40 MeV for the  $^{27}\text{Al}$  nucleus, where the experimental cross section exceeds its theoretical counterpart considerably.

Figure 3 displays the experimental and theoretical data for nuclei from the mass-number range  $48 \leq A \leq 142$ . Here, the effect of the isospin splitting on the structure of giant dipole resonances in nuclei

like  $^{48}\text{Ti}$ ,  $^{54}\text{Fe}$ , and  $^{63}\text{Cu}$  is worthy of special note. The effect of the broadening of the cross sections for photoabsorption on the  $^{82}\text{Se}$ ,  $^{116,120}\text{Sn}$ , and  $^{142}\text{Nd}$  nuclei because of the configuration splitting of giant dipole resonances is also of interest. In addition, it can be seen from Fig. 3 that, despite the smallness of the  $T_>$  component, the isospin splitting explains some special features in the photoabsorption cross sections for heavy nuclei like  $^{116,120}\text{Sn}$  and  $^{142}\text{Nd}$ . For the  $^{72}\text{Ge}$  nucleus, there are serious discrepancies between the theoretical and experimental results in the energy range 30–40 MeV. However, they are most likely due to the incorrectness of the experimental data. Some distinctions between the shapes of the theoretical and experimental photoabsorption curves for the vibrational nucleus  $^{63}\text{Cu}$  may probably be attributed to the effect of surface nuclear vibrations on the structure of the respective giant dipole resonance. The origin of the high-energy tails in the experimental

cross sections for photoabsorption on the  $^{116,120}\text{Sn}$  nuclei remains unclear.

Figure 4 shows data for deformed and transition nuclei in the mass range  $150 \leq A \leq 182$ . One can see from this figure that, in all cases, the calculation faithfully reproduces the shape of the experimental photoabsorption cross sections. As might have been expected, the oscillator strengths of  $E1$  transitions in strongly deformed nuclei are grouped into two main states corresponding to longitudinal and transverse dipole vibrations. In transition nuclei, configuration splitting leads to a more complicated structure of giant dipole resonances. It is very interesting that, for some nuclei (see the data for the  $^{156}\text{Gd}$ ,  $^{178}\text{Hf}$ ,  $^{181}\text{Ta}$ , and  $^{182}\text{W}$  nuclei), the experimental values of the photoabsorption cross sections in the region of  $T_>$  states are in excess of their theoretical counterparts. Possibly, this is the region where there occur narrow  $T_>$  resonances, which, according to (23), may arise in heavy nuclei (see the discussion of this issue in Section 3).

The data on the nuclei from the mass-number range  $184 \leq A \leq 239$  in Fig. 5 can be interpreted in a similar way.

## 5. CONCLUSIONS

Let us formulate basic conclusions following from the above analysis.

(i) Although the parameters used in the calculations have not been fitted individually in describing photoabsorption cross sections, the generalized model of giant-dipole-resonance splitting has enabled us to develop a satisfactory explanation of the gross structure of giant resonances in the mass-number range  $10 \lesssim A \lesssim 240$ .

(ii) The configuration and the isospin splitting of giant dipole resonances play an important role not only in light and medium-mass but also in heavy nuclei. In particular, configuration splitting enhances considerably the total width of a giant dipole resonance in heavy nonmagic nuclei, while isospin splitting generates, despite the smallness of the  $T_>$  component, a number of structural features in the behavior of the photoabsorption cross section in the mass-number region  $A \gtrsim 100$ .

(iii) There can exist narrow  $T_>$  resonances.

## ACKNOWLEDGMENTS

We are grateful to V.V. Varlamov, M.E. Stepanov, and V.V. Chesnokov from the Center for Data from Photonuclear Experiments at the Institute of Nuclear Physics (Moscow State University) for assistance in selecting experimental data required for the present analysis.

## REFERENCES

1. M. Danos, Bull. Am. Phys. Soc. **1**, 135 (1956); Nucl. Phys. **5**, 23 (1958).
2. K. Okamoto, Prog. Theor. Phys. **15**, 75 (1956); Phys. Rev. **110**, 143 (1958).
3. B. Goulard and S. Fallieros, Can. J. Phys. **45**, 3221 (1967).
4. V. M. Novikov and M. G. Urin, Yad. Fiz. **3**, 419 (1966) [Sov. J. Nucl. Phys. **3**, 302 (1966)].
5. D. F. Petersen and C. J. Veje, Phys. Lett. B **24B**, 449 (1967).
6. H. Ejiri and K. Ikeda, Phys. Rev. **176**, 1277 (1968).
7. V. G. Neudatchin and V. G. Shevchenko, Phys. Lett. **12**, 18 (1964).
8. R. A. Eramzhyan, B. S. Ishkhanov, I. M. Kapitonov, *et al.*, Phys. Rep. **136**, 230 (1986).
9. B. S. Ishkhanov, N. P. Yudin, and R. A. Éramzhyan, Fiz. Élem. Chastits At. Yadra **31**, 313 (2000).
10. B. S. Ishkhanov, I. M. Kapitonov, V. G. Neudachin, *et al.*, Fiz. Élem. Chastits At. Yadra **31**, 1343 (2000).
11. B. S. Ishkhanov and V. N. Orlin, Yad. Fiz. **66**, 615 (2003) [Phys. At. Nucl. **66**, 659 (2003)].
12. S. G. Nilsson, K. Dan, Vidensk. Selsk. Mat. Fys. Medd. **29**, No. 16 (1955).
13. A. Bohr and B. R. Mottelson, *Nuclear Structure, Vol. 2: Nuclear Deformations* (Benjamin, New York, 1975; Mir, Moscow, 1977).
14. A. S. Davydov, *Theory of Atomic Nucleus* (Gosizdat, Moscow, 1958).
15. F. C. Williams, Nucl. Phys. A **166**, 231 (1971).
16. B. S. Ishkhanov and V. N. Orlin, Yad. Fiz. **65**, 1978 (2002) [Phys. At. Nucl. **65**, 1809 (2002)].
17. C. Gustafson *et al.*, Ark. Fys. **36**, 613 (1967).
18. B. S. Ishkhanov and V. N. Orlin, Yad. Fiz. **65**, 1858 (2002) [Phys. At. Nucl. **65**, 1809 (2002)].
19. Nuclear Reaction Base Data, <http://depni.npi.msu.ru/cdf/service/index.html>

*Translated by A. Isaakyan*

## Polarization Phenomena in Elastic Proton Scattering on Odd Nuclei

Yu. A. Berezhnoy and V. P. Mikhailiyuk<sup>1)</sup>

*Kharkov State University, pl. Svobody 4, Kharkov, 310077 Ukraine*

Received August 2, 2002; in final form, February 26, 2003

**Abstract**—Polarization observables of elastic proton scattering on  $^{13}\text{C}$  and  $^{13}\text{N}$  nuclei are calculated by using the theory of multiple diffractive scattering and the  $\alpha$ -cluster model with dispersion. The  $^{13}\text{C}$  and  $^{13}\text{N}$  nuclei are considered as those that consist of a deformed core and an additional cluster (nucleon) occurring with the highest probability inside the core. It is shown that this assumption on the structure of these nuclei makes it possible to match the calculated and measured observables without resort to adjustable parameters. © 2004 MAIK “Nauka/Interperiodica”.

The structure and the properties of light nuclei have been studied intensively for many years (see, for example, [1] and references therein). Presently, there are experimental data on the polarization observables for elastic nucleon scattering on odd nuclei [2–6]—in particular, elastic proton scattering on spin-1/2  $^{13}\text{C}$  nuclei. In this case, polarization phenomena are more diversified and intricate than in particle scattering on spinless nuclei; this allows one to obtain more information about the nuclear structure and about the character and strength of spin-orbit and spin-spin interactions. In addition, there appears the possibility of studying polarized spin states of nuclei, the coefficients of spin correlations belonging to the beam-target type, and other observables that are absent in the case of nucleon scattering on spinless nuclei.

In order to describe elastic proton scattering on spinless nuclei completely, it is necessary to measure three independent observables [7]. Usually, the spin-rotation function  $Q$  is chosen to be the third independent observable in addition to the differential cross section  $d\sigma/d\Omega$  and the polarization  $P$ . In the case of the scattering of spin-1/2 particles, it is necessary to measure at least 11 independent observables [8]. In order to describe experimental data on the scattering of two spin-1/2 particles theoretically, it is therefore of paramount importance to choose the target-nucleus model and the parameters of the “elementary” amplitude for the projectile interaction with the structural components of the nucleus (for example, the nucleon–nucleon amplitude) appropriately.

Various approaches were used to describe elastic proton scattering on  $^{13}\text{C}$  nuclei. For example, these

were the nonrelativistic impulse approximation involving an effective nucleon–nucleon amplitude in [9] and the relativistic impulse approximation combined with the relativistic distorted-wave method (relativistic extension of the distorted-wave impulse approximation) in [2, 10–12]. The optical potential used in [2, 10–12] was determined from data on elastic  $p^{12}\text{C}$  scattering and was then applied to describing  $p^{13}\text{C}$  scattering. In those studies, the parameters of the nucleon–nucleon amplitude were considered to be adjustable. In [13], the observables of elastic  $p^{13}\text{C}$  scattering were calculated by solving the Lippmann–Schwinger equation. The calculated observables were in qualitative agreement with experimental data.

In [8], the polarization observables of elastic  $p^{13}\text{C}$  and  $p^{13}\text{N}$  scattering were calculated within the theory of multiple diffractive scattering and the model of independent nucleons. The observables calculated in [8] were in agreement with available experimental data. The nucleon–nucleon amplitude used in those calculations was obtained from the results of a partial-wave analysis for nucleon–nucleon scattering. Among other things, it was shown in [8] that the polarization properties of elastic  $p^{13}\text{C}$  and  $p^{13}\text{N}$  scattering differ only slightly.

A cluster structure often manifests itself in light nuclei. An  $\alpha$ -cluster model with dispersion was proposed in [14] to describe the nuclear-matter distribution and the size of the  $^{12}\text{C}$  nucleus; in this model, the carbon nucleus is assumed to consist of three alpha-particle clusters located at the vertices of an equilateral triangle. The possibility that these alpha-particle clusters are displaced from their most probable equilibrium positions was taken into account in [14]. This model was extended in [15, 16] to the case of the  $^{16}\text{O}$  and  $^{20}\text{Ne}$  nuclei. The  $^{16}\text{O}$  nucleus was assumed to

<sup>1)</sup>Institute for Nuclear Research, National Academy of Sciences of Ukraine, pr. Nauki 47, Kiev, Ukraine.  
e-mail: [mikhailiyuk@ukr.net](mailto:mikhailiyuk@ukr.net), [mikhailiyuk@kinr.kiev.ua](mailto:mikhailiyuk@kinr.kiev.ua)

consist of four alpha-particle clusters located at the vertices of an equilateral tetrahedron, while the  $^{20}\text{Ne}$  nucleus was taken to involve a deformed core ( $^{16}\text{O}$  nucleus) and an additional alpha-particle cluster. It was shown in [17] that this alpha-particle cluster is most probably located inside the core.

Such an approach is often used to calculate the structural properties of loosely bound (see [1, 18], for example) and compact (see [19], for example) nuclei. However, the internal structure of the core is usually disregarded in such calculations.

In the present study, the model proposed in [16] is extended to the  $^{13}\text{C}$  and  $^{13}\text{N}$  nuclei. These nuclei are assumed to consist of a deformed core ( $^{12}\text{C}$  nucleus) and an additional nucleon, which is most probably located inside the core.

Within this approach, the multiparticle densities of the  $^{13}\text{C}$  and  $^{13}\text{N}$  nuclei can be represented in the form

$$\rho(\boldsymbol{\xi}, \boldsymbol{\eta}, \boldsymbol{\chi}) = \rho_{\Delta}^{(12\text{C})}(\boldsymbol{\xi}, \boldsymbol{\eta})\rho^{(N)}(\boldsymbol{\chi}), \quad (1)$$

where  $\rho_{\Delta}^{(12\text{C})}(\boldsymbol{\xi}, \boldsymbol{\eta})$  is the core density (that of the  $^{12}\text{C}$  nucleus),  $\rho^{(N)}(\boldsymbol{\chi})$  is the density of the additional nucleon,  $\boldsymbol{\xi}$  and  $\boldsymbol{\eta}$  are the Jacobi coordinates of the alpha-particle clusters of the  $^{12}\text{C}$  nucleus, and  $\boldsymbol{\chi}$  is the coordinate of the additional nucleon.

In accordance with the  $\alpha$ -cluster model with dispersion, the density of the  $^{12}\text{C}$  nucleus has the form [14]

$$\rho_{\Delta}^{(12\text{C})}(\boldsymbol{\xi}, \boldsymbol{\eta}) = \int d^3\xi' d^3\eta' \rho_0(\boldsymbol{\xi}', \boldsymbol{\eta}') \quad (2)$$

$$\times \Phi_{\Delta}(\boldsymbol{\xi} - \boldsymbol{\xi}', \boldsymbol{\eta} - \boldsymbol{\eta}'),$$

$$\rho_0(\boldsymbol{\xi}, \boldsymbol{\eta}) = \frac{1}{4\sqrt{3}\pi^2 d^2} \delta(\xi - d) \delta\left(\eta - \frac{\sqrt{3}}{2}d\right) \delta(\boldsymbol{\xi} \cdot \boldsymbol{\eta}), \quad (3)$$

$$\Phi_{\Delta}(\boldsymbol{\xi}, \boldsymbol{\eta}) = \frac{1}{(\sqrt{3}\pi\Delta^2)^3} \exp\left(-\frac{\xi^2 + \frac{4}{3}\eta^2}{2\Delta^2}\right). \quad (4)$$

In these formulas, the parameters  $d$  and  $\Delta$  characterize the distance between the  $\alpha$  clusters and the possibility of their displacement from their most probable equilibrium positions at the vertices of an equilateral triangle.

We take the density of the additional nucleon in the form

$$\rho^{(N)}(\boldsymbol{\chi}) = \frac{1}{(\lambda\sqrt{\pi})^3} \exp\left(-\frac{\chi^2}{\lambda^2}\right), \quad (5)$$

where the parameter  $\lambda$  characterizes the distance between the additional nucleon and the center of mass of the core. It is evident from formulas (1) and (5) that,

within this approach, the additional nucleon resides most probably inside the core. In other words, the additional nucleon executes vibrations about its most probable equilibrium position at the center of mass of the core.

The values of the parameters  $d$ ,  $\Delta$ , and  $\lambda$  can be determined by fitting the calculated form factors for the nuclei in question to their measured counterparts. The  $^{13}\text{N}$  nucleus is not stable, and its electric form factor has not been measured experimentally; in view of this and the fact that the polarization observables calculated for the  $^{13}\text{C}$  and  $^{13}\text{N}$  nuclei in [12] differ only slightly, experimental value of the charge form factor for the  $^{13}\text{C}$  nucleus from [20] can be used to assess the density parameters of the nuclei in question. It should be noted that, within the present  $\alpha$ -cluster model with dispersion, we neglect the possibility of nucleon exchange between the alpha-particle clusters. The calculations performed in [14, 15] revealed that the effect of nucleon exchange between the alpha-particle clusters and the effect of antisymmetrization of the wave function for the nucleus on the cross-section value are small, because the time of projectile-target interaction is much shorter than the characteristic time of intranuclear motion. In other words, this interaction time is too short for the projectile to feel nucleon exchange between the alpha-particle clusters, which occurs rather rarely and slowly. Moreover, the projectile energy exceeds considerably the Fermi energy, so that the correlations between the nucleons in the nucleus that are caused by the Pauli exclusion principle cannot play a noticeable role in elastic scattering of such a particle.

The charge form factor for the  $^{13}\text{N}$  nucleus can be represented as

$$F^{(13\text{N})}(q) = \frac{12}{13} \exp\left(-\frac{1}{6}q^2\langle r^2 \rangle_{\alpha} - \frac{1}{6}q^2\Delta^2\right) \quad (6)$$

$$\times j_0\left(\frac{qd}{\sqrt{3}}\right) + \frac{1}{13} \frac{1}{(1+r_0^2q^2)^2} \exp\left(-\frac{q^2\lambda^2}{4}\right),$$

where  $j_0(x)$  is a spherical Bessel function,  $\langle r^2 \rangle_{\alpha}^{1/2} = 1.61$  fm is the root-mean-square radius of the alpha-particle clusters of the core,  $\mathbf{q}$  is the momentum transfer, and  $r_0 = 0.234$  fm is the proton radius.

Neglecting the neutron charge form factor, we represent the form factor for the  $^{13}\text{C}$  nucleus as

$$F^{(13\text{C})}(q) = \exp\left[-\frac{1}{6}q^2(\langle r^2 \rangle_{\alpha} + \Delta^2)\right] j_0\left(\frac{qd}{\sqrt{3}}\right). \quad (7)$$

The mean-square radii of the  $^{13}\text{C}$  and  $^{13}\text{N}$  nuclei are

$$\langle r^2 \rangle_{13\text{C}} = \langle r^2 \rangle_{\alpha} + \frac{1}{3}d^2 + \Delta^2, \quad (8)$$

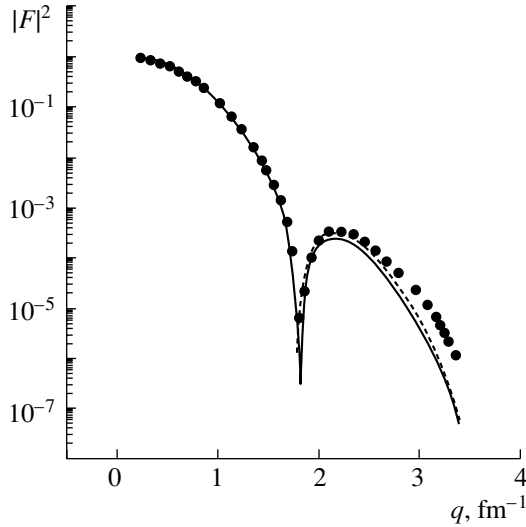


**Fig. 1.** Elastic form factors for the  $^{13}\text{C}$  and  $^{13}\text{N}$  nuclei (the solid and the dashed curve, respectively) versus the momentum transfer. The displayed experimental data (points) were borrowed from [20].

$$\langle r^2 \rangle_{^{13}\text{N}} = \frac{12}{13} \left( \langle r^2 \rangle_{\alpha} + \frac{1}{3}d^2 + \Delta^2 + \frac{1}{8}\lambda^2 + \frac{1}{2}r_0^2 \right). \quad (9)$$

Figure 1 shows the calculated form factors for the  $^{13}\text{C}$  and  $^{13}\text{N}$  nuclei (the solid and the dashed curve, respectively) along with experimental data on the  $^{13}\text{C}$  nucleus from [20]. It can be seen that the form factors that we calculated for the  $^{13}\text{C}$  and  $^{13}\text{N}$  nuclei differ only slightly and are in agreement with available experimental data within the momentum-transfer region  $q \leq 3 \text{ fm}^{-1}$ .

Having compared the form factors calculated for the  $^{13}\text{C}$  and  $^{13}\text{N}$  nuclei with the measured  $^{13}\text{C}$  form factor [20], we obtained the following values of the density parameters:  $d = 3.0 \text{ fm}$  and  $\Delta = 0.59 \text{ fm}$  for the  $^{13}\text{C}$  nucleus and  $d = 3.031 \text{ fm}$ ,  $\Delta = 0.45 \text{ fm}$ , and  $\lambda = 2.1 \text{ fm}$  for the  $^{13}\text{N}$  nucleus. The root-mean-square radii calculated for the  $^{13}\text{C}$  and  $^{13}\text{N}$  nuclei with these values of the density parameters are the following:  $\langle r^2 \rangle_{^{13}\text{C}}^{1/2} = 2.4372 \text{ fm}$  and  $\langle r^2 \rangle_{^{13}\text{N}}^{1/2} = 2.4373 \text{ fm}$ . These values of the root-mean-square radii of the  $^{13}\text{C}$  and  $^{13}\text{N}$  nuclei are close to the experimentally measured value of  $\langle r^2 \rangle_{^{13}\text{C}}^{1/2}(\text{expt}) = 2.44 \text{ fm}$  [21]. We note that the value measured experimentally for the root-mean-square radius of the  $^{13}\text{C}$  nucleus is less than that for the  $^{12}\text{C}$  nucleus ( $\langle r^2 \rangle_{^{12}\text{C}}^{1/2}(\text{expt}) = 2.472 \text{ fm}$  [21]).

In accordance with the theory of multiple diffractive scattering, the amplitude of elastic proton scat-

tering on  $^{13}\text{C}$  and  $^{13}\text{N}$  nuclei can be represented as

$$F(\mathbf{q}) = \frac{ik}{2\pi} \int d^2bd^3\xi d^3\eta d^3\chi e^{i\mathbf{q}\cdot\mathbf{b}} \rho(\boldsymbol{\xi}, \boldsymbol{\eta}, \boldsymbol{\chi}) \quad (10)$$

$$\times \Omega(\mathbf{b}, \{\mathbf{r}_j\}),$$

$$\Omega(\mathbf{b}, \{\mathbf{r}_j\}) = 1 \quad (11)$$

$$- \prod_{j=1}^4 \left[ 1 - \frac{1}{2\pi ik} \int d^2q \exp[-i\mathbf{q}(\mathbf{b} - \mathbf{r}_j)] \tilde{f}(\mathbf{q}) \right],$$

where  $\mathbf{b}$  is the impact parameter;  $\mathbf{r}_j$  are the coordinates of the target-nucleus clusters;  $\mathbf{k}$  is the wave vector of the incident proton; and  $\tilde{f}(\mathbf{q}) = f_{NN}(q)$  and  $f_{p\alpha}(\mathbf{q})$  are the elementary amplitudes for, respectively, nucleon–nucleon interaction and proton interaction with the target-nucleus clusters. We note that, in this approach, the additional nucleon of the nucleus is actually considered as yet another cluster.

In general, the nucleon–nucleon amplitude is an operator in the spin–isospin space of colliding nucleons. Taking into account the invariance of the amplitude under spatial rotations and reflections, we represent the amplitude  $f_{NN}(q)$  in the most general form

$$f_{NN}(\mathbf{q}) = f_1(\mathbf{q}) + qf_2(\mathbf{q})(\boldsymbol{\sigma}_0 \cdot \mathbf{n} + \boldsymbol{\sigma}_1 \cdot \mathbf{n}) \quad (12)$$

$$+ f_3(\mathbf{q})(\boldsymbol{\sigma}_0 \cdot \boldsymbol{\sigma}_1) + f_4(\mathbf{q})(\boldsymbol{\sigma}_0 \cdot \mathbf{q})(\boldsymbol{\sigma}_1 \cdot \mathbf{q})$$

$$+ f_5(\mathbf{q})(\boldsymbol{\sigma}_0 \cdot \mathbf{p})(\boldsymbol{\sigma}_1 \cdot \mathbf{p}),$$

where  $\boldsymbol{\sigma}_0$  and  $\boldsymbol{\sigma}_1$  are the operators of the spins of, respectively, the incident proton and the additional nucleon of the target nucleus;  $\mathbf{n} = [\mathbf{k}, \mathbf{k}']/|\mathbf{k}, \mathbf{k}'|$ ,  $\mathbf{k}$  and  $\mathbf{k}'$  being the wave vectors of, respectively, the incident and the scattered proton,  $\mathbf{q} = \mathbf{k} - \mathbf{k}'$ ; and  $\mathbf{p} = (\mathbf{k} + \mathbf{k}')/|\mathbf{k} + \mathbf{k}'|$ . The vectors  $\mathbf{n}$ ,  $\mathbf{p}$ , and  $-\mathbf{q}/|\mathbf{q}|$  form a right-hand triplet of orthonormal vectors. Neglecting the isospin part of the nucleon–nucleon interaction, we represent the amplitudes  $f_i(\mathbf{q})$  as

$$f_i(\mathbf{q}) = kH_i \exp(-\gamma_i q^2), \quad 1 \leq i \leq 5. \quad (13)$$

The numerical values of the parameters  $H_i$  and  $\gamma_i$  were obtained in [8] from a partial-wave analysis of nucleon–nucleon scattering and are quoted in Table 1.

Let us represent the amplitude of proton scattering on the alpha-particle clusters of the target nucleus as [15]

$$f_{p\alpha}(\mathbf{q}) = k \sum_{i=1}^2 (G_{ci} \exp(-\beta_{ci} q^2) \quad (14)$$

$$+ qG_{si} \exp(-\beta_{si} q^2)(\boldsymbol{\sigma}_0 \cdot \mathbf{n})).$$

The parameters  $G_{c1}$ ,  $\beta_{c1}$ ,  $G_{s1}$ , and  $\beta_{s1}$  are adjustable. They were determined from a comparison of the calculated and measured observables for elastic

**Table 1.** Parameters of the nucleon–nucleon amplitude

	$E_p = 547 \text{ MeV}$		$E_p = 800 \text{ MeV}$	
	$pp$	$pn$	$pp$	$pn$
$H_1 (\text{GeV}/c)^{-2}$	$3.49 - i1.32$	$3.40 + i0.57$	$4.84 + i0.03$	$3.91 + i1.40$
$\gamma_1 (\text{GeV}/c)^{-2}$	$5.84 - i0.65$	$5.42 - i7.13$	$5.82 - i0.85$	$4.87 - i3.0$
$H_2 (\text{GeV}/c)^{-3}$	$-1.06 - i6.91$	$-2.25 - i6.53$	$-2.29 - i6.15$	$-2.55 - i4.51$
$\gamma_2 (\text{GeV}/c)^{-2}$	$3.09 + i0.47$	$4.96 + i0.25$	$3.70 + i0.19$	$3.93 + i0.47$
$H_3 (\text{GeV}/c)^{-2}$	$-0.49 + i1.07$	$-0.55 - i0.99$	$-0.25 + i0.71$	$0.0 - i0.69$
$\gamma_3 (\text{GeV}/c)^{-2}$	$3.49 - i0.56$	$5.86 - i0.05$	$3.92 - i0.82$	$2.05 + i1.68$
$H_4 (\text{GeV}/c)^{-4}$	$-1.45 - i30.01$	$1.59 + i28.74$	$-4.53 - i16.87$	$-1.73 + i6.87$
$\gamma_4 (\text{GeV}/c)^{-2}$	$9.67 + i0.81$	$5.54 - i0.19$	$5.71 + i1.95$	$2.84 - i1.08$
$H_5 (\text{GeV}/c)^{-2}$	$0.99 - i0.04$	$0.54 + i0.60$	$1.07 - i0.33$	$0.29 + i0.73$
$\gamma_5 (\text{GeV}/c)^{-2}$	$7.07 + i0.61$	$4.91 + i0.60$	$3.52 - i1.68$	$3.65 + i1.87$

**Table 2.** Parameters of the  $p\alpha$  amplitude

$E_p, \text{ MeV}$	$\beta_{c1}, \text{ fm}^2$	$G_{c1}, \text{ fm}^2$	$\beta_{s1}, \text{ fm}^2$	$G_{s1}, \text{ fm}^3$
500	$0.393 - i0.079$	$-0.217 + i1.042$	$0.464 + i0.076$	$0.194 + i0.413$
800	$0.424 - i0.025$	$-0.330 + i1.258$	$0.490 + i0.052$	$0.177 + i0.295$

$p^4\text{He}$  scattering. The parameters  $G_{c2}$ ,  $\beta_{c2}$ ,  $G_{s2}$ , and  $\beta_{s2}$  are expressed in terms of  $G_{c1}$ ,  $\beta_{c1}$ ,  $G_{s1}$ , and  $\beta_{s1}$  by using the following relations from [15]:

$$G_{c2} = \frac{3iG_{c1}^2}{32\beta_{c1}}, \quad \beta_{c2} = \frac{1}{2}\beta_{c1}, \quad (15)$$

$$G_{s2} = \frac{3iG_{c1}G_{s1}\beta_{c1}}{8(\beta_{c1} + \beta_{s1})^2}, \quad \beta_{s2} = \frac{\beta_{c1}\beta_{s1}}{\beta_{c1} + \beta_{s1}}. \quad (16)$$

The parameters of the  $p\alpha$  amplitude are given in Table 2.

Substituting (11)–(14) into (10), we recast the amplitude of elastic proton scattering on  $^{13}\text{C}$  nuclei into the form

$$F^{(13\text{C})}(\mathbf{q}) = F^{(12\text{C})}(\mathbf{q}) + \tilde{F}(\mathbf{q}), \quad (17)$$

$$F^{(12\text{C})}(\mathbf{q}) = 3F_1^{(12\text{C})}(\mathbf{q}) - 3F_2^{(12\text{C})}(\mathbf{q}) + F_3^{(12\text{C})}(\mathbf{q}), \quad (18)$$

$$\tilde{F}(\mathbf{q}) = \tilde{F}_1(\mathbf{q}) - 3\tilde{F}_2(\mathbf{q}) + 3\tilde{F}_3(\mathbf{q}) - \tilde{F}_4(\mathbf{q}), \quad (19)$$

where  $F^{(12\text{C})}(\mathbf{q})$  is the amplitude of elastic proton scattering on the alpha-particle clusters of the core ( $^{12}\text{C}$  nucleus) and the amplitude  $\tilde{F}(\mathbf{q})$  arises owing to the multiple scattering of the incident proton on the

alpha-particle clusters of the core and on the additional nucleon of the target nucleus. The amplitudes  $F_i^{(12\text{C})}(\mathbf{q})$  and  $\tilde{F}_i(\mathbf{q})$  are associated with the single, double, triple, and quadruple scattering of the incident proton on the clusters of the target nucleus.

We note that the calculated amplitudes of elastic proton scattering on  $^{13}\text{C}$  and  $^{13}\text{N}$  nuclei coincide in this approach. The distinctions between the calculated observables of elastic  $p^{13}\text{C}$  and  $p^{13}\text{N}$  scattering are caused by the distinctions between the parameters of the proton–proton ( $pp$ ) and proton–neutron ( $pn$ ) amplitudes (Table 1).

Performing integration in (10), we obtain

$$F(\mathbf{q}) = A + E(\boldsymbol{\sigma}_0 \cdot \mathbf{n}) + M(\boldsymbol{\sigma}_1 \cdot \mathbf{n}) \quad (20) \\ + B(\boldsymbol{\sigma}_0 \cdot \mathbf{n})(\boldsymbol{\sigma}_1 \cdot \mathbf{n}) + C(\boldsymbol{\sigma}_0 \cdot \mathbf{q})(\boldsymbol{\sigma}_1 \cdot \mathbf{q}) \\ + D(\boldsymbol{\sigma}_0 \cdot \mathbf{p})(\boldsymbol{\sigma}_1 \cdot \mathbf{p}).$$

As was indicated above, it is necessary to measure at least 11 independent observables in order to describe the elastic scattering of spin-1/2 particles completely. So far, the most detailed experimental measurement of polarization observables for such processes has been performed for elastic  $p^{13}\text{C}$  scattering at 500 MeV. In [2–6], the following observables were measured versus the scattering angle  $\theta$ :

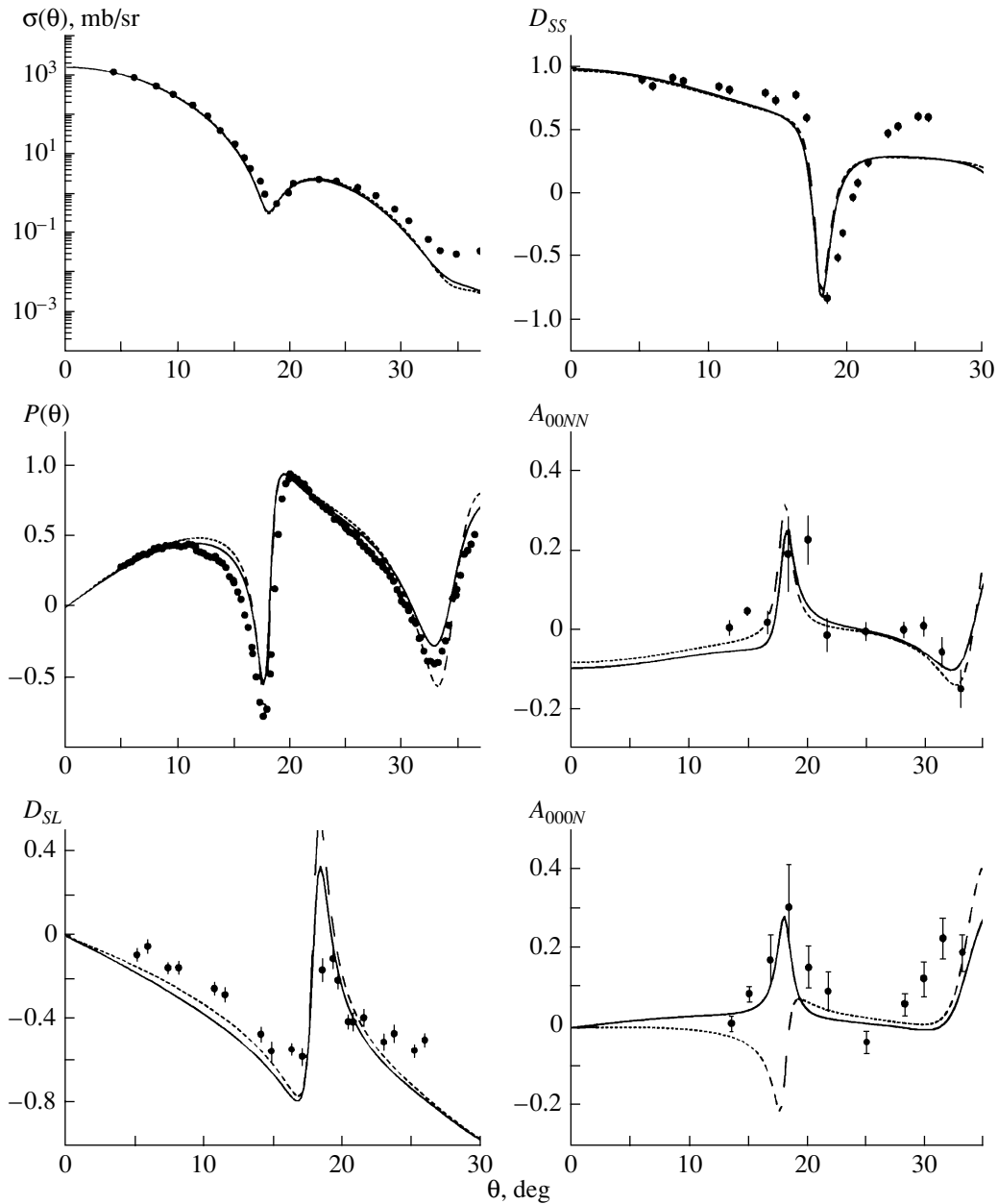


**Fig. 2.** Differential cross sections  $\sigma(\theta)$  and polarization observables for elastic proton scattering on  $^{13}\text{C}$  and  $^{13}\text{N}$  nuclei at 500 MeV (the solid and the dashed curve, respectively). The displayed experimental data (points) were borrowed from [2, 3].

the differential cross section  $\sigma(\theta) \equiv d\sigma/d\Omega$  (mb/sr); the polarization (asymmetry)  $P(\theta)$ ; the depolarization parameters  $D_{LS}(\theta)$ ,  $D_{SS}(\theta)$ , and  $D_{NN}(\theta)$ ; and the analyzing powers  $A_{000N}(\theta)$  and  $A_{00NN}(\theta)$ . These quantities are related to the amplitudes  $A$ ,  $B$ ,  $C$ ,  $D$ ,  $E$ , and  $M$  by the equations [10]

$$\sigma = |A|^2 + |B|^2 + |C|^2 + |D|^2 + |E|^2 + |M|^2, \quad (21)$$

$$\sigma P = 2\text{Re}(A^*E + B^*M), \quad (22)$$

$$\sigma D_{LS} = 2\text{Re}(A^*E - B^*M), \quad (23)$$

$$\sigma D_{SS} = |A|^2 - |B|^2 + |C|^2 - |D|^2 \quad (24)$$

$$- |E|^2 + |M|^2,$$

$$\sigma D_{NN} = |A|^2 + |B|^2 - |C|^2 - |D|^2 \quad (25)$$

$$+ |E|^2 + |M|^2,$$

$$\sigma A_{000N} = 2\text{Re}(A^*M + B^*E), \quad (26)$$

$$\sigma A_{00NN} = 2\text{Re}(A^*B - C^*D + E^*M). \quad (27)$$

Figures 2–5 show the calculated polarization observables for elastic  $p^{13}\text{C}$  and  $p^{13}\text{N}$  scattering (solid and dashed curves, respectively) at 500, 547, and 800 MeV, along with respective experimental data

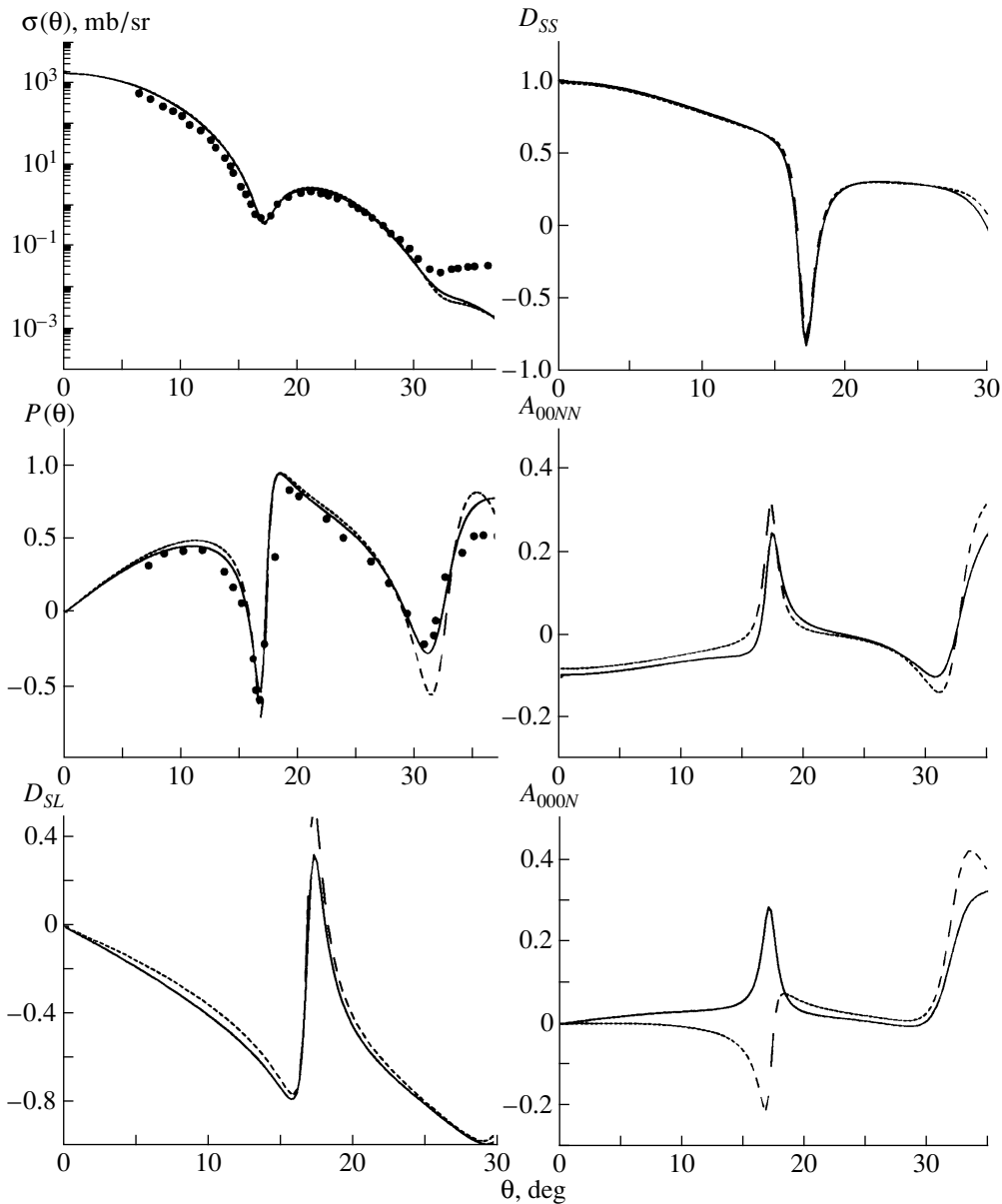


Fig. 3. As in Fig. 2, but for 547 MeV. The displayed experimental data (points) were borrowed from [5].

from [2–6]. The same value of the parameter  $\lambda$  was used in calculating the observables of elastic proton scattering on  $^{13}\text{C}$  and  $^{13}\text{N}$  nuclei. It can be seen from these figures that the calculated observables are in agreement with available experimental data. We note that the observables of elastic proton scattering on  $^{13}\text{C}$  and  $^{13}\text{N}$  nuclei were calculated without adjustable parameters.

Our calculations revealed that the cluster structure manifests itself quite clearly in the  $^{13}\text{C}$  and  $^{13}\text{N}$  nuclei. The proposed model, where the  $^{13}\text{C}$  and  $^{13}\text{N}$  nuclei consist of a deformed core ( $^{12}\text{C}$  nucleus) and an additional nucleon, which is most probably located inside the core, makes it possible to describe avail-

able experimental data without adjustable parameters, the calculated observables for elastic  $p^{13}\text{C}$  and  $p^{13}\text{N}$  scattering differing only slightly. Experimental measurements of the maximum possible number of observables for such processes would allow one to assess the applicability range of this model more reliably and to obtain additional information about the nucleon–nucleon interaction, nuclear forces, and the structure of light nuclei.

It should be noted that the phenomenological densities of target nuclei were used here in calculating the observables of elastic  $p^{13}\text{C}$  and  $p^{13}\text{N}$  scattering. A similar arrangement of the clusters for determining the density of the aforementioned nuclei can be ob-

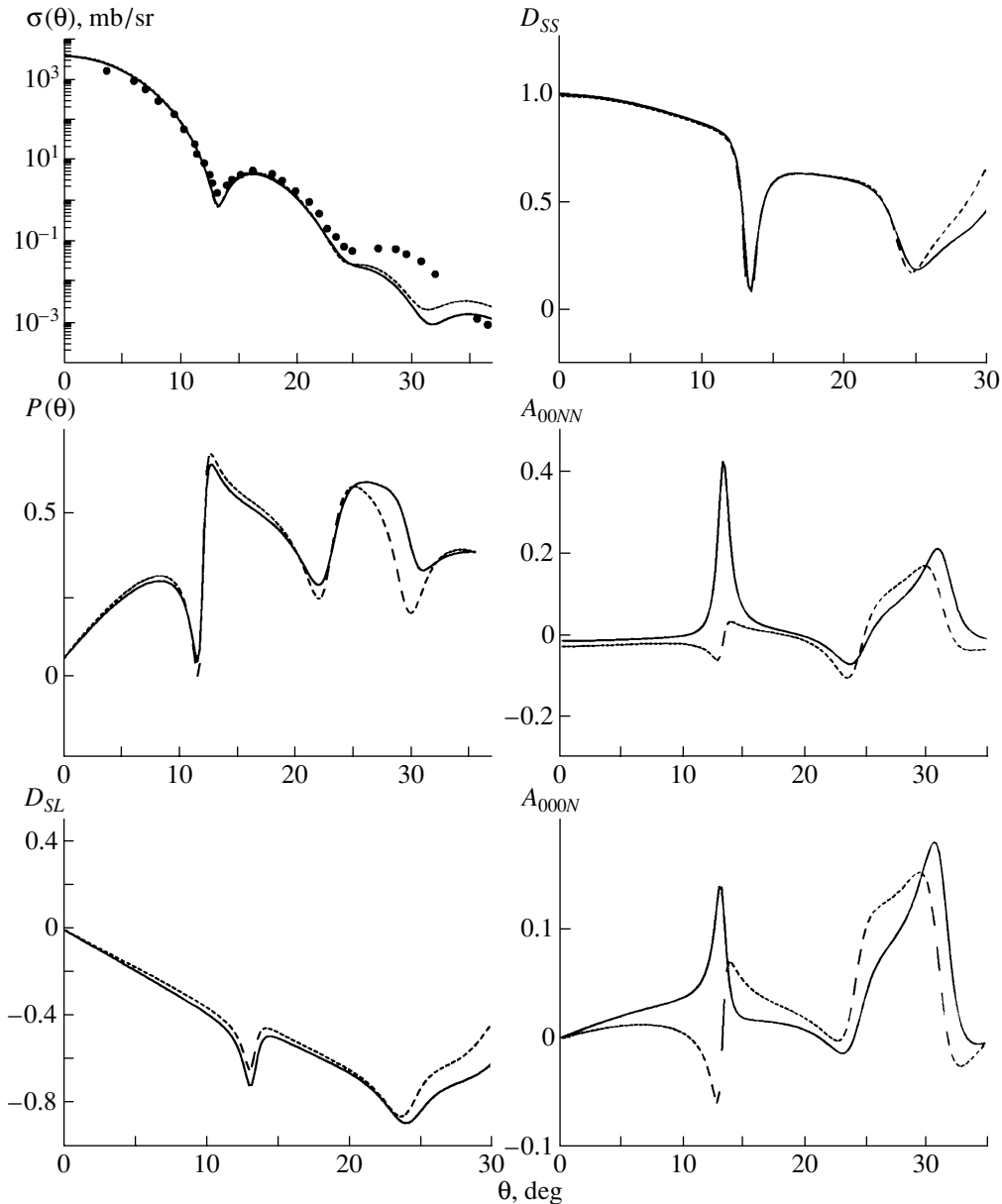
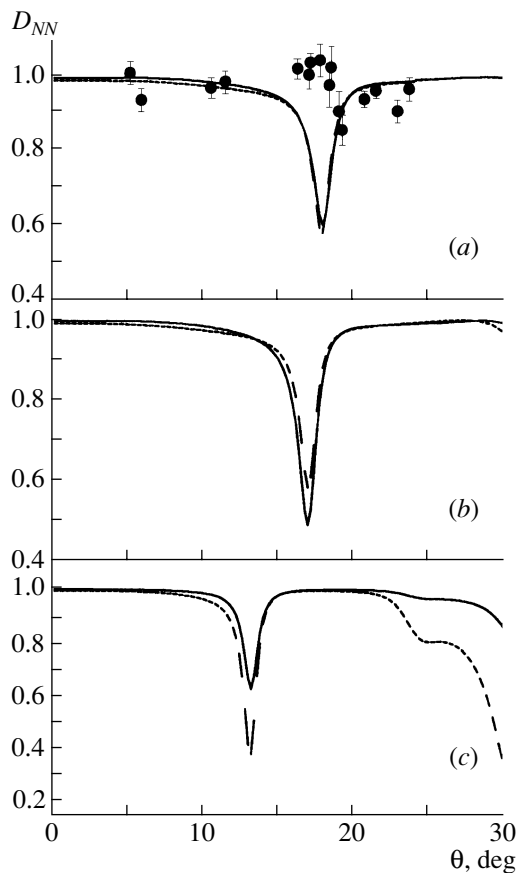


Fig. 4. As in Fig. 2, but for 800 MeV. The displayed experimental data (points) were borrowed from [6].

tained from calculations based on microscopic cluster models. For example, the multicluster model was used in [22] to study the properties of the  $^{12,13,14}\text{C}$ ,  $^{15}\text{N}$ , and  $^{16}\text{O}$  nuclei. Within this approach, three alpha-particle clusters entering into the composition of these nuclei are located with the highest probability at the vertices of an equilateral triangle, while the additional cluster is located at the vertex of the tetrahedron formed by all four clusters. It was shown in [22] that use of this approach makes it possible to describe the binding energies and the spectroscopic properties of the aforementioned nuclei better than within the usual shell model.

Unfortunately, the polarization observables of elastic  $p^{13}\text{C}$  and  $p^{13}\text{N}$  scattering have not yet been calculated by using the microscopic cluster wave functions. The optical model with shell wave functions [2, 9–12] or the theory of multiple diffractive scattering with the single-particle density of the target nucleus [8] was usually used to calculate these observables. In this case, the parameters of the nucleon–nucleon amplitude were considered to be adjustable for matching the calculated and measured observables [2, 9–12], while the behavior of the depolarization parameters calculated in [8] within the theory of multiple diffractive scattering and the model of independent nucleons was not quite correct. Good



**Fig. 5.** Depolarization parameters  $D_{NN}(\theta)$  for elastic proton scattering on  $^{13}\text{C}$  and  $^{13}\text{N}$  (solid and dashed curves, respectively) at (a) 500, (b) 547, and (c) 800 MeV. The displayed experimental data (points) were borrowed from [2, 4].

agreement between the calculated and measured observables within the cluster model was obtained in studying the polarization properties of elastic proton scattering on lighter nuclei ( $^6\text{Li}$ ,  $^9\text{Be}$ ) at intermediate energies (see [23] and references therein). However, only the differential cross sections and polarization (asymmetry) were calculated in those studies, but these properties are less sensitive to the choice of model density for the target nucleus and to the parameters of the nucleon–cluster amplitude than the depolarization parameters and the analyzing power, which were considered in the present study.

## ACKNOWLEDGMENTS

We are grateful to V.V. Pilipenko and Yu.A. Pozdnyakov for stimulating discussions.

## REFERENCES

1. A. Ozawa, T. Suzuki, and I. Tanihata, Nucl. Phys. A **693**, 32 (2001).
2. G. W. Hoffman, M. L. Barlett, D. Ciskowski, *et al.*, Phys. Rev. C **41**, 1651 (1990).
3. G. W. Hoffman, M. L. Barlett, W. Kielhorn, *et al.*, Phys. Rev. Lett. **65**, 3096 (1990).
4. G. W. Hoffman, L. Ray, D. Read, *et al.*, Phys. Rev. C **53**, 1974 (1996).
5. S. J. Seestrom-Morris *et al.*, Phys. Rev. C **30**, 270 (1984).
6. G. S. Blanpied *et al.*, Phys. Rev. C **32**, 2152 (1985).
7. P. Osland and R. J. Glauber, Nucl. Phys. A **326**, 225 (1979).
8. I. N. Kudryavtsev and A. P. Soznik, J. Phys. G **15**, 1377 (1989).
9. L. Ray, Phys. Rev. C **41**, 2816 (1990).
10. L. Ray, G. W. Hoffman, M. L. Barlett, *et al.*, Phys. Rev. C **37**, 1169 (1988).
11. L. Ray, Phys. Rev. C **45**, 1394 (1992).
12. L. Ray, Phys. Rev. C **47**, 2990 (1993).
13. T. Mefford, R. H. Landau, L. Berge, and K. Amos, Phys. Rev. C **50**, 1648 (1994).
14. Yu. A. Berezhnoy, V. V. Pilipenko, and G. A. Khomenko, J. Phys. G **10**, 63 (1984).
15. Yu. A. Berezhnoy, V. P. Mikhailyuk, and V. V. Pilipenko, J. Phys. G **18**, 85 (1992).
16. Yu. A. Berezhnoy and V. P. Mikhailyuk, Yad. Fiz. **63**, 783 (2000) [Phys. At. Nucl. **63**, 715 (2000)].
17. Yu. A. Berezhnoy and V. P. Mikhailyuk, Izv. Akad. Nauk, Ser. Fiz. **65**, 721 (2001).
18. J. S. Al-Khalili, A. Tostevin, and I. J. Thompson, Phys. Rev. C **54**, 1843 (1996).
19. T. Wada and H. Horiuchi, Phys. Rev. Lett. **58**, 2190 (1987).
20. P. Bydzovsky, R. Mach, and S. S. Kamalov, Nucl. Phys. A **574**, 685 (1994).
21. H. de Vries, C. W. de Jager, and C. de Vries, At. Data Nucl. Data Tables **36**, 495 (1987).
22. M. Dufour and P. Descouvemont, Nucl. Phys. A **605**, 160 (1996).
23. M. A. Zhusupov and E. T. Ibraeva, Fiz. Élem. Chastits At. Yadra **31**, 1427 (2000).

*Translated by E. Kozlovsky*

---

---

**ELEMENTARY PARTICLES AND FIELDS**  
**Theory**

---

---

## Description of Composite Systems in the Spectral Integration Technique: The Gauge Invariance and Analyticity Constraints for the Radiative Decay Amplitudes\*

V. V. Anisovich and M. A. Matveev

*Petersburg Nuclear Physics Institute, Russian Academy of Sciences, Gatchina, 188350 Russia*

Received April 2, 2003

**Abstract**—The constraints following from gauge invariance and analyticity are considered for the amplitudes of radiative transitions of composite systems, when composite systems are treated in terms of spectral integrals. We discuss gauge-invariant amplitudes for the transitions  $S \rightarrow \gamma S$  and  $V \rightarrow \gamma S$ , with scalar  $S$  and vector  $V$  mesons being two-particle composite systems of scalar (or pseudoscalar) constituents, and we demonstrate the mechanism of cancellation of false kinematical singularities. Furthermore, we explain how to generalize this consideration for quark–antiquark systems, in particular, for the reaction  $\phi(1020) \rightarrow \gamma f_0(980)$ . Here, we also consider in more detail the quark-model nonrelativistic approach for this reaction. © 2004 MAIK “Nauka/Interperiodica”.

### 1. INTRODUCTION

Presently, there exists rich information for radiative decays of mesons with masses at 1000–1800 MeV, and one may expect the appearance of more data in the future (see, e.g., [1–4] and references therein). The data on partial widths of radiative decays provide us with important knowledge about the quark–gluon structure of hadrons. However, to suffice this expectation and avoid misleading conclusions, one needs to work with an adequate technique for the description of radiative processes involving composite systems.

To describe the low-lying hadronic states, namely,  $S$ -wave mesons of the 36-plet and baryons of the 56-plet in terms of the  $SU(6)$  symmetry, the nonrelativistic quark-model approach is an appropriate technique. The investigation of radiative decays carried out decades ago played a crucial role in establishing the quark model, by operating with a constituent quark as a universal object for mesons and baryons [5]. However, for higher states, e.g., for the  $P$ -wave quark–antiquark states, relativistic effects become important. Nevertheless, until now, the use of nonrelativistic formulas for radiative decays of mesons with masses of about 1000–1500 MeV has been rather common practice.

Thus, there is a necessity to use relativistic technique for the description of radiative decays. The scheme of relativistic description of the composite system interacting with an electromagnetic field was suggested in [6–9]. Within this approach, form

factors of composite systems are represented as double spectral integrals over the masses of composite systems. The spectral integration technique is a direct generalization of nonrelativistic quantum-mechanical approximation, and the processes considered within this technique are time-ordered, as in quantum mechanics. The energy in the intermediate state is not conserved, but the particles are mass-on-shell. In this method, vertex functions of the transitions *composite system*  $\rightarrow$  *constituents* are defined by the scattering amplitude of constituents.

The scheme applied to the composite-system form factors in [6] is as follows: partial scattering amplitude  $A^{(J)}(s)$  ( $s$  is total energy squared of the scattered constituents and  $J$  is the total angular momentum) is considered within the dispersion  $N/D$  representation [10]. In this technique, the amplitude is represented as a sum of dispersion  $N/D$  loop diagrams shown in Fig. 1a. In the case where the  $D$  function does not have CDD poles [11], the partial amplitude of the  $J$  state is

$$A^{(J)} = Q_{\mu_1 \dots \mu_J}^{(J)}(p_\perp) \frac{N_J(s)}{1 - B_J(s)} Q_{\mu_1 \dots \mu_J}^{(J)}(p'_\perp), \quad (1)$$

where  $Q_{\mu_1 \dots \mu_J}^{(J)}(p_\perp)$  is a covariant angular momentum- $J$  operator which depends on the relative momentum of particles 1 and 2:  $p_{\perp\mu} = g_{\mu\nu}^\perp p_\nu$ ; here,  $p = p_1 - p_2$ , and  $g_{\mu\nu}^\perp$  is the metric tensor, which works in the space, orthogonal to  $P = p_1 + p_2$ :  $g_{\mu\nu}^\perp = g_{\mu\nu} - P_\mu P_\nu / P^2$  (for equal particle masses 1 and 2, one has  $p_\perp = p$ ). If the scattered particles are spinless and

---

\*This article was submitted by the authors in English.

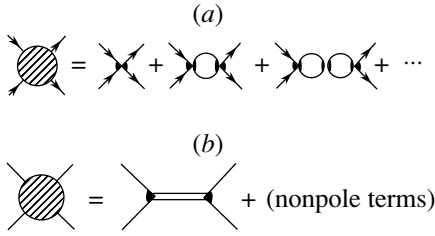


**Fig. 1.** (a) Representation of partial scattering amplitude as a set of dispersion loop diagrams. (b) Partial amplitude at energies close to the mass of a bound state: the main contribution is given by the pole at  $s = M^2$ .

$J = L$ , where  $L$  is the orbital momentum of the system, we replace  $Q_{\mu_1 \dots \mu_J}^{(J)}(p_\perp) \rightarrow X_{\mu_1 \dots \mu_L}^{(L)}(p_\perp)$ , where for the lowest waves, according to [12], the operators  $X_{\mu_1 \dots \mu_L}^{(L)}(p_\perp)$  are determined as follows:

$$X^{(0)}(p_\perp) = 1, \quad X_\mu^{(1)}(p_\perp) = p_{\perp\mu}, \quad (2)$$

$$X_{\mu_1 \mu_2}^{(2)}(p_\perp) = \frac{3}{2} \left( p_{\perp\mu_1} p_{\perp\mu_2} - \frac{1}{3} p_\perp^2 g_{\mu_1 \mu_2}^\perp \right), \dots$$

When particles 1 and 2 are fermions, like quarks or nucleons, then the operators  $Q_{\mu_1 \dots \mu_J}^{(J)}$  are constructed by using  $\gamma$  matrices (see [12] for details).

If there is a bound state with mass  $M$  in the partial wave, the sum of diagrams shown in Fig. 1a creates a pole at  $s = M^2$  (see Fig. 1b), and the vertex of the pole diagram determines the wave function of the bound state.

The form factor of bound state can be defined by the process of Fig. 2a when the photon is emitted by interacting constituents. The amplitudes of the initial state (interaction block before the photon emission) and final one (that after photon emission) contain the poles  $s = M^2$  and  $s' = M'^2$  (see Fig. 2b), so the two-pole amplitude defines the form factor of the composite system: the form factor is the residue in these poles; it is shown separately in Fig. 2c.

To be more understandable in explaining the form factor calculus within gauge invariance and analyticity constraints, we use a simplified variant of the  $N$  function, with separable forces. The hypothesis of separability of the interaction blocks can be successfully applied to the realistic description of composite systems such as the deuteron [6]. Here, we use this hypothesis to simplify a rather cumbersome presentation, and this simplification does not influence the principal statements. Correspondingly, we use separable interaction with  $N_J(s) \rightarrow g_J^2(s)$ . Then the amplitude of Fig. 2a for the emission of a photon by the two-particle system with total angular momenta

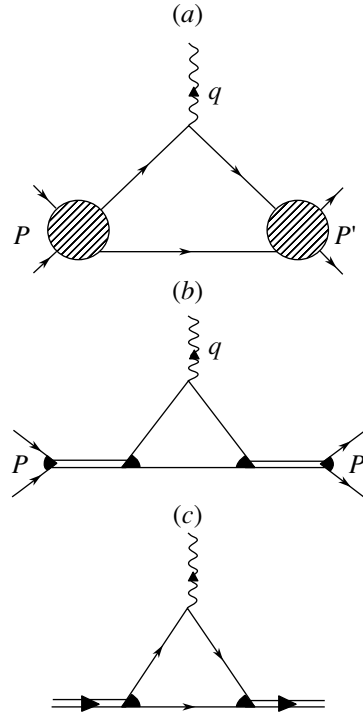


**Fig. 2.** Diagrams determining the form factor of the composite system: (a) the photon emission by interacting constituents; (b) diagram a near pole corresponding to bound states; (c) form factor of bound state determined as a residue of the amplitude of diagram b at the poles at  $s = M^2$  and  $s' = M'^2$ .

$J$  and  $J'$  in the initial and final states, respectively, reads as follows:

$$A_\alpha^{(J \rightarrow J')} = Q_{\mu_1 \dots \mu_J}^{(J)}(p_\perp) \frac{g_J(s)}{1 - B_J(s)} \quad (3)$$

$$\times \Gamma_{\mu_1 \dots \mu_J \alpha \nu_1 \dots \nu_{J'}}^{(J \rightarrow J')}(P, P'; q) \frac{g_{J'}(s')}{1 - B_{J'}(s')} Q_{\nu_1 \dots \nu_{J'}}^{(J')}(p'_\perp),$$

where  $\Gamma_{\mu_1 \dots \mu_J \alpha \nu_1 \dots \nu_{J'}}^{(J \rightarrow J')}$  is the three-point interaction amplitude at  $P^2 = s$  and  $P'^2 = s'$ . The amplitude  $A_\alpha^{(J \rightarrow J')}$  is represented by Fig. 3a as a chain of loop diagrams; the three-point interaction amplitude is depicted in Fig. 3a in the middle of the chain of loop diagrams.

The loop diagram  $B_J(s)$ , under the ansatz of separable interaction, is equal to

$$B_J(s) = \int_{(m_1+m_2)^2}^{\infty} \frac{d\tilde{s}}{\pi} \frac{g_J^2(\tilde{s})}{\tilde{s} - s - i0} \rho_J(\tilde{s}), \quad (4)$$

where  $m_1$  and  $m_2$  are the masses of scattered particles and  $\rho_J(s)$  is the phase space in the state with total angular momentum  $J$ . For scalar constituent particles and total angular momentum  $J = 0$ , the

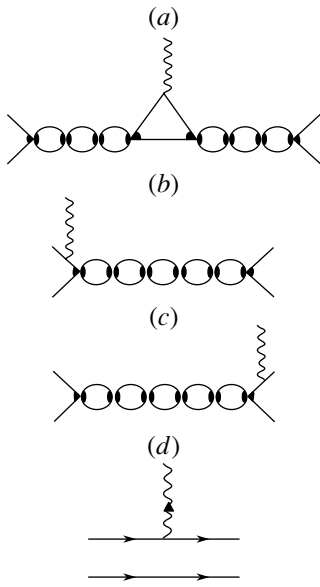


**Fig. 3.** (a) The process shown diagrammatically in Fig. 2a in terms of the dispersion loop diagrams; diagrams with the photon interaction in the (b) initial and (c) final states; (d) emission of photon by noninteracting constituents.

phase volume is defined as follows:

$$\rho(s) = \int d\Phi_2(P; p_1, p_2), \quad (5)$$

$$d\Phi_2(P; p_1, p_2) = \frac{1}{2} \frac{d^3 p_1}{2p_{10}(2\pi)^3}$$

$$\times \frac{d^3 p_2}{2p_{20}(2\pi)^3} (2\pi)^4 \delta^{(4)}(P - p_1 - p_2),$$

where we have redenoted  $\rho_0(s) \rightarrow \rho(s)$ . For  $J \neq 0$ , the convolution of the operators  $Q_{\mu_1 \dots \mu_J}^{(J)}(p_\perp) \times Q_{\mu_1 \dots \mu_J}^{(J)}(p_\perp)$  should be inserted on the right-hand side of (5) for the calculation of  $\rho_J(s)$ .

The  $D$ -function zeros at  $s = M^2$  and  $s' = M'^2$  correspond to the existence of bound states

$$1 - B_J(M^2) = 0, \quad 1 - B_{J'}(M'^2) = 0. \quad (6)$$

In this way, the  $D$  functions near the pole read

$$1 - B_J(s) \simeq \frac{dB_J(M^2)}{ds} (M^2 - s), \quad (7)$$

$$1 - B_{J'}(s') \simeq \frac{dB_{J'}(M'^2)}{ds'} (M'^2 - s').$$

Therefore, the amplitude (3) near the poles takes the form

$$A_\alpha^{(J \rightarrow J')} \simeq Q_{\mu_1 \dots \mu_J}^{(J)}(p_\perp) \frac{G_J(s)}{M^2 - s} \quad (8)$$

$$\times \frac{\Gamma_{\mu_1 \dots \mu_J \alpha \nu_1 \dots \nu_{J'}}^{(J \rightarrow J')}(P, P'; q)}{\sqrt{(dB_J(M^2)/ds)(dB_{J'}(M'^2)/ds')}} \\ \times \frac{G_{J'}(s')}{M'^2 - s'} Q_{\nu_1 \dots \nu_{J'}}^{(J')}(p'_\perp),$$

where  $G_J(s) = g_J(s)/\sqrt{dB_J(M^2)/ds}$ .

One can introduce the wave functions as follows:

$$\psi_J(s) = \frac{G_J(s)}{M^2 - s}, \quad \psi_{J'}(s') = \frac{G_{J'}(s')}{M'^2 - s'}. \quad (9)$$

The radiative transition amplitude meson- $J \rightarrow$  meson- $J'$  is determined by residues at the poles  $s = M^2$  and  $s' = M'^2$ :

$$\Gamma_{\mu_1 \dots \mu_J \alpha \nu_1 \dots \nu_{J'}}^{(J \rightarrow J')}(P, P'; q) \quad (10)$$

$$= \frac{\left[ \Gamma_{\mu_1 \dots \mu_J \alpha \nu_1 \dots \nu_{J'}}^{(J \rightarrow J')}(P, P'; q) \right]_{s=M^2, s'=M'^2}}{\sqrt{(dB_J(M^2)/ds)(dB_{J'}(M'^2)/ds')}}.$$

In this way, the magnitudes  $M^2$  and  $M'^2$  are fixed in (9). This means that we should discriminate between analytic properties of the amplitude of photon emission by unbound particles and those of radiative transition amplitude meson- $J \rightarrow$  meson- $J'$ . Analytic properties of the amplitude as a function of  $s$  and  $s'$  for the emission of a photon by unbound particles are determined by all diagrams shown in Fig. 3.

In studying the analytic amplitude, one should take into account that moment operators, which give the spin dependence of the form factor  $\Gamma_{\mu_1 \dots \mu_J \alpha \nu_1 \dots \nu_{J'}}^{(J \rightarrow J')}(P, P'; q)$ , may have false kinematical singularities. In the whole amplitude of Fig. 3, just these singularities should cancel each other.

This paper is devoted to the problem of cancellation of false singularities: we use as an example the processes when  $J = J' = 0$  (Section 2) and  $J = 1, J' = 0$  (Section 3). We deal with scalar (or pseudoscalar) constituent particles with equal masses,  $m_1 = m_2 = m$ : this does not affect generality but simplifies cumbersome calculations. Furthermore, in Section 4 we present the generalization for quark constituents.

In Section 2, the transition  $(J = 0) \rightarrow (J' = 0)$  is considered; we denote this transition as  $S \rightarrow \gamma S$ . The three-point amplitude for this transition  $\Gamma_\alpha^{(0 \rightarrow 0)}(P, P'; q)$  can be expanded with respect to two spin operators: the transverse one,  $(P_\perp + P'_\perp)_\alpha = 2(P_\alpha - q_\alpha(Pq)/q^2)$ , and longitudinal one,  $q_\alpha$ . The transverse spin operator contains the kinematical singularity  $1/q^2$ , which should be canceled in the whole amplitude.

The necessity to use transverse and longitudinal spin operators, which are orthogonal to each other,

$(P_{\perp} + P'_{\perp})_{\alpha} q_{\alpha} = 0$ , is dictated by the specifics of the spectral-representation method for form factors of the  $S \rightarrow \gamma S$  transition. The vertex function of the photon emission is expanded with respect to independent and orthogonal operators  $(P_{\perp} + P'_{\perp})_{\alpha}$  and  $q_{\alpha}$  as follows:

$$\Gamma_{\alpha}^{(0 \rightarrow 0)}(P, P'; q) = (P_{\perp} + P'_{\perp})_{\alpha} \quad (11)$$

$$\times F_T^{(0 \rightarrow 0)}(s, s', q^2) + q_{\alpha} F_L^{(0 \rightarrow 0)}(s, s', q^2).$$

Then,  $F_T^{(0 \rightarrow 0)}(s, s', q^2)$  and  $F_L^{(0 \rightarrow 0)}(s, s', q^2)$  are defined by dispersion integrals over  $s$  and  $s'$ , which are in due course determined by transverse and longitudinal components of the triangle diagram only.

The mechanism of singularity cancellation in  $\Gamma_{\alpha}^{(0 \rightarrow 0)}(P, P'; q)$  was considered in [6] for the variant of  $F_T^{(0 \rightarrow 0)}(s, s', q^2)$  being a double spectral integral without subtraction terms. However, as was shown in [6], one cannot deal without subtraction terms at all: subtraction terms in  $F_L^{(0 \rightarrow 0)}(s, s', q^2)$  are important for canceling false singularities in (11). In Section 2, we consider a more general case of  $\Gamma_{\alpha}^{(0 \rightarrow 0)}(P, P'; q)$  with a subtraction term in  $F_T^{(0 \rightarrow 0)}(s, s', q^2)$ : such a variant serves as a guide to consider transition form factors with angular momenta  $J = 1, J' = 0$ .

The vertex function for the transition ( $J = 1$ )  $\rightarrow$  ( $J' = 0$ ), or  $V \rightarrow \gamma S$ , is considered in Section 3. The spin structure of such a vertex,  $\Gamma_{\mu\alpha}^{(1 \rightarrow 0)}(P, P'; q)$ , is determined by two independent tensors: one of them can be chosen as a metric tensor operating in two-dimensional space and being orthogonal to  $P$  and  $q$ ,

$$g_{\mu\alpha}^{\perp\perp} = g_{\mu\alpha} + \frac{q^2}{(Pq)^2 - P^2q^2} P_{\mu} P_{\alpha} \quad (12)$$

$$+ \frac{P^2}{(Pq)^2 - P^2q^2} q_{\mu} q_{\alpha}$$

$$- \frac{(Pq)}{(Pq)^2 - P^2q^2} (P_{\mu} q_{\alpha} + q_{\mu} P_{\alpha}),$$

while the second tensor is defined as

$$4L_{\mu\alpha} = \frac{q^2}{(Pq)^2 - P^2q^2} P_{\mu} P_{\alpha} \quad (13)$$

$$+ \frac{P^2}{(Pq)^2 - P^2q^2} q_{\mu} q_{\alpha} - \frac{(Pq)}{(Pq)^2 - P^2q^2} P_{\mu} q_{\alpha}$$

$$- \frac{P^2q^2}{[(Pq)^2 - P^2q^2](Pq)} q_{\mu} P_{\alpha}.$$

These two tensors satisfy gauge-invariance requirements

$$P_{\mu} g_{\mu\alpha}^{\perp\perp} = 0, \quad g_{\mu\alpha}^{\perp\perp} q_{\alpha} = 0, \quad (14)$$

$$P_{\mu} L_{\mu\alpha} = 0, \quad L_{\mu\alpha} q_{\alpha} = 0,$$

and  $L_{\mu\alpha}$  is constructed to be orthogonal to  $g_{\mu\alpha}^{\perp\perp}$ :

$$L_{\mu\alpha} g_{\mu\alpha}^{\perp\perp} = 0. \quad (15)$$

The vertex function for  $V \rightarrow \gamma S$  is defined by two form factors that correspond to operators in the form (12) and (13):

$$\Gamma_{\mu\alpha}^{(1 \rightarrow 0)}(P, P'; q) = g_{\mu\alpha}^{\perp\perp} F_T^{(1 \rightarrow 0)}(s, s', q^2) \quad (16)$$

$$+ L_{\mu\alpha} F_L^{(1 \rightarrow 0)}(s, s', q^2).$$

The operators written in (12) and (13) are singular: they contain poles at  $(Pq)^2 - P^2q^2 = 0$  and  $(Pq) = 0$ . In (16), these singularities must be compensated by zeros of the form factors  $F_T^{(1 \rightarrow 0)}(s, s', q^2)$  and  $F_L^{(1 \rightarrow 0)}(s, s', q^2)$ ; the corresponding mechanism is considered in detail in Section 3. We demonstrate that, to compensate false singularities in the reactions  $V \rightarrow \gamma S$ , the subtraction terms play an important role; from this point of view, the compensation mechanisms in the amplitudes  $S \rightarrow \gamma S$  and  $V \rightarrow \gamma S$  are similar.

At  $q^2 = 0$ , the only form factor  $F_T^{(1 \rightarrow 0)}(s, s', q^2)$  determines the transition amplitude  $V \rightarrow \gamma S$ . In Section 3, we discuss in detail the problem of unambiguous determination of the amplitude in terms of the spectral integration technique. The point is that, at  $q^2 \rightarrow 0$ , one of the independent operators of (12) and (13) becomes nilpotent. Indeed,

$$g_{\mu\alpha}^{\perp\perp}(0) = g_{\mu\alpha} + \frac{4s}{(s - s')^2} q_{\mu} q_{\alpha} \quad (17)$$

$$- \frac{2}{s - s'} (P_{\mu} q_{\alpha} + q_{\mu} P_{\alpha}),$$

$$L_{\mu\alpha}(0) = \frac{s}{(s - s')^2} q_{\mu} q_{\alpha} - \frac{1}{2(s - s')} P_{\mu} q_{\alpha},$$

and the second operator has a zero norm:

$$L_{\mu\alpha}(0) L_{\mu\alpha}(0) = 0. \quad (18)$$

Due to Eqs. (15) and (18), any combination of  $g_{\mu\alpha}^{\perp\perp}(0)$  and  $L_{\mu\alpha}(0)$ ,

$$g_{\mu\alpha}^{\perp\perp}(0) + C(s, s') L_{\mu\alpha}(0), \quad (19)$$

can be equally used to define the transverse form factor  $F_T(s, s', 0)$ . In Section 3, this property is demonstrated directly by considering two sets of operators, the first one given by (17) and the second set appearing after the substitution as follows:

$$g_{\mu\alpha}^{\perp\perp}(0) \rightarrow g_{\mu\alpha}^{\perp\perp}(0) + 4L_{\mu\alpha}(0) = g_{\mu\alpha} - \frac{2}{s - s'} q_{\mu} P_{\alpha}. \quad (20)$$

Such a choice of operators for the illustration of (19) is motivated by the existing statements (for example, see [13]) that only the form of (20) provides us with a correct operator expansion of transition amplitude for  $V \rightarrow \gamma(q^2 = 0)S$ . However, our consideration performed in Section 3 proves directly that it is not so.

Concerning analytic properties of amplitudes in the transitions  $V \rightarrow \gamma S$ , with emission of a photon ( $q^2 = 0$ ), they are as follows.

The whole amplitude of the transition of unbound particles is a sum of three contributions shown in Figs. 3a, 3b, and 3c:

$$\frac{g_1(s)}{1 - B_1(s)} [g_{\mu\alpha}^{\perp\perp}(0)T(s, s', 0) + L_{\mu\alpha}(0)L(s, s', 0)] \frac{g_0(s')}{1 - B_0(s')}. \quad (21)$$

The analyticity of this amplitude requires that the transverse component  $T(s, s', 0)$  have a zero of the first order at  $s = s'$ , namely,  $T(s, s, 0) = 0$ , while the combination  $L(s, s', 0) + 4T(s, s', 0)$  should have a zero of the second order.

The transverse amplitude for the transition of bound vector state to bound scalar state,  $F_T^{(1 \rightarrow 0)}(s = M^2, s' = M'^2, 0)$ , which is defined by the diagram of Fig. 2c, is not required to be zero at  $\omega = M - M' = 0$ .

In Section 4, we show the way to generalize our results for constituent quarks. We present the additive-quark-model contribution for the form factor of the decay  $\phi(1020) \rightarrow \gamma f_0(980)$  both in the form of a relativistic spectral integral [7] and in a nonrelativistic approach. Direct calculations performed for the additive-quark-model diagram, in both relativistic and nonrelativistic approximations, demonstrate the absence of a zero in the amplitude for  $\omega \rightarrow 0$ . This is in accordance with the general result obtained in the analysis of the whole amplitude (21).

In the Conclusion, we summarize briefly the results focusing our attention on advantages of the spectral integration technique and the problems that this method faces.

## 2. INTERACTION OF SCALAR TWO-PARTICLE COMPOSITE SYSTEM IN THE STATE $J^P = 0^+$ WITH ELECTROMAGNETIC FIELD: $S \rightarrow \gamma S$

A diagrammatical representation of the interaction amplitude in terms of the dispersion-relation graphs is shown in Fig. 3. These diagrams are obtained by coupling the photon to all the constituents (both internal and external) in the diagrams related to the constituent scattering amplitude. In addition, there

is an uncoupled diagram of Fig. 3d corresponding to noninteracting constituents.

We assume that two constituents may form the bound state, and the form factor of the composite system is determined by residues in the amplitude poles (see Fig. 2b).

For the sake of simplicity, the constituent masses are set equal to each other,  $m_1 = m_2 = m$ , though constituents are not identical; in this way, we do not symmetrize the states of constituents.

### 2.1. Diagrams of Fig. 3a Type

Consider the sum of the diagrams shown in Fig. 3a, when constituents interact in the  $S$ -wave state both before and after the emission of a photon. The sum of diagrams of such a type is written as

$$A_\alpha^{(0 \rightarrow 0)}(P, P'; q) = \frac{g_0(s)}{1 - B_0(s)} \times \Gamma_\alpha^{(0 \rightarrow 0)}(P, P'; q) \frac{g_0(s')}{1 - B_0(s')}, \quad (22)$$

where  $\Gamma_\alpha^{(0 \rightarrow 0)}$  is the three-point function shown separately in Fig. 4a; its representation through form factors  $F_T^{(0 \rightarrow 0)}(s, s', q^2)$  and  $F_L^{(0 \rightarrow 0)}(s, s', q^2)$  is given in (11).

The dispersion representation of the triangle graph can be found in [6–9]. Here, we briefly repeat the scheme, keeping in mind to apply it not only to three-point diagrams but also to the two-point ones describing the photon emission by constituents in the initial and final states (see Figs. 4b and 4c).

Let us start with the Feynman expression for the triangle diagram  $\Gamma_\alpha^{(0 \rightarrow 0)}(P, P'; q)$ :

$$\int \frac{d^4 k_1}{i(2\pi)^4} \frac{g_0(\tilde{P}^2; k_1^2, k_2^2)(k_1 + k_1')_\alpha g_0(\tilde{P}'^2; k_1'^2, k_2'^2)}{(m^2 - k_1^2)(m^2 - k_2^2)(m^2 - k_1'^2)}. \quad (23)$$

The following steps are necessary to write the dispersion integral starting from this amplitude:

(i) We should calculate the double discontinuity of the Feynman diagram (23), with fixed energy squared of initial and final states,  $\tilde{P}^2 = \tilde{s}$  and  $\tilde{P}'^2 = \tilde{s}'$ . This implies the substitution of operators in the intermediate states as follows:

$$(m^2 - k_1^2)^{-1}(m^2 - k_2^2)^{-1} \rightarrow \theta(k_{10})\delta(k_1^2 - m^2)\theta(k_{20})\delta(k_2^2 - m^2), \\ (m^2 - k_1'^2)^{-1} \rightarrow \theta(k_{10}')\delta(k_1'^2 - m^2), \quad (24)$$

as well as integration over three-particle phase space in both channels at fixed  $\tilde{s}$  and  $\tilde{s}'$ :

$$\frac{d^4 k_1}{(2\pi)^4} \delta(m^2 - k_1^2) \delta(m^2 - k_1'^2) \delta(m^2 - k_2^2) \quad (25)$$

$$\rightarrow d\Phi_{\text{tr}}(\tilde{P}, \tilde{P}'; k_1, k'_1, k_2),$$

$$d\Phi_{\text{tr}}(\tilde{P}, \tilde{P}'; k_1, k'_1, k_2) = d\Phi_2(\tilde{P}; k_1, k_2) \\ \times d\Phi_2(\tilde{P}'; k'_1, k'_2) 2k_{20} (2\pi)^3 \delta^3(\mathbf{k}_2 - \mathbf{k}'_2).$$

The constituents in the intermediate state are mass-on-shell. The double discontinuity is calculated at  $\tilde{q} = \tilde{P} - \tilde{P}' \neq q$  but  $\tilde{q}^2 = q^2$ .

(ii) The vertex functions are to be replaced as

$$g_0(\tilde{P}^2; k_1^2, k_2^2) g_0(\tilde{P}'^2; k_1'^2, k_2'^2) \rightarrow g_0(\tilde{s}) g_0(\tilde{s}'), \quad (26)$$

which actualizes the treatment of the composite system as a true two-particle state.

(iii) The invariant part of the triangle diagram should be singled out by expanding the spin factor  $(k_1 + k'_1)_\alpha$  in the vectors  $(\tilde{P} + \tilde{P}')_\perp$  and  $\tilde{q} = \tilde{P} - \tilde{P}'$ :

$$(k_1 + k'_1)_\alpha = \alpha(\tilde{s}, \tilde{s}', q^2) \quad (27) \\ \times \left( \tilde{P}_\alpha + \tilde{P}'_\alpha - \frac{\tilde{s} - \tilde{s}'}{q^2} \tilde{q}_\alpha \right) + \beta(\tilde{s}, \tilde{s}', q^2) \tilde{q}_\alpha.$$

The coefficients  $\alpha(\tilde{s}, \tilde{s}', q^2)$  and  $\beta(\tilde{s}, \tilde{s}', q^2)$  are given below, in Eq. (30). As a result, we have the following expressions for double discontinuities (double spectral densities) for the triangle diagram:

$$\text{disc}_{\tilde{s}} \text{disc}_{\tilde{s}'} F_T^{(0 \rightarrow 0)}(\tilde{s}, \tilde{s}', q^2) = \alpha(\tilde{s}, \tilde{s}', q^2) g_0(\tilde{s}) \quad (28) \\ \times g_0(\tilde{s}') d\Phi_{\text{tr}}(\tilde{P}, \tilde{P}'; k_1, k_2, k'_1),$$

$$\text{disc}_{\tilde{s}} \text{disc}_{\tilde{s}'} F_L^{(0 \rightarrow 0)}(\tilde{s}, \tilde{s}', q^2) = \beta(\tilde{s}, \tilde{s}', q^2) g_0(\tilde{s}) \\ \times g_0(\tilde{s}') d\Phi_{\text{tr}}(\tilde{P}, \tilde{P}'; k_1, k_2, k'_1).$$

The form factor  $F_i^{(0 \rightarrow 0)}(s, s', q^2)$  is determined by its spectral density as follows:

$$F_i^{(0 \rightarrow 0)}(s, s', q^2) = f_i^{(0 \rightarrow 0)}(s, s', q^2) \quad (29) \\ + \int_{4m^2}^{\infty} \frac{d\tilde{s}}{\pi} \frac{d\tilde{s}'}{\pi} \frac{\text{disc}_{\tilde{s}} \text{disc}_{\tilde{s}'} F_i^{(0 \rightarrow 0)}(\tilde{s}, \tilde{s}', q^2)}{(\tilde{s} - s - i0)(\tilde{s}' - s' - i0)},$$

where  $f_i^{(0 \rightarrow 0)}(s, s', q^2)$  are the subtraction terms with zero double spectral density. Within the approach where the partial amplitude is described by a set of dispersion diagrams of Fig. 1a, the subtraction term  $f_i^{(0 \rightarrow 0)}(s, s', q^2)$  is an arbitrary function determined by diagrams where a photon interacts with other particles, not constituents, for example, with mesons which determine the forces between constituents.

The expansion coefficients (27) are calculated under the orthogonality requirements. Indeed, by projecting (27) onto  $(\tilde{P}_\alpha + \tilde{P}'_\alpha - \tilde{q}_\alpha(\tilde{s} - \tilde{s}')/q^2)$  and

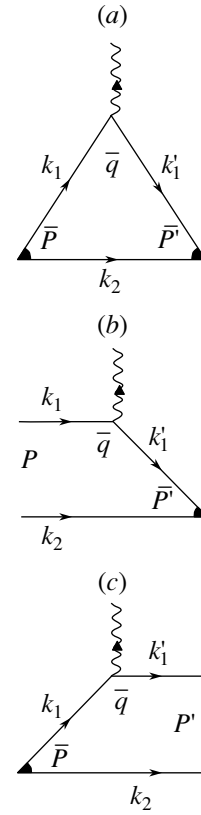


Fig. 4. (a) Three-point form factor amplitude. The blocks for the emission of a photon in the (b) initial and (c) final states.

$\tilde{q}_\alpha$ , we obtain the equations for  $\alpha(\tilde{s}, \tilde{s}', q^2)$  and  $\beta(\tilde{s}, \tilde{s}', q^2)$ :

$$\alpha(\tilde{s}, \tilde{s}', q^2) = -\frac{q^2(\tilde{s} + \tilde{s}' - q^2)}{\lambda(\tilde{s}, \tilde{s}', q^2)}, \quad (30)$$

$$\beta(\tilde{s}, \tilde{s}', q^2) = 0,$$

$$\lambda(\tilde{s}, \tilde{s}', q^2) = -2q^2(\tilde{s} + \tilde{s}') + q^4 + (\tilde{s} - \tilde{s}')^2.$$

Here, we took into account that  $k_i^2 = m^2$  and  $(k_1 - k'_1)^2 = q^2$ . Therefore,  $F_L^{(0 \rightarrow 0)}(s, s', q^2)$  has zero double spectral density, and it is defined by the subtraction term only:

$$F_L^{(0 \rightarrow 0)}(s, s', q^2) = f_L^{(0 \rightarrow 0)}(s, s', q^2). \quad (31)$$

For  $F_T^{(0 \rightarrow 0)}(s, s', q^2)$ , after integrating in (25) over the momenta  $k_1, k'_1$ , and  $k_2$  at fixed  $s$  and  $s'$ , we obtain the following equation:

$$F_T^{(0 \rightarrow 0)}(s, s', q^2) = f_T^{(0 \rightarrow 0)}(s, s', q^2) \quad (32) \\ + \int_{4m^2}^{\infty} \frac{d\tilde{s} d\tilde{s}'}{\pi^2} \frac{g_0(\tilde{s}) g_0(\tilde{s}')}{\tilde{s} - s \tilde{s}' - s'}$$

$$\times \frac{\Theta(-\tilde{s}\tilde{s}'q^2 - m^2\lambda(\tilde{s}, \tilde{s}', q^2))}{16\sqrt{\lambda(\tilde{s}, \tilde{s}', q^2)}}\alpha(\tilde{s}, \tilde{s}', q^2).$$

Here, the  $\Theta$  function is defined as follows:  $\Theta(X) = 1$  at  $X \geq 0$  and  $\Theta(X) = 0$  at  $X < 0$ .

Now, let us come back to the requirements that the amplitude should obey. First, as was said above, it must be an analytic function; that is, kinematical singularities should be absent. Concerning the  $q^2 = 0$  singularity of the considered amplitude, the term in which we are interested is

$$-\frac{s-s'}{q^2}F_T^{(0\rightarrow 0)}(s, s', q^2)q_\alpha. \tag{33}$$

Let us calculate the form factor in the limit  $q^2 \rightarrow 0$ . To this aim, let us introduce new variables in (32),

$$\sigma = \frac{1}{2}(\tilde{s} + \tilde{s}'); \quad \Delta = \tilde{s} - \tilde{s}', \quad Q^2 = -q^2, \tag{34}$$

and then consider the case of interest,  $Q^2 \rightarrow 0$ . The form factor formula reads

$$F_T^{(0\rightarrow 0)}(s, s', q^2) = f_T^{(0\rightarrow 0)}(s, s', q^2) + \int_{4m^2}^{\infty} \frac{d\sigma}{\pi} \frac{g_0^2(\sigma)}{(\sigma-s)(\sigma-s')} \int_{-b}^b d\Delta \frac{\alpha(\sigma, \Delta, Q^2)}{16\pi\sqrt{\Delta^2 + 4\sigma Q^2}}, \tag{35}$$

where

$$b = \frac{Q}{m}\sqrt{\sigma(\sigma - 4m^2)}, \tag{36}$$

$$\alpha(\sigma, \Delta, Q^2) = \frac{2\sigma Q^2}{\Delta^2 + 4\sigma Q^2}.$$

As a result, we have

$$F_T^{(0\rightarrow 0)}(s, s', 0) = f_T^{(0\rightarrow 0)}(s, s', 0) + \frac{B_0(s) - B_0(s')}{s - s'}, \tag{37}$$

where  $B_0(s)$  is the loop diagram:

$$B_0(s) = \int_{4m^2}^{\infty} \frac{d\tilde{s}}{\pi} \frac{g_0^2(\tilde{s})}{\tilde{s} - s} \rho(\tilde{s}), \tag{38}$$

$$\rho(s) = \frac{1}{16\pi} \sqrt{\frac{s - 4m^2}{s}}.$$

In (38), the index  $J$  for the phase volume with  $J = 0$  is omitted.

In the limit  $q^2 \rightarrow 0$ , the amplitude takes the form

$$\Gamma_\alpha^{(0\rightarrow 0)}(P, P'; q^2 \rightarrow 0) = \left( P_\alpha + P'_\alpha - \frac{s-s'}{q^2}q_\alpha \right) \times \left[ f_T^{(0\rightarrow 0)}(s, s', q^2 \rightarrow 0) + \frac{B_0(s) - B_0(s')}{s - s'} \right]$$

$$+ q_\alpha f_L^{(0\rightarrow 0)}(s, s', q^2 \rightarrow 0).$$

The amplitude (39) should not have pole singularity  $1/q^2$ : the presence on the right-hand side of (39) of singular factor  $q_\alpha(s-s')/q^2$  is an artifact of our expansion of the amplitude  $\Gamma_\alpha^{(0\rightarrow 0)}$  in the transverse and longitudinal components. Therefore, the subtraction term in  $f_L^{(0\rightarrow 0)}(s, s', q^2 \rightarrow 0)$  must contain expressions that cancel the singularity  $1/q^2$ . The cancellation of singular terms leads to the requirement

$$f_L^{(0\rightarrow 0)}(s, s', q^2 \rightarrow 0) = \frac{1}{q^2} \left( (s-s')f_T^{(0\rightarrow 0)}(s, s', 0) + B_0(s) - B_0(s') \right). \tag{40}$$

After the fulfillment of (40), we have for  $\Gamma_\alpha^{(0\rightarrow 0)}(s, s'; 0)$

$$\Gamma_\alpha^{(0\rightarrow 0)}(s, s'; 0) = (P_\alpha + P'_\alpha) \times \left( f_T^{(0\rightarrow 0)}(s, s', 0) + \frac{B_0(s) - B_0(s')}{s - s'} \right). \tag{41}$$

This formula has been obtained in [6] for the case of  $f_T^{(0\rightarrow 0)} \equiv 0$ . In this approximation, we come to a well-known Ward identity for the triangle diagram:  $q_\alpha \Gamma_\alpha^{(0\rightarrow 0)}(s, s', 0) = B_0(s) - B_0(s')$ . With a nonzero subtraction term, the Ward identity looks as follows:

$$q_\alpha \Gamma_\alpha^{(0\rightarrow 0)}(s, s'; 0) = (s-s')f_T^{(0\rightarrow 0)}(s, s', 0) + B_0(s) - B_0(s'). \tag{42}$$

### 2.2. Diagrams of Figs. 3b, 3c Type

Consider the amplitude for the diagram of Fig. 3b; it reads as follows:

$$A_\alpha^{(\rightarrow 0)}(P, P'; q) = \Gamma_\alpha^{(\rightarrow 0)}(P, P'; q) \frac{g_0(s')}{1 - B_0(s')}. \tag{43}$$

Here,  $\Gamma_\alpha^{(\rightarrow 0)}$  stands for the vertex representing the emission of a photon by the incoming constituent; it is shown in Fig. 4b.

By singling out the  $S$ -wave state from the initial state of the amplitude of Fig. 4b,  $\Gamma_\alpha^{(\rightarrow 0)} \rightarrow \Gamma_\alpha^{(S\rightarrow 0)}$ , we can represent  $\Gamma_\alpha^{(S\rightarrow 0)}$  as the spectral integral. In this way, the amplitude is written as follows:

$$\Gamma_\alpha^{(S\rightarrow 0)}(P, P'; q) = \left( P_\alpha + P'_\alpha - \frac{s-s'}{q^2}q_\alpha \right) \times F_T^{(S\rightarrow 0)}(s, s', q^2) + q_\alpha F_L^{(S\rightarrow 0)}(s, s', q^2). \tag{44}$$

The spectral integrals for  $F_T^{(S\rightarrow 0)}$  and  $F_L^{(S\rightarrow 0)}$  are obtained in the same way as before. Namely, we project the Feynman diagram of Fig. 4b on the  $S$ -wave state

by averaging over the phase space of initial particles,  $k_1$  and  $k_2$ :

$$\int \frac{d\Phi_2(P; k_1, k_2)}{\rho(s)} (k_1 + k'_1)_\alpha \frac{g_0(\tilde{P}^2; k_1'^2, k_2^2)}{m^2 - k_1'^2}. \quad (45)$$

The discontinuity of the amplitude (44) is calculated for the mass-on-shell constituent

$$(m^2 - k_1'^2)^{-1} \rightarrow \theta(k_{10}') \delta(k_1'^2 - m^2), \quad (46)$$

with the phase-space integration in the channel  $s'$ :

$$(2\pi)^3 \cdot 2k_{20} \delta^{(3)}(\mathbf{k}_2 - \mathbf{k}'_2) d\Phi_2(P'; k'_1, k'_2). \quad (47)$$

In addition, it is necessary to expand the spin factor  $(k_1 + k'_1)_\alpha$  in the vectors  $P_\alpha$ ,  $\tilde{P}'_\alpha$ , and  $\tilde{q}$  with the constraint  $\tilde{q}^2 = q^2$ . Invariant expansion coefficients,  $\alpha(s, \tilde{s}', q^2)$  and  $\beta(s, \tilde{s}', q^2)$ , are given by Eqs. (27) and (30).

After the substitution  $g_0(\tilde{P}^2; k_1'^2, k_2^2) \rightarrow g_0(\tilde{s}')$  and spectral integration, we have the following representation for  $F_i^{(S \rightarrow 0)}(s, s', q^2)$ :

$$F_T^{(S \rightarrow 0)}(s, s', q^2) = f_T^{(S \rightarrow 0)}(s, s', q^2) + \int_{4m^2}^{\infty} \frac{d\tilde{s}'}{\pi} \alpha(s, \tilde{s}', q^2) \frac{g_0(\tilde{s}')}{\tilde{s}' - s'} d\Phi_{\text{tr}}(P, \tilde{P}'; k_1, k'_1, k_2),$$

$$F_L^{(S \rightarrow 0)}(s, s', q^2) = f_L^{(S \rightarrow 0)}(s, s', q^2). \quad (48)$$

Here, we took into account that  $\beta(s, \tilde{s}', q^2) = 0$  [see (30)]; the equation for  $F_L^{(S \rightarrow 0)}(s, s', q^2)$  has zero double spectral density, and it is completely determined by its subtraction term.

For  $F_T^{(S \rightarrow 0)}(s, s', q^2)$ , after integrating over  $k_1$ ,  $k'_1$ , and  $k_2$  at fixed  $s'$ , we have the following expression:

$$F_T^{(S \rightarrow 0)}(s, s', q^2) = f_T^{(S \rightarrow 0)}(s, s', q^2) + \int_{4m^2}^{\infty} \frac{d\tilde{s}'}{\pi} \frac{g_0(\tilde{s}')}{\tilde{s}' - s' - i0} \times \frac{\Theta(-s\tilde{s}'q^2 - m^2\lambda(s, \tilde{s}', q^2))}{16\sqrt{\lambda(s, \tilde{s}', q^2)}} \alpha(s, \tilde{s}', q^2). \quad (49)$$

For the factor  $F_T^{(S \rightarrow 0)}(s, s', q^2)$  in the limit  $q^2 \rightarrow 0$ , after the same calculations as for previous diagrams, we obtain

$$F_T^{(S \rightarrow 0)}(s, s', 0) = f_T^{(S \rightarrow 0)}(s, s', 0) + \frac{g_0(s)}{s - s'}. \quad (50)$$

The amplitude (44) in the limit  $q^2 \rightarrow 0$  has the form

$$\Gamma_\alpha^{(S \rightarrow 0)}(P, P'; q^2 \rightarrow 0) = \left( P_\alpha + P'_\alpha - \frac{s - s'}{q^2} q_\alpha \right) \quad (51)$$

$$\times \left[ f_T^{(S \rightarrow 0)}(s, s', q^2 \rightarrow 0) + \frac{g_0(s)}{s - s'} \right] + q_\alpha f_L^{(S \rightarrow 0)}(s, s', q^2 \rightarrow 0),$$

and the requirement of absence of singularity  $1/q^2$  in the amplitude  $\Gamma_\alpha^{(S \rightarrow 0)}(P, P'; q^2 \rightarrow 0)$  leads to the formula

$$f_L^{(S \rightarrow 0)}(s, s', q^2 \rightarrow 0) = \frac{1}{q^2} \left( (s - s') f_T^{(S \rightarrow 0)}(s, s', 0) + g_0(s) \right). \quad (52)$$

Taking this condition into account for the vertex  $\Gamma_\alpha^{(S \rightarrow 0)}(P, P'; 0)$ , one obtains

$$\Gamma_\alpha^{(S \rightarrow 0)}(P, P'; 0) = (P_\alpha + P'_\alpha) \left( f_T^{(S \rightarrow 0)}(s, s', 0) + \frac{g_0(s)}{s - s'} \right). \quad (53)$$

The amplitude for diagrams of Fig. 3c type is treated similarly. After the  $S$  wave is extracted for outgoing constituents, we have

$$A_\alpha^{(0 \rightarrow S)}(P, P'; q) = \frac{g_0(s)}{1 - B_0(s)} \Gamma_\alpha^{(0 \rightarrow S)}(P, P'; q), \quad (54)$$

where

$$\Gamma_\alpha^{(0 \rightarrow S)}(P, P'; q) = \left( P_\alpha + P'_\alpha - \frac{s - s'}{q^2} q_\alpha \right) \times F_T^{(0 \rightarrow S)}(s, s', q^2) + q_\alpha F_L^{(0 \rightarrow S)}(s, s', q^2), \quad (55)$$

and

$$F_L^{(0 \rightarrow S)}(s, s', q^2) = f_L^{(0 \rightarrow S)}(s, s', q^2), \quad (56)$$

$$F_T^{(0 \rightarrow S)}(s, s', q^2) = f_T^{(0 \rightarrow S)}(s, s', q^2) + \int_{4m^2}^{\infty} \frac{d\tilde{s}}{\pi} \frac{g_0(\tilde{s})}{\tilde{s} - s} \times \frac{\Theta(-\tilde{s}s'q^2 - m^2\lambda(\tilde{s}, s', q^2))}{16\sqrt{\lambda(\tilde{s}, s', q^2)}} \alpha(\tilde{s}, s', q^2).$$

In the limit  $q^2 \rightarrow 0$ , the amplitude takes the form

$$\Gamma_\alpha^{(0 \rightarrow S)}(P, P'; q^2 \rightarrow 0) = \left( P_\alpha + P'_\alpha - \frac{s - s'}{q^2} q_\alpha \right) \times \left[ f_T^{(0 \rightarrow S)}(s, s', q^2 \rightarrow 0) - \frac{g_0(s')}{s - s'} \right] + q_\alpha f_L^{(0 \rightarrow S)}(s, s', q^2 \rightarrow 0), \quad (57)$$

and the requirement of cancellation of the singularity  $1/q^2$  produces the following formula:

$$f_L^{(0 \rightarrow S)}(s, s', q^2 \rightarrow 0) \quad (58)$$

$$= \frac{1}{q^2} \left( (s - s') f_T^{(0 \rightarrow S)}(s, s', 0) - g_0(s') \right).$$

This results in

$$\Gamma_\alpha^{(0 \rightarrow S)}(P, P'; 0) = (P_\alpha + P'_\alpha) \quad (59)$$

$$\times \left( f_T^{(0 \rightarrow S)}(s, s', 0) - \frac{g_0(s')}{s - s'} \right).$$

### 2.3. Connected Diagrams in the Limit $q^2 \rightarrow 0$

First, consider the case when there are no subtraction terms in the transverse form factor,  $f_T^{(S \rightarrow 0)}(s, s', 0) = f_T^{(0 \rightarrow S)}(s, s', 0) = 0$ : such a variant has been considered in [6]. It is easy to see that the sum of all connected diagrams of Figs. 3a, 3b, and 3c is equal to zero in this limit. Indeed, according to (41), (53), and (59), it is equal to

$$(P_\alpha + P'_\alpha) \left[ \frac{g_0(s)}{s - s'} \frac{g_0(s')}{1 - B_0(s')} \right. \quad (60)$$

$$+ \frac{g_0(s)}{1 - B_0(s)} \frac{B_0(s) - B_0(s')}{s - s'} \frac{g_0(s')}{1 - B_0(s')} - \left. \frac{g_0(s)}{1 - B_0(s)} \frac{g_0(s')}{s - s'} \right] = 0.$$

Generally, when subtraction terms differ from zero, the amplitude  $A_\alpha^{(\text{connected})}(P, P', q^2)$  should also go to zero at  $q^2 \rightarrow 0$ :

$$A_\alpha^{(\text{connected})}(P, P', q^2 \rightarrow 0) \quad (61)$$

$$= A_\alpha^{(S \rightarrow 0)}(P, P', q^2 \rightarrow 0)$$

$$+ A_\alpha^{(0 \rightarrow 0)}(P, P', q^2 \rightarrow 0)$$

$$+ A_\alpha^{(0 \rightarrow S)}(P, P', q^2 \rightarrow 0) = 0;$$

this is equivalent to the requirement [see formulas (41), (53), (59)]

$$f_T^{(0 \rightarrow 0)}(s, s', 0) = \frac{B_0(s) - 1}{g_0(s)} f_T^{(S \rightarrow 0)}(s, s', 0) \quad (62)$$

$$+ f_T^{(0 \rightarrow S)}(s, s', 0) \frac{B_0(s') - 1}{g_0(s')}.$$

Let us direct our attention to the following. The existence of a bound state requires  $B_0(M^2) = 1$ ; therefore, we have on the basis of (62)

$$f_T^{(0 \rightarrow 0)}(M^2, M^2, 0) = 0. \quad (63)$$

This means that the charge form factor of the composite system  $F(q^2) = F_T^{(0 \rightarrow 0)}(M^2, M^2, q^2)$  is determined at  $q^2 = 0$  by the triangle graph only, without subtraction terms. Such a property is not surprising: relying on  $B_0(M^2) = 1$ , we actually assumed that the

composite system is a true two-particle one, and the condition for the charge form factor of the composite system,

$$F(0) = 1, \quad (64)$$

is the normalization condition for the wave function of this system.

Accounting for (63), one can impose the more general constraint

$$f_T^{(0 \rightarrow 0)}(M^2, M^2, q^2) = 0, \quad (65)$$

which is equivalent to the suggestion that charge form factor of the composite system is defined by a double spectral integral only. Within this approximation, the form factor of a deuteron as a two-nucleon system was calculated in [6], as well as the form factor of the pion treated as a  $q\bar{q}$  system [8].

### 3. TRANSITION $V \rightarrow \gamma S$

Consider now the transition of a vector state to a scalar one,  $V \rightarrow \gamma S$ : this is the transition of the  $P$ -wave two-constituent state to the  $S$ -wave one. Such a reaction, as in the previous case, is represented by a set of diagrams shown in Figs. 3a, 3b, and 3c. The vertex function for  $V \rightarrow \gamma S$ ,  $\Gamma_{\mu\alpha}^{(1 \rightarrow 0)}$ , depends on the two spin indices:  $\mu$  stands for the vector state of constituents and  $\alpha$ , as before, is related to the photon.

In the diagrams shown in Figs. 4a, 4b, and 4c, the following factor carries spin indices:

$$(k_1 - k_2)_\mu (k_1 + k'_1)_\alpha, \quad (66)$$

where  $(k_1 - k_2)_\mu$  provides the  $P$  wave of the initial state and  $(k_1 + k'_1)_\alpha$  determines the gauge-invariant vertex *photon-constituent*. Let us expand the factor  $(k_1 - k_2)_\mu (k_1 + k'_1)_\alpha$  in the spin operators. As was said in the Introduction, there exists some freedom in the choice of expansion operators. To reveal the consequences of this freedom for spectral amplitudes, consider in parallel two sets of operators. In the first case, the operators are as follows:

$$\text{Expansion I: } g_{\mu\alpha}^{\perp\perp}, \quad L_{\mu\alpha}; \quad (67)$$

and in the second one:

$$\text{Expansion II: } \tilde{g}_{\mu\alpha}^{\perp\perp} = g_{\mu\alpha} - \frac{q_\mu P_\alpha}{(Pq)} \quad (68)$$

$$= g_{\mu\alpha}^{\perp\perp} - 4L_{\mu\alpha}, \quad L_{\mu\alpha}.$$

Recall that the operators  $g_{\mu\alpha}^{\perp\perp}$  and  $L_{\mu\alpha}$  were introduced in (12) and (13).

The convolutions of operators  $g_{\mu\alpha}^{\perp\perp}$ ,  $\tilde{g}_{\mu\alpha}^{\perp\perp}$ , and  $L_{\mu\alpha}$  are equal to

$$g_{\mu\alpha}^{\perp\perp} g_{\mu\alpha}^{\perp\perp} = 2, \quad L_{\mu\alpha} L_{\mu\alpha} = \frac{q^2 P^2}{16(Pq)^2}, \quad (69)$$

$$L_{\mu\alpha}g_{\mu\alpha}^{\perp\perp} = 0, \quad \tilde{g}_{\mu\alpha}^{\perp\perp}\tilde{g}_{\mu\alpha}^{\perp\perp} = 2 + \frac{q^2P^2}{(Pq)^2},$$

$$L_{\mu\alpha}\tilde{g}_{\mu\alpha}^{\perp\perp} = \frac{q^2P^2}{4(Pq)^2}.$$

We see that the operators from the second set are not orthogonal to one another, but the orthogonality is restored at  $q^2 \rightarrow 0$ . At  $q^2 = 0$ , one has

$$g_{\mu\alpha}^{\perp\perp}(0)g_{\mu\alpha}^{\perp\perp}(0) = 2, \quad L_{\mu\alpha}(0)L_{\mu\alpha}(0) = 0, \quad (70)$$

$$L_{\mu\alpha}(0)g_{\mu\alpha}^{\perp\perp}(0) = 0, \quad \tilde{g}_{\mu\alpha}^{\perp\perp}(0)\tilde{g}_{\mu\alpha}^{\perp\perp}(0) = 2,$$

$$L_{\mu\alpha}(0)\tilde{g}_{\mu\alpha}^{\perp\perp}(0) = 0,$$

which means the equivalence of both sets of operators.

In terms of the considered operators, the spin factor,

$$S_{\mu\alpha} = (k_1 - k_2)_\mu (k_1 + k'_1)_\alpha, \quad (71)$$

is represented as

$$\text{Expansion I: } S_{\mu\alpha} = \xi_T(s, s', q^2)g_{\mu\alpha}^{\perp\perp} + \xi_L(s, s', q^2)L_{\mu\alpha}, \quad (72)$$

$$\xi_T(s, s', q^2) = 2 \left( m^2 + \frac{ss'q^2}{\lambda(s, s', q^2)} \right),$$

$$\xi_L(s, s', q^2) = \frac{2(s + s' - q^2)(s - s' - q^2)(s - s' + q^2)}{\lambda(s, s', q^2)};$$

$$\text{Expansion II: } S_{\mu\alpha} = \tilde{\xi}_T(s, s', q^2)\tilde{g}_{\mu\alpha}^{\perp\perp} + \tilde{\xi}_L(s, s', q^2)L_{\mu\alpha}, \quad (73)$$

$$\tilde{\xi}_T(s, s', q^2) = 2 \left( m^2 + \frac{ss'q^2}{\lambda(s, s', q^2)} \right),$$

---


$$\tilde{\xi}_L(s, s', q^2) = 2 \left( 4m^2 + \frac{4ss'q^2 + (s + s' - q^2)(s - s' - q^2)(s - s' + q^2)}{\lambda(s, s', q^2)} \right),$$


---

with function  $\lambda(s, s', q^2)$  given in (30) (the calculation of coefficients is carried out in Appendix A). As one can see,

$$\xi_T(s, s', q^2) = \tilde{\xi}_T(s, s', q^2), \quad (74)$$

and this is important for the discussion.

### 3.1. The Amplitude of Fig. 3a

The whole amplitude is a sum of amplitudes of three types represented by Figs. 3a, 3b, and 3c. Let us start with the diagram of Fig. 3a, which contains a double pole term. The corresponding amplitude is written as follows:

$$A_\alpha^{(1 \rightarrow 0)}(s, s', q^2) = (p_1 - p_2)_\mu \frac{g_1(s)}{1 - B_1(s)} \times \Gamma_{\mu\alpha}^{(1 \rightarrow 0)}(P, P'; q) \frac{g_0(s')}{1 - B_0(s')}. \quad (75)$$

The functions  $g_1(s)$  and  $g_0(s')$  are vertices of vector and scalar states;  $\Gamma_{\mu\alpha}$  is the three-point amplitude of Fig. 4a, for which the expressions for different choices of operators read

$$\text{Expansion I: } \Gamma_{\mu\alpha}^{(1 \rightarrow 0)}(P, P'; q) = g_{\mu\alpha}^{\perp\perp} F_T^{(1 \rightarrow 0)}(s, s', q^2) + L_{\mu\alpha} F_L^{(1 \rightarrow 0)}(s, s', q^2);$$

$$\text{Expansion II: } \Gamma_{\mu\alpha}^{(1 \rightarrow 0)}(P, P'; q) = \tilde{g}_{\mu\alpha}^{\perp\perp} \tilde{F}_T^{(1 \rightarrow 0)}(s, s', q^2) + L_{\mu\alpha} \tilde{F}_L^{(1 \rightarrow 0)}(s, s', q^2).$$

Here,  $F_T^{(1 \rightarrow 0)}$ ,  $F_L^{(1 \rightarrow 0)}$  and  $\tilde{F}_T^{(1 \rightarrow 0)}$ ,  $\tilde{F}_L^{(1 \rightarrow 0)}$  are the form factors, for which the dispersion relations can be written similarly to what was described in the previous section.

The form factor  $F_i^{(1 \rightarrow 0)}(s, s', q^2)$  in Expansion I reads

$$F_i^{(1 \rightarrow 0)}(s, s', q^2) = f_i^{(1 \rightarrow 0)}(s, s', q^2) + \int_{4m^2}^{\infty} \frac{d\tilde{s} d\tilde{s}'}{\pi \pi} \frac{\text{disc}_{\tilde{s}} \text{disc}_{\tilde{s}'} F_i^{(1 \rightarrow 0)}(\tilde{s}, \tilde{s}', q^2)}{(\tilde{s} - s - i0)(\tilde{s}' - s' - i0)}, \quad i = T, L. \quad (77)$$

Here,  $f_i^{(1 \rightarrow 0)}(s, s', q^2)$  is the subtraction term, and the double spectral density is

$$\text{disc}_{\tilde{s}} \text{disc}_{\tilde{s}'} F_i^{(1 \rightarrow 0)}(\tilde{s}, \tilde{s}', q^2) = \xi_i(\tilde{s}, \tilde{s}', q^2) g_1(\tilde{s}) g_0(\tilde{s}') d\Phi_{\text{tr}}(\tilde{P}, \tilde{P}'; k_1, k'_1, k_2). \quad (78)$$

The form factor  $\tilde{F}_i^{(1 \rightarrow 0)}(s, s', q^2)$  in Expansion II is written similarly to (77) but with differently defined double spectral density given by (78): one should substitute  $\xi_i(\tilde{s}, \tilde{s}', q^2) \rightarrow \tilde{\xi}_i(\tilde{s}, \tilde{s}', q^2)$ .

Using dispersion relations for the form factors, one can investigate these two variants for any  $q^2$ . But the subject of our interest is the case of  $q^2 \rightarrow 0$ , so we just concentrate our attention here. At  $q^2 \rightarrow 0$ , the amplitude in Expansion I takes the form

$$\Gamma_{\mu\alpha}^{(1 \rightarrow 0)}(s, s'; q^2 \rightarrow 0) \quad (79)$$

$$\begin{aligned}
 &= \left[ g_{\mu\alpha} + \frac{4s}{(s-s')^2} q_\mu q_\alpha - \frac{2}{s-s'} (P_\mu q_\alpha + q_\mu P_\alpha) \right] \\
 &\quad \times F_T^{(1\rightarrow 0)}(s, s', 0) \\
 &+ \left[ \frac{s}{(s-s')^2} q_\mu q_\alpha - \frac{1}{2(s-s')} P_\mu q_\alpha \right] \\
 &\quad \times F_L^{(1\rightarrow 0)}(s, s', 0) \\
 &= \left[ g_{\mu\alpha} - \frac{2}{s-s'} q_\mu P_\alpha \right] F_T^{(1\rightarrow 0)}(s, s', 0) \\
 &+ \left[ \frac{s}{(s-s')^2} q_\mu q_\alpha - \frac{1}{2(s-s')} P_\mu q_\alpha \right] \\
 &\quad \times \left( F_L^{(1\rightarrow 0)}(s, s', 0) + 4F_T^{(1\rightarrow 0)}(s, s', 0) \right).
 \end{aligned}$$

Hence, one has

$$\begin{aligned}
 \tilde{F}_T^{(1\rightarrow 0)}(s, s', 0) &= F_T^{(1\rightarrow 0)}(s, s', 0), \\
 \tilde{F}_L^{(1\rightarrow 0)}(s, s', 0) &= F_L^{(1\rightarrow 0)}(s, s', 0) + 4F_T^{(1\rightarrow 0)}(s, s', 0).
 \end{aligned} \tag{80}$$

The calculation of three-point form factors in the limit  $q^2 \rightarrow 0$  is given in Appendix B for both expansion types; it is similar to the calculation of the three-point amplitude performed in the previous section for the transition  $S \rightarrow \gamma S$ . Here, we present the case of Expansion I only, since the amplitudes of Expansion II are defined by (80). One gets in Expansion I

$$\begin{aligned}
 F_i^{(1\rightarrow 0)}(s, s', 0) &= f_i^{(1\rightarrow 0)}(s, s', 0) \tag{81} \\
 &+ \frac{B_i^{(1\rightarrow 0)}(s) - B_i^{(1\rightarrow 0)}(s')}{s - s'}, \quad i = T, L,
 \end{aligned}$$

where the loop diagram  $B_i^{(1\rightarrow 0)}(s)$  is equal to

$$B_i^{(1\rightarrow 0)}(s) = \int_{4m^2}^{\infty} \frac{d\tilde{s}}{\pi} \frac{g_1(\tilde{s})g_0(\tilde{s})}{\tilde{s} - s} \rho(\tilde{s})\zeta_i(\tilde{s}), \tag{82}$$

$$\zeta_T(s) = 2m^2 \sqrt{\frac{s}{s-4m^2}} \ln \frac{1 + \sqrt{(s-4m^2)/s}}{1 - \sqrt{(s-4m^2)/s}} - s,$$

$$\zeta_L(s) = 4s \left[ \sqrt{\frac{s}{s-4m^2}} \ln \frac{1 + \sqrt{(s-4m^2)/s}}{1 - \sqrt{(s-4m^2)/s}} - 2 \right].$$

Here, we come to a key result of our study: the form factor related to the transverse component (80) does not depend on the choice of expansion operators. The choice of the expansion results in the definition of  $F_L^{(1\rightarrow 0)}(s, s', 0)$ , but the amplitude  $A_{L\mu\alpha}^{(1\rightarrow 0)}$ , in turn, does not contribute to cross sections of physical processes with real photons, because  $A_{L\mu\alpha}^{(1\rightarrow 0)}\epsilon_\alpha^{(\gamma)} = 0$ .

Summing up, we conclude that, in the limit  $q^2 \rightarrow 0$ , the amplitude of Fig. 3a-type diagrams is determined unambiguously:

$$\begin{aligned}
 A_\alpha^{(1\rightarrow 0)}(s, s'; 0) &= (p_1 - p_2)_\mu \frac{g_1(s)}{1 - B_1(s)} \tag{83} \\
 &\quad \times \Gamma_{\mu\alpha}^{(1\rightarrow 0)}(s, s'; 0) \frac{g_0(s')}{1 - B_0(s')},
 \end{aligned}$$

where  $\Gamma_{\mu\alpha}^{(1\rightarrow 0)}(s, s'; 0)$  is given by (79).

### 3.2. The Amplitudes for the Processes of Figs. 3b, 3c

Furthermore, consider the diagram of Fig. 3b, when the photon interacts with constituents in the initial state. The corresponding amplitude for diagrams of such type is given by (43); recall that  $\Gamma_\alpha^{(-0)}(P, P'; q)$  is a function represented diagrammatically by Fig. 4b. By studying the transitions  $V \rightarrow \gamma S$ , one needs to single out the  $P$ -wave component in the initial state of the pole amplitude of Fig. 4b. In Appendix C, the expansion of the pole diagram in partial waves is presented in more detail. After singling out the  $P$  wave, the amplitude  $\Gamma_\alpha^{(-0)}(P, P'; q)$  turns into  $\Gamma_{\mu\alpha}^{(P\rightarrow 0)}(P, P'; q)$ :

$$\begin{aligned}
 \Gamma_{\mu\alpha}^{(P\rightarrow 0)}(P, P'; q) &= \frac{3}{p^2} \int \frac{d\Phi_2(P; p_1, p_2)}{\rho(s)} \tag{84} \\
 &\quad \times (p_1 - p_2)_\mu \Gamma_\alpha^{(-0)}(P, P'; q),
 \end{aligned}$$

where  $p^2 = (p_1 - p_2)^2 = 4m^2 - s$ .

Therefore, the amplitude for diagrams with the  $P$ -wave initial state takes the form

$$\begin{aligned}
 A_\alpha^{(P\rightarrow 0)}(P, P'; q) &= (p_1 - p_2)_\mu \Gamma_{\mu\alpha}^{(P\rightarrow 0)}(P, P'; q) \frac{g_0(s')}{1 - B_0(s')}. \tag{85}
 \end{aligned}$$

Now we can perform an expansion similar to what has been done in Section 3.1, namely,

$$\begin{aligned}
 \text{Expansion I: } \Gamma_{\mu\alpha}^{(P\rightarrow 0)}(P, P'; q) &= g_{\mu\alpha}^{\perp\perp} F_T^{(P\rightarrow 0)}(s, s', q^2) + L_{\mu\alpha} F_L^{(P\rightarrow 0)}(s, s', q^2); \tag{86}
 \end{aligned}$$

$$\begin{aligned}
 \text{Expansion II: } \Gamma_{\mu\alpha}^{(P\rightarrow 0)}(P, P'; q) &= \tilde{g}_{\mu\alpha}^{\perp\perp} \tilde{F}_T^{(P\rightarrow 0)}(s, s', q^2) + L_{\mu\alpha} \tilde{F}_L^{(P\rightarrow 0)}(s, s', q^2).
 \end{aligned}$$

The form factors  $F_T^{(P\rightarrow 0)}$ ,  $F_L^{(P\rightarrow 0)}$  and  $\tilde{F}_T^{(P\rightarrow 0)}$ ,  $\tilde{F}_L^{(P\rightarrow 0)}$  entering this expression may be found in the same way as for  $S \rightarrow \gamma S$  (see also Appendix C). For Expansion I, we have

$$F_i^{(P\rightarrow 0)}(s, s', q^2) = f_i^{(P\rightarrow 0)}(s, s', q^2) \tag{87}$$

$$\begin{aligned}
 & + \frac{3}{p^2} \int_{4m^2}^{\infty} \frac{d\tilde{s}'}{\pi} \frac{g_0(\tilde{s}')}{\tilde{s}' - s'} \xi_i(s, \tilde{s}', q^2) \\
 & \times d\Phi_{\text{tr}}(P, \tilde{P}'; k_1, k'_1, k_2), \quad i = T, L,
 \end{aligned}$$

with factors  $\xi_i(s, \tilde{s}', q^2)$  determined by formula (72). The formulas for  $\tilde{F}_i^{(P \rightarrow 0)}(s, s', q^2)$  are given by an equation similar to (87), with the substitution  $\xi_i(s, \tilde{s}', q^2) \rightarrow \tilde{\xi}_i(s, \tilde{s}', q^2)$ .

In the limit  $q^2 \rightarrow 0$ , the amplitude (86) reads

$$\begin{aligned}
 & \Gamma_{\mu\alpha}^{(P \rightarrow 0)}(s, s', q^2 \rightarrow 0) \quad (88) \\
 & = \left[ g_{\mu\alpha} + \frac{4s}{(s - s')^2} q_{\mu} q_{\alpha} - \frac{2}{s - s'} (P_{\mu} q_{\alpha} + q_{\mu} P_{\alpha}) \right] \\
 & \quad \times F_T^{(P \rightarrow 0)}(s, s', 0) \\
 & \quad + \left[ \frac{s}{(s - s')^2} q_{\mu} q_{\alpha} - \frac{1}{2(s - s')} P_{\mu} q_{\alpha} \right] \\
 & \quad \times F_L^{(P \rightarrow 0)}(s, s', 0) \\
 & = \left[ g_{\mu\alpha} - \frac{2}{s - s'} q_{\mu} P_{\alpha} \right] F_T^{(P \rightarrow 0)}(s, s', 0) \\
 & \quad + \left[ \frac{s}{(s - s')^2} q_{\mu} q_{\alpha} - \frac{1}{2(s - s')} P_{\mu} q_{\alpha} \right] \\
 & \quad \times \left( F_L^{(P \rightarrow 0)}(s, s', 0) + 4F_T^{(P \rightarrow 0)}(s, s', 0) \right).
 \end{aligned}$$

Hence, the form factors in Expansions I and II are related to each other as

$$\begin{aligned}
 & \tilde{F}_T^{(P \rightarrow 0)}(s, s', 0) = F_T^{(P \rightarrow 0)}(s, s', 0), \quad (89) \\
 & \tilde{F}_L^{(P \rightarrow 0)}(s, s', 0) = F_L^{(P \rightarrow 0)}(s, s', 0) \\
 & \quad + 4F_T^{(P \rightarrow 0)}(s, s', 0),
 \end{aligned}$$

which is similar to (80). The calculation of form factors in the limit  $q^2 \rightarrow 0$  is performed in Appendix B for Expansion I. We have

$$\begin{aligned}
 & \text{Expansion I: } F_i^{(P \rightarrow 0)}(s, s', 0) \quad (90) \\
 & = f_i^{(P \rightarrow 0)}(s, s', 0) + \frac{g_0(s)}{s - s'} \frac{3\zeta_i(s)}{4m^2 - s}, \quad i = T, L,
 \end{aligned}$$

where  $\zeta_T(s)$  and  $\zeta_L(s)$  are given in (82). Let us emphasize that the factor  $\xi_i(s)/(4m^2 - s)$  in (90) is analytic at  $s = 4m^2$ , since  $\xi_i(4m^2) = 0$ .

The amplitude for diagrams of Fig. 3c type, with a separated  $S$  wave in the final state, reads as follows:

$$\begin{aligned}
 & A_{\alpha}^{(1 \rightarrow S)}(P, P'; q) \quad (91) \\
 & = (p_1 - p_2)_{\mu} \frac{g_1(s)}{1 - B_1(s)} \Gamma_{\mu\alpha}^{(1 \rightarrow S)}(s, s'; q^2).
 \end{aligned}$$

Here,  $\Gamma_{\mu\alpha}^{(1 \rightarrow S)}$  is the function represented by Fig. 4c, where the separation of the  $S$  wave has been carried out. For Expansion I, this function is written as follows:

$$\begin{aligned}
 & \Gamma_{\mu\alpha}^{(1 \rightarrow S)}(P, P'; q) \quad (92) \\
 & = g_{\mu\alpha}^{\perp\perp} F_T^{(1 \rightarrow S)}(s, s', q^2) + L_{\mu\alpha} F_L^{(1 \rightarrow S)}(s, s', q^2).
 \end{aligned}$$

The calculation of  $F_i^{(1 \rightarrow S)}$  and  $\tilde{F}_i^{(1 \rightarrow S)}$  can be done quite similarly to a former case. As a result, we have the following expressions for the form factors:

$$\begin{aligned}
 & \text{Expansion I: } F_{T,L}^{(1 \rightarrow S)}(s, s', q^2) \quad (93) \\
 & = f_{T,L}^{(1 \rightarrow S)}(s, s', q^2) + \int_{4m^2}^{\infty} \frac{d\tilde{s}}{\pi} \frac{g_1(\tilde{s})}{\tilde{s} - s} \\
 & \quad \times \xi_{T,L}(\tilde{s}, s', q^2) d\Phi_2(\tilde{P}; k_1, k_2).
 \end{aligned}$$

In the limit  $q^2 \rightarrow 0$ , which is just one subject of our investigation, we have

$$\begin{aligned}
 & \text{Expansion I: } F_{T,L}^{(1 \rightarrow S)}(s, s', 0) \quad (94) \\
 & = f_{T,L}^{(1 \rightarrow S)}(s, s', 0) + \frac{g_1(s')}{s' - s} \zeta_i(s').
 \end{aligned}$$

For Expansion I, the final amplitude at  $q^2 \rightarrow 0$  reads

$$\begin{aligned}
 & A_{\alpha}^{(1 \rightarrow S)}(s, s'; 0) = (p_1 - p_2)_{\mu} \quad (95) \\
 & \quad \times \frac{g_1(s)}{1 - B_1(s)} \left[ \left( g_{\mu\alpha} + \frac{4s}{(s - s')^2} q_{\mu} q_{\alpha} \right. \right. \\
 & \quad \left. \left. - \frac{2}{s - s'} (P_{\mu} q_{\alpha} + q_{\mu} P_{\alpha}) \right) \right. \\
 & \quad \times \left( f_T^{(1 \rightarrow S)}(s, s', 0) + \frac{g_1(s')}{s' - s} \zeta_T(s') \right) \\
 & \quad + \left( \frac{s}{(s - s')^2} q_{\mu} q_{\alpha} - \frac{1}{2(s - s')} P_{\mu} q_{\alpha} \right) \\
 & \quad \times \left. \left( f_L^{(1 \rightarrow S)}(s, s', 0) + \frac{g_1(s')}{s' - s} \zeta_L(s') \right) \right].
 \end{aligned}$$

It can be easily rewritten in the form of Expansion II:

$$\begin{aligned}
 & A_{\alpha}^{(1 \rightarrow S)}(s, s'; 0) = (p_1 - p_2)_{\mu} \frac{g_1(s)}{1 - B_1(s)} \quad (96) \\
 & \quad \times \left[ \left( g_{\mu\alpha} - \frac{2}{s - s'} q_{\mu} P_{\alpha} \right) \right. \\
 & \quad \times \left( f_T^{(1 \rightarrow S)}(s, s', 0) + \frac{g_1(s')}{s' - s} \zeta_T(s') \right) \\
 & \quad + \left( \frac{s}{(s - s')^2} q_{\mu} q_{\alpha} - \frac{1}{2(s - s')} P_{\mu} q_{\alpha} \right) \\
 & \quad \times \left. \left( f_L^{(1 \rightarrow S)}(s, s', 0) + 4f_T^{(1 \rightarrow S)}(s, s', 0) \right) \right]
 \end{aligned}$$

$$+ \frac{g_1(s')}{s' - s} (\zeta_L(s') + 4\zeta_T(s')) \Big].$$

3.3. Analytic Properties of the Amplitude  $V \rightarrow \gamma S$

Now, let us turn to the whole amplitude, which is the sum of processes shown in Figs. 3a, 3b, and 3c, and investigate its analytic properties in the limit  $q^2 \rightarrow 0$ .

For the two representations of the amplitude corresponding to Expansions I and II, one has

$$A_{\mu\alpha}^{(\text{connected})}(s, s'; 0) = \frac{g_1(s)}{1 - B_1(s)} \quad (97)$$

$$\times \left[ \left( g_{\mu\alpha} + \frac{4s}{(s - s')^2} q_\mu q_\alpha \right. \right.$$

$$\left. - \frac{2}{s - s'} (P_\mu q_\alpha + q_\mu P_\alpha) \right) T(s, s', 0)$$

$$+ \left( \frac{s}{(s - s')^2} q_\mu q_\alpha - \frac{1}{2(s - s')} P_\mu q_\alpha \right)$$

$$\times L(s, s', 0) \Big] \frac{g_0(s')}{1 - B_0(s')} = \frac{g_1(s)}{1 - B_1(s)}$$

$$\times \left[ \left( g_{\mu\alpha} - \frac{2}{s - s'} q_\mu P_\alpha \right) T(s, s', 0) \right.$$

$$+ \left( \frac{s}{(s - s')^2} q_\mu q_\alpha - \frac{1}{2(s - s')} P_\mu q_\alpha \right)$$

$$\times (L(s, s', 0) + 4T(s, s', 0)) \Big] \frac{g_0(s')}{1 - B_0(s')},$$

where

$$T(s, s', 0) = \frac{1 - B_1(s)}{g_1(s)} f_T^{(P \rightarrow 0)}(s, s', 0) \quad (98)$$

$$+ \frac{1 - B_1(s)}{g_1(s)} \frac{g_0(s)}{s - s'} \frac{3\zeta_T(s)}{4m^2 - s} + f_T^{(1 \rightarrow 0)}(s, s', 0)$$

$$+ \frac{B_T^{(1 \rightarrow 0)}(s) - B_T^{(1 \rightarrow 0)}(s')}{s - s'} + f_T^{(1 \rightarrow S)}(s, s', 0)$$

$$\times \frac{1 - B_0(s')}{g_0(s')} + \frac{g_1(s')}{s' - s} \zeta_T(s') \frac{1 - B_0(s')}{g_0(s')}$$

and

$$L(s, s', 0) = \frac{1 - B_1(s)}{g_1(s)} f_L^{(P \rightarrow 0)}(s, s', 0) \quad (99)$$

$$+ \frac{1 - B_1(s)}{g_1(s)} \frac{g_0(s)}{s - s'} \frac{3\zeta_L(s)}{4m^2 - s} + f_L^{(1 \rightarrow 0)}(s, s', 0)$$

$$+ \frac{B_L^{(1 \rightarrow 0)}(s) - B_L^{(1 \rightarrow 0)}(s')}{s - s'} + f_L^{(1 \rightarrow S)}(s, s', 0)$$

$$\times \frac{1 - B_0(s')}{g_0(s')} + \frac{g_1(s')}{s' - s} \zeta_L(s') \frac{1 - B_0(s')}{g_0(s')}.$$

Looking at the last equation in (97), which corresponds to Expansion II, we conclude that the analyticity of the amplitude  $A_{\mu\alpha}^{(\text{connected})}(s, s', 0)$  requires that the following ultimate expressions be fulfilled at  $s \rightarrow s'$ :

$$[T(s, s', 0)]_{s \rightarrow s'} = 0, \quad (100)$$

and

$$[L(s, s', 0) + 4T(s, s', 0)]_{s \rightarrow s'} = 0, \quad (101)$$

$$\left[ \frac{L(s, s', 0) + 4T(s, s', 0)}{s - s'} \right]_{s \rightarrow s'} = 0.$$

After satisfying the requirements given by (100) and (101), the point  $s = s'$  is not singular for  $A_{\mu\alpha}^{(\text{connected})}(s, s', 0)$ .

First, consider the condition (100) for the transverse amplitude  $T(s, s', 0)$ . This amplitude is defined in (98); it contains pole singularities  $1/(s - s')$ , which are due to both  $A_{\mu\alpha}^{(P \rightarrow 0)}(s, s', 0)$  and  $A_{\mu\alpha}^{(1 \rightarrow S)}(s, s', 0)$  [see (94)]. These singularities should be canceled by similar singular points, correspondingly, in  $f_T^{(P \rightarrow 0)}(s, s', 0)$  and  $f_T^{(1 \rightarrow S)}(s, s', 0)$ . Namely, at  $s \rightarrow s'$ , we should deal with finite limits for

$$f_T^{(P \rightarrow 0)}(s, s', 0) + \frac{g_0(s)}{s - s'} \frac{3\zeta_T(s)}{4m^2 - s} \equiv l_T(s, s', 0), \quad (102)$$

$$f_T^{(1 \rightarrow S)}(s, s', 0) - \frac{g_1(s')}{s - s'} \zeta_T(s') \equiv r_T(s, s', 0). \quad (103)$$

Therefore,  $l_T(s, s, 0)$  and  $r_T(s, s, 0)$  should be analytic functions of  $s$ . In terms of  $l_T(s, s, 0)$  and  $r_T(s, s, 0)$ , Eq. (100) reads

$$-f_T^{(1 \rightarrow 0)}(s, s, 0) \quad (104)$$

$$= \frac{1 - B_1(s)}{g_1(s)} l_T(s, s, 0) + F_T^{(1 \rightarrow 0)}(s, s, 0)$$

$$+ r_T(s, s, 0) \frac{1 - B_0(s)}{g_0(s)}.$$

Here, we use the equality

$$F_T^{(1 \rightarrow 0)}(s, s', 0) = \frac{B_T^{(1 \rightarrow 0)}(s) - B_T^{(1 \rightarrow 0)}(s')}{s - s'}, \quad (105)$$

which results in  $F_T^{(1 \rightarrow 0)}(s, s, 0) = dB_T^{(1 \rightarrow 0)}(s)/ds$ . The freedom in choosing subtraction terms makes fulfillment of (104) a reality. Assuming that the transition form factor of composite systems is defined

by a double spectral integral only, the following requirement should be imposed:

$$f_T^{(1\rightarrow 0)}(M_1^2, M_0^2, q^2) = 0, \quad (106)$$

in particular, at  $q^2 = 0$ :  $f_T^{(1\rightarrow 0)}(M_1^2, M_0^2, 0) = 0$ . We see that the requirement (106) does not contradict the amplitude analyticity constraint given by (104).

Likewise, using the freedom for the choice of subtraction functions,

$$f_L^{(P\rightarrow 0)}(s, s', 0), \quad f_L^{(1\rightarrow 0)}(s, s', 0), \quad f_L^{(1\rightarrow S)}(s, s', 0), \quad (107)$$

one can satisfy the analyticity constraints given by (101); however, we will not present these constraints explicitly, for they are rather cumbersome and do not teach us anything new.

#### 4. ADDITIVE-QUARK MODEL

Rewriting formulas of Sections 2 and 3 for composite fermion–antifermion systems does not present any problems. For such a case, one needs to introduce spin variables and substitute vertices of scalar (pseudoscalar) constituents by fermion ones:

$$g_0 \rightarrow (\bar{u}u)g_0, \quad (108)$$

$$p_{\perp\mu}g_1 \rightarrow (\bar{u}\gamma_{\mu}^{\perp}u)g_1,$$

where  $u$  is the four-spinor. Then the consideration of the fermion–antifermion composite system  $f\bar{f}$  remains in principle the same as for scalar (pseudoscalar) constituents. Namely, one should consider the  $f\bar{f}$  scattering amplitude of Fig. 1, and the pole of the amplitude  $f\bar{f} \rightarrow f\bar{f}$  determines the bound state of the  $f\bar{f}$  system. Its form factor is defined by the triangle graph of Fig. 2c, which is a residue in the amplitude poles of the transition  $(f\bar{f})_{\text{in}} \rightarrow \gamma + (f\bar{f})_{\text{out}}$  (Fig. 2b). The triangle diagram shown separately in Fig. 4a determines the form factor of a composite particle in the additive model.

Still, quarks do not leave the confinement trap as free particles do, so one cannot use for quarks the above-described scheme on a full scale.

The logic of the quark model tells us that we may treat constituent quarks inside the confinement region as free particles, and the region where they are "allowed" to be free is determined by the quark wave function. This means that, within the quark model, one can calculate the three-point form-factor amplitudes, which refer to the interaction of a photon in the intermediate state: these are the diagrams of Fig. 4a type. The diagrams with a photon interacting with an incoming/outgoing particle (Figs. 4b and 4c type) should be treated using hadronic language. Thus,

we come to a combined approach, where incoming/outgoing particles in the processes of Fig. 3 are mesons, while constituents of the triangle diagram are quarks. It is obvious that, in such a combined approach to the amplitude, relations (100) and (101) imposed by analyticity are kept; they may be satisfied, without any problem, by constraints similar to (104) and (106). Triangle diagrams determined as residues in amplitude poles (see Fig. 2b) stand for quark form factors, which are obtained in accordance with gauge invariance and analyticity constraints.

Now, to illustrate the above statements, let us repeat the main items of the method of singling out the quark form factor of the transition  $\phi(1020) \rightarrow \gamma f_0(980)$  from hadronic processes. We cannot directly use the process  $(q\bar{q})_{\text{in}} \rightarrow \gamma(q\bar{q})_{\text{out}}$  for the definition of quark form factor: being rigorous, we are not allowed to treat quarks as free particles at large distances. In this way, the reaction of the type  $K\bar{K} \rightarrow \gamma\pi\pi$  is to be considered; then, the amplitude  $\phi(1020) \rightarrow \gamma f_0(980)$  should be extracted as a double residue at the amplitude poles for complex masses. The amplitude itself,  $\phi(1020) \rightarrow \gamma f_0(980)$ , may be considered in terms of constituent quarks, namely, as a triangle diagram with constituent quarks.

The form-factor amplitude for radiative transition of a vector meson to a scalar one, of the type of  $\phi(1020) \rightarrow \gamma f_0(980)$ , was calculated in terms of constituent quarks [7, 9]. The spectral integral for  $F_T^{(1\rightarrow 0)}(M_V^2, M_S^2, 0)$  was given by Eq. (32) of [9]; it was denoted there as  $A_{V\rightarrow\gamma S}(0)$ . Up to the charge factor  $Z_{V\rightarrow\gamma S}$ , which we omit here, it reads

$$F_T^{(1\rightarrow 0)}(M_V^2, M_S^2, 0) = \int_{4m^2}^{\infty} \frac{ds}{\pi} \Psi_V(s) \Psi_S(s) \quad (109)$$

$$\times \left[ \frac{m}{4\pi} \sqrt{s(s-4m^2)} - \frac{m^3}{2\pi} \ln \frac{\sqrt{s} + \sqrt{s-4m^2}}{\sqrt{s} - \sqrt{s-4m^2}} \right].$$

The quark wave functions for vector and scalar states,  $\Psi_V(s)$  and  $\Psi_S(s)$ , are normalized as follows:

$$\int_{4m^2}^{\infty} \frac{ds}{\pi} \Psi_V^2(s) \frac{s+2m^2}{12\pi} \sqrt{\frac{s-4m^2}{s}} = 1, \quad (110)$$

$$\int_{4m^2}^{\infty} \frac{ds}{\pi} \Psi_S^2(s) \frac{s-4m^2}{8\pi} \sqrt{\frac{s-4m^2}{s}} = 1.$$

Masses of light constituent quarks  $u$  and  $d$  are of the order of 350 MeV, and the strange-quark mass is  $\sim 500$  MeV.

The function in square brackets of the integrand of (109) is positive at  $s > 4m^2$ , so the transition form

factor  $F_T^{(1\rightarrow 0)}(M_V^2, M_S^2, 0) \neq 0$  at arbitrary  $M_V$  and  $M_S$ ,  $M_V = M_S$  included, if the wave functions  $\Psi_V(s)$  and  $\Psi_S(s)$  do not change sign, and just this feature (absence of zeros in the radial wave function) is a signature of basic states with the radial quantum number  $n = 1$ .

One point needs special discussion, that is, the possibility of applying the spectral-integration technique, with mass-on-shell intermediate states, to the calculation of quark diagrams of Fig. 4a. The fact that quarks—constituents do not fly off at large distances does not directly restrain the calculation technique: calculations may be performed with mass-on-shell particles in the intermediate states as well as mass-off-shell ones, like Feynman integrals. Recall that, in nonrelativistic quantum mechanics, that is, in the nonrelativistic quark model, the particles in the intermediate states are mass-on-shell, which does not prevent the use of confinement models. The flying-off of quarks at large distances corresponds to threshold singularities of the amplitude: in the triangle diagram of Fig. 4a, they are at  $s = 4m^2$  and  $s' = 4m^2$ . The suppression of contribution from large distances means the suppression in the momentum space from the regions  $s \sim 4m^2$  and  $s' \sim 4m^2$ . Such a suppression is implemented by the properties of vertices, or wave functions, of composite systems. As concerns the threshold singularities, they are present in other techniques too, like Feynman or light-cone ones. Therefore, in all representations, one should suppress the contributions from the regions  $s \sim 4m^2$  and  $s' \sim 4m^2$ . The spectral-integration technique provides us with a possibility to control the near-threshold contributions.

### Transition ${}^3S_1 q\bar{q} \rightarrow {}^3P_0 q\bar{q}$ in the Nonrelativistic Approach

In the nonrelativistic limit, formula (109) turns into the standard expression of the additive-quark-model transition  ${}^3S_1 \rightarrow {}^3P_0$ , and the amplitude is obtained by expanding the expression in square brackets in a series with respect to relative quark momentum squared  $k^2$ , where  $k^2 = s/4 - m^2$ . Here, we present the form factor  $F_T^{(1\rightarrow 0)}(M_V^2, M_S^2, 0)$  in the nonrelativistic approach: this very transition is responsible for the decays  $\phi(1020) \rightarrow \gamma f_0(980)$  and  $\phi(1020) \rightarrow \gamma a_0(980)$ , if  $f_0(980)$  and  $a_0(980)$  are the  $q\bar{q}$  states.

In the nonrelativistic approximation, after redefinition  $\Psi_V(s) \rightarrow \psi_V(k^2)$  and  $\Psi_S(s) \rightarrow \psi_S(k^2)$ , Eq. (109) becomes

$$F_T^{(1\rightarrow 0)}(M_V^2, M_S^2, 0) \rightarrow \left[ F_T^{(1\rightarrow 0)}(M_V^2, M_S^2, 0) \right]_{\text{nonrelativistic}} \quad (111)$$

$$= \int_0^\infty \frac{dk^2}{\pi} \psi_V(k^2) \psi_S(k^2) \frac{8}{3\pi} k^3.$$

Normalization conditions for wave functions  $\psi_V(k^2)$  and  $\psi_S(k^2)$  should also be rewritten in the nonrelativistic limit; they read

$$1 = \int_0^\infty \frac{dk^2}{\pi} \psi_S^2(k^2) \frac{2k^3}{\pi m}, \quad (112)$$

$$1 = \int_0^\infty \frac{dk^2}{\pi} \psi_V^2(k^2) \frac{mk}{2\pi}.$$

For exponential parametrization of wave functions,

$$\psi_S(k^2) = N_S e^{-b_S k^2}, \quad \psi_V(k^2) = N_V e^{-b_V k^2}, \quad (113)$$

one can easily calculate integrals (111) and (112). Normalization constants are determined as

$$N_S^2 = \frac{8\sqrt{2}}{3} \pi^{3/2} m b_S^{5/2}, \quad N_V^2 = 2\sqrt{2} \pi^{3/2} \frac{1}{m} b_S^{3/2}, \quad (114)$$

and the transition form factor is equal to

$$\left[ F_T^{(1\rightarrow 0)}(M_V^2, M_S^2, 0) \right]_{\text{nonrelativistic}} = 8\sqrt{\frac{2}{3}} \frac{b_V^{3/4} b_S^{5/4}}{(b_V + b_S)^{5/2}}. \quad (115)$$

At  $b_V \simeq b_S = b$ , one has

$$\left[ F_T^{(1\rightarrow 0)}(M_V^2, M_S^2, 0) \right]_{\text{nonrelativistic}} \simeq \frac{2}{\sqrt{3}b}. \quad (116)$$

For loosely bound systems,  $1/b \sim \sqrt{m\epsilon}$ , where  $\epsilon$  is the binding energy, so the right-hand side of Eq. (116) contains the suppression factor inherent to the  $E1$  transition.

In Fig. 5, we demonstrate the calculated form factors  $F_T^{(1\rightarrow 0)}$  for the transition  $\phi(1020) \rightarrow \gamma f_0(980)$  for both the nonrelativistic approximation, Eq. (111), and the relativistic spectral integrals, Eq. (109), with the  $n\bar{n}$  and  $s\bar{s}$  components. We use  $b_V = 10 \text{ GeV}^{-2}$ , which corresponds to the  $\phi$ -meson radius of the order of the pion radius, and for the  $f_0$  meson we change the wave-function slope within the limits  $2 < b_S < 12 \text{ GeV}^{-2}$ , which means the change of the radius squared in the interval  $0.5R_\pi^2 < R_{f_0}^2 < 2R_\pi^2$  (for more detail, see [7, 9]).

It is seen that form factors calculated in both relativistic and nonrelativistic approaches do not differ significantly one from another, which makes puzzling the statement about problematic quark-model

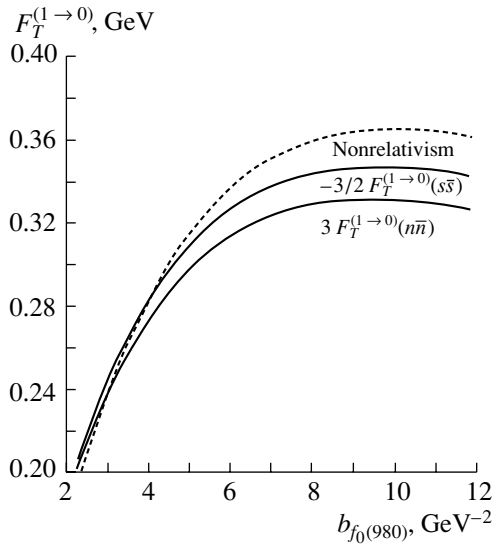


**Fig. 5.** Form factor  $F_T^{(1 \rightarrow 0)}(M_V^2, M_S^2)$  for the decay  $\phi(1020) \rightarrow \gamma f_0(980)$  calculated in the relativistic (for  $n\bar{n}$  and  $s\bar{s}$  components) and nonrelativistic approaches.

description of the reactions  $\phi(1020) \rightarrow \gamma f_0(980)$  and  $\phi(1020) \rightarrow \gamma a_0(980)$  under the assumption of  $f_0(980)$  and  $a_0(980)$  being  $q\bar{q}$  states: recall that the data can indeed be described [7, 9] by using spectral-integral formula (109).

## 5. CONCLUSION

The use of the dispersion technique for the calculation of form factors of the composite system has certain advantages, of which we would underline two:

(i) In the dispersion technique, or in the spectral-integration technique, the content of the bound state is controlled. The interaction of constituents with each other due to meson exchanges does not lead to the appearance of new components in the bound state related to these mesons.

(ii) The dispersion technique, as well as the spectral integration technique, works with the energy-off-shell amplitudes, and the particles in the intermediate states are mass-on-shell. This provides us with an easy possibility to construct spin operators, which in turn allows one to consider, without any problems, the amplitudes for composite particles with a large spin (see [12] for more detail).

However, as often happens, the advantages make it necessary to take special care regarding other aspects of the approach: in the spectral-integration technique, when radiative processes are considered, one should impose “by hand” the constraints related to gauge invariance and analyticity. In [6], this problem was considered in connection with charge form factors, for example, for the transitions of ( $S \rightarrow \gamma S$ )

type, where  $S$  is a scalar meson. However, more complicated radiative processes were investigated later on [8], such as  $V \rightarrow \gamma S$  ( $V$  is a vector meson) and  $P \rightarrow \gamma\gamma$ ,  $S \rightarrow \gamma\gamma$ ,  $T \rightarrow \gamma\gamma$  ( $P$  and  $T$  are pseudoscalar and tensor mesons). In these cases, the spin structure of the amplitude is more complicated; hence, more complicated constraints for amplitudes are needed, which is related to gauge-invariant operators that perform the moment-operator expansion. Although, in principle, the reconstruction of analyticity and transition form factors is analogous to that used in [6], the statements of [13] concerning transition form factors need our attention.

In the present paper, we have carried out the study of more complicated processes using as an example the process  $V \rightarrow \gamma S$ . The consideration of different processes within the spectral-integration technique has much in common, so we discuss here basic principles of treating the transition  $S \rightarrow \gamma S$ , though in a more general way than in [6]. As the first step, we take the mesons  $V$  and  $S$  to be two-particle composite systems of scalar or pseudoscalar particles—constituents (Section 3). Such an approach makes calculations simple, less cumbersome, without affecting basic points. This approach can be generalized for the fermion–antifermion system without principal complications, and the necessary changes are related only to the phase space (spin factors should be included) and the form of vertices. In this way, one can generalize the present results for quark–antiquark systems (Section 4); i.e., one can apply the method to the consideration of radiative decays of  $q\bar{q}$  mesons too.

Concerning the transition  $V \rightarrow \gamma S$ , we demonstrate that two independent operators are responsible for the spin structure of this reaction,  $g_{\mu\alpha}^{\perp\perp}$  and  $L_{\mu\alpha}$  given by (12) and (13). The operators  $g_{\mu\alpha}^{\perp\perp}$  and  $L_{\mu\alpha}$  determine the transverse and longitudinal amplitudes; at  $q^2 = 0$ , the longitudinal operator turns into a nilpotent one,  $L_{\mu\alpha}(0)L_{\mu\alpha}(0) = 0$ . In the spectral integration technique, the essential point is the use of operators, which are responsible for total spin space, that is, two orthogonal operators  $g_{\mu\alpha}^{\perp\perp}$  and  $L_{\mu\alpha}$ , with  $g_{\mu\alpha}^{\perp\perp}L_{\mu\alpha} = 0$ .

Also, we demonstrate that meson-decay form factors are determined by residues in the poles of scattering blocks. For example, the form factor for the decay  $\phi(1020) \rightarrow \gamma f_0(980)$  is given by the residue of the amplitude of the reaction  $\phi(1020) \rightarrow \gamma\pi\pi$  at the pole for complex-valued  $M_{\pi\pi}$  masses so analytic properties of these two amplitudes are different. In particular, the amplitude of the transition  $\phi(1020) \rightarrow \gamma\pi\pi$  should be zero at  $(M_\phi - M_{\pi\pi}) \rightarrow 0$ , while for the transition  $\phi(1020) \rightarrow \gamma f_0(980)$  an analogous

requirement is absent for  $M_\phi = M_{f_0}$ . Moreover, if  $\phi(1020)$  and  $f_0(980)$  are the members of the basic  $q\bar{q}$  nonets,  $1^3S_1$  and  $1^3P_0$ , the transition amplitude cannot be zero because the wave functions do not change sign.

The present investigation does not confirm the use of a unique form of the spin operator in  $S \rightarrow \gamma V$  declared in [13]: generally, at  $q^2 \neq 0$ , two independent spin operators exist related to the transverse and longitudinal amplitudes. At  $q^2 \rightarrow 0$ , one operator turns into a nilpotent one, thus giving us freedom in writing the spin operator for the transition with a real photon.

### ACKNOWLEDGMENTS

We thank A.V. Anisovich, Ya.I. Azimov, L.G. Dakhno, M.N. Kobrinsky, D.I. Melikhov, V.N. Nikonov, and V.A. Sarantsev for helpful discussions of problems involved.

This work is supported by the Russian Foundation for Basic Research, project nos. 01-02-17861 and 00-15-96610.

### APPENDIX A

*Coefficients  $\xi_T(s, s', q^2)$  and  $\xi_L(s, s', q^2)$*

Let us calculate coefficients in the expansion (72) for spin factor  $S_{\mu\alpha}$ . To this aim, we need the convolutions as follows:

$$g_{\mu\alpha}(k_1 - k_2)_\mu(k_1 + k'_1)_\alpha = 4m^2 - \frac{1}{2}(s + s' + q^2), \quad (\text{A.1})$$

$$\begin{aligned} P_\mu P_\alpha(k_1 - k_2)_\mu(k_1 + k'_1)_\alpha &= 0, \\ q_\mu q_\alpha(k_1 - k_2)_\mu(k_1 + k'_1)_\alpha &= 0, \\ P_\mu q_\alpha(k_1 - k_2)_\mu(k_1 + k'_1)_\alpha &= 0, \\ q_\mu P_\alpha(k_1 - k_2)_\mu(k_1 + k'_1)_\alpha \\ &= \frac{1}{4}(s + s' - q^2)(-s + s' + q^2). \end{aligned}$$

Projecting  $S_{\mu\alpha}$  on the operators  $g_{\mu\alpha}^{\perp\perp}$  and  $L_{\mu\alpha}$ , one obtains

$$\xi_T(s, s', q^2) \left(g_{\mu\alpha}^{\perp\perp}\right)^2 = 4 \left(m^2 + \frac{ss'q^2}{\lambda(s, s', q^2)}\right), \quad (\text{A.2})$$

$$\begin{aligned} &\xi_L(s, s', q^2) (L_{\mu\alpha})^2 \\ &= -\frac{q^2 s}{2\lambda(s, s', q^2)} \frac{(s + s' - q^2)(-s + s' + q^2)}{(s - s' + q^2)}. \end{aligned}$$

As a result, we have the coefficients given in (72). Taking into account that  $g_{\mu\alpha}^{\perp\perp} = \tilde{g}_{\mu\alpha}^{\perp\perp} + 4L_{\mu\alpha}$ , we obtain coefficients for Expansion II,  $\tilde{\xi}_T(s, s', q^2)$  and  $\tilde{\xi}_L(s, s', q^2)$ .

### APPENDIX B

*Form Factors in the Limit  $q^2 \rightarrow 0$*

*Form Factors of the Three-Point Diagram of Fig. 4a*

Let us calculate form factors in the limit  $q^2 \rightarrow 0$  for the diagram of Fig. 4a for two variants of the expansion given by (76).

**Expansion I.** To get formula (77) for form factors in the limit  $q^2 \rightarrow 0$ , let us insert new variables,  $\sigma$ ,  $\Delta$ , and  $Q^2$  [see (34)], and integrate over phase space, which leads at small  $Q^2$  to

$$\begin{aligned} F_i^{(1 \rightarrow 0)}(s, s', q^2 \rightarrow 0) &= f_i^{(1 \rightarrow 0)}(s, s', q^2 \rightarrow 0) \quad (\text{A.3}) \\ &+ \int_{4m^2}^{\infty} \frac{d\sigma}{\pi} \frac{g_1(\sigma)g_0(\sigma)}{(\sigma - s)(\sigma - s')} \int_{-b}^b d\Delta \frac{\xi_i(\sigma, \Delta, Q^2)}{16\pi\sqrt{\Delta^2 + 4\sigma Q^2}}, \end{aligned}$$

where  $b$  is defined in (36) and

$$\begin{aligned} \xi_T(\sigma, \Delta, Q^2) &= 2 \left( m^2 - \frac{Q^2\sigma^2}{\Delta^2 + 4\sigma Q^2} \right), \quad (\text{A.4}) \\ \xi_L(\sigma, \Delta, Q^2) &= 4\sigma \left( \frac{\Delta^2}{\Delta^2 + 4\sigma Q^2} \right). \end{aligned}$$

Integrating over  $\Delta$ , we obtain the final formula for form factors in Expansion I [see (81) and (82)].

**Expansion II.** Likewise, the same procedure is carried out for Expansion II, though with other coefficients defining the double discontinuity of the form factor:

$$\begin{aligned} \tilde{\xi}_T(\sigma, \Delta, Q^2) &= \xi_T(\sigma, \Delta, Q^2), \quad (\text{A.5}) \\ \tilde{\xi}_L(\sigma, \Delta, Q^2) &= 4 \left( 2m^2 + \frac{\sigma(\Delta^2 - 2\sigma Q^2)}{\Delta^2 + 4\sigma Q^2} \right). \end{aligned}$$

As a result, we obtain

$$\tilde{F}_T^{(1 \rightarrow 0)}(s, s', q^2) = F_T^{(1 \rightarrow 0)}(s, s', 0)$$

and

$$\begin{aligned} \tilde{F}_L^{(1 \rightarrow 0)}(s, s', q^2) &= \tilde{f}_L^{(1 \rightarrow 0)}(s, s', 0) \quad (\text{A.6}) \\ &+ \frac{\tilde{B}_L^{(1 \rightarrow 0)}(s) - \tilde{B}_L^{(1 \rightarrow 0)}(s')}{s - s'}, \end{aligned}$$

$$\tilde{B}_L^{(1 \rightarrow 0)}(s) = \int_{4m^2}^{\infty} \frac{d\tilde{s}}{\pi} \frac{g_1(\tilde{s})g_0(\tilde{s})}{\tilde{s} - s} \rho(\tilde{s}) \tilde{\zeta}_L(\tilde{s}),$$

$$\begin{aligned} \tilde{\zeta}_L(s) &= 4 \left[ (2m^2 + s) \sqrt{\frac{s}{4m^2 - s}} \right. \\ &\left. \times \ln \frac{1 + \sqrt{(s - 4m^2)/s}}{1 - \sqrt{(s - 4m^2)/s}} - 3s \right]. \end{aligned}$$

Form Factors of the Two-Point Diagram of Fig. 4b

For the diagram of Fig. 4b, the form-factor calculation in the limit  $q^2 \rightarrow 0$  [see (87)] is carried out as before, by using the variables  $\sigma$ ,  $\Delta$ , and  $Q^2$  defined in (34):

$$\begin{aligned} F_i^{(P \rightarrow 0)}(s, s', q^2 \rightarrow 0) & \quad (A.7) \\ &= f_i^{(P \rightarrow 0)}(s, s', q^2 \rightarrow 0) + \frac{3}{p^2} \\ & \times \int_{4m^2}^{\infty} \frac{d\sigma}{\pi} \frac{g_0(\sigma)}{\sigma - s'} \pi \delta(\sigma - s) \int_{-b}^b d\Delta \frac{\xi_i(\sigma, \Delta, Q^2 \rightarrow 0)}{16\pi \sqrt{\Delta^2 + 4\sigma Q^2}}, \end{aligned}$$

where  $\xi_i(s, s', q^2)$  are given by (A.4). Performing calculations analogous to the ones above, we obtain (90).

### APPENDIX C

Separation of the P Wave in the Initial State of the Process of Fig. 4b

The Feynman diagram shown in Fig. 4b reads

$$\Gamma_{\alpha}^{(\rightarrow 0)} = (p_1 + k'_1)_{\alpha} \frac{g_0(P'^2; k_1'^2, k_2'^2)}{m^2 - k_1'^2}. \quad (A.8)$$

The amplitude  $\Gamma_{\alpha}^{(\rightarrow 0)}$  can be expanded in a series with respect to orbital momenta of the initial states as follows:

$$\begin{aligned} \Gamma_{\alpha}^{(\rightarrow 0)} &= \Gamma_{\alpha}^{(S \rightarrow 0)} + (p_1 - p_2)_{\mu} \Gamma_{\mu\alpha}^{(P \rightarrow 0)} \\ &+ X_{\mu_1\mu_2}^{(2)}(p) \Gamma_{\mu_1\mu_2\alpha}^{(D \rightarrow 0)} + \dots \end{aligned} \quad (A.9)$$

There is summation over  $\mu$  and  $\mu_1, \mu_2$ . To find  $\Gamma_{\mu\alpha}^{(P \rightarrow 0)}$ , one should multiply  $\Gamma_{\alpha}^{(\rightarrow 0)}$  by

$$(p_1 - p_2)_{\mu} \equiv p_{\mu} \quad (A.10)$$

and integrate over  $d\Omega/(4\pi)$  or  $\int d\Phi_2(P; p_1, p_2)/\rho(s)$ . The right-hand side of (A.9) gives us

$$\begin{aligned} \int \frac{d\Phi_2(P; p_1, p_2)}{\rho(s)} (p_1 - p_2)_{\mu} & \quad (A.11) \\ \times (p_1 - p_2)_{\mu} \Gamma_{\mu\alpha}^{(P \rightarrow 0)} &= \frac{p^2}{3} \Gamma_{\mu\alpha}^{(P \rightarrow 0)}, \end{aligned}$$

for one can replace in the integrand of (A.11)

$$\begin{aligned} (p_1 - p_2)_{\mu} (p_1 - p_2)_{\mu'} & \rightarrow g_{\mu\mu'}^{\perp} \frac{p^2}{3}, \\ p^2 &= 4m^2 - s. \end{aligned} \quad (A.12)$$

The left-hand side of (A.9) with account of (A.8) gives us

$$\int \frac{d\Phi_2(P; k_1, k_2)}{\rho(P^2)} (k_1 - k_2)_{\mu} \quad (A.13)$$

$$\times (k_1 + k'_1)_{\alpha} \frac{g_0(P'^2; k_1'^2, k_2'^2)}{m^2 - k_1'^2}.$$

In the integrand, we redenoted the momenta  $p_1$  and  $p_2$  as  $k_1$  and  $k_2$ . To get the spectral integral, let us calculate the discontinuity; to this aim, we consider the intermediate state as mass-on-shell,

$$(m^2 - k_1'^2)^{-1} \rightarrow \theta(k_{10}') \delta(m^2 - k_1'^2), \quad (A.14)$$

and substitute the vertex function as follows:

$$g_0(\tilde{P}'^2; k_1'^2, k_2'^2) \rightarrow g_0(\tilde{s}'). \quad (A.15)$$

Then we expand the spin factor of the amplitude:

$$\begin{aligned} (k_1 - k_2)_{\mu} (k_1 + k'_1)_{\alpha} & \quad (A.16) \\ &= g_{\mu\alpha}^{\perp\perp} \xi_T(s, \tilde{s}', q^2) + L_{\mu\alpha} \xi_L(s, \tilde{s}', q^2), \end{aligned}$$

with the coefficients  $\xi_T$  and  $\xi_L$  given in (72). As a result, the discontinuity in the  $s'$  channel reads

$$\begin{aligned} \text{disc}_{s'} F_{T,L}^{(P \rightarrow 0)}(s, s', q^2) &= \frac{1}{\rho(s)} \xi_{T,L}(s, \tilde{s}', q^2) \\ &\times g_0(\tilde{s}') d\Phi_{\text{tr}}(P, P'; k_1, k_1', k_2). \end{aligned} \quad (A.17)$$

Thus, we have the following dispersion representation for the pole diagram of Fig. 4b:

$$\begin{aligned} F_{T,L}^{(P \rightarrow 0)}(s, s', q^2) &= f_{T,L}^{(P \rightarrow 0)}(s, s', q^2) \\ &+ \frac{3}{p^2} \frac{1}{\rho(s)} \int_{4m^2}^{\infty} \frac{d\tilde{s}'}{\pi} \frac{g_0(\tilde{s}')}{\tilde{s}' - s'} \xi_{T,L}(s, \tilde{s}', q^2) \\ &\times d\Phi_{\text{tr}}(P, P'; k_1, k_1', k_2), \end{aligned} \quad (A.18)$$

which gives (87).

### REFERENCES

1. M. N. Kinzle-Focacci, in *Proc. of the VIII Blois Workshop, Protvino, Russia, 1999*, Ed. by V. A. Petrov and A. V. Prokudin (World Sci., Singapore, 2000); V. A. Schegelsky, *Talk Given in Open Session of HEP Division of PNPI "On the Eve of the XXI Century"* (2000).
2. E. Klempt, hep-ex/0101031.
3. KLOE Collab. (A. Aloisio *et al.*), hep-ex/0204012.
4. T. Barnes, hep-ph/0202157.
5. V. V. Anisovich, A. A. Anselm, Ya. I. Azimov, *et al.*, Phys. Lett. **16**, 194 (1965); W. E. Tiring, Phys. Lett. **16**, 335 (1965); L. D. Soloviev, Phys. Lett. **16**, 345 (1965); C. Becchi and G. Morpurgo, Phys. Rev. **140**, 687 (1965).
6. V. V. Anisovich, M. N. Kobrinsky, D. I. Melikhov, and A. V. Sarantsev, Nucl. Phys. A **544**, 747 (1992); Yad. Fiz. **55**, 1773 (1992) [Sov. J. Nucl. Phys. **55**, 982 (1992)].
7. A. V. Anisovich, V. V. Anisovich, and V. A. Nikonov, Eur. Phys. J. A **12**, 103 (2001).

8. V. V. Anisovich, D. I. Melikhov, and V. A. Nikonov, Phys. Rev. D **52**, 5295 (1995); **55**, 2918 (1997); A. V. Anisovich, V. V. Anisovich, D. V. Bugg, and V. A. Nikonov, Phys. Lett. B **456**, 80 (1999).
9. A. V. Anisovich, V. V. Anisovich, V. N. Markov, and V. A. Nikonov, Yad. Fiz. **65**, 523 (2002) [Phys. At. Nucl. **65**, 497 (2002)].
10. G. F. Chew and S. Mandelstam, Phys. Rev. **119**, 467 (1960).
11. L. Castellejo, F. J. Dyson, and R. H. Dalitz, Phys. Rev. **101**, 453 (1956).
12. A. V. Anisovich, V. V. Anisovich, V. N. Markov, *et al.*, J. Phys. G **28**, 15 (2002).
13. N. N. Achasov, hep-ph/0110059; N. N. Achasov and V. V. Gubin, hep-ph/0101024 v2.

## A New Look at the KLOE Data on the Decay $\phi \rightarrow \eta\pi^0\gamma^*$

N. N. Achasov\*\* and A. V. Kiselev\*\*\*

Sobolev Institute for Mathematics, Siberian Division, Russian Academy of Sciences, Novosibirsk, 630090 Russia

Received February 4, 2003

**Abstract**—We present an analysis of recent high-statistical KLOE data on  $\phi \rightarrow \eta\pi^0\gamma$  decay. This decay mainly goes through the  $a_0\gamma$  intermediate state, which makes it possible to investigate properties of the  $a_0$ . It is shown that KLOE data prefer a higher  $a_0$  mass and a considerably larger  $a_0$  coupling to the  $K\bar{K}$  than those obtained in the analysis of the KLOE group. © 2004 MAIK “Nauka/Interperiodica”.

### 1. INTRODUCTION

The lightest scalar mesons  $a_0(980)$  and  $f_0(980)$ , discovered more than thirty years ago, became a hard problem for the naive quark–antiquark ( $q\bar{q}$ ) model from the outset. On the one hand, the almost exact degeneration of the masses of the isovector  $a_0(980)$  and isoscalar  $f_0(980)$  states seemingly revealed a structure similar to the structure of the vector  $\rho$  and  $\omega$  mesons, and on the other hand, the strong coupling of  $f_0(980)$  with the  $K\bar{K}$  channel pointed unambiguously to a considerable part of the strange quark pair  $s\bar{s}$  in the wave function of  $f_0(980)$ . It was noted in late 1970s that, in the MIT bag model, there are light four-quark scalar states and it was suggested that  $a_0(980)$  and  $f_0(980)$  might be these states [1]. From that time,  $a_0(980)$  and  $f_0(980)$  resonances became beloved children of light quark spectroscopy (see, for example, [2–4]).

Ten years later, there was a proposal [5] to study radiative  $\phi$  decays  $\phi \rightarrow a_0\gamma \rightarrow \eta\pi^0\gamma$  and  $\phi \rightarrow f_0\gamma \rightarrow \pi^0\pi^0\gamma$  to solve the puzzle of the lightest scalar mesons. Over the next ten years before the experiments (in 1998), this question was examined from different points of view [6–10].

Now, these decays have been studied not only theoretically but also experimentally. The first measurements have been reported by the SND [11–14] and CMD-2 [15] Collaborations, which obtained the following branching ratios:

$$\text{Br}(\phi \rightarrow \gamma\pi^0\eta) = (8.8 \pm 1.4 \pm 0.9) \times 10^{-5} \quad [13],$$

$$\text{Br}(\phi \rightarrow \gamma\pi^0\pi^0) = (12.21 \pm 0.98 \pm 0.61) \times 10^{-5} \quad [14],$$

$$\text{Br}(\phi \rightarrow \gamma\pi^0\eta) = (9.0 \pm 2.4 \pm 1.0) \times 10^{-5} \quad [15],$$

$$\text{Br}(\phi \rightarrow \gamma\pi^0\pi^0) = (9.2 \pm 0.8 \pm 0.6) \times 10^{-5} \quad [15].$$

More recently, the KLOE Collaboration has measured [16, 17]

$$\text{Br}(\phi \rightarrow \gamma\pi^0\eta) = (8.51 \pm 0.51 \pm 0.57) \times 10^{-5} \quad \text{in } \eta \rightarrow \gamma\gamma \quad [16],$$

$$\text{Br}(\phi \rightarrow \gamma\pi^0\eta) = (7.96 \pm 0.60 \pm 0.40) \times 10^{-5} \quad \text{in } \eta \rightarrow \pi^+\pi^-\pi^0 \quad [16],$$

$$\text{Br}(\phi \rightarrow \gamma\pi^0\pi^0) = (10.9 \pm 0.3 \pm 0.5) \times 10^{-5} \quad [17]$$

in agreement with the Novosibirsk data [13–15] but with a considerably smaller error.

In this work, we present a new analysis of the recent KLOE data on  $\phi \rightarrow \eta\pi^0\gamma$  decay [16, 18]. In contradistinction to [16], we

(1) treat the  $a_0$  mass  $m_{a_0}$  as a free parameter of the fit;

(2) fit the phase  $\delta$  of the interference between  $\phi \rightarrow a_0\gamma \rightarrow \eta\pi^0\gamma$  (signal) and  $\phi \rightarrow \rho^0\pi^0 \rightarrow \eta\pi^0\gamma$  (background) reactions;

(3) use new, more precise experimental values of the input parameters.

All formulas for the  $\phi \rightarrow (a_0\gamma + \rho^0\pi^0) \rightarrow \eta\pi^0\gamma$  reaction taking the background into account are shown in Section 2. The results of the five different fits are presented in Section 3. A brief summary is given in Section 4.

### 2. THE FORMALISM OF THE $\phi \rightarrow a_0\gamma \rightarrow \eta\pi^0\gamma$ AND $\phi \rightarrow \rho^0\pi^0 \rightarrow \eta\pi^0\gamma$ REACTIONS

In [19], it was shown that the process  $\phi \rightarrow a_0\gamma \rightarrow \eta\pi^0\gamma$  dominates in  $\phi \rightarrow \eta\pi^0\gamma$  decay (see also [5, 7], where it was predicted in four-quark model). This was confirmed in [16, 18]. Nevertheless, the main

\*This article was submitted by the authors in English.

\*\* e-mail: achasov@math.nsc.ru

\*\*\* e-mail: kiselev@math.nsc.ru

background process  $\phi \rightarrow \rho\pi^0 \rightarrow \eta\pi^0\gamma$  should also be taken into account (see [16, 19]).

The amplitude of the background process  $\phi(p) \rightarrow \pi^0\rho^0 \rightarrow \gamma(q)\pi^0(k_1)\eta(k_2)$  is [19]

$$M_B = \frac{g_{\phi\rho\pi}g_{\rho\eta\gamma}}{D_\rho(p-k_1)}\phi_\alpha k_{1\mu}p_\nu\epsilon_\delta(p-k_1)_\omega q_\epsilon\epsilon_{\alpha\beta\mu\nu}\epsilon_{\beta\delta\omega\epsilon}. \quad (1)$$

According to the one-loop mechanism of the decay  $\phi \rightarrow K^+K^- \rightarrow \gamma a_0$  suggested in [5], the amplitude of the signal  $\phi \rightarrow \gamma a_0 \rightarrow \gamma\pi^0\eta$  has the form

$$M_a = g(m)\frac{g_{a_0K^+K^-}g_{a_0\pi\eta}}{D_{a_0}(m)}\left((\phi\epsilon) - \frac{(\phi q)(\epsilon p)}{(pq)}\right), \quad (2)$$

where  $m^2 = (k_1 + k_2)^2$ , and  $\phi_\alpha$  and  $\epsilon_\mu$  are the polarization vectors of the  $\phi$  meson and photon. The forms of  $g_R(m)$  and  $g(m) = g_R(m)/g_{RK^+K^-}$  everywhere over the region  $m$  are given in [5] and [20], respectively:

For  $m < 2m_{K^+}$ ,

$$g(m) = \frac{e}{2(2\pi)^2}g_{\phi K^+K^-} \quad (3)$$

$$\times \left\{ 1 + \frac{1 - \rho^2(m^2)}{\rho^2(m_\phi^2) - \rho^2(m^2)} \left[ 2|\rho(m^2)| \right. \right.$$

$$\times \arctan \frac{1}{|\rho(m^2)|} - \rho(m_\phi^2)\lambda(m_\phi^2) + i\pi\rho(m_\phi^2)$$

$$\left. - (1 - \rho^2(m_\phi^2))\left(\frac{1}{4}(\pi + i\lambda(m_\phi^2))^2 \right. \right.$$

$$\left. \left. - \left(\arctan \frac{1}{|\rho(m^2)|}\right)^2 \right) \right] \right\},$$

where

$$\rho(m^2) = \sqrt{1 - \frac{4m_{K^+}^2}{m^2}}, \quad (4)$$

$$\lambda(m^2) = \ln \frac{1 + \rho(m^2)}{1 - \rho(m^2)}, \quad \frac{e^2}{4\pi} = \alpha = \frac{1}{137}.$$

For  $m \geq 2m_{K^+}$ ,

$$g(m) = \frac{e}{2(2\pi)^2}g_{\phi K^+K^-} \quad (5)$$

$$\times \left\{ 1 + \frac{1 - \rho^2(m^2)}{\rho^2(m_\phi^2) - \rho^2(m^2)} \left[ \rho(m^2)(\lambda(m^2) - i\pi) \right. \right.$$

$$\left. - \rho(m_\phi^2)(\lambda(m_\phi^2) - i\pi) - \frac{1}{4}(1 - \rho^2(m_\phi^2)) \right.$$

$$\left. \left. \times \left( (\pi + i\lambda(m_\phi^2))^2 - (\pi + i\lambda(m^2))^2 \right) \right] \right\}.$$

The mass spectrum is

$$\frac{d\Gamma(\phi \rightarrow \gamma\pi^0\eta, m)}{dm} = \frac{d\Gamma_{a_0}(m)}{dm} \quad (6)$$

$$+ \frac{d\Gamma_{\text{back}}(m)}{dm} + \frac{d\Gamma_{\text{int}}(m)}{dm},$$

where the mass spectrum for the signal is

$$\frac{d\Gamma_{a_0}(m)}{dm} = \frac{2}{\pi} \frac{m^2\Gamma(\phi \rightarrow \gamma a_0, m)\Gamma(a_0 \rightarrow \pi^0\eta, m)}{|D_{a_0}(m)|^2} \quad (7)$$

$$= \frac{2|g(m)|^2 p_{\eta\pi}(m_\phi^2 - m^2)}{3(4\pi)^3 m_\phi^3} \left| \frac{g_{a_0K^+K^-}g_{a_0\pi\eta}}{D_{a_0}(m)} \right|^2.$$

The mass spectrum for the background process  $\phi \rightarrow \pi^0\rho \rightarrow \gamma\pi^0\eta$  is [19]

$$\frac{d\Gamma_{\text{back}}(m)}{dm} = \frac{(m_\phi^2 - m^2)p_{\pi\eta}}{128\pi^3 m_\phi^3} \int_{-1}^1 dx A_{\text{back}}(m, x), \quad (8)$$

where

$$A_{\text{back}}(m, x) = \frac{1}{3} \sum |M_B|^2 \quad (9)$$

$$= \frac{1}{24} \left( m_\eta^4 m_\pi^4 + 2m^2 m_\eta^2 m_\pi^2 \tilde{m}_\rho^2 - 2m_\eta^4 m_\pi^2 \tilde{m}_\rho^2 \right.$$

$$\left. - 2m_\eta^2 m_\pi^4 \tilde{m}_\rho^2 + 2m^4 \tilde{m}_\rho^4 - 2m^2 m_\eta^2 \tilde{m}_\rho^4 \right.$$

$$\left. + m_\eta^4 \tilde{m}_\rho^4 - 2m^2 m_\pi^2 \tilde{m}_\rho^4 + 4m_\eta^2 m_\pi^2 \tilde{m}_\rho^4 \right.$$

$$\left. + m_\pi^4 \tilde{m}_\rho^4 + 2m^2 \tilde{m}_\rho^6 - 2m_\eta^2 \tilde{m}_\rho^6 - 2m_\pi^2 \tilde{m}_\rho^6 \right.$$

$$\left. + \tilde{m}_\rho^8 - 2m_\eta^4 m_\pi^2 m_\phi^2 - 2m^2 m_\eta^2 m_\phi^2 \tilde{m}_\rho^2 \right.$$

$$\left. + 2m_\eta^2 m_\pi^2 m_\phi^2 \tilde{m}_\rho^2 - 2m^2 m_\phi^2 \tilde{m}_\rho^4 + 2m_\eta^2 m_\phi^2 \tilde{m}_\rho^4 \right.$$

$$\left. - 2m_\phi^2 \tilde{m}_\rho^6 + m_\eta^4 m_\phi^4 + m_\phi^4 \tilde{m}_\rho^4 \right) \left| \frac{g_{\phi\rho\pi}g_{\rho\eta\gamma}}{D_\rho(\tilde{m}_\rho)} \right|^2$$

and

$$\tilde{m}_\rho^2 = m_\eta^2 + \frac{(m^2 + m_\eta^2 - m_\pi^2)(m_\phi^2 - m^2)}{2m^2} \quad (10)$$

$$- \frac{(m_\phi^2 - m^2)x}{m} p_{\pi\eta},$$

$$p_{\pi\eta} = \frac{\sqrt{(m^2 - (m_\eta - m_\pi)^2)(m^2 - (m_\eta + m_\pi)^2)}}{2m},$$

where  $x$  is the cosine of the angle between  $\eta$  and  $\gamma$  momenta in the  $\eta-\pi^0$  c.m. Note that there is a misprint in Eq. (6) of [19], which describes  $A_{\text{back}}(m, x)$ : the seventh term in the brackets “ $+2m_\eta^4\tilde{m}_\rho^4$ ” should be replaced by “ $+m_\eta^4\tilde{m}_\rho^4$ ,” as above in Eq. (9). We emphasize that all evaluations in [19] were done with the correct formula.

The term for the interference between the signal and the background processes is written in the following way:

$$\frac{d\Gamma_{\text{int}}(m)}{dm} = \frac{(m_\phi^2 - m^2)p_{\pi\eta}}{128\pi^3 m_\phi^3} \int_{-1}^1 dx A_{\text{int}}(m, x), \quad (11)$$

where

$$\begin{aligned} A_{\text{int}}(m, x) &= \frac{2}{3} \text{Re} \sum M_a M_B^* \quad (12) \\ &= \frac{1}{3} \left( (m^2 - m_\phi^2) \tilde{m}_\rho^2 + \frac{m_\phi^2 (\tilde{m}_\rho^2 - m_\eta^2)^2}{m_\phi^2 - m^2} \right) \\ &\times \text{Re} \left\{ \frac{e^{i\delta} g(m) g_{a_0 K^+ K^-} - g_{a_0 \pi\eta} g_{\phi\rho\pi} g_{\rho\eta\gamma}}{D_\rho^*(\tilde{m}_\rho) D_{a_0}(m)} \right\}. \end{aligned}$$

Note that the phase  $\delta$  is not taken into account in [19]. The inverse propagator of the scalar meson  $R$  ( $a_0$  in our case) is presented in [5, 7, 21, 22]:

$$\begin{aligned} D_R(m) &= m_R^2 - m^2 \quad (13) \\ &+ \sum_{ab} [\text{Re}\Pi_R^{ab}(m_R^2) - \Pi_R^{ab}(m^2)], \end{aligned}$$

where  $\sum_{ab} [\text{Re}\Pi_R^{ab}(m_R^2) - \Pi_R^{ab}(m^2)] = \text{Re}\Pi_R(m_R^2) - \Pi_R(m^2)$  takes into account the finite width corrections of the resonance which are the one-loop contribution to the self-energy of the  $R$  resonance from the two-particle intermediate  $ab$  states.

For the pseudoscalar  $ab$  mesons and  $m_a \geq m_b$ ,  $m \geq m_+$  one has [3, 9, 21–23]<sup>1)</sup>

$$\begin{aligned} \Pi_R^{ab}(m^2) &= \frac{g_{Rab}^2}{16\pi} \left[ \frac{m_+ m_-}{\pi m^2} \ln \frac{m_b}{m_a} \quad (14) \right. \\ &\left. + \rho_{ab} \left( i + \frac{1}{\pi} \ln \frac{\sqrt{m^2 - m_-^2} - \sqrt{m^2 - m_+^2}}{\sqrt{m^2 - m_-^2} + \sqrt{m^2 - m_+^2}} \right) \right]. \end{aligned}$$

For  $m_- \leq m < m_+$ ,

$$\begin{aligned} \Pi_R^{ab}(m^2) &= \frac{g_{Rab}^2}{16\pi} \left[ \frac{m_+ m_-}{\pi m^2} \ln \frac{m_b}{m_a} \quad (15) \right. \\ &\left. - |\rho_{ab}(m)| + \frac{2}{\pi} |\rho_{ab}(m)| \arctan \frac{\sqrt{m_+^2 - m^2}}{\sqrt{m^2 - m_-^2}} \right]; \end{aligned}$$

for  $m < m_-$ ,

$$\Pi_R^{ab}(m^2) = \frac{g_{Rab}^2}{16\pi} \left[ \frac{m_+ m_-}{\pi m^2} \ln \frac{m_b}{m_a} \quad (16) \right.$$

<sup>1)</sup>Note that, in [21],  $\Pi_R^{ab}(m^2)$  differs by a real constant from those determined in other enumerated works in the case of  $m_a \neq m_b$ , but obviously it has no effect on Eq. (13).

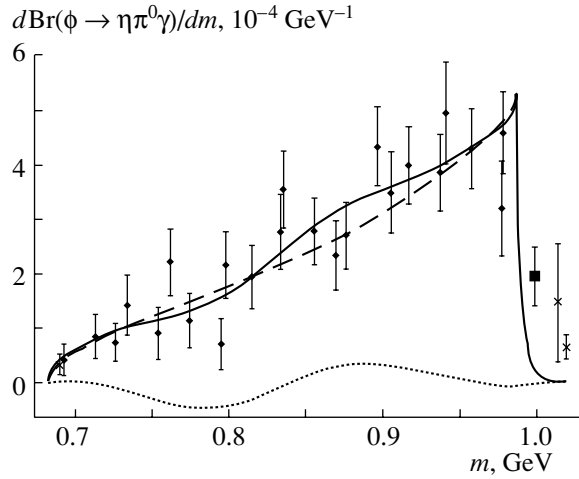


**Fig. 1.** Plot of the fit-1 results (solid curve) and the KLOE data (points). The signal contribution and the interference term are shown with the dashed and the dotted curves, respectively. Cross points are omitted in fitting; the square point (0.999 GeV) is omitted in fits 3 and 4.

$$- \frac{1}{\pi} \rho_{ab}(m) \ln \frac{\sqrt{m_+^2 - m^2} - \sqrt{m_-^2 - m^2}}{\sqrt{m_+^2 - m^2} + \sqrt{m_-^2 - m^2}}];$$

and

$$\begin{aligned} \rho_{ab}(m) &= \sqrt{\left(1 - \frac{m_+^2}{m^2}\right) \left(1 - \frac{m_-^2}{m^2}\right)}, \quad (17) \\ m_\pm &= m_a \pm m_b. \end{aligned}$$

The constants  $g_{Rab}$  are related to the width

$$\Gamma(R \rightarrow ab, m) = \frac{g_{Rab}^2}{16\pi m} \rho_{ab}(m). \quad (18)$$

In our case, we take into account intermediate states  $ab = \eta\pi^0, K\bar{K},$  and  $\eta'\pi^0$ :

$$\Pi_{a_0} = \Pi_{a_0}^{\eta\pi^0} + \Pi_{a_0}^{K^+K^-} + \Pi_{a_0}^{K^0\bar{K}^0} + \Pi_{a_0}^{\eta'\pi^0}, \quad (19)$$

$g_{a_0 K^+ K^-} = -g_{a_0 K^0 \bar{K}^0}$ . Note that the  $\eta'\pi^0$  contribution is of small importance due to the high threshold. Even fitting with  $|g_{a_0 \eta'\pi^0}| = 0$  changes the results by less than 10% of their errors. We set  $|g_{a_0 \eta'\pi^0}| = |1.13g_{a_0 K^+ K^-}|$  according to the four-quark model, but this is practically the same as the two-quark model prediction  $|g_{a_0 \eta'\pi^0}| = |1.2g_{a_0 K^+ K^-}|$  (see [5]).

The inverse propagator of the  $\rho$  meson has the following expression:

$$D_\rho(m) = m_\rho^2 - m^2 - im^2 \frac{g_{\rho\pi\pi}^2}{48\pi} \left(1 - \frac{4m_\pi^2}{m^2}\right)^{3/2}. \quad (20)$$

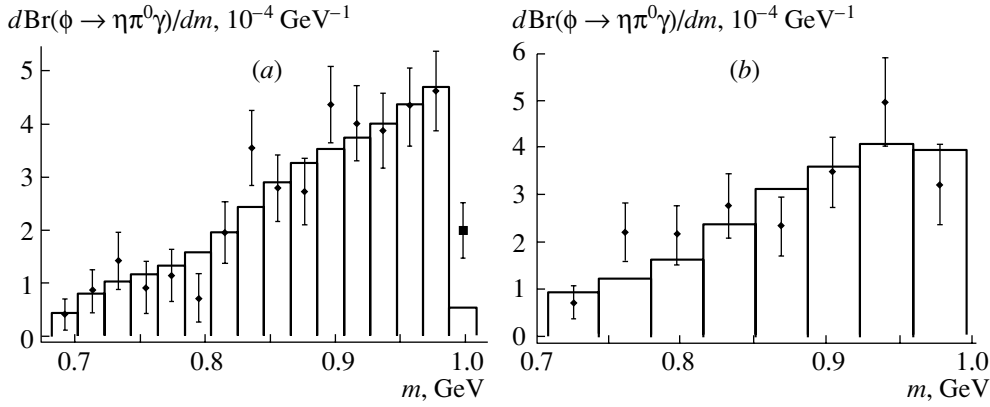


**Fig. 2.** The comparison of fit 1 and the KLOE data. Histograms show fit-1 results averaged around each bin [see Eqs. (22), (24)] for (a)  $\phi \rightarrow \eta\pi^0\gamma$ ,  $\eta \rightarrow \gamma\gamma$  and (b)  $\phi \rightarrow \eta\pi^0\gamma$ ,  $\eta \rightarrow \pi^+\pi^-\pi^0$  samples.

The coupling constants  $g_{\phi K^+K^-} = 4.376 \pm 0.074$  and  $g_{\phi\rho\pi} = 0.814 \pm 0.018 \text{ GeV}^{-1}$  are taken from the new most precise measurement [24]. Note that, in [16, 19], the value  $g_{\phi K^+K^-} = 4.59$  was obtained using the data of [25]. The coupling constant  $g_{\rho\eta\gamma} = 0.56 \pm 0.05 \text{ GeV}^{-1}$  is obtained from the data of [26] with the help of the expression

$$\Gamma(\rho \rightarrow \eta\gamma) = \frac{g_{\rho\eta\gamma}^2}{96\pi m_\rho^3} (m_\rho^2 - m_\eta^2)^3. \quad (21)$$

### 3. RESULTS

The KLOE data on  $\phi \rightarrow \eta\pi^0\gamma$  decay may be found in Table 5 of [18] (see also Figs. 1, 2). The data are separated into two samples: the first consists of events in which  $\eta$  decays into  $2\gamma$ , while events in which  $\eta$  decays into  $3\pi$  correspond to the second sample (see Fig. 2). Note that, as in [16, 18], we do not fit the 1st, 10th, and 27th points of this table (cross points in Fig. 1). We emphasize that the 10th (1.014 GeV) and 27th (1.019 GeV) points are obvious artifacts because the mass spectrum behavior on the right slope of the resonance has the form (photon energy)<sup>3</sup> according to gauge invariance.

In the experiment, the whole mass region ( $m_\eta + m_{\pi^0}$ ,  $m_\phi$ ) is divided into some number of bins. Experimenters measure the average value  $\bar{B}_i$  (“ $i$ ” is the bin number) of  $d\text{Br}(\phi \rightarrow \eta\pi^0\gamma)/dm$  around each  $i$ th bin:

$$\bar{B}_i = \frac{1}{m_{i+1} - m_i} \int_{m_i}^{m_{i+1}} d\text{Br}(\phi \rightarrow \eta\pi^0\gamma)/dm. \quad (22)$$

In this case, one should define the  $\chi^2$  function as

$$\chi^2 = \sum_i \frac{(\bar{B}_i^{\text{th}} - \bar{B}_i^{\text{exp}})^2}{\sigma_i^2}, \quad (23)$$

where  $\bar{B}_i^{\text{exp}}$  are the experimental results,  $\sigma_i$  are the experimental errors, and

$$\bar{B}_i^{\text{th}} = \frac{1}{m_{i+1} - m_i} \int_{m_i}^{m_{i+1}} d\text{Br}^{\text{th}}(\phi \rightarrow \eta\pi^0\gamma)/dm \quad (24)$$

( $d\text{Br}^{\text{th}}(\phi \rightarrow \eta\pi^0\gamma)/dm$  is the theoretical curve).

The free parameters of the fit are  $m_{a_0}$ ,  $g_{a_0K^+K^-}^2/4\pi$ , the phase  $\delta$  (we assume it is constant), and the ratio  $g_{a_0\eta\pi}/g_{a_0K^+K^-}$ . The quality of the fit is good; the results are shown in Table 1 (fit 1) and Figs. 1, 2.

Note that fitting without averaging the theoretical curve (changing  $\bar{B}_i^{\text{th}} \rightarrow d\text{Br}^{\text{th}}(\phi \rightarrow \eta\pi^0\gamma)/dm|_{m=(m_{i+1}+m_i)/2}$ ) gives a worse  $\chi^2/\text{n.d.f.} = 28.8/20$ . The results in this case are consistent within errors with those obtained with averaging the theoretical curve.

We also check the importance of omitting the experimental points. Taking these points into account leads to an increasing  $\chi^2/\text{n.d.f.}$  value up to 38.4/23 (C.L. = 4.8%), while the obtained values of the parameters change by less than a quarter of their errors.<sup>2)</sup>

The phase  $\delta$  is consistent with zero, so we make a fit with  $\delta = 0$  (fit 2 in Table 1).

To check the correctness of treating the phase  $\delta$  as a constant, we have done a fit with  $\delta$  taken in the form  $\delta(m) = b\rho_{\eta\pi}(m)$  (the phase of the elastic background in  $\eta\pi^0$  scattering may have such behavior) and found

<sup>2)</sup>All three omitted points correspond to bins whose bounds lie below (or above) the lower (upper) threshold of the reaction ( $m_\eta + m_{\pi^0} = 682.4 \text{ MeV}$  and  $m_\phi = 1019.4 \text{ MeV}$ , respectively); see Table 5 in [18]. We assume that the experimental data relate only to the “physical” parts of the bins.

**Table 1**

Fit	$m_{a_0}$ , MeV	$g_{a_0K^+K^-}^2/4\pi$ , GeV <sup>2</sup>	$g_{a_0\eta\pi}/g_{a_0K^+K^-}$	$\delta$ , deg	$\chi^2/\text{n.d.f.}$	C.L., %
1	$1003_{-13}^{+32}$	$0.82_{-0.27}^{+0.81}$	$1.06_{-0.27}^{+0.20}$	$27 \pm 29$	24.2/20	23
2	$995_{-8}^{+22}$	$0.65_{-0.18}^{+0.42}$	$1.17_{-0.24}^{+0.17}$	0	25.2/21	24
3	$994_{-8}^{+22}$	$0.62_{-0.17}^{+0.4}$	$1.21_{-0.24}^{+0.17}$	$21 \pm 30$	16.3/19	63
4	$992_{-7}^{+14}$	$0.55_{-0.13}^{+0.27}$	$1.26_{-0.2}^{+0.16}$	0	16.9/20	66
5	$991_{-7}^{+14}$	$0.59_{-0.15}^{+0.3}$	$1.25_{-0.29}^{+0.15}$	–	26.0/21	21

**Table 2**

Fit	$\Gamma_{a_0\eta\pi^0}$ , MeV	$R$	$\text{Br}(\phi \rightarrow (a_0\gamma + \rho\pi^0) \rightarrow \eta\pi^0\gamma) \times 10^5$	$\text{Br}(\phi \rightarrow a_0\gamma \rightarrow \eta\pi^0\gamma) \times 10^5$
1	$153_{-17}^{+22}$	$3.4 \pm 1.7$	$7.6 \pm 0.4$	$7.3 \pm 0.4$
2	$148_{-15}^{+17}$	$4.3 \pm 1.7$	$7.6 \pm 0.4$	$7.1 \pm 0.4$
3	$149_{-16}^{+19}$	$4.5 \pm 1.7$	$7.6 \pm 0.4$	$7.2 \pm 0.4$
4	$146_{-15}^{+17}$	$5.0 \pm 1.6$	$7.6 \pm 0.4$	$7.1 \pm 0.4$
5	$153_{-14}^{+16}$	$4.7 \pm 1.5$	$7.6 \pm 0.4$	$7.6 \pm 0.4$

that the constant  $b = 2.8 \pm 3.2 \text{ GeV}^{-1}$  is also consistent with zero. Change of the other values is not important.

Since the discrepancy between fits and the experimental point number 26 (0.999 GeV) in Table 5 of [18] (the square point in Fig. 1) is about three standard deviations (i.e., this point may also be an artifact), we make another fit without this point (fit 3). The phase  $\delta$  is again consistent with zero, so we make a fit without it (fit 4).

To understand the situation at all, we have done a fit (fit 5) by setting the constant  $g_{\phi\rho\pi^0}$  to zero and thus neglecting the background reaction  $\phi \rightarrow \rho\pi^0 \rightarrow \eta\pi^0\gamma$ . While the confidence level is good, it does not mean, of course, that we should neglect the background. The point is that the data can be described without background, but we exactly know that it exists, so we must take it into account, especially since the difference between the results of fit 1 and fit 5 is not small (see Table 1).

In Table 2, we present the results on the total branching ratio  $\text{Br}(\phi \rightarrow (a_0\gamma + \rho\pi^0) \rightarrow \eta\pi^0\gamma)$ , the signal contribution  $\text{Br}(\phi \rightarrow a_0\gamma \rightarrow \eta\pi^0\gamma)$ ,  $\Gamma_{a_0\eta\pi^0} \equiv \Gamma(a_0 \rightarrow \eta\pi^0, m_{a_0}) = g_{a_0\eta\pi}^2 \rho_{\eta\pi^0}(m_{a_0}) / (16\pi m_{a_0})$ , and the ratio  $R = g_{f_0K^+K^-}^2 / g_{a_0K^+K^-}^2$ . The last one is obtained using the value  $g_{f_0K^+K^-}^2 / (4\pi) = 2.79 \pm 0.12 \text{ GeV}^2$  [17]. The branching ratio of the back-

ground  $\text{Br}(\phi \rightarrow \rho\pi^0 \rightarrow \eta\pi^0\gamma)$  accounts for  $(0.5 \pm 0.1) \times 10^{-5}$ .

#### 4. CONCLUSION

Note that the obtained value of the ratio  $g_{a_0\eta\pi} / g_{a_0K^+K^-}$  does not contradict the first predictions based on the four-quark model of the  $a_0$ :  $g_{a_0\eta\pi} / g_{a_0K^+K^-} \approx 0.85$  [5].<sup>3)</sup> But even if  $g_{a_0\eta\pi} / g_{a_0K^+K^-}$  deviates from 0.85, there is no tragedy, because this variant of the four-quark model is rather rough and should be considered as a guide.

The results shown in Table 1 are in excellent agreement with the first SND poor-statistical measurement [13], where  $m_{a_0} = 994_{-8}^{+33} \text{ MeV}$  and  $g_{a_0K^+K^-}^2 / (4\pi) = 1.05_{-0.25}^{+0.36} \text{ GeV}^2$  are obtained under the assumption  $g_{a_0\eta\pi} / g_{a_0K^+K^-} = 0.85$ , based on the four-quark model (see [5]).

For all fits, the obtained value of  $R$  differs from the value  $R = 7.0 \pm 0.7$  [16]. Thus, the conclusion that the constant  $g_{a_0K^+K^-}^2 / (4\pi)$  is small, obtained in [16, 18] ( $g_{a_0K^+K^-}^2 / (4\pi) = 0.4 \pm 0.04 \text{ GeV}^2$ ), is the result of the parameter restrictions, especially fixing  $m_{a_0}$  at the PDG-2000 value 984.8 MeV. Note that a

<sup>3)</sup>Note that the prediction  $g_{a_0\eta\pi} / g_{a_0K^+K^-} \approx 0.93$  made in [1] was corrected in [27].

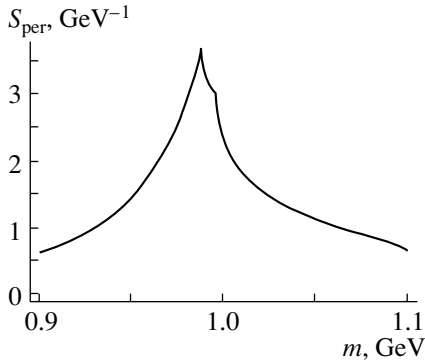


Fig. 3. Plot of the function  $S_{\text{per}}(m)$  for fit-1 results.

high  $a_0$  mass is also needed to describe a  $\gamma\gamma \rightarrow \eta\pi^0$  experiment (see [28]).

There should be no confusion due to the large  $a_0$  width. In the peripheral production of the  $a_0$  (for example, in the reaction  $\pi^- p \rightarrow \eta\pi^0 n$ ), the mass spectrum is given by the relation

$$\frac{dN_{\eta\pi^0}}{dm} \sim S_{\text{per}}(m) = \frac{2m^2 \Gamma(a_0 \rightarrow \eta\pi^0, m)}{\pi |D_{a_0}(m)|^2}. \quad (25)$$

The effective (visible) width of this distribution is much less than the nominal width  $\Gamma_{a_0\eta\pi^0}$ . For example, for the fit-1 results (Table 1), the effective width is  $\sim 60$  MeV (see Fig. 3).

As is noted [29], there is no tragedy with the relation between branching ratios of  $a_0$  and  $f_0$  production in  $\phi$  radiative decays. The early predictions [5] are based on the one-loop mechanism  $\phi \rightarrow K^+K^- \rightarrow a_0\gamma \rightarrow \eta\pi^0\gamma$  and  $\phi \rightarrow K^+K^- \rightarrow f_0\gamma \rightarrow \pi\pi\gamma$  at  $m_{a_0} = 980$  MeV,  $m_{f_0} = 975$  MeV, and  $g_{a_0K^+K^-} = g_{f_0K^+K^-}$ ,<sup>4)</sup> which leads to  $\text{Br}(\phi \rightarrow a_0\gamma \rightarrow \eta\pi^0\gamma) \approx \text{Br}(\phi \rightarrow f_0\gamma \rightarrow \pi\pi\gamma)$ . But it is shown in [7] that the relation between branching ratios of  $a_0$  and  $f_0$  production in  $\phi$  radiative decays essentially depends on  $a_0$ - $f_0$  mass splitting. This strong mass dependence is the result of gauge invariance, the (photon energy)<sup>3</sup> law on the right slope of the resonance. Our present analysis confirms this conclusion. Note that a noticeable deviation from the naive four-quark model equality  $g_{a_0K^+K^-} = g_{f_0K^+K^-}$  is not crucial. What is more important is the mechanism of the production of the  $a_0$  and  $f_0$  through the charged kaon loop, i.e., the four-quark transition. As is shown in [4], this gives strong evidence in favor of the four-quark model of the  $a_0$  ( $f_0$ ).

Note that the constant  $g_{f_0K^+K^-}^2/(4\pi)$  also can differ a lot from those obtained in [17]. The point is

<sup>4)</sup>We emphasize that the isotopic invariance does not require  $g_{a_0K^+K^-} = g_{f_0K^+K^-}$ .

that the extraction of this constant is very model dependent. For example, fitting by taking into account the mixing of the resonances can decrease the value of  $g_{f_0K^+K^-}^2/(4\pi)$  considerably. For instance, fitting the data of [14] without mixing, one has  $g_{f_0K^+K^-}^2/(4\pi) = 2.47_{-0.51}^{+0.37}$  GeV<sup>2</sup> [14], while fitting by taking the mixing into account gives  $g_{f_0K^+K^-}^2/(4\pi) = 1.29 \pm 0.017$  GeV<sup>2</sup> [19]. Note also that, in [17], the phase  $\delta_B$  of the background is taken from [19], where it is obtained by the simultaneous fitting of the  $m_{\pi^0\pi^0}$  spectrum and the phase  $\delta_0$  of the  $\pi\pi$  scattering, taking into account the mixing of the resonances. In [17], the mixing is not taken into account, so an additional phase dealing with it is omitted.

We emphasize once more that the KLOE data do not leave any doubt about the  $K^+K^-$ -loop mechanism of  $\phi \rightarrow a_0\gamma$  decay suggested in [5].

## ACKNOWLEDGMENTS

We thank C. Bini very much for providing useful information, discussions, and kind contacts.

This work was supported in part by the Russian Foundation for Basic Research (project no. 02-02-16061) and by a presidential grant (no. 2339.2003.2) for support of Leading Scientific Schools.

A.V. Kiselev thanks the Dynasty Foundation and ICFPM for financial support (scholarship).

## REFERENCES

1. R. L. Jaffe, Phys. Rev. D **15**, 267 (1977); **15**, 281 (1977).
2. L. Montanet, Rep. Prog. Phys. **46**, 337 (1983); F. E. Close, Rep. Prog. Phys. **51**, 833 (1988); L. G. Landsberg, Usp. Fiz. Nauk **160**, 3 (1990) [Sov. Phys. Usp. **33**, 169 (1990)]; M. R. Pennington, in *Proc. of the 6th Int. Conf. on Hadron Spectroscopy, HADRON'95, Manchester, UK, 1995*, Ed. by M. C. Birse, G. D. Lafferty, and J. A. McGovern (World Sci., Singapore, 1996), p. 3; T. Barnes, *Hadron Spectroscopy, VII Int. Conf., Upton, 1997*, Ed. by S. U. Chung and H. J. Willutzki; AIP Conf. Proc. **432**, 3 (1998); C. Amsler, Rev. Mod. Phys. **70**, 1293 (1998); Muneyuki Ishida, Shin Ishida, and Taku Ishida, Prog. Theor. Phys. **99**, 1031 (1998); S. Godfrey and J. Napolitano, Rev. Mod. Phys. **71**, 1411 (1999); P. Minkowski and W. Ochs, Eur. Phys. J. C **9**, 283 (1999); O. Black, A. Fariborz, F. Sannino, and J. Schechter, Phys. Rev. D **59**, 074026 (1999); S. Spanier and N. A. Törnqvist, Eur. Phys. J. C **15**, 437 (2000); H. Y. Cheng, hep-ph/0212117.

3. N. N. Achasov, S. A. Devyanin, and G. N. Shestakov, *Usp. Fiz. Nauk* **142**, 361 (1984) [*Sov. Phys. Usp.* **27**, 161 (1984)]; N. N. Achasov and G. N. Shestakov, *Usp. Fiz. Nauk* **161** (6), 53 (1991) [*Sov. Phys. Usp.* **34**, 471 (1991)]; N. N. Achasov, *Nucl. Phys. B (Proc. Suppl.)* **21**, 189 (1991); *Usp. Fiz. Nauk* **168**, 1257 (1998); N. N. Achasov, *Nucl. Phys. A* **675**, 279c (2000); *Yad. Fiz.* **65**, 573 (2002) [*Phys. At. Nucl.* **65**, 546 (2002)].
4. N. N. Achasov, *AIP Conf. Proc.* **619**, 112 (2002); hep-ph/0201299.
5. N. N. Achasov and V. N. Ivanchenko, *Nucl. Phys. B (Proc. Suppl.)* **315**, 465 (1989); Preprint No. 87-129 (Inst. Nucl. Phys., Novosibirsk, 1987).
6. A. Bramon, A. Grau, and G. Pancheri, *Phys. Lett. B* **289**, 97 (1992); F. E. Close, N. Isgur, and S. Kumano, *Nucl. Phys. B (Proc. Suppl.)* **389**, 513 (1993); J. L. Lucio and M. Napsuciale, *Phys. Lett. B* **331**, 418 (1994).
7. N. N. Achasov and V. V. Gubin, *Phys. Rev. D* **56**, 4084 (1997); *Yad. Fiz.* **61**, 274 (1998) [*Phys. At. Nucl.* **61**, 224 (1998)].
8. N. N. Achasov, V. V. Gubin, and V. I. Shevchenko, *Phys. Rev. D* **56**, 203 (1997); *Int. J. Mod. Phys. A* **12**, 5019 (1997); *Yad. Fiz.* **60**, 89 (1997) [*Phys. At. Nucl.* **60**, 81 (1997)].
9. N. N. Achasov, V. V. Gubin, and E. P. Solodov, *Phys. Rev. D* **55**, 2672 (1997); *Yad. Fiz.* **60**, 1279 (1997) [*Phys. At. Nucl.* **60**, 1152 (1997)].
10. N. N. Achasov and V. V. Gubin, *Phys. Rev. D* **57**, 1987 (1998); *Yad. Fiz.* **61**, 1473 (1998) [*Phys. At. Nucl.* **61**, 1367 (1998)].
11. M. N. Achasov *et al.*, *Phys. Lett. B* **438**, 441 (1998).
12. M. N. Achasov *et al.*, *Phys. Lett. B* **440**, 442 (1998).
13. M. N. Achasov *et al.*, *Phys. Lett. B* **479**, 53 (2000).
14. M. N. Achasov *et al.*, *Phys. Lett. B* **485**, 349 (2000).
15. R. R. Akhmetshin *et al.*, *Phys. Lett. B* **462**, 380 (1999).
16. KLOE Collab. (A. Aloisio *et al.*), *Phys. Lett. B* **536**, 209 (2002).
17. KLOE Collab. (A. Aloisio *et al.*), *Phys. Lett. B* **537**, 21 (2002).
18. C. Bini, P. Gauzzi, S. Giovannella, *et al.*, KLOE Note 173 06/02, <http://www.lnf.infn.it/kloe/>
19. N. N. Achasov and V. V. Gubin, *Phys. Rev. D* **63**, 094007 (2001); *Yad. Fiz.* **65**, 1566 (2002) [*Phys. At. Nucl.* **65**, 1528 (2002)].
20. N. N. Achasov and V. V. Gubin, *Phys. Rev. D* **64**, 094016 (2001); *Yad. Fiz.* **65**, 1939 (2002).
21. N. N. Achasov, S. A. Devyanin, and G. N. Shestakov, *Yad. Fiz.* **32**, 1098 (1980) [*Sov. J. Nucl. Phys.* **32**, 566 (1980)].
22. N. N. Achasov, S. A. Devyanin, and G. N. Shestakov, *Z. Phys. C* **22**, 56 (1984).
23. N. N. Achasov, *The Second DAΦNE Physics Handbook*, Ed. by L. Maiani, G. Pancheri, and N. Paver (Laboratory Nazionali di Frascati, Frascati, 1995), Vol. II, p. 671.
24. M. N. Achasov *et al.*, *Phys. Rev. D* **63**, 072002 (2001).
25. Particle Data Group (D. E. Groom *et al.*), *Eur. Phys. J. C* **15**, 1 (2000).
26. Particle Data Group (K. Hagiwara *et al.*), *Phys. Rev. D* **66**, 010001 (2002).
27. N. N. Achasov, S. A. Devyanin, and G. N. Shestakov, *Phys. Lett. B* **108B**, 134 (1982); *Z. Phys. C* **16**, 55 (1982).
28. N. N. Achasov and G. N. Shestakov, *Z. Phys. C* **41**, 309 (1988).
29. N. N. Achasov and A. V. Kiselev, *Phys. Lett. B* **534**, 83 (2002).

---

## ELEMENTARY PARTICLES AND FIELDS

### Theory

---

# Thermal Effects and Flat Direction Baryogenesis\*

A. Yu. Anisimov\*\*

Santa Cruz Institute for Particle Physics, Santa Cruz, USA

Received November 6, 2002

**Abstract**—We provide a detailed numerical study of the influence of thermal effects on the original picture of the Affleck–Dine baryogenesis. These effects are found to modify the results greatly in some cases. We estimate the baryon/entropy ratio and provide numerical results on the typical behavior of the charge as a function of the strength of the potential and other parameters. © 2004 MAIK “Nauka/Interperiodica”.

## 1. INTRODUCTION

Affleck–Dine (AD) baryogenesis from flat directions [1, 2] is a natural mechanism to explain the baryon/entropy ratio. The current known value of  $\Omega_b h^2$  is  $0.019 \pm 0.002$  from nucleosynthesis and  $0.031 \pm 0.005$  from BOOMERANG data [3]. This corresponds to  $n_B/n_\gamma \approx 5.1 \times 10^{-9}$  and  $n_B/n_\gamma \approx 8.3 \times 10^{-9}$ , respectively. The ingredients needed in general to generate the baryon asymmetry are  $CP$ -violating  $A$  terms, terms which lift flat directions, and supersymmetry-breaking terms in the early Universe, which give rise to negative mass squared of order of  $H^2$ , where  $H$  is the Hubble constant. At the level of renormalizable interactions, there are several flat directions that can be found in MSSM, i.e., directions, where  $F$  and  $D$  terms in the potential vanish. A simple example is the  $H_u L$  flat direction. These flat directions can be lifted by nonrenormalizable terms that we might imagine to be associated with the Planck scale, i.e., suppressed by some power of  $M_*$ .<sup>1)</sup> In that situation, as a result of the balance between the soft induced supersymmetry-breaking potential and higher order nonrenormalizable terms, the field can acquire a large expectation value which evolves as some power of  $t$ . Eventually, the negative-mass-squared term, which decreases as  $1/t^2$ , becomes comparable with the  $m_{3/2}^2$  term and the AD field starts to oscillate. This is the moment when baryon charge, which is generated by the torque due to the different phases and time dependence of  $A$  terms, “freezes” at some value. Terms that lift the flat direction in general have the form  $\phi^{2n+4}/M_*^{2n}$ . We will principally consider  $n = 1, 2, 3$  and refer to these as the  $n = 1, 2, 3$  cases. One then can do a simple estimate to

obtain the ratio  $n_B/n_\gamma$ . For example, in the  $n = 1$  case,  $n_B/n_\gamma$  is of order  $(m_{3/2}/M_*)^{1/2} \sin(\delta) \sim 10^{-8} \sin(\delta)$  or so.<sup>2)</sup> The resulting baryon/entropy ratio is a bit lower because one has to take into account that, for example, in the case of the  $H_u L$  direction, lepton number is produced first, which later has to be converted to baryon number. Also, the AD condensate interacts with thermalized inflaton decay products and some part of it can be evaporated before the charge is produced. There is a related issue of  $Q$ -ball formation and the corresponding evaporation rate, which is different from that of homogeneous condensate. There have been a number of papers on the subject in which the authors considered thermal effects relative to AD baryogenesis as well as  $Q$ -ball formation. In this paper, we will consider AD baryogenesis in the absence of  $Q$  balls. Taking into account the formation of  $Q$  balls will alter the whole picture. We refer the reader to [4] for more detail on this subject.

Recently, it was noticed [5] that, due to the evolution of the AD condensate in the background of inflaton decay products, there is an interesting effect that takes place in addition to the physics of the original scenario. It was observed that superpotential interactions couple the flat directions to other fields. These fields acquire masses induced by the flat-direction VEV, but they may be sufficiently small, so that fields come to thermal equilibrium with the inflaton decay products. In such cases, the flat direction starts to oscillate at an earlier time than usually estimated because it acquires thermal mass  $y^2 T^2$ ,<sup>3)</sup> which decreases with time as  $1/t$ . Since  $-H^2$  falls more rapidly with time, the difference  $y^2 T^2 - H^2$  eventually becomes positive. That normally happens much earlier than  $t \sim m_{3/2}^{-1}$ .

---

\*This article was submitted by the author in English.

\*\* e-mail: [anisimov@eron.itep.ru](mailto:anisimov@eron.itep.ru)

<sup>1)</sup>By  $M_*$ , we denote reduced Planck mass,  $M_* = 10^{18}$  GeV.

<sup>2)</sup>By  $\delta$ , we denote  $CP$ -violating phase.

<sup>3)</sup>Here,  $y$  is the coupling constant and  $T$  is the temperature.

It was also argued that the main source for generating baryon asymmetry in that case is  $A$  terms which are proportional to  $T$ . In [6], it was pointed out that such  $A$  terms are suppressed, in general, by symmetries, so that there is no temperature enhancement of the  $A$  term. However, it was noted that there is an additional source of  $A$  terms that can be efficient in the  $n = 2, 3$  cases. It was also shown that there is an additional thermal contribution to the potential of the form  $T^4 \log(|\phi|^2)$ . In the  $n = 2, 3$  cases, this defines the time when the condensate starts to oscillate, rather than the  $y^2 T^2$  contribution found in [5].

In this paper, we further investigate this scenario. We consider different types of thermal effects that are relevant for different choices of  $n$ . We analyze the parameter space in greater detail, i.e., the dependence of the resulting baryon/entropy ratio on the parameters of the Lagrangian. These parameters are the Yukawa constant, gauge coupling constant, the relative phase between  $A$  terms, and the coefficients in front of the  $A$  terms.

The  $n = 1$  case is found not to generate sufficiently large  $n_B/n_\gamma$ , but the  $n = 2, 3$  cases can rather easily generate the needed number for a wide range of parameters. Throughout, we assume for simplicity that the ratio of the inflaton mass to the reduced Planck mass is of the order of  $10^{-5}$ , taking, in general, the mass of inflaton  $m_I$  to be  $10^{13}$  GeV and reduced Planck mass  $M_*$  to be  $10^{18}$  GeV. These parameters appear in the estimate of the reheating temperature  $T_R$  as well as in the estimate of the baryon-number-violating terms. Therefore, the choice of these parameters is important for the estimate of  $n_B/n_\gamma$ . We discuss this in detail in Section 4.

This paper is organized as follows. In Section 2, we discuss the origin of two thermal effects as well as their relevance in the  $n = 1, 2, 3$  cases. In Section 3, we introduce additional  $A$  terms that will be the sources for generating the baryon asymmetry. In Section 4, we provide the estimates and numerical results for the baryon/entropy ratio. In Section 5, we give some details of the numerical simulations.

## 2. THERMAL EFFECTS

As was argued in [5] and [6], there are two types of thermally induced contributions to the potential. The first is due to the following mechanism. Consider some field  $\chi$  that couples to the flat direction via the superpotential  $W \sim y\chi\chi\phi$  and interacts with the dilute plasma produced by the inflaton decay. Because of  $\chi$  coupling to the flat direction,  $\chi$  acquires mass  $m_\chi = y\phi$ . If this mass is less than the temperature of the thermal plasma, this field will come to thermal equilibrium, giving an effective temperature-dependent mass to the flat direction. Let us do some

estimates to see when this effect might be important. Consider the case  $n = 1$ . Since  $T = (H\Gamma_d M_*^2)^{1/4}$ <sup>4</sup> and  $\phi = (HM_*)^{1/2}$ , the condition  $y\phi < T$  leads to

$$H_{\text{th}} < \frac{T_R^2}{y^4 M_*}, \tag{1}$$

where  $H_{\text{th}}$  is the value of Hubble constant when thermalization of  $\chi$  occurs. Taking  $M_*$  to be  $10^{18}$  GeV and  $T_R = 10^{10}$  GeV, one obtains

$$H_{\text{th}} < \left(\frac{0.01}{y}\right)^4 \times 10^{10} \text{ GeV}. \tag{2}$$

On the other hand, if  $\phi$  gets a thermal mass, oscillations start when  $yT \sim H$ , which gives the value of the Hubble constant  $H_o$  at this moment

$$H_o \sim y^{4/3} T_R^{2/3} M_*^{1/3} = \left(\frac{y}{0.01}\right)^{4/3} \times 10^{10} \text{ GeV}. \tag{3}$$

In order for this thermal term to be relevant, oscillations have to start no later than when  $\chi$  becomes thermalized, so that we have  $H_o/H_{\text{th}} \leq 1$ , which means  $y \leq 0.01$ . Provided  $y$  is sufficiently small, there is a  $y^2 T^2 |\phi|^2$  contribution to the potential, which affects the time when oscillation of  $\phi$  begins. If  $y$  is bigger than 0.01, then oscillations start when the  $y^2 T^2$  term is generated, which means that  $H_o$  is defined by  $H_{\text{th}}$ . Estimating  $H_{\text{th}}$  for the  $n = 2$  case gives

$$H_{\text{th}} < \frac{T_R^6}{y^{12} M_*^5} = \left(\frac{0.01}{y}\right)^{12} \times 10^{-6} \text{ GeV}, \tag{4}$$

which is too late for the thermalization process to have any effect on  $V(\phi)$  unless  $y \leq 0.001$ . For  $n = 3$ , from the condition  $y\phi < T$ , one obtains  $(y/0.01) < 10^{-2}$ . We conclude that, in the  $n = 2, 3$  cases, this effect does not take place unless  $y$  is very small.

The other contribution to the potential comes from the modification of the coupling constant when some sfermions, which are coupled to the flat direction, gain masses. The effective potential for  $\phi$  (see [6]) is then

$$V_{\text{eff}} \sim \alpha^2 T^4 \log(|\phi|^2), \tag{5}$$

where  $\alpha$  is the gauge coupling. This contribution causes  $\phi$  to oscillate when  $H^2 \sim \partial V_{\text{eff}}/\partial|\phi|^2$ . For  $n = 1$ ,  $\phi$  starts to oscillate at  $H_o \sim \alpha T_R = (\alpha/0.01) \times 10^8$  GeV. For  $n = 2$ ,  $H_o \sim \alpha^{6/5} T_R (T_R/M_*)^{1/5} = (\alpha/0.01)^{6/5} \times 10^6$  GeV, while, for  $n = 3$ ,  $H_o \sim \alpha^{4/3} T_R (T_R/M_*)^{1/3} = (\alpha/0.01)^{4/3} \times 10^5$  GeV. If we now look at the ratio of  $H_o$  due to both thermal contributions in the  $n = 1$  case, we see that

$$\frac{H_o^{(1)}}{H_o^{(2)}} \sim \frac{y^{4/3}}{\alpha} M_*/T_R = \frac{y^{4/3}}{\alpha} \times 10^3, \tag{6}$$

<sup>4</sup> $\Gamma_d$  is the inflaton decay rate.

where by  $H_o^{(1)}$  and  $H_o^{(2)}$  we denote the values of the Hubble constant when the AD field starts to oscillate if there is only an  $\alpha^2 T^4 \log(|\phi|^2)$  or  $y^2 T^2$  thermal contribution to the potential, respectively.

That estimate shows that, in the  $n = 1$  case, the  $y^2 T^2$  term dominates over the  $\alpha^2 T^4 \log(|\phi|^2)$  potential unless the ratio  $y^{4/3}/\alpha \leq 10^{-3}$ . Therefore, we will analyze the  $n = 1$  case with the  $y^2 T^2$  term only, while for  $n = 2, 3$  we will consider only the logarithmic thermal term.

### 3. A TERMS

To build up a baryon or lepton asymmetry, one needs to have corresponding  $U(1)$ -violating  $A$  terms. The misalignment between their phases then exerts a torque, making  $\phi$  roll down towards one of the discrete minima along the angular direction and settle there. In the original scenario [2], there were two  $A$  terms:  $Am_{3/2}\phi^{n+3}/M_*^n$ , which is the usual supersymmetry-breaking  $A$  term, and  $aH\phi^{n+3}/M_*^n$ , which is induced because of the finite energy density in the Universe during inflation.<sup>5)</sup> At later times ( $H < m_{3/2}$ ), because of its dependence on  $H$ , the second term is no longer important, but at times  $H \sim m_{3/2}$ , when the flat direction starts to oscillate, this term is of comparable size with the first one and a sufficient amount of charge is produced.

As we learned in the previous section,  $\phi$  oscillations generically start much earlier than  $H \sim m_{3/2}$ . One might then consider some other sources of  $A$  terms, which can be relevant in this case. These additional  $A$  terms may arise in the following way: consider the superpotential

$$\delta W = \int d^4\theta f(I) \frac{\phi^{n+3}}{M_*^n}, \tag{7}$$

where  $f(I)$  is some holomorphic function of the inflaton field  $I$ . Taking the first two terms in the polynomial expansion of  $f(I)$  in powers of  $I/M_*$  leads to the superpotential

$$\delta W = \frac{1}{M_*} \left( aI + b \frac{I^2}{M_*} \right) \frac{\phi^{n+3}}{M_*^n}, \tag{8}$$

where, in general,  $a$  and  $b$  are complex constants which do not need to have the same phase.  $I$  decreases as  $I_0(t_0/t)$ , so that the second term is somewhat suppressed with respect to the first, but at the time when oscillations of the  $\phi$  field start, this is not necessarily a large suppression and one might expect to generate a reasonable baryon number. We will investigate this particular case in greater detail in the next section.

<sup>5)</sup>  $A$  and  $a$  are some complex constants.

### 4. $n_B/n_\gamma$ : ESTIMATES AND NUMERICAL RESULTS

Before we move to the discussion of numerical results, let us provide some crude estimates for the baryon number. In the  $n = 1$  case, we assume that  $y \leq 0.01$  and  $y^2 T^2$  dominates over the logarithmic term. Then,  $H_o \sim y^{4/3} T_R (M_*/T_R)^{1/3}$ . We take the equation

$$\frac{dn_B}{dt} = |V_B| \sin(\delta), \tag{9}$$

where  $\delta$  is some effective phase that comes from the phase difference of two  $A$  terms, and  $V_B$  is the baryon-number-violating part of the potential. For the  $A$  terms that come from superpotential

$$\delta W = \frac{1}{M_*} \left( aI + b \frac{I^2}{M_*} \right) \frac{\phi^{n+3}}{M_*^n}$$

would be the phase of  $b$  after we redefine the phase of  $\phi$  to make the  $aI$  term real.<sup>6)</sup>

Taking the initial amplitude of  $I$  to be of the order of  $M_*$  and replacing  $dn_B/dt$  by the product  $n_B H_o$ , one obtains

$$\begin{aligned} n_B t^2 &= \frac{b H_o}{M_*} \frac{\phi^4}{M_*} \frac{1}{H_o^2} \\ &= b y^{4/3} T_R^{2/3} M_*^{1/3} \approx b \left( \frac{y}{0.01} \right)^{4/3} \times 10^{11} \text{ GeV}. \end{aligned} \tag{10}$$

We compute  $n_B t^2$  instead of  $n_B$  because it is more convenient, since, after the oscillations begin, the baryon density decreases as  $1/t^2$ . For the same reason, it is more convenient to compute  $n_\gamma t^2 = T_R^3 t_d^2$ , where  $t_d = (\Gamma_d)^{-1}$  and  $\Gamma_d \approx m_I^3/M_*^2$  is the inflaton-decay rate. Since  $T = (H\Gamma_d M_*^2)^{1/4}$ , the reheating temperature is given by  $T_R = (\Gamma_d M_*)^{1/2}$ . Then,  $T_R^3 t_d^2 = M_*^{3/2} t_d^{1/2}$ . Taking  $m_I \approx 10^{13}$  GeV, one obtains  $\Gamma_d \approx 10^3$  GeV,  $T_R \approx 10^{10}$  GeV, and  $n_\gamma t^2 \approx 10^{25}$  GeV. The value of  $T_R$  is somewhat large from the perspective of the gravitino problem. The baryon/entropy ratio for the  $n = 1$  case is

$$\frac{n_B}{n_\gamma} \approx b \left( \frac{y}{0.01} \right)^{4/3} \times 10^{-14} \sin(\delta_b), \tag{11}$$

which turns out to be too small unless  $y \sim 1$ . Actual numerical study shows that, for a wide range (see Fig. 1) of  $y$ , the resulting baryon/entropy ratio is somewhat larger,

$$\frac{n_B}{n_\gamma} \approx b \sin(\delta_b) \times (10^{-14} - 10^{-13}), \tag{12}$$

<sup>6)</sup> The phase of  $I$  is assumed to be a constant, so that one can absorb its phase in  $b$  and consider the inflaton to be real.

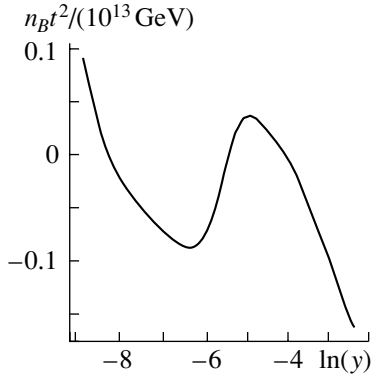


**Fig. 1.** The asymptotic value of  $n_B t^2$  as a function of  $\ln(y)$  for  $n = 1$ . The choice of parameters here is  $a = b = 1$ ;  $\delta_b = \pi/3$ .

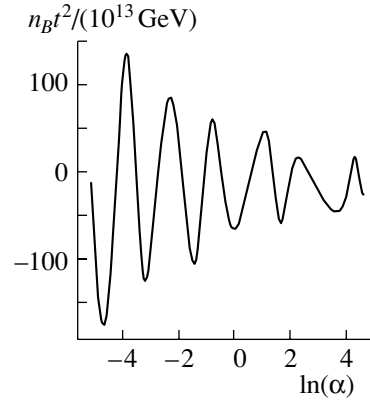


**Fig. 2.** The asymptotic value of  $n_B t^2$  as a function of  $\ln(\alpha)$  for  $n = 2$ . The choice of parameters here is  $a = b = 1$ ;  $\delta_b = \pi/3$ .

and almost independent of  $y$ . There is some uncertainty that depends on the choice of  $M_*$  as well as  $m_I$ . However, in order for the  $n = 1$  case to be viable, we would need to consider a much smaller ratio of  $M_*/m_I$  than  $10^5$ .

One can also consider  $\Gamma_d = \epsilon m_I^3 / M_*^2$ , where  $\epsilon$  is some new parameter, i.e.,  $\Gamma_d = m_I^3 / \Lambda^2$ , where  $\Lambda$  is some new scale different from  $M_*$ . Then,  $T_R$  is lower than before by a factor of  $\epsilon^{1/2}$ . For  $\epsilon \sim 10^{-4}$ ,  $T_R \sim 10^8$  GeV, which is an upper bound on  $T_R$  to avoid the gravitino problem. If one combines the result of Eq. (10) and the value for  $T_R^3 t_d^2$  in terms of  $\epsilon$ , the inflaton mass, and  $M_*$ , one finds that  $n_B/n_\gamma = b y^{4/3} \epsilon^{5/6} (m_I/M_*)^{5/2}$ . This is an even smaller number than at  $T_R = 10^{10}$  GeV. Thus, if one tries to fit the value of  $T_R$  in a consistent way to avoid the gravitino problem, one finds that the  $n = 1$  case seems to be even less acceptable. In the literature, sometimes the value of  $T_R$  is considered as a free parameter. In that case, the value of the ratio  $n_B/n_\gamma \sim T_R^{-7/3}$  is very sensitive to the value of the reheating temperature and our estimate for the resulting baryon/entropy ratio changes by several orders of magnitude. For example, if one takes  $T_R = 10^8$  GeV again and keeps  $\Gamma_d \approx 10^3$  GeV, one will obtain  $n_B/n_\gamma \sim 10^{-9}$ . One can also treat  $t_d$  as a free parameter as well. This, in fact, would significantly relax constraints on  $n_B t^2$  and would soften our conclusions. There was also discussion in the literature [7] that the gravitino problem can actually be avoided even at temperatures higher than  $10^{10}$  GeV. In this paper, we stick to  $T_R \approx 10^{10}$  GeV according to the estimate that we get from the expression  $T = (H \Gamma_d M_*^2)^{1/4}$  for the temperature during the inflation at  $H \approx \Gamma_d$  as well as the estimate for  $\Gamma_d$  mentioned above. Therefore, for that choice of parameters, we can conclude that the  $n = 1$  case can

hardly be acceptable. However, with all the remarks above, one can probably consider the  $n = 1$  case to be a borderline case.

In the case of  $n = 2$ , a similar analysis gives  $H_o \sim \alpha^{6/5} T_R^{6/5} M_*^{-1/5}$  (now there is no  $y^2 T^2$  term and oscillations start due to the logarithmic contribution). Since  $\phi$  behaves as  $(HM_*^2)^{1/3}$ , one obtains the following estimate for  $n_B t^2$  in the  $n = 2$  case:

$$n_B t^2 \approx b \alpha^{4/5} T_R^{4/5} M_*^{1/5} \approx b \left(\frac{\alpha}{0.1}\right)^{4/5} \times 10^{11} \text{ GeV}; \tag{13}$$

the corresponding baryon/entropy ratio is

$$\frac{n_B}{n_\gamma} \approx b \left(\frac{\alpha}{0.1}\right)^{4/5} \times 10^{-13} \sin(\delta_b). \tag{14}$$

This is very different from the numerical result, which is

$$\frac{n_B}{n_\gamma} \approx b \sin(\delta_b) \times (10^{-10} - 10^{-9}) \tag{15}$$

for wide range of  $\alpha$  (see Figs. 2, 3). We want to point out here that, as in the case  $n = 1$ , the dependence of the result on the coupling constant is rather weak, as opposed to what one gets estimating  $n_B/n_\gamma$  analytically.

Before we explain why the numerical result is so different from the naive estimate, we want to repeat the analysis above for the  $n = 3$  case. In that case,  $\phi = (HM_*^3)^{1/4}$ ; the operator which creates the charge is  $\frac{bH^2}{M_*} \frac{\phi^6}{M_*^3}$ . Estimating  $n_B t^2$  at  $H = H_o$ , one gets  $n_B t^2 \approx b H_o^{1/2} M_*^{1/2} \sin(\delta_b)$ . Since  $H_o \approx \alpha^{4/3} T_R^{4/3} / M_*^{1/3}$ ,

$$n_B t^2 \approx b \alpha^{2/3} \sin(\delta_b) T_R^{2/3} M_*^{1/3}. \tag{16}$$

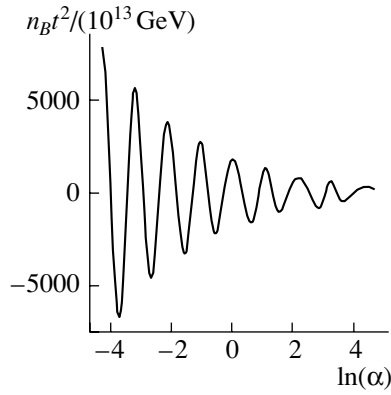


**Fig. 3.** The asymptotic value of  $n_B t^2$  as a function of  $\ln(\alpha)$  for  $n = 3$ . The choice of parameters here is  $a = b = 1$ ;  $\delta_b = \pi/3$ .

Taking  $T_R = 10^{10}$  GeV and  $M_* = 10^{18}$  GeV, one gets

$$n_B t^2 \approx b \alpha^{2/3} \sin(\delta_b) \times 10^{12} \text{ GeV}, \quad (17)$$

and the corresponding baryon/entropy ratio

$$\frac{n_B}{n_\gamma} = \frac{n_B t^2}{T_R^3 t_d^2} \approx b \alpha^{4/5} \sin(\delta_b) \times 10^{-13}, \quad (18)$$

which is too small for all reasonable values of  $b$ ,  $y$ , and  $\sin(\delta_b)$ . One can notice that this rough estimate predicts the decrease in the baryon/entropy ratio as  $y$  gets smaller as well as in the  $n = 2$  case. Actual numerical study, as in the case  $n = 2$ , gives quite a different value of that ratio. The baryon/entropy ratio for a wide range of  $\alpha$  is

$$\frac{n_B}{n_\gamma} \approx b \sin(\delta_b) \times (10^{-8} - 10^{-9}), \quad (19)$$

which could be consistent with the experimentally known value if  $b \sim 0.1 - 0.01$  and  $\delta_b \sim 1$ .

The naive expectation fails because the approximation of  $dn_B/dt$  by  $n_B H_o$  is too crude with respect to actual integration. One can understand why the amplitude of  $n_B t^2$  grows as  $y$  gets smaller, when looking at the behavior of  $n_B t^2$  at some values of  $y$  as a function of time. From numerical results, it is clear that the later the oscillations of  $\phi$  start, the more oscillations  $n_B t^2$  undergoes before it “freezes.” With each oscillation, the operator that is responsible for the charge production contributes more and more to the amplitude of  $n_B t^2$ . That might explain the unexpected behavior of charge in the  $n = 2, 3$  cases. One can see that the behavior of the charge for  $n = 1$  with the  $y^2 T^2$  term is quite different from its behavior for  $n = 2, 3$  with the logarithmic term. Namely, for  $n = 2, 3$ , before the value of a charge “freezes,” it experiences many more oscillations than in the  $n = 1$

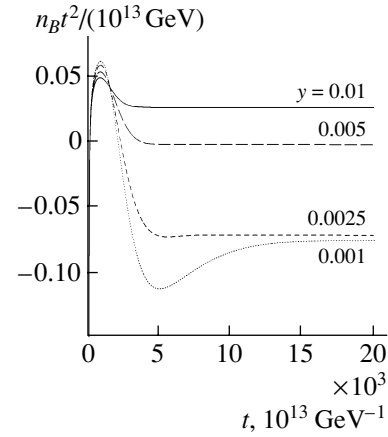


**Fig. 4.** The value  $n_B t^2$  as a function of time in the  $n = 1$  case for  $y = 0.01, 0.005, 0.0025$ , and  $0.001$ . The values of other parameters are taken to be  $\delta_b = \pi/3$ ,  $a = b = 1 = \lambda$ .

case, gaining a larger amplitude with each of them. One can see this from numerical results in Figs. 1–6, which show the evolution of the charge with time and with the strength of the potential (Yukawa coupling in the case  $n = 1$  and gauge coupling in the  $n = 2, 3$  cases). The first three plots demonstrate the expected behavior of the charge; i.e., it oscillates at the time  $t < t_o$  and freezes afterwards. The difference between  $n = 1$  and  $n = 2, 3$  is that, for  $n = 1$ , the charge typically oscillates one or two times, while in the  $n = 2, 3$  cases it oscillates much more. Correspondingly, for  $n = 1$ , the numerical result is close to the naive estimate, but for  $n = 2, 3$  the numerical value is much larger.

Figures 1–3 further distinguish these cases. One can see that changing the Yukawa coupling in the phenomenologically interesting region does not produce major changes in the amplitude of  $n_B t^2$  in the  $n = 1$  case. However, if one changes the value of the gauge coupling in the  $n = 2, 3$  cases, one can see that  $n_B t^2$  oscillates with  $\ln(\alpha)$  and its amplitude grows with decreasing  $\alpha$ , which is against the naive analytical estimate. We believe that this happens due to the logarithmic nature of the thermal potential in these cases.

The dependence of the numerical result of the baryon/entropy ratio on  $b$  and  $\delta_b$  does not bring any surprises with respect to the crude estimate above. In Fig. 7, one can see that the dependence on  $\delta_b$  is  $\sin(\delta_b)$ , and from Fig. 8 the dependence on  $b$  is a linear function. Thus, for any  $b$  and  $\delta_b$ , one knows how to reproduce the baryon/entropy ratio from the results in Eqs. (12), (15), and (19).

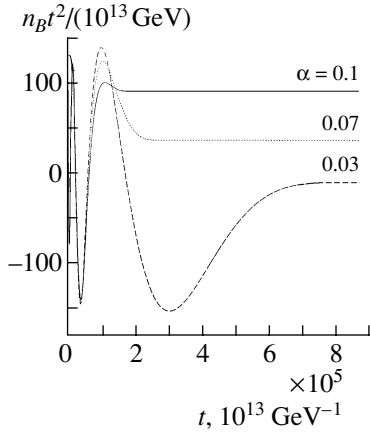


**Fig. 5.** The value  $n_B t^2$  as a function of time in the  $n = 2$  case for  $\alpha = 0.1, 0.07$ , and  $0.03$ . The values of other parameters are taken to be  $\delta_b = \pi/3$ ,  $a = b = 1 = \lambda$ .

## 5. DETAILS OF THE NUMERICAL SIMULATIONS

The equation for the evolution of  $\phi$  is

$$\ddot{\phi} + 3H\dot{\phi} + \frac{\partial V}{\partial \phi^*} = 0. \quad (20)$$

In general,  $V$  has the form  $V = V_0(|\phi|^2) + V_B(\phi) + V_B(\phi^*)$ , where  $V_0$  determines the evolution of  $|\phi|$  and  $V_B$  is the part of the potential that is responsible for creating the baryon charge. It also has a minor effect on evolution of  $|\phi|$ , which can be neglected in the cases we consider. The potentials we wish to study have the form

$$V_0 = (-H^2 + m_{3/2}^2)|\phi|^2 + V_{\text{th}}(T) + \left| \frac{\partial W}{\partial \phi} \right|^2, \quad (21)$$

$$V_B = aHW + b \frac{H^2}{M_*} W + Am_{3/2}W.$$

As we discussed before, the terms that are proportional to  $m_{3/2}$  are not important. Dropping them, we have for  $n = 1$

$$V = (-H^2 + y^2 T^2)|\phi|^2 + \lambda^2 \frac{|\phi|^6}{M_*^2} + \left( aH \frac{\phi^4}{M_*} + b \frac{H^2}{M_*} \frac{\phi^4}{M_*} + \text{h.c.} \right), \quad (22)$$

for  $n = 2$

$$V = -H^2|\phi|^2 + \alpha^2 T^4 \log(|\phi|^2) + \lambda^2 \frac{|\phi|^8}{M_*^4} + \left( aH \frac{\phi^5}{M_*^2} + b \frac{H^2}{M_*} \frac{\phi^5}{M_*^2} + \text{h.c.} \right), \quad (23)$$

and for  $n = 3$

$$V = -H^2|\phi|^2 + \alpha^2 T^4 \log(|\phi|^2) + \lambda^2 \frac{|\phi|^{10}}{M_*^6} + \left( aH \frac{\phi^6}{M_*^3} + b \frac{H^2}{M_*} \frac{\phi^6}{M_*^3} + \text{h.c.} \right). \quad (24)$$

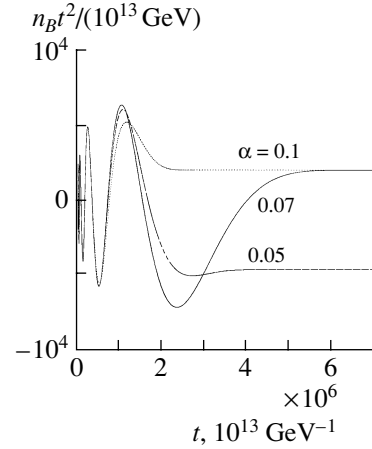


**Fig. 6.** The value  $n_B t^2$  for  $n = 3$  for  $\alpha = 0.1, 0.07$ , and  $0.05$ . The values of other parameters are taken to be  $\delta_b = \pi/3$ ,  $a = b = 1 = \lambda$ .

We took into account that different thermal effects are relevant for  $n = 1$  and  $n = 2, 3$ . Introducing radial and angular parts of  $\phi$  by  $\phi = R e^{i\Omega}$ , one gets the corresponding equations for  $R$  and  $\Omega$ :

for  $n = 1$ ,

$$\ddot{R} + 3H\dot{R} + \left( -H^2 - \dot{\Omega}^2 + y^2 T^2 + \frac{\lambda^2 R^4}{M_*^2} \right) R = 0, \quad (25)$$

$$\ddot{\Omega} + \left( 3H + \frac{2\dot{R}}{R} \right) \dot{\Omega} = |a| \frac{R^2 H}{M_*} \sin(4\Omega) + |b| \frac{R^2 H^2}{M_*^2} \sin(4\Omega - \delta_b);$$

for  $n = 2$ ,

$$\ddot{R} + 3H\dot{R} + \left( -H^2 - \dot{\Omega}^2 + \alpha^2 T^4 / R^2 + \frac{\lambda^2 R^6}{M_*^4} \right) R = 0, \quad (26)$$

$$\ddot{\Omega} + \left( 3H + \frac{2\dot{R}}{R} \right) \dot{\Omega} = |a| \frac{R^3 H}{M_*^2} \sin(5\Omega) + |b| \frac{R^3 H^2}{M_*^3} \sin(5\Omega - \delta_b);$$

for  $n = 3$ ,

$$\ddot{R} + 3H\dot{R} + \left( -H^2 - \dot{\Omega}^2 + \alpha^2 T^4 / R^2 + \frac{\lambda^2 R^8}{M_*^6} \right) R = 0, \quad (27)$$

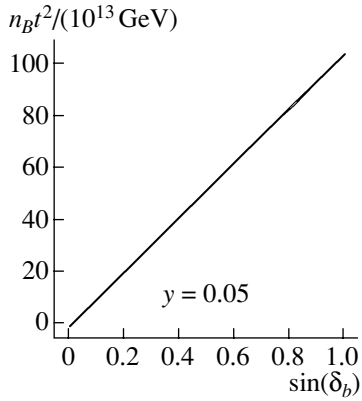


**Fig. 7.** The asymptotic value of  $n_B t^2$  as a function of  $\sin(\delta_b)$  for  $n = 2$ . The choice of parameters here is  $a = b = 1$ ;  $\alpha = 0.05$ .

$$\ddot{\Omega} + \left(3H + \frac{2\dot{R}}{R}\right) \dot{\Omega} = |a| \frac{R^4 H}{M_*^3} \sin(6\Omega) + |b| \frac{R^4 H^2}{M_*^4} \sin(6\Omega - \delta_b).$$

We drop the contribution from  $V_B$  at  $t < t_o$  to the equations for  $R$  for the following reasons. Let us compare the behavior of  $R$  induced by the  $\lambda^2 R^4 / M_*^2$  and the  $|a| (R^2 H / M_*) \cos(4\Omega)$  terms separately ( $n = 1$  case). We know that the first term causes  $R$  to behave as  $(HM_*)^{1/2}$ . The second term causes  $R$  to behave in the same way, provided  $\Omega$  is small, so that  $\cos(4\Omega) \approx 1$ . The smallness of  $\Omega$  is guaranteed by its equation of evolution and, in fact, is well seen in numerical results. Therefore, qualitatively, it does not bring any changes to the evolution of  $R$ .<sup>7)</sup> The other term, which is proportional to  $|b|$ , is suppressed by  $(m_I / M_*)$  and falls more rapidly with time with respect to the  $A$  term. Hence, neglecting these terms in the equation for  $R$  makes sense, since that does not change the evolution of  $R$  and simplifies the numerical and analytical analysis of the equations.

For numerical simulations it is more convenient to introduce a dimensionless field  $r = Rt$  and to scale everything by  $m_I$ , which we take to be  $10^{13}$  GeV. Then, the equations above with all the simplifications that were discussed before take the following form:

<sup>7)</sup>In fact, one can also neglect the  $\dot{\Omega}^2$  term in the equation for  $R$  since this term is small compared to the others for any  $H > H_o$ . It becomes, however, important after the oscillations start. At this moment, baryon charge is already produced and fixed. Later evolution of the baryon number is not interesting because of that and one does not need to run simulations further.

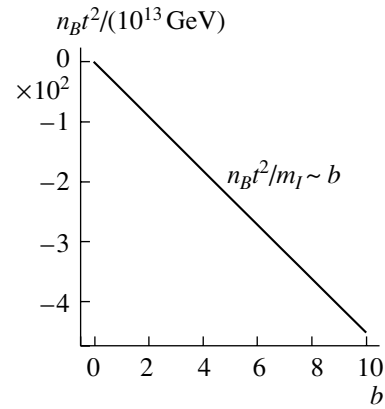


**Fig. 8.** The asymptotic value  $n_B t^2$  as a function of  $b$  for  $n = 2$ . The choice of parameters here is  $a = 1$ ,  $\delta_b = \pi/3$ ,  $\alpha = 0.03$ .

for  $n = 1$ ,

$$\ddot{r} + \left(-H^2 + y^2 T^2 + \epsilon^2 \frac{\lambda^2 r^4}{t^4}\right) r = 0, \quad (28)$$

$$\ddot{\Omega} + \frac{2\dot{r}}{r} \dot{\Omega} = |a| \epsilon \frac{r^2 H}{t^2} \sin(4\Omega) + |b| \epsilon^2 \frac{r^2 H^2}{t^2} \sin(4\Omega - \delta_b);$$

for  $n = 2$ ,

$$\ddot{r} + \left(-H^2 + \alpha^2 t^2 T^4 / r^2 + \epsilon^4 \frac{\lambda^2 r^6}{t^6}\right) r = 0, \quad (29)$$

$$\ddot{\Omega} + \frac{2\dot{r}}{r} \dot{\Omega} = |a| \epsilon^2 \frac{r^3 H}{t^3} \sin(5\Omega) + |b| \epsilon^3 \frac{r^3 H^2}{t^3} \sin(5\Omega - \delta_b);$$

for  $n = 3$ ,

$$\ddot{r} + \left(-H^2 + \alpha^2 t^2 T^4 / r^2 + \epsilon^6 \frac{\lambda^2 r^8}{t^8}\right) r = 0, \quad (30)$$

$$\ddot{\Omega} + \frac{2\dot{r}}{r} \dot{\Omega} = |a| \epsilon^3 \frac{r^4 H}{t^4} \sin(6\Omega) + |b| \epsilon^4 \frac{r^4 H^2}{t^4} \sin(6\Omega - \delta_b),$$

where  $\epsilon = m_I / M_* \approx 10^{-5}$ . Solving these equations numerically and noting that  $n_B t^2 = r^2 \dot{\Omega}$ , we can plot the behavior of  $n_B t^2$  as a function of time as well as find its asymptotic value as a function of different parameters.

At this point, it is rather easy to analyze the behavior of the charge. In fact, the equation for  $r$  is no longer dependent on  $\Omega$ , so that the second equation

describes the evolution of  $\Omega$  in the “background” of the radial component, which, in turn, is given by the first equation in each case. The evolution of  $r$  is easy to understand just by looking at its equation. First, it falls as some power of  $t$ , which depends on  $n$ , and then at  $H \sim H_o$  starts to oscillate. Numerical comparison of the full system of equations without all these simplifications made above shows that, at  $t < t_o$ , this approximation is reliable.

## 6. CONCLUSIONS

Clearly, thermal effects are important in the evolution of AD condensate and modify the original mechanism of AD baryogenesis. We find that, in the  $n = 1$  case, it is difficult to reproduce the known value of the baryon/entropy ratio even if we take into account some uncertainty due to the choice of the value of the reheating temperature, so that this case should probably be considered borderline at best. However, the  $n = 2, 3$  cases give plausible results for a wide range of the parameters of the potential. We have shown that the naive estimate of  $n_B/n_\gamma$  fails by several orders of magnitude to reproduce the observed numerical value. This effect is most clearly seen in the  $n = 2, 3$  cases, when the radial component of the AD field evolves in the logarithmic potential. This happens due to the behavior of the charge before it freezes, which might seem a bit surprising. Instead of decreasing with  $H_o$ , it actually grows slightly. We

have also shown numerically that the dependence on a few other parameters of the potential, such as the phase difference between the  $A$  terms and the coefficient of the  $A$  term  $b$ , is of the expected form.

## ACKNOWLEDGMENTS

I would like to thank M. Dine and M. Graesser for useful conversations and for the discussion of the results of this paper.

## REFERENCES

1. I. Affleck and M. Dine, Nucl. Phys. B **249**, 361 (1985).
2. M. Dine, L. Randall, and S. Thomas, Nucl. Phys. B **458**, 291 (1995); hep-ph/9507453.
3. P. de Bernardis *et al.*, astro-ph/0011469; C. B. Netterfield, astro-ph/0104460; J. Bond, astro-ph/0011378; W. Hu, M. Fukugita, M. Zaldarriaga, and M. Tegmark, astro-ph/0006436.
4. M. Fujii, K. Hamaguchi, and T. Yanagida, Phys. Rev. D **63**, 123513 (2001); hep-ph/0102187; S. Kasuya and M. Kawasaki, hep-ph/0106119.
5. R. Allahverdi, B. A. Campbell, and J. Ellis, Nucl. Phys. B **579**, 355 (2000); hep-ph/0001122.
6. A. Anisimov and M. Dine, Nucl. Phys. B **619**, 729 (2001); hep-ph/0008058.
7. K. Hamaguchi, H. Murayama, and T. Yanagida, hep-ph/0109030.

## **Relativistic Description of Polarized-Deuteron Fragmentation Accompanied by the Emission of Protons of High Transverse Momenta**

**L. S. Azhgirey and N. P. Yudin**

Available experimental data on the tensor analyzing power of nuclear relativistic-deuteron fragmentation accompanied by the emission of protons of high transverse momenta are analyzed within light-front quantum mechanics. It is shown that, in contrast to calculations with standard wave functions, calculations employing the relativistic deuteron wave function obtained by V.A. Karmanov and his coauthors on the basis of light-front dynamics can explain the entire body of data without resort to additional degrees of freedom.

## **Description of Scattering and of a Bound State in the System of Two Nucleons on the Basis of the Bargmann Representation of the $S$ Matrix**

**V. A. Babenko and N. M. Petrov**

For the effective-range function  $k \cot \delta$ , a pole approximation that involves a small number of parameters is derived on the basis of the Bargmann representation of the  $S$  matrix. The parameters of this representation, which have a clear physical meaning, are related to the parameters of the Bargmann  $S$  matrix by simple equations. By using a polynomial least squares fit to the function  $k \cot \delta$  at low energies, the triplet low-energy parameters of neutron-proton scattering are obtained for the latest experimental data of Arndt's group on phase shifts. The results are  $a_t = 5.4030$  fm,  $r_t = 1.7494$  fm, and  $v_2 = 0.163$  fm<sup>3</sup>. With allowance for the values found for the low-energy parameters and for the pole parameter, the pole approximation of the function  $k \cot \delta$  provides an excellent description of the triplet phase shift for neutron-proton scattering over a wide energy range ( $T_{\text{lab}} \lesssim 1000$  MeV), substantially improving the description at low energies as well. For the experimental phase shifts of Arndt's group, the triplet shape parameters  $v_n$  of the effective-range expansion are obtained by using the pole approximation. It turns out that they are positive and decrease with increasing  $n$ . The description of the phase shift by means of the effective-range expansion featuring values found for the low-energy parameters of scattering proves to be fairly accurate over a broad energy region extending to energy values approximately equal to the energy at which this phase shift changes sign, this being indicative of a high accuracy and a considerable value of the effective-range expansion in describing experimental data on nucleon-nucleon scattering. The properties of the deuteron that were calculated by using various approximations of the effective-range function comply well with their experimental values.

## **New Possibilities for Investigating Nucleon Resonances in Reactions of $\pi^+\pi^-$ -Pair Production by Polarized Electrons on an Unpolarized Proton**

**V. Burkert, V. I. Mokeev, M. Ripani, M. Anghinolfi, M. Battaglieri, A. A. Boluchevsky, E. V. Golovach,  
R. De Vita, L. Elouadhiri, B. S. Ishkhanov, M. V. Osipenko, G. Ricco, M. Taiuti, G. V. Fedotov, E. L. Isupov,  
N. S. Markov, and N. V. Shvedunov**

The difference of the cross sections for the electroproduction of  $\pi^+\pi^-$  pairs in the scattering of opposite-helicity electrons on an unpolarized proton is calculated within the phenomenological model developed previously. The nucleon-resonance electromagnetic form factors and the parameters of nonresonance processes were borrowed from the last data of the CLAS Collaboration on the production of charged-pion pairs on a proton by virtual photons. The effect of the longitudinal excitations of the  $P_{11}(1440)$  and  $D_{13}(1520)$  states on the difference of the helicity cross-section components is investigated. The sensitivity of this quantity to the contribution of nucleon resonances opens the possibility of employing it both in extracting the Coulomb form factors for nucleon resonances and in seeking new baryon states. Signals from one of these states were possibly contained in the last data of the CLAS Collaboration.

## Energy Resolution of Experiments with Quasimonoenergetic Annihilation Photons and Structure of a Giant Dipole Resonance

V. V. Varlamov, B. S. Ishkhanov, D. S. Rudenko, and M. E. Stepanov

The reasons behind the known systematic discrepancies between the results of photonuclear experiments performed with different photon beams are investigated in detail. Information about the cross sections obtained for the reactions  $^{63}\text{Cu}(\gamma, n)^{62}\text{Cu}$  and  $^{197}\text{Au}(\gamma, xn)$  at all stages of experiments with quasimonoenergetic photons from relativistic positrons annihilating in flight is studied, and a comparison with the data of experiments with beams of bremsstrahlung gamma radiation is performed. Data obtained in experiments for the reaction  $^{16}\text{O}(\gamma, xn)$  are used in the present analysis. It is shown that the typical difference procedure of experiments with quasimonoenergetic annihilation photons hinders the estimation of the actual energy resolution, this leading to a considerable distortion of information about the structure of cross sections for photonuclear reactions.

## Search for Single-Spin Asymmetry in the Inclusive Central Production of Neutral Pions at the Proton-Beam Energy of 70 GeV

A. N. Vasil'ev, V. N. Grishin, A. M. Davidenko, A. A. Derevshchikov, Yu. A. Matulenko, Yu. M. Mel'nik, A. P. Meshchanin, V. V. Mochalov, L. V. Nogach, S. B. Nurushev, A. F. Prudkoglyad, P. A. Semenov, L. F. Solov'ev, V. L. Solov'yanov<sup>†</sup>, V. Yu. Khodyrev, K. E. Shestermanov, A. E. Yakutin, N. S. Borisov, V. N. Matafonov, A. B. Neganov, Yu. A. Plis, Yu. A. Usov, A. N. Fedorov, and A. A. Lukhanin  
The PROZA-M Collaboration

The results obtained by measuring single-spin asymmetry in the inclusive production of neutral pions in the reaction  $p + p \uparrow \rightarrow \pi^0 + X$  at  $x_F \approx 0$  are presented. Protons of energy 70 GeV were extracted directly from the vacuum chamber of the accelerator by means of a bent single crystal. For transverse momenta in the range  $1.0 < p_T < 3.0$  GeV/ $c$ , the single-spin asymmetry independently measured by two detectors is zero within the errors. This result is in agreement with data obtained at Fermilab for 200 GeV, but it is at odds with CERN data obtained for 24 GeV.

## Measurement of Single-Spin Asymmetry in the Inclusive Production of Neutral Pions at 40 GeV in the Region of Polarized-Target Fragmentation

A. N. Vasil'ev, V. N. Grishin, A. A. Derevshchikov, V. I. Kravtsov, Yu. A. Matulenko, V. A. Medvedev, Yu. M. Mel'nik, A. P. Meshchanin, D. A. Morozov, V. V. Mochalov, A. I. Mysnik, L. V. Nogach, S. B. Nurushev, A. F. Prudkoglyad, P. A. Semenov, L. F. Solov'ev, V. L. Solov'yanov<sup>†</sup>, M. N. Ukhanov, Yu. V. Kharlov, V. Yu. Khodyrev, B. V. Chuiko, K. E. Shestermanov, A. E. Yakutin, N. S. Borisov, V. N. Matafonov, A. B. Neganov, Yu. A. Plis, Yu. A. Usov, A. N. Fedorov, and A. A. Lukhanin  
The PROZA-2 Collaboration

The single-spin asymmetry  $A_N$  in the inclusive production of neutral pions in the region of polarized-target fragmentation in the reaction  $\pi^- p \uparrow \rightarrow \pi^0 X$  at a beam energy of 40 GeV is measured. The result is  $A_N = -(13.8 \pm 3.8)\%$  for  $-0.8 < x_F < -0.4$  and  $1 < p_T < 2$  GeV/ $c$  and is compatible with zero for  $-0.4 < x_F < -0.1$  and  $0.5 < p_T < 1.5$  GeV/ $c$ . Both in the central region and in the region of target fragmentation, the asymmetry becomes nonvanishing at a c.m. neutral-pion momentum of about 1.75 GeV/ $c$ . The behavior of the asymmetry is similar to that in the E704 (FNAL, 200 GeV) and STAR (BNL, 20 TeV) experiments in the region of polarized-proton-beam fragmentation.

## Theoretical Investigation of the Angular-Momentum Dependence of the Mean Time of Fission of Excited Nuclei

I. I. Gontchar, N. A. Ponomarenko, V. V. Turkin, and L. A. Litnevsky

Mean times of nuclear fission at excitation energies of 80 to 400 MeV were recently measured at GANIL by the shadowing technique. These experiments served as a motivation for us to perform systematic calculations of time distributions of fission events and of mean fission times versus the angular momentum, the initial excitation energy, and the fissility of the primary excited nucleus. The mean fission times are represented here versus the orbital angular momentum  $L$ . The calculations are performed on the basis of a refined version of

the combined dynamical–statistical model. It turns out that the  $L$  dependence of the mean fission time has a resonance character if the fission-barrier height at  $L = 0$  is noticeably greater than the neutron binding energy. Both statistical calculations and the dynamical simulation of the process with allowance for friction leads to this behavior of the mean fission time  $\langle t_f \rangle$ . It is shown that the dependence of  $\langle t_f \rangle$  on  $L$  develops a maximum owing to the fission of nuclei that have lost a considerable part of the initial excitation energy in the process of neutron emission. A major part of the calculations were performed for  $^{190}\text{Pt}$  at an initial excitation energy of 150 MeV. It is shown that the resonance behavior disappears as the fissility increases, but it survives over a wide range of initial excitation energies.

### **Employing the Reaction $(n, n'\gamma)$ to Rule out Nuclear Levels Erroneously Introduced in Other Investigations: On the $3_1^-$ Level in $^{56}\text{Fe}$**

**A. M. Demidov, L. I. Govor, V. A. Kurkin, and I. V. Mikhailov**

Since  $(n, n'\gamma)$  reactions proceed through the stage of a compound nucleus, excitation cross sections do not depend, as a rule, on the nature of a level. Accordingly, all excited states must manifest themselves through  $\gamma$  transitions (with allowance for their internal conversion). In performing a comparison of energy-level and  $\gamma$ -transition diagrams obtained in studying gamma radiation induced by the inelastic scattering of fast reactor neutrons with the diagrams published in the last issues of Nuclear Data Sheets, it was found that 120 levels in 34 nuclei must be excluded from the adopted data since  $\gamma$  transitions expected from them are not observed. The case of a dubious first  $3_1^-$  level in  $^{56}\text{Fe}$  at an energy of 3076 keV is considered by way of example. It is concluded that there is no such level in  $^{56}\text{Fe}$ .

### **Elastic Hadron Scattering on Lithium Isotopes at Intermediate Energies**

**M. A. Zhusupov, E. T. Ibraeva, and O. Imambekov**

The elastic scattering of hadrons (protons, charged pions, and positively charged kaons) on  $^{6,7,8}\text{Li}$  nuclei is analyzed on the basis of Glauber–Sitenko diffraction theory. A few nuclear-wave-function versions found within two- and three-particle potential cluster models are used in the calculations. It is shown that the application of these functions in diffraction theory makes it possible to describe adequately the experimental differential cross sections and analyzing powers in hadron scattering at intermediate energies. In this study, particular attention is given to a comparison of the scattering of different particles on the same target nucleus, as well as to a comparison of scattering of particles of the same sort on different target nuclei.

### **Magnetic Catalysis of Stability of Quark Matter in the Nambu–Jona-Lasinio Model**

**K. G. Klimenko and D. Ebert**

The effect of an external magnetic field  $H$  on the stability of quark matter is studied on the basis of the Nambu–Jona-Lasinio model. It is shown that, at  $H = 0$ , lumps of quark matter are stable only in the case where the coupling constant  $G$  is greater than some value  $G_{\text{bag}}$ . If  $H \neq 0$ , stable multiquark formations may exist even for  $G < G_{\text{bag}}$  (magnetic catalysis of stability). For  $G > G_{\text{bag}}$ , a magnetic field facilitates the formation of stable quark matter.

### **Exact Inclusion of the Coulomb Field in Photo–Beta Decay of Nuclei and Problem of Avoided Elements**

**I. V. Kopytin, K. N. Karelin, and A. A. Nekipelov**

The probability of endothermic  $\beta^-$  decay of nuclei that is stimulated by an electromagnetic field of Planck frequency spectrum (photo–beta decay) is calculated, the effect of the Coulomb field on a relativistic electron and a virtual relativistic positron being exactly taken into account in this calculation. It is shown that the inclusion of Coulomb effects is of paramount importance and that the results of the calculations may differ by an order of magnitude from those obtained previously in the plane-wave approximation, depending on the energy range being considered. A model for the synthesis of avoided elements in the substance of massive stars is proposed on the basis of the mechanism of photo–beta decay of stable elements that originate from  $s$  and  $r$  processes.

## Use of Low-Power Reactors in Investigating the Mixing Parameter $\sin^2(2\theta_{13})$

V. N. Kornoukhov and A. S. Starostin

Measurement of the mixing parameter  $\sin^2(2\theta_{13})$  is one of the pressing problems in neutrino physics. Projects of reactor experiments characterized by a sensitivity of  $\sin^2(2\theta_{13}) \approx 0.01$  are being presently discussed. Almost all of them are based on the *one reactor—two detectors* scheme. Within this methodological approach, one employs an NPP reactor of power about a few GW for a neutrino source and two detectors of identical configurations that are arranged at different distances from the reactor. In such experiments, the systematic error may be about 1%, which ensures a precision of about 0.01. In the present study, it is proposed to use, in a measurement of  $\sin^2(2\theta_{13})$ , the existing SuperKamiokande (SK) facility combined with its own antineutrino source, a nuclear reactor of low thermal power about 300 MW (LPR). Such an experiment can be realized within a rather short time. An analysis that studied various detection mechanisms revealed that a combination of LPR and SK makes it possible to attain a sensitivity of  $\sin^2(2\theta_{13}) \approx 0.002$ .

## New Method for Calculating the Potential Energy of Deformed Nuclei in the Liquid-Drop Model

R. S. Kurmanov and G. I. Kosenko

The method that we previously developed for going over from double volume integrals to double surface integrals in calculating the Coulomb energy of nuclei that have a sharp edge is generalized to the case of nuclei where the range of nuclear forces is finite and where the nuclear surface is diffuse. New formulas for calculating the Coulomb and nuclear energy of deformed nuclei are obtained. For a spherically symmetric nucleus, in which case there is an analytic solution to the problem in question, the results are compared with those that are quoted in the literature, and it is shown that the respective results coincide identically. A differential formulation of the method developed previously by Krappé, Nix, and Sierk for going over from double volume to double surface integrals is proposed here on the basis of the present approach.

## Solving Relativistic Inverse Scattering Problem with Allowance for Inelasticity Effects on the Basis of $N/D$ Equations and Application of the Results to an Analysis of Nucleon—Nucleon Interaction

A. N. Safronov and A. A. Safronov

A manifestly Poincaré-invariant approach to solving the inverse scattering problem is developed with allowance for inelasticity effects. The equations of the  $N/D$  method are used as dynamical equations in this approach. Two versions of the approach are considered. In the first version (method A), the required equations are constructed on the basis of the maximal-analyticity principle, which underlies the dynamical theory of the  $S$  matrix. In formulating the second version (method B), it is assumed that a partial-wave amplitude may develop dynamical singularities that violate the requirement of maximal analyticity. The dynamics of interaction components that violate maximal analyticity is described within the model of a nonlocal separable potential. The method is used to analyze nucleon—nucleon interaction in the  $^1S_0$  and  $^3S_1$  states. The results obtained by solving the inverse scattering problem for potential functions are compared with the predictions of a one-boson-exchange model.

## $D_s^+ \rightarrow \pi^+ \pi^+ \pi^-$ Decay: The $1^3P_0 s\bar{s}$ Component in Scalar—Isoscalar Mesons

V. V. Anisovich, L. G. Dakhno, and V. A. Nikonov

We calculate the processes  $D_s \rightarrow \pi^+ s\bar{s}$  and  $D_s \rightarrow \pi^+ resonance$ , correspondingly, in the spectator and  $W$ -annihilation mechanisms. The data on the reaction  $D_s \rightarrow \pi^+ \rho^0$ , which owes itself to the  $W$ -annihilation mechanism only, point to a negligibly small contribution of the  $W$  annihilation to the production of scalar—isoscalar resonances  $D_s \rightarrow \pi^+ f_0$ . As to the spectator mechanism, we evaluate the  $1^3P_0 s\bar{s}$  component in the resonances  $f_0(980)$ ,  $f_0(1300)$ , and  $f_0(1500)$  and broad state  $f_0(1200–1600)$  on the basis of data on the  $D_s^+ \rightarrow \pi^+ f_0/D_s \rightarrow \pi^+ \phi$  decay ratios. The data point to a large  $s\bar{s}$  component in the  $f_0(980)$ :  $40\% \lesssim s\bar{s} \lesssim 70\%$ . Nearly 30% of the  $1^3P_0 s\bar{s}$  component flows to the mass region 1300–1500 MeV being shared by  $f_0(1300)$ ,  $f_0(1500)$ , and broad state  $f_0(1200–1600)$ ; the interference of these states results in a peak near 1400 MeV with the width

around 200 MeV. Our calculations show that the yield of radial excitation state  $2^3P_0s\bar{s}$  is relatively suppressed,  $\Gamma(D_s \rightarrow \pi^+(2^3P_0s\bar{s}))/\Gamma(D_s \rightarrow \pi^+(1^3P_0s\bar{s})) < 0.05$ .

## Scattering and Pair Production by a Potential Barrier

A. I. Nikishov

Scattering and electron–positron pair production by a one-dimensional electric barrier is considered in the framework of the  $S$ -matrix formalism. The solutions of the Dirac equation are classified according to frequency sign. The Bogolyubov transformation relating the in- and out-states are given. We show that the norm of a solution of the wave equation is determined by the largest amplitude of its asymptotic form when  $x_3 \rightarrow \pm\infty$ . For the Sauter-type potential, we give the explicit expressions for the complete in- and out-sets of orthonormalized wave functions. We note that, in principle, virtual vacuum processes in an external field influence the phase of the wave function of a scattered particle.